Non-classical effects in straight-fibre and tow-steered composite beams and plates

Rainer Maria Johannes Groh

Department of Aerospace Engineering
University of Bristol

A dissertation submitted to the University of Bristol in accordance with the requirements for award of the degree of Doctor of Philosophy in the Faculty of Engineering.

October 2015

Words in Text: Sixty-One Thousand Eight Hundred

Abstract

Multilayered composites are widespread in load-bearing structures of the aeronautical and wind energy industries. Increasingly, advanced composites are spreading into the mass-market automotive sector, where the lightweight advantages of composites improve structural efficiencies and thereby enable a new generation of electric cars.

Composite laminates are mostly employed in thin-walled semi-monocoque structures as the manufacturing processes, such as pre-preg curing and resin infusion, are amenable to this type of construction. However, their imminent diversification to new applications will benefit from extending the range of possible laminate configurations in terms of layer material properties, stacking sequences and laminate thicknesses, as well as the nature of service loading.

Such a diversification can add significant complexity when, for example, the layer material properties differ by multiple orders of magnitude or when the composite comprises of relatively thick cross-sections. In case of the former, the structural response is non-intuitive and cannot be modelled adequately using classical lamination theory. The latter adds non-classical effects due to transverse shearing and transverse normal stresses, which are particularly pernicious due to the lack of reinforcing material in the stacking direction and can lead to the delamination of layers.

Reliable design of these multilayered structures requires tools for accurate stress analysis that account for these non-classical higher-order effects. Despite offering high fidelity, three-dimensional (3D) finite element models are prohibitive for iterative design studies due to their high computational expense. Consequently, a large number of approximate higher-order two-dimensional (2D) theories have been formulated over the last decades, with the aim of predicting accurate 3D stress fields while maintaining superior computational efficiency. The majority of these formulations have focused on purely displacement-based approaches that typically require post-processing steps to recover accurate transverse stresses.

The work presented here uses the Hellinger-Reissner mixed-variational principle to derive a higher-order 2D equivalent single-layer formulation that predicts variationally consistent 3D stress fields in laminated beams and plates with *3D heterogeneity*, i.e. laminates comprised of layers with material properties that differ by multiple orders of magnitude and that also vary continuously in-plane. The formulation is shown to be accurate to within a few percent of 3D elasticity and 3D finite element solutions. A novelty of the present approach is that the computational expense is reduced by basing all stress fields on the same set of unknowns. Furthermore, by enforcing Cauchy's equilibrium equations in the variational statement via Lagrange multipliers, and then solving the ensuing governing equations in the strong form using spectral methods, boundary layers in the 3D stress fields are captured robustly.

The present formulation is then used to ascertain the relative effects of transverse shear, transverse normal and zig-zag deformations. By studying non-traditional materials and stacking sequences with pronounced transverse anisotropy, the results presented herein provide physical insight into the governing factors that drive non-classical effects, with the aim of aiding the intuition of structural engineers in preliminary design stages. Finally, to showcase a possible application, the model is applied in an optimisation study that tailors the through-thickness stress fields in a beam in order to reduce the likelihood of delaminations. In the author's opinion, the general formulation presented herein is well-suited for accurate and computationally efficient stress analysis in industrial applications.

To Mom and Dad

Meine Arbeit in Eurer Handschrift

"Sie sind so jung, so vor allem Anfang, und ich möchte Sie, so gut ich es kann, bitten, lieber Herr, Geduld zu haben gegen alles Ungelöste in Ihrem Herzen und zu versuchen, die Fragen selbst liebzuhaben wie verschlossene Stuben und wie Bücher, die in einer sehr fremden Sprache geschrieben sind. Forschen Sie jetzt nicht nach den Antworten, die Ihnen nicht gegeben werden können, weil Sie sie nicht leben könnten. Und es handelt sich darum, alles zu leben. Leben Sie jetzt die Fragen. Vielleicht leben Sie dann allmählich, ohne es zu merken, eines fernen Tages in die Antwort hinein."

– Rainer Maria Rilke, *Briefe an Einen Jungen Poeten*

"You are so young, so much before all beginning, and I would like to beg you, dear Sir, as well as I can, to have patience with everything unresolved in your heart and to try to love the questions themselves as if they were locked rooms or books written in a very foreign language. Don't search for the answers, which could not be given to you now, because you would not be able to live them. And the point is, to live everything. Live the questions now. Perhaps then, someday far in the future, you will gradually, without even noticing it, live your way into the answer."

– Rainer Maria Rilke, *Letters to a Young Poet*

Acknowledgements

The completion of this thesis would not have been possible without the support from a number of key people.

First and foremost, I would like to thank my mother and father for their unwavering support in all of my endeavours, both sportive and academic, and the freedom they have granted me to pursue my passions. Your early admonitions that intelligence and hard work are worthless without integrity have been a guiding beacon on this scientific exploration. I would not be writing these words without your guidance and the countless opportunities you have enabled.

Second, I am forever indebted to my supervisor Prof. Paul Weaver, who has been an incredible mentor and continues to teach me invaluable lessons in the world of structural mechanics. Over the last three years, he has granted me ample freedom to explore and test different ideas, while providing timely guidance when dead ends deemed to halt all progress. I believe we are both wiser as a result of our efforts, and I am proud of what we have achieved.

I would also like to thank NASA Langley Research Center for hosting me at the National Institute of Aerospace under the Advanced Composites Project. Working at NASA was a dream come true. In this respect, Dr Alexander Tessler requires special mention for inviting me to collaborate with world-leading engineers and scientists at this prestigious and historic institution. I look forward to continuing our work in the future.

Special acknowledgements are due to my colleagues, specifically Simon White, Broderick Coburn, Dr Gangadharan Raju, Ettore Lamacchia and Dr Alberto Pirrera, who have been co-explorers on this journey, are always ready for an insightful technical discussion, and have provided invaluable feedback on many papers and presentations. Thank you!

Furthermore, I would like to sincerely thank the Engineering and Physical Sciences Research Council for funding this work through the EPSRC Centre for Doctoral Training at the Advanced Composites Centre for Innovation and Science [grant number EP/G036772/1] at the University of Bristol.

These acknowledgements would not be complete without mentioning the vast body of literature that preceded and served as an inspiration for this thesis. In whatever way this dissertation contributes to the field of solid mechanics is due to your education. I truly stand on the shoulders of giants.

Finally, this research exercise has been a humbling lesson in realising that Science is the ultimate teacher of ignorance. Even as I write this, I must submit to the uncertainty that accompanies the work I present herein. In this respect, I need to thank the great physicist Richard Feynman, whose writings have been a sanitary guide in my struggles to appreciate that doubt is an inherent driver of Science. In his words, the first principle is that I shall not fool myself, and indeed, I am the easiest person to fool.

Bristol, October 2015 R.M.J.G.

Author's Declaration

I declare that the work in this dissertation was carried out in accordance with the requirements of the University's Regulations and Code of Practice for Research Degree Programmes and that it has not been submitted for any other academic award. Except where indicated by specific reference in the text, the work is the candidate's own work. Work done in collaboration with, or with the assistance of, others, is indicated as such. Any views expressed in the dissertation are those of the author.

Signed: ..... Date: .....

Rainer Maria Johannes Groh

List of Publications

Some of the topics outlined in this thesis have been published in peer-reviewed journals and/or presented at international conferences. Furthermore, additional work on the buckling and post-buckling analysis of variable-stiffness, variable-thickness shell structures that were investigated but are not elucidated in detail herein are listed for completeness.

Journal articles

[1] RMJ. Groh, PM. Weaver, S. White, G. Raju, and Z. Wu. A 2D equivalent single-layer formulation for the effect of transverse shear on laminated plates with curvilinear fibres. *Composite Structures*, 100:464-478, 2013.

[2] RMJ. Groh and PM. Weaver. Buckling analysis of variable angle tow, variable thickness panels with transverse shear effects. *Composite Structures*, 107:482-493, 2014.

[3] RMJ. Groh and PM. Weaver. Static inconsistencies in certain axiomatic higher-order shear deformation theories for beams, plates and shells. *Composite Structures*, 120:231-245, 2015.

[4] RMJ. Groh and PM. Weaver. On displacement-based and mixed-variational equivalent single layer theories for modelling highly heterogeneous laminated beams. *International Journal of Solids and Structures*, 59:147-170, 2015.

[5] RMJ. Groh and PM. Weaver. A computationally efficient 2D model for inherently equilibrated 3D stress predictions in heterogeneous laminated plates. Part I: Model formulation. *Composite Structures*, Accepted for publication.

[6] RMJ. Groh and PM. Weaver. A computationally efficient 2D model for inherently equilibrated 3D stress predictions in heterogeneous laminated plates. Part II: Model validation. *Composite Structures*, Accepted for publication.

Reports

[7] RMJ. Groh, PM. Weaver, and A. Tessler. Application of the Refined Zigzag Theory to the modeling of delaminations in laminated composites. NASA/TM-2015-218808, 2015.

Conference papers and presentations

[8] RMJ. Groh and PM. Weaver. Buckling analysis of variable angle tow, variable thickness panels with transverse shear effects. In 17th *International Conference on Composite Structures*, Porto, Portugal, 17-21 June 2013.[1]

[9] RMJ. Groh and PM. Weaver. A mixed-variational, higher-order zig-zag theory for highly heterogeneous layered structures. In 18th *International Conference on Composite Structures*,

[1] Awarded the Ian Marshall's Award for Best Student Paper by Conference Chair Prof. António JM. Ferreira.

Lisbon, Portugal, 15-18 June 2015.

[10] RMJ. Groh and PM. Weaver. Full-field stress tailoring of composite laminates. In 20th *International Conference on Composite Materials*, Copenhagen, Denmark, 19-24 July 2015.

Related work on buckling and postbuckling

[11] RMJ. Groh and PM. Weaver. Buckling analysis of variable angle tow, variable thickness panels. In 19th *International Conference on Composite Materials*, Montréal, Canada, 28 July - 2 August 2013.

[12] RMJ. Groh and PM. Weaver. Post-buckling analysis of variable angle, variable thickness panels manufactured by Continuous Tow Shearing. In 1st *International Conference on Mechanics of Composites*, Stony Brook University, Long Island, USA, 8-12 June 2014.

[13] RMJ. Groh and PM. Weaver. Mass optimization of variable angle tow, variable thickness panels with static failure and buckling constraints. In 56th *AIAA/ASME/ASCE/AHS/ASC Structures, Structural Dynamics and Materials Conference*, AIAA 2015-0452, Kissimmee, USA, 5-9 January 2015[2].

Use of published work in this thesis

The literature reviews of references [2], [3], [4] and [13] above have served as a foundation for Chapter 2. Furthermore, Chapter 3 is based on the work previously published in [3], and Chapters 4 and 5 draw from the work in [4] and [10]. Note also that the author discusses pertinent topics regarding composite materials on his personal website `aerospaceengineeringblog.com`, and some of his previous observations regarding the future of composites have been used in Chapter 1.

[2] Awarded the Collier Research HyperSizer/AIAA Structures Best Paper Award.

Contents

List of Figures

List of Tables

Nomenclature

List of common abbreviations

1D,2D,3D	One-, two- and three-dimensional, respectively
AFP	Advanced fibre placement
AHOT	Advanced higher-order theory
AMT	Ambartsumyan multilayered theory
CLA	Classical laminate analysis
CTP	Classical theory of plates
CTS	Continuous tow shearing
CUF	Carrera's unified formulation
DQ	Differential quadrature
DQM	Differential quadrature method
ESLT	Equivalent single-layer theory
EWL	Externally weak layer
FEM	Finite element method
FSDT	First-order shear deformation theory
GA	Genetic algorithm
GDQ	Generalised differential quadrature
GUF	Generalised unified formulation
HOT	Higher-order shear deformation theory
HR	Hellinger-Reissner
HW	Hu-Washizu
IA	In-plane anisotropy
IC	Interlaminar continuity
LMT	Lekhnitskii multilayered theory
LWT	Layerwise theory
MZZF	Murakami's zig-zag function
PMCE	Principle of minimum complementary energy
PMPE	Principle of minimum potential energy
PVD	Principle of virtual displacements
PVF	Principle of virtual forces
PVW	Principle of virtual work
RMVT	Reissner mixed-variational theory
RPT	Refined plate theory
RZT	Refined zig-zag theory
TA	Transverse anisotropy
VAT	Variable angle tow
ZZ	Zig-zag

Roman symbols

$\boldsymbol{A}$	Laminate membrane stiffness matrix
$A_{ij}^{(n)}$	DQM weighting coefficients of the nth derivative
a	Length of laminate in the global x-direction
$\boldsymbol{a}$	Laminate membrane compliance matrix
$\boldsymbol{a}^{(k)}$	Integration constants of the transverse shear stresses
$\boldsymbol{B}$	Laminate in-plane/bending coupling stiffness matrix
b	Width of laminate in the global y-direction
$\boldsymbol{b}$	Laminate in-plane/bending coupling compliance matrix
$\boldsymbol{b}^{(k)}$	Integration constants of the transverse normal stress
C_1	Perimeter curve of a 2D surface with prescribed displacements
C_2	Perimeter curve of a 2D surface with prescribed stress resultants
C_z^0	Zeroth-order continuity of functions in transverse z-direction
C_{ijkl}	3D linear stiffness tensor of Hooke's Law
$\boldsymbol{c}^{(k)}$	Layerwise expansion functions of the transverse shear stresses
D	1D bending rigidity
$\boldsymbol{D}$	Laminate bending stiffness matrix, or differential operator matrix
$\boldsymbol{D}^F$	Differential operator matrix
$\boldsymbol{D}^g$	Global differential operator matrix
$\boldsymbol{D}^l$	Local differential operator matrix
$\boldsymbol{d}$	Laminate bending compliance matrix
E	1D first-order/higher-order coupling bending rigidity, or effective "springs-in-parallel" axial stiffness
E_{ii}	Young's Moduli in normal ii-direction
E_{ts}	Normalised maximum error in the transverse shear energy residual
$E^{(k)}$	Equivalent unidirectional Young's Modulus of kth layer
$\mathcal{E}$	Array of equivalent single-layer in-plane strain unknowns
$e^{(k)}$	Ratio of kth-layer reduced axial stiffness to effective axial stiffness
$\boldsymbol{e}^{(k)}$	Layerwise expansion functions of the transverse normal stress
$\hat{e}_i$	Unit vectors
F	1D higher-order bending rigidity
F_b	Discretised nodal loads in the boundary equations
F_i	Discretised nodal loads in the internal field equations
F_τ	Spatial expansion functions of CUF
$\mathcal{F}$	Array of equivalent single-layer stress resultants
$\mathcal{F}_{bc}$	Transformed boundary stress resultants
$\mathcal{F}^g$	Array of global equivalent single-layer stress resultants
$\mathcal{F}^l$	Array of local equivalent single-layer stress resultants
$\mathcal{F}^*$	Array of equivalent single-layer stress resultants, excluding stress resultant related to derivative of the ZZ function
f	Delamination initiation metric
$f(z)$	Higher-order through-thickness shape function

f_i	Body force in i^{th} direction
$\boldsymbol{f}$	Array of through-thickness expansion functions
$\boldsymbol{f}^g$	Array of global through-thickness expansion functions
$\boldsymbol{f}^l$	Array of local, layerwise through-thickness expansion functions
$\boldsymbol{f}_u^{(k)}$	Array of through-thickness displacement field expansion functions
$\boldsymbol{f}_u^g$	Array of global through-thickness displacement field expansion functions
$\boldsymbol{f}_u^l$	Array of local, layerwise through-thickness displacement field expansion functions
$\boldsymbol{f}_\epsilon^{(k)}$	Array of through-thickness in-plane strain field expansion functions
$\boldsymbol{f}_\epsilon^g$	Array of global through-thickness in-plane strain field expansion functions
$\boldsymbol{f}_\epsilon^l$	Array of local, layerwise through-thickness in-plane strain field expansion functions
G	1D transverse shear rigidity, or effective "springs-in-series" transverse shear stiffness
G_i	Equivalent "springs-in-series" stiffness of RZT
G_{ij}	Shear Moduli in ij-direction
$G^{(k)}$	Equivalent unidirectional shear modulus of kth layer
$\boldsymbol{G}^{(k)}$	Matrix of shear moduli of kth layer
$g^{(k)}$	Ratio of effective transverse shear rigidity to k^{th}-layer transverse shear rigidity
$\boldsymbol{g}^{(k)}$	Array of through-thickness expansion functions of the transverse shear stresses
H	1D first-order/higher-order transverse shear coupling rigidity
$\boldsymbol{h}^{(k)}$	Array of through-thickness expansion functions of the transverse normal stress
I	1D higher-order transverse shear rigidity
$\boldsymbol{I}_i$	Identity matrix of size $i \times i$
$\boldsymbol{K}$	Stiffness matrix of numerical solution technique
k	Pertinent shear correction factor
L	A characteristic length, or higher-order ZZ moment
$\mathcal{L}_{bc}$	Array of Lagrange multipliers in the boundary conditions
$\mathcal{L}_{eq}$	Array of Lagrange multipliers in the equilibrium equations
$\mathcal{L}_i$	An arbitrary differential operator
M_i	Bending moment in i^{th} direction
M_i^ϕ	ZZ bending moment in i^{th} direction
$\mathcal{M}$	Array of bending moments
N_i	In-plane membrane stress resultant in i^{th} direction
N_l	Total number of layers in a laminate
N_o	Order of expansion of a model
N_{og}	Global number of variables in higher-order theory
N_{ol}	Local, layerwise number of variables in higher-order theory
N_p	Number of numerical discretisation points
$\check{N}$	Interlaminar tensile strength
$\mathcal{N}$	Array of membrane stress resultants

$\boldsymbol{n}$	Boundary normal vector n_i
O_i	Second-order stress resultant in i^{th} direction
$\mathcal{O}$	Length of stress resultant array $\mathcal{F}$, or order of error
o_p	Order of expansion of the in-plane displacements
o_z	Order of expansion of the transverse displacement
P_i	Third-order stress resultant in i^{th} direction
$\hat{P}_b$	Prescribed normal traction on the bottom laminate surface
$\hat{P}_t$	Prescribed normal traction on the top laminate surface
p	Perturbation parameter
Q_i	Transverse shear force in i^{th} direction
Q_i^{ϕ}	ZZ transverse shear force in i^{th} direction
$\boldsymbol{Q}^{(k)}$	Reduced stiffness matrix of Hooke's Law for k^{th} layer
$\bar{\boldsymbol{Q}}^{(k)}$	Transformed reduced stiffness matrix of Hooke's Law for k^{th} layer
$\mathcal{Q}$	Array of first-order transverse shear stress resultants
q	Distributed transverse loading on beams
q_0	Transverse loading magnitude on beams
R_i	Second-order transverse shear force in i^{th} direction
R_{ij}	Reduced compliance terms with plane strain in the y-direction
R_{ts}	Transverse shear energy residual
$\bar{R}_i$	Normalised equilibrium residuals in the ith direction
$\bar{R}_z^t$	Normalised transverse equilibrium equation residual at the top surface
$\boldsymbol{R}_i^{(k)}$	Through-thickness expansion functions of transverse shear stresses
r_{ts}	Ratio of transverse shear bending deflection components
r_w	Ratio of total bending deflections
S	Boundary surface of a body in 3D Cartesian coordinates
S_1	Part of the boundary surface of a body with prescribed displacements
S_2	Part of the boundary surface of a body with prescribed tractions
S_{ijkl}	3D linear compliance tensor of Hooke's Law
$\check{S}$	Interlaminar shear strength
$\boldsymbol{S}$	Equivalent single-layer, higher-order stiffness matrix
$\boldsymbol{s}$	Equivalent single-layer, higher-order compliance matrix
T_0	Local fibre angle at the centre of a variable stiffness panel
T_1	Local fibre angle at the edges of a variable stiffness panel
$\hat{T}_b$	Prescribed shear tractions on the bottom laminate surface
$\hat{T}_t$	Prescribed shear tractions on the top laminate surface
$\check{T}$	Interlaminar shear strength
$\boldsymbol{T}$	Transformation matrix
$\boldsymbol{T}_{bc}$	Boundary transformation matrix
$\boldsymbol{T}_n$	Contracted transformation matrix
$\mathcal{T}$	Array of higher-order transverse shear stress resultants
t	Laminate total thickness
$t^{(k)}$	Thickness of kth layer

$t_0^{(k)}$	CTS sheared thickness of layer k
$\boldsymbol{t}$	Vector of surface tractions t_i
U	Strain energy of a 3D body
U_0	Strain energy density function
U_b	Array of DQ boundary unknowns
U_i	Array of DQ internal field unknowns
U^*	Complementary energy of a 3D body
U_0^*	Complementary energy density function
$\mathcal{U}, \mathcal{U}_{xy}$	Array of equivalent single-layer in-plane displacement unknowns
$\mathcal{U}_{bc}$	Array of in-plane displacement unknowns in normal-tangential coordinates
$\mathcal{U}^g$	Array of global equivalent single-layer in-plane displacement unknowns
$\mathcal{U}^l$	Array of local equivalent single-layer in-plane displacement unknowns
u_{0i}	In-plane displacement of an equivalent single layer in i^{th} direction
$\boldsymbol{u}$	Displacement vector field of a solid u_i
$\boldsymbol{u}_\tau$	Array of unknown displacement variables
V	Volume of a body in 3D Cartesian coordinates
V_e	Work done by external forces
V_e^*	Complementary work done by external forces
$\boldsymbol{v}$	Velocity vector v_i
W	Work done by internal and external forces
W^*	Complementary work done by internal and external forces
$\mathcal{W}$	Array of equivalent single-layer transverse displacement unknowns
w, w_0	Transverse deflection of an equivalent single layer
X_i	Location of the grid points in direction X
x_A, x_B	Two ends of a plate in the x-direction
$\boldsymbol{x}$	Cartesian coordinates in 3D space $(x_1, x_2, x_3) = (x, y, z)$
y_A, y_B	Two ends of a plate in the y-direction
$\boldsymbol{Z}_i^p$	Identity matrix of size $i \times i$ multiplied by scalar z^p
z_k	Through-thickness location of the interface between layers k and $(k+1)$
$z_m^{(k)}$	Through-thickness location of the mid-plane of layer k

Greek symbols

$\alpha^{(k)}$	Local fibre angle of kth layer
$\beta_i^{(k)}$	ZZ slopes of layer k
δ	Variational operator
Γ	Boundary line of an equivalent single layer
γ_i	Transverse shear rotation in i^{th} direction
γ_{ij}	Linear shear components of the Green-Lagrangian strain dyad
$\gamma^{(k)}$	CTS shearing angle in ply k
$\boldsymbol{\gamma}^{nbc}$	Transverse shear correction factors of the applied surface shear tractions in the boundary equations of the beam theory
ϵ	Equivalent single layer in-plane stretching and flexural strains

ϵ_i	Linear normal components of the Green-Lagrangian strain dyad
ϵ^g	Global equivalent single-layer in-plane stretching and flexural strains
ϵ^l	Local equivalent single-layer in-plane stretching and flexural strains
$\boldsymbol{\epsilon}$	Linear Green-Lagrangian strain dyad ϵ_{ij}
ζ_i	Second-order in-plane displacement in i^{th} direction
$\boldsymbol{\eta}$	Transverse shear correction factors of the plate theory
$\boldsymbol{\eta}^n$	Transverse normal correction factors of the beam theory
$\boldsymbol{\eta}^s$	Transverse shear correction factors of the beam theory
θ_i	First-order cross-sectional bending rotation in i^{th} direction
$\kappa(\boldsymbol{K})$	Condition number of stiffness matrix $\boldsymbol{K}$
κ_i	Curvature of an equivalent single layer in i^{th} direction
$\boldsymbol{\Lambda}_{bc}$	Array of Lagrange multipliers in the boundary conditions
$\boldsymbol{\Lambda}_{eq}$	Array of Lagrange multipliers in the equilibrium equations
λ_i	Nondimensional orthotropy ratios in i^{th} direction
$\boldsymbol{\mu}^{nbc}$	Transverse shear correction factors of the applied surface normal tractions in the boundary equations of the beam theory
$\nu_{xy}^{(k)}, \nu_{yx}^{(k)}$	Major and minor Poisson's ratio of kth layer
ξ_i	Third-order bending rotation in i^{th} direction
Π	Total potential energy of an elastic body
Π_{HR}	Total potential energy of the Hellinger-Reissner mixed-variational principle
Π_{HW}	Total potential energy of the Hu-Washizu mixed-variational principle
Π^*	Total complementary energy of an elastic body
ρ	Volumetric mass density
$\boldsymbol{\rho}^{nbc}$	Transverse shear correction factors of the boundary equations in the beam theory
σ_i	Normal stress components of the Cauchy stress dyad
$\boldsymbol{\sigma}$	Cauchy stress dyad σ_{ij}
τ_{ij}	Shear stress components of the Cauchy stress dyad
Φ	Rotation of variable stiffness fibre path with respect to x-axis
ϕ_i^A	Ambartsumyan shear functions in i^{th} direction
ϕ_i^{RZT}	RZT ZZ function in i^{th} direction
$\phi_i^{(k)}$	General ZZ function in i^{th} direction
$\phi_{MZZF}^{(k)}$	Murakami's ZZ function
$\phi_{RZT}^{(k)}$	Unidirectional RZT ZZ function
$\boldsymbol{\chi}$	Transverse shear correction factors of the applied surface shear tractions in the plate theory
$\boldsymbol{\chi}^n$	Transverse normal correction factors of the applied surface shear tractions in the beam theory
$\boldsymbol{\chi}^s$	Transverse shear correction factors of the applied surface shear tractions in the beam theory
ψ_i	ZZ variable in i^{th} direction
Ω	Internal surface of an equivalent single layer

$\boldsymbol{\omega}^n$	Transverse normal correction factors of the applied surface normal tractions in the beam theory

Superscripts

0	Initial conditions
bc	Quantities corresponding to the boundary conditions
g	Quantity corresponding to global through-thickness shape function
(k)	Quantities corresponding to the kth layer
l	Quantity corresponding to local, layerwise through-thickness shape function
n	Quantities corresponding to transverse normal correction factors
s	Quantities corresponding to transverse shear correction factors
$\top$	Matrix transpose operator
$*$	Complementary energy quantities, or contracted shear stress resultants

Subscripts

0	Magnitude of sinusoidal variable assumptions
b	Quantity corresponding to boundary discretisation points
bc	Quantity corresponding to boundary conditions
eq	Quantity corresponding to equilibrium equations
i	Quantity corresponding to internal field discretisation points
k	Quantity corresponding to the interface between the k and $k+1$ layers

Superimposed characters

$\cdot$	Derivative with respect to time
$\bar{}$	Normalised quantity for displacements and stresses, or reduced stiffness matrix
$\check{}$	Mechanical material strength
$\hat{}$	Prescribed quantity such as boundary conditions and applied loads

Chapter 1

Introduction

1.1 Background

The use of multilayered composites in load-bearing structures, particularly in the aeronautical, marine and renewable energy industries is on the rise. In fact, in any engineering structure that features heavy moving machinery, be it an aircraft, sea-faring vessel or turbine blade, structural mass is a primary design driver. Oftentimes, the benefits of saving weight are not linear but lead to beneficial second-order effects.

On an aircraft, for example, every gram saved in the structure of the wings and fuselage can be replaced by more payload, and hence, increases revenue for the operating airline. Alternatively, the aircraft can be flown at reduced weight, which means the propulsive system can accelerate the aircraft to the same velocity at lower power output, i.e. at improved fuel efficiency. In the ideal scenario shedding structural mass induces a beneficial feedback loop. First, lighter aircraft require smaller engines to achieve the same cruising speed and smaller wings to keep the aircraft aloft. In turn, smaller engines and a more compact aircraft are naturally lighter and also reduce drag, thereby further reducing the engine power output requirements.

What prevents this virtuous cycle from repeating *ad infinitum* is the economic goal of the operating airline to turn over a profit. From the perspective of the airline, the ultimate goal is not to fly the lightest or smallest aircraft but to make money for the shareholders of the company. In this respect, economies of scale play a big role on the bottom line, such that bigger aircraft are preferred to smaller ones. The greater the payload and passengers the aircraft can carry, the greater the revenue for the airline and the smaller the operating costs per passenger. Additionally, structural mass saved can be replaced by comfort or luxury items, such as private cabins, reclining seats and entertainment systems, that warrant higher prices and improved gross margins on sales. Finally, legislative goals by the European Commission to reduce CO_2 emissions by 75% per passenger kilometre, and to eliminate taxiing emissions completely by 2050, pose serious threats in terms of financial penalties [1].

Thus, from the perspective of the operating airline, savings in aircraft dry mass lead to a trifecta of benefits to the bottom line: an increase in revenue, a reduction in operating costs per passenger, and an improvement in fuel efficiency. As a result, original equipment manufacturers, such as Airbus, Boeing, Bombardier and Embraer, are incentivised to design more efficient aircraft. Due to the higher specific strength (strength/density) and specific stiffness (stiffness/density) of advanced fibre-reinforced plastics compared to standard metallic aerospace materials, advanced composites are finding increasing application in primary aircraft structures. Most recently, Boeing replaced the 767-type aircraft with the 787 Dreamliner, the first commercial airplane with a composite fuselage and composite wings, resulting in an overall composite usage of 50% by weight [2]. In early 2015, Airbus shipped its competitor aircraft, the A350

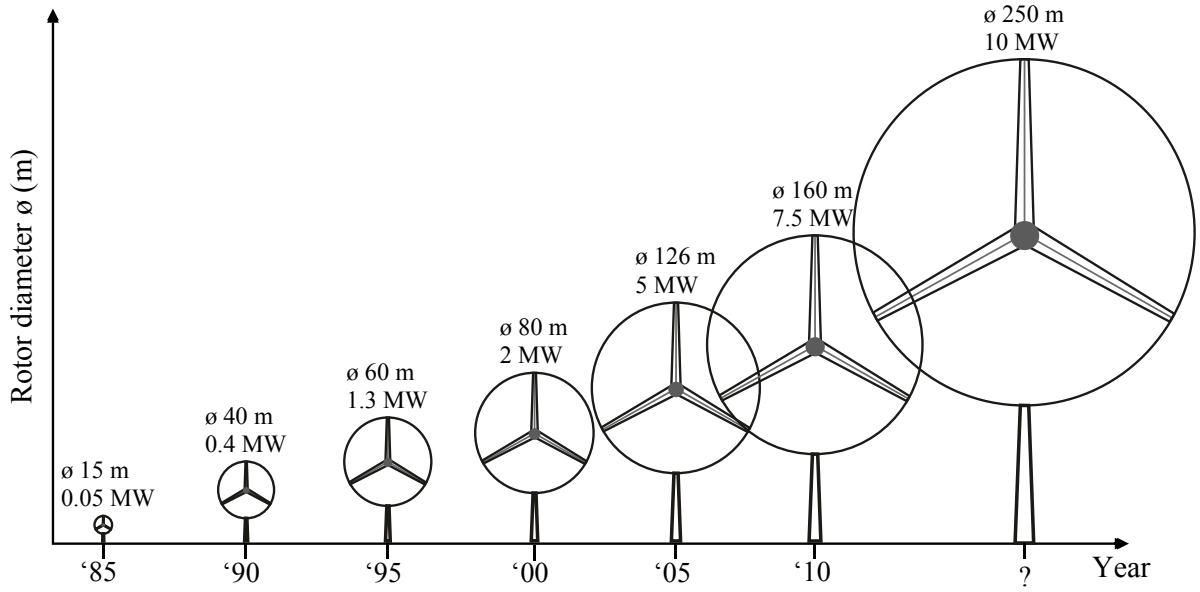

Figure 1.1: A progression of wind turbine rotor sizes and power output ratings from 1985-2010. Data reproduced from the 2011 *UpWind* research report [3]. All drawings are not to scale.

XWB, made primarily from carbon fibre-reinforced plastics.

Similarly, other industries are taking advantage of the high specific strength and stiffness of composites in lightweight design. BMW's i3 urban electric car is the first mass production vehicle to predominantly use carbon fibre-reinforced plastics for the internal structure. Although the lightweight structural properties of composites have been employed in high-performance racing cars for more than two decades, the use of carbon fibre composites in large-scale automotive applications is expected to grow considerably in the coming years [4].

The notion of an impending world energy crisis, with threats of peak oil and global warming, have increased demand for renewable energy sources, such as wind power. In the last 25-30 years the use of wind turbines for electricity generation has grown from a grass-root green initiative to a financially sustainable primary energy resource [5]. The increasing maturity of the industry can be traced from the small 50-150 kW turbines constructed throughout the 1980s to the large 2-5 MW projects installed both on- and offshore today (see Figure 1.1). This growth can largely be attributed to innovations in the integration of lightweight fibre-reinforced plastics as the high specific stiffness of these materials limits tip deflections, reduces gravity-induced loading and decreases rotor inertia. Furthermore, the excellent fatigue resistance of composites helps to minimise material degradation and maintenance costs over the 20-year design lifespan [6]. As governmental subsidies run out, the long-term economic sustainability of wind technology depends on increasing the energy capture efficiency, which is primarily driven by the swept area of the turbine and therefore the turbine blade lengths. It has been shown statistically that the weight of a turbine blade scales proportional to the cubic of the blade length [7], such that gravity-induced bending moments vary with the *fourth* power of the blade length. Thus, achieving the goals of a 20 MW turbine with 100 m long blades, as outlined in the

2011 *UpWind* research report [3], requires further innovations in terms of lightweight structural design on multiple fronts.

In high-performance applications, multiple layers of advanced fibre-reinforced plastics are typically laminated into a multilayered assembly. By rotating the fibre orientation of individual layers within a laminate, the engineer is endowed with enhanced design freedom to tailor the structural behaviour on a micro- and macromechanical level. By creating balanced/unbalanced and symmetric/non-symmetric laminations, for example, the designer can exploit anisotropic coupling effects between different orthogonal deformation modes that are impossible with isotropic structures.

The ability to discretely build up the thickness of a laminate while tailoring the material properties of individual layers, extends the lightweight benefits of composites from the *material* to the *structural* level. In fact, as multiple layers of dry fibre mats can be prearranged in a mould and injected with liquid resin, the distinction between the creation of the fibre-reinforced material and laminated structure is blurred. Automated manufacturing processes, such as tow-steering, now allow the fibre orientation to be controlled continuously within the plane to create so-called variable-stiffness laminates. In combination with three-dimensional (3D) printing techniques, modern manufacturing techniques are slowly converging to the bottom-up construction used by nature. Thus, material is grown or deposited at smaller length scales and then assembled to form subsequent structural units on an incrementally greater length scale. In this manner, stiffness and strength can be allocated and removed *pro re nata*, and facilitate the combination of the materials with different functional properties. Hence, the multilayered, multimaterial composites of the future pave the way for more optimised, multifunctional structures.

1.2 Research motivation and objectives

Within the traditional applications of the aerospace and high-performance automobile industries, composite laminates are typically employed in thin-walled semi-monocoque structures. However, with the diversification of laminated composites to primary load-bearing structures in novel applications, the range of possible laminate configurations in terms of layer material properties, stacking sequences and overall laminate thicknesses, as well as the nature of service loading, is likely to extend simultaneously.

For example, laminated safety glass that remains intact when shattered is not only applied for ballistic protection in cars but increasingly used as a structural material in modern office buildings. In these laminates, layers of stiff and brittle glass are joined by soft and ductile interlayers of polyvinyl butyral or ethylene-vinyl acetate. As the material properties of glass and interlayer can differ by multiple orders of magnitude, the structural response to external stimuli is non-intuitive and not accurately captured using classical lamination theory.

Furthermore, the use of composite laminates in regions that require thicker cross-sections, such as wind turbine blade roots, is increasing as well, and these thicker aspect ratios are known to induce non-classical effects (see Figure 1.2) from significant transverse shearing and transverse normal deformations. In laminated composites, these transverse effects are exacerbated by a the lack of stiff reinforcing material in the stacking direction. These transverse stresses require

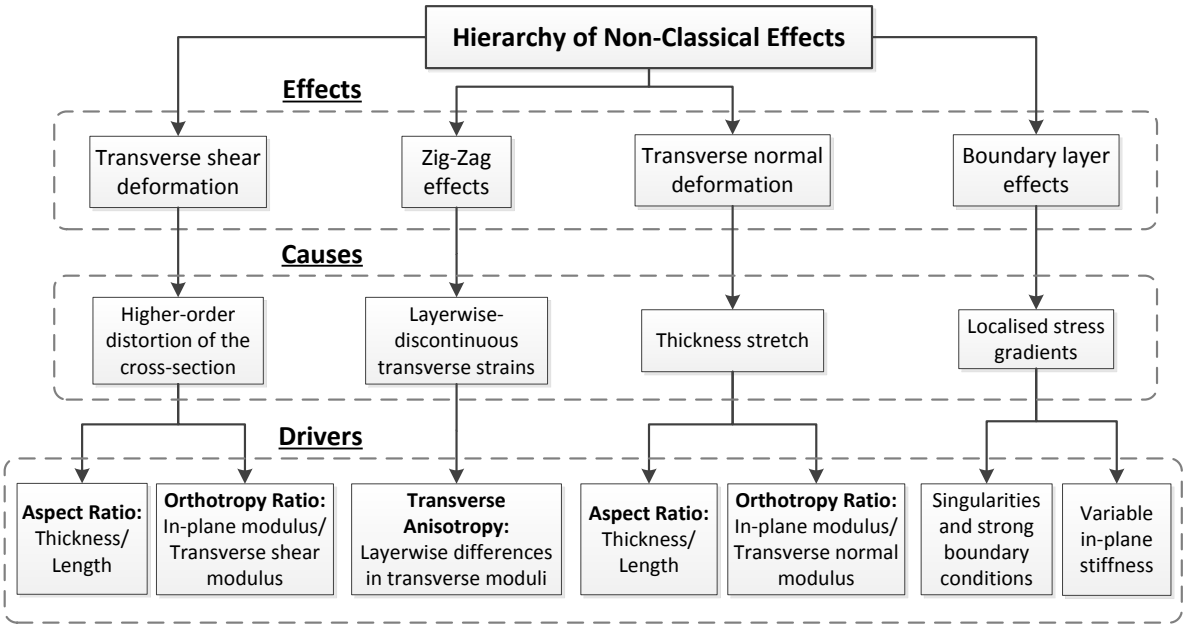

Figure 1.2: A hierarchy of non-classical effects relevant to multilayered composite structures. The chart highlights the four classes of non-classical effects investigated herein, and identifies their driving factors and influence on the structural behaviour.

particular attention as they are major drivers of common failure modes in laminated structures, such as delamination and debonding of layers.

Consider Figure 1.2 which highlights the four major non-classical effects relevant to multilayered composite structures studied in this work. Transverse shearing of the cross-section reduces the bending stiffness of a laminate, and also leads to higher-order distortions of the cross-section that channel stresses towards the surfaces. Similarly, transverse normal deformation results in changes in laminate thickness, which is particularly pernicious for sandwich laminates with soft cores. The zig-zag effect is a phenomenon that only arises in multilayered structures with discrete layerwise changes in transverse shear and transverse normal moduli, and results in non-intuitive internal load redistributions. Finally, localised boundary layers towards clamped edges and free surfaces exacerbate all three of the previously mentioned effects, and similar stress gradients can be induced remote from boundaries using variable-stiffness composites.

Thus, the reliable design of multilayered structures requires tools for accurate stress predictions that account for these non-classical effects. Currently, the standard approach in industry is to use 3D finite element models to predict accurate 3D stress fields. However, these approaches are computationally prohibitive in iterative design studies as multiple elements are needed for each layer. Therefore, these models are only used in areas of high stress concentration or for safety-critical components.

Over recent decades, a large number of approximate, higher-order 2D theories have been formulated with the aim of predicting accurate 3D stress fields while maintaining low computational expense. The present research follows in these footsteps with particular focus on laminated beams and plates with so-called *3D heterogeneity*, i.e. laminates comprised of layers with material properties that may differ by multiple orders of magnitude and that also vary

continuously in the plane of the beam or plate. The overall aims of the research are summarised as follows:

1. To develop a robust higher-order modelling framework that predicts variationally consistent 3D stress fields in laminated beams and plates with *3D heterogeneity* to within a few percent of 3D elasticity and 3D finite element solutions.

2. To implement the higher-order model numerically via a computer code that allows 3D stress fields, and stress gradients towards boundaries and singularities to be captured in a computationally efficient manner, i.e. using the smallest number of degrees of freedom. In order to maximise the model's potential use in industrial design applications, the numerical solution technique should be extendable to structures of arbitrary shape.

3. To compare the results of the present framework against other higher-order formulations in order to elucidate certain advantages and disadvantages of the present and other commonly-used 2D higher-order and 3D finite element techniques.

4. To provide physical insight into the governing factors that drive non-classical effects by studying non-traditional materials and stacking sequences with pronounced transverse anisotropy, with the aim of aiding the intuition of structural engineers in preliminary design stages.

5. To elucidate differences in the transverse stress response of straight-fibre and tow-steered composites, and to subsequently tailor the through-thickness stress fields via in-plane stiffness variations in order to minimise the likelihood of delaminations.

1.3 Thesis outline

The thesis is structured as follows:

- Chapter 2 begins with a detailed review of the literature on the fundamental variational principles of mechanics, and then leads into a treatise of different higher-order equivalent single-layer theories (ESLTs) that can be derived by means of these principles. Research into ESLTs has received considerable attention throughout the last century and has led to an extensive corpus of work. It is therefore not possible, nor indeed in the intention of the author, to mention all papers and different theories that have been published. Rather, the author has attempted to classify different formulations into groups and to discuss the seminal works therein. In an attempt to elucidate the advantages and disadvantages of certain formulations, a large number of models were implemented numerically throughout this research project. Thus, the author has given special attention to those models that have most aided the author's appreciation and understanding of the field. The chapter concludes with a review of the recent literature on tow-steered composites and the differential quadrature method, where the latter has been found to be a versatile numerical technique for solving the variable-coefficient partial differential equations that govern the mechanics of tow-steered composites.

- Chapter 3 discusses certain static inconsistencies that arise in displacement-based, axiomatic, higher-order theories that enforce the condition of vanishing transverse shear strains *a priori*. This condition leads to a physically inaccurate essential boundary condition at a clamped edge, and causes an inconsistency between the shear stress resultants derived from the equilibrium and constitutive equations of elasticity. A more consistent approach is to use generalised higher-order theories written in the form of a power series, as is done in generalised theories. Finally, Chapter 3 introduces a nondimensional parameter that can be used to gauge the accuracy of a higher-order theory.

- In Chapter 4, the governing equations[1] of a higher-order model for highly heterogeneous, variable-stiffness beams is derived using a contracted Hellinger-Reissner functional. This functional reduces the number of variables in the governing equations by basing the transverse stress assumptions on integrations of the axial stress. The model is derived using a generalised Taylor series notation, such that any order of theory can be chosen *a priori* without re-deriving the governing equations.

- In Chapter 5, the higher-order, mixed-variational formulation derived in Chapter 4 is implemented in a computer code using the differential quadrature method, and then used to analyse a comprehensive set of straight-fibre composite and sandwich beams in stretching and bending. The accuracy of the model is validated against 3D elasticity and 3D finite element solutions, and also compared to a second mixed-variational formulation that is commonly implemented in the literature. The model is then used to study the mechanics and origin of stress gradients towards clamped edges, and used to assess the importance of different higher-order effects on the structural behaviour.

- Chapter 6 extends the analysis of Chapter 5 to tow-steered, variable-stiffness beams. The results of the present formulation are again compared against 3D finite element solutions, and the correlation of the stress fields with the benchmark solution demonstrate the successful application of the model to layered structures with material properties that vary continuously or discretely in all three dimensions. The model is also used to analyse transverse boundary layers towards external surfaces, which are not modelled rigorously by 3D finite elements. Finally, the model is implemented in an optimisation study that tailors the 3D stress fields to find a compromise between maximising bending stiffness and minimising the chance of delaminations.

- In Chapter 7, the higher-order model for laminated one-dimensional beams presented in Chapter 4 is extended to two-dimensional plates. The derivation of the model is based on the notion that accurate transverse shear and normal stress fields can be derived by integrating the in-plane stresses of displacement-based, higher-order theories in Cauchy's 3D equilibrium equations. It is proven mathematically that the ensuing transverse stress assumptions always obey the interfacial and surface equilibrium conditions when applied

[1] Note that throughout this monograph the term "governing equations" is used to refer to the combined set of governing field equations *and* boundary conditions of a continuum. If referred to separately, the terms "governing field equations" and "boundary conditions" will be used as such.

within a variational statement that enforces Cauchy's 3D equilibrium equations as constraint conditions, hence the Hellinger-Reissner mixed-variational statement. Note that the formulation presented here is *generalised*, i.e. the order of the theory can adapted without having to rewrite the governing equations, but it is not *unified* as other displacement-based or mixed-variational theories are not included in the formalism.

- In Chapter 8, the mixed stress/displacement-based, higher-order plate theory derived in Chapter 7 is applied to the bending of orthotropic, anisotropic and variable-stiffness plates and sandwich laminates for different boundary conditions and applied surface tractions. The accuracy of the plate model is compared against 3D elasticity solutions and 3D finite element models. Different orders of the model are implemented and compared to establish useful guidelines recommending the order of expansion required for different laminates. Finally, the relative influence of transverse shear deformation on tow-steered composites, compared to a quasi-isotropic and homogeneous straight-fibre laminate, is assessed.

- Chapter 9 summarises the contributions of this thesis and makes suggestions for future work. In particular, the findings on displacement-based theories, the newly derived Hellinger-Reissner model and new insights into the higher-order behaviour of *3D heterogeneous* beams and plates are highlighted. Finally, suggestions regarding the extension of the presented Hellinger-Reissner framework to curved arches and shells, and more general topologies using the finite element method are made.

Chapter 2

Literature Review

2.1 Variational principles of solid mechanics

Any body in Cartesian three-dimensional space $\mathbb{R}^3 = (x_1, x_2, x_3)$, as depicted in Figure 2.1, subjected to certain force and displacement boundary conditions is defined by 15 unknown quantities - three displacements (u_1, u_2, u_3), six strain components $(\epsilon_{11}, \epsilon_{22}, \epsilon_{33}, \epsilon_{23}, \epsilon_{13}, \epsilon_{12})$ and six stress components $(\sigma_{11}, \sigma_{22}, \sigma_{33}, \sigma_{23}, \sigma_{13}, \sigma_{12})$. With proper boundary conditions there exists a unique equilibrium state that can be determined by solving the six kinematic, six constitutive and three equilibrium equations of elasticity. For a body deforming isothermally and linearly in $\mathbb{R}^3$, the governing field equations in indicial notation are

$$\textbf{Kinematics:} \quad \epsilon_{ij} = \frac{1}{2}\left(u_{i,j} + u_{j,i}\right), \quad i,j = 1,2,3 \tag{2.1a}$$

$$\textbf{Constitutive:} \quad \sigma_{ij} = C_{ijkl}\epsilon_{kl}, \quad C_{ijkl} = C_{klij}, \quad i,j = 1,2,3 \tag{2.1b}$$

$$\text{or:} \quad \epsilon_{ij} = S_{ijkl}\sigma_{kl}, \quad S_{ijkl} = S_{klij}, \quad i,j = 1,2,3$$

$$\textbf{Equilibrium:} \quad \sigma_{ij,j} + f_i = \rho\ddot{u}_i, \quad \sigma_{ij} = \sigma_{ji}, \quad i,j = 1,2,3 \tag{2.1c}$$

where f_i are applied body forces, ρ is the volumetric mass density of the body, C_{ijkl} and S_{ijkl} are components of the fourth-order stiffness and compliance tensors, respectively, ϵ_{ij} and σ_{ij} are the components of the linear Green-Lagrangian strain and Cauchy stress dyads, respectively, and the comma notation is used henceforth to denote partial differentiation. Furthermore, the superposed dot indicates differentiation with respect to time, and repeated roman indices j imply summation over the indicated range $j = 1,2,3$. To guarantee a unique solution, these governing field equations are combined with pertinent initial and boundary conditions of the following form:

Initial conditions (time = 0 and x_i inside body):

$$u_i = u_i^0, \quad \dot{u}_i = v_i^0 \tag{2.2a}$$

Boundary conditions (time ≥ 0 and x_i on boundary surface):

$$\text{Essential conditions: } u_i = \hat{u}_i, \quad \text{Natural conditions: } \sigma_{ij}n_j = \hat{t}_i \tag{2.2b}$$

where u_i^0 and v_i^0 are initial displacements and velocities within the body, and $\hat{u}_i$ and $\hat{t}_i$[1] are the specified displacements and tractions on the boundary surface with normal vector $\boldsymbol{n}$.

Finding an accurate solution to the system of equations (2.1) under conditions (2.2) is the primary goal of solid mechanics. Depending on the type of boundary conditions enforced in the problem, i.e. of essential or natural type, the system of governing equations can be solved using

[1] Throughout this monograph, a hat ˆ indicates a quantity prescribed on the boundary.

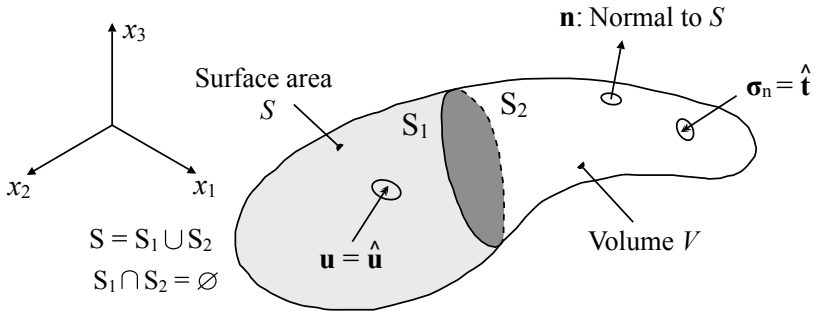

Figure 2.1: A linear elastic body of volume V in static equilibrium. The boundary surface $S : S_1 \cup S_2$ is split into S_1 on which surface displacements $\hat{\boldsymbol{u}}$ are prescribed, and S_2 on which surface tractions $\hat{\boldsymbol{t}}$ are prescribed.

three distinct approaches:

1. Displacement-based problems: With a certain displacement field $\hat{\boldsymbol{u}}$ specified over the entire boundary surface S of the body, the governing field equations are recast in terms of the displacement field $\boldsymbol{u} = u_i$ only by eliminating the stresses in the equilibrium equation (2.1c) using a combination of the constitutive equations (2.1b) and the kinematics Eq. (2.1a).

2. Stress-based problems: With certain tractions $\hat{\boldsymbol{t}}$ specified over the entire boundary surface S of the body, the governing field equations are recast in terms of stresses $\boldsymbol{\sigma} = \sigma_{ij}$ only by taking the constitutive equation (2.1b) in terms of the compliance tensor S_{ijkl} and substituting this into the kinematic equations (2.1a), which is then simplified using the equilibrium equations (2.1c).

3. Mixed problems: With certain displacements $\hat{\boldsymbol{u}}$ specified over one portion of the boundary surface S_1 and tractions $\hat{\boldsymbol{t}}$ specified over the remaining portion S_2, the displacement and stress fields $\boldsymbol{u}$ and $\boldsymbol{\sigma}$ are solved for simultaneously. The large majority of problems in solid mechanics are of this type.

In general, some form of displacement and/or stress assumptions that satisfy boundary conditions (2.2) are made to solve the three problems outlined above. However, finding an exact solution to linear elasticity problems at *each* material point within volume V is a very strong requirement. The variational principles of solid mechanics are powerful techniques for finding *approximate* solutions to elasticity problems by solving the equations in the sense of an integral. In this manner, some of the governing field equations, e.g. kinematic equations (2.1a) and constitutive relations (2.1b), are satisfied exactly, whereas other equations, e.g. the equilibrium equations (2.1c), produce a residual and hence, an approximate solution is found. Variational principles are expressed in terms of an energy balance of geometrically admissible displacement and/or statically admissible stress fields, and the minimisation of the associated energy functional by means of the calculus of variations, leads to the intrinsic Euler-Lagrange equations. The functionals involved typically refer to physical quantities that are invariant under coordinate transformations. This property makes the variational approach a powerful tool for

structural analysis, as formulating the variational principle in one coordinate system means that the governing equations in another can easily be derived by rewriting the functional and performing the variations. This obviates the need for deriving equilibrium equations from free body diagrams, which can become complex for curvilinear coordinate systems or geometrically nonlinear problems. Finally, auxiliary variational statements are readily derived by substitutions of other potential functions, or by applying constraint conditions via Lagrange multipliers.

The basis of variational methods in solid mechanics is the Principle of Virtual Displacements (PVD), which is an application of the Principle of Virtual Work (PVW) to the study of solid mechanics, and is discussed in many books on the topic e.g. [8, 9]. It states that a body constrained by a certain set of geometric conditions, i.e. essential boundary conditions, may displace into a large set of possible *admissible* configurations. However, only one unique configuration exists that satisfies the equilibria of forces and moments, and this corresponds to the actual configuration of the body. Thus, a mechanical system is in equilibrium if the sum of the virtual work δW, done by the external and internal forces acting on the system when the body is perturbed by arbitrary, yet geometrically admissible virtual displacements $\delta \boldsymbol{u} = (\delta u_1, \delta u_2, \delta u_3)$ from the true configuration $\boldsymbol{u} = (u_1, u_2, u_3)$, is zero. Hence, $\delta W = 0$ for equilibrium.

Following the notation in Figure 2.1, an elastic body is subjected to body forces $\boldsymbol{f}$ acting throughout its volume V, displacements $\hat{\boldsymbol{u}}$ on the boundary surface S_1 and surface tractions $\hat{\boldsymbol{t}}$ on the boundary surface S_2, where S_1 and S_2 are disjoint and their sum is equal to the total boundary surface S. The equilibrium condition of the PVD, stating that all internal and boundary forces must remain in equilibrium if the body is displaced from its true configuration $\boldsymbol{u}$ by a geometrically admissible variation $\delta \boldsymbol{u}$, is now enforced in a weak sense using the method of weighted residuals. Thus, equilibrium equations (2.1c) and natural boundary conditions (2.2b) are evaluated in an integral sense with the virtual displacements $\delta \boldsymbol{u}$ acting as weighting functions,

$$\delta W = -\int_V \left(\sigma_{ij,j} + f_i\right) \delta u_i \mathrm{d}V + \int_S \left(\sigma_{ij} n_j - \hat{t}_i\right) \delta u_i \mathrm{d}S = 0 \tag{2.3}$$

where $\mathrm{d}V = \mathrm{d}x\mathrm{d}y\mathrm{d}z$ and $\mathrm{d}S$ are the differential volume and surface area elements in Cartesian $\mathbb{R}^3$ coordinates, respectively. By applying the divergence theorem on $\sigma_{ij,j}$ in the volume integral of Eq. (2.3), and combining the ensuing derivatives of the weighting functions $\delta u_{i,j}$ by means of the variation of the kinematic equation $\delta \epsilon_{ij} = \frac{1}{2}\left(\delta u_{i,j} + \delta u_{j,i}\right)$, we get

$$\delta W = \int_V \left(\sigma_{ij} \delta \epsilon_{ij} - f_i \delta u_i\right) \mathrm{d}V - \int_{S_2} \hat{t}_i \delta u_i \mathrm{d}S = 0 \tag{2.4}$$

where a sum on repeated indices is implied, and the boundary integrals of terms $\sigma_{ij} n_j$ in Eq. (2.3) cancel with the boundary integrals that arise by applying the divergence theorem. In the variational statement of the PVD in Eq. (2.4), the weighting functions $\delta \boldsymbol{u}$ must satisfy the geometric boundary conditions, and therefore, by definition, $\delta \boldsymbol{u} = 0$ on S_1. Thus, the boundary integral in Eq. (2.4) is only evaluated over S_2 where $\delta \boldsymbol{u}$ is arbitrary and not defined *a priori*.

As no explicit constitutive assumptions are made, the PVD is independent of any material system, and thus applies to elastic and inelastic continuum problems. In general, the PVD is

applied with a certain admissible, axiomatic displacement assumption $\delta\boldsymbol{u}$ which is then used to calculate the strains $\boldsymbol{\epsilon}$ via the kinematic equations (2.1a), thereby inherently satisfying the compatibility of strains. In this manner, minimising the energy functional δW using the calculus of variations yields the equations of equilibrium and natural boundary conditions as the Euler-Lagrange equations.

A complementary principle to the PVD is the Principle of Virtual Forces (PVF). This variational statement stipulates that of all statically admissible stress fields $\boldsymbol{\sigma}$, i.e. those that equilibrate with the tractions $\boldsymbol{t}$ on boundary surface S_2, the stress state that enforces the compatibility condition of displacements $\boldsymbol{u}$ and strains $\boldsymbol{\epsilon}$ when the body is perturbed by a virtual stress field $\delta\boldsymbol{\sigma}$ from the current equilibrium state, is the true stress state. In the PVF, the virtual stresses $\delta\boldsymbol{\sigma}$ are used as weighting functions to enforce the compatibility of strains $\boldsymbol{\epsilon}$ and displacements $\boldsymbol{u}$ in an integral sense. The ensuing functional of the PVF reads

$$\delta W^* = \int_V \left[\epsilon_{ij} - \frac{1}{2}\left(u_{i,j} + u_{j,i}\right)\right] \delta\sigma_{ij} \mathrm{d}V + \int_S \left(u_i - \hat{u}_i\right) \delta t_i \mathrm{d}S = 0 \tag{2.5}$$

where δW^* is known as the complementary virtual work. By means of applying the divergence theorem on $u_{i,j}$ in the volume integral, Eq. (2.5) is transformed into

$$\delta W^* = \int_V \left(\epsilon_{ij}\delta\sigma_{ij} + u_i\delta\sigma_{ij,j}\right) \mathrm{d}V - \int_{S_1} \hat{u}_i \delta t_i \mathrm{d}S + \int_{S_2} u_i \left(\delta t_i - n_j \delta\sigma_{ij}\right) \mathrm{d}S = 0. \tag{2.6}$$

By requiring that the virtual stresses $\delta\sigma_{ij}$ satisfy the equilibrium equation $\delta\sigma_{ij,j} = -\delta f_i$, and the boundary condition of prescribed tractions $\delta\sigma_{ij}n_j = \delta t_i$ on S_2, the above variational statement Eq. (2.6) is simplified to

$$\delta W^* = \int_V \left(\epsilon_{ij}\delta\sigma_{ij} - u_i\delta f_i\right) \mathrm{d}V - \int_{S_1} \hat{u}_i \delta t_i \mathrm{d}S = 0. \tag{2.7}$$

Note, the PVF is valid irrespective of the chosen material system and thus applies to elastic and inelastic continuum problems. In general, the PVF is used to derive the governing equations for a certain axiomatic stress assumption $\delta\boldsymbol{\sigma}$ that satisfies the equilibrium equations and natural boundary condition $\delta\boldsymbol{t} = 0$ on S_2. In this manner, minimising the energy functional δW^* using the calculus of variations yields kinematic compatibility and essential boundary conditions as the Euler-Lagrange equations.

A number of additional variational statements can be derived directly from the PVD and the PVF. First, if we assume that a positive-definite strain energy per unit volume function U_0 can be written in terms of the strains ϵ_{ij} at any point throughout the body, then in the absence of temperature variations and non-conservative forces, the stresses within the elastic body can be derived directly from the strain energy density $U_0(\epsilon_{ij})$ via the constitutive equation. Hence,

$$\sigma_{ij} = \frac{\partial U_0(\epsilon_{ij})}{\partial \epsilon_{ij}}. \tag{2.8}$$

Introducing the constitutive equation (2.8) into the PVD of Eq. (2.4) gives

$$\int_V f_i \delta u_i \mathrm{d}V + \int_{S_2} \hat{t}_i \delta u_i \mathrm{d}S = \int_V \frac{\partial U_0}{\partial \epsilon_{ij}} \delta \epsilon_{ij} \mathrm{d}V = \int_V \delta U_0 \mathrm{d}V = \delta U \tag{2.9}$$

where U is the strain energy of the entire body. Furthermore, the expression on the left hand side of Eq. (2.9) is defined as the variation of the potential of the external applied loads δV_e with respect to $\boldsymbol{u}$. Hence,

$$V_e = \int_V f_i u_i \mathrm{d}V + \int_{S_2} \hat{t}_i u_i \mathrm{d}S. \tag{2.10}$$

Thus, the PVD can now be written in terms of the energy functionals U and V_e in Eqs. (2.9) and (2.10), respectively, such that

$$\delta \Pi(\boldsymbol{u}) \equiv \delta \left(U - V_e \right) = 0 \tag{2.11}$$

where the sum $U - V_e = \Pi$ is called the total potential energy of the elastic body and the variational statement in Eq. (2.11) is known as the Principle of Minimum Potential Energy (PMPE). By introducing the kinematic relations Eq. (2.1a), the PMPE is typically written in terms of the displacements $\boldsymbol{u}$ and hence, the PMPE states that among all the geometrically admissible fields $\boldsymbol{u}$ the actual displacements are those that minimise the total potential energy. Note that by introducing the constitutive equation into the PVD, the PMPE is only valid for linear and nonlinear elastic bodies, i.e. stresses are conservative and all deformations are isothermal.

Similarly, by assuming that a positive-definite complementary energy per unit volume function U_0^* exists, which can be written in terms of the stresses σ_{ij} at any point throughout the body, stresses and strains are related by the following constitutive relation

$$\epsilon_{ij} = \frac{\partial U_0^*(\sigma_{ij})}{\partial \sigma_{ij}}. \tag{2.12}$$

Introducing the constitutive equation (2.12) into the PVF of Eq. (2.7) gives

$$\int_V u_i \delta f_i \mathrm{d}V + \int_{S_1} \hat{u}_i \delta t_i \mathrm{d}S = \int_V \frac{\partial U_0^*}{\partial \sigma_{ij}} \delta \sigma_{ij} \mathrm{d}V = \int_V \delta U_0^* \mathrm{d}V = \delta U^* \tag{2.13}$$

where U^* is the complementary energy of the entire body. Furthermore, the expression on the left hand side of Eq. (2.13) is the variation of the potential of the external applied displacements δV_e^* with respect to $\boldsymbol{f}$ and $\boldsymbol{t}$. Hence,

$$V_e^* = \int_V u_i f_i \mathrm{d}V + \int_{S_1} \hat{u}_i t_i \mathrm{d}S. \tag{2.14}$$

Thus, the PVD can now be written in terms of the energy functionals U^* and V_e^* in Eqs. (2.13) and (2.14), respectively, such that

$$\delta \Pi^*(\boldsymbol{\sigma}) \equiv \delta \left(U^* - V_e^* \right) = 0 \tag{2.15}$$

where the sum $U^* - V_e^* = \Pi^*$ is called the total complementary energy of the elastic body, and the variational statement in Eq. (2.15) is known as the Principle of Minimum Complementary Energy (PMCE). The PMCE states that among all the statically admissible fields $\boldsymbol{\sigma}$, the actual stresses are those that minimise the total complementary energy. Again, note that by introducing the constitutive equation into the PVF, the PMCE is only valid for elastic bodies with either linear or nonlinear constitutive behaviour. For inelastic bodies, e.g. nonconservative systems where the work potential is a function of the path taken, the stresses and strains cannot be mapped via a potential function, and the PMCE does not hold.

It is worth noting that for linear stress-strain relations we have $U_0(\epsilon_{ij}) = U_0^*(\sigma_{ij})$, and both functions carry the same physical meaning of internal strain energy. In this case we can write

$$U_0(\epsilon_{ij}) = \frac{1}{2}C_{ijkl}\epsilon_{ij}\epsilon_{kl} \quad \text{and} \quad U_0^*(\sigma_{ij}) = \frac{1}{2}S_{ijkl}\sigma_{ij}\sigma_{kl}. \tag{2.16}$$

However, when the stress-strain relations are nonlinear, the two quantities are different and given by the respective areas underneath the stress-strain curves. Hence,

$$U_0 = \int_0^{\epsilon_{ij}} \sigma_{ij}\mathrm{d}\epsilon_{ij} \quad \text{and} \quad U_0^* = \int_0^{\sigma_{ij}} \epsilon_{ij}\mathrm{d}\sigma_{ij}. \tag{2.17}$$

Thus, U_0 and U_0^* are complementary to each other in terms of expressing the sum of respective stress-strain products, i.e. $U_0 + U_0^* = \sigma_{ij}\epsilon_{ij}$.

A characterisation of the relation between the PVD and the PVF is succinctly given by Reissner [10]. In the PMPE, the displacements are taken as the unknowns, and a constitutive relation between stresses and derivatives of displacements is defined *a priori*, such that the differential equations of equilibrium are derived as the variational Euler-Lagrange equations. In the PMCE, the stresses are taken as the unknowns, and the differential equations of equilibrium serve to constrain the class of statically admissible stresses, such that the variational Euler-Lagrange equations yield the pertinent stress-displacement relations. Therefore, the solutions to the PMPE and the PMCE result in approximate solutions to the boundary value problem, whereby one part of the complete system of differential equations, either the stress-displacement relations or the equilibrium equations, is enforced *explicitly*, whereas the other is satisfied only *approximately*.

In applying these variational statements, the structural engineer needs to remain wary of the approximate nature of these solutions. For example, consider the popular displacement-based Finite Element Method (FEM) as derived from the PVD. This method may provide excellent predictions for the displacements of the body if the admissible shape functions are chosen to accurately satisfy the geometric boundary conditions. However, the derivation of the stresses is not as reliable for two reasons. First, the exact equilibrium equations and natural boundary conditions are solved in their weak weighted-integral form, which is not equivalent to the strong form in a finite-dimensional solution space. Hence, the equilibrium and natural boundary conditions are therefore only satisfied globally in an average sense. Second, stresses are derived from the differentiation of displacements and this operation is not as accurate as treating the stresses directly as functional unknowns [9]. Thus, in the displacement-based FEM approach, the exact equilibrium equations of elasticity and the natural boundary conditions

are not enforced point-by-point, and may be violated locally. As a result, the approximate solutions obtained by the displacement-based FEM are always smaller than the real solution, i.e. the lowest energy solution, such that the solution makes the system stiffer than the true 3D elasticity solution [11].

Another form of the PMPE and the PMCE are the so-called mixed-variational statements, which allow simultaneous assumptions of displacements and stress fields, some of which take the role of constraint conditions. In this manner, approximate solutions to the 3D boundary value problem are found that do not give "preferential treatment" [10] to either set of stress-displacement or equilibrium equations. As a result, both the stress-displacement relations and the differential equations of equilibrium are obtained as the variational Euler-Lagrange equations.

For example, in the derivation of the PMPE, the compatibility condition of the strains is explicitly enforced by replacing $\boldsymbol{\epsilon}$ directly with geometrically admissible displacements $\boldsymbol{u}$ via the kinematic equations (2.1a). This statement can be generalised by introducing the strains as functional unknowns in the variational statement, and enforcing the compatibility condition and essential boundary conditions in a variational sense via Lagrange multipliers. Thus, the kinematic equations (2.1a) and essential displacement boundary conditions Eq. (2.2b) are introduced as variational constraints, with the stresses $\boldsymbol{\sigma}$ and surface tractions $\boldsymbol{t}$ serving as Lagrange multipliers. Hence,

$$\delta\Pi_{HW}(\boldsymbol{u},\boldsymbol{\epsilon},\boldsymbol{\sigma}) = \delta\left\{\int_V \left[U_0(\epsilon_{ij}) - f_i u_i\right]\mathrm{d}V - \int_{S_2} \hat{t}_i u_i \mathrm{d}S - \int_V \left[\epsilon_{ij} - \frac{1}{2}\left(u_{i,j} + u_{j,i}\right)\right]\sigma_{ij}\mathrm{d}V - \int_{S_1}\left(u_i - \hat{u}_i\right) t_i \mathrm{d}S\right\} = 0. \quad (2.18)$$

This approach, known as the Hu-Washizu (HW) variational principle, is a generalisation of the PMPE in that it allows 15 independent assumptions in terms of displacements $\boldsymbol{u}$, strains $\boldsymbol{\epsilon}$ and stresses $\boldsymbol{\sigma}$, such that kinematic equations, constitutive stress-strain relations, equilibrium equations, and both essential displacement and natural force boundary conditions are derived as Euler-Lagrange equations.

Similarly, in the PMCE, it is assumed that the stresses $\boldsymbol{\sigma}$ equilibrate and are statically admissible on the boundary by enforcing this condition explicitly in the PVF. This condition can be imposed in a variational sense by adding the equilibrium equations (2.1c) and natural boundary conditions (2.2b) as constraint conditions to the PMCE via Lagrange multipliers. In this case, the Lagrange multipliers equal the three displacements $\boldsymbol{u}$. Hence,

$$\delta\Pi_{HR}(\boldsymbol{u},\boldsymbol{\sigma}) = \delta\left\{\int_V U_0^*(\sigma_{ij})\mathrm{d}V - \int_{S_1}\hat{u}_i t_i \mathrm{d}S + \int_V \left(\sigma_{ij,j} + f_i\right) u_i \mathrm{d}V - \int_{S_2}\left(\sigma_{ij}n_j - \hat{t}_i\right) u_i \mathrm{d}S\right\} = 0. \quad (2.19)$$

This variational statement is known as the Hellinger-Reissner (HR) variational principle, and allows nine independent assumptions in terms of displacements $\boldsymbol{u}$ and stresses $\boldsymbol{\sigma}$, such that equilibrium equations, differential stress-displacement relations, and essential and natural boundary

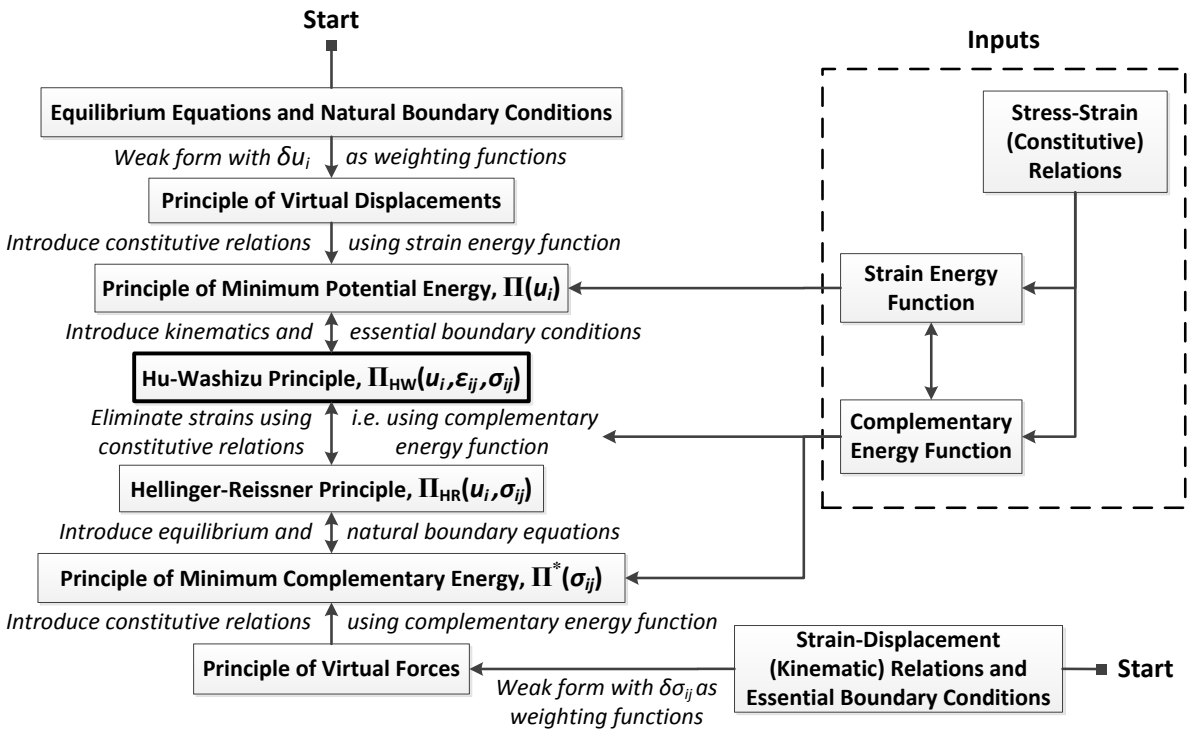

Figure 2.2: Relationship of different variational statements. Adapted from Washizu [9].

conditions are derived as the Euler-Lagrange equations. Furthermore, the HR principle can be interpreted as a special case of the generalised HW principle in that the strains $\boldsymbol{\epsilon}$ are no longer independent but specified *a priori* using a constitutive relation of the form Eq. (2.12). The advantage of eliminating the strain components is that the number of unknowns is reduced.

Due to the relation between the HR and HW principles, it is evident that the derivation of mixed-variational principles from the PMPE and the PMCE is reciprocal and equivalent for small displacements. This relationship is depicted schematically in Figure 2.2. The HW principle is the most general principle as it allows independent assumptions of all 15 unknowns. The HR principle and the PMPE are derived directly from this generalised principle by eliminating certain variables and constraint conditions. For detailed mathematical derivations of the HW and HR principles, as well as proofs of the validity of all variational statements, the interested reader is directed to Chapters 1 and 2 in the comprehensive monograph by Washizu [9].

The variational statements introduced herein are especially useful for deriving the governing differential equations for 2D plates and shells. In these theories, the 3D problem is condensed onto an equivalent single layer by integrating in the direction of the smallest dimension. Therefore, the governing field equations (2.1) and boundary conditions (2.2) in the remaining two dimensions need to be adapted accordingly. One aim of the present work is to show that the HR principle is a powerful technique for deriving computationally efficient 2D theories that allow accurate computations of 3D stress fields, including local stress gradients towards boundaries.

2.2 Higher-order structural modelling of composite laminates

In practical applications, composite laminates are typically modelled as thin plates and shells because the thickness dimension t is at least an order of magnitude smaller than representative in-plane dimensions L_x and L_y. This feature allows the problem to be reduced from a 3D to a 2D one coincident with a chosen reference surface of the plate or shell. The major advantage of this approximation is a significant reduction in the total number of variables and computational effort required. Such a theory is aptly called an Equivalent Single-Layer Theory (ESLT) as the through-thickness properties are compressed onto a reference layer by integrating properties of interest through the thickness. Many ESLTs are based on the axiomatic approach, whereby intuitive postulations of the displacement and/or stress fields in the thickness z-direction are made. Appropriate displacement-based, stress-based or mixed-variational formulations are then used to derive variationally consistent governing field equations and boundary conditions.

A second possible 2D approach is the asymptotic method, whereby the 3D governing equations are expanded in terms of a small perturbation parameter p and the terms related by the same power of p^i are grouped together. For example,

$$\mathcal{L}_{3D} \approx \mathcal{L}_1 p^1 + \mathcal{L}_2 p^2 + \cdots + \mathcal{L}_{N_o} p^{N_o} \tag{2.20}$$

where $\mathcal{L}_i$ is some differential operator and N_o is the order of the theory. The perturbation parameter is often chosen to be the thickness to length ratio $p = t/L$, such that governing equations related to the same order of p model the significant effects at the specific length scale $(t/L)^p$. As a result, the accuracy of the solution is refined by sequentially solving the governing equations $\mathcal{L}_1$, $\mathcal{L}_2$ and so on. The disadvantage of asymptotic methods is that large number of terms in the power series Eq. (2.20) may be needed to guarantee convergence as the thickness increases [12]. Second, consistent analysis is complicated by the fact that higher-order effects are also driven by the orthotropy ratios E_{11}/G_{13}, E_{22}/G_{23} and E_{11}/E_{22}. Therefore, mechanical-layerwise perturbation parameters may also be needed to capture the full structural behaviour.

The ad-hoc displacement and/or stress assumptions of axiomatic approaches facilitate an intuitive understanding of the underlying physical behaviour. For this reason, the rest of this literature review, and indeed the rest of this thesis, focuses on axiomatic theories. The reader interested in the application of asymptotic methods to problems in structural mechanics is directed to the textbook by Ciarlet et al. [13] and a review article on the variational asymptotic method by Yu et al. [14].

2.2.1 Displacement-based axiomatic theories

The most prominent example of an axiomatic ESLT is the Classical Theory of Plates (CTP) developed by Kirchhoff [15] and then revisited by Love [16], and its extension to laminated structures, namely Classical Laminate Analysis (CLA) [17]. The principle assumptions of Kirchhoff's theory are that:

1. Transverse normals to the reference surface before deformation are inextensible and remain

normal after deformation.

2. Plane sections remain plane, i.e. there is no distortion of the cross-section.

3. The transverse normal stress may be neglected in comparison with the stresses acting in the direction parallel to the reference surface.

4. All strains are sufficiently small, i.e. $\epsilon \ll 1$, and Hooke's law applies.

These assumptions mean that the effects of through-thickness shear and normal strains are ignored, the in-plane displacement fields u_x and u_y are assumed to vary linearly through the thickness, and the transverse displacement u_z is assumed to be constant. Thus, the 3D displacement field is assumed to obey

$$u_i(x, y, z) = u_{0i} - z w_{0,i}, \quad i = x, y \tag{2.21a}$$

$$u_z(x, y) = w_0. \tag{2.21b}$$

This approach reduces the number of displacement unknowns to three, namely the two axial stretching deformations u_{0x} and u_{0y}, and the constant transverse deflection w_0 of the reference plane.

The design of primary load-bearing structures requires accurate tools for stress analysis. When used around areas of stress concentration or in fail-safe design frameworks, composite laminates are often designed to have thicker cross-sections. Under these circumstances, non-classical effects, such as transverse shear and normal deformations, become important factors in the failure event. Furthermore, the analysis of layered composite structures is significantly more cumbersome due to a plethora of new features, such as in-plane anisotropy (IA); transverse anisotropy (TA); and interlaminar displacement, transverse shear and transverse normal stress continuity (IC). For example, composite laminae often exhibit much greater values of Young's modulus orthotropic ratio ($E_{11}/E_{22} = E_{11}/E_{33} \approx 140/10 = 14$), i.e. in-plane orthotropy, than isotropic materials ($E_{xx} = E_{yy} = E_{zz}$).

Furthermore, the induced error of Kirchhoff's hypothesis for isotropic plates is around 5% for thickness to characteristic length ratios t/L of around 1/10 [8]. For fibre-reinforced plastics, transverse shear deformations are more pronounced because the ratio of longitudinal to shear modulus is approximately one order of magnitude greater ($E_{iso}/G_{iso} = 2.6$, $E_{11}/G_{13} \approx 140/5 = 28$). The nondimensional ratios $\lambda_x = E_{11}/G_{13}(t/L_x)^2$ and $\lambda_y = E_{22}/G_{23}(t/L_y)^2$ drive what Everstine and Pipkin [18] called the "stress-channelling" effect on axial stress, as shown in Figure 2.3. Weaver [19] showed that as the nondimensional ratios λ_i increase, the cross-section shears exceedingly and transitions from a constant rotation to a higher-order distortion field. This nonlinear distortion is equivalent to a channelling of the axial stresses towards the surfaces. Due to the greater value of E_{11}/G_{13} and E_{22}/G_{23} in composites, the "stress channelling" effect is more pronounced in composite laminates than for isotropic plates of the same thickness to characteristic length ratio t/L_i.

Most notably, transverse anisotropy, i.e. the difference in layerwise transverse shear and normal moduli, leads to sudden changes in slope of the three displacement fields u_x, u_y, u_z at layer interfaces. This is known as the zig-zag (ZZ) phenomenon. In fact, Carrera [21] points

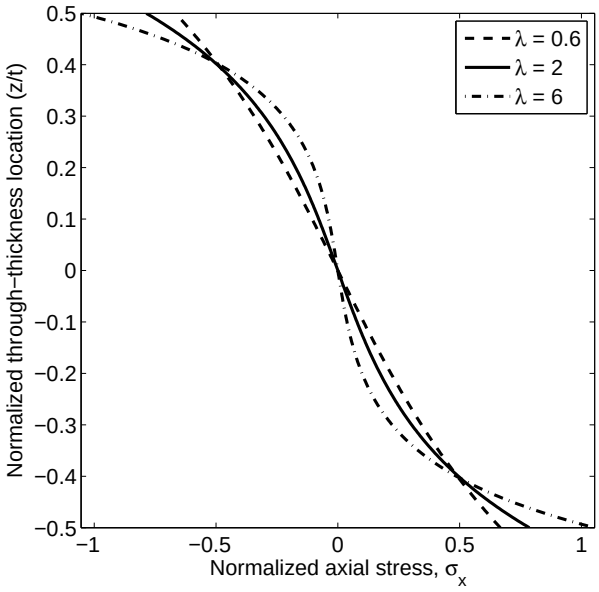

Figure 2.3: Variation of normalised in-plane stress profile $\bar{\sigma}_x$ through the thickness of a [0] laminate for different values of $\lambda = E_{11}/G_{13}(t/L_x)^2$. Results from Pagano's 3D elasticity solution [20].

out that "compatibility and equilibrium, i.e., ZZ and IC, are strongly connected to each other." Thus, while IC of the displacements requires u_x, u_y, u_z to be C^0 continuous at interfaces, IC of the transverse stresses forces the displacement fields to be C^1-*discontinuous*. Motivated by these considerations, Demasi [22] showed that the ZZ form of the in-plane displacements u_x, u_y and u_z can be derived directly from the continuity of τ_{xz}, τ_{yz} and σ_z, respectively. Therefore, an accurate model for multilayered composite and sandwich structures should ideally address the modelling issues denoted as C_z^0-requirements by Carrera [12, 23]:

1. Through-thickness continuous displacements and transverse stresses, i.e. the IC condition.

2. Discontinuous z-wise displacement derivatives at layer interfaces where transverse mechanical properties change, i.e. the zig-zag effect.

At the same time, the accuracy of the model should not come at the cost of excessive computational expense if the model is to be used for iterative design studies in industry.

Due to the complexities of modelling displacement and stress fields in layered structures, high-fidelity 3D finite element methods (FEM) are often employed for accurate structural analysis. However, these models can become computationally prohibitive when employed for laminates with large number of layers; optimisation studies; nonlinear problems that require iterative solution techniques; or for progressive failure analyses. Another class of model is the so-called Layerwise Theory (LWT), where each layer within the laminate stack is given its unique set of displacement unknowns, stress unknowns, or both. Whereas LWTs are able to satisfy both IC and ZZ requirements, the added accuracy comes at a much greater computational cost. This is because the number of variables of the theory scales with the number of layers in the laminate.

In cases where 3D FEM techniques are required due to the presence of very localised stress gradients or layerwise boundary conditions, LWTs can become a viable alternative [24].

Thus, with the aim of developing rapid, yet robust design tools for industrial purposes there remains a need for further efficient modelling techniques. In this regard, particular focus is required on ESLTs because the number of unknowns in these formulations is independent of the number of layers. A full comprehensive review of all axiomatic higher-order theories that have been published throughout the last century is beyond the scope of this literature review. Thus, the author has focused on the theories that have aided in developing the ideas and formulations presented in the following chapters.

Since the first half of the 20th century, a number of models have been published that partially or completely revoke at least one of Kirchhoff's original assumptions, known collectively as Love's Second Approximation Theories. One of the earliest examples is the First-Order Shear Deformation Theory (FSDT), which assumes that normals to the reference surface do not remain normal after deformation. Thus, rotations of the cross-section with respect to the undeformed state, θ_x and θ_y, are introduced as new degrees of freedom into the displacement field assumptions. Hence,

$$u_i(x, y, z) = u_{0i} + z\theta_i, \quad i = x, y \tag{2.22a}$$

$$u_z(x, y) = w_0. \tag{2.22b}$$

In FSDT, the effect of shear deformation on the cross-section is captured in an average sense. Timoshenko [25] famously applied this hypothesis to the classical model for isotropic Euler-Bernoulli beams, whereas a 2D extension for isotropic and single-layer plates was presented by Mindlin [26], and then extended to multilayered plates by Yang, Norris and Stavsky [27]. FSDT improves the predictions for global structural phenomena, such as bending displacement and low-frequency buckling and vibrational modes, but does not improve localised strain and stress predictions. Especially for highly heterogeneous and thick composite and sandwich laminates, FSDT is limited by its uniform transverse shear strain assumption [28]. Furthermore, FSDT produces piecewise-constant transverse shear stresses that violate continuity at layer interfaces, and do not disappear at the top and bottom surfaces. Finally, as the actual transverse shear stress profile is at least quadratic, shear correction factors are needed to energetically adjust the constant through-thickness strain profile. Determining the magnitude of these shear correction factors is not a straightforward task, especially in the case of highly heterogeneous laminates, and various methods addressing such concerns have been published in the literature [29–31]. In this regard, a new approach based on an asymptotic power series expansion for highly-orthotropic single-layers is presented in Chapter 3.

To account for the actual higher-order distribution of transverse shear stresses τ_{xz} and τ_{yz} through the thickness, and to guarantee that these disappear at the top and bottom surfaces when no shear tractions are applied, the so-called Higher-Order Shear Deformation Theory (HOT) was introduced. In general, the cross-section is allowed to deform in any form by including higher-order terms in the axiomatic expansions of the in-plane displacements u_x and

Table 2.1: Different higher-order shearing shape functions.

Model	$f(z)$ function
Ambartsumyan [35]	$\frac{z}{2}\left[\frac{t^2}{4}-\frac{z^2}{3}\right]$
Reddy [36]	$z\left[1-\frac{4z^2}{3t^2}\right]$
Touratier [37]	$\frac{t}{\pi}\sin\left(\frac{\pi z}{t}\right)$
Soldatos [38]	$t\sinh\frac{z}{t}-z\cosh\frac{1}{2}$
Karama [39]	$z\mathrm{e}^{-2(z/t)^2}$

u_y. Hence,

$$u_i(x,y,z) = u_{0i} + z\theta_i + z^2\zeta_i + z^3\xi_i + \ldots, \quad i = x, y \tag{2.23a}$$

$$u_z(x,y) = w_0 \tag{2.23b}$$

where the displacement unknowns associated with z coefficients of even power are higher-order membrane deformations, and the unknowns associated with odd power coefficients of z are higher-order bending rotations. A generalised expansion can be based on a number of different polynomial expansions of z, e.g. power series as in Eq. (2.23) above, Lagrange polynomials or Legendre polynomials, but the advantage of using the latter two orthogonal polynomials is that the associated deformation variables u_{0i}, θ_i, ζ_i, ξ_i, etc. are mathematically independent.

Vlasov [32] refined Mindlin's theory by guaranteeing that transverse shear strains and stresses disappear at the top and bottom surfaces in the absence of shear tractions. Taking Vlasov's condition into consideration, Levinson [33] proposed a third-order displacement field for the axial deformation u_x of a beam with a constant transverse displacement $u_z = w_0$. By enforcing the shear strain to vanish at the top and bottom surfaces, the Euler-Bernoulli rotation $w_{0,x}$ was introduced into the in-plane expansion u_x, thereby reducing the number of variables to that of Timoshenko beam theory. The associated bending moment and shear force were substituted into the well-known beam equilibrium equations, resulting in a variationally *inconsistent* fourth-order differential equation featuring only the transverse displacement w_0. Reddy [34] extended Levinson's theory to 2D problems featuring u_x, u_y and u_z and derived the governing field and boundary conditions in a variationally consistent manner using the PVD.

Thus, both Levinson [33] and Reddy [34] modified the general higher-order displacement field of Eq. (2.23) by truncating the series of u_x after the cubic z^3 term, and then enforced the physical boundary conditions of vanishing transverse shear strains at the top and bottom surfaces. As a result, the higher-order membrane stretching terms ζ_i are eliminated and the higher-order rotations ξ_i are rewritten in terms of $w_{0,i}$ and θ_i. These steps have led to a class of theories that are collectively written as

$$u_i(x,y,z) = u_{0i} - zw_{0,i} + f(z)\gamma_i, \quad i = x, y \tag{2.24a}$$

$$u_z(x,y) = w_0. \tag{2.24b}$$

Here the unknown variables γ_i capture the magnitude of the cross-sectional distortion, where $f(z)$ is a pertinent shape function that approximates the parabolic distribution of the transverse shear strains through the thickness, while guaranteeing that transverse shear strains vanish at the surfaces. A large number of different shear shape functions $f(z)$ have been published ranging from polynomial [35, 36, 40] and trigonometric [37, 41–44], to hyperbolic [38, 45] and exponential [39, 46], some of which are shown in Table 2.1. Karama et al. [39] point out that expansions based on the combinations of exponential and linear functions in z are superior to trigonometric functions as the former functions feature all even and odd powers in the displacement expansion, and the coefficients of higher-order terms do not decay as quickly. However, as shown in Chapter 3, the presence of the Kirchhoff rotations $w_{0,i}$ in the expansions of the displacement assumptions for u_x and u_y in Eq. (2.24) leads to a static inconsistency at clamped edges.

Another type of HOT, known as the Refined Plate Theory (RPT), was introduced by Shimpi [47]. In RPT, the transverse displacement is split into separate bending and transverse shear components, and the axial displacement is a function of individual bending and transverse shearing rotations. As a result, the bending components do not contribute towards transverse shear forces, and shearing components do not contribute towards bending moments. The advantages of this approach are that the governing equations maintain an intuitive resemblance to CPT, and allow the development of linear, isoparametric finite elements that are free from shear locking.

In a so-called Advanced Higher-Order Theory (AHOT), the transverse normal strain is incorporated in the displacement assumption by expanding the out-of-plane displacement u_z as a higher-order field in z. Here, the class of theory is generally denoted by $\{o_p, o_z\}$ where o_p refers to the order of expansion of the in-plane displacements u_x and u_y, and o_z refers to the order of the transverse displacement u_z. These theories obey *Koiter's Recommendation* which postulates that refinements of CPT should account for both transverse shear and transverse normal strains [48]. Milestone works were presented by Hildebrand, Reissner and Thomas [49], and Lo, Christensen and Wu [50], where the latter is a $\{3, 2\}$ AHOT given by

$$u_i(x, y, z) = u_{0i} + z\theta_i + z^2\zeta_i + z^3\xi_i, \quad i = x, y \tag{2.25a}$$

$$u_z(x, y, z) = w_0 + z\theta_z + z^2\zeta_z \tag{2.25b}$$

where θ_z and ζ_z are higher-order thickness stretch variables. Further examples of AHOTs are given in [50–53]. Generally, AHOTs only provide improvements that are worth their additional computational effort for thick plates with characteristic length to thickness ratios less than 5:1; sandwich panels with compliant, thick cores [22]; or for sandwich panels with one face-laminate considerably stiffer than the other [54]. Also note that Eq. (2.25) is a generalised expansion of the displacement field that does not enforce the boundary conditions of vanishing transverse shear strains at the top and bottom surfaces *a priori*, as is the case for the class of theories summarised by Eq. (2.24).

2.2.2 Mixed-variational axiomatic theories

All of the previously discussed theories are based on displacement formulations where the displacements u_x, u_y and u_z are treated as the unknown variables. Consequently, all strains and stresses are derived from the displacement assumptions using the kinematic and constitutive equations, respectively. The governing equations are typically derived in a variationally consistent manner using the PVD. A disadvantage of these displacement-based theories is that once the governing equations are solved for the displacement unknowns, accurate transverse strains and by extension accurate transverse stresses are not recovered accurately from the kinematic relations and the constitutive equations [21], respectively. For example, the transverse shear stresses typically violate the C_z^0-requirements of interfacial traction continuity. More accurate transverse stresses are often recovered *a posteriori* by integrating the in-plane stresses in Cauchy's 3D indefinite equilibrium equations [55]. The disadvantage of this technique is that the post-processed transverse stresses no longer satisfy the underlying governing field equations, and are therefore variationally inconsistent.

This post-processing operation can be precluded if some form of stress assumption is made. One class of model is based on applying the HR mixed-variational principle. Here, the strain energy is written in complementary form in terms of in-plane and transverse stresses, and Cauchy's 3D equilibrium equations are introduced as constraints via Lagrange multipliers (see Eq.(2.19)). Reissner [56, 57] was the first to use the HR principle to derive a new first-order theory for isotropic plates by assuming linear stress and displacement field assumptions through the thickness of the plate.

Batra and Vidoli [58] and Batra et al. [59] used the HR principle to develop a higher-order theory for studying vibrations and plane waves in piezoelectric and anisotropic plates, accounting for both transverse shear and transverse normal deformations, with all functional unknowns expanded in the thickness direction using orthonormal Legendre polynomials. The researchers showed that the major advantage of the HR principle is that by enforcing stresses to satisfy the natural boundary conditions at the top and bottom surfaces, and by deriving transverse stresses from the plate equations directly, the stress fields are closer to 3D elasticity solutions than a displacement-based equivalent that relies on Hooke's law to derive the stress fields. In particular, this means that boundary layers near clamped and free edges, and asymmetric stress profiles due to surface tractions on one surface only, can be captured accurately.

Cosentino and Weaver [60] applied the HR principle to symmetrically laminated straight-fibre composites to develop a single sixth-order differential equation in just two variables: transverse deflection w_0 and stress function Ω. The formulation of this theory is an extension of Reissner's original first-order approach for isotropic plates [56, 57] to anisotropic composite laminates. The approach by Cosentino and Weaver [60] is less general than the one proposed by Batra and Vidoli [58] as the in-plane and transverse stress assumptions are based on the same set of functional unknowns in order to minimise the computational cost. In fact, the in-plane stresses of CLA are integrated in Cauchy's equilibrium equations to derive an *a priori* equilibrated assumption for the transverse shear stresses. Chapters 4-8 show that the approach by Cosentino and Weaver [60] can be generalised further into a computationally efficient modelling framework of arbitrary order that can predict accurate 3D stress fields for laminates of arbitrary

stacking sequence and layer properties.

Forty years after publishing his work on the HR principle mentioned above, Reissner [61] had the insight that when considering multilayered structures, it is sufficient to restrict the stress assumptions to the transverse stresses because only these have to be specified independently to guarantee the IC requirements. This variational statement is known as Reissner's Mixed-Variational Theory (RMVT), and makes model assumptions for the three displacements u_x, u_y, u_z and independent assumptions for the transverse stresses $\tau_{xz}, \tau_{yz}, \sigma_z$. Compatibility of the transverse strains derived from the kinematic relations, i.e. from u_x, u_y and u_z, and the constitutive equations, i.e. from τ_{xz}, τ_{yz} and σ_z, is enforced by means of Lagrange multipliers. In this manner, the IC of transverse stresses and compatibility of strains is enforced *a priori* in RMVT, whereas equilibrium of the 3D stress fields is not enforced explicitly as in the HR principle. The relative benefits of these two mixed-variational approaches is studied in detail in Chapter 5.

Another interesting contribution to the field of mixed-variational statements for composite laminates is the work by Auricchio and Sacco [62]. In this work, the authors combine a HW-type functional for the in-plane response, written in terms of the midplane strains and curvatures of CLA, with a HR-type functional for the transverse shear response. The transverse shear stresses are either based on independent piecewise-quadratic functions of z, or alternatively on equilibrated stress assumptions as in the work by Cosentino and Weaver [60]. The researchers conclude that the latter approach is the more suitable for accurate transverse shear stress results. Note that the approach by Auricchio and Sacco [62] is more computationally expensive than the model by Cosentino and Weaver [60] as the combination of HW and HR functionals in the former depends on displacement, strain and stress unknowns, whereas the HR functional of the latter only depends on displacement and stress variables.

2.2.3 Displacement-based and mixed-variational zig-zag theories

HOTs and AHOTs provide considerable improvements in terms of transverse stress profiles and accurate modelling of global structural effects. However, these theories are not capable of explicitly capturing ZZ effects as the in-plane variables u_x, u_y are defined to be at least C_z^1-continuous. In this regard ESLTs that incorporate ZZ kinematics present a good compromise between local, layerwise accuracy and computational cost. Based on an historical review of the topic by Carrera [63] the ZZ theories can generally be divided into three groups:

1. Lekhnitskii Multilayered Theory (LMT)

2. Ambartsumyan Multilayered Theory (AMT)

3. Reissner Multilayered Theory (RMT)

Lekhnitskii [64] appears to be the first author to propose a ZZ theory originally formulated for multilayered beams. This was later extended to the analysis of plates by Ren [65, 66]. Ambartsumyan [35, 67] developed a ZZ theory for symmetric, specially orthotropic laminates by making an assumption for the two transverse shear stresses based on a linear combination

between the shear resultants Q_x and Q_y, an unknown through-thickness function $f(z) = 1 - 4(z/t)^2$, and two shear functions $\phi_x^A(x,y)$ and $\phi_y^A(x,y)$. Hence,

$$\tau_{xz}(x,y,z) = [Q_{55}^{(k)} f(z) + a_{55}^{(k)}]\phi_x^A(x,y) \tag{2.26a}$$

$$\tau_{yz}(x,y,z) = [Q_{44}^{(k)} f(z) + a_{44}^{(k)}]\phi_y^A(x,y) \tag{2.26b}$$

where the constants $a_{55}^{(k)}$ and $a_{44}^{(k)}$ are found by enforcing transverse shear stress equilibrium at layer interfaces, and at the top and bottom surfaces . The shear strains γ_{xz} and γ_{yz} are consequently expressed in terms of G_{xz} and G_{yz} using the constitutive equations, and the displacements u_x and u_y found by integrating the shear strains in the thickness z-direction with $u_z = w_0(x,y)$. Constants of integration are removed by enforcing that u_x, u_y disappear at the midplane and by enforcing interlaminar continuity. Whitney [68] later extended the analysis to symmetric laminates with off-axis plies and noted that the theory provides excellent results for global laminate behaviour when compared to the 3D elasticity solutions of cylindrical bending provided by Pagano [20, 69, 70]. However, Whitney also pointed out that the theory does not give good local agreement for transverse shear stresses as it fails to capture the large slope discontinuity at layer interfaces. The main reason for this is that the magnitude of the interface discontinuity is driven by the ratio of G_{13}/G_{23} in the Ambartsumyan theory, whereas in the exact elasticity solution the driving ratio is E_{11}/E_{22}. Later the effects of transverse normal strain [71] were included, and the theory was applied to shells and dynamic problems [72].

Di Sciuva [73, 74] introduced a displacement based ZZ theory where piecewise-linear ZZ contributions in the thickness direction enhance a FSDT expansion for u_x and u_y. The slopes of the layerwise ZZ functions are obtained by enforcing the same transverse shear stress for all layers, and by defining the ZZ function to vanish across the bottom layer. As a result, the transverse shear stress in all layers is identical to that of the bottom layer, causing a bias towards the transverse shear stiffness of this layer. To overcome this counterintuitive property, Averill [75] and Averill and Yip [76] introduced a penalty term in the variational principle that enforces continuity of the transverse shear stresses as the penalty term becomes large. Tessler et al. [77] note that the formulations based on Di Sciuva's early works present two major issues:

1. The in-plane strains are functions of the second derivative of transverse deflection w_0. This fact means that less attractive C^1 continuous shape functions of w_0 are required for implementation in FE codes.

2. The physical transverse shear forces derived from the first derivatives of the bending moments are different from the transverse shear forces derived by integrating the transverse shear stresses over the plate cross-section, thus creating a modelling inconsistency.

To remedy these drawbacks, Tessler, Di Sciuva and Gherlone developed the Refined Zigzag Theory (RZT) [77–80]. The kinematics of RZT are essentially those of FSDT enhanced by ZZ variables $\psi_i(x,y)$ that are multiplied by piecewise continuous transverse functions $\phi_i^{(k)}$. Hence,

in RZT

$$u_i^{(k)}(x,y,z) = u_{0i} + z\theta_i + \phi_i^{(k)}(z)\psi_i, \quad i = x, y \tag{2.27a}$$

$$u_z(x,y) = w_0(x,y). \tag{2.27b}$$

In this theory, the ZZ slopes $\beta_x^{(k)} = \partial\phi_x^{(k)}/\partial z$ and $\beta_y^{(k)} = \partial\phi_y^{(k)}/\partial z$ for u_x and u_y, respectively, are defined by the difference between the transverse shear rigidities $G_{xz}^{(k)}$ and $G_{yz}^{(k)}$ of layer k, and the effective transverse shear rigidity G_x and G_y of the entire layup,

$$\beta_i^{(k)} = \frac{G_i}{G_{iz}^{(k)}} - 1, \quad \text{and} \quad G_i = \left[\frac{1}{t}\sum_{k=1}^{N_l}\frac{t^{(k)}}{G_{iz}^{(k)}}\right]^{-1}, \quad i = x, y \tag{2.28}$$

where N_l is the total number of layers, and $t^{(k)}$ and t are the thickness of layer k and the total laminate thickness, respectively. RZT has shown excellent results compared to the 3D elasticity solutions by Pagano [20, 69] for both general composite laminations and sandwich constructions. RZT has also been extended to include transverse normal stretching and higher-order displacements for a ZZ theory of order {2,2} [81].

However, this first, displacement-based version of RZT still requires post-processing steps for accurate transverse stress predictions. To remedy this, Tessler [82] recently developed a mixed-variational approach for 1D beams using RMVT in a novel way, essentially splitting the variation of the full RMVT functional into two separate operations: first, a variation of the Lagrange multiplier functional for the compatibility condition, and second, a variation of the strain energy functional. The first step is used to derive an accurate assumption for the transverse shear stress. Integrating the RZT in-plane stress in Cauchy's axial equilibrium equation derives an expression for τ_{xz} in terms of second derivatives of the RZT in-plane displacement variables and known through-thickness functions. The second derivative terms are then replaced by ad-hoc stress functions that are determined in terms of the displacement unknowns themselves using the first variation of the Lagrange multiplier functional. Thus, the strain compatibility condition is not minimised as part of the full RMVT as was originally defined by Reissner [61]. The governing equations of the new theory, denoted by RZT$^{(m)}$, are then derived as the Euler-Lagrange equations of the strain-energy functional, and are found to provide accurate transverse shear stress results from the derived transverse shear stress assumption. In follow-up works, the formulation was extended to plates [83, 84] and then further to a $\{3, 2\}$ HOT [85].

In a similar manner, Murakami [86] enhanced the axiomatic FSDT expansion by including a zig-zag function, herein denoted as Murakami's ZZ function (MZZF), that alternatively takes the values of +1 or -1 at layer interfaces. Therefore, the slope purely depends on geometric differences between plies and is not based on transverse shear moduli. In addition, Murakami made independent, piecewise-parabolic assumptions for the transverse shear stresses and applied RMVT to obtain new governing equations. MZZF was subsequently applied to an AHOT of degree $\{3, 2\}$ by Toledano and Murakami [87]. In recent years, MZZF has been applied to functionally graded materials [45], sandwich structures [88,89] and in the framework of the Carrera Unified Formulation (CUF) [90,91]. Carrera [92] investigated the effect of including MZZF in first-order and higher-order displacement-based and mixed-variational theories, showing that

superior representation of displacements and stresses, combined with less computational cost, can be achieved by including a single ZZ term than a higher-order continuous term. On the other hand, Gherlone [54] showed that MZZF leads to inferior results than the RZT ZZ function for sandwiches with large face-to-core stiffness ratios and laminates with general layups. Thus, an accurate choice of the ZZ function seems to be of paramount importance. The relative accuracies of the RZT ZZ function and MZZF are compared further in Chapter 5 and 8.

2.2.4 Generalised and unified formulations

A multiscale approach for modelling the multifaceted structural behaviour of composite laminates in one unified model has been proposed by Williams [93]. The theory uses a general framework with nonlinear von Kármán displacement fields, and additional temperature and solute diffusion variables on two length scales, namely global and local, with the transverse basis functions of the two length scales enforced to be independent. This results in two sets of variationally consistent governing equations, such that the theory is capable of capturing, in a coupled fashion, the thermo-mechanical-diffusional phenomena of laminates at the micro-, meso- and macro levels simultaneously. The use of interfacial constitutive models allows the theory to account for delamination initiation and growth, as well as nonlinear elastic or inelastic interfacial constitutive relations, in a unified form. Williams [94] has shown that multi-length scale theories can be more computationally efficient than pure layerwise models as the order of the theory can be increased on both local and global levels. The displacement-based theory features $3(N_{og} + N_{ol}N_l)$ unknowns where N_{og} and N_{ol} are the global and local number of variables and N_l the number of layers. In general, $N_{og} = N_{ol} = 3$ is sufficient for accurate 3D stress field predictions as derived from the constitutive relations. In later work, Williams [95] developed an improved formulation by deriving the governing equations from the method of moments over different length scales, and enforcing the interfacial continuity of transverse stresses in a strong sense.

The notion of a generalised axiomatic expansion was developed further by Carrera in what is known as Carrera's Unified Formulation (CUF) [23, 96, 97], and its extension the Generalized Unified Formulation by Demasi (GUF) [24]. CUF is a hierarchical formulation where Taylor series or Lagrange polynomials are used to approximate the displacement fields throughout the cross-section [97]. This allows the order of the theory to be expressed as an input to the analysis. In this manner, the governing field equations are formulated based on a generalised axiomatic expansion. Theories of different order are easily implemented computationally without the need for separately deriving new field equations. The Taylor series or Lagrange polynomial expansion is not strictly limited to a function of the z-coordinate, such that bi-axial bending, torsion and warping can be modelled by expanding in the x- and y-coordinates. Thus, in the framework of CUF, the displacement field is expressed as the expansion of generic functions F_τ,

$$\boldsymbol{u} = F_\tau \boldsymbol{u}_\tau, \quad \tau = 1, 2, \ldots, N_o \tag{2.29}$$

where F_τ are individual functions of the coordinates x, y and z; $\boldsymbol{u}_\tau$ is the vector of displacement unknowns; N_o is the number of terms in the expansion, and according to the Einstein notation,

repeated indices denote summation. For example,

$$
\begin{aligned}
&u_x(x,y,z) = u_{x_1} + xu_{x_2} + yu_{x_3} + zu_{x_4} = F_\tau u_{x_\tau} \\
&u_y(x,y,z) = u_{y_1} + xu_{y_2} + yu_{y_3} + zu_{y_4} = F_\tau u_{y_\tau} \\
&u_z(x,y,z) = u_{z_1} + xu_{z_2} + yu_{z_3} + zu_{z_4} = F_\tau u_{z_\tau} \\
&\text{where} \quad F_1 = 1, \quad F_2 = x, \quad F_3 = y, \quad F_4 = z.
\end{aligned}
\tag{2.30}
$$

This compact notation allows the finite element stiffness matrix of the theory to be expressed in terms of a few fundamental nuclei that are through-thickness integrals of material stiffness terms multiplied by a combination of F_τ terms. Furthermore, the notation in Eq. (2.29) can be generalised to incorporate mixed-variational statements, such as RMVT. In this manner, classical and non-classical effects can be accounted for by increasing the order of the assumed fields without the need for further ad-hoc formulations. In this manner, CUF and GUF are powerful tools for benchmarking and comparing the accuracies of various theories.

2.3 Variable-stiffness laminates

The idea of tailoring the structural performance of composite laminates by spatially varying the pointwise fibre orientations has been explored since the early 1970's [98]. For example, early work by Hyer and Lee [99] and Hyer and Charette [100] showed that such variable angle tow (VAT) laminates can alleviate stress concentrations around holes by aligning the fibre paths with the directions of principle stress.

In recent years, the use of fibre reinforced composites in primary aircraft structures has led to increased interest in VAT technology. Numerous works have shown that tailoring the in-plane stiffness over the plate planform allows prebuckling stresses to be redistributed to supported regions, thereby increasing the critical buckling load [101–109]. Specifically, Gürdal et al. [102] have shown that varying the stiffness of the panel perpendicular to the direction of applied end compression results in greater improvements than varying the stiffness in the direction of loading. In this manner, van den Brink et al. [110] improved the buckling performance of a composite fuselage window section by 12% compared to an equivalent straight fibre laminate [110], whereas Alhajahmad et al. [111] alleviated the pressure pillowing of fuselage sections. Furthermore, Coburn et al. [112] investigated the concept of using VAT technology to design blade-stiffened wing panels with greater critical buckling loads, and lower Poisson's ratio mismatch between base plate and stiffener foot. In a follow-up study, the researchers reduced the mass of a representative blade-stiffened wing panel subject to static failure, buckling, compressive strain and manufacturing constraints by 10% compared to a baseline design [113].

Recent results show that VAT plates with linear fibre variations can be designed to exhibit smaller stiffness reductions in the postbuckling regime than their straight-fibre counterparts [114]. Furthermore, the optimum fibre orientations for increasing the buckling load are similar to those for minimising the transverse displacement in the postbuckling regime [115]. In this regard, an interesting application of variable-stiffness composites is in designing cylindrical shells with stable postbuckling paths. It is well known in the engineering community that

cylindrical shells are prone to collapse when loaded in axial compression beyond the buckling load. A direct consequence of this postbuckling instability is an extreme sensitivity to initial geometric imperfections and loading conditions, which can lead to actual buckling loads less than 50% of analytical predictions from linear eigenvalue analyses [116]. White and Weaver [117] have shown that this imperfection sensitivity can be effectively eliminated, thereby creating stable, plate-like postbuckling responses by tailoring the fibre paths across the surface of the cylindrical shell. The idea of introducing flat, plate-like behaviour in shells was also exploited by applying the variable stiffness concept to decouple the linear membrane-bending coupling that is characteristic of curved structures [118].

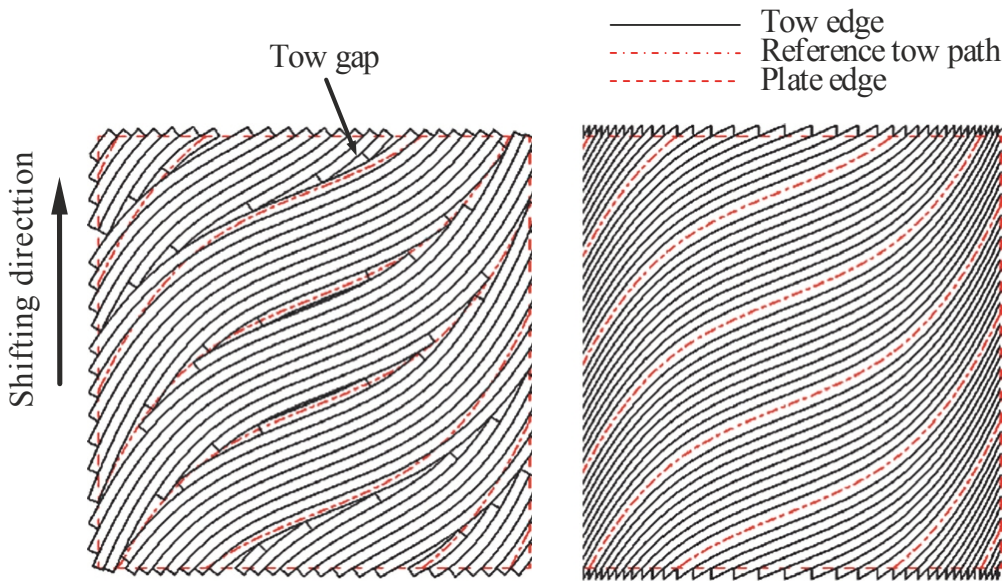

(a) AFP **(b)** CTS

Figure 2.4: Arrangements of steered fibre tows on a substrate manufactured using (a) the AFP and (b) the CTS technique. Due to the finite thickness of tows, tow overlaps or gaps (shown here) are inherently produced in AFP when shifting a tow perpendicular to a reference path. In CTS, the tows can be tessellated without gaps or overlaps. The figures have been reproduced and annotated from reference [119].

To date, the primary technology for manufacturing VAT laminates is Automated Fibre Placement (AFP), a manufacturing process originally developed in the 1980's to automate lamination of straight fibre laminates. AFP uses a robotic fibre placement head that deposits multiple pre-impregnated tows of "slit-tape" allowing cutting, clamping and restarting of single tows. While the robotic head follows a specific fibre path, tows are heated shortly before deposition and then compacted onto the substrate using a special roller. Due to the high fidelity of current robot technology, AFP machines can provide high productivity and handle complex geometries [120]. However, in AFP, steering is accomplished by bending the tows in-plane, which leads to local fibre buckling on the inside radii of the curved tow, and thus limits the steering radius of curvature [121]. Furthermore, if individual tows are placed next to each other by shifting the reference path along a specific direction, tow gaps and overlaps are inevitably required to cover the whole surface. Fayazbakhsh et al. [122] showed that the presence of gaps may reduce the optimised buckling load by up to 15% compared to pristine

designs.

To overcome the drawbacks of AFP machines the Continuous Tow Shearing (CTS) technique, which uses shear deformation to steer fibres at the point of application, was developed [119]. By tessellating tows on the substrate, this technique not only allows much tighter radii of curvature but tow gaps and overlaps are also avoided (see Figure 2.4). In recent characterisation work, Kim et al. [123] showed that CTS can produce impregnation quality similar to commercial prepreg. Most importantly for structural applications, CTS produces VAT laminates with fibre paths curved more than ten times those available from conventional AFP machines without producing tow cuts or resin pockets.

One feature of CTS is that in order to maintain the volume fraction of fibre the thickness of a tow inherently increases as it is sheared. The relation between unsheared tow thickness $t_0^{(k)}$ and sheared tow thickness $t^{(k)}$ of layer k is

$$t^{(k)} = \frac{t_0^{(k)}}{\cos\gamma^{(k)}} = t_0^{(k)} \sec\gamma^{(k)} \tag{2.31}$$

where $\gamma^{(k)}$ is the shearing angle of the tow at the point of application. Consequently, the thickness of a ply may locally increase by a factor of three if the fibre tow is sheared through an angle of 70°. As the laminate is cured on a tool plate, one side of the laminate remains flat, whereas the other resembles a curved panel. The effects of this asymmetric profile in terms of local three-dimensional stress fields, buckling loads and postbuckling behaviour is relatively unexplored. As part of this research project, the present author has published some work on the buckling and postbuckling behaviour of these variable-stiffness, variable-thickness panels [124, 125], and found that the structural behaviour is governed more by curved "shell-like" than flat "plate-like" kinematics. The details of this work are not elucidated further herein, and the interested reader is directed to references [124, 125].

Variable-stiffness composites are a promising technology for improving the efficiency of engineering structures due to the increased design space available for tailoring. To fully take account of this enhanced design freedom, efficient optimisation strategies have to be developed to allow rapid iterative design in industrial settings. Due to its modelling versatility and numerical robustness, most previous optimisation work has focused on designing AFP manufactured variable-stiffness panels using the Finite Element Method (FEM). Setoodeh et al. [103] performed an optimisation study in FE where the fibre orientation angles at the nodes are treated as design variables. A generalised reciprocal approximation was used that allowed the maximisation of buckling load to be carried out at each node separately. The authors noted that due to the non-convexity of the problem the optimisation results depend on the starting points. Ijsselmuiden et al. [126] addressed the problem of non-convexity by using lamination parameters as the design variables, and demonstrated buckling load improvements in excess of 100% compared to the optimum constant-stiffness designs. In a follow-up study, van Campen et al. [127] proposed a methodology for converting the optimal lamination parameter distribution into realistic fibre paths, taking into account constraints on in-plane fibre path curvature. Using a surrogate-based genetic algorithm (GA), Nik et al. [128] performed a multi-objective optimisation of in-plane stiffness and buckling load of a laminated plate with curvilinear fibre

paths. The researchers found that varying the fibre direction perpendicular to the direction of compression can improve the buckling load of a flat plate with unconstrained lateral edges by 116% compared to an optimised quasi-isotropic laminate. Later it was shown that gaps degrade and overlaps improve the structural performance along the in-plane stiffness/buckling load Pareto front, respectively [129].

The drawback of using the FEM in optimisation studies of VAT laminates is their computational cost. Even though buckling is a global structural phenomenon, improvements in buckling load due to variable fibre paths arise as a result of local stress redistributions, and to capture these accurately, local fibre variations need to be represented precisely using fine meshes. A number of optimisation studies have implemented numerical solution techniques that reduce the computational effort compared to FE solvers. Wu et al. [106] used a GA in combination with the Rayleigh-Ritz solution technique, and this technique was extended by Coburn et al. [113] to the study of blade-stiffened wing panels. Liu and Butler [108] performed a gradient-based mass-minimisation strategy with buckling load constraints for VAT panels specifically manufactured using the CTS technique. This study idealised the CTS panel as a flat plate with symmetric thickness variation and therefore did not account for curved shell kinematics. Groh and Weaver [125] used a differential quadrature implementation (see Section 2.4) of an asymptotic numerical method to conduct a minimum-mass optimisation study on CTS panels, accounting for the influence of the coupled fibre angle-thickness variations, as well as the ensuing geometric effects of the asymmetric cross-sectional profile. Raju et al. [130] solved the prebuckling, buckling and initial postbuckling problems of flat VAT plates using a similar differential quadrature numerical scheme, and then minimised the end-shortening strain in the postbuckling regime for a fixed compressive load. This latter work is based on the two-step optimisation framework developed by Wu, Raju and Weaver [131]. In the first step, an optimum layup in lamination parameter space, which is represented using B-splines, is sought via a gradient-based globally convergent method of moving asymptotes. The convexity property of B-splines between interpolation grid points means that the lamination parameters automatically satisfy predefined feasibility constraints between discretisation points, even if the feasibility constraints are only explicitly specified at the interpolation points. The second step then involves retrieving feasible fibre orientations to match the lamination parameter space using a GA.

Whereas a number of works in the literature deal with global structural phenomena of tow-steered composites laminates, such as vibration and buckling, relatively little work has been conducted on localised higher-order effects in these laminates. Akhavan and Ribeiro [132] and Akhavan et al. [133] investigated the natural modes of vibration, and nonlinear bending deflections and stresses of tow-steered composites. A Reddy-type third-order shear deformable theory was solved via a p-version FEM approach, and a variety of different edge conditions, including plates clamped along all four edges, were investigated. As mentioned in Section 2.2.1 and elucidated in detail in Chapter 3, the Reddy-type model used by these researchers leads to static inconsistencies at the clamped boundaries. Furthermore, as a displacement-based theory, the transverse shear stresses were derived by integrating the in-plane stresses in Cauchy's equilibrium equations via a post-processing step. In further work, Akhavan and Ribeiro [134] extended the vibrational analysis into the nonlinear regime using a FSDT model. Akhavan and

Ribeiro also point out that tow-steered laminates can be used effectively to tailor deflections and stresses locally in order to improve damage resistance in certain applications. Coburn et al. [112, 113] accounted for the effect of transverse shear deformation on the buckling behaviour of tow-steered, blade-stiffened wing panels. Akbarzadeh et al. [135] studied the effects of transverse shear deformation on the vibrational and buckling response of moderately thick AFP panels with gaps and overlaps using a Reddy-type third-order shear deformable theory. The authors corroborate the findings of the present author published in [136] that transverse shear deformation has a bigger impact on tow-steered than straight-fibre laminates. Yazdani and Ribeiro [137] and Yazdani et al. [138] recently published LWT extensions of the earlier works by Akhavan and co-workers cited above. Finally, Tornabene et al. [139] studied the free vibrations of doubly curved, variable-stiffness shells using a generalised higher-order model implemented via CUF using a local differential quadrature method. Overall, there is very little work in the literature regarding detailed analyses of full 3D stress fields in tow-steered laminates and how these could be tailored to optimise structures for specific objectives. Hence, the present work aims to contribute research in this field.

2.4 Differential quadrature method

The Differential Quadrature Method (DQM) has been shown to be a fast, accurate and computationally efficient technique for solving the variable-coefficient, higher-order differential equations for bending [136], buckling [107, 124], and postbuckling of VAT plates [109, 140] and cylindrical shells [117, 125, 141]. Raju et al. [140] validated the accuracy of the DQM approach in modelling variable-stiffness plates for free, simply-supported and clamped plate boundary conditions. In comprehensive surveys by Viola, Tornabene and Fantuzzi, the DQM was effectively applied to analyse the free vibration [142, 143] and static behaviour [144] of doubly-curved, straight-fibre laminates based on a large number of higher-order shear deformation theories.

Differential quadrature (DQ) is a numerical discretisation technique proposed by Bellman et al. [145], that approximates the partial derivative of a functional field with respect to a specific spatial variable using a linear weighted sum of all the functional values in the domain. For example, the nth partial derivative of function $f(x)$ at the ith discretisation point is

$$\frac{\partial^n f(x_i)}{\partial x^n} = A_{ij}^{(n)} f(x_j), \quad i = 1, 2, \ldots, N_p \tag{2.32}$$

where x_i is the set of N_p discretisation points in the x-direction, typically defined by the non-uniform Gauss-Lobatto-Chebychev distribution, $A_{ij}^{(n)}$ are the weighting coefficients of the nth derivative, and repeated index j means summation from 1 to N_p. The same technique is easily extended to the remaining two spatial dimensions to compute mixed derivatives.

The key to applying DQ is finding the value of the weighting coefficients for any order derivative. Bellman et al. [145] originally proposed two methods to obtain the weighting coefficients. The first solves a set of linear algebraic equations of the Vandermonde form exactly, thereby fitting a generalised $N_p - 1$ polynomial through the N_p grid points, and solving for the polynomial coefficients by satisfying the linear constrained relation between all polynomials. The second computes the weighting coefficients using Legendre polynomials, whereby the

discretisation points are constrained to the roots of the nth order shifted Legendre polynomials. In the former approach, the weighting coefficients cannot be determined robustly due to ill-conditioning of the Vandermonde coefficient matrix when $N_p > 13$, and in the latter, the fixed grid distribution restricts the application of DQM to specific problems.

To overcome these deficiencies, Shu and Richard [146,147] proposed the Generalised Differential Quadrature (GDQ). The key insight in GDQ is that when the interpolating polynomials are based on Lagrange polynomials, Lagrange trigonometric polynomials or the cardinal sine functions, the coefficient matrix of the underlying set of interpolation equations is the identity matrix, and therefore always invertible. In this manner, the interpolation coefficient matrix g_k for a Lagrangian polynomial basis [148] is given by

$$\begin{aligned} g_k(x) &= \frac{m(x)}{(x-x_k)m^{(1)}(x_k)}, \quad k = 1, 2, \ldots, N_p \\ \text{where} \quad m(x) &= \prod_{j=1}^{N_p}(x-x_j) \quad \text{and} \quad m^{(1)}(x_i) = \prod_{k=1,k\neq i}^{N_p}(x_i - x_k) \end{aligned} \tag{2.33}$$

and this leads to the weighting coefficients of the derivatives $A_{ij}^{(n)}$,

$$A_{ij}^{(1)} = \frac{1}{x_j - x_i} \prod_{k=1,k\neq i,j}^{N_p} \frac{x_i - x_k}{x_j - x_k} \quad \text{for} \quad i \neq j \quad \text{and} \quad A_{ii}^{(1)} = \sum_{k=1,k\neq i}^{N_p} \frac{1}{x_i - x_k}. \tag{2.34}$$

Subsequently, all higher order weighting coefficients are obtained by direct matrix multiplication, i.e. $[A^{(m)}] = [A^{(1)}][A^{(m-1)}]$, with $m = 2, 3, \ldots, N_p - 1$ [149]. In this manner, any set of linear differential equations can be written as a linear system of algebraic equations by replacing the differential operators with the weighting matrix in Eq. (2.32). Thus, the unknown functional values $f(x_i)$ at each grid point are found by solving the system of equations with the appropriate boundary conditions. A comprehensive historical survey of the GDQ and detailed derivations of the weighting coefficients are provided in the recent review by Tornabene et al. [150].

The advantage of the DQM is that the differential-algebraic relation of Eq. (2.32) allows differential equations to be solved in the strong form, i.e. the differential relations are solved exactly at each grid point, rather than in an average sense over the whole domain, as is the case in the classic weak-form FEM based on the generalised Galerkin method of weighted residuals. This means that both essential and natural boundary conditions are enforced along the boundary points, and as a result local stress gradients towards boundaries are captured with relatively few degrees of freedom. In the weak-form FEM, the natural boundary conditions are not enforced explicitly but the solution generally converges to satisfy the natural boundary condition with increasing mesh density.

Recently, a research group at the University of Bologna has shown the merits of a strong-form FEM by discretising the computational domain into multiple GDQ elements, and enforcing continuity of displacements and stresses at the interfaces [150]. The latter feature of stress continuity is especially valuable in post-processing accurate transverse stresses from Cauchy equilibrium equations [151], whereas classic weak-form C^0-continuous finite elements often require smoothing algorithms [152]. This coupled DQM-FEM approach furthers the applicability of the

classic GDQ from the relatively simple geometries typically analysed in research environments to more general applications by taking advantage of the fidelity of the FEM to model arbitrarily shaped domains. Furthermore, GDQ elements form the basis of a versatile hp-type FEM as the interpolating polynomial order and number of elements in the mesh are easily adaptable in numerical codes due to the existence of closed-form solutions for the GDQ weighting matrix $A_{ij}^{(n)}$ for any number of grid points.

As the DQM solves boundary value problems in the strong form, the appropriate displacement and force boundary conditions must be satisfied to guarantee a unique and converged solution. If there is only one boundary condition at each discretised boundary point, the application of the boundary conditions is straightforward. However, when there is more than one boundary condition at each boundary point, say a displacement and stress resultant condition in plate bending problems, different methods for applying these dual boundary conditions are possible, and a number of different techniques are discussed in the following.

The first method, introduced by Bert et al. [153], is the so called δ-technique. The appropriate essential conditions are discretised directly at the boundary points, whereas the appropriate natural conditions are applied at the adjacent points at a distance δ from the boundary. As the natural condition is not directly implemented at the boundary point, the accuracy of the results depends on the magnitude of δ. In general, the smaller the value of δ the more accurately the natural condition is defined. On the other hand, if the mesh spacing δ is considerably smaller than all others in the grid, then the DQM weighting coefficient may become ill-conditioned and lead to oscillations in the results [149].

Wang and Bert [154] presented a method to overcome the drawbacks of the δ-technique. The essential boundary condition is still implemented numerically, whereas the natural boundary conditions are included in the DQM weighting coefficient matrices. This approach exactly satisfies the natural condition and thus provides very accurate results for homogeneous boundary conditions, for example, simply-supported boundary conditions. However, for non-homogeneous conditions, the implementation is more cumbersome [155] and produces large errors for clamped boundary conditions.

Shu and Du [156] substituted the essential boundary conditions directly into the governing field equilibrium equations, whereas the natural conditions were discretised in DQM form. By coupling the natural conditions of the two sets of opposite edges, the functional values at these points can be found and then substituted back into the governing field equations. Although this method efficiently implements the boundary conditions, it becomes very difficult and time consuming to couple the natural conditions when all functional values in the computational domain are present.

Du et al. [157, 158] introduced another methodology to overcome the difficulties of implementing the dual boundary condition. They noted that the boundary conditions introduce a redundancy in the equilibrium equations at the boundary grid points and the set of adjacent grid points. Thus, they replaced the governing field equations at the boundary and the adjacent grid points with the discretised boundary equations. In essence, this means that individual rows in the DQ stiffness matrix, which pertain to governing field equations at the boundary points, are replaced with new rows that represent the discretised boundary conditions. The advantage

of this approach is its numerical versatility and ease of implementation, and also introduced the notion of separating the domain into sets of internal and boundary points.

Shu and Du [159] then generalised this approach for the application to any set of boundary equations by writing both the essential and natural conditions in algebraic DQM form. One set of boundary conditions, typically the essential boundary conditions, are taken as the equations for the boundary points themselves, whereas the second set of boundary conditions is taken for the adjacent interior points. The computational domain is then split into an array of interior points with functional unknowns U_i, and an array of boundary points with boundary unknowns U_b. The governing field equations are discretised in DQM form at the interior points, whereas boundary equations are discretised at the boundary points. As a result, there are two sets of governing equations written in terms of the unknown arrays U_i and U_b,

$$\text{Field equations:} \quad \boldsymbol{K_{ii}} U_i + \boldsymbol{K_{ib}} U_b = F_i \tag{2.35a}$$

$$\text{Boundary conditions:} \quad \boldsymbol{K_{bi}} U_i + \boldsymbol{K_{bb}} U_b = F_b \tag{2.35b}$$

where $\boldsymbol{K_{ii}}$ and $\boldsymbol{K_{ib}}$ are the stiffness matrices of the governing field equations multiplying the arrays of internal and boundary unknowns, respectively, $\boldsymbol{K_{bi}}$ and $\boldsymbol{K_{bb}}$ are the analogous stiffness matrices for the boundary equations, and F_i and F_b are the arrays of externally applied loads of the internal field and boundary equations, respectively. Therefore the functional values U_i and U_b at the internal and boundary grid points can be found separately as follows:

$$U_i = \left[\boldsymbol{K_{ii}} - \boldsymbol{K_{ib}} \boldsymbol{K_{bb}}^{-1} \boldsymbol{K_{bi}}\right]^{-1} \cdot \left(F_i - \boldsymbol{K_{ib}} \boldsymbol{K_{bb}}^{-1} F_b\right) \tag{2.36a}$$

$$U_b = \boldsymbol{K_{bb}}^{-1} \cdot \left(F_b - \boldsymbol{K_{bi}} U_i\right). \tag{2.36b}$$

Due to its general applicability, this latter approach by Shu and Du [159] is implemented for all problems analysed herein. For these problems, the stiffness matrices $\boldsymbol{K_{ii}}$, $\boldsymbol{K_{ib}}$, $\boldsymbol{K_{bi}}$ and $\boldsymbol{K_{bb}}$ are comprised of products of the DQ weighting matrices $A_{ij}^{(n)}$ and laminate structural properties, such as membrane and bending rigidities, and transverse shear and normal correction factors.

Chapter 3

Displacement-Based Axiomatic Theories

Displacement-based axiomatic theories have received the most attention in the field of HOTs. These theories are based on relatively intuitive ad-hoc displacement field assumptions from which the governing field equations and boundary conditions are derived using the PVD. A particular set of HOTs can be formulated using Eq. (2.24) and the different shear shape functions in Table 2.1. One commonality of these theories is that Kirchhoff rotations $w_{0,x}$ and $w_{0,y}$ feature explicitly in the displacement field assumptions. The inclusion of the Kirchhoff rotations maintains an intuitive resemblance to the CLA displacement field, and is featured in the pioneering works of Ambartsumyan [35] as early as 1958. Later, Reddy [34] derived a third-order theory with the same number of unknowns as FSDT by enforcing shear tractions to vanish at the top and bottom surfaces. This variable condensation step invariably introduced the Kirchhoff rotations into the displacement assumption. Reddy's theory has received significant amount of attention in the literature and is a popular benchmarking solution for new HOTs.

This chapter reveals certain static inconsistencies that arise in this particular class of displacement-based HOT written in the form of Eq. (2.24). Section 3.1 shows that the essential boundary condition of vanishing Kirchhoff rotations perpendicular to clamped edges that arises in these theories, i.e. $w_{0,x} = 0$ and $w_{0,y} = 0$, is physically inaccurate as the rotation can be non-zero in the presence of transverse shear deformation. Furthermore, this boundary condition overconstrains the structure leading to underpredictions in transverse bending deflections and overpredictions of axial stresses. Finally, in these theories, the transverse shear force derived from the constitutive equations erroneously vanishes at clamped edges.

Next, Section 3.2 shows that generalised higher-order theories written in the form of a power series, as in Carrera's [23] or the Generalized Unified Formulation [24], do not produce this inconsistency. Indeed, the condition of vanishing transverse shear tractions at the top and bottom surfaces should not be applied *a priori* in the displacement-based theories as the transverse shear strains inherently vanish if the order of the theory is sufficient to capture all higher-order effects. Finally, a metric for assessing the order of the expansion required to model a particular laminate is developed, and a material- and geometry-dependent shear correction factor is derived, that provides more accurate solutions of bending deflection than the classical value of 5/6.

3.1 Static inconsistencies in higher-order theories

3.1.1 Definition of a baseline problem

As shown in Figure 3.1, the analysis presented herein pertains to a plate of thickness t, infinitely wide in the lateral y-direction, with finite length L in the x-direction, and support conditions

defined along the infinitely wide edges $x = x_A$ and $x = x_B$, which are henceforth referred to as the ends of the plate. This configuration is chosen to reduce the structural complexity by enforcing all unknown fields to be functions of the x- and z-coordinates only, i.e. reducing the analysis to a beam in plane strain. As a result, the discussion only deals with the essential boundary condition $\delta w_{0,x} = 0$ at edges $x = x_A$ and $x = x_B$ allowing for simpler derivations and clearer discussion of the arguments made. However, without loss of generality, all comments apply to two-dimensional plates and shells because the inclusion of the lateral displacement field u_y in the principle of virtual displacements introduces the essential boundary condition $\delta w_{0,y} = 0$ at clamped edges $y = y_A$ and $y = y_B$.

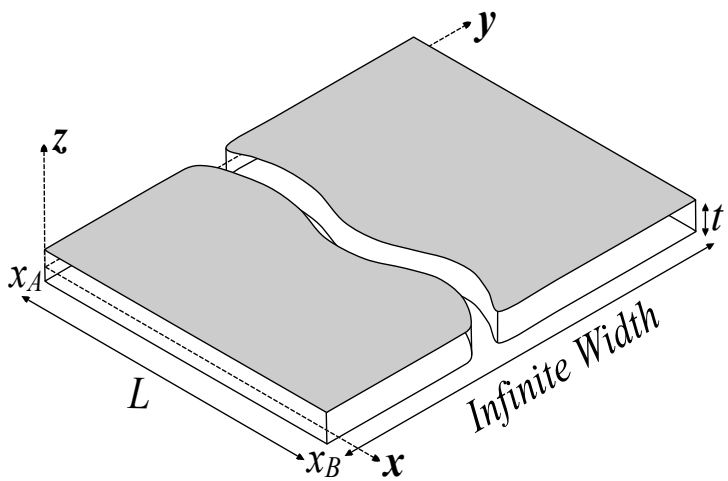

Figure 3.1: Schematic diagram of an infinitely wide plate with arbitrary boundary conditions at the two supports $x = x_A$ and $x = x_B$.

Consider an infinitely wide 0° orthotropic layer in cylindrical bending loaded by an arbitrary transverse loading of magnitude q_0. All analytical formulations presented are solved in the strong form using an implementation of the DQM in Matlab. This pseudo-spectral numerical technique was introduced in Section 2.4, and allows the governing differential equations to be converted into algebraic ones by replacing the differential operators with weighting matrices that operate on the functional unknowns at the grid points. Based on an initial mesh convergence study, a non-uniform Chebychev-Gauss-Lobatto grid with 31 points was chosen. For all problems solved, the deflection and stress results are stated as normalised quantities defined as follows:

$$\bar{w} = \frac{E_{11}t^2}{q_0 L^4}\int_{-\frac{t}{2}}^{\frac{t}{2}} u_z \mathrm{d}z, \qquad \bar{\sigma}_x = \frac{t^2}{q_0 L^2}\sigma_x, \qquad \bar{\tau}_{xz} = \frac{1}{q_0}\tau_{xz}. \tag{3.1}$$

Therefore, absolute magnitudes of material properties play no role, only the orthotropy ratio E_{11}/G_{13}, thickness to length ratio t/L, the Poisson's ratios $v_{12} = v_{13} = 0.25$, and the boundary conditions are of significance.

A 3D FEM model was implemented in the commercial software package Abaqus and used as a benchmark to validate the results. For all cases considered, the plate was discretised with 400 and 200 linear C3D8R elements along the axial length and through the thickness, respectively. To enforce the plane-strain condition in the lateral direction, a single C3D8R element was applied along the width and lateral expansion prevented. The ensuing model of

80,000 elements yields converged results to within 0.1% for all results presented. All externally applied transverse loading is split equally between the top and bottom surfaces of the plate in order to minimise local through-thickness deformations.

3.1.2 First-order shear deformation theory

To begin, we analyse the cylindrical bending of the infinitely wide plate using FSDT. One variant of FSDT is Mindlin's plate theory in which the functional unknowns are the midplane displacement u_0, the transverse deflection w_0 and the average rotation of the cross-section θ. The average rotation of the cross-section may be assumed to include the Kirchhoff bending rotation $-w_{0,x}$ and an average shear rotation γ. Thus, an alternative way of writing the in-plane displacement assumption of Mindlin's theory is to replace θ with $-w_{0,x} + \gamma$. In the following two examples, we investigate the effect this has on the governing field equations and boundary conditions as derived in a variationally consistent manner from the PVD.

3.1.2.1 Mindlin plate

For cylindrical bending, Mindlin's plate theory assumes axial and transverse displacements in the following form:

$$u_x = u_0 + z\theta \tag{3.2a}$$

$$u_z = w_0. \tag{3.2b}$$

Using the kinematic relations between strains and displacements, the axial strain ϵ_x and transverse shear strain γ_{xz} are given by

$$\epsilon_x = u_{x,x} = u_{0,x} + z\theta_{,x} \tag{3.3a}$$

$$\gamma_{xz} = u_{z,x} + u_{x,z} = w_{0,x} + \theta. \tag{3.3b}$$

The principle of virtual displacements states that a body is in equilibrium if the virtual work done by the equilibrium forces when the body is perturbed by a virtual amount $\delta\boldsymbol{u}$ from the true configuration $\boldsymbol{u}$, is zero. With regard to an infinitely wide plate subjected to cylindrical bending in the plane-strain condition, the virtual work done by the virtual displacement $\delta\boldsymbol{u}$ is

$$\delta\Pi = \int_V \left(\sigma_x \delta\epsilon_x + \tau_{xz}\delta\gamma_{xz}\right) \mathrm{d}V - \int q\delta w_0 \mathrm{d}x - \int_{S_2} \left(\hat{\sigma}_x \delta u_x + \hat{\tau}_{xz}\delta w_0\right) \mathrm{d}S_2 = 0 \tag{3.4}$$

where q is the net transverse pressure on the top and bottom surfaces of the plate, and S_2 is the boundary surface on which the stresses $\hat{\sigma}_x$ and $\hat{\tau}_{xz}$ are prescribed. Substituting the strains of Eq. (3.3) into the PVD statement Eq. (3.4) yields

$$\delta\Pi = \int_V \left[\sigma_x \delta\left(u_{0,x} + z\theta_{,x}\right) + \tau_{xz}\delta\left(w_{0,x} + \theta\right)\right] \mathrm{d}V - \int q\delta w_0 \mathrm{d}x - \int_{S_2} \left[\hat{\sigma}_x \delta\left(u_0 + z\theta\right) + \hat{\tau}_{xz}\delta w_0\right] \mathrm{d}S_2 = 0. \tag{3.5}$$

The stresses σ_x and τ_{xz} are integrated through the thickness to define the stress resultants N, M and Q as follows:

$$N = \int_{-t/2}^{t/2} \sigma_x \mathrm{d}z, \quad M = \int_{-t/2}^{t/2} z\sigma_x \mathrm{d}z, \quad Q = \int_{-t/2}^{t/2} k\tau_{xz} \mathrm{d}z \tag{3.6}$$

where N is the in-plane load per unit width, M is the bending moment per unit width, Q is the transverse shear force per unit width and k is the pertinent shear correction factor. The shear correction factor is needed to energetically account for the actual parabolic shear stress profile, and is assumed to be equal to 5/6 [25]. Thus, Eq. (3.5) reduces to

$$\delta\Pi = \int \left[N\delta u_{0,x} + M\delta\theta_{,x} + Q\delta w_{0,x} + Q\delta\theta\right] \mathrm{d}x - \int q\delta w_0 \mathrm{d}x - \left[\hat{N}\delta u_0 + \hat{M}\delta\theta + \hat{Q}\delta w_0\right]_{x_A,x_B} = 0. \tag{3.7}$$

where x_A and x_B are the two supported ends of the infinitely wide plate. The governing field equations and boundary conditions are derived using the calculus of variations. Integrating by parts those variational terms that feature derivatives gives

$$\delta\Pi = -\int \left[N_{,x}\delta u_0 + M_{,x}\delta\theta + Q_{,x}\delta w_0 - Q\delta\theta\right] \mathrm{d}x - \int q\delta w_0 \mathrm{d}x + \left[\left(N - \hat{N}\right)\delta u_0 + \left(M - \hat{M}\right)\delta\theta + \left(Q - \hat{Q}\right)\delta w_0\right]_{x_A,x_B} = 0. \tag{3.8}$$

The governing field equations and boundary conditions are derived from the Euler-Lagrange equations of the integral expressions and the expression evaluated at x_A and x_B, respectively. These governing field equations are

$$\delta u_0 : \quad N_{,x} = 0 \tag{3.9a}$$

$$\delta\theta : \quad M_{,x} - Q = 0 \tag{3.9b}$$

$$\delta w_0 : \quad Q_{,x} - q = 0 \tag{3.9c}$$

whereas the essential and natural boundary conditions are

$$\delta u_0 = 0 \quad \text{or} \quad N - \hat{N} = 0 \tag{3.10a}$$

$$\delta\theta = 0 \quad \text{or} \quad M - \hat{M} = 0 \tag{3.10b}$$

$$\delta w_0 = 0 \quad \text{or} \quad Q - \hat{Q} = 0. \tag{3.10c}$$

Modelling a clamped boundary condition in Mindlin's plate theory is relatively straightforward. Assuming that both ends x_A and x_B are rigidly built-in, then the in-plane displacement, transverse displacement and plate cross-sectional rotation are zero. Thus,

$$u_0 = \theta = w_0 = 0 \tag{3.11}$$

Note, this boundary condition does not specify that the rotational component $w_{0,x} = 0$ at the ends x_A and x_B. In fact, we may have a non-zero value of $w_{0,x}$ due to the presence of transverse shearing. Furthermore, we know from basic equilibrium that a non-zero shear force

Q is required at the clamped edges. Using the definition of Q in Eq. (3.6) with the transverse shear constitutive equation and kinematics, we have

$$Q = \int_{-t/2}^{t/2} k\tau_{xz}\mathrm{d}z = \int_{-t/2}^{t/2} kG_{xz}\gamma_{xz}\mathrm{d}z = \int_{-t/2}^{t/2} kG_{xz}\left(w_{0,x} + \theta\right)\mathrm{d}z. \tag{3.12}$$

Thus, for a clamped edge with $\theta = 0$ the value of $w_{0,x}$ defines the magnitude of the shear force at the support. In Kirchhoff's plate theory, the shear rotation is assumed to be zero, such that the clamped boundary condition needs to be enforced by setting $w_{0,x} = 0$. Physically, this boundary condition is reached asymptotically as the thickness to length ratio t/L of the plate approaches zero. Because all plates have finite thickness, and thus finite shear deformation, imposing the condition $w_{0,x} = 0$ is physically incorrect in a shear-deformable theory and leads to inaccuracies as the thickness increases.

3.1.2.2 Alternative first-order shear theory

The observations of the previous section are compared to a theory where the average rotation of the cross-section θ is replaced by a sum of the Kirchhoff rotation $w_{0,x}$ and the shear rotation γ. Under these circumstances the displacement field is given by

$$u_x = u_0 + z\left(\gamma - w_{0,x}\right) \tag{3.13a}$$

$$u_z = w_0 \tag{3.13b}$$

which leads to the new strain field

$$\epsilon_x = u_{x,x} = u_{0,x} + z\left(\gamma_{,x} - w_{0,xx}\right) \tag{3.14a}$$

$$\gamma_{xz} = u_{z,x} + u_{x,z} = \gamma. \tag{3.14b}$$

Performing the same variational analysis outlined in the previous section, using the PVD definition Eq. (3.4) and the new strain field Eq. (3.14), results in

$$\begin{aligned}\delta\Pi = &-\int\left[N_{,x}\delta u_0 + M_{,x}\delta\gamma + M_{,xx}\delta w_0 - Q\delta\gamma\right]\mathrm{d}x - \int q\delta w_0\mathrm{d}x + \\ &\left[\left(N - \hat{N}\right)\delta u_0 + \left(M - \hat{M}\right)\delta\gamma + \left(\hat{M} - M\right)\delta w_{0,x} + \left(M_{,x} - \hat{Q}\right)\delta w_0\right]_{x_A,x_B} = 0\end{aligned} \tag{3.15}$$

where N, M and Q are as previously defined in Eq. (3.6). The governing field equations derived from the integral expressions are

$$\delta u_0: \quad N_{,x} = 0 \tag{3.16a}$$

$$\delta\gamma: \quad M_{,x} - Q = 0 \tag{3.16b}$$

$$\delta w_0: \quad M_{,xx} + q = 0 \tag{3.16c}$$

whereas the essential and natural boundary conditions at x_A and x_B are

$$\delta u_0 = 0 \quad \text{or} \quad N - \hat{N} = 0 \tag{3.17a}$$

$$\delta\gamma = 0 \quad \text{or} \quad M - \hat{M} = 0 \tag{3.17b}$$

$$\delta w_{0,x} = 0 \quad \text{or} \quad \hat{M} - M = 0 \tag{3.17c}$$

$$\delta w_0 = 0 \quad \text{or} \quad M_{,x} - \hat{Q} = 0. \tag{3.17d}$$

A number of striking observations can be made about this system of equations. First, the third equilibrium equation Eq. (3.16c) is the same as the governing field equation of Kirchhoff's theory, and can be derived from Mindlin's equilibrium equations by combining Eq. (3.9b) and (3.9c). This means that in the present theory, the second equilibrium equation Eq. (3.16b) is already incorporated in the third equilibrium equation Eq. (3.16c). This result suggests that Eq. (3.16b) is redundant and can be eliminated, which reverts the equations back to Kirchhoff's classical theory.

The same redundancy is also shown in the boundary conditions. The natural boundary conditions in Eq. (3.17b) and (3.17c) are the same. Solving the boundary value problem of differential equilibrium equations (3.16) in a mathematically consistent manner requires four boundary conditions at each end, i.e. eight boundary conditions in total. For simply supported boundary conditions, with $M = 0$ at either end, we thus only have six boundary conditions to apply due to this redundancy. It is of course still possible to solve the governing field equations by assuming mode shapes for u_0, w_0 and γ that satisfy the boundary conditions. However, the problem in itself is not mathematically well-determined.

In fact, if we consider clamped boundary conditions we fail to solve the problem at all. If both x_A and x_B are both rigidly built-in, the boundary conditions $u_0 = w_0 = 0$ need to be satisfied. The bending moment M is non-zero at both ends, such that a value for both γ and $w_{0,x}$ needs to be prescribed on the boundary. For a generic loading q, the values of both γ and $w_{0,x}$ are unknown as both γ and w_0 are variables of the theory. Thus, the only condition we can apply to adequately constrain the boundary value problem is $\gamma = w_{0,x} = 0$ if we are not to prescribe an arbitrary non-zero value to either of these variables.

This statement causes two anomalies. First, we know that $w_{0,x}$ is in fact non-zero at the boundary due to the presence of transverse shearing. Second, if $\gamma(x_A, x_B) = 0$ then the transverse shear force vanishes at the boundary. Hence,

$$Q_{x_A,x_B} = \int_{-t/2}^{t/2} k\tau_{xz}(x_A, x_B)\mathrm{d}z = \int_{-t/2}^{t/2} kG_{xz}\gamma_{xz}(x_A, x_B)\mathrm{d}z = \int_{-t/2}^{t/2} kG_{xz}\gamma(x_A, x_B)\mathrm{d}z = 0 \tag{3.18}$$

where the shear strain $\gamma_{xz} = \gamma$ according to Eq. (3.14b). However, from the equilibrium of bending moments and transverse shear forces we know that the shear force is finite at the supports x_A and x_B.

3.1.3 Higher-order theories featuring Kirchhoff rotation

In FSDT, the presence of the Kirchhoff rotation $w_{0,x}$ introduces two critical inconsistencies. The argument presented in the previous section is now extended to higher-order theories. Reddy's third-order theory is used as an example but the observations apply to any higher-order theory that is written in the general form of Eq. (2.24). These include, but are not limited to, the

theories of Ambartsumyan [35], Touratier [37], Soldatos [38] and Karama [39].

3.1.3.1 Reddy's third-order theory

To derive Reddy's third-order theory we start with a cubic expansion of the in-plane displacement field,

$$u_x = u_0 + z\theta + z^2\zeta + z^3\xi \tag{3.19a}$$

$$u_z = w_0 \tag{3.19b}$$

where θ is the average rotation of the cross-section, and ζ and ξ are higher-order rotations. The tractions at the top and bottom surfaces $z = \pm t/2$ are known *a priori* and this boundary condition is thus enforced in the in-plane displacement field. The transverse shear from the kinematic relations is given by

$$\gamma_{xz} = u_{x,z} + u_{z,x} = (w_{0,x} + \theta) + 2z\zeta + 3z^2\xi. \tag{3.20}$$

Assuming zero shear tractions at the top and bottom surfaces $z = \pm t/2$, the transverse shear strain must vanish accordingly. Hence,

$$\begin{aligned} \gamma_{xz}\left(\pm t/2\right) = 0 \Rightarrow \left(w_{0,x} + \theta\right) \pm t\zeta + \frac{3}{4}t^2\xi = 0 \\ \therefore \zeta = 0 \quad \text{and} \quad \xi = -\frac{4}{3t^2}\left(w_{0,x} + \theta\right). \end{aligned} \tag{3.21}$$

Thus, the second-order rotation ζ is eliminated from the in-plane displacement expansion Eq. (3.19a) due to symmetry, and the third-order rotation ξ is replaced by a term involving the average rotation θ and Kirchhoff rotation $w_{0,x}$. The modified displacement field reads

$$u_x = u_0 + z\theta - \frac{4}{3t^2}z^3\left(w_{0,x} + \theta\right) \tag{3.22a}$$

$$u_z = w_0 \tag{3.22b}$$

and the strain field is given by

$$\epsilon_x = u_{0,x} + z\theta_{,x} - \frac{4}{3t^2}z^3\left(w_{0,xx} + \theta_{,x}\right) \tag{3.23a}$$

$$\gamma_{xz} = \left(\theta + w_{0,x}\right)\left(1 - \frac{4}{t^2}z^2\right). \tag{3.23b}$$

The governing field equations and boundary conditions are derived by substituting the new strain field Eq. (3.23) into the PVD of Eq. (3.4). Thus,

$$\begin{aligned} \delta\Pi = -\int \left[N_{,x}\delta u_0 + M_{,x}\delta\theta + c_1P_{,xx}\delta w_0 - c_1P_{,x}\delta\theta + Q_{,x}\delta w_0 - Q\delta\theta - c_2R_{,x}\delta w_0 + c_2R\delta\theta\right]\mathrm{d}x \\ - \int q\delta w_0 \mathrm{d}x + \left[\left(N - \hat{N}\right)\delta u_0 + \left(M - \hat{M} - c_1P + c_1\hat{P}\right)\delta\theta + \right. \end{aligned}$$

$$\left(Q - \hat{Q} - c_2 R + c_1 P_{,x}\right) \delta w_0 + \left(c_1 \hat{P} - c_1 P\right) \delta w_{0,x}\Big]_{x_A, x_B} = 0 \quad (3.24)$$

where $c_1 = \dfrac{4}{3t^2}$ and $c_2 = \dfrac{4}{t^2}$, and N and M are as previously defined in Eq. (3.6). The higher-order moment P, transverse shear force Q and higher-order transverse shear force R are given by

$$P = \int_{-t/2}^{t/2} z^3 \sigma_x \mathrm{d}z, \quad Q = \int_{-t/2}^{t/2} \tau_{xz} \mathrm{d}z, \quad R = \int_{-t/2}^{t/2} z^2 \tau_{xz} \mathrm{d}z. \quad (3.25)$$

Note that the shear correction factor k is no longer required in the definition of the transverse shear force Q because a parabolic shear strain profile is assumed.

The governing field equations and boundary conditions are the Euler-Lagrange equations of the virtual displacement statement Eq. (3.24). The field equations from the integral expressions are

$$\delta u_0 : \quad N_{,x} = 0 \quad (3.26a)$$

$$\delta \theta : \quad M_{,x} - c_1 P_{,x} - Q + c_2 R = 0 \quad (3.26b)$$

$$\delta w_0 : \quad c_1 P_{,xx} + Q_{,x} - c_2 R_{,x} + q = 0 \quad (3.26c)$$

and the boundary conditions at the ends x_A and x_B are

$$\delta u_0 = 0 \quad \text{or} \quad N - \hat{N} = 0 \quad (3.27a)$$

$$\delta \theta = 0 \quad \text{or} \quad M - \hat{M} - c_1 \left(P - \hat{P}\right) = 0 \quad (3.27b)$$

$$\delta w_{0,x} = 0 \quad \text{or} \quad P - \hat{P} = 0 \quad (3.27c)$$

$$\delta w_0 = 0 \quad \text{or} \quad c_1 P_{,x} + Q - c_2 R - \hat{Q} = 0. \quad (3.27d)$$

First, note that the force boundary condition on the higher-order moment P in Eq. (3.27c) also features in Eq. (3.27b). Thus, we face the same problem of boundary condition uniqueness and conditions of a well-defined boundary value problem described in the previous section. For simply supported boundary conditions,

$$w_0 = N = M = P = 0 \quad \text{at} \quad x_A \text{ and } x_B \quad (3.28)$$

and it is possible to define mode shapes that satisfy the boundary conditions exactly, and then solve for the unknown coefficients. However, when solving a problem with built-in supports, the situation is more difficult. The conditions

$$u_0 = w_0 = \theta = 0 \quad \text{at} \quad x_A \text{ and } x_B \quad (3.29)$$

are readily applied at either end as there can be no in-plane movement u_0, no transverse deflection w_0 and no average rotation θ of the cross-section. This leaves the third boundary condition Eq. (3.27c), where either the higher-order moment P or the Kirchhoff rotation $w_{0,x}$ need to be defined. Both the bending moment M and higher-order moment P are non-zero at the supports because of a unique axial stress σ_x at this location. Furthermore, for a generic

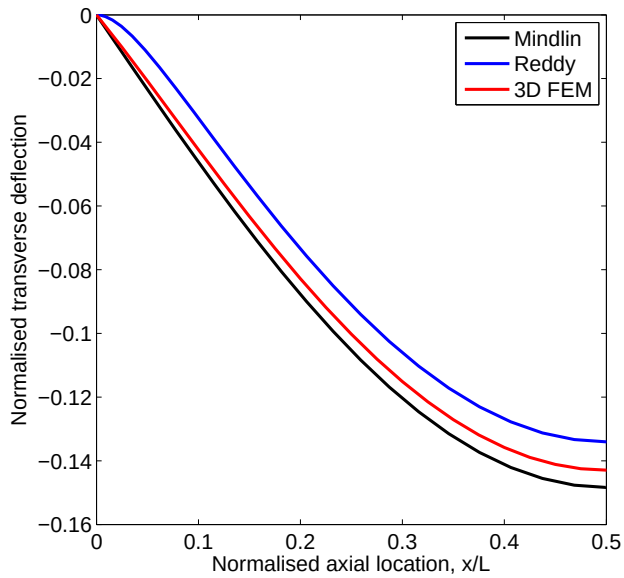

Figure 3.2: Comparison of transverse deflection $\bar{w}$ for an infinitely wide plate clamped at two ends, $t/L = 1:8$, $E_{11}/G_{13} = 50$, and loaded by a uniformly distributed pressure. A half-span plot is shown with the symmetry condition at $x/L = 0.5$.

distributed transverse load q, the value of P at the supports is not known *a priori*. Therefore, we are forced to define a displacement boundary condition $w_{0,x}$ to sufficiently constrain the problem. In his textbook "Mechanics of Laminated Composite Plates and Shells" [160, Eq. 11.5.17, p. 704], Reddy applies the following boundary conditions

$$u_0 = w_0 = w_{0,x} = \theta = 0 \tag{3.30}$$

for clamped edges. The same boundary condition is applied in references [39, 161–165] for various other HOTs as well. As described in Section 3.1.2, the boundary condition $w_{0,x} = 0$ in Eq. (3.30) is physically inaccurate due to the presence of finite transverse shearing at a clamped edge.

Consider, for example, the transverse deflection plots of an infinitely wide plate with thickness to length ratio $t/L = 1:8$ and orthotropy ratio $E_{11}/G_{13} = 50$, clamped at both ends and loaded with a uniformly distributed pressure. Figure 3.2 shows the discrepancy of the rotation at the support when compared to Mindlin's theory and 3D FEM. Whereas $w_{0,x}$ is non-zero in Mindlin's theory and in 3D FEM due to the presence of transverse shearing, the rotation $w_{0,x}$ is forced to vanish in Reddy's theory. The plot shows that the boundary condition $w_{0,x} = 0$ overconstrains the structure leading to overall stiffer behaviour. Mindlin's theory overpredicts the 3D FEM solution because higher-order effects are important for the chosen configuration. Specifically, Mindlin's theory does not capture the "stress-channelling" of axial stress σ_x towards the surfaces, thereby underpredicting the maximum stress and overpredicting the transverse deflection.

Furthermore, enforcing boundary condition Eq. (3.30) causes the transverse shear force Q

and higher-order transverse shear force R to erroneously vanish at the supports,

$$\begin{aligned}\begin{bmatrix} Q_{x_A,x_B} & R_{x_A,x_B} \end{bmatrix} &= \int_{-t/2}^{t/2} \begin{bmatrix} 1 & z^2 \end{bmatrix} \tau_{xz}(x_A, x_B)\mathrm{d}z = \int_{-t/2}^{t/2} G_{xz} \begin{bmatrix} 1 & z^2 \end{bmatrix} \gamma_{xz}(x_A, x_B)\mathrm{d}z \\ &= \int_{-t/2}^{t/2} G_{xz} \begin{bmatrix} 1 & z^2 \end{bmatrix} \left[\{\theta(x_A, x_B) + w_{0,x}(x_A, x_B)\} \left(1 - \frac{4}{t^2} z^2\right) \right] \mathrm{d}z = 0 \end{aligned} \tag{3.31}$$

as $w_{0,x} = \theta = 0$ at x_A and x_B.

Thus, at a clamped edge, Reddy's third-order theory leads to an inconsistency between the transverse shear forces obtained from constitutive and equilibrium equations. To overcome this inconsistency, a non-zero value of $w_{0,x}$ could be defined. Alternatively, a boundary condition on $w_{0,x}$ could be left undefined. The former is not possible as the slope $w_{0,x}$ depends on the loading condition, plate dimensions and material properties, and is thus a quantity to be determined as a result of solving the problem. The latter option is infeasible as this additional boundary condition is required to properly define the boundary value problem.

3.1.3.2 Transverse shear force in Reddy's third-order theory

Consider a cantilevered, infinitely wide plate of thickness to length ratio $t/L = 1 : 10$ and orthotropy ratio $E_{11}/G_{13} = 25$ subject to a transverse shear traction q_0 at the free end. From simple equilibrium of forces and moments, we know that the shear force must be constant along the length of the plate. The spanwise distribution of the transverse shear force from the constitutive equation and equilibrium condition, as derived from Reddy's third-order theory, is shown in Figure 3.3a. It is apparent that at the built-in support $x = 0$ there is a discrepancy between the constitutive shear force Q of Eq. (3.25) and the shear force $V = M_{,x}$ derived from equilibrium. Furthermore, the constitutive shear force can be seen to converge from zero to the correct value of unity some distance away from the built-in support. Figure 3.3b shows an equivalent plot for an infinitely wide plate that is clamped at both ends and loaded by a uniformly distributed pressure of magnitude q_0. In this case, the constitutive shear force vanishes at both supports and converges to the linearly varying distribution derived from equilibrium some distance away from the supports.

In both Figures 3.3a and 3.3b, the convergence distance depends on the magnitude of the thickness to length ratio t/L and the orthotropy ratio E_{11}/G_{13} as these ratios are the governing factors of transverse shear flexibility. The variation of the constitutive shear force along the length of the cantilevered plate for different thickness to length ratios t/L is shown in Figure 3.4a, and that for different orthotropy ratios E_{11}/G_{13} is shown in Figure 3.4b. As t/L and E_{11}/G_{13} increase, so does the distance required for convergence. For $t/L \to 0$ and $E_{11}/G_{13} \to 0$, the convergence distance tends to zero because the plate approaches the idealised condition of pure bending with $w_{0,x} = 0$. However, this trend is asymptotic, such that the transverse shear force at the support condition is always equal to zero for any finite thickness to length ratio t/L and orthotropy ratio E_{11}/G_{13}. In Mindlin's plate theory, no constraint is placed on $w_{0,x}$ at the boundary, and therefore results in the same transverse shear force along the length of the infinitely wide plate for both the constitutive and equilibrium derivations.

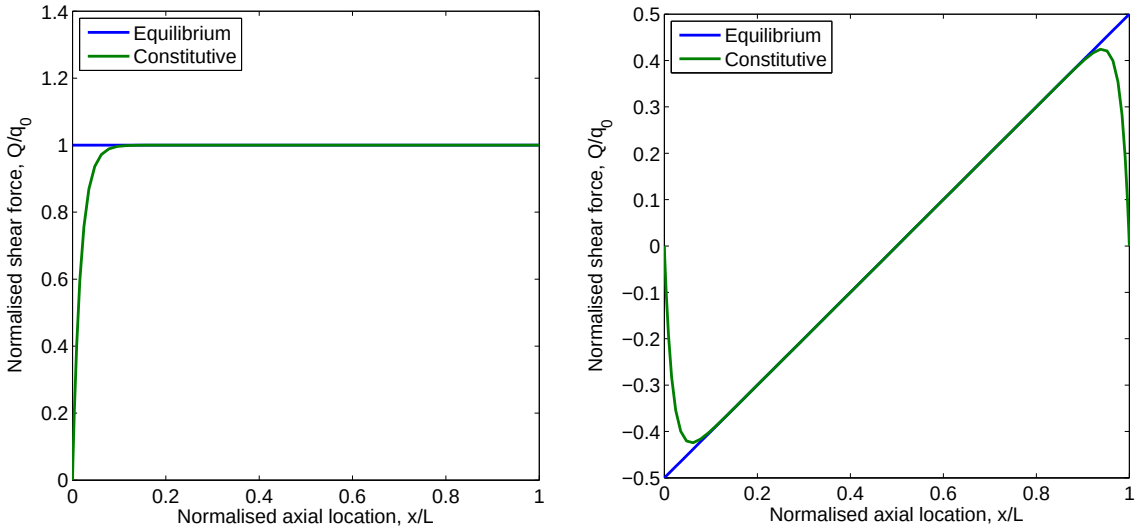

(a) Cantilevered plate

(b) Plate clamped at two ends

Figure 3.3: Comparison of normalised transverse shear force along the length of an infinitely wide plate with $t/L = 1:10$ and $E_{11}/G_{13} = 25$, as derived from constitutive and equilibrium equations of Reddy's third-order theory, for two different boundary conditions.

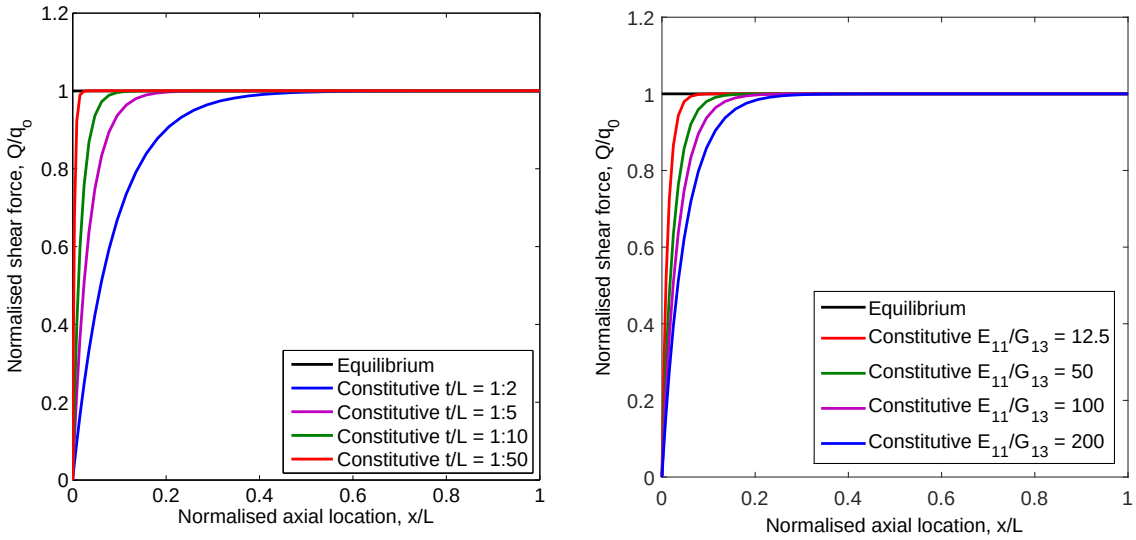

(a) Varying t/L with $E_{11}/G_{13} = 25$

(b) Varying E_{11}/G_{13} with $t/L = 1:10$

Figure 3.4: Variation of the constitutive transverse shear force of Reddy's third-order theory along the length of a cantilevered plate for different thickness to length ratios t/L and different orthotropy ratios E_{11}/G_{13}.

Table 3.1: Normalised transverse displacement $\bar{w}$ of 3D FEM results compared to Mindlin's (FSDT), Reddy's third-order (RTOT), generalised third-order (3HOT) and fifth-order (5HOT) solutions for an infinitely wide plate clamped at two ends and loaded by a uniformly distributed pressure.

Normalised transverse deflection $\bar{w}$ at $x/L = 0.5$						
$\frac{t}{L}$	$\frac{E_{11}}{G_{13}}$	**3D FEM**	**FSDT (%)**	**RTOT (%)**	**3HOT (%)**	**5HOT (%)**
1:100		0.0315	0.27	0.26	0.27	0.27
1:50		0.0326	0.13	0.06	0.10	0.10
1:20	**25**	0.0404	0.41	-0.39	0.09	0.12
1:10		0.0678	1.32	-2.51	-0.25	-0.10
1:5		0.1772	2.26	-9.44	-1.49	-1.00

Table 3.2: Normalised transverse displacement $\bar{w}$ of 3D FEM results compared to Mindlin's (FSDT), Reddy's third-order (RTOT), generalised third-order (3HOT) and fifth-order (5HOT) solutions for an infinitely wide plate clamped at two ends and loaded by a uniformly distributed pressure.

Normalised transverse deflection $\bar{w}$ at $x/L = 0.5$						
$\frac{t}{L}$	$\frac{E_{11}}{G_{13}}$	**3D FEM**	**FSDT (%)**	**RTOT (%)**	**3HOT (%)**	**5HOT (%)**
	12.5	0.0496	0.56	-1.28	-0.19	-0.12
	25	0.0678	1.32	-2.51	-0.25	-0.10
1:10	**50**	0.1036	2.51	-4.56	-0.37	-0.10
	100	0.1738	4.22	-7.70	-0.62	-0.12
	200	0.3113	6.39	-12.44	-1.06	-0.16

The physically incorrect boundary condition $w_{0,x} = 0$ also influences the bending deflection and stress results as a whole. Because the plate can shear at the clamped boundary, the boundary condition $w_{0,x} = 0$ overconstrains the structure and leads to unconservative transverse deflection results. The inaccuracy increases with increasing thickness to length ratio t/L and increasing orthotropy ratio E_{11}/G_{13}. A comparison of the normalised transverse midspan deflection $\bar{w}$ of Mindlin's first-order (FSDT) and Reddy's third-order theory (RTOT) against the high-fidelity 3D FEM solution for different thickness to length ratios t/L is shown in Table 3.1. The same comparison for varying orthotropy ratio E_{11}/G_{13} is shown in Table 3.2. The normalised solution of 3D FEM is stated explicitly and the errors in FSDT and RTOT are given as percentages. The solutions are calculated for an infinitely wide plate clamped at both ends and loaded by a uniformly distributed pressure q_0 across the span L.

Table 3.1 shows that the accuracy of $\bar{w}$ for FSDT and RTOT are similar for small values of t/L. However, as the thickness increases, Reddy's third-order theory is less accurate than Mindlin's first-order theory. The results show that RTOT always leads to an underprediction of $\bar{w}$ compared to 3D FEM, which arises due to the stiffening effect of $w_{0,x} = 0$ at the boundary. For FSDT, the error is always on the conservative side. Furthermore, for $t/L = 1:5$ the 9.44% error of RTOT is more than three times the magnitude of the FSDT error. Finally, the $\bar{w}$ results in Table 3.2 show similar trends of increasing inaccuracy for both FSDT and RTOT as the orthotropy ratio E_{11}/G_{13} increases, with the error of RTOT generally two times greater than that of FSDT.

The errors in FSDT may largely be attributed to neglecting higher-order effects that become important as t/L and E_{11}/G_{13} increase. RTOT on the other hand captures higher-order effects due to the cubic displacement formulation, and the errors stem largely from the erroneous boundary condition $w_{0,x} = 0$. In Section 3.2.4, t/L and E_{11}/G_{13} are combined into a single non-dimensional metric that governs the structural behaviour of the plate.

3.2 General higher-order theories

Based on the previous findings, a formulation is sought that:

1. Captures higher-order effects.

2. Allows transverse shear stresses to vanish at the surfaces.

3. Gives a meaningful, non-zero shear force at a clamped edge, i.e. the Kirchhoff rotation $w_{0,x}$ does not appear in the axial displacement field.

To achieve this, a general higher-order theory following Carrera et al. [23, 96, 97] is presented.

3.2.1 Model derivation

The most expedient way to achieve the conditions outlined above is by a natural extension to Mindlin's first-order theory, i.e. the axial displacement field u_x is expanded as a linear

combination of a power series in z and an unknown displacement field $\mathcal{U}$. Hence,

$$u_x = u_0 + z\theta + z^2\zeta + z^3\xi + \cdots = \begin{bmatrix} 1 & z & z^2 & z^3 & \dots \end{bmatrix} \begin{Bmatrix} u_0 & \theta & \zeta & \xi & \dots \end{Bmatrix}^\top = \boldsymbol{f}(z)\mathcal{U} \quad (3.32a)$$

$$u_z = w_0 \quad (3.32b)$$

where θ is the average rotation of the cross-section, and ζ and ξ are linear and parabolic distortion variables of the cross-section, respectively. Row vector $\boldsymbol{f}(z)$ is the deformation function of the cross-section, whereas column vector $\mathcal{U}$ contains all displacement variables. The zeroth and even exponent terms of z pertain to stretching deformation variables, whereas the odd exponent terms of z pertain to bending terms.

The generalised strain fields are given by

$$\epsilon_x = \boldsymbol{f}\mathcal{U}_{,x} \quad (3.33a)$$

$$\gamma_{xz} = w_{0,x} + \boldsymbol{f}_{,z}\mathcal{U}. \quad (3.33b)$$

The transverse shear strain is not forced to vanish at the top and bottom surfaces explicitly. The transverse shear strain and stress profiles are of higher-order but are free to "float" away from zero at the surfaces, and in doing so, provide an indication of modelling error. In the following, it is shown that the transverse shear strain automatically vanishes at the surfaces if the order of the expansion adequately captures the structural behaviour. The greater the value of the thickness to length ratio t/L and orthotropy ratio E_{11}/G_{13}, the more terms in the expansion are required to achieve this. Thus, enforcing the transverse shear strain to vanish *a priori*, as in RTOT, is not necessary and the inconsistency due to the $w_{0,x}$ term is prevented.

Substituting the new strain field of Eq. (3.33) into the PVD statement of Eq. (3.4) gives

$$\delta\Pi = \int_V \left[\sigma_x \boldsymbol{f}\delta\mathcal{U}_{,x} + \tau_{xz}\delta\left(w_{0,x} + \boldsymbol{f}_{,z}\mathcal{U}\right)\right] \mathrm{d}V - \int q\delta w_0 \mathrm{d}x - \int_{S_2} \left[\hat{\sigma}_x \boldsymbol{f}\delta\mathcal{U} + \hat{\tau}_{xz}\delta w_0\right] \mathrm{d}S_2 = 0.$$

Defining the following stress resultants

$$\mathcal{F}^\top = \int_{-t/2}^{t/2} \sigma_x \boldsymbol{f} \mathrm{d}z, \quad \mathcal{T}^\top = \int_{-t/2}^{t/2} \tau_{xz} \boldsymbol{f}_{,z} \mathrm{d}z, \quad Q = \int_{-t/2}^{t/2} \tau_{xz} \mathrm{d}z, \quad (3.34)$$

where $\top$ is the transpose operator, and then integrating by parts results in

$$\delta\Pi = -\int \left[\mathcal{F}_{,x}^\top \delta\mathcal{U} + Q_{,x}\delta w_0 - \mathcal{T}^\top \delta\mathcal{U}\right] \mathrm{d}x - \int q\delta w_0 \mathrm{d}x + \left[\left(\mathcal{F}^\top - \hat{\mathcal{F}}^\top\right)\delta\mathcal{U} + \left(Q - \hat{Q}\right)\delta w_0\right]_{x_A, x_B} = 0. \quad (3.35)$$

Note, that no shear correction factor is required for $\mathcal{T}$ or Q due to the presence of higher-order terms. The generalised set of governing field equations is derived by setting the integral expressions to zero. Hence,

$$\delta\mathcal{U}: \quad \mathcal{F}_{,x}^\top - \mathcal{T}^\top = 0 \quad (3.36a)$$

$$\delta w_0: \quad Q_{,x} + q = 0 \quad (3.36b)$$

Table 3.3: Normalised axial stress $\bar{\sigma}_x$ of 3D FEM results compared to Mindlin's (FSDT), Reddy's third-order (RTOT), generalised third-order (3HOT) and fifth-order (5HOT) solutions for an infinitely wide plate clamped at two ends and loaded by a uniformly distributed pressure.

Normalised axial stress $\bar{\sigma}_x$ at $x/L = 0.5$						
$\frac{t}{L}$	$\frac{E_{11}}{G_{13}}$	**3D FEM**	**FSDT (%)**	**RTOT (%)**	**3HOT (%)**	**5HOT (%)**
1:100		0.2484	0.66	0.76	0.76	0.76
1:50		0.2496	0.17	0.57	0.57	0.55
1:20	**25**	0.2550	-1.97	0.49	0.49	0.49
1:10		0.2740	-8.76	0.39	0.39	0.33
1:5		0.3459	-27.73	1.25	0.32	-0.25

The essential and natural boundary conditions at x_A and x_B are

$$\delta\mathcal{U} = 0 \quad \text{or} \quad \mathcal{F}^\top - \hat{\mathcal{F}}^\top = 0 \tag{3.37a}$$

$$\delta w_0 = 0 \quad \text{or} \quad Q - \hat{Q} = 0. \tag{3.37b}$$

The equilibrium equations corresponding to $\delta\mathcal{U}$ are hierarchical and the total number depends on the order of the axial displacement expansion. The transverse equilibrium equation corresponding to δw_0, on the other hand, is always fixed. At a clamped boundary, all displacement variables and the transverse deflection are equal to zero, i.e. $\mathcal{U}(x_A, x_B) = w_0(x_A, x_B) = 0$. This generalised formulation results in a finite transverse shear force at the support. Hence,

$$Q_{x_A,x_B} = \int_{-t/2}^{t/2} G_{xz} \left[w_{0,x}(x_A, x_B) + \boldsymbol{f}_{,z}\mathcal{U}(x_A, x_B) \right] \mathrm{d}z = \int_{-t/2}^{t/2} G_{xz} w_{0,x}(x_A, x_B) \mathrm{d}z. \tag{3.38}$$

Also note that the shear stress at a clamped edge $\tau_{xz} = G_{xz} w_{0,x}$ is independent of the higher-order field $\boldsymbol{f}_{,z}$. Therefore this theory assumes that the whole cross-section is sheared by the same amount and the shear stress τ_{xz} at the built-in support is constant and non-zero throughout the whole thickness.

3.2.2 Comparison with Mindlin's first-order and Reddy's third-order theories

Tables 3.1 and 3.2, previously used to compare the results of normalised transverse deformation $\bar{w}$ at the midspan for FSDT and RTOT, also include the results of cubic (3HOT) and quintic (5HOT) generalised theories. As expected, the fifth-order theory provides slightly more accurate results than the third-order theory for both increasing thickness to length ratio t/L and orthotropy ratio E_{11}/G_{13}. Also, both 3HOT and 5HOT considerably improve on the accuracy of RTOT as the inconsistency due to the $w_{0,x}$ boundary condition is removed. The difference is especially striking for $E_{11}/G_{13} = 200$ in Table 3.2, where the error of 3HOT and 5HOT are one and two orders of magnitude smaller than RTOT, respectively.

The maximum normalised axial stress $\bar{\sigma}_x$ at the midspan of the plate, as predicted by FSDT,

Table 3.4: Normalised axial stress $\bar{\sigma}_x$ of 3D FEM results compared to Mindlin's (FSDT), Reddy's third-order (RTOT), generalised third-order (3HOT) and fifth-order (5HOT) solutions for an infinitely wide plate clamped at two ends and loaded by a uniformly distributed pressure.

Normalised axial stress $\bar{\sigma}_x$ at $x/L = 0.5$						
$\frac{t}{L}$	$\frac{E_{11}}{G_{13}}$	**3D FEM**	**FSDT (%)**	**RTOT (%)**	**3HOT (%)**	**5HOT (%)**
	12.5	0.2619	-4.53	0.25	0.25	0.25
	25	0.2740	-8.76	0.39	0.39	0.33
1:10	**50**	0.2978	-16.06	0.77	0.71	0.59
	100	0.3420	-26.90	2.42	1.48	0.90
	200	0.4165	-39.97	8.14	2.01	1.47

RTOT, 3HOT and 5HOT, is compared against 3D FEM in Table 3.3 for increasing thickness to length ratio t/L. FSDT significantly underpredicts the maximum stress for large t/L values. This behaviour is to be expected as the linear stress assumption cannot capture the higher-order "stress-channelling" effect that occurs for large t/L ratios. Even though the boundary condition on $w_{0,x}$ in RTOT leads to inaccurate transverse deflection results, the stress solutions maintain good accuracy for all t/L presented. Thus, it seems that strain and stress results, being based on derivatives of the displacements, are not affected to the same degree as the displacements themselves. Nevertheless, both 3HOT and 5HOT always outperform RTOT.

A similar trend is shown in Table 3.4 for increasing orthotropy ratio E_{11}/G_{13}. As the orthotropy ratio increases, the plate becomes relatively more flexible in transverse shear. As a result, the distortion of the plate's cross-section, and by extension, the higher-order "stress-channelling" effects increase. Thus, the stress profile through the thickness transitions from predominantly linear, to cubic, to quintic and to further higher-order fields. Both 3HOT and 5HOT considerably improve upon FSDT and RTOT, resulting in nominal overall errors. For increasing E_{11}/G_{13}, the axial stress $\bar{\sigma}_x$ from RTOT shows errors up to 8%. This is more than four times the percentage error magnitude of 3HOT and 5HOT.

3.2.3 Hierarchical modelling

One of the characteristics of RTOT is that the transverse shear stresses are forced to vanish at the top and bottom surfaces. However, enforcing this constraint introduces the Kirchhoff rotation $w_{0,x}$ into the formulation and leads, as we have seen, to underpredictions of transverse displacement and vanishing of the transverse shear force at clamped boundaries. In 3HOT and 5HOT, the transverse shear strain is not enforced to vanish at the top and bottom surfaces. Nevertheless, if the chosen order of the theory adequately captures the structural behaviour, the transverse shear stress naturally disappears at the top and bottom surfaces.

As an example, consider an infinitely wide plate of thickness to length ratio $t/L = 1 : 10$ and orthotropy ratio $E_{11}/G_{13} = 50$. The plate is simply supported at either end and loaded by a sinusoidally distributed pressure $q = q_0 \sin\left(\frac{\pi x}{L}\right)$. This loading configuration is chosen as it allows the through-thickness results to be compared to Pagano's 3D elasticity solution [20].

Under this loading condition, and due to the midplane symmetry of the layer, the in-plane stretching displacements u_0, ζ, etc. in Eq. (3.32) vanish.

In Figure 3.5a, the normalised axial stress $\bar{\sigma}_x$ at the midspan of the plate is plotted through the thickness for the Pagano, FSDT, 3HOT and 5HOT solutions. The linear profile of FSDT fails to capture the higher-order field but both the 3HOT and 5HOT are accurate throughout the whole cross-section. As a result, the normalised transverse shear stress profile $\bar{\tau}_{xz}$ at the support $x = 0$ is accurately predicted by both 3HOT and 5HOT (Figure 3.5b). For 5HOT, the transverse shear stress vanishes exactly at the top and bottom surfaces, whereas for 3HOT, a small residual remains.

Now consider an infinitely wide plate $t/L = 1 : 8$ and $E_{11}/G_{13} = 200$ under the same loading conditions. Figure 3.6a shows that the "stress-channelling" of $\bar{\sigma}_x$ towards the outside surfaces is more pronounced. Whereas 5HOT remains close to Pagano's solutions throughout the whole thickness, there are some inaccuracies for 3HOT. Because fifth-order effects are significant for this plate configuration, there is a considerable residual in $\bar{\tau}_{xz}$ at the surfaces for 3HOT, whereas the solution for 5HOT remains accurate throughout and vanishes on the surfaces (Figure 3.6b).

One possible hypothesis is that this behaviour is a direct result of the minimisation technique employed in the PVD. In essence, each theory accounts for the average total potential energy through the volume of the body (volume integral) as permitted by the order of the theory. If the true 3D behaviour of the structure is governed by higher-order behaviour, as in Figure 3.6, the linear profile of FSDT must underpredict in some parts and overpredict in others to arrive at a similar magnitude of total potential energy. The same argument holds for the transverse shear stress of 3HOT in Figure 3.6b. The quadratic transverse shear stress expansion of 3HOT cannot model the actual higher-order behaviour accurately. Thus, the shear stress magnitude is overpredicted at the surfaces and at the midplane, and underpredicted at other points throughout the cross-section. This effect is eliminated in 5HOT as enough degrees of freedom are included in the model to accurately capture the higher-order stress profile.

The adequacy of a higher-order model can be ascertained by analysing the residual of the transverse shear stress at the surfaces. The energy associated with this residual is given by

$$R_{ts} = \frac{1}{2}\tau_{xz}\gamma_{xz}\bigg|_{z=t/2}. \tag{3.39}$$

If this residual is three orders of magnitude less than the average transverse shear energy through the thickness, then the error associated with this residual is assumed to be negligible. Consequently, the order of the theory is deemed adequate if

$$E_{ts} = \max_{x\in[0,L]}\left\{\frac{\tau_{xz}\gamma_{xz}\,|_{z=t/2}}{\frac{1}{t}\int_{-t/2}^{t/2}\tau_{xz}\gamma_{xz}\mathrm{d}z}\right\} = \mathcal{O}(10^{-3}). \tag{3.40}$$

The values of E_{ts} from Eq. (3.40) for the two cases in Figures 3.5 and 3.6 are shown in Table 3.5. The tabulated results support the qualitative observations made regarding Figure 3.6b that 3HOT inadequately captures the higher-order effects in the plate with $t/L = 1 : 8$ and $E_{11}/G_{13} = 200$. This result has been underlined in the table.

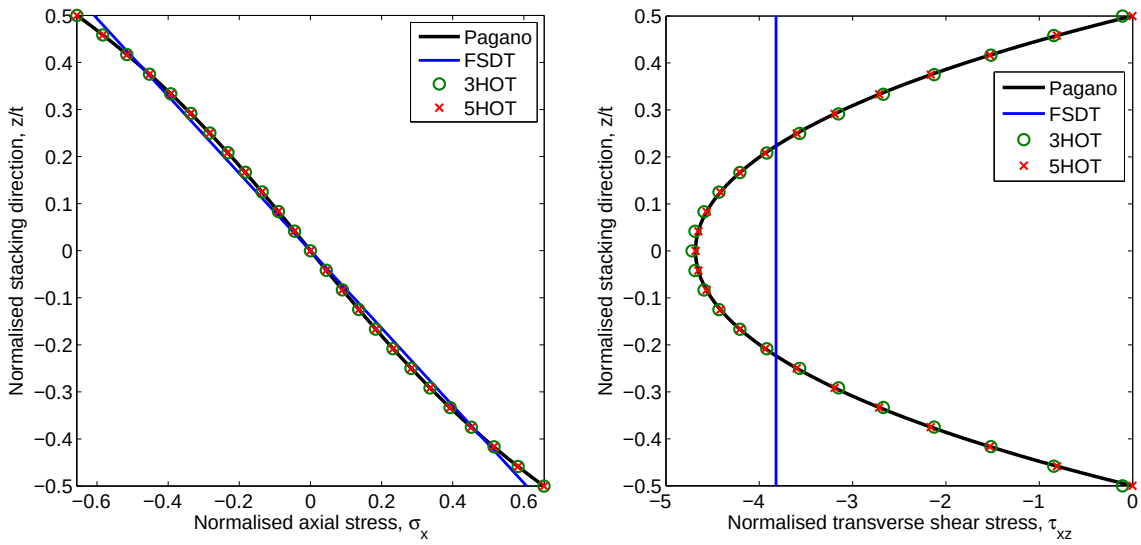

(a) $\bar{\sigma}_x$ at $x = L/2$ **(b)** $\bar{\tau}_{xz}$ at $x = 0$

Figure 3.5: Pagano's normalised axial and transverse shear stresses of a simply supported, infinitely wide plate with $t/L = 1:10$ and $E_{11}/G_{13} = 50$, compared to first-order, third-order and fifth-order theories.

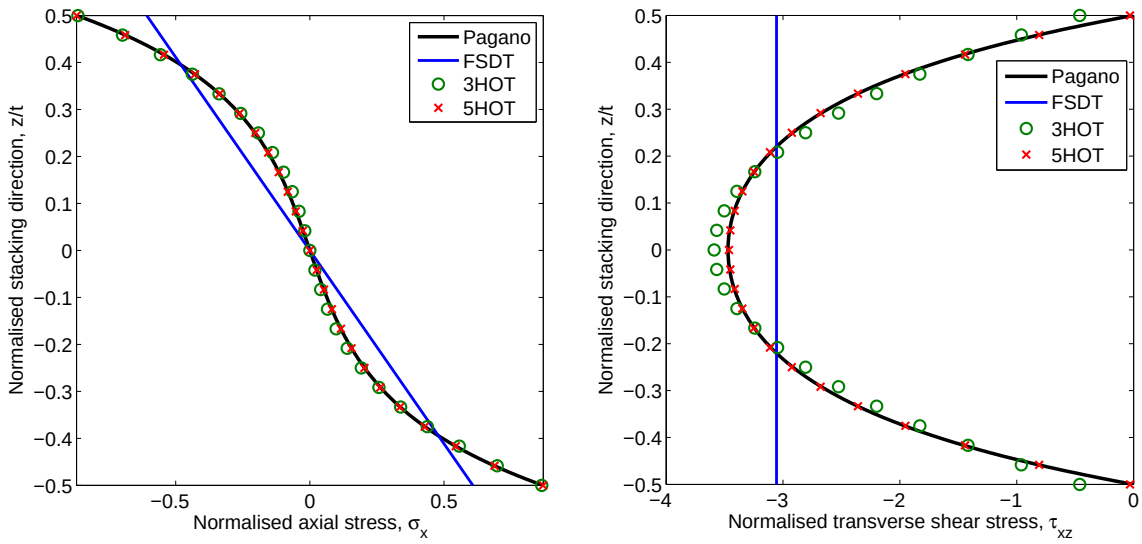

(a) $\bar{\sigma}_x$ at $x = L/2$ **(b)** $\bar{\tau}_{xz}$ at $x = 0$

Figure 3.6: Pagano's normalised axial and transverse shear stresses of a simply supported, infinitely wide plate with $t/L = 1:8$ and $E_{11}/G_{13} = 200$, compared to first-order, third-order and fifth-order theories.

Table 3.5: Transverse shear residual E_{ts} for 3HOT and 5HOT calculated for two different load cases. The 3HOT case where E_{ts} is greater than the acceptable tolerance is underlined.

$\frac{t}{L}$	$\frac{E_{11}}{G_{13}}$	Residual E_{ts} 3HOT	Residual E_{ts} 5HOT
1:10	50	1.17×10^{-3}	1.72×10^{-7}
1:8	200	$\underline{3.28 \times 10^{-2}}$	1.44×10^{-4}

3.2.4 Asymptotic expansion

The previous sections showed that the structural behaviour of an infinitely wide plate in cylindrical bending is a function of both the orthotropy ratio E_{11}/G_{13} and the thickness to length ratio t/L. It is possible to combine these two factors into a single metric which governs the structural behaviour of the plate.

Consider an infinitely wide, simply supported plate as depicted in Figure 3.1, which is loaded by a sinusoidally distributed pressure $q = q_0 \sin\left(\frac{\pi x}{L}\right)$. The governing equations (3.9b)-(3.9c) for FSDT written in terms of w_0 and θ are

$$\delta\theta : D\theta_{,xx} - kG\left(w_{0,x} + \theta\right) = 0 \tag{3.41a}$$

$$\delta w_0 : kG\left(w_{0,xx} + \theta_{,x}\right) + q = 0 \tag{3.41b}$$

where k is a pertinent shear correction factor, D is the bending rigidity and G the shear rigidity of the single layer. These rigidities are defined as follows:

$$D = \frac{E_{11}}{1-\upsilon^2}\frac{t^3}{12} = Q_{11}\frac{t^3}{12} \quad \text{and} \quad G = G_{13}t \tag{3.42}$$

where the term $Q_{11} = E_{11}/\left(1-\upsilon^2\right)$ has been defined. The ad-hoc assumptions

$$w_0 = W_0 \sin\left(\frac{\pi x}{L}\right) \quad \text{and} \quad \theta = \Theta\cos\left(\frac{\pi x}{L}\right) \tag{3.43}$$

satisfy the boundary conditions exactly. Substituting Eq. (3.43) into the governing field equations (3.41) and solving for the unknown coefficients W_0 and Θ gives

$$\Theta = -\frac{q_0}{D}\frac{L^3}{\pi^3} \tag{3.44a}$$

$$W_0 = \frac{q_0 L^4}{D\pi^4}\left(1 + \frac{D}{kG}\frac{\pi^2}{L^2}\right). \tag{3.44b}$$

Substituting Eq. (3.42) into Eq. (3.44) yields

$$W_0^{FSDT} = \frac{q_0 L^4}{D\pi^4}\left[1 + \frac{\pi^2}{12k}\left\{\frac{Q_{11}}{G_{13}}\left(\frac{t}{L}\right)^2\right\}\right] = \frac{q_0 L^4}{D\pi^4}\left[1 + \frac{\pi^2}{12k}\lambda\right] \tag{3.45}$$

where $\lambda = \dfrac{Q_{11}}{G_{13}}\left(\dfrac{t}{L}\right)^2$ is a layup dependent ratio that governs the influence of transverse shear deformation. The origin of this parameter is discussed by Hu et al. [166], and has been used extensively in the literature to assess the effect of transverse shear deformation on the structural behaviour of beams, plates and shells. As FSDT only captures first-order effects, the order of λ in Eq. (3.45) is one.

A similar analysis is conducted for 3HOT by writing the governing field equations (3.36) in terms of the unknown variables θ, ζ and w_0,

$$\delta\theta : D\theta_{,xx} + E\zeta_{,xx} - G\left(w_{0,x} + \theta\right) - H\zeta = 0 \tag{3.46a}$$

$$\delta\zeta : E\theta_{,xx} + F\zeta_{,xx} - H\left(w_{0,x} + \theta\right) - I\zeta = 0 \tag{3.46b}$$

$$\delta w_0 : G\left(w_{0,xx} + \theta_{,x}\right) + H\zeta_{,x} + q = 0 \tag{3.46c}$$

where D and G are as previously defined in Eq. (3.42), F and I are the higher-order bending and transverse shear rigidities, respectively, and E and H are the first-order/higher-order coupling bending and transverse shear rigidities, respectively. These terms are defined as follows:

$$E = Q_{11}\frac{t^5}{80}, \quad F = Q_{11}\frac{t^7}{448}, \quad H = G_{13}\frac{t^3}{4} \quad \text{and} \quad I = G_{13}\frac{9t^5}{80}. \tag{3.47}$$

The assumptions

$$w = W_0 \sin\left(\frac{\pi x}{L}\right) \quad \text{and} \quad (\theta,\ \zeta) = (\Theta,\ Z)\cos\left(\frac{\pi x}{L}\right) \tag{3.48}$$

satisfy the boundary conditions exactly. Substituting Eq. (3.48) into the governing field equations (3.46) and solving for the unknown coefficients W_0, Θ and Z gives

$$Z = q_0\frac{L}{\pi}\eta \quad \text{where} \quad \eta = \frac{\frac{H}{G} - \frac{E}{D}}{\frac{\pi^2}{L^2}\left(\frac{E^2}{D} - F\right) + \frac{H^2}{G} - I} \tag{3.49a}$$

$$\Theta = -\frac{q_0}{D}\frac{L^3}{\pi^3}\left(1 + E\frac{\pi^2}{L^2}\eta\right) \tag{3.49b}$$

$$W_0 = \frac{q_0 L^4}{D\pi^4}\left[1 + \frac{D}{G}\frac{\pi^2}{L^2} + \frac{\pi^2}{L^2}\left(E - \frac{DH}{G}\right)\eta\right]. \tag{3.49c}$$

Substituting Eq. (3.47) into Eq. (3.49) yields

$$W_0^{3HOT} = \frac{q_0 L^4}{D\pi^4}\left[1 + \frac{\pi^2}{12}\lambda + \frac{\pi^2}{60}\frac{\lambda}{1 + \frac{\pi^2}{140}\lambda}\right] \tag{3.50}$$

which shows that the transverse displacement is now a higher-order function of λ. The expression in Eq. (3.50) is expanded via a binomial series and compared to the FSDT expression in Eq. (3.45). Thus, expanding Eq. (3.50) as a power series gives

$$W_0^{3HOT} = \frac{q_0 L^4}{D\pi^4}\left[1 + \frac{\pi^2}{12}\lambda + \frac{\pi^2}{60}\lambda - \frac{\pi^4}{8400}\lambda^2 + \mathcal{O}(\lambda^3)\right] = \frac{q_0 L^4}{D\pi^4}\left[1 + \frac{\pi^2}{10}\lambda - \frac{\pi^4}{8400}\lambda^2 + \mathcal{O}(\lambda^3)\right]. \tag{3.51}$$

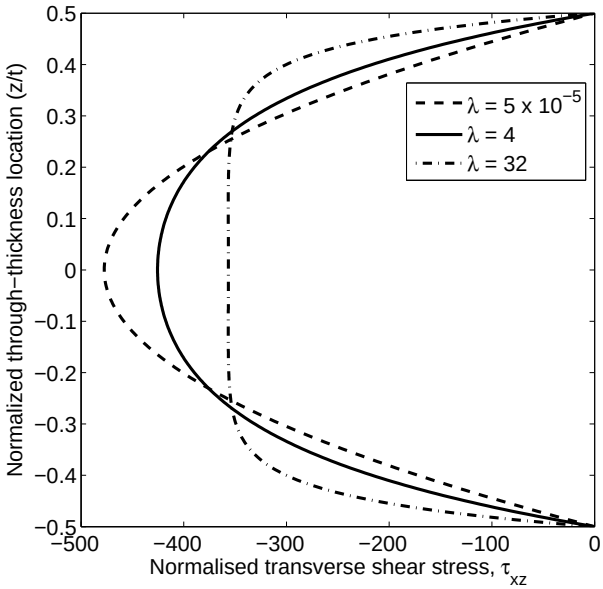

Figure 3.7: Variation of the normalised transverse shear stress $\bar{\tau}_{xz}$ through the thickness of a [0] laminate for three values of λ. Results are calculated using Pagano's 3D elasticity solution [20].

The above equation shows that if the shear correction factor for FSDT is chosen to be $k = 5/6$, i.e. the original value found by Reissner [56], then the first-order coefficients of λ in Eq. (3.45) and Eq. (3.51) are equal. Thus, the shear correction factor of $k = 5/6$ guarantees that FSDT accounts for the first-order structural effects associated with λ. The shear correction factor is generalised to include all the higher-order terms of λ explicit in 3HOT by equating Eq. (3.45) and Eq. (3.50). Hence,

$$1 + \frac{\pi^2}{12k}\lambda = 1 + \frac{\pi^2}{12}\lambda + \frac{\pi^2}{60}\frac{\lambda}{1 + \frac{\pi^2}{140}\lambda} \quad \Rightarrow \quad k = \left[\frac{1}{5}\left(1 + \frac{\pi^2}{140}\lambda\right)^{-1} + 1\right]^{-1}. \tag{3.52}$$

The expression in Eq. (3.52) shows that the shear correction factor $k \to 5/6$ as $\lambda \to 0$. Furthermore, as $\lambda \to \infty$ the value of $k \to 1$. This result suggests that a shear correction factor of $k = 5/6$ pertains to a fictitious layer of infinitesimal thickness or infinite length with perfectly linear and parabolic through-thickness variations of σ_x and τ_{xz}, respectively. As λ increases, and the "stress-channelling" effect becomes more significant, the through-thickness variations of σ_x and τ_{xz} transition to increasingly higher-order profiles (see Figures 3.5 and 3.6). As a result of σ_x channelling towards the outside surfaces, the transverse shear stress τ_{xz} is more evenly distributed at the centre (see Figure 3.7), an effect which is analogous to the behaviour observed in a sandwich beam with stiff face layers and compliant core. With more of the cross-section sheared by the same amount, the shear correction factor consequently increases from $k = 5/6$ because the energetic difference between the constant shear stress profile of FSDT and the actual profile is decreasing. Thus, in the limiting case of constant shear stress through the thickness, the shear correction factor approaches unity.

Table 3.6: Normalised transverse displacement $\bar{w}$ of an infinitely wide plate simply supported at two ends and loaded by a sinusoidally distributed pressure. The results of Pagano's 3D elasticity solution [20] are compared to two Mindlin (FSDT) solutions with different shear correction factors k.

$\frac{t}{L}$	$\frac{E_{11}}{G_{13}}$	**Pagano**	**FSDT (%)** k = 5/6	**FSDT (%)** k = Eq. (3.52)
0.1	**50**	0.1829	0.41	0.22
0.2		0.3605	1.53	0.14
0.1	**100**	0.2428	0.70	0.15
0.2		0.5923	2.85	-0.16

In essence, Eq. (3.52) generalises the shear correction factor for a plate of finite thickness to a chosen order of λ up to the accuracy inherent in 3HOT. In Table 3.6, the normalised transverse deflection from FSDT calculated using the generalised shear correction factor of Eq. (3.52) and the classical value of $k = 5/6$ are compared. The table shows that the percentage error with respect to Pagano's 3D elasticity solution [20] is significantly reduced when the shear correction factor in Eq. (3.52) is used.

The local axial stress results of the two FSDT solutions are unchanged because the through-thickness stress assumption remains linear. Substituting the solutions for the displacement variables of FSDT in Eq. (3.44) into the kinematic and constitutive relations, the axial stress field for FSDT is given by

$$\sigma_x^{FSDT} = Q_{11}\frac{q_0 L^2}{D\pi^2} z \cdot \sin\frac{\pi x}{L} \tag{3.53}$$

and this is unchanged from the CLA solution. This observation that FSDT improves predictions of global structural phenomena but not of the stress fields was first made by Whitney [28]. Similarly, using the solution for the displacement variables of 3HOT in Eq. (3.49), the axial stress reads as follows

$$\sigma_x^{3HOT} = \sigma_x^{FSDT}\left[1 - \frac{\pi^2\lambda}{1+\frac{\pi^2}{140}\lambda}\left\{\frac{1}{40} - \frac{1}{6}\left(\frac{z}{t}\right)^2\right\}\right]. \tag{3.54}$$

Expanding Eq. (3.54) as a power series of λ, i.e.

$$\frac{\sigma_x^{3HOT}}{\sigma_x^{FSDT}} = 1 - \left(\frac{\pi^2}{40}\lambda - \frac{\pi^4}{5600}\lambda^2 + \mathcal{O}(\lambda^3)\right) + \left(\frac{\pi^2}{6}\lambda - \frac{\pi^4}{840}\lambda^2 + \mathcal{O}(\lambda^3)\right)\left(\frac{z}{t}\right)^2 \tag{3.55}$$

shows that the higher-order solution modifies the FSDT axial stress field in two ways. First, the average slope of the through-thickness field is modified by the power series coefficient in the first bracket of Eq. (3.55). Second, a higher-order component that governs the extent of "stress-channelling" is given by the power series coefficient of $(z/t)^2$. In this particular case, the higher-order component has a leading coefficient that is 20/3 times greater than the leading coefficient of the average slope change. Thus, the inclusion of the cubic term z^3 in the displacement field refines the axial stress more through the higher-order "stress-channelling" effects than by correcting the linear component.

Finally, the solution process presented above is extended to 5HOT and 7HOT in order

Table 3.7: Convergence of the normalised transverse deflection $W_0 \dfrac{D\pi^4}{q_0 L^4}$ with increasing order of λ^n for three different materials with thickness to length ratio $t/L = 0.3$. The convergence is compared to the full series solution ($n \to \infty$) of 3HOT, 5HOT and 7HOT.

		Expansion up to λ^n term					Full	Full	Full
Material	λ	n=1	n=2	n=3	n=4	n=5	3HOT	5HOT	7HOT
Isotropic $\left(\dfrac{E_{11}}{G_{13}} = 2.6\right)$	0.234	1.2309	1.2303	1.2303	1.2303	1.2303	1.2303	1.2303	1.2303
IM7 8552 $\left(\dfrac{E_{11}}{G_{13}} = 40\right)$	3.6	4.5531	4.4028	4.4621	4.4368	4.4478	4.4332	4.4444	4.4445
Highly Ortho. $\left(\dfrac{E_{11}}{G_{13}} = 100\right)$	9	9.8826	8.9433	9.8704	8.8812	9.9590	9.3080	9.3940	9.3957

to derive shear correction factors that correct FSDT to an order consistent with 5HOT and 7HOT. For 5HOT and 7HOT, Eqs. (3.46) now feature five and seven governing field equations, respectively, in terms of five and seven displacement unknowns. The algebraic derivations are straightforward but rather involved and, for brevity, only the final result is shown here. Hence, the transverse deflection magnitudes W_0^{5HOT} and W_0^{7HOT} are given by

$$W_0^{5HOT} = \frac{q_0 L^4}{D\pi^4}\left[1 + \frac{\pi^2}{12}\lambda + \frac{\frac{\pi^2}{60}\lambda + \frac{\pi^4}{9240}\lambda^2}{1 + \frac{3\pi^2}{220}\lambda + \frac{\pi^4}{55440}\lambda^2}\right] \tag{3.56}$$

$$W_0^{7HOT} = \frac{q_0 L^4}{D\pi^4}\left[1 + \frac{\pi^2}{12}\lambda + \frac{\frac{\pi^2}{60}\lambda + \frac{\pi^4}{6300}\lambda^2 + \frac{\pi^6}{3931200}\lambda^3}{1 + \frac{\pi^2}{60}\lambda + \frac{\pi^4}{18200}\lambda^2 + \frac{\pi^6}{43243200}\lambda^3}\right]. \tag{3.57}$$

The expressions for W_0^{3HOT} of Eq. (3.51), and W_0^{5HOT} and W_0^{7HOT} of Eqs. (3.56) and (3.57), respectively, are now expanded up to the fifth order of λ. Hence,

$$W_0^{3HOT} = \frac{q_0 L^4}{D\pi^4}\left[1 + \frac{\pi^2}{10}\lambda - \frac{\pi^4}{8400}\lambda^2 + \frac{\pi^6}{1176000}\lambda^3 - \frac{\pi^8}{1.646 \times 10^8}\lambda^4 + \frac{\pi^{10}}{2.305 \times 10^{10}}\lambda^5 + \mathcal{O}(\lambda^6)\right] \tag{3.58}$$

$$W_0^{5HOT} = \frac{q_0 L^4}{D\pi^4}\left[1 + \frac{\pi^2}{10}\lambda - \frac{\pi^4}{8400}\lambda^2 + \frac{\pi^6}{756000}\lambda^3 - \frac{37\pi^8}{2.328 \times 10^9}\lambda^4 + \frac{127\pi^{10}}{6.586 \times 10^{11}}\lambda^5 + \mathcal{O}(\lambda^6)\right] \tag{3.59}$$

$$W_0^{7HOT} = \frac{q_0 L^4}{D\pi^4}\left[1 + \frac{\pi^2}{10}\lambda - \frac{\pi^4}{8400}\lambda^2 + \frac{\pi^6}{756000}\lambda^3 - \frac{37\pi^8}{2.328 \times 10^9}\lambda^4 + \frac{59\pi^{10}}{3.027 \times 10^{11}}\lambda^5 + \mathcal{O}(\lambda^6)\right]. \tag{3.60}$$

Comparing Eqs. (3.59), (3.60) and (3.58), it is evident that the higher-order theories progressively correct higher-order terms in λ. As a result, the expansion of 3HOT converges to λ^2, 5HOT to λ^4 and 7HOT to λ^6. Even though the expression for w_0 can be seen to follow a decaying progression, no closed-form holonomic sequence could be determined herein.

Table 3.7 shows the convergence of normalised transverse deflection $w_0 \dfrac{D\pi^4}{q_0 L^4}$ with increasing order of λ^n up to $n = 5$ for three different materials with thickness to length ratio $t/L = 0.3$. The three materials are a metallic isotropic material with Poisson's ratio $\upsilon = 0.3$, an industrial grade carbon-fibre pre-preg IM7 8552 and a highly orthotropic lamina. The results show that for metallic isotropic materials the solution converges for $n = 1$, i.e. a first-order theory solution. For materials with $\lambda \approx 3$, such as a very thick IM7 8552 composite, the solution converges for $n = 4$, i.e. a third-order theory solution. For the highly orthotropic material the full series solutions between 5HOT and 7HOT are similar but a power series solution in terms of λ^n needs to be expanded beyond $n = 5$ to achieve convergence. It is important to note that the higher-order solutions past 5HOT may be meaningless. The structural behaviour for large values of λ, where these higher-order theories are necessary, may be influenced to a greater extent by transverse normal deformation, which has been ignored in the present analysis.

3.3 Conclusions

Static inconsistencies in modelling clamped boundary conditions using displacement-based, axiomatic, higher-order theories have been discussed. Enforcing the boundary condition of vanishing transverse shear strain at the top and bottom surfaces *a priori* introduces the Kirchhoff rotations $w_{0,x}$ and $w_{0,y}$ into the expansion for u_x and u_y, respectively. If the governing differential equations are derived using the PVD, an essential boundary condition on $w_{0,i}$ perpendicular to an edge arises, which needs to be prescribed to properly constrain the boundary value problem. At a clamped edge the ensuing condition $w_{0,i} = 0$ is physically inaccurate as the plate can rotate at the clamped edge due to the presence of transverse shearing. Furthermore, this condition causes the transverse shear force, as derived from constitutive equations, to vanish at the clamped edge. Such a condition is erroneous when compared to simple transverse equilibrium conditions. Finally, constraining $w_{0,i} = 0$ at the clamped edge overconstrains the structure, leading to underpredictions of transverse deflections and overpredictions of axial stresses.

When the in-plane displacement fields are written as a general power series in terms of the transverse coordinate z, as proposed in Carrera's Unified Formulation, this inconsistency does not occur. Furthermore, if the order of the theory is sufficient to capture all higher-order effects, the transverse shear stresses automatically vanish at the top and bottom surfaces, thereby obviating the need for enforcing this constraint explicitly *a priori*. Based on this insight, a nondimensional parameter based on the transverse shear strain energy at the surfaces was introduced to gauge the accuracy of a higher-order theory. Finally, it was shown that the structural behaviour of a single layer plate in bending is a function of the parameter $\lambda = \dfrac{Q_{11}}{G_{13}} \left(\dfrac{t}{L}\right)^2$. The parameter λ can be used to derive shear correction factors for FSDT that allow the transverse bending deflection results of the single layer to match any higher-order theory.

Chapter 4

Hellinger-Reissner Model for Heterogeneous Laminated Beams

The previous chapter showed that displacement-based theories that enforce equilibrium of transverse shear stresses on the top and bottom surfaces using the kinematic and constitutive equations lead to static inconsistencies at clamped edges. The discussion in Chapter 3 focused on a single layer, and therefore did not address the interlaminar continuity condition present in laminated structures. In fact, for typical higher-order displacement-based theories, such as Reddy's third-order theory [34], the transverse stresses are derived from kinematic and constitutive equations, and do not satisfy the interlaminar continuity condition of transverse stresses even when equilibrium of the surface tractions is enforced via the displacement field.

Some higher-order theories, such as the ZZ theories by Ambartsumyan [67] and Whitney [68], derive the displacement field directly from a layerwise-continuous assumption of the transverse shear stresses, and thus guarantee interlaminar and surface equilibrium of the transverse stresses. However, this derivation typically introduces the Kirchhoff rotation $w_{0,i}$ into the displacement assumption, thereby leading to the mathematical inconsistency at a clamped edge discussed in Chapter 3.

One alternative is to increase the number of variables in the general displacement-based theories until the transverse interfacial conditions are naturally satisfied. However, such an approach is associated with relatively high computational cost due to the large number of degrees of freedom required. The accepted trade-off in the literature is to use higher-order displacement-based theories that produces transverse shear and transverse normal stresses that violate interfacial equilibrium conditions, and then recover more accurate transverse stresses by integrating the in-plane stresses in Cauchy's indefinite equilibrium equations. The drawback of this post-processing approach is that the derived transverse stresses do not satisfy the equilibrium equations of the underlying model, and are thus variationally inconsistent.

Thus, there exists a need for ESLTs that predict accurate 3D stress fields from the underlying model assumptions, thereby preventing static inconsistencies at clamped edges and precluding post-processing steps. A promising approach towards this end are mixed-variational theories based on both displacement and stress variables. The most commonly used of these statements for multilayered structures is RMVT, developed by Reissner [61] particularly for the analysis of layered structures. Similarly, the HR principle is another mixed-variational approach that, in terms of calculating accurate 3D stresses, has the beneficial characteristic of forcing the ad-hoc stress assumptions to explicitly obey Cauchy's 3D equilibrium equations in the variational statement. In most other variational statements this condition is not enforced explicitly. The results in the following chapters show that this characteristic means that transverse stresses are accurately computed from the underlying model assumptions and boundary layer effects

towards boundaries are captured robustly.

In Section 4.1, the origin of the ZZ effect is elucidated using a physically intuitive analogy of a system of springs in series combined with a system of springs in parallel. A higher-order model based on a global, continuous deformation field coupled with a local, layer-wise ZZ deformation field is derived in Section 4.2 using the HR principle. The transverse stress assumptions are derived from integrations of the axial stress in Cauchy's equilibrium equations, such that all stress fields are based on the same set of unknowns. This allows a condensed form of the HR functional to be used, which only enforces the membrane and bending equilibrium equations via Lagrange multipliers. All other higher-order equilibrium equations are not enforced explicitly as the equilibrated transverse stress assumptions inherently satisfy these. Even though local layerwise properties are taken into account via a ZZ function, all functional unknowns are independent of the number of layers, and therefore the model is an equivalent single-layer formulation. The governing equations[1] are derived in a generalised framework that allows the order of the theory to be specified *a priori*, eliminating the need for rederiving the governing equations as the order is increased.

4.1 Mechanics of zig-zag displacements

In the following section the mechanics of the ZZ effect are elucidated using the simple example of a beam in bending. The mechanical origins of the ZZ displacements are discussed, and this physical insight is then used to phenomenologically depict the laminated beam using an equivalent system of springs in series coupled with a system of springs in parallel. The analogous mechanical system is used to interpret the physical meaning of the RZT ZZ function, which, as discussed in Section 2.2.3, has been shown to provide accurate results for highly heterogeneous laminates.

4.1.1 Origin of zig-zag displacements

Consider an N_l layer composite beam of arbitrary constitutive properties as depicted in Figure 4.1. The beam may be of entirely anisotropic or sandwich construction, and is subjected to external tractions causing it to deflect transversely to the stacking direction. The x-direction is defined to be along the principle beam axis (0° fibre-direction), whereas the z-axis is in the transverse stacking direction. For the purpose of this explanation, it is assumed that transverse normal strain is negligible but that transverse shear deformation cannot be neglected.

To prevent individual layers from sliding, the IC conditions for the displacement field u_x and the transverse shear stress τ_{xz} need to be satisfied. Hence,

$$u_x^{(k)}(z_k) = u_x^{(k+1)}(z_k) \quad \text{and} \quad \tau_{xz}^{(k)}(z_k) = \tau_{xz}^{(k+1)}(z_k), \quad k = 1 \dots N_l - 1 \tag{4.1}$$

where subscripts k and superscripts (k) indicate layerwise and interfacial quantities, respectively. If the composite beam is comprised of layers with different transverse shear moduli, then the IC condition on transverse shear stress inherently results in discontinuous transverse shear strains

[1] Governing field equations and boundary conditions.

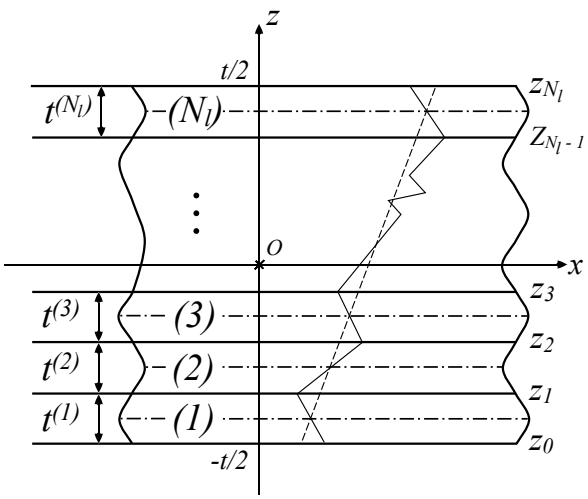

Figure 4.1: Arbitrary laminate configuration with coordinate system and approximate in-plane displacements. The broken line pertains to a classical displacement field, whereas the solid line captures the ZZ effect.

across ply interfaces. Assuming a linear geometric deformation, the kinematic relation for the transverse shear strain is given by

$$\gamma_{xz} = u_{z,x} + u_{x,z} \quad \Rightarrow \quad u_{x,z} = \gamma_{xz} - u_{z,x}. \tag{4.2}$$

As the transverse normal strain is assumed to be negligible the displacement u_z is constant for all layers, such that, according to Eq. (4.2), discontinuous transverse shear strains lead to changes in $u_{x,z}$ across ply interfaces. Thus, the slope of the displacement field u_x in the thickness direction changes at ply interfaces, giving rise to the so-called "zig-zag" displacement field. This effect is depicted graphically by the in-plane displacement u_x, transverse shear stress τ_{xz}, and transverse shear strain γ_{xz} plots through the thickness of a [90/0/90/0/90] laminate in Figure 4.2. Here, the transverse shear modulus G_{xz} of the 90° layers is 2.5 times smaller than the value of G_{xz} for the 0° oriented layers, which causes a step change in transverse shear strain at the ply interfaces.

Figure 4.2 also shows an example of a laminate with "Externally Weak Layers" (EWLs). As discussed by Gherlone [54], these laminates have external layers ($k = 1$ or $k = N_l$) with transverse shear moduli lower than the adjacent internal layers ($k = 2$ and $k = N_l - 1$, respectively), and do not appear to have a ZZ discontinuity at these interfaces. Thus, Gherlone introduced a slight modification to the calculation of the RZT ZZ slopes introduced in Eq. (2.28). Hence, when calculating the RZT ZZ function

$$\begin{aligned} &\bullet \text{ If } G_{xz}^{(1)} < G_{xz}^{(2)}, \text{ then } G_{xz}^{(1)} = G_{xz}^{(2)} \\ &\bullet \text{ If } G_{xz}^{(N)} < G_{xz}^{(N-1)}, \text{ then } G_{xz}^{(N)} = G_{xz}^{(N-1)}. \end{aligned} \tag{4.3}$$

Gherlone attributed the EWL phenomenon to the stiffer inner layers dominating the more compliant external layers. However, there is in fact a slope discontinuity at the interfaces of the EWL. This discontinuity is considerably smaller than at the interface between the internal 0°

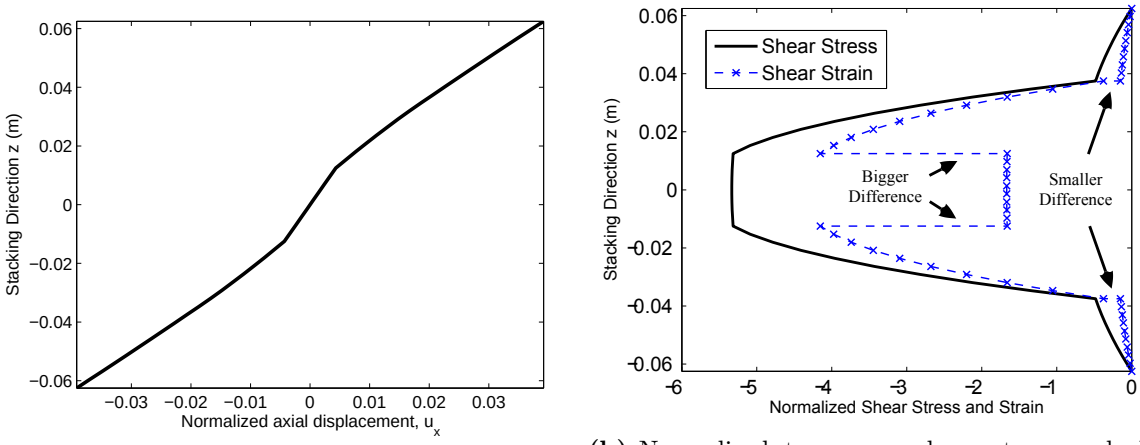

(a) Normalised in-plane deflection

(b) Normalised transverse shear stress and shear strain

Figure 4.2: Pagano's through-thickness solution [20] of normalised in-plane deflection and transverse shear stress for a [90/0/90/0/90] laminate. This laminate is an example of EWLs indicated by the lack of zig-zag discontinuity at the outermost ply interfaces.

and 90° layers, and is consequently not noticed as easily. This phenomenon may be explained by observing the general shape of the transverse shear stress and transverse shear strain profiles of the [90/0/90/0/90] laminate shown in Figure 4.2b. The transverse shear stress at the interface between the outer layers is an order of magnitude smaller than the transverse shear stress at the inner interfaces. Therefore the discontinuity in transverse shear strain is much larger for the inner layers than for the outer layers, such that it appears as if there is no ZZ effect for the outermost interfaces. Even though the ratio of shear strains at the outer and inner [90/0] interface remains the same, the *difference* in magnitude is considerably larger for the inner layers. It is this *difference* in transverse shear strains, rather than their *ratio* that drives the slope discontinuity of the displacement field. Thus, the magnitude of the ZZ discontinuity is both a function of the ratio of transverse shear moduli and the magnitude of the transverse shear stresses at the interface.

This also means that EWL laminates with less than three layers, such as [0/90], [90/0] and [90/0/90] laminates, always show the same degree of ZZ effect at the interfaces. Thus, Gherlone [54] was forced to specify an exception to the EWL implementation rule of the RZT ZZ slopes of Eq. (4.3); namely, the rule does not apply if the condition reduces the laminate to have the same transverse shear moduli for all layers, as would be the case for the [0/90], [90/0] and [90/0/90] laminates.

The difficulty in accurately modelling the ZZ phenomenon is that the displacement and transverse shear stress fields are dependent. To solve any 3D elasticity problem, the full set of 15 equations, namely 6 kinematic equations, 3 equilibrium equations and 6 constitutive equations, are required to solve for all 3 displacement variables, 6 stress and 6 strain fields. The interaction between the 15 unknowns is shown graphically in Figure 4.2, whereby the layerwise slopes of the ZZ displacement field u_x depend on the transverse shear stress distribution, and the transverse shear stress is a function of the kinematic equations. Thus, the ZZ effect arises from

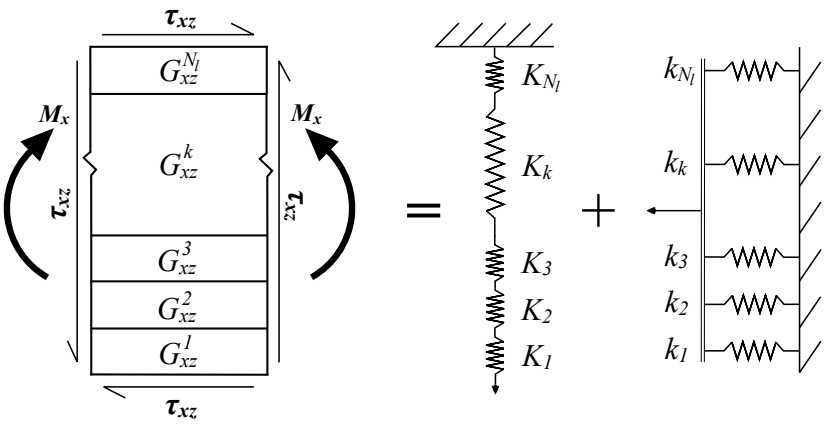

Figure 4.3: Schematic diagram of a composite laminate with varying layerwise transverse shear moduli $G_{xz}^{(k)}$ loaded by a transverse shear load and bending moment. The structure is modelled by an analogous system of mechanical springs.

the interaction of the full set of displacement, strain and stress variables in the 3D elasticity equations.

It is therefore a challenge to derive a mechanically consistent 2D approach that accurately models this inherently 3D effect. For axiomatic, displacement-based theories, the difficulty lies in the fact that assumptions for the displacement variables need to incorporate ZZ unknowns that lead to accurate transverse shear stresses that obey the interlaminar continuity conditions. In the reverse case, Ambartsumyan-type models [67] based on initial transverse shear stress assumptions, need to include all pertinent variables that influence the distributions of the transverse shear stresses, and also lead to accurate through-thickness distributions of the displacement fields.

4.1.2 Spring model for zig-zag displacements

As depicted in Figure 4.3, the IC requirements on in-plane displacements and transverse shear stresses are mechanically similar to a combined system of "springs-in-series" and "springs-in-parallel". For example, a set of springs in series acted upon by a constant force extends the springs by different amounts. By analogy, a constant transverse shear stress acting on a laminate with layers of different shear moduli results in different shear strains in the layers, which are smeared, average values of the actual piecewise-parabolic distributions. At the same time, a system of springs in parallel elongated by a common displacement develops different reaction forces in the springs. This case is interpreted as layerwise transverse shear stresses concentrated in the areas of highest stiffness. Conceptually, these two spring systems combine to capture the interplay between transverse shear stress and displacements as influenced by the IC conditions.

Following this line of reasoning, the average transverse shear stress condition of the "springs-in-series" model is expressed via Hooke's law as an effective shear modulus G multiplied by an average shear strain $\bar{\gamma}_{xz}$. Thus,

$$\tau_{xz} = G\bar{\gamma}_{xz}. \tag{4.4}$$

The effective shear modulus G is found using the reciprocal stiffness equation of a set of springs

in series

$$G = \left[\frac{t^{(1)}/t}{G_{xz}^{(1)}} + \frac{t^{(2)}/t}{G_{xz}^{(2)}} + \cdots + \frac{t^{(N_l)}/t}{G_{xz}^{(N_l)}} \right]^{-1} = \left[\frac{1}{t} \sum_{k=1}^{N_l} \frac{t^{(k)}}{G_{xz}^{(k)}} \right]^{-1}. \tag{4.5}$$

Note that the shear modulus of each layer is normalised by the layer thickness fraction $t^{(k)}/t$ to guarantee that $G = G_{xz}$ for a laminate with layers of equal shear moduli. The change in displacement slope $u_{x,z}$ at layer interfaces depends on the difference in transverse shear strain at the layer interfaces. By inserting Eq. (4.4) into the transverse shear constitutive equation,

$$\gamma_{xz}^{(k)} = \frac{\tau_{xz}^{(k)}}{G_{xz}^{(k)}} = \frac{G}{G_{xz}^{(k)}} \bar{\gamma}_{xz} = g^{(k)} \bar{\gamma}_{xz} \tag{4.6}$$

we see that the transverse shear strain is a function of the layerwise stiffness ratio $g^{(k)} = G/G_{xz}^{(k)}$. This ratio is used to capture the differences in layerwise displacement slopes, and is in fact very similar to the RZT slope function defined in Eq. (2.28).

Figure 4.2b shows that the shear stress profile of a multilayered beam differs from a single layer beam in that the z-direction curvature of the transverse shear stress profile in the stiffer $0°$ plies is increased, whereas the curvature in the more compliant $90°$ is reduced. Integrating the axial stress σ_x derived from CLA for a zero B-matrix laminate in Cauchy's first equilibrium equation,

$$\sigma_x = \bar{Q}^{(k)} \epsilon_x = \bar{Q}^{(k)} z \kappa_x \quad \text{and} \quad \tau_{xz} = -\int \frac{\mathrm{d}\sigma_x}{\mathrm{d}x} \mathrm{d}z = -\bar{Q}^{(k)} \frac{z^2}{2} \kappa_x + C \tag{4.7}$$

shows that the magnitude of the quadratic term z^2 is influenced by the transformed layer stiffness $\bar{Q}^{(k)}$, noting that κ_x is the flexural curvature. The "springs-in-series" analogy is now used to define an effective in-plane stiffness E,

$$E = \frac{1}{t} \sum_{k=1}^{N_l} t^{(k)} \bar{Q}^{(k)} \quad \text{such that} \quad e^{(k)} = \frac{\bar{Q}^{(k)}}{E}. \tag{4.8}$$

The change in layerwise z-direction curvature of the transverse shear stress profile is a function of the relative magnitude of $\bar{Q}^{(k)}$ to the equivalent laminate stiffness. Therefore, a layerwise in-plane stiffness ratio $e^{(k)}$ is defined to quantify the change in transverse shear stress curvature of each layer.

The layerwise stiffness ratios $e^{(k)}$ and $g^{(k)}$ are used in a study by the present author [167] to locally modify a parabolic transverse shear stress assumption, which is then used to derive an Ambartsumyan-type displacement-based model with just two unknowns. This simple and efficient phenomenological approach results in predictions of bending deformation, axial stress and transverse shear stress to within 5% of Pagano's 3D elasticity solution [20] for laminates with thickness-to-length ratios up to 1 : 10, without the need for post-processing steps. However, this approach can lead to errors greater than 50% for non-symmetric laminations and for cases where the ZZ effect is pronounced. Although the derivation of the layerwise stiffness ratios $g^{(k)}$ and $e^{(k)}$ via Eqs. (4.6) and (4.8), respectively, sheds light onto the physics of the ZZ effect, a more rigorous approach is needed to capture the ZZ effect efficiently and accurately.

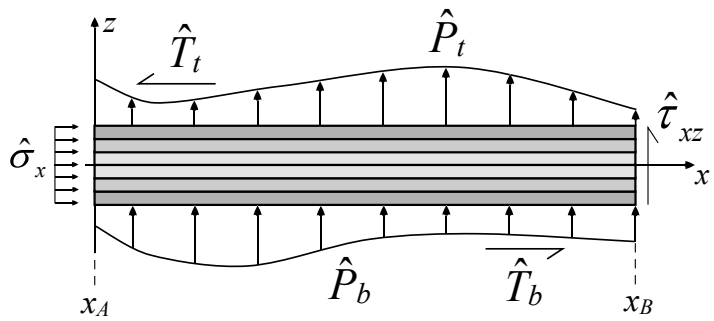

Figure 4.4: A composite beam loaded by distributed loads on the top and bottom surfaces and subjected to pertinent boundary conditions at ends A and B.

4.2 Hellinger-Reissner higher-order zig-zag model

Previous studies [55,77,78] have shown that accurate transverse stress fields can be derived in a post-processing step by indefinitely integrating the axial stresses of displacement-based theories in Cauchy's equilibrium equations. It is expedient to perform this step *a priori* and to then derive new sets of governing equations using the inherently equilibrated stress fields. Such an approach was applied within the framework of the HR principle by Cosentino and Weaver [60], but the authors restricted the model to symmetric laminations of straight-fibre composites, did not include higher-order effects in the formulation, and assumed equal transverse shear rigidity $G_{xz}^{(k)} = G_{yz}^{(k)}$ for all layers k. This previous work is generalised herein to account for a wider range of highly heterogeneous, highly orthotropic and variable-stiffness laminates. Additionally, the present work provides detailed physical insight into the significance of the derived equations and shows why the equilibrium of the transverse stresses is rigorously guaranteed. The model is thus applicable for the analysis of a wide range of industrial engineering structures, but also provides insights and interesting observations into extreme mechanical behaviour.

4.2.1 Higher-order zig-zag axial stress field

Consider a multilayered continuum as represented in Figure 4.4 undergoing static deformations under a specific set of externally applied loads and boundary conditions. The continuum is bounded by two boundary surfaces S_1 and S_2 on which the displacement and traction boundary conditions are specified, respectively, and where the complete bounding surface $S = S_1 \cup S_2$. The continuum has total thickness t and is comprised of N_l perfectly bonded laminae with layer thicknesses $t^{(k)}$. The initial configuration of the plate is referenced in orthogonal Cartesian coordinates (x, y, z), with (x, y) defining the two in-plane dimensions and $z \in [-t/2, t/2]$ defining the thickness coordinate. From hereon, it is assumed that the structural behaviour of this continuum is independent of the y-direction, such that a 1D beam formulation can be used.

Thus, within an equivalent single-layer framework, this multilayered structure is compressed onto a line element Ω coincident with the x-axis by integrating the structural properties and 3D governing equations in the direction of the smallest dimension z. The intersection of the bounding surface S and the reference line element Ω represents the two boundary points of the equivalent single layer. If displacement conditions are specified on a boundary point, this is

denoted by C_1 and in the case of traction boundary conditions we refer to point C_2. The plate is assumed to undergo static deformations under a specific set of externally applied shear and normal tractions $\left(\hat{T}_b, \hat{P}_b\right)$ and $\left(\hat{T}_t, \hat{P}_t\right)$ in the (x, z)-directions on the bottom and top surfaces of the 3D body, respectively. Note that henceforth a superposed "hat" ˆ refers to a prescribed quantity.

This equivalent single layer is assumed to deform according to a generalised in-plane and transverse displacement field,

$$\begin{aligned} u_x^{(k)}(x,z) &= u_0 + z\theta + z^2\zeta + z^3\xi + \cdots + \phi^{(k)}(z)\psi \\ u_z^{(k)}(x,z) &= w_0 \end{aligned} \tag{4.9}$$

where u_0 is the reference surface axial displacement, θ is the rotation of the beam cross-section, $\zeta, \xi, \ldots$ are higher-order rotations, ψ is the ZZ rotation, and $\phi^{(k)}$ is a pertinent ZZ function of layer k. In condensed matrix form Eq. (4.9) reads

$$u_x^{(k)}(x,z) = \boldsymbol{f}^g \mathcal{U}^g + \phi^{(k)}\psi = \begin{bmatrix} \boldsymbol{f}^g & \phi^{(k)} \end{bmatrix} \begin{Bmatrix} \mathcal{U}^g \\ \psi \end{Bmatrix} = \boldsymbol{f}_u^{(k)} \mathcal{U} \tag{4.10}$$

where $\mathcal{U}^g$ and ψ are the global and local displacement fields, respectively, and the global row vector $\boldsymbol{f}^g$ describes the global through-thickness displacement variation. Hence,

$$\boldsymbol{f}^g(z) = \begin{bmatrix} 1 & z & z^2 & z^3 & \ldots \end{bmatrix}, \qquad \mathcal{U}^g = \begin{bmatrix} u_0 & \theta & \zeta & \xi & \ldots \end{bmatrix}^\top \tag{4.11}$$

where the superscript $\top$ denotes the matrix transpose. The in-plane strain is given by the first derivative of Eq. (4.10) in the x-direction. Thus,

$$\epsilon_x^{(k)} = u_{x,x}^{(k)} = \boldsymbol{f}^g \mathcal{U}_{,x}^g + \phi_{,x}^{(k)}\psi + \phi^{(k)}\psi_{,x} = \boldsymbol{f}^g \epsilon^g + \boldsymbol{f}^l \epsilon^l \tag{4.12}$$

where the comma notation is employed to denote differentiation, the global strain field $\epsilon^g = \mathcal{U}_{,x}^g$, and the local strain field ϵ^l and local row vector $\boldsymbol{f}^l$ are given by

$$\boldsymbol{f}^l(z) = \begin{bmatrix} \phi_{,x}^{(k)} & \phi^{(k)} \end{bmatrix}, \qquad \epsilon^l = \begin{bmatrix} \psi & \psi_{,x} \end{bmatrix}^\top. \tag{4.13}$$

The axial strain field in Eq. (4.12) is written as a combination of a global higher-order strain field (independent of local ply properties) and a local ZZ strain field (dependent on local ply properties). Most ZZ functions in the literature can be written in the linear form

$$\phi^{(k)}(z) = m^{(k)} z + c^{(k)}. \tag{4.14}$$

As outlined in the work by Tessler et al. [78], the RZT ZZ function $\phi_{RZT}^{(k)}$ is defined by

$$\phi_{RZT}^{(1)} = \left(z + \frac{t}{2}\right)\left(\frac{G}{G_{xz}^{(1)}} - 1\right) \tag{4.15a}$$

$$\phi_{RZT}^{(k)} = \left(z + \frac{t}{2}\right)\left(\frac{G}{G_{xz}^{(k)}} - 1\right) + \sum_{i=2}^{k} t^{(i-1)}\left(\frac{G}{G_{xz}^{(i-1)}} - \frac{G}{G_{xz}^{(k)}}\right) \tag{4.15b}$$

where G is the equivalent "springs-in-series" stiffness defined in Eq. (4.5). The RZT ZZ function is derived from transverse material properties and may vary with location x for variable-stiffness laminates. A second ZZ function, namely MZZF [86], is given by

$$\phi_{MZZF}^{(k)} = (-1)^k \frac{2}{t^{(k)}} \left(z - z_m^{(k)} \right) \tag{4.16}$$

where $z_m^{(k)}$ is the midplane coordinate of layer k. Thus, MZZF assumes alternating values of $+1$ and -1 at the top and bottom interfaces regardless of axial location. In this case, the derivative $\phi_{,x}^{(k)}$ and the associated displacement unknown ψ vanish in Eqs. (4.12) and (4.13). In the following Chapters 5 and 6 the accuracy of the RZT ZZ function and MZZF are compared for a number of different composite laminates and sandwich beams.

Using the constitutive equation, the axial stress field is derived from the axial strain in Eq. (4.12) as follows:

$$\sigma_x^{(k)} = \bar{Q}^{(k)} \epsilon_x^{(k)} = \bar{Q}^{(k)} \left(\boldsymbol{f}^g \epsilon^g + \boldsymbol{f}^l \epsilon^l \right) \tag{4.17}$$

where $\bar{Q}^{(k)}$ is the reduced stiffness matrix, assuming either a plane strain or a plane stress condition in y. Next, the in-plane stress resultants are derived by integrating the axial stress of Eq. (4.17), weighted by the expansion functions $\boldsymbol{f}^l$ and $\boldsymbol{f}^g$, through the thickness. Hence,

$$\mathcal{F}^g = \int_{-t/2}^{t/2} \boldsymbol{f}^{g^\top} \sigma_x^{(k)} \mathrm{d}z = \int_{-t/2}^{t/2} \left(\boldsymbol{f}^{g^\top} \bar{Q}^{(k)} \boldsymbol{f}^g \epsilon^g + \boldsymbol{f}^{g^\top} \bar{Q}^{(k)} \boldsymbol{f}^l \epsilon^l \right) \mathrm{d}z = \boldsymbol{S}_{gg} \epsilon^g + \boldsymbol{S}_{gl} \epsilon^l \tag{4.18}$$

$$\mathcal{F}^l = \int_{-t/2}^{t/2} \boldsymbol{f}^{l^\top} \sigma_x^{(k)} \mathrm{d}z = \int_{-t/2}^{t/2} \left(\boldsymbol{f}^{l^\top} \bar{Q}^{(k)} \boldsymbol{f}^g \epsilon^g + \boldsymbol{f}^{l^\top} \bar{Q}^{(k)} \boldsymbol{f}^l \epsilon^l \right) \mathrm{d}z = \boldsymbol{S}_{lg} \epsilon^g + \boldsymbol{S}_{ll} \epsilon^l \tag{4.19}$$

where $\boldsymbol{S}_{gg}$, $\boldsymbol{S}_{gl}$, $\boldsymbol{S}_{lg}$ and $\boldsymbol{S}_{ll}$ are the global, local and global-local coupling stiffness matrices,

$$\boldsymbol{S}_{gg} = \int_{-t/2}^{t/2} \boldsymbol{f}^{g^\top} \bar{Q}^{(k)} \boldsymbol{f}^g \mathrm{d}z, \quad \boldsymbol{S}_{gl} = \int_{-t/2}^{t/2} \boldsymbol{f}^{g^\top} \bar{Q}^{(k)} \boldsymbol{f}^l \mathrm{d}z, \tag{4.20}$$

$$\boldsymbol{S}_{lg} = \int_{-t/2}^{t/2} \boldsymbol{f}^{l^\top} \bar{Q}^{(k)} \boldsymbol{f}^g \mathrm{d}z, \quad \boldsymbol{S}_{ll} = \int_{-t/2}^{t/2} \boldsymbol{f}^{l^\top} \bar{Q}^{(k)} \boldsymbol{f}^l \mathrm{d}z. \tag{4.21}$$

Therefore, the relation between stress resultants and strain variables is given by

$$\begin{Bmatrix} \mathcal{F}^g \\ \mathcal{F}^l \end{Bmatrix} = \begin{bmatrix} \boldsymbol{S}_{gg} & \boldsymbol{S}_{gl} \\ \boldsymbol{S}_{lg} & \boldsymbol{S}_{ll} \end{bmatrix} \begin{Bmatrix} \epsilon^g \\ \epsilon^l \end{Bmatrix} \quad \Rightarrow \quad \mathcal{F} = \boldsymbol{S}\epsilon \quad \text{and} \quad \epsilon = \boldsymbol{s}\mathcal{F} \quad \text{where} \quad \boldsymbol{s} = \boldsymbol{S}^{-1} \tag{4.22}$$

where $\boldsymbol{S}$ is the higher-order stiffness matrix of membrane and flexural rigidities, and its inverse $\boldsymbol{s}$ is the higher-order compliance matrix. These matrices relate the stress resultants $\mathcal{F}$ to the strain measures ϵ of the reference plane, and vice versa. The equation for in-plane stress in Eq. (4.17) is now recast in terms of stress resultants $\mathcal{F}$ by eliminating the strains ϵ,

$$\sigma_x^{(k)} = \bar{Q}^{(k)} \begin{bmatrix} \boldsymbol{f}^g & \boldsymbol{f}^l \end{bmatrix} \begin{Bmatrix} \epsilon^g \\ \epsilon^l \end{Bmatrix} = \bar{Q}^{(k)} \boldsymbol{f}_\epsilon^{(k)} \epsilon = \bar{Q}^{(k)} \boldsymbol{f}_\epsilon^{(k)} \boldsymbol{s}\mathcal{F} \tag{4.23}$$

where $\boldsymbol{f}_\epsilon^{(k)} = \begin{bmatrix} \boldsymbol{f}^g & \boldsymbol{f}^l \end{bmatrix}$. The axial stress field of this higher-order model written in terms of the

stress resultants $\mathcal{F}$ is used to derive expressions for the transverse shear and transverse normal stress fields.

4.2.2 Derivation of transverse shear and transverse normal stresses

An expression for the transverse shear stress is found by integrating the axial stress of Eq. (4.23) in Cauchy's axial equilibrium equation,

$$\tau_{xz}^{(k)} = -\int \frac{\mathrm{d}\sigma_x}{\mathrm{d}x}\,\mathrm{d}z = -\frac{\mathrm{d}}{\mathrm{d}x}\left[\bar{Q}^{(k)}\left(\int \boldsymbol{f}_{\epsilon}^{(k)}\,\mathrm{d}z\right)\boldsymbol{s}\mathcal{F}\right] = -\frac{\mathrm{d}}{\mathrm{d}x}\left[\bar{Q}^{(k)}\boldsymbol{g}^{(k)}\boldsymbol{s}\mathcal{F}\right] + \boldsymbol{a}^{(k)} \tag{4.24}$$

where $\boldsymbol{g}^{(k)}(z)$ captures the variation of $\tau_{xz}^{(k)}$ through the thickness of each ply k,

$$\boldsymbol{g}^{(k)}(z) = \begin{bmatrix} z & \dfrac{z^2}{2} & \dfrac{z^3}{3} & \dots & \dfrac{m_{,x}^{(k)}z^2}{2} + c_{,x}^{(k)}z & \dfrac{m^{(k)}z^2}{2} + c^{(k)}z \end{bmatrix}. \tag{4.25}$$

Note, the derivative $\mathrm{d}/\mathrm{d}x$ is applied to all terms within the square brackets in Eq. (4.24) as both the material dependent quantities $\bar{Q}^{(k)}$, $\boldsymbol{g}^{(k)}$ and $\boldsymbol{s}$, as well as the stress resultants $\mathcal{F}$ can vary along the length of a variable-stiffness beam. At this point, the product rule is not applied to expand the derivatives in order to keep the derivations as concise as possible.

The N_l layerwise constants $\boldsymbol{a}^{(k)}$ are found by enforcing N_l-1 interfacial continuity conditions $\tau_{xz}^{(k)}(z_{k-1}) = \tau_{xz}^{(k-1)}(z_{k-1})$ for $k = 2\dots N_l$ and one of the prescribed surface tractions, i.e. either the bottom surface $\tau_{xz}^{(1)}(z_0) = \hat{T}_b$ or the top surface $\tau_{xz}^{(N_l)}(z_{N_l}) = \hat{T}_t$. Here we choose to enforce the bottom surface traction, such that the layerwise integration constants $\boldsymbol{a}^{(k)}$ are found to be

$$\boldsymbol{a}^{(k)} = \sum_{i=1}^{k}\frac{\mathrm{d}}{\mathrm{d}x}\left[\left\{\bar{Q}^{(i)}\boldsymbol{g}^{(i)}(z_{i-1}) - \bar{Q}^{(i-1)}\boldsymbol{g}^{(i-1)}(z_{i-1})\right\}\boldsymbol{s}\mathcal{F}\right] + \hat{T}_b = \frac{\mathrm{d}}{\mathrm{d}x}\left[\boldsymbol{\alpha}^{(k)}\boldsymbol{s}\mathcal{F}\right] + \hat{T}_b \tag{4.26}$$

where by definition $\bar{Q}^0 = 0$. Substituting the integration constants of Eq. (4.26) back into Eq. (4.24) gives an expression for the transverse shear stress in terms of the shape functions $\boldsymbol{g}^{(k)}$, material properties $\bar{Q}^{(k)}$, higher-order compliance matrix $\boldsymbol{s}$, and the unknown stress resultants $\mathcal{F}$. Hence,

$$\tau_{xz}^{(k)} = \frac{\mathrm{d}}{\mathrm{d}x}\left[\left\{-\bar{Q}^{(k)}\boldsymbol{g}^{(k)} + \boldsymbol{\alpha}^{(k)}\right\}\boldsymbol{s}\mathcal{F}\right] + \hat{T}_b. \tag{4.27}$$

In the derivation of Eq. (4.26) the surface traction on the top surface is not enforced explicitly. However, this condition is automatically satisfied if equilibrium of the axial stress field Eq. (4.23) and the transverse shear stress Eq. (4.27) is enforced. As we are dealing with an equivalent single layer, Cauchy's axial equilibrium equation is integrated through the thickness z-direction to give

$$\int_{z_0}^{z_{N_l}} \sigma_{x,x}\mathrm{d}z + \int_{z_0}^{z_{N_l}} \tau_{xz,z}\mathrm{d}z = N_{,x} + \tau_{xz}^{(N_l)}(z_{N_l}) - \tau_{xz}^{(1)}(z_0) = 0 \tag{4.28}$$

where N is the membrane stress resultant of CLA. An expression for $N_{,x}$ is easily derived by differentiating Eq. (4.23) along the x-direction and then integrating in the z-direction. These

steps result in the following expression

$$N_{,x} = \sum_{k=1}^{N_l} \frac{\mathrm{d}}{\mathrm{d}x} \left[\left\{ \bar{Q}^{(k)} \boldsymbol{g}^{(k)}(z_k) - \bar{Q}^{(k)} \boldsymbol{g}^{(k)}(z_{k-1}) \right\} \boldsymbol{s}\mathcal{F} \right]. \tag{4.29}$$

Now the only undefined quantity in Eq. (4.28) is $\tau_{xz}^{(N_l)}(z_{N_l})$ and an expression for this is derived by calculating τ_{xz} at $z = z_{N_l}$ using Eq. (4.27). Hence,

$$\begin{aligned} \tau_{xz}^{(N_l)}(z_{N_l}) &= \frac{\mathrm{d}}{\mathrm{d}x} \left[\left\{ -\bar{Q}^{(N_l)} \boldsymbol{g}^{(N_l)}(z_{N_l}) + \boldsymbol{\alpha}^{(N_l)} \right\} \boldsymbol{s}\mathcal{F} \right] + \hat{T}_b \\ &= -\sum_{k=1}^{N_l} \frac{\mathrm{d}}{\mathrm{d}x} \left[\left\{ \bar{Q}^{(k)} \boldsymbol{g}^{(k)}(z_k) - \bar{Q}^{(k)} \boldsymbol{g}^{(k)}(z_{k-1}) \right\} \boldsymbol{s}\mathcal{F} \right] + \hat{T}_b. \end{aligned}$$

Inserting Eq. (4.29) in the above expression gives

$$\tau_{xz}^{(N_l)}(z_{N_l}) = -N_{,x} + \hat{T}_b. \tag{4.30}$$

Therefore, substituting Eq. (4.30) back into the Cauchy equilibrium equation (4.28) we have

$$N_{,x} + \left(-N_{,x} + \hat{T}_b \right) - \tau_{xz}^{(1)}(z_0) = 0 \tag{4.31}$$

and as $\tau_{xz}^{(1)}(z_0) = \hat{T}_b$ the expression in Eq. (4.31) is satisfied. This is the first significant finding of the present formulation: as long as Eq. (4.28) is satisfied when deriving the governing equations from a variational statement, equilibrium of the interfacial and surface shear tractions is automatically enforced.

An expression for the transverse normal stress is derived in a similar fashion. Integrating the transverse shear stress of Eq. (4.27) in Cauchy's transverse equilibrium equation yields

$$\begin{aligned} \sigma_z^{(k)} &= -\int \frac{\mathrm{d}\tau_{xz}}{\mathrm{d}x} \mathrm{d}z = \frac{\mathrm{d}^2}{\mathrm{d}x^2} \left[\int \left(\bar{Q}^{(k)} \boldsymbol{g}^{(k)} - \boldsymbol{\alpha}^{(k)} \right) \mathrm{d}z \boldsymbol{s}\mathcal{F} \right] - \hat{T}_{b,x} z \\ &= \frac{\mathrm{d}^2}{\mathrm{d}x^2} \left[\left\{ \bar{Q}^{(k)} \boldsymbol{h}^{(k)} - \boldsymbol{\alpha}^{(k)} z \right\} \boldsymbol{s}\mathcal{F} \right] - \hat{T}_{b,x} z + \boldsymbol{b}^{(k)} \end{aligned} \tag{4.32}$$

where $\boldsymbol{h}^{(k)}(z)$ captures the variation of $\sigma_z^{(k)}$ through the thickness of each ply k,

$$\boldsymbol{h}^{(k)}(z) = \left[\frac{z^2}{2} \quad \frac{z^3}{6} \quad \frac{z^4}{12} \quad \dots \quad \frac{m_{,x}^{(k)} z^3}{6} + \frac{c_{,x}^{(k)} z^2}{2} \quad \frac{m^{(k)} z^3}{6} + \frac{c^{(k)} z}{2} \right]. \tag{4.33}$$

The N_l layerwise constants $\boldsymbol{b}^{(k)}$ are found by enforcing the $N_l - 1$ continuity conditions $\sigma_z^{(k)}(z_{k-1}) = \sigma_z^{(k-1)}(z_{k-1})$ for $k = 2 \dots N_l$ and one of the prescribed surface tractions, i.e. either the bottom surface $\sigma_z^{(1)}(z_0) = \hat{P}_b$ or the top surface $\sigma_z^{(N_l)}(z_{N_l}) = \hat{P}_t$. Hence, by enforcing the $N_l - 1$ continuity conditions and $\sigma_z^{(1)}(z_0) = \hat{P}_b$ we have

$$\begin{aligned} \boldsymbol{b}^{(k)} &= \sum_{i=1}^{k} \frac{\mathrm{d}^2}{\mathrm{d}x^2} \left[\left\{ \bar{Q}^{(i-1)} \boldsymbol{h}^{(i-1)}(z_{i-1}) - \bar{Q}^{(i)} \boldsymbol{h}^{(i)}(z_{i-1}) + \left(\boldsymbol{\alpha}^{(i)} - \boldsymbol{\alpha}^{(i-1)} \right) z_{i-1} \right\} \boldsymbol{s}\mathcal{F} \right] + \hat{T}_{b,x} z_0 + \hat{P}_b \\ \boldsymbol{b}^{(k)} &= \frac{\mathrm{d}^2}{\mathrm{d}x^2} \left[\boldsymbol{\beta}^{(k)} \boldsymbol{s}\mathcal{F} \right] + \hat{T}_{b,x} z_0 + \hat{P}_b \end{aligned} \tag{4.34}$$

where by definition $\bar{Q}^0 = \boldsymbol{\alpha}^0 = 0$. Thus, substituting the integration constants of Eq. (4.34) back into Eq. (4.32) gives an expression for the transverse normal stress,

$$\sigma_z^{(k)} = \frac{\mathrm{d}^2}{\mathrm{d}x^2}\left[\left\{\bar{Q}^{(k)}\boldsymbol{h}^{(k)} - \boldsymbol{\alpha}^{(k)}z + \boldsymbol{\beta}^{(k)}\right\}\boldsymbol{s}\mathcal{F}\right] - \hat{T}_{b,x}\left(z - z_0\right) + \hat{P}_b. \tag{4.35}$$

In the derivation of Eq. (4.34) the traction condition on the top surface is not enforced explicitly. However, this condition is automatically satisfied if equilibrium of the transverse shear stress field Eq. (4.27) and the transverse normal stress Eq. (4.35) is enforced. Integrating Cauchy's transverse equilibrium equation in the thickness z-direction,

$$\int_{z_0}^{z_{N_l}} \tau_{xz,x}\mathrm{d}z + \int_{z_0}^{z_{N_l}} \sigma_{z,z}\mathrm{d}z = Q_{,x} + \sigma_z^{(N_l)}(z_{N_l}) - \sigma_z^{(1)}(z_0) = 0 \tag{4.36}$$

where Q is the transverse shear force. An expression for $Q_{,x}$ is derived by integrating Eq. (4.27) from the bottom surface of the laminate $z = z_0$ to the top surface $z = z_{N_l}$ and differentiating in the x-direction. Hence,

$$Q_{,x} = \sum_{k=1}^{N_l} \frac{\mathrm{d}^2}{\mathrm{d}x^2}\left[\left\{\bar{Q}^{(k)}\left(\boldsymbol{h}^{(k)}(z_{k-1}) - \boldsymbol{h}^{(k)}(z_k)\right) + \boldsymbol{\alpha}^{(k)}t^{(k)}\right\}\boldsymbol{s}\mathcal{F}\right] + \sum_{k=1}^{N_l}\hat{T}_{b,x}t^{(k)} \tag{4.37}$$

where $t^{(k)}$ is the thickness of the kth layer. An expression for $\sigma_z^{(N_l)}(z_{N_l})$ is defined by computing Eq. (4.35) at $z = z_{N_l}$,

$$\begin{aligned}\sigma_z^{(N_l)}(z_{N_l}) &= \frac{\mathrm{d}^2}{\mathrm{d}x^2}\left[\left\{\bar{Q}^{(N_l)}\boldsymbol{h}^{(N_l)}(z_{N_l}) - \boldsymbol{\alpha}^{(N_l)}z_{N_l} + \boldsymbol{\beta}^{(N_l)}\right\}\boldsymbol{s}\mathcal{F}\right] - \hat{T}_{b,x}\left(z_{N_l} - z_0\right) + \hat{P}_b \\ &= \sum_{k=1}^{N_l}\frac{\mathrm{d}^2}{\mathrm{d}x^2}\left[\left\{\bar{Q}^{(k)}\left(\boldsymbol{h}^{(k)}(z_k) - \boldsymbol{h}^{(k)}(z_{k-1})\right) - \boldsymbol{\alpha}^{(k)}t^{(k)}\right\}\boldsymbol{s}\mathcal{F}\right] - \sum_{k=1}^{N_l}\hat{T}_{b,x}t^{(k)} + \hat{P}_b.\end{aligned}$$

Substituting Eq. (4.37) into the above expression gives

$$\sigma_z^{(N_l)}(z_{N_l}) = -Q_{,x} + \hat{P}_b. \tag{4.38}$$

Finally, Eq. (4.38) is inserted back into Eq. (4.36), such that

$$Q_{,x} + \left(-Q_{,x} + \hat{P}_b\right) - \sigma_z^{(1)}(z_0) = 0 \tag{4.39}$$

and as $\sigma_z^{(1)}(z_0) = \hat{P}_b$ the expression in Eq. (4.39) is satisfied. This is the second significant finding of the present formulation: as long as Eq. (4.36) is enforced in the variational statement then equilibrium of the interfacial and surface normal tractions is guaranteed.

The layerwise reduced stiffness term $\bar{Q}^{(k)}$ and through-thickness shape functions in Eqs. (4.27) and (4.35) are each combined conveniently into single layerwise vectors. Thus,

$$\tau_{xz}^{(k)} = \frac{\mathrm{d}}{\mathrm{d}x}\left[\boldsymbol{c}^{(k)}\boldsymbol{s}\mathcal{F}\right] + \hat{T}_b \tag{4.40}$$

$$\sigma_z^{(k)} = \frac{\mathrm{d}^2}{\mathrm{d}x^2}\left[\boldsymbol{e}^{(k)}\boldsymbol{s}\mathcal{F}\right] - \hat{T}_{b,x}\left(z - z_0\right) + \hat{P}_b. \tag{4.41}$$

4.2.3 A contracted Hellinger-Reissner functional

A new set of governing equations is derived by means of minimising the potential energy functional Π_{HR} of the HR mixed-variational principle introduced in Eq. (2.19) of Chapter 2. For a 3D continuum independent of variations in the y-direction, the HR functional reads

$$\Pi_{HR}(\boldsymbol{u},\boldsymbol{\sigma}) = \int_V U_0^*(\sigma_{ij})\mathrm{d}V - \int_{S_1} \hat{u}_i t_i \mathrm{d}S + \int_V u_i\left(\sigma_{ij,j} + f_i\right)\mathrm{d}V - \int_{S_2} u_i\left(t_i - \hat{t}_i\right)\mathrm{d}S \quad i,j = x,z. \tag{4.42}$$

where $U_0^*(\sigma_{ij})$ is the complementary energy density written in terms of the Cauchy stress tensor σ_{ij}. The displacements u_i are the Lagrange multipliers that enforce Cauchy's equilibrium equations $\sigma_{ij,j} + f_i$ in a variational sense throughout the volume of the continuum, as well as the traction boundary conditions $t_i - \hat{t}_i$ on the boundary surface S_2. The tractions $t_i = (\sigma_x, \sigma_{xz})$ are the tractions in the (x,z) directions acting on the boundary surface.

In the present work, the model assumption of the axial displacements is given by Eq. (4.10), i.e. $u_x^{(k)} = \boldsymbol{f}_u^{(k)}\mathcal{U}$, whereas the transverse displacement $u_z = w_0$ is constant throughout the thickness. Thus, the term $\Pi_{\mathcal{L}}$ associated with Cauchy's equilibrium equations in the HR functional in the absence of body forces, where $\mathcal{L}$ refers to Lagrange multipliers, is written as

$$\Pi_{\mathcal{L}} = \int_V u_i\sigma_{ij,j}\mathrm{d}V = \int_V \left[\mathcal{U}^\top \boldsymbol{f}_u^{(k)^\top}\left(\frac{\mathrm{d}\sigma_x^{(k)}}{\mathrm{d}x} + \frac{\mathrm{d}\tau_{xz}^{(k)}}{\mathrm{d}z}\right) + w_0\left(\frac{\mathrm{d}\tau_{xz}^{(k)}}{\mathrm{d}x} + \frac{\mathrm{d}\sigma_z^{(k)}}{\mathrm{d}z}\right)\right]\mathrm{d}V \tag{4.43}$$

where all quantities are defined as in the previous two sections. Taking the first variation of this functional with respect to the displacement variables, i.e. $\delta\mathcal{U}$ and δw_0 results in the higher-order equilibrium equations of the theory. By integrating the $\mathcal{U}$-coefficient term in Eq. (4.43) by parts in the z-direction (note, $\mathcal{U}$ is independent of z), and then taking the first variation we have

$$\begin{aligned}\delta\Pi_{\mathcal{L}_1} &= \iint_{-t/2}^{t/2} \delta\mathcal{U}^\top\left(\boldsymbol{f}_u^{(k)^\top}\frac{\mathrm{d}\sigma_x^{(k)}}{\mathrm{d}x} - \frac{\mathrm{d}\boldsymbol{f}_u^{(k)^\top}}{\mathrm{d}z}\tau_{xz}^{(k)}\right)\mathrm{d}z\mathrm{d}x + \int \delta\mathcal{U}^\top\ \boldsymbol{f}_u^{(k)^\top}\tau_{xz}^{(k)}\Big|_{-t/2}^{t/2}\mathrm{d}x \\ &= \int \delta\mathcal{U}^\top\left[\frac{\mathrm{d}\mathcal{F}^*}{\mathrm{d}x} - \mathcal{T} + \boldsymbol{f}_u^{(N_l)^\top}(z_{N_l})\hat{T}_t - \boldsymbol{f}_u^{(1)^\top}(z_0)\hat{T}_b\right]\mathrm{d}x.\end{aligned} \tag{4.44}$$

The vector of stress resultants $\mathcal{F}^*$ used in Eq. (4.44) is defined in the same manner as $\mathcal{F}$ in Eqs. (4.18) and (4.19), i.e.

$$\mathcal{F}^* = \int_{-t/2}^{t/2} \boldsymbol{f}_u^{(k)^\top}\sigma_x^{(k)}\mathrm{d}z \tag{4.45}$$

but does not contain the stress resultants associated with the derivative of the ZZ function $\phi_{,x}^{(k)}$ as this term is not included in $\boldsymbol{f}_u^{(k)}$. Finally, a vector of higher-order shear forces $\mathcal{T} = (0, Q, \ldots, Q^\phi)$ that balances the derivative of the stress resultants $\mathcal{F}^*$ in the higher-order equilibrium equations has been defined as follows

$$\mathcal{T} = \int_{-t/2}^{t/2} \frac{\mathrm{d}\boldsymbol{f}_u^{(k)^\top}}{\mathrm{d}z}\tau_{xz}^{(k)}\mathrm{d}z. \tag{4.46}$$

When the first variation is set to zero, the term in square brackets of Eq. (4.44) represents the collection of equilibrium equations of the equivalent single-layer written in matrix form. These are the same higher-order equilibrium equations that are derived from the assumed displacement

field if the PVD is applied. The equilibrium equations and associated Lagrange multipliers for a first-order theory with ZZ functionality are

$$\begin{aligned} \delta u_0 &: N_{,x} + \hat{T}_t - \hat{T}_b = 0 \\ \delta\theta &: M_{,x} - Q + z_{N_l}\hat{T}_t - z_0\hat{T}_b = 0 \\ \delta\psi &: M^{\phi}_{,x} - Q^{\phi} + \phi^{(N_l)}(z_{N_l})\hat{T}_t - \phi^{(1)}(z_0)\hat{T}_b = 0 \end{aligned} \tag{4.47}$$

where the comma notation is used to denote differentiation; N, M and Q are the classical membrane force, bending moment and transverse shear force respectively, whereas M^{ϕ} and Q^{ϕ} are the ZZ bending moment and ZZ transverse shear force, respectively.

For a general assumption of displacements $\boldsymbol{u}$ and stresses $\boldsymbol{\sigma}$, the entire set of higher-order equilibrium equations in Eq. (4.44) needs to be satisfied. However, in the present work, the assumption of the transverse shear stress is based explicitly on the integration of the in-plane stress in Cauchy's equilibrium equations. As shown in the following, this means that the equilibrium equations of Eq. (4.44) are automatically satisfied and do not need to be enforced in the variational statement. Returning to the definition of the transverse shear stress resultants of Eq. (4.46) and integrating by parts,

$$\mathcal{T} = \int_{-t/2}^{t/2} \frac{\mathrm{d}\boldsymbol{f}_u^{(k)^\top}}{\mathrm{d}z}\tau_{xz}^{(k)}\mathrm{d}z = \boldsymbol{f}_u^{(k)^\top}\tau_{xz}^{(k)}\Big|_{-t/2}^{t/2} - \int_{-t/2}^{t/2} \boldsymbol{f}_u^{(k)^\top}\frac{\mathrm{d}\tau_{xz}^{(k)}}{\mathrm{d}z}\mathrm{d}z. \tag{4.48}$$

As the model assumption for the transverse shear stresses is derived exactly from Cauchy's axial equilibrium equation in Eq. (4.24), we can replace $\tau_{xz,z}^{(k)}$ with $-\sigma_{x,x}^{(k)}$. Hence,

$$\mathcal{T} = \boldsymbol{f}_u^{(N_l)^\top}(z_{N_l})\hat{T}_t - \boldsymbol{f}_u^{(1)^\top}(z_0)\hat{T}_b + \int_{-t/2}^{t/2} \boldsymbol{f}_u^{(k)^\top}\frac{\mathrm{d}\sigma_x^{(k)}}{\mathrm{d}x}\mathrm{d}z \tag{4.49}$$

and by using the expression in Eq. (4.45)

$$\mathcal{T} = \boldsymbol{f}_u^{(N_l)^\top}(z_{N_l})\hat{T}_t - \boldsymbol{f}_u^{(1)^\top}(z_0)\hat{T}_b + \frac{\mathrm{d}\mathcal{F}^*}{\mathrm{d}x}. \tag{4.50}$$

Thus, substituting Eq. (4.50) back into Eq. (4.44), the equilibrium equations in the square brackets vanish identically when using the present, inherently equilibrated stress assumptions. However, as was shown in Section 4.2.2, the axial and transverse Cauchy equilibrium equations need to be satisfied to guarantee that the transverse stresses are recovered accurately. Thus, these two equations are enforced in a variational sense using two Lagrange multipliers, resulting in a *contracted* version of the HR principle with fewer degrees of freedom and less computational cost. All other higher-order equilibrium equations are automatically satisfied due to the inherently equilibrated axial and transverse stress assumptions.

The axial and transverse Cauchy equilibrium equations are derived by integrating the equilibrium equations in the thickness z-direction. Thus,

$$\int_{z_0}^{z_{N_l}} \sigma_{x,x}\mathrm{d}z + \int_{z_0}^{z_{N_l}} \tau_{xz,z}\mathrm{d}z = N_{,x} + \tau_{xz}^{(N_l)}(z_{N_l}) - \tau_{xz}^{(1)}(z_0) = N_{,x} + \hat{T}_t - \hat{T}_b = 0 \tag{4.51}$$

$$\int_{z_0}^{z_{N_l}} \tau_{xz,x} \mathrm{d}z + \int_{z_0}^{z_{N_l}} \sigma_{z,z} \mathrm{d}z = Q_{,x} + \sigma_z^{(N_l)}(z_{N_l}) - \sigma_z^{(1)}(z_0) = Q_{,x} + \hat{P}_t - \hat{P}_b = 0. \tag{4.52}$$

Next, transverse shear force Q is eliminated from Eq. (4.52) using the first-order moment equilibrium condition,

$$\begin{aligned} &\int_{z_0}^{z_{N_l}} z\left(\sigma_{x,x} + \tau_{xz,z}\right) \mathrm{d}z = M_{,x} - Q + z_{N_l}\hat{T}_t - z_0\hat{T}_b = 0 \\ &\therefore Q = M_{,x} + z_{N_l}\hat{T}_t - z_0\hat{T}_b. \end{aligned} \tag{4.53}$$

Therefore, the equilibrium equation (4.52) now reads

$$M_{,xx} + z_{N_l}\hat{T}_{t,x} - z_0\hat{T}_{b,x} + \hat{P}_t - \hat{P}_b = 0. \tag{4.54}$$

For equilibrium of the system, the first variation of the functional Π must vanish in such a manner that equilibrium equations (4.51) and (4.54) are satisfied over the whole beam domain $x \in [x_A, x_B]$. Following the HR principle this condition is enforced using the displacement Lagrange multipliers u_0 and w_0. Hence,

$$\begin{aligned} \delta\Pi =& \delta\left[\frac{1}{2}\int_V U_0^*(\mathcal{F})\mathrm{d}V - \int_{S_1}\left(\sigma_x \hat{u}_x^{(k)} + \tau_{xz}\hat{w}_0\right)\mathrm{d}S - \int_{S_2}\left\{u_x^{(k)}\left(\sigma_x - \hat{\sigma}_x\right) + w_0\left(\tau_{xz} - \hat{\tau}_{xz}\right)\right\}\mathrm{d}S \right. \\ &\left. + \int u_0\left(N_{,x} + \hat{T}_t - \hat{T}_b\right)\mathrm{d}x + \int w_0\left(M_{,xx} + z_{N_l}\hat{T}_{t,x} - z_0\hat{T}_{b,x} + \hat{P}_t - \hat{P}_b\right)\mathrm{d}x\right] = 0 \end{aligned} \tag{4.55}$$

where $\hat{u}_x^{(k)}$ and $\hat{w}_0$ are the displacements defined on the boundary surface S_1, and $\hat{\sigma}_x$ and $\hat{\tau}_{xz}$ are the tractions defined on the boundary surface S_2.

The strain energy $U_0^*(\mathcal{F}) = \sigma_x\epsilon_x + \tau_{xz}\gamma_{xz} + \sigma_z\epsilon_z$ in Eq. (4.55) is written in complementary form by replacing the strains via a constitutive relation. The quantities σ_x, τ_{xz} and σ_z are defined by Eqs. (4.23), (4.40) and (4.41), respectively. The transverse shear strain $\gamma_{xz}^{(k)}$ is defined using the constitutive relation

$$\gamma_{xz}^{(k)} = \frac{\tau_{xz}^{(k)}}{G_{xz}^{(k)}} = \frac{1}{G_{xz}^{(k)}}\left[\frac{\mathrm{d}}{\mathrm{d}x}\left(\boldsymbol{c}^{(k)}\boldsymbol{s}\mathcal{F}\right) + \hat{T}_b\right]. \tag{4.56}$$

The transverse normal strain $\epsilon_z^{(k)}$ is derived from Hooke's Law, written in terms of the full compliance matrix S_{ij} in a state of plane strain in y as this is the condition assumed throughout the model validation in Chapters 5 and 6. Thus,

$$\begin{aligned} \epsilon_z^{(k)} &= R_{13}^{(k)}\sigma_x^{(k)} + R_{33}^{(k)}\sigma_z^{(k)} \quad \text{where} \quad R_{ij} = S_{ij} - \frac{S_{i2}S_{j2}}{S_{22}} \\ &= R_{13}^{(k)}\bar{Q}^{(k)}\boldsymbol{f}_\epsilon^{(k)}\boldsymbol{s}\mathcal{F} + R_{33}^{(k)}\left[\frac{\mathrm{d}^2}{\mathrm{d}x^2}\left(\boldsymbol{e}^{(k)}\boldsymbol{s}\mathcal{F}\right) - \hat{T}_{b,x}\left(z - z_0\right) + \hat{P}_b\right]. \end{aligned} \tag{4.57}$$

The new set of governing equations is derived by substituting all stress and strain expressions Eqs. (4.23), (4.40), (4.41), (4.56) and (4.57) into Eq. (4.55) and setting the first variation to zero. The resulting Euler-Lagrange field equations in terms of the functional unknowns u_0, w_0

and $\mathcal{F}$ are,

$$\delta u_0 : \; N_{,x} + \hat{T}_t - \hat{T}_b = 0 \tag{4.58a}$$

$$\delta w_0 : \; M_{,xx} + z_{N_l}\hat{T}_{t,x} - z_0\hat{T}_{b,x} + \hat{P}_t - \hat{P}_b = 0 \tag{4.58b}$$

$$\begin{aligned}\delta\mathcal{F}^\top : \; &(\boldsymbol{s} + \boldsymbol{\eta}^s + \boldsymbol{\eta}^n)\,\mathcal{F} + (\boldsymbol{\eta}^s_x + \boldsymbol{\eta}^n_x)\,\mathcal{F}_{,x} + (\boldsymbol{\eta}^s_{xx} + \boldsymbol{\eta}^n_{xx})\,\mathcal{F}_{,xx} + \boldsymbol{\eta}^n_{xxx}\mathcal{F}_{,xxx} + \boldsymbol{\eta}^n_{xxxx}\mathcal{F}_{,xxxx} + \\ &\hat{T}_b\boldsymbol{\chi}^s + \hat{T}_{b,x}\,(\boldsymbol{\chi}^s_x + \boldsymbol{\chi}^n_x) + \hat{T}_{b,xx}\boldsymbol{\chi}^n_{xx} + \hat{T}_{b,xxx}\boldsymbol{\chi}^n_{xxx} + \hat{P}_b\boldsymbol{\omega}^n + \hat{P}_{b,x}\boldsymbol{\omega}^n_x + \hat{P}_{b,xx}\boldsymbol{\omega}^n_{xx} + \boldsymbol{\Lambda}_{eq} = \mathbf{0}.\end{aligned} \tag{4.58c}$$

The pertinent essential and natural boundary conditions are given by,

$$\begin{aligned}\text{on } C_1 \quad \delta\mathcal{F}^\top : \; &\left(\boldsymbol{\eta}^{sbc} + \boldsymbol{\eta}^{nbc}\right)\mathcal{F} + \left(\boldsymbol{\eta}^{sbc}_x + \boldsymbol{\eta}^{nbc}_x\right)\mathcal{F}_{,x} + \boldsymbol{\eta}^{nbc}_{xx}\mathcal{F}_{,xx} + \boldsymbol{\eta}^{nbc}_{xxx}\mathcal{F}_{,xxx} + \\ &\hat{T}_b\boldsymbol{\chi}^{sbc} + \hat{T}_{b,x}\boldsymbol{\chi}^{nbc}_x + \hat{T}_{b,xx}\boldsymbol{\chi}^{nbc}_{xx} + \hat{P}_b\boldsymbol{\omega}^{nbc} + \hat{P}_{b,x}\boldsymbol{\omega}^{nbc}_x + \boldsymbol{\Lambda}_{bc_1} = \hat{\mathcal{U}}_{bc}\end{aligned} \tag{4.59a}$$

$$\text{on } C_1 \quad \delta\mathcal{F}^\top_{,x} : \boldsymbol{\rho}^{nbc}\mathcal{F} + \boldsymbol{\rho}^{nbc}_x\mathcal{F}_{,x} + \boldsymbol{\rho}^{nbc}_{xx}\mathcal{F}_{,xx} + \hat{T}_{b,x}\boldsymbol{\gamma}^{nbc}_x + \hat{P}_b\boldsymbol{\mu}^{nbc} + \boldsymbol{\Lambda}_{bc_2} = \hat{\mathcal{W}}. \tag{4.59b}$$

$$\text{on } C_2 \quad \delta\mathcal{U}^\top : \mathcal{F}^* = \hat{\mathcal{F}}^* \tag{4.59c}$$

$$\text{on } C_2 \quad \delta w_0 : Q = \hat{Q} \tag{4.59d}$$

Note, the full derivation of the above governing equations, including details of all coefficients, is given in Appendix A.

The governing field equations and boundary conditions related to $\delta\mathcal{F}^\top$ are written in matrix notation, with each row defining a separate equation. Eqs. (4.58c) are an enhanced version of the 1D CLA constitutive equation for beams, namely

$$\begin{Bmatrix} u_{0,x} \\ -w_{0,xx} \end{Bmatrix} = \begin{bmatrix} A & B \\ B & D \end{bmatrix}^{-1} \begin{Bmatrix} N \\ M \end{Bmatrix} = \boldsymbol{s}\mathcal{F} \tag{4.60}$$

where $u_{0,x}$ and $-w_{0,xx}$ are the reference surface stretching strain and curvature, respectively, but additionally accounting for higher-order effects in $\boldsymbol{s}$ and $\mathcal{F}$. The members of $\boldsymbol{\eta}$ are correction factors related to either transverse shear stresses (superscript s) or transverse normal stresses (superscript n). The addition of the superscript bc to s and n denotes correction factors for the boundary equations. Similarly, members of row vectors $\boldsymbol{\chi}$ and $\boldsymbol{\omega}$ are correction factors related to the surface shear and normal tractions, respectively. The terms $\boldsymbol{\rho}$, $\boldsymbol{\gamma}$ and $\boldsymbol{\mu}$ in the second set of boundary equations $\delta\mathcal{F}^\top_{,x}$ stem only from transverse normal stresses. Column vectors $\boldsymbol{\Lambda}$ only include the Lagrange multipliers u_0, w_0 and their derivatives. Specifically, $\boldsymbol{\Lambda}_{eq}$ is a column vector that captures the reference surface stretching strain and curvature,

$$\boldsymbol{\Lambda}_{eq} = \begin{bmatrix} -u_{0,x} & w_{0,xx} & 0 & \dots \end{bmatrix}^\top. \tag{4.61}$$

Similarly, $\boldsymbol{\Lambda}_{bc1}$ and $\hat{\mathcal{U}}_{bc}$ are column vectors of the boundary displacement and Kirchhoff rotation, and prescribed displacement variables, respectively,

$$\boldsymbol{\Lambda}_{bc1} = \begin{bmatrix} u_0 & -w_{0,x} & 0 & \dots \end{bmatrix}^\top \quad \text{and} \quad \hat{\mathcal{U}}_{bc} = \begin{bmatrix} \hat{\mathcal{U}}^g & 0 & \hat{\psi} \end{bmatrix}^\top. \tag{4.62}$$

whereas $\boldsymbol{\Lambda}_{bc2}$ and $\hat{\mathcal{W}}$ are column vectors that include the unknown field and prescribed boundary

transverse displacement, respectively,

$$\mathbf{\Lambda}_{bc2} = \begin{bmatrix} 0 & w_0 & 0 & \dots \end{bmatrix}^\top \quad \text{and} \quad \hat{\mathcal{W}} = \begin{bmatrix} 0 & \hat{w}_0 & 0 & \dots \end{bmatrix}^\top . \tag{4.63}$$

The displacement boundary conditions in Eq. (4.59a) indicate that the Kirchhoff rotation normal to the boundary curve $w_{0,x}$ is modified by transverse shear correction factors. Therefore the static inconsistency that occurs for Reddy-type models discussed in Chapter 3 is prevented because the slope of the beam at the support can be non-zero. Finally, the traction boundary conditions on C_2 refer to $\mathcal{F}^*$, which are the stress resultants without the stress resultant associated with $\phi_{,x}^{(k)}$, as previously defined in Eq. (4.45). Finally, the expression in Eq. (4.59a) is used to determine the deformation vector $\mathcal{U}$ of the reference surface from the stress resultants, whereas the second row of Eq. (4.59b) is used to find an expression for the bending deflection w_0 throughout the entire domain.

4.3 Conclusions

In this chapter the governing equations of a higher-order model for highly heterogeneous, variable-stiffness beams was derived using a contracted HR functional that only enforces the membrane and bending equilibrium equations via Lagrange multipliers. All other higher-order equilibrium equations are automatically satisfied by basing the transverse stresses on integrations of the axial stress. As a result, the number of variables in the model is greatly reduced. Higher-order fidelity is introduced in the model by a Taylor series expansion of the in-plane stress field including the effect of ZZ moments.

Section 4.1.2 investigated the fundamental mechanics of the ZZ effect in multilayered structures. The ZZ effect was attributed to differences in transverse shear strains at layer interfaces that require discrete changes in the slope of the in-plane deformation field in order to satisfy the kinematic relations. The dual requirement of transverse shear stress and displacement continuity at layer interfaces led to the notion of modelling the transverse shear mechanics of a multilayered structure using a combination of "springs-in-series" and "springs-in-parallel" systems. Such an approach invariably leads to the RZT ZZ function proposed by Tessler et al. [77], which is based on the ratios of layerwise transverse shear moduli and the equivalent, average transverse rigidity of the entire laminate. Hence, this approach incorporates the physical insight that the ZZ effect is driven by differences in the transverse shear properties through the laminate thickness. Alternatively, MZZF [86], which is extensively used and cited in the literature, only accounts for differences in layer thicknesses.

The derivation of the HR formulation in Section 4.2 is based on the notion that accurate transverse shear and normal stress fields can be derived by integrating the axial stresses of displacement-based higher-order theories in Cauchy's equilibrium equations. In the present model this post-processing step is precluded by using these equilibrated 3D stress fields, written in terms of stress resultants, as *a priori* model assumptions in the HR variational principle. It was shown that by enforcing the classical membrane and bending equilibrium equations of an equivalent single layer in a variational statement using Lagrange multipliers, the interlaminar continuity conditions and equilibrium of surface tractions are guaranteed.

Chapter 5

Global and Local Phenomena in Straight-Fibre Composite Beam Bending

In the previous chapter, the governing equations of a higher-order ZZ theory for highly heterogeneous, variable-stiffness beams was derived using a *contracted* HR functional. Hence, this functional was derived by enforcing only the classical membrane and bending equilibrium equations in the PMCE via Lagrange multipliers. All other higher-order equilibrium equations are automatically satisfied due to the inherently equilibrated stress field assumptions. This model is now applied to analyse the bending of a comprehensive set of heterogeneous straight-fibre composite laminates and sandwich beams. The results in this chapter include the benchmarking of the model against 3D elasticity solutions (Section 5.2), a discussion of the relative effects of transverse shear, transverse normal and ZZ deformations on the flexural behaviour of straight-fibre laminates (Section 5.3), and the analysis of boundary layer effects towards clamped edges (Section 5.4).

A third-order form of the HR model is implemented with two different ZZ functions; MZFF, denoted by HR3-MZZF and the RZT ZZ function, denoted by HR3-RZT. In the latter case, Gherlone's modified version of the RZT ZZ function of Eq. (4.3) is used. A third-order formulation was chosen as the linear z-wise function in the first-order formulation fails to model higher-order "stress-channelling" effects towards the outer surface as discussed in Chapter 3. Furthermore, Carrera [92] has pointed out that including a single ZZ variable gives more accurate results for equal computational effort than multiple higher-order continuous terms. These findings are corroborated here and suggests that a fifth-order term is not needed to model higher-order effects that arise in most composite laminates and sandwich beams.

For all results shown herein, the governing equations for HR3-RZT and HR3-MZZF are derived for laminated beams in plane strain in the lateral y-direction. This condition allows the results to be compared against Pagano's 3D elasticity solution [20] of an infinitely wide plate. However, the HR formulation is readily modified to the application of plane stress by changing the definition of the stiffness term from $\bar{Q}^{(k)} = E_x^{(k)} / \left(1 - \nu_{xy}^{(k)} \nu_{yx}^{(k)}\right)$ in plane strain to $\bar{Q}^{(k)} = E_x^{(k)}$ in plane stress, and similarly altering the definition of R_{ij} in Eq. (4.57).

5.1 Load case and model implementation

Consider a multilayered, laminated beam comprising N_l orthotropic, straight-fibre composite layers as illustrated in Figure 5.1 with the midplane and normal to the beam aligned with the Cartesian x- and z-axes. The layers can be arranged in any general fashion with different ply thicknesses, material properties or material orientations. The beam is assumed to be simply

supported at the two ends $x_A = 0$ and $x_B = a$ as shown in Figure 5.2, and is considered to undergo isothermal static deformation in plane strain under the applied sinusoidally distributed load equally divided between the top and bottom surfaces $\hat{P}_b = -\hat{P}_t = q_0/2 \cdot \sin(\pi x/a)$.

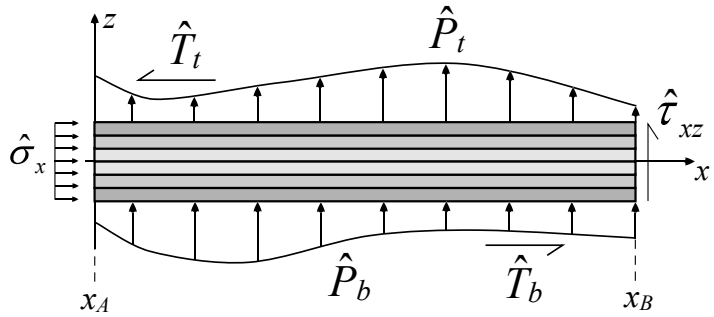

Figure 5.1: A composite beam loaded by distributed loads on the top and bottom surfaces and subjected to pertinent boundary conditions at ends A and B.

This boundary value problem is analysed using the governing field equations (4.58). A third-order expansion of the global displacement and stress field is chosen in order to take account of the "stress-channelling" effects that arise in highly-orthotropic laminates. Thus, the infinite series in Eq. (4.9) is truncated after the z^3 term, such that there are four global stress resultants in vector $\mathcal{F}$. For straight-fibre laminates, the ZZ moment associated with $\phi^{(k)}_{,x}$ vanishes as the ZZ function does not vary along the length of the beam. Furthermore, some of the terms in governing field equations (4.58) disappear because their associated shear correction coefficients, e.g. $\boldsymbol{\eta}^n_x, \boldsymbol{\eta}^s_x, \boldsymbol{\eta}^n_{xxx}, \boldsymbol{\chi}^s, \boldsymbol{\chi}^n_{xx}$ and $\boldsymbol{\omega}^n_x$, are purely functions of axial derivatives of material properties.

Variable assumptions that satisfy the simply supported boundary conditions,

$$\hat{\mathcal{W}} = \mathcal{F} = \mathbf{0} \quad \text{at} \quad x = 0, a. \tag{5.1}$$

are given by

$$(w_0, \mathcal{F}) = (W_0, \mathcal{F}_0) \cdot \sin\left(\frac{\pi x}{a}\right) \tag{5.2a}$$

$$u_0 = U_0 \cdot \cos\left(\frac{\pi x}{a}\right) \tag{5.2b}$$

The boundary condition $N = 0$ at $x = 0, a$ in Eq. (5.1), combined with the absence of surface shear tractions $\hat{T}_b = \hat{T}_t = 0$, means that the membrane force N vanishes over the whole beam domain. Therefore the membrane force amplitude $N_0 = 0$ in Eq. (5.2a) and equilibrium equation (4.58a) need not be considered.

Substituting the assumptions in Eq. (5.2) into the governing field equations (4.58b)-(4.58c) results in six simultaneous algebraic equations with six unknown variables,

$$\boldsymbol{v} = \begin{bmatrix} M_0 & O_0 & P_0 & L_0 & U_0 & W_0 \end{bmatrix}^\top, \tag{5.3}$$

hence, bending moment magnitude M_0, higher-order membrane force magnitude O_0, higher-order bending moment magnitude P_0, ZZ moment magnitude L_0, and two displacement mag-

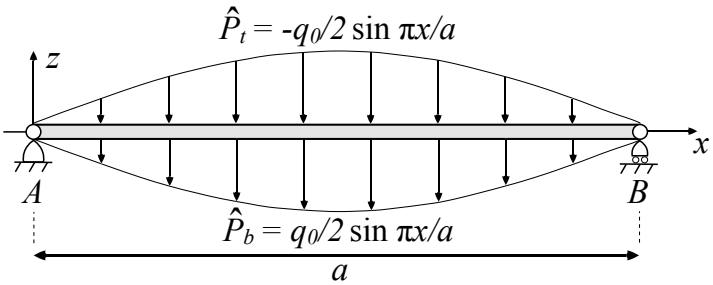

Figure 5.2: A simply supported multilayered beam loaded by a sinusoidal distributed load. This load case is used to assess the accuracies of different HR models with the 3D elasticity solution of Pagano [20] serving as a benchmark.

Table 5.1: Mechanical properties of materials p (Pagano), m (Murakami), pvc, and h (honeycomb) nondimensionalised by the in-plane shear modulus $G_{12}^{(h)}$ of material h.

Material	$\frac{E_1}{G_{12}^{(h)}}$	$\frac{E_2}{G_{12}^{(h)}}$	$\frac{E_3}{G_{12}^{(h)}}$	$\frac{G_{12}}{G_{12}^{(h)}}$	$\frac{G_{13}}{G_{12}^{(h)}}$	$\frac{G_{23}}{G_{12}^{(h)}}$
p	25×10^6	1×10^6	1×10^6	5×10^5	5×10^5	2×10^5
m	32.57×10^6	1×10^6	10×10^6	6.5×10^5	8.21×10^6	3.28×10^6
pvc	25×10^4	25×10^4	25×10^4	9.62×10^4	9.62×10^4	9.62×10^4
h	250	250	2500	1	875	1750

Material	ν_{12}	ν_{13}	ν_{23}
p	0.25	0.25	0.25
m	0.25	0.25	0.25
pvc	0.3	0.3	0.3
h	0.9	3×10^{-5}	3×10^{-5}

nitudes U_0 and W_0. These equations are readily solved by matrix inversion,

$$\boldsymbol{v} = \boldsymbol{K}^{-1}\boldsymbol{q} \tag{5.4}$$

where the stiffness matrix $\boldsymbol{K}$ is comprised of the coefficients of the $\mathcal{F}$, u_0 and w_0 terms in Eqs. (4.58b)-(4.58c) and the column load vector $\boldsymbol{q}$ is comprised of the terms associated with $\hat{T}_b$, $\hat{T}_t$, $\hat{P}_b$ and $\hat{P}_t$.

In order to emphasize the effects of transverse shear and ZZ deformability, relatively deep beams of length-to-thickness ratios $t/a = 1 : 8$ are considered herein. The material properties and stacking sequences are shown in Tables 5.1 and 5.2, respectively. Material p was originally defined by Pagano [20] and is representative of a carbon-fibre reinforced plastic, whereas material m features increased transverse stiffness and is based on the work by Toledano and Murakami [168]. Material pvc is a closed-cell polyvinyl chloride foam modelled as an isotropic material. The honeycomb core h is modelled as transversely isotropic and features significantly lower transverse shear stiffness than material p to exacerbate the ZZ effect. As all results in Section 5.2 are presented in nondimensional form, the material properties in Table 5.1 are nondimensionalised as well, in this case with respect to the shear modulus G_{12} of material h.

Table 5.2: Analysed stacking sequences with $t/a = 1:8$. Laminates A-H are zero B-matrix layups and laminates I-M are arbitrary layups. Subscripts indicate the repetition of a property over the corresponding number of layers.

Laminate	Thickness Ratio	Material	Stacking Sequence
A	$[(1/3)_3]$	$[p_3]$	[0/90/0]
B	$[0.2_5]$	$[p_5]$	[0/90/0/90/0]
C	$[0.2_5]$	$[p_5]$	[90/0/90/0/90]
D	$[(1/51)_{51}]$	$[p_{51}]$	$[0/(90/0)_{25}]$
E	$[(1/30)_3/0.8/(1/30)_3]$	$[p_3/pvc/p_3]$	$[0/90/0_3/90/0]$
F	$[(1/30)_3/0.8/(1/30)_3]$	$[p_3/h/p_3]$	$[0/90/0_3/90/0]$
G	$[0.1_2/0.2_3/0.1_2]$	$[p_2/pvc/h/pvc/p_2]$	$[90/0_5/90]$
H	$[(1/12)_{12}]$	$[p_{12}]$	$[\pm 45/\mp 45/0/90_2/0/\mp 45/\pm 45]$
I	[0.3/0.7]	$[p_2]$	[0/90]
J	$[0.25_4]$	$[p_4]$	[0/90/0/90]
K	[0.1/0.3/0.35/0.25]	$[p_2/m/p]$	$[0/90/0_2]$
L	[0.3/0.2/0.15/0.25/0.1]	$[p_3/m/p]$	$[0/90/0_2/90]$
M	[0.1/0.7/0.2]	[m/pvc/p]	$[0_3]$

The stacking sequences in Table 5.2 are split into a group of zero B-matrix laminates A-H and general laminates I-M. Laminates A-D are symmetric cross-ply composite laminates with 0° and 90° layers progressively more dispersed through the thickness. Even though thick blocks of 0° and 90° plies (as in laminate A) are not commonly used in industry due to transverse cracking issues, this stacking sequence maximises the ZZ effect for validation purposes. Laminates E-G are symmetric thick-core sandwich beams with unidirectional or cross-ply outer skins. Laminate G may be considered as a challenging test case in that the sandwich construction maximises the ZZ effect and the stacking sequence is a combination of three distinct materials. Laminate J is an example of an anti-symmetrically laminated beam with zero B-matrix terms. As Pagano's 3D elasticity solution does not include modelling of off-axis anisotropic layers, the ±45° plies were modelled with effective orthotropic material properties using the transformed axial rigidity $\bar{Q}^{(k)}$ and transverse shear moduli $\bar{G}_{xz}^{(k)}$. Laminates I and J are non-symmetric counterparts to the cross-ply laminates A-D mentioned above. Finally, laminates K-M are highly heterogeneous laminates with general laminations in terms of fibre orientations, ply thicknesses and layer material properties.

Normalised quantities of the bending deflection w_0, axial stress σ_x, transverse shear stress τ_{xz} and transverse normal stress σ_z are used as metrics to assess the accuracy of the different HR models. These normalised quantities are defined as follows:

$$\bar{w} = \frac{10^6 t^2}{q_0 a^4} \int_{-\frac{t}{2}}^{\frac{t}{2}} u_z\left(\frac{a}{2}, z\right) \mathrm{d}z, \quad \bar{\sigma}_x = \frac{t^2}{q_0 a^2} \sigma_x\left(\frac{a}{2}, z\right), \quad \bar{\tau}_{xz} = \frac{1}{q_0} \tau_{xz}\left(0, z\right), \quad \bar{\sigma}_z = \frac{1}{q_0} \sigma_z\left(\frac{a}{2}, z\right) \tag{5.5}$$

and are calculated at the indicated locations (x, z) of the beam domain. The normalised deflection $\bar{w}$ of the HR models is constant through the thickness and thus compared against Pagano's normalised average through-thickness deflection.

5.2 Model validation

The relative percentage errors with respect to Pagano's 3D elasticity solution of the normalised metrics $\bar{w}$, the maximum through-thickness values $\bar{\sigma}_x^{max}$ and $\bar{\tau}_{xz}^{max}$ for the zero B-matrix laminates A-H are shown in Table 5.3. In each case, errors greater than 3% have been underlined to indicate an error outside the acceptable accuracy margin. For comparison, the table also includes the results of a third-order RMVT implementation using the cubic in-plane displacement assumption of Lo, Christensen and Wu [50] (see Eq. (2.25)) enhanced by a ZZ variable, combined with the piecewise, parabolic transverse shear stress assumption of Murakami [86]. This RMVT implementation with the RZT ZZ function is denoted by RMVT3-RZT, whereas the MZZF implementation is denoted by RMVT3-MZZF. Similarly, the results for the general laminates I-M are shown in Table 5.4. To qualitatively compare the stress fields through the thickness of the laminates, the normalised axial stresses $\bar{\sigma}_x$ and transverse shear stresses $\bar{\tau}_{xz}$ are plotted in Figures 5.3-5.15.

For all laminates analysed herein, the accuracy of HR3-RZT is within 1% for all three metrics $\bar{w}$, $\bar{\sigma}_x^{max}$ and $\bar{\tau}_{xz}^{max}$. The corresponding through-thickness plots in Figures 5.3-5.15 show that both axial stress and transverse shear stress profiles are closely matched to Pagano's 3D elasticity solution for any type of laminate. Most importantly, the transverse shear stress profile is captured accurately from the *a priori* model assumption.

An interesting phenomenon is shown in Figures 5.8b and 5.9b where a reversal of the transverse shear stress in the stiffer face layers is observed. This behaviour only occurs for extreme cases of transverse orthotropy when the transverse shear rigidity of an inner layer is insufficient to support the peak transverse shear stress of the adjacent outer layer. In essence, it is a load redistribution effect that arises because the transverse shear force, i.e. the through-thickness integral of τ_{xz}, remains constant for a specific transverse loading condition regardless of the stacking sequence. Thus, as the transverse shear orthotropy between different layers is increased, the transverse shear stress is shifted towards the stiffer layers. The extreme case of transverse orthotropy occurs when stiffer outer layers are bending independently with fully reversed transverse shear profiles, i.e. the inner core carries no transverse shear loading.

Moreover, the through-thickness plots of $\bar{\sigma}_z$ in Figures 5.16-5.22 show that the transverse normal stress field is also modelled accurately using the HR3-RZT model. Thus, the results presented here suggest that the HR3-RZT model provides accurate 3D stress field predictions to within nominal errors of Pagano's 3D elasticity solution for arbitrarily laminated, thick, anisotropic composite and sandwich beams without the need for stress recovery post-processing steps. At the same time, the computational expense of the model is relatively benign compared to layerwise and 3D FEM models as the number of variables is independent of the number of layers.

The accuracy of the HR3-MZZF formulation is within the same range as HR3-RZT for most laminates, and for cross-ply laminates A, B, D and I the results are identical. Small discrepancies exist for cross-ply laminates C and J because of the presence of EWLs which are not taken account of in MZZF. For laminates with at least three unique plies, the HR3-MZZF model generally gives less accurate results for all three metrics $\bar{w}$, $\bar{\sigma}_x^{max}$ and $\bar{\tau}_{xz}^{max}$ (laminates E, F, G, H, K, L and M). For laminates E, K and M the difference between the two theories is

Table 5.3: Zero B-matrix laminates A-H: Normalised results of maximum transverse deflection, maximum absolute axial stress and maximum absolute transverse shear stress for Pagano's solution [20] with model results given by percentage errors. Errors greater than 3% are underlined.

Laminate	Model	$\bar{w}$	$\bar{\sigma}_x^{max}$	$\bar{\tau}_{xz}^{max}$
A	**Pagano**	**0.0116**	**0.7913**	**3.3167**
	HR3-RZT (%)	0.06	-0.23	-0.04
	HR3-MZZF (%)	0.05	-0.23	-0.04
	RMVT3-RZT (%)	0.07	-2.03	0.55
	RMVT3-MZZF (%)	0.07	-2.03	0.55
B	**Pagano**	**0.0124**	**0.8672**	**3.3228**
	HR3-RZT (%)	0.07	-0.92	-0.23
	HR3-MZZF (%)	0.07	-0.92	-0.23
	RMVT3-RZT (%)	0.08	-1.10	-1.40
	RMVT3-MZZF (%)	0.08	-1.10	-1.40
C	**Pagano**	**0.0303**	**1.6307**	**5.3340**
	HR3-RZT (%)	0.24	-0.49	0.03
	HR3-MZZF (%)	0.24	1.05	0.07
	RMVT3-RZT (%)	-0.66	-0.48	0.37
	RMVT3-MZZF (%)	-1.49	0.45	18.06
D	**Pagano**	**0.0154**	**1.2239**	**3.6523**
	HR3-RZT (%)	0.11	0.34	-0.05
	HR3-MZZF (%)	0.11	0.34	-0.05
	RMVT3-RZT (%)	-0.62	-1.15	19.22
	RMVT3-MZZF (%)	-0.62	-1.15	19.22
E	**Pagano**	**0.0309**	**1.9593**	**2.8329**
	HR3-RZT (%)	0.06	0.02	-0.16
	HR3-MZZF (%)	0.09	-0.88	-0.33
	RMVT3-RZT (%)	0.13	0.08	31.96
	RMVT3-MZZF (%)	-1.18	-0.04	218.78
F	**Pagano**	**1.0645**	**13.9883**	**8.1112**
	HR3-RZT (%)	-0.28	-0.24	0.05
	HR3-MZZF (%)	-0.25	7.96	-0.29
	RMVT3-RZT (%)	-0.32	-0.15	16.74
	RMVT3-MZZF (%)	-62.92	-54.24	2697.28
G	**Pagano**	**0.4590**	**6.3417**	**5.6996**
	HR3-RZT (%)	-0.02	0.02	0.04
	HR3-MZZF (%)	7.11	10.66	-0.13
	RMVT3-RZT (%)	-0.08	0.07	5.53
	RMVT3-MZZF (%)	-88.80	-70.05	188.93
H	**Pagano**	**0.0224**	**0.6157**	**4.0096**
	HR3-RZT (%)	0.40	0.26	0.05
	HR3-MZZF (%)	0.48	2.75	1.07
	RMVT3-RZT (%)	0.45	-0.06	-0.26
	RMVT3-MZZF (%)	-3.15	-0.64	42.11

Table 5.4: Arbitrary laminates I-M: Normalised results of maximum transverse deflection, maximum absolute axial stress and maximum absolute transverse shear stress for Pagano's solution [20] with model results given by percentage errors. Errors greater than 3% are underlined.

Laminate	Model	$\bar{w}$	$\bar{\sigma}_x^{max}$	$\bar{\tau}_{xz}^{max}$
	Pagano	**0.0482**	**2.0870**	**4.8799**
	HR3-RZT (%)	0.64	-0.59	0.17
I	HR3-MZZF (%)	0.64	-0.59	0.17
	RMVT3-RZT (%)	0.57	-1.84	0.41
	RMVT3-MZZF (%)	0.57	-1.84	0.41
	Pagano	**0.0195**	**1.2175**	**4.3539**
	HR3-RZT (%)	0.36	-0.94	0.06
J	HR3-MZZF (%)	0.36	0.67	0.10
	RMVT3-RZT (%)	-0.39	-2.22	<u>3.71</u>
	RMVT3-MZZF (%)	-0.81	-0.69	<u>11.38</u>
	Pagano	**0.0100**	**0.9566**	**4.1235**
	HR3-RZT (%)	0.39	-0.06	-0.48
K	HR3-MZZF (%)	0.39	0.19	0.11
	RMVT3-RZT (%)	<u>-5.48</u>	<u>-4.42</u>	<u>8.95</u>
	RMVT3-MZZF (%)	-0.67	-1.05	<u>13.56</u>
	Pagano	**0.0115**	**1.0368**	**3.8037**
	HR3-RZT (%)	0.29	0.61	-0.12
L	HR3-MZZF (%)	0.53	<u>6.16</u>	0.17
	RMVT3-RZT (%)	0.12	0.05	0.91
	RMVT3-MZZF (%)	<u>-12.48</u>	<u>-3.93</u>	<u>195.58</u>
	Pagano	**0.0226**	**1.4902**	**2.8969**
	HR3-RZT (%)	0.05	0.51	-0.06
M	HR3-MZZF (%)	0.06	1.11	0.05
	RMVT3-RZT (%)	0.03	0.47	-0.22
	RMVT3-MZZF (%)	0.05	0.98	<u>3.91</u>

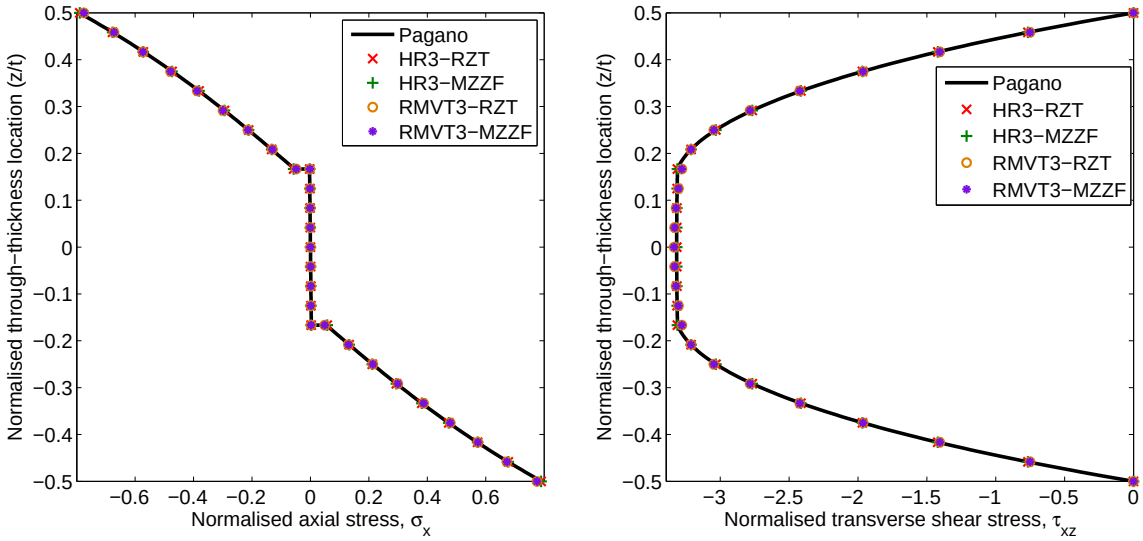

(a) Normalised axial stress, $\bar{\sigma}_x$ **(b)** Normalised transverse shear stress, $\bar{\tau}_{xz}$

Figure 5.3: Laminate A: Through-thickness distribution of the normalised axial stress and transverse shear stress.

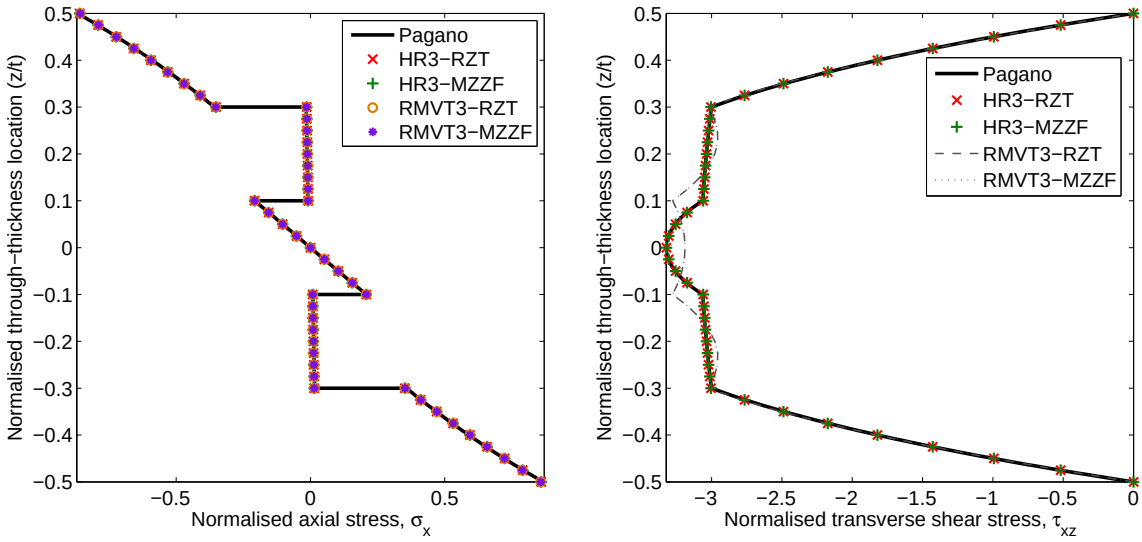

(a) Normalised axial stress, $\bar{\sigma}_x$ **(b)** Normalised transverse shear stress, $\bar{\tau}_{xz}$

Figure 5.4: Laminate B: Through-thickness distribution of the normalised axial stress and transverse shear stress.

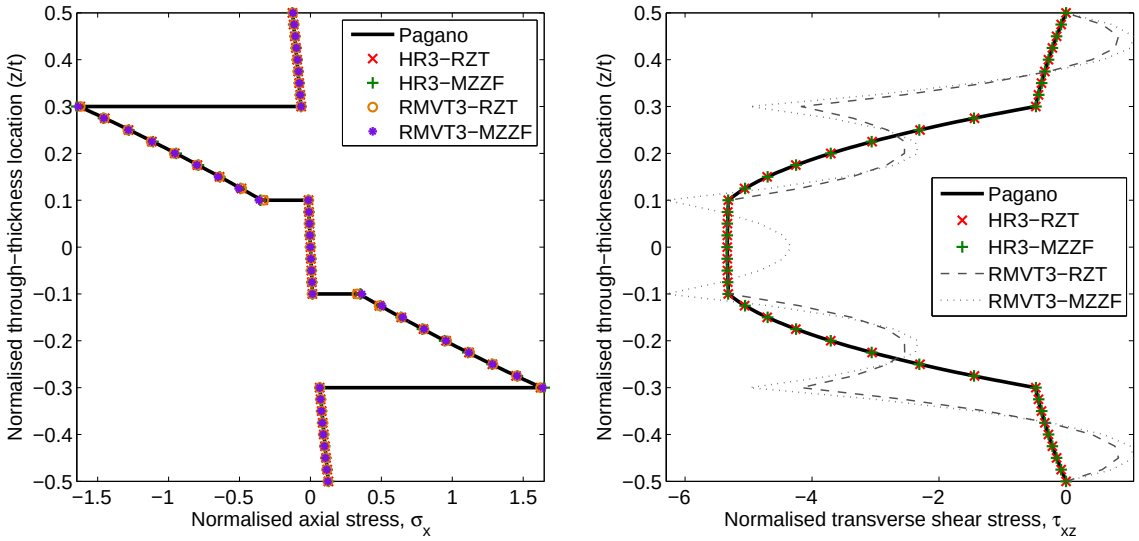

(a) Normalised axial stress, $\bar{\sigma}_x$ **(b)** Normalised transverse shear stress, $\bar{\tau}_{xz}$

Figure 5.5: Laminate C: Through-thickness distribution of the normalised axial stress and transverse shear stress.

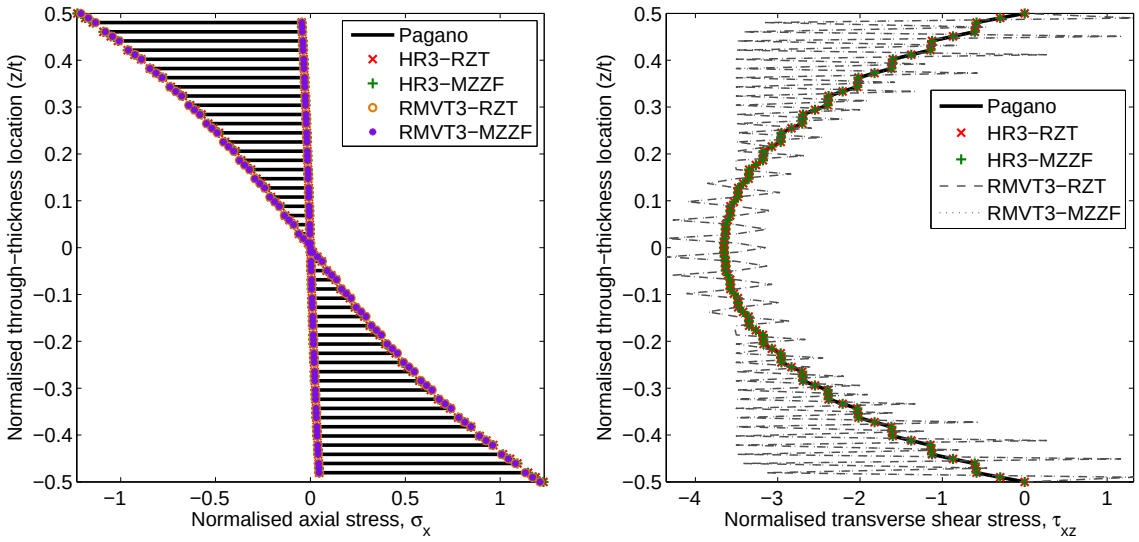

(a) Normalised axial stress, $\bar{\sigma}_x$ **(b)** Normalised transverse shear stress, $\bar{\tau}_{xz}$

Figure 5.6: Laminate D: Through-thickness distribution of the normalised axial stress and transverse shear stress.

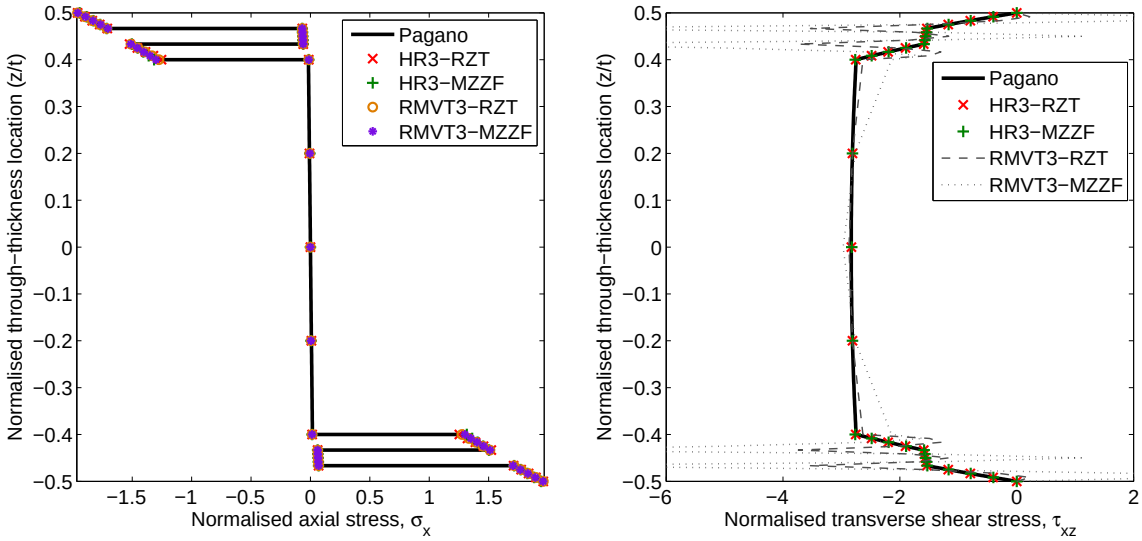

(a) Normalised axial stress, $\bar{\sigma}_x$ **(b)** Normalised transverse shear stress, $\bar{\tau}_{xz}$

Figure 5.7: Laminate E: Through-thickness distribution of the normalised axial stress and transverse shear stress.

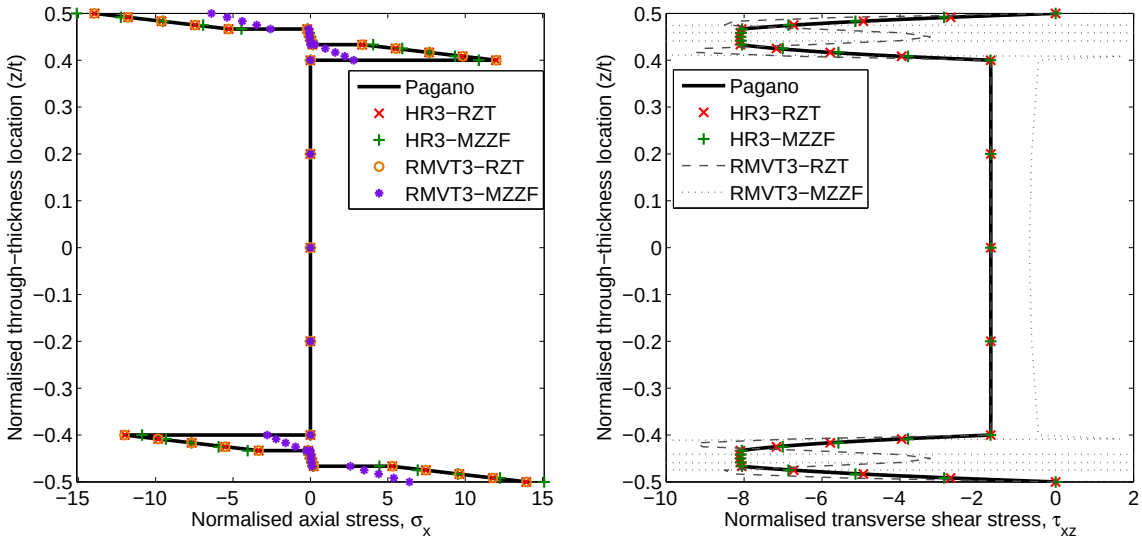

(a) Normalised axial stress, $\bar{\sigma}_x$ **(b)** Normalised transverse shear stress, $\bar{\tau}_{xz}$

Figure 5.8: Laminate F: Through-thickness distribution of the normalised axial stress and transverse shear stress.

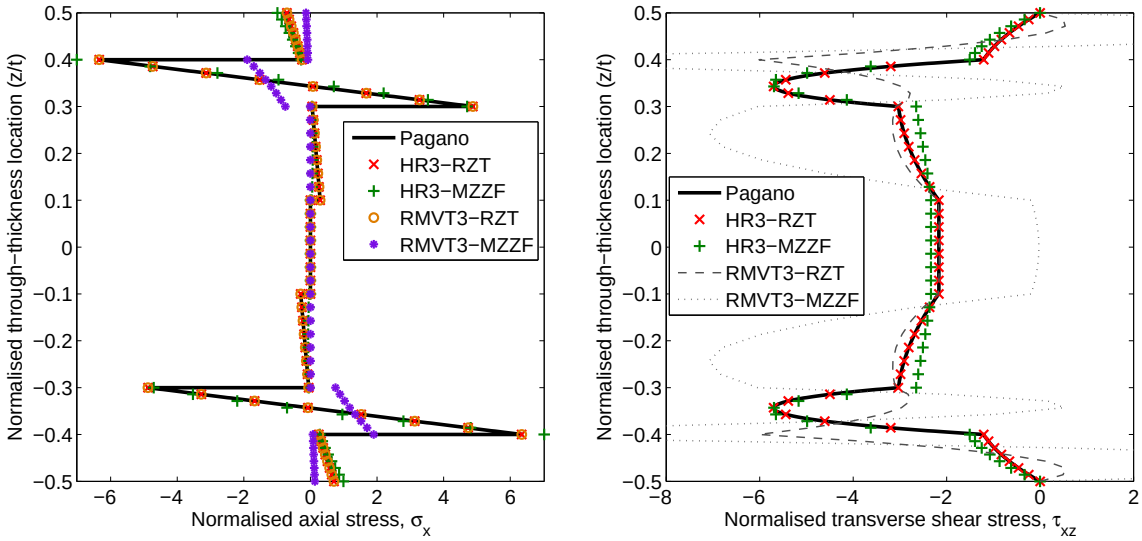

(a) Normalised axial stress, $\bar{\sigma}_x$ **(b)** Normalised transverse shear stress, $\bar{\tau}_{xz}$

Figure 5.9: Laminate G: Through-thickness distribution of the normalised axial stress and transverse shear stress.

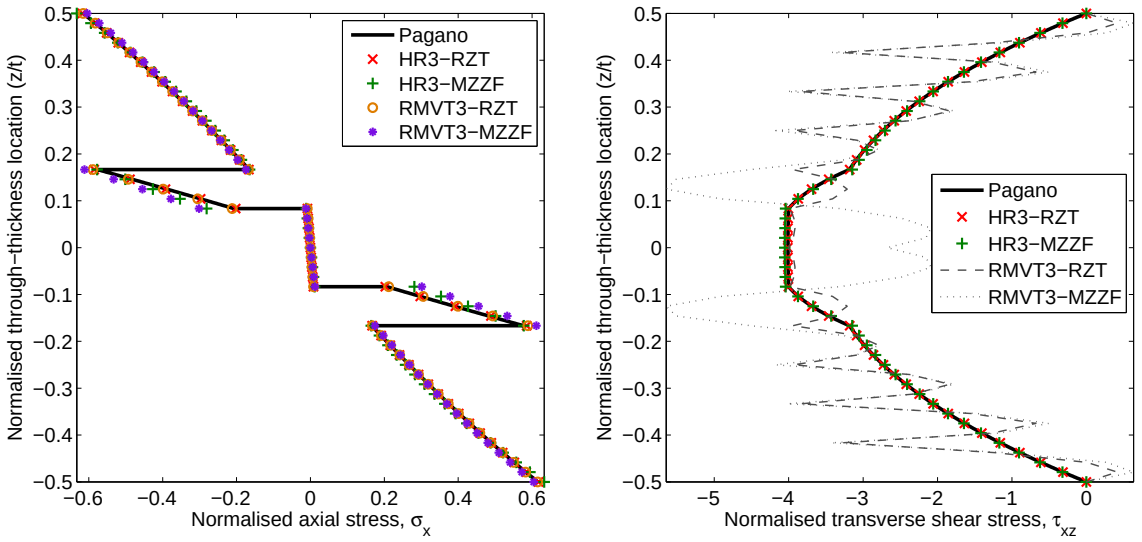

(a) Normalised axial stress, $\bar{\sigma}_x$ **(b)** Normalised transverse shear stress, $\bar{\tau}_{xz}$

Figure 5.10: Laminate H: Through-thickness distribution of the normalised axial stress and transverse shear stress.

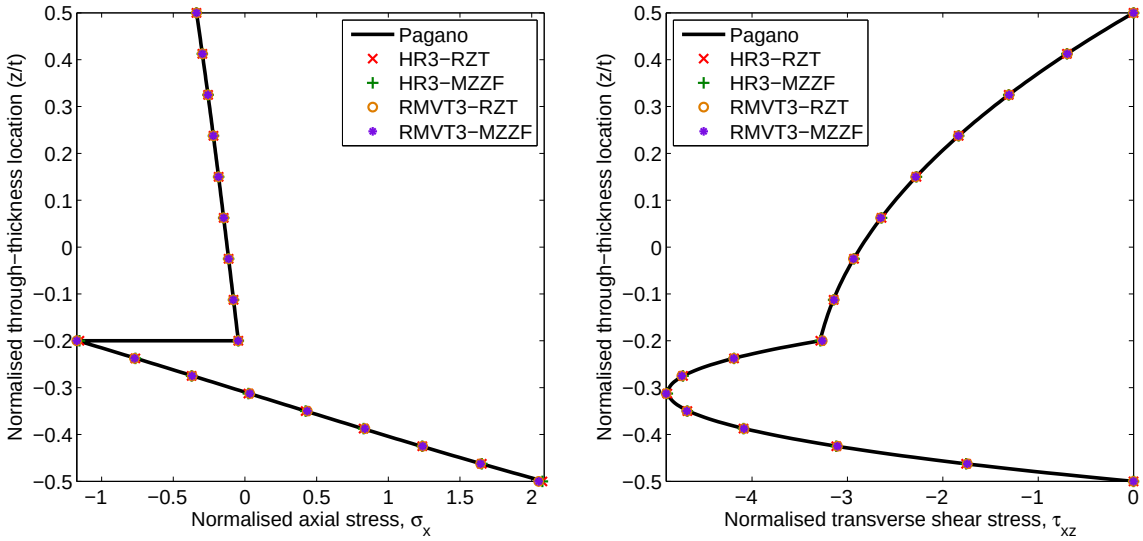

(a) Normalised axial stress, $\bar{\sigma}_x$ **(b)** Normalised transverse shear stress, $\bar{\tau}_{xz}$

Figure 5.11: Laminate I: Through-thickness distribution of the normalised axial stress and transverse shear stress.

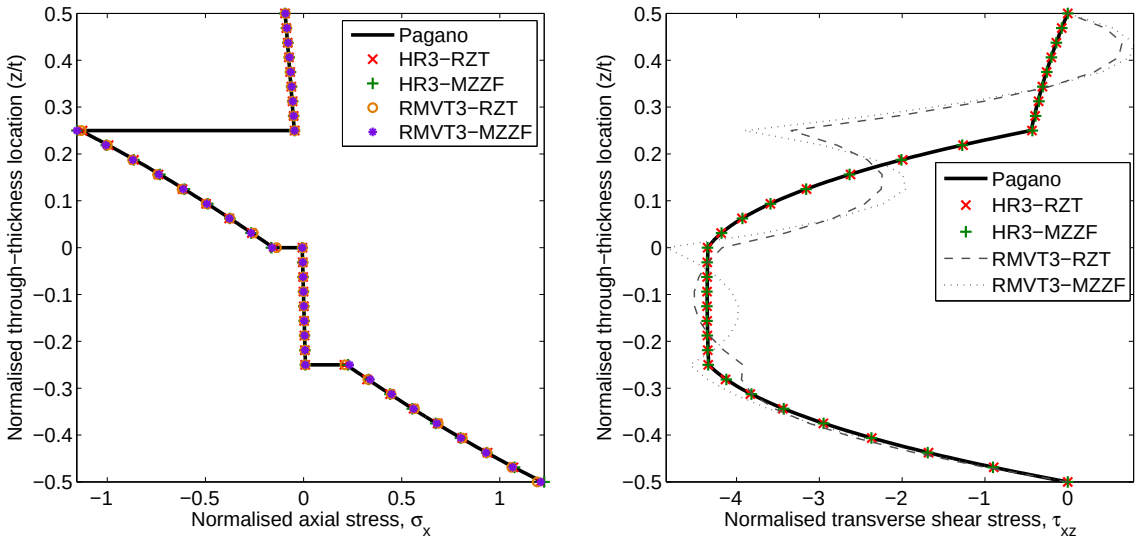

(a) Normalised axial stress, $\bar{\sigma}_x$ **(b)** Normalised transverse shear stress, $\bar{\tau}_{xz}$

Figure 5.12: Laminate J: Through-thickness distribution of the normalised axial stress and transverse shear stress.

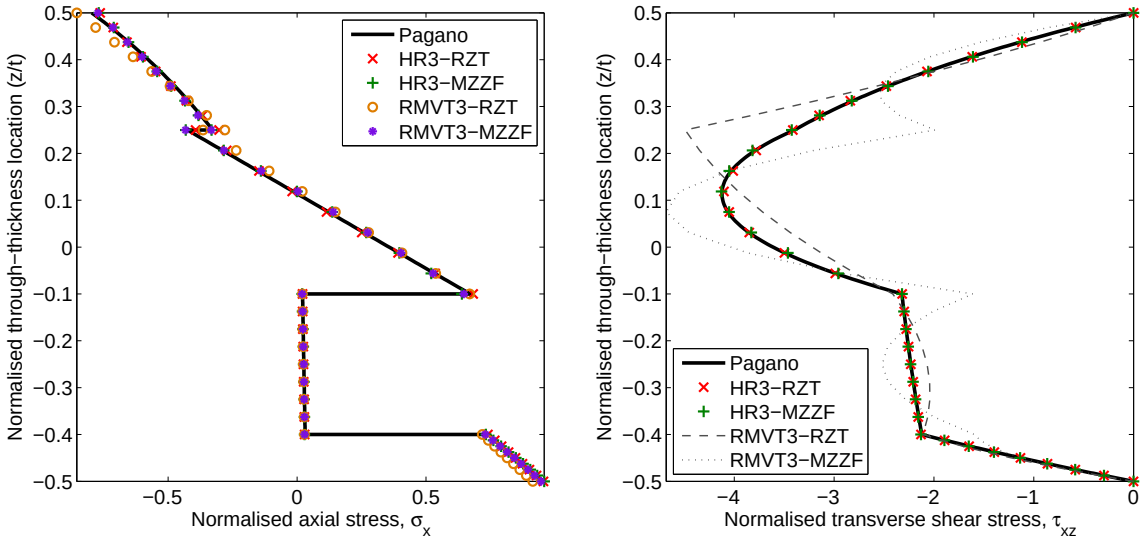

(a) Normalised axial stress, $\bar{\sigma}_x$ **(b)** Normalised transverse shear stress, $\bar{\tau}_{xz}$

Figure 5.13: Laminate K: Through-thickness distribution of the normalised axial stress and transverse shear stress.

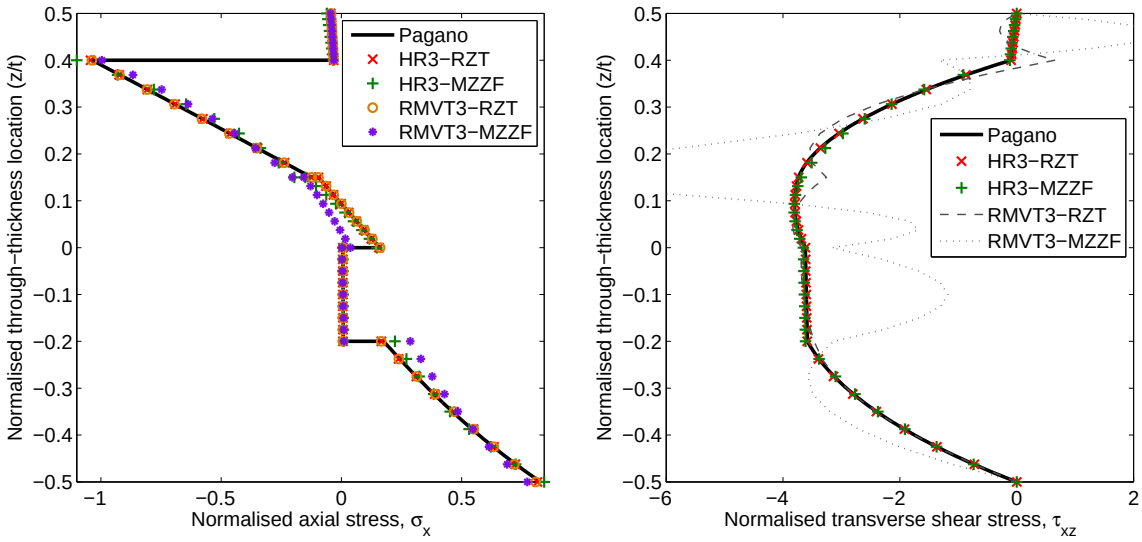

(a) Normalised axial stress, $\bar{\sigma}_x$ **(b)** Normalised transverse shear stress, $\bar{\tau}_{xz}$

Figure 5.14: Laminate L: Through-thickness distribution of the normalised axial stress and transverse shear stress.

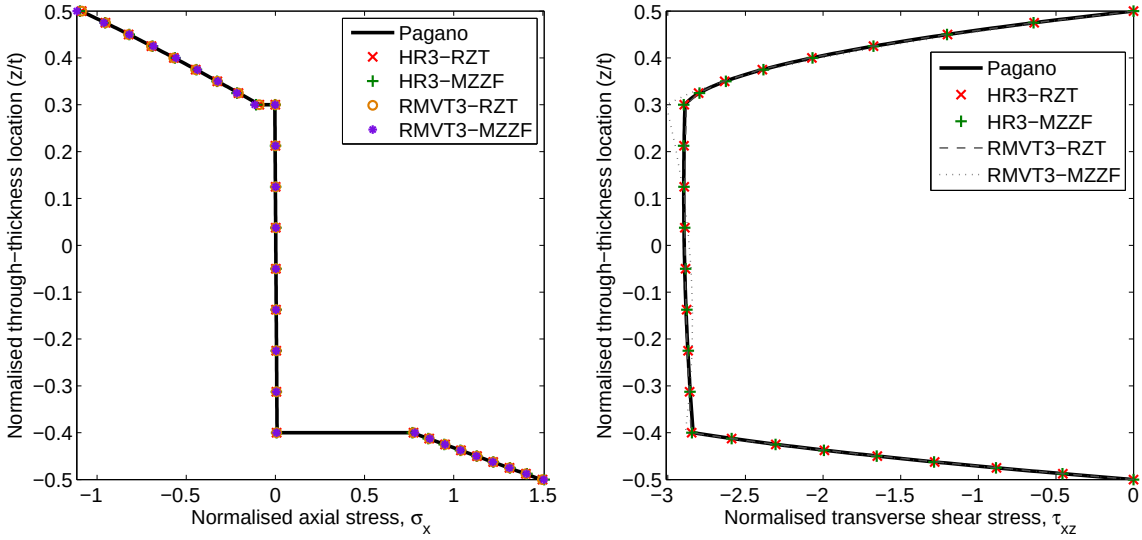

(a) Normalised axial stress, $\bar{\sigma}_x$ **(b)** Normalised transverse shear stress, $\bar{\tau}_{xz}$

Figure 5.15: Laminate M: Through-thickness distribution of the normalised axial stress and transverse shear stress.

marginal, whereas for laminates F, G, H and L the error in $\bar{\sigma}_x^{max}$ of HR3-MZZF is an order of magnitude greater than for HR3-RZT. In fact, the HR3-MZZF error in $\bar{\sigma}_x^{max}$ for laminates F, G and L, and $\bar{w}$ for laminate G is more than double the 3% threshold. Furthermore, Figures 5.10a and 5.14a show that for laminates H and L there are visible discrepancies in the $\bar{\sigma}_x$ through-thickness profile with respect to Pagano's solution. The numerical errors in Table 5.3 and Table 5.4 suggest that HR3-MZZF captures the maximum value of the transverse shear stress through the thickness accurately for all laminates. However, the through-thickness profiles show that this is not generally the case for throughout the entire thickness. For example, in Figure 5.9b the transverse shear stress is accurately captured in the outer 0° p-layers of laminate G, whereas there are visible discrepancies in the stress profiles of all other layers.

The inherently equilibrated model assumption for transverse shear stress in the HR model gives superior results to Murakami's [86] model assumption used in the RMVT formulation. The transverse shear stress profiles for laminates with a small number of layers, such as A, B, I and M, follow Pagano's solution closely for both RMVT3-RZT and RMVT3-MZZF. As the number of layers increases, the transverse shear profiles of both formulations oscillate around the 3D elasticity solution, and this is most clearly shown in Figure 5.6b. For laminates E, F, G, H and L, the oscillations in the RMVT3-MZZF solution significantly increase the maximum value of the transverse shear stress $\bar{\tau}_{xz}^{max}$ as indicated by the 2700% error for laminate F in Table 5.3.

In RMVT, two independent assumptions are made for the displacement and transverse shear stress fields, and these are enforced to be kinematically compatible in the variational statement. However, as was shown in Section 4.1, the ZZ effect in the displacement field is directly related to the presence of C^1-discontinuous transverse shear strains that result from continuity requirements on transverse shear stresses at layer interfaces, and, as such, the independence of the two fields is not absolute. Whereas the minimisation of the strain energy in RMVT guarantees that

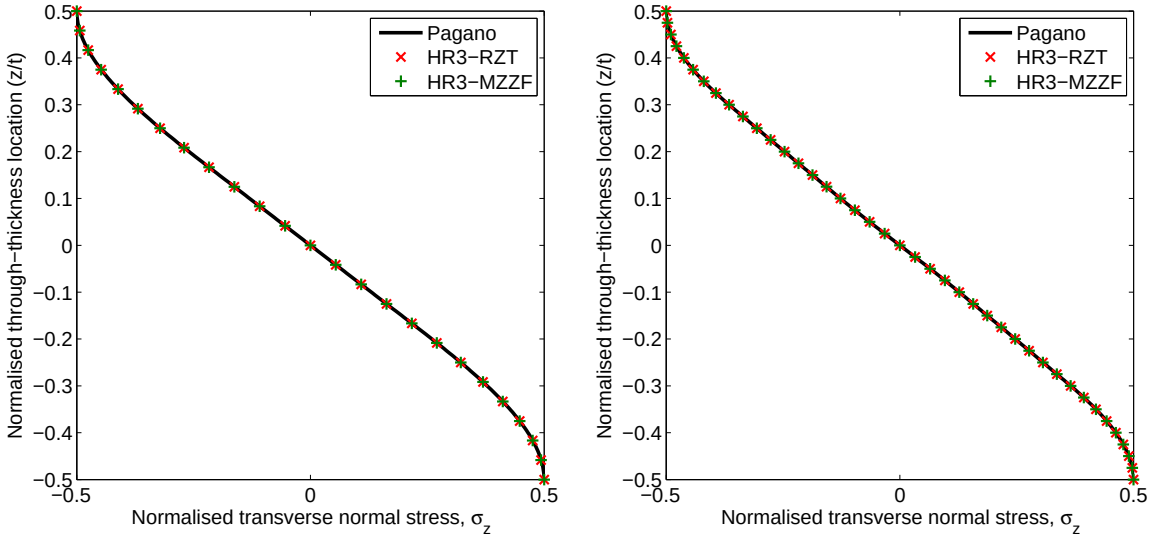

(a) $\bar{\sigma}_z$ Laminate A

(b) $\bar{\sigma}_z$ Laminate B

Figure 5.16: Through-thickness distribution of the normalised transverse normal stress for laminates A and B.

the geometric and assumed model shear strains are compatible, there is no such condition on equilibrium between the axial stress and the transverse shear stress. In the HR functional, the situation is reversed in that compatibility of geometric and assumed model strains is not guaranteed, whereas equilibrium of stresses is enforced. In terms of deriving accurate stress fields, which are the critical measures for failure analyses, it seems that enforcing the equilibrium of stresses leads to better results than enforcing displacement compatibility, and hence, the HR formulation performs better than RMVT for this purpose.

As discussed above, the RMVT3-RZT through-thickness profiles of $\bar{\tau}_{xz}$ show major discrepancies compared with Pagano's solution. On the other hand, the through-thickness plots of $\bar{\sigma}_x$ closely match Pagano's solution. Thus, the RMVT3-RZT axial stress fields may be integrated in the equilibrium equations to compute more accurate transverse stresses, a step which was advised by Toledano and Murakami in their original papers on RMVT [168], and was later reinforced by Carrera [169]. The third-order HR formulation introduced herein features seven functional unknowns, whereas the third-order RMVT formulation only features six variables. Thus, the overall computational efficiency of the RMVT formulation with respect to the HR formulation depends on the computational effort involved in this extra post-processing step.

Finally, consider Figures 5.8a, 5.9a and 5.14a, which show significant discrepancies between the RMVT3-MZZF through-thickness profiles of $\bar{\sigma}_x$ compared to Pagano's solution. Combined with the previous observations that the HR3-RZT model is more accurate than the HR3-MZZF model, these findings corroborate the comments by Gherlone [54] that MZZF may lead to inferior results for some laminates. This occurs because the RZT ZZ function is based on transverse shear properties and layer thicknesses, which are the actual drivers behind the ZZ effect (see Section 4.1), whereas MZZF only accounts for the relative thicknesses of different layers. In fact, Toledano and Murakami point out in their original work that the "inclusion of the zig-zag shaped C^0 function was motivated by the displacement micro-structure of *periodic* laminated

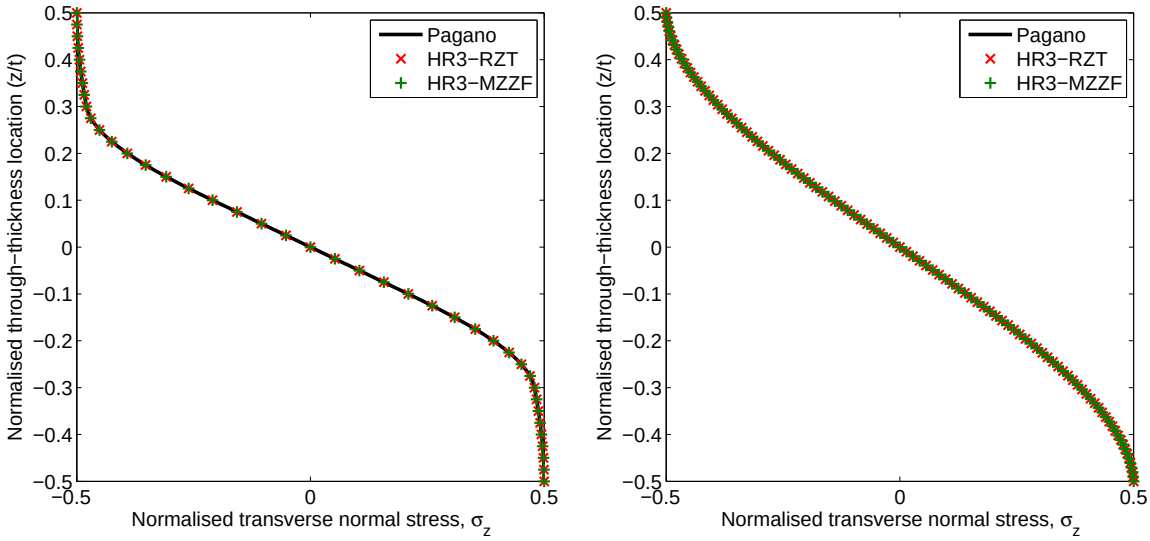

(a) $\bar{\sigma}_z$ Laminate C **(b)** $\bar{\sigma}_z$ Laminate D

Figure 5.17: Through-thickness distribution of the normalised transverse normal stress for laminates C and D.

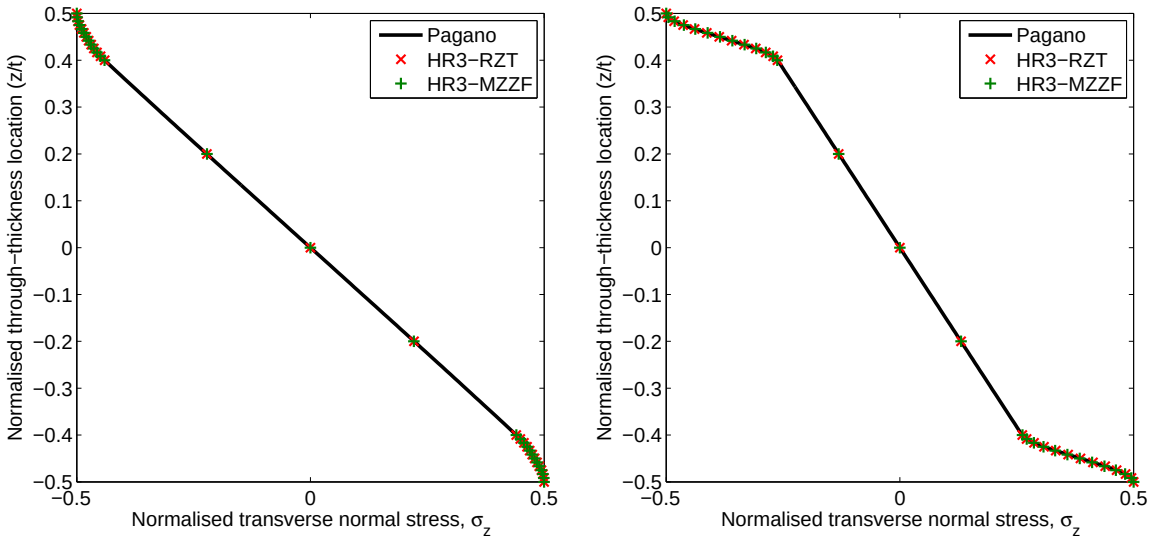

(a) $\bar{\sigma}_z$ Laminate E **(b)** $\bar{\sigma}_z$ Laminate F

Figure 5.18: Through-thickness distribution of the normalised transverse normal stress for laminates E and F.

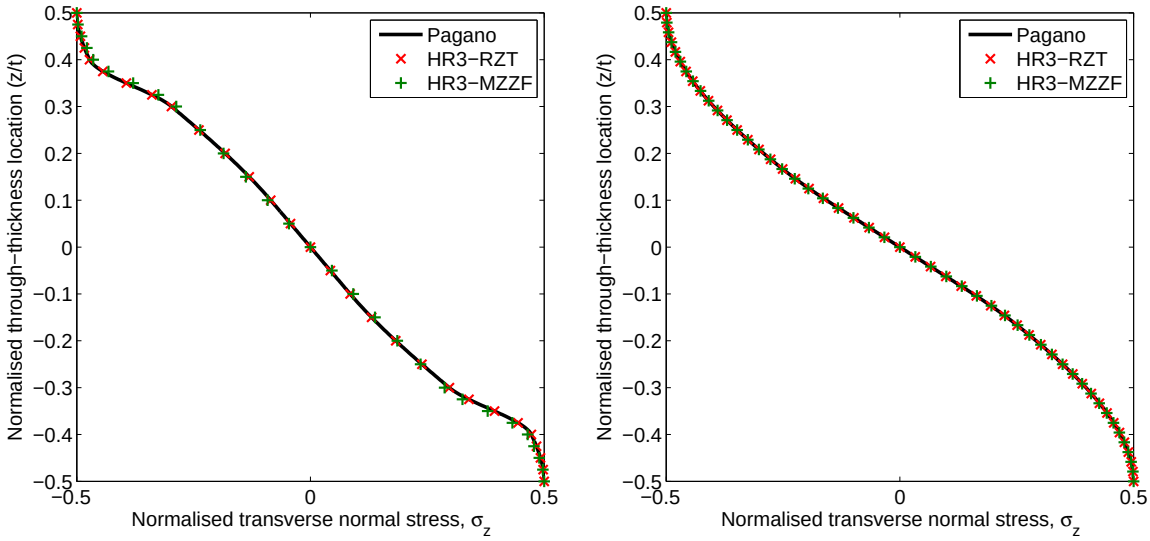

(a) $\bar{\sigma}_z$ Laminate G **(b)** $\bar{\sigma}_z$ Laminate H

Figure 5.19: Through-thickness distribution of the normalised transverse normal stress for laminates G and H.

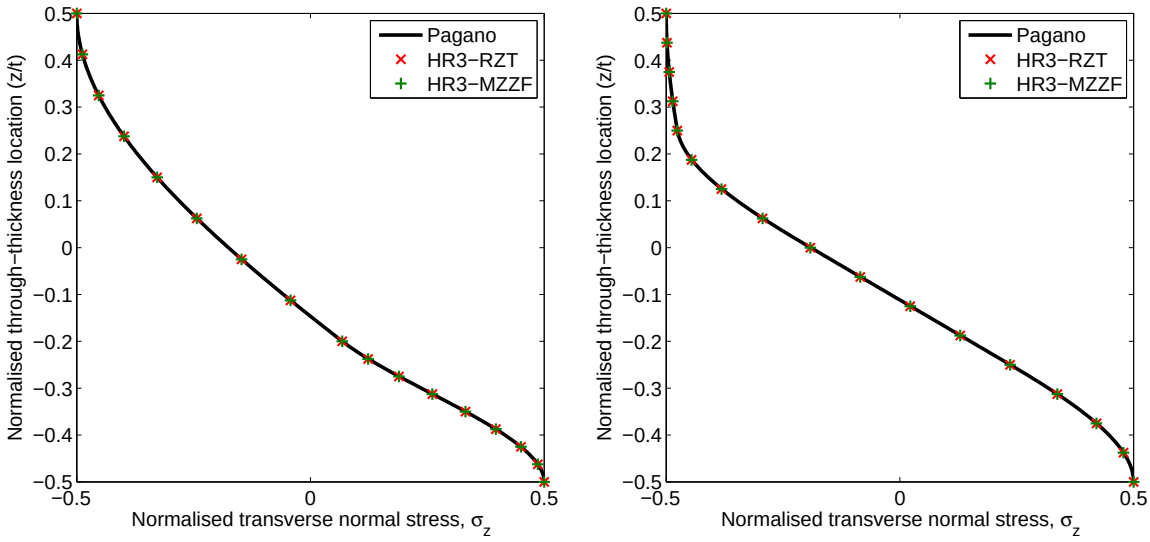

(a) $\bar{\sigma}_z$ Laminate I **(b)** $\bar{\sigma}_z$ Laminate J

Figure 5.20: Through-thickness distribution of the normalised transverse normal stress for laminates I and J.

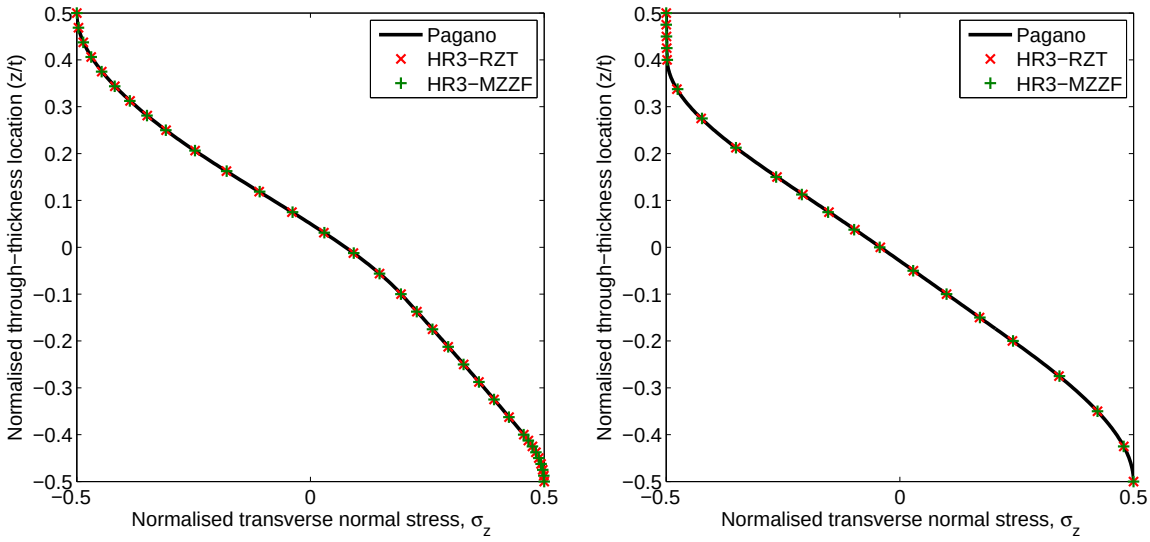

(a) $\bar{\sigma}_z$ Laminate K **(b)** $\bar{\sigma}_z$ Laminate L

Figure 5.21: Through-thickness distribution of the normalised transverse normal stress for laminates K and L.

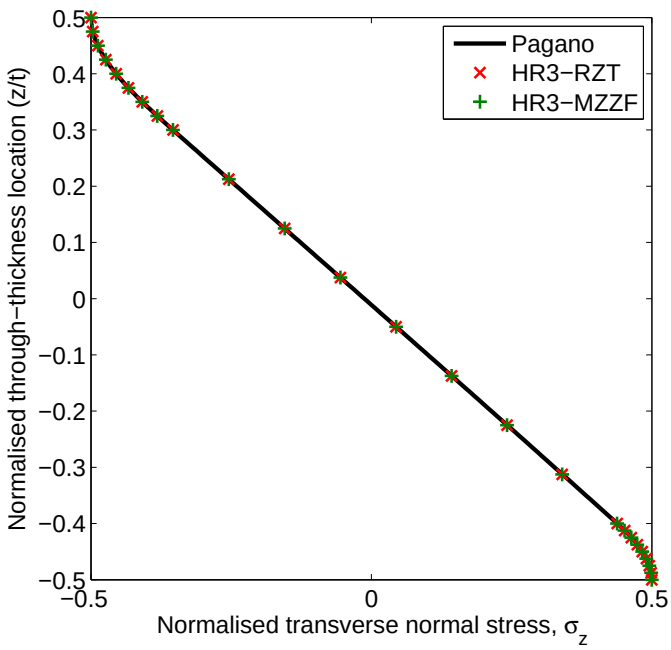

Figure 5.22: Through-thickness distribution of the normalised transverse normal stress for laminate M.

composites", and that "for general laminate configurations, this periodicity is destroyed", such that the "theory should be expected to break down in these particular cases" [168]. Overall, MZZF results in nominal errors for most commonly used laminates when employed in a third-order theory coupled with the HR mixed-variational statement. However, for sandwich beams with very flexible cores or heterogeneous laminates comprised of more than three unique materials, the constitutive independence of MZZF may lead to large errors.

In conclusion, the third-order HR3-RZT formulation is the most accurate of the formulations investigated herein for predicting bending deflections, axial bending stresses and transverse bending stresses from *a priori* model assumptions. This is because the RZT ZZ function is derived from actual transverse material properties, and because equilibrium of the 3D stresses is enforced in the variational statement using Lagrange multipliers. The RMVT3-RZT model provides similar accuracy for axial stresses but requires a *posteriori* stress recovery step for accurate transverse shear stresses. In terms of computational efficiency, there is a trade-off between the extra degree of freedom of the HR3-RZT formulation and the extra post-processing step required in the RMVT3-RZT formulation.

5.3 Assessment of transverse shear, transverse normal and zig-zag effects

Previous authors [78, 86, 92] have shown that ignoring the ZZ effect may lead to significant underestimations of the peak axial and transverse stresses. The inaccuracies are especially pronounced for sandwich beams because of the large degree of transverse orthotropy between the flexible core and the stiff face layers. Even though a relatively large thickness to length ratio of 1:8 was analysed in this study, the ZZ effect is important for longer and thinner sandwich beams as well.

However, for commonly used composite laminates, the ZZ effect may not be as significant. Many industrial lamination guidelines prevent the use of thick blocks of same orientation plies to prevent problems associated with transverse cracking. As such, laminates A-C in Table 5.2 are not representative of typical laminates used in practice, and the results for laminate D in Figure 5.6 show that dispersing the 0° and 90° layers throughout the thickness greatly reduces the ZZ effect.

The relative effects of transverse shear deformation, transverse normal deformation and the ZZ effect may be analysed numerically using the bending displacement of the HR model. For simplicity, we examine straight-fibre symmetric laminates (all membrane stress resultants vanish) and ignore all higher-order bending moments, hence, resulting in a first-order ZZ formulation of the HR model. The transverse pressure acts on the top surface, such that $\hat{P}_b = 0$ and $\hat{P}_t = q_0 \sin \pi x/a$, and both ends of the beam are simply supported. To begin, the effect of ZZ deformation is initially ignored to compare the relative importance of transverse shear and transverse normal deformation.

Under these assumptions the governing field equations (4.58) of the first-order HR model

are

$$M_{,xx} + \hat{P}_t = 0 \tag{5.6a}$$

$$s^{CLA} M + \left(\eta^s_{xx} + \eta^n_{xx}\right) M_{,xx} + \eta^n_{xxxx} M_{,xxxx} + w_{0,xx} = 0 \tag{5.6b}$$

where M is the classic bending moment of CLA. The boundary condition Eq. (4.59b) is required to calculate the transverse deflection,

$$u_z = \rho^{nbc} M + \rho^{nbc}_{xx} M_{,xx} + w_0 \tag{5.7}$$

from the bending moment M and Lagrange multiplier w_0. The term $\rho^{nbc} M + \rho^{nbc}_{xx} M_{,xx}$ in Eq. (5.7) corrects the displacement Lagrange multiplier w_0 to account for transverse normal effects. Note that $s^{CLA} = 1/D^{CLA}$ where D is the classic bending rigidity of CLA, and the shear correction factors η and ρ are also scalars due to the single unknown stress resultant M. Using the solution assumption of Eq. (5.2a) and $u_z = U_{z0} \sin(\pi x/a)$ in Eqs. (5.6) and (5.7) results in

$$\begin{aligned} -M_0 \frac{\pi^2}{a^2} + q_0 &= 0 \\ s^{CLA} M_0 - \left(\eta^s_{xx} + \eta^n_{xx}\right) \frac{\pi^2}{a^2} M_0 + \eta^n_{xxxx} \frac{\pi^4}{a^4} M_0 - W_0 \frac{\pi^2}{a^2} &= 0 \\ \rho^{nbc} M_0 - \rho^{nbc}_{xx} \frac{\pi^2}{a^2} M_0 + W_0 &= U_{z0}. \end{aligned} \tag{5.8}$$

Using the fact that $\rho^{nbc}_{xx} = \eta^n_{xxxx}$ as shown in Eq. (A.8e) in Appendix A, the algebraic system of equations in Eq. (5.8) is readily solved for bending amplitude U_{z0},

$$U_{z0} = \frac{a^4}{\pi^4} \left[s^{CLA} - \frac{\pi^2}{a^2} \left(\eta^s_{xx} + \eta^n_{xx}\right) + \frac{\pi^2}{a^2} \rho^{nbc} \right] q_0. \tag{5.9}$$

Note, that the transverse normal correction factor η^n_{xxxx} vanishes in the derivation of the bending deflection U_{z0} in Eq. (5.9). Transverse normal deformation only affects the bending displacement via the boundary condition term ρ^{nbc}. Eq. (A.8p) in Appendix A shows that for straight-fibre laminates, i.e. when all axial derivatives of material properties vanish, ρ^{nbc} is a function of the transverse-axial Poisson's coupling term $R^{(k)}_{13}$ only, i.e. the transverse normal term $R^{(k)}_{33}$ does not play a role.

The bending deflection is normalised into three separate entities by dividing by a factor of $q_0 s^{CLA} a^4/\pi^4$. This leads to

$$\begin{aligned} &\bar{w} = \bar{w}_{CLA} + \bar{w}_{TS} + \bar{w}_{TN} \quad \text{where} \\ &\bar{w}_{CLA} = 1, \quad \bar{w}_{TS} = -\frac{\eta^s_{xx}}{s^{CLA}} \frac{\pi^2}{a^2}, \quad \bar{w}_{TN} = -\frac{\eta^n_{xx} - \rho^{nbc}}{s^{CLA}} \frac{\pi^2}{a^2} \end{aligned} \tag{5.10}$$

where $\bar{w}_{TS}$ and $\bar{w}_{TN}$ refer to transverse shear and transverse normal deflection components, respectively. These three factors are plotted against the thickness to length ratio (t/a) in Figure 5.23 for laminate D. Furthermore, this plot shows a comparison between the total normalised

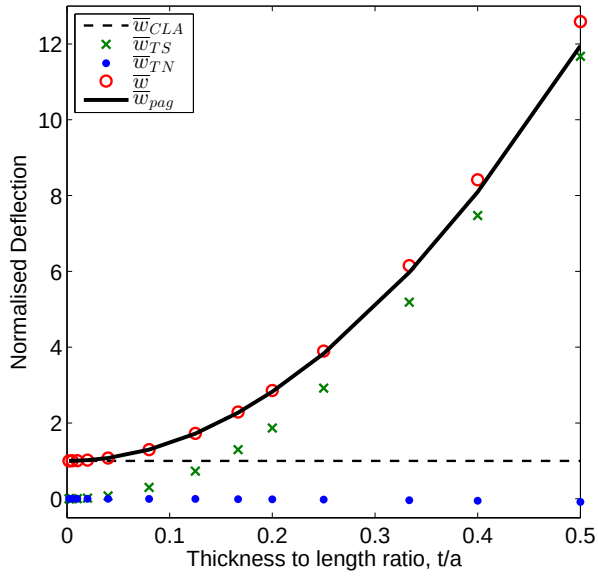

Figure 5.23: Laminate D: Change in normalised CLA, transverse shear and transverse normal bending deflection components versus thickness to length ratio t/a.

deflection $\bar{w}$ and Pagano's normalised solution $\bar{w}_{pag}$. Laminate D is chosen to minimise the ZZ effect in Pagano's 3D elasticity solution and therefore allows a fair comparison between $\bar{w}$ and $\bar{w}_{pag}$. The comparison between $\bar{w}$ and $\bar{w}_{pag}$ shows that the HR model accurately predicts the bending deflection up to very deep aspect ratios of $t/a = 0.4$.

Figure 5.23 also shows the parabolic relationship of $\bar{w}_{TS}$ with respect to the beam thickness ratio t/a, which plays a more significant role than the transverse normal deflection. In fact, the transverse normal component is negative, i.e. it stiffens the structure. This arises because $\bar{w}_{TN}$ only captures the Poisson's effect of σ_z on the bending deformation, as indicated by the presence of the Poisson's term $R_{13}^{(k)}$ in the definition of ρ^{nbc} in Eq. (A.8p) in Appendix A. If normal compressibility effects are to be included, this has to be factored into the initial assumption of the displacement field in Eq. (4.9) that underlies the derivation of the model. Therefore the transverse displacement field $u_z^{(k)}$ has to be expanded in a power series of z and its effect included in the derivation of $\sigma_x^{(k)}$ via the Poisson's ratio υ_{zx} and strain $\epsilon_z^{(k)}$. Based on the excellent correlation of the 3D stress fields between the HR3-RZT and Pagano's solution in Figures 5.3-5.15, the argument is made that for laminates with thickness to length ratio of 1:8 such a refinement is not necessary. Although the transverse normal correction factor ρ^{nbc} varies with layup, a numerical study showed that for commonly used carbon- and glass-reinforced composite and sandwich panels the magnitude of this factor is always negligible compared to the transverse shear factor η_{xx}^{s}.

As discussed by Gherlone [54], transverse normal effects are accentuated for moderately thick laminates when one half of the laminate has significantly less transverse normal stiffness than the other half. Under these circumstances, transverse normal loading leads to local transverse normal deformations in the softer regions, and these need to be accounted for as detailed above. However, for most laminates used in industrial engineering structures, the transverse

normal modulus of the constituent layers is within 8-12 GPa, such that a uniform transverse displacement assumption is warranted.

Next, the influence of the ZZ effect on the bending behaviour is investigated by ignoring the effect of transverse normal deformation in the governing field equations (4.58). Under these conditions, the governing field equations of the HR1-RZT formulation, as derived from Eq. (4.58), are

$$\begin{aligned} M_{,xx} + \hat{P}_t &= 0 \\ s_{11}M + s_{12}L + \eta^s_{xx_{11}} M_{,xx} + \eta^s_{xx_{12}} L_{,xx} + w_{0,xx} &= 0 \\ s_{12}M + s_{22}L + \eta^s_{xx_{12}} M_{,xx} + \eta^s_{xx_{22}} L_{,xx} &= 0 \end{aligned} \tag{5.11}$$

where M is the CLA bending moment, L the ZZ moment, and s_{ij} and $\eta^s_{xx_{ij}}$ are coefficients of the bending compliance matrix $\boldsymbol{s}$ and the shear correction matrix $\boldsymbol{\eta}^s_{xx}$. Substituting the variable assumptions Eq. (5.2a) and $w_0 = W_0^{ZZ} \sin(\pi x/a)$ into Eqs. (5.11) results in

$$\begin{aligned} -M_0 \frac{\pi^2}{a^2} + q_0 &= 0 \\ s_{11}M_0 + s_{12}L_0 - \eta^s_{xx_{11}} \frac{\pi^2}{a^2} M_0 - \eta^s_{xx_{12}} \frac{\pi^2}{a^2} L_0 - W_0^{ZZ} \frac{\pi^2}{a^2} &= 0 \\ s_{12}M_0 + s_{22}L_0 - \eta^s_{xx_{12}} \frac{\pi^2}{a^2} M_0 - \eta^s_{xx_{22}} \frac{\pi^2}{a^2} L_0 &= 0. \end{aligned} \tag{5.12}$$

Next, the algebraic system of equations (5.12) is solved for bending amplitude W_0^{ZZ} to give

$$W_0^{ZZ} = \left[s_{11} \frac{a^4}{\pi^4} - \frac{\left(s_{12} \frac{a^2}{\pi^2} - \eta^s_{xx_{12}} \right)^2}{s_{22} - \eta^s_{xx_{22}} \frac{\pi^2}{a^2}} - \eta^s_{xx_{11}} \frac{a^2}{\pi^2} \right] q_0. \tag{5.13}$$

The bending deflection in Eq. (5.13) is normalised into $\bar{w}^{ZZ}$ by dividing W_0^{ZZ} by the factor $q_0 s^{CLA} a^4/\pi^4$. Hence,

$$\begin{aligned} \bar{w}^{ZZ} &= \frac{\pi^4}{q_0 s^{CLA} a^4} \left[\left(s^{CLA} + s_{11} - s^{CLA} \right) \frac{a^4}{\pi^4} - \frac{\left(s_{12} \frac{a^2}{\pi^2} - \eta^s_{xx_{12}} \right)^2}{s_{22} - \eta^s_{xx_{22}} \frac{\pi^2}{a^2}} - \eta^s_{xx_{11}} \frac{a^2}{\pi^2} \right] q_0 \\ \bar{w}^{ZZ} &= 1 + \frac{s_{11} - s^{CLA}}{s^{CLA}} - \frac{\left(s_{12} - \eta^s_{xx_{12}} \frac{\pi^2}{a^2} \right)^2}{s^{CLA} \left(s_{22} - \eta^s_{xx_{22}} \frac{\pi^2}{a^2} \right)} - \frac{\eta^s_{xx_{11}}}{s^{CLA}} \frac{\pi^2}{a^2}. \end{aligned} \tag{5.14}$$

The expression in Eq. (5.14) is separated into three components

$$\begin{aligned} &\bar{w}^{ZZ} = \bar{w}_{CLA} + \bar{w}^{ZZ}_{CLA} + \bar{w}^{ZZ}_{TS} \quad \text{where} \\ &\bar{w}_{CLA} = 1, \quad \bar{w}^{ZZ}_{CLA} = \frac{s_{11} - s^{CLA}}{s^{CLA}} - \frac{\left(s_{12} - \eta^s_{xx_{12}} \frac{\pi^2}{a^2} \right)^2}{s^{CLA} \left(s_{22} - \eta^s_{xx_{22}} \frac{\pi^2}{a^2} \right)}, \quad \bar{w}^{ZZ}_{TS} = -\frac{\eta^s_{xx_{11}}}{s^{CLA}} \frac{\pi^2}{a^2}. \end{aligned} \tag{5.15}$$

Note that the bending flexibility s^{CLA} and s_{11} are not equal. The two terms are related by a

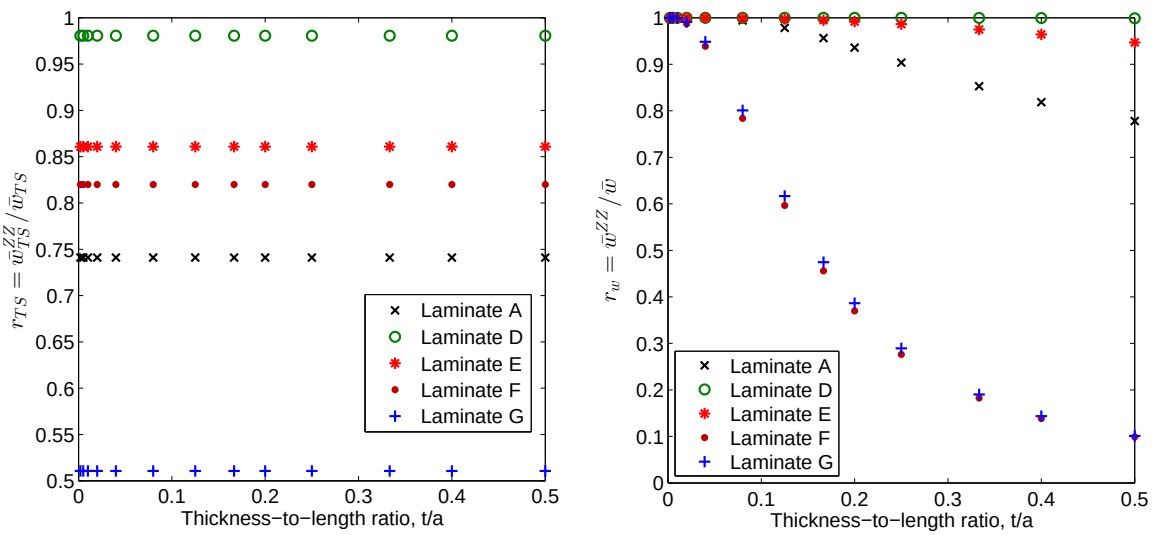

(a) Ratio of transverse shear components

(b) Ratio of total deflection

Figure 5.24: Ratio of transverse shear components and ratio of total deflection, as calculated from the HR1-RZT model with and without ZZ effects, versus thickness to length ratio (t/a) for different laminates in Table 5.2.

constant of proportionality that is independent of the laminate thickness t. The two components $\bar{w}_{CLA}^{ZZ}$ and $\bar{w}_{TS}^{ZZ}$ are ZZ bending deformations related to the difference between ZZ and CLA, and the action of the transverse shear deformation, respectively.

The quantities in Eq. (5.15) are compared to the corresponding bending components that ignore the ZZ effect in Eq. (5.10). Thus, the total deflection ratio $r_w = \bar{w}^{ZZ}/\bar{w}$ and shear deflection ratio $r_{TS} = \bar{w}_{TS}^{ZZ}/\bar{w}_{TS}$ are used as metrics to assess the influence of the ZZ effect on the bending displacement. The term $\bar{w}_{CLA}^{ZZ}$ can be used as a standalone metric to express the normalised difference between classic bending deformation, and the deformation of direct ZZ effects and the coupling effects of ZZ-transverse shear deformations.

Figure 5.24a shows that the ratio of transverse shear components is invariant with t/a but may vary with the stacking sequence. Furthermore, the ZZ effect always reduces the magnitude of transverse shear deformation. Figure 5.24b shows that the ZZ effect reduces the overall bending deflection of all analysed laminates and that this effect is greatest for the two honeycomb core sandwich beams F and G, i.e. stiffening is most for laminates with the greatest ZZ effect. For the non-sandwich beams A, D and E, the ZZ effect can be ignored up to $t/a = 0.1$ which includes the large majority of composite laminates used in industry. Furthermore, the reduction in bending displacement is non-linear in t/a and converges to a constant value as the thickness of the beam approaches the length. In a state of equilibrium, the internal strain energy must equate to the work done by the external loads. To maintain this balance, the stiffening effect of the ZZ moments must result in an increase in the internal stress of the beam. The axial stress plot for sandwich beam F in Figure 5.8a shows exactly this phenomenon; here, the ZZ effect increases the z-wise slope of the stress field in the outer layers, thereby increasing the maximum stress magnitude throughout the thickness.

Figure 5.25 plots the ZZ deformation metric $\bar{w}_{CLA}^{ZZ}$ versus the thickness to length ratio t/a.

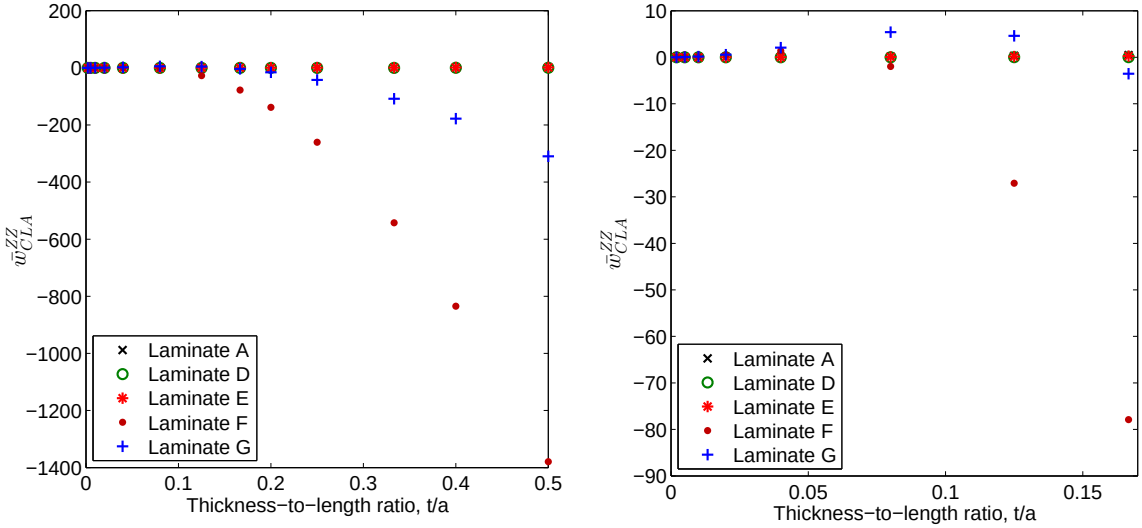

(a) $t/a \in [.002, 0.5]$ **(b)** $t/a \in [.002, 0.166]$

Figure 5.25: Normalised ratio $\bar{w}^{ZZ}_{CLA}$ of classic bending deformation to the deformation of direct ZZ effects and the coupling of ZZ-transverse shear deformations versus thickness to length ratio (t/a) for different laminates in Table 5.2. Plot (b) is the same as plot (a) but over s smaller range of t/a values.

The figure shows that the term is initially positive for small values of t/a and then changes sign for greater values of t/a. The $\bar{w}^{ZZ}_{CLA}$ term vanishes when the ZZ effect is ignored, which means that for small values of t/a, when $\bar{w}^{ZZ}_{CLA}$ is positive, the ZZ stiffness and ZZ-transverse shear coupling terms are reducing the rigidity of the beam, i.e. making it more flexible. However, because Figure 5.24b shows that the ZZ effect always decreases the total deflection $\bar{w}^{ZZ}_{0}$ of the beam, i.e. increasing the stiffness, this reduction must be a result of the decreased effect of direct transverse shear deformation (Figure 5.24a) when ZZ effects are important.

In conclusion, the stiffness term associated with ZZ deformation reduces the classic bending rigidity of the beam, but at the same time increases the transverse shear rigidity (Figure 5.24a). The increase in transverse shear rigidity outweighs the reduction in classic bending rigidity and therefore the total deflection decreases (Figure 5.24b). Finally, the sum of the two normalised coefficients $\bar{w}^{ZZ}_{CLA}$ and $\bar{w}^{ZZ}_{TS}$, calculated for a specific laminate, can be compared against a known sandwich beam, and used to gauge the effects of ZZ deformation.

5.4 Modelling boundary layers towards clamped edges

Some authors in the literature have pointed out that models derived from the HR variational principle can be used to capture boundary layer effects and localised stress gradients towards boundaries [59]. This is possible because the stresses are treated as fundamental unknowns and forced to obey Cauchy's equilibrium equations in the variational statement. This feature creates a stronger condition than simply post-processing the stresses from the displacement unknowns in the kinematic and constitutive relations. A second feature particular to the present work is that the governing field equations are solved in the strong form using the pseudo-

spectral DQM. This has the advantage that both essential and natural boundary conditions are enforced explicitly. Thus, the satisfaction of equilibrium and natural boundary conditions does not depend on the mesh density as is the case in the classic, weak displacement-based finite element formulations. Hence, the governing field equations are solved at every single grid point within the domain, rather than in an average sense over the whole domain. Coupled with the enforcement of Cauchy's equilibrium equations and the use of stress-based variables, this means that equilibrium of stresses is guaranteed at each location within the solution domain, and boundary layer effects are captured more robustly.

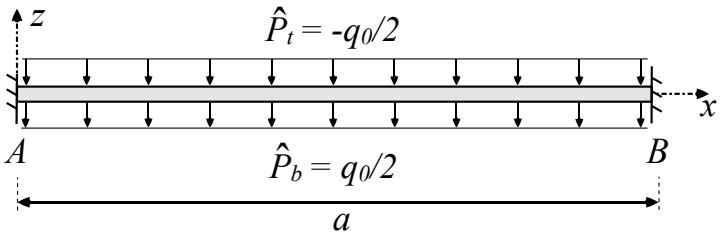

Figure 5.26: A multilayered beam clamped at both ends and loaded by a uniformly distributed load on the top and bottom surfaces.

The problem presented in Section 5.1 is revisited with the multilayered beam now clamped at both ends $x_A = 0$ and $x_B = a$ with a uniformly distributed load equally divided between the top and bottom surfaces, i.e. $\hat{P}_b = -\hat{P}_t = q_0/2$ as shown in Figure 5.26. The clamped support induces a boundary layer effect in the 3D stress field that is modelled using the HR3-RZT formulation. Two laminates shown in Table 5.5 are considered, where laminate 1 is a non-symmetric composite laminate, and laminate 2 is a non-symmetric sandwich beam. Both beams have thickness-to-length ratio $t/a = 1 : 10$ and are comprised of materials p and pvc previously defined in Table 5.1

Following the description of the DQM in Section 2.4, the governing differential equations are converted into algebraic ones by replacing the differential operators with weighting matrices that operate on all functional unknowns within the domain. Thus, each differential operator is converted into a linear weighted sum of the functional unknowns at pre-determined grid points, such that the system of differential equations is written as a system of algebraic equations in matrix form. A non-uniform Chebychev-Gauss-Lobatto grid with 31 points is chosen here based on an initial mesh convergence study.

As shown in Eq. (2.35), the governing field equations Eq. (4.58) are discretised at the internal grid points, whereas the boundary conditions Eq. (4.59) are discretised at the boundary points. Both sets of equations are written in terms of two unknown vectors; a vector of internal field unknowns and a vector of boundary unknowns. In this manner, the complete set of governing equations is substructured into four matrices that allow the boundary unknowns to be eliminated, as shown in Eq. (2.36a). Thus, the final matrix inversion problem includes both the discretised field and boundary equations in one matrix, and is solved for the vector of internal field unknowns only. The unknowns on the boundary are subsequently post-processed from the internal field variables and boundary equations using Eq. (2.36b) .

Table 5.5: Composite laminate and sandwich beam stacking sequences with $t/a = 1:10$ used to investigate boundary layers. Subscripts indicate the repetition of a property over the corresponding number of layers.

Laminate	t/a	Thickness Ratio	Material	Stacking Sequence
1	1:10	$[(1/4)_4]$	$[p_4]$	[0/90/0/90]
2	1:10	$[(1/8)_2/0.5/(1/8)_2]$	$[p_2/pvc/p_2]$	$[0/90/0_2/90]$

The third-order ZZ HR model for straight-fibre laminates has two displacement unknowns u_0 and w_0, and five stress unknowns $\mathcal{F} = \begin{bmatrix} N & M & O & P & L \end{bmatrix}^\top$, where N and O are the classic and second-order membrane stress resultants, respectively; M and P are the classic bending moment and second-order bending moment, respectively; and L is the ZZ moment.

For the load case shown in Figure 5.26, the stress resultants do not vanish at the clamped ends $x = 0$ and $x = a$ but all displacements vanish, i.e. $\hat{\mathcal{U}}_{bc} = \mathbf{0}$, such that the boundary condition Eq. (4.59a)

$$\left(\boldsymbol{\eta}_x^{sbc} + \boldsymbol{\eta}_x^{nbc}\right)\mathcal{F}_{,x} + \boldsymbol{\eta}_{xxx}^{nbc}\mathcal{F}_{,xxx} + \hat{T}_b\boldsymbol{\chi}^{sbc} + \hat{T}_{b,xx}\boldsymbol{\chi}_{xx}^{nbc} + \hat{P}_{b,x}\boldsymbol{\omega}_x^{nbc} + \boldsymbol{\Lambda}_{bc_1} = \mathbf{0} \tag{5.16}$$

needs to be satisfied. Note, that the shear and normal correction factors in Eq. (4.59a) that only depend on variable-stiffness properties are eliminated in Eq. (5.16). Furthermore, the axial derivatives of the membrane stress resultant $N_{,x} = 0$ at the clamped ends as the membrane stress resultant does not vary along the length of the beam for the current load case. However, the axial derivatives of all other stress resultants remain undefined. Therefore, the boundary condition in Eq. (4.59b) is split into the following two parts,

$$N_{,x} = 0 \quad \text{from} \quad \delta\mathcal{F}_{,x}^\top = 0 \tag{5.17a}$$

$$\begin{bmatrix} \rho_{21}^{nbc} & \rho_{22}^{nbc} & \rho_{23}^{nbc} & \rho_{24}^{nbc} & \rho_{25}^{nbc} \\ \rho_{31}^{nbc} & \rho_{32}^{nbc} & \rho_{33}^{nbc} & \rho_{34}^{nbc} & \rho_{35}^{nbc} \\ \rho_{41}^{nbc} & \rho_{42}^{nbc} & \rho_{43}^{nbc} & \rho_{44}^{nbc} & \rho_{45}^{nbc} \\ \rho_{51}^{nbc} & \rho_{52}^{nbc} & \rho_{53}^{nbc} & \rho_{54}^{nbc} & \rho_{55}^{nbc} \end{bmatrix} \begin{Bmatrix} N \\ M \\ O \\ P \\ L \end{Bmatrix} + \begin{bmatrix} \rho_{xx21}^{nbc} & \rho_{xx22}^{nbc} & \rho_{xx23}^{nbc} & \rho_{xx24}^{nbc} & \rho_{xx25}^{nbc} \\ \rho_{xx31}^{nbc} & \rho_{xx32}^{nbc} & \rho_{xx33}^{nbc} & \rho_{xx34}^{nbc} & \rho_{xx35}^{nbc} \\ \rho_{xx41}^{nbc} & \rho_{xx42}^{nbc} & \rho_{xx43}^{nbc} & \rho_{xx44}^{nbc} & \rho_{xx45}^{nbc} \\ \rho_{xx51}^{nbc} & \rho_{xx52}^{nbc} & \rho_{xx53}^{nbc} & \rho_{xx54}^{nbc} & \rho_{xx55}^{nbc} \end{bmatrix} \begin{Bmatrix} N_{,xx} \\ M_{,xx} \\ O_{,xx} \\ P_{,xx} \\ L_{,xx} \end{Bmatrix}$$
$$+ \hat{T}_{b,x} \begin{Bmatrix} \gamma_{x_2}^{nbc} \\ \gamma_{x_3}^{nbc} \\ \gamma_{x_4}^{nbc} \\ \gamma_{x_5}^{nbc} \end{Bmatrix} + \hat{P}_b \begin{Bmatrix} \mu_2^{nbc} \\ \mu_3^{nbc} \\ \mu_4^{nbc} \\ \mu_5^{nbc} \end{Bmatrix} + \begin{Bmatrix} w_0 \\ 0 \\ 0 \\ 0 \end{Bmatrix} = \mathbf{0} \tag{5.17b}$$

where the first equation associated with membrane stress resultant N is not included in Eq. (5.17b) because it satisfies the condition in Eq. (5.17a). Thus, by writing the governing field equations (4.58) and boundary conditions Eq. (5.16) and (5.17) in DQ matrix form, the functional unknowns at the DQ grid points are found using standard matrix operations. In the present work the numerical solution procedure was implemented in Matlab.

As Pagano's 3D elasticity solution [20] is only valid for simply supported beams, a 3D

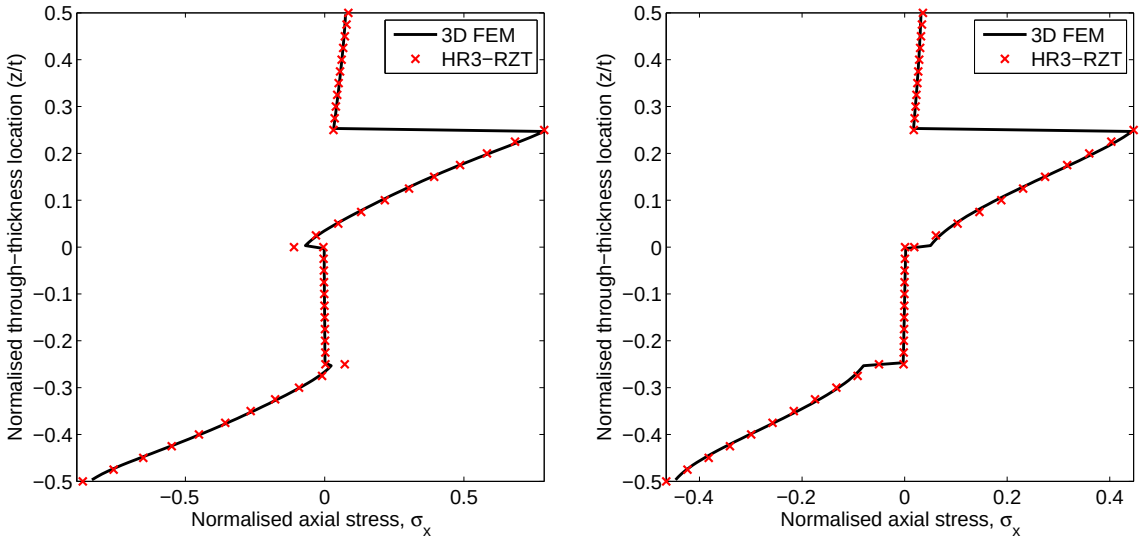

(a) $\bar{\sigma}_x$ at 5% **(b)** $\bar{\sigma}_x$ at 10%

Figure 5.27: Laminate 1: Through-thickness plot of normalised axial stress $\bar{\sigma}_x$ at locations 5% and 10% of the beam span from clamped end x_A.

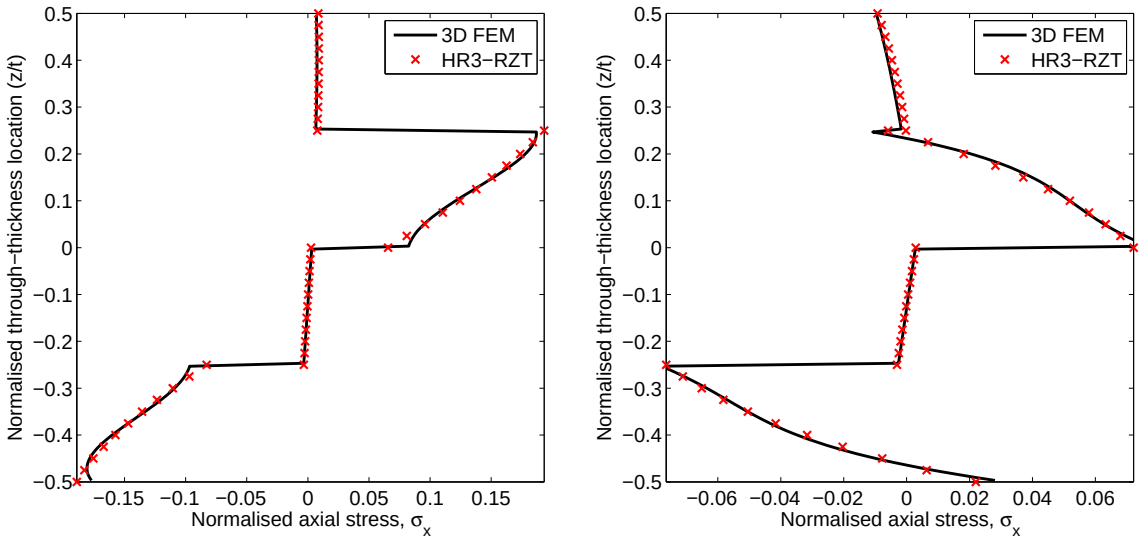

(a) $\bar{\sigma}_x$ at 15% **(b)** $\bar{\sigma}_x$ at 20%

Figure 5.28: Laminate 1: Through-thickness plot of normalised axial stress $\bar{\sigma}_x$ at locations 15% and 20% of the beam span from clamped end x_A.

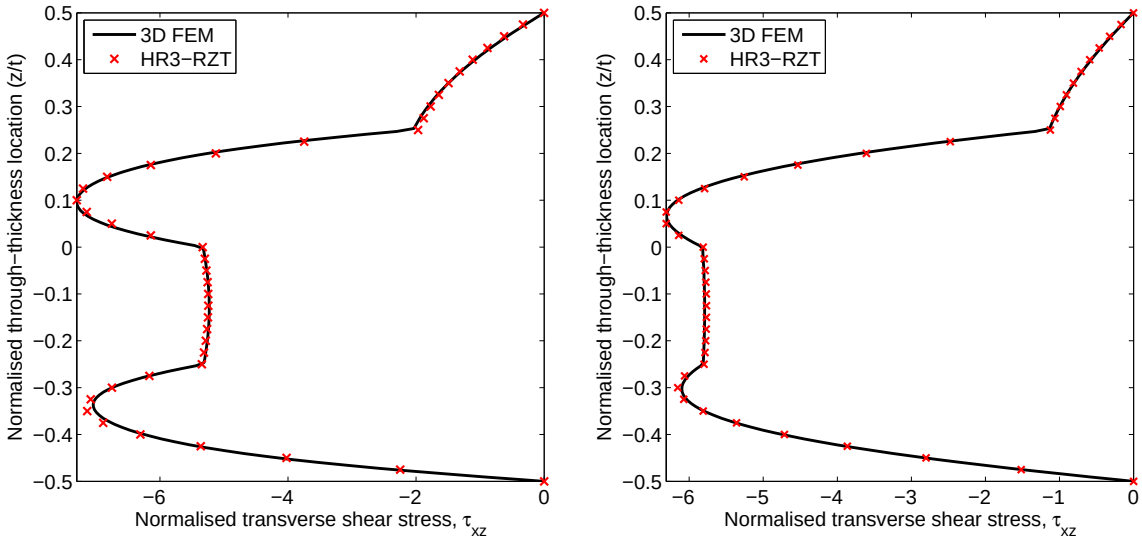

(a) $\bar{\tau}_{xz}$ at 5% **(b)** $\bar{\tau}_{xz}$ at 10%

Figure 5.29: Laminate 1: Through-thickness plot of normalised transverse shear stress $\bar{\tau}_{xz}$ at locations 5% and 10% of the beam span from clamped end x_A.

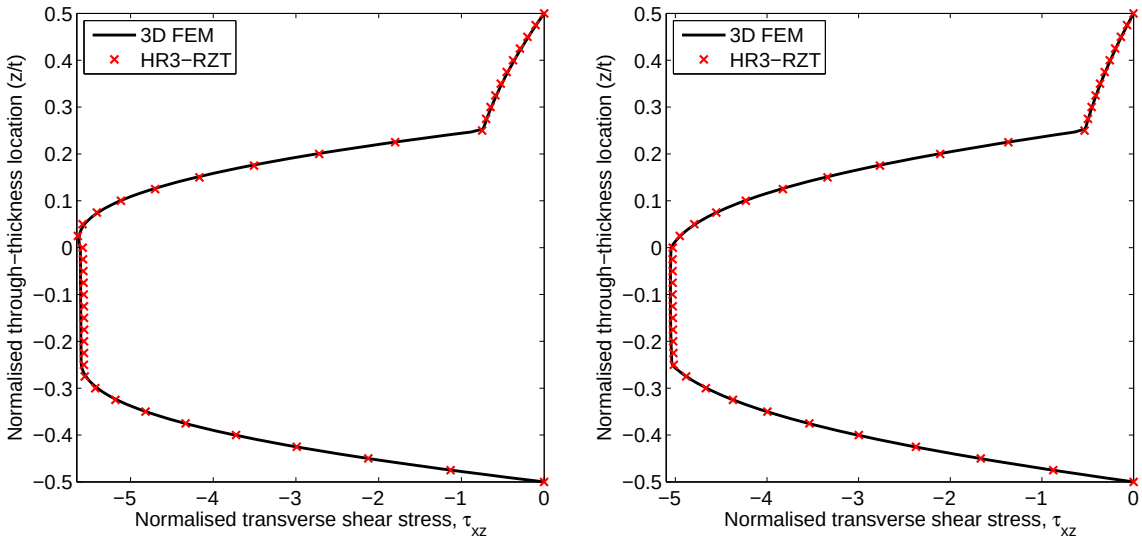

(a) $\bar{\tau}_{xz}$ at 15% **(b)** $\bar{\tau}_{xz}$ at 20%

Figure 5.30: Laminate 1: Through-thickness plot of normalised transverse shear stress $\bar{\tau}_{xz}$ at locations 15% and 20% of the beam span from clamped end x_A.

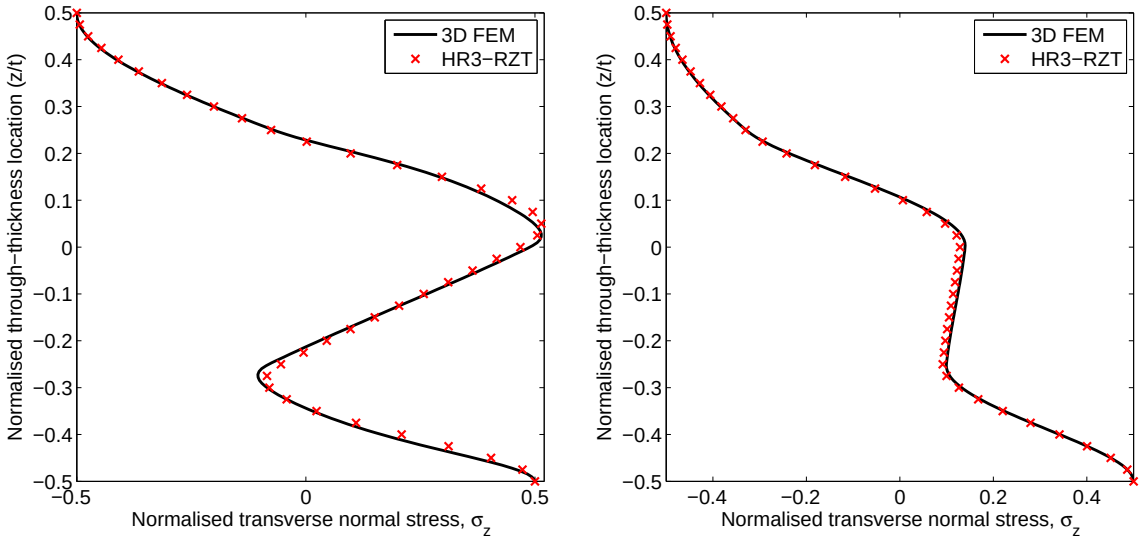

(a) $\bar{\sigma}_z$ at 5% **(b)** $\bar{\sigma}_z$ at 10%

Figure 5.31: Laminate 1: Through-thickness plot of normalised transverse normal stress $\bar{\sigma}_z$ at locations 5% and 10% of the beam span from clamped end x_A.

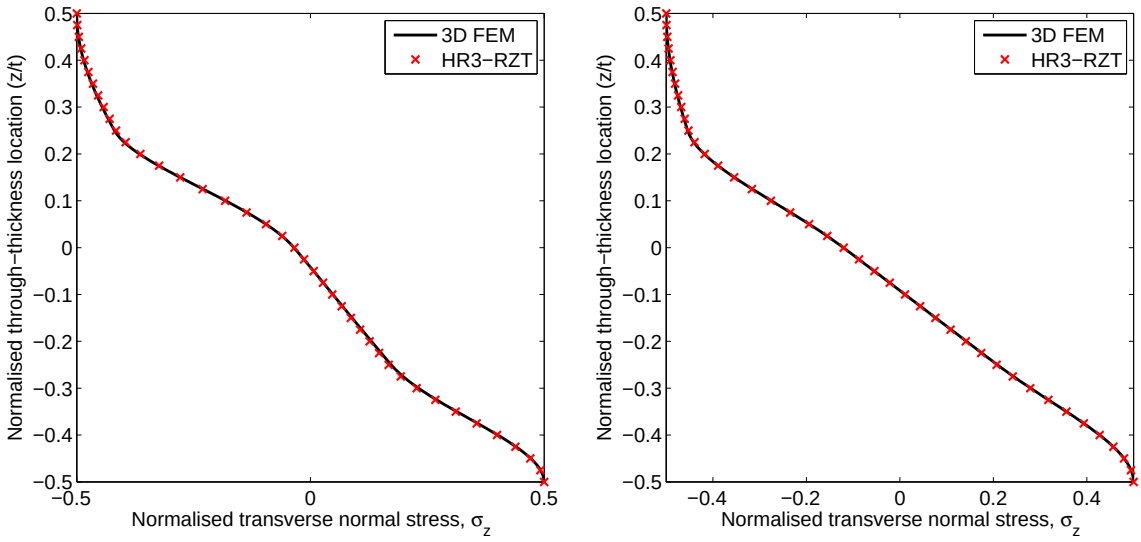

(a) $\bar{\sigma}_z$ at 15% **(b)** $\bar{\sigma}_z$ at 20%

Figure 5.32: Laminate 1: Through-thickness plot of normalised transverse normal stress $\bar{\sigma}_z$ at locations 15% and 20% of the beam span from clamped end x_A.

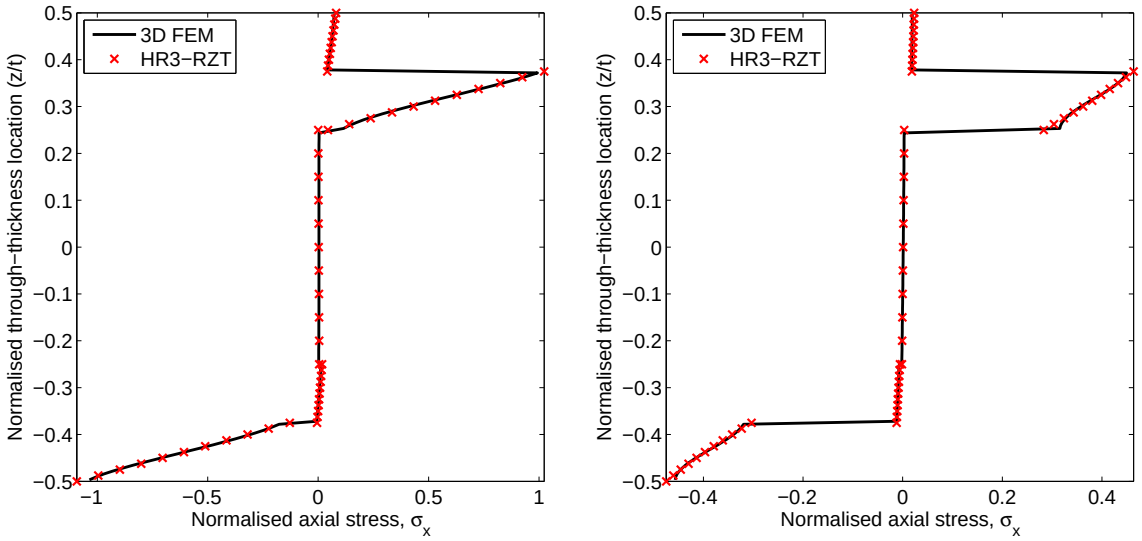

(a) $\bar{\sigma}_x$ at 5% **(b)** $\bar{\sigma}_x$ at 10%

Figure 5.33: Laminate 2: Through-thickness plot of normalised axial stress $\bar{\sigma}_x$ at locations 5% and 10% of the beam span from clamped end x_A.

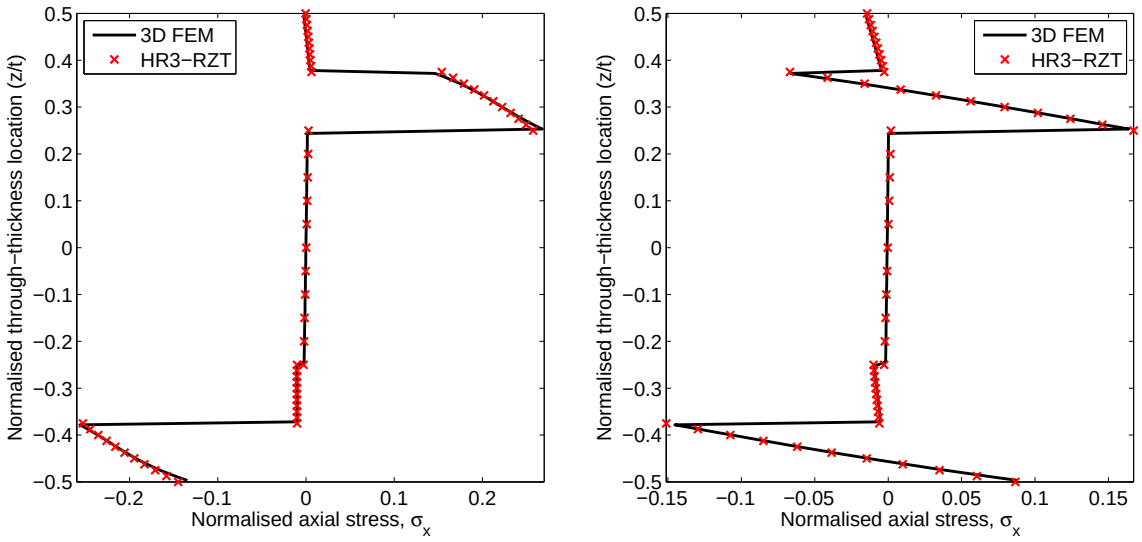

(a) $\bar{\sigma}_x$ at 15% **(b)** $\bar{\sigma}_x$ at 20%

Figure 5.34: Laminate 2: Through-thickness plot of normalised axial stress $\bar{\sigma}_x$ at locations 15% and 20% of the beam span from clamped end x_A.

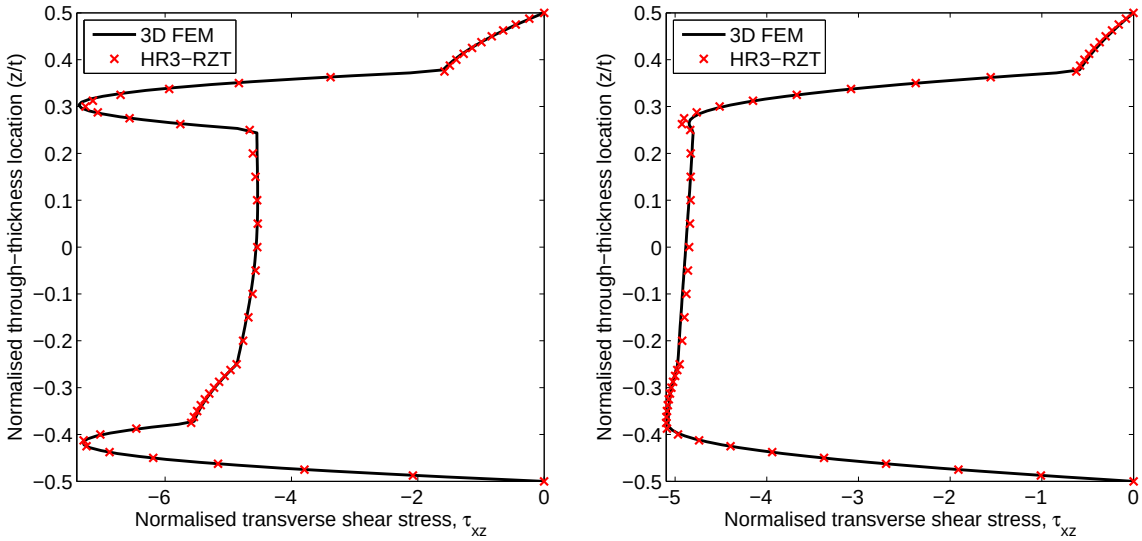

(a) $\bar{\tau}_{xz}$ at 5% **(b)** $\bar{\tau}_{xz}$ at 10%

Figure 5.35: Laminate 2: Through-thickness plot of normalised transverse shear stress $\bar{\tau}_{xz}$ at locations 5% and 10% of the beam span from clamped end x_A.

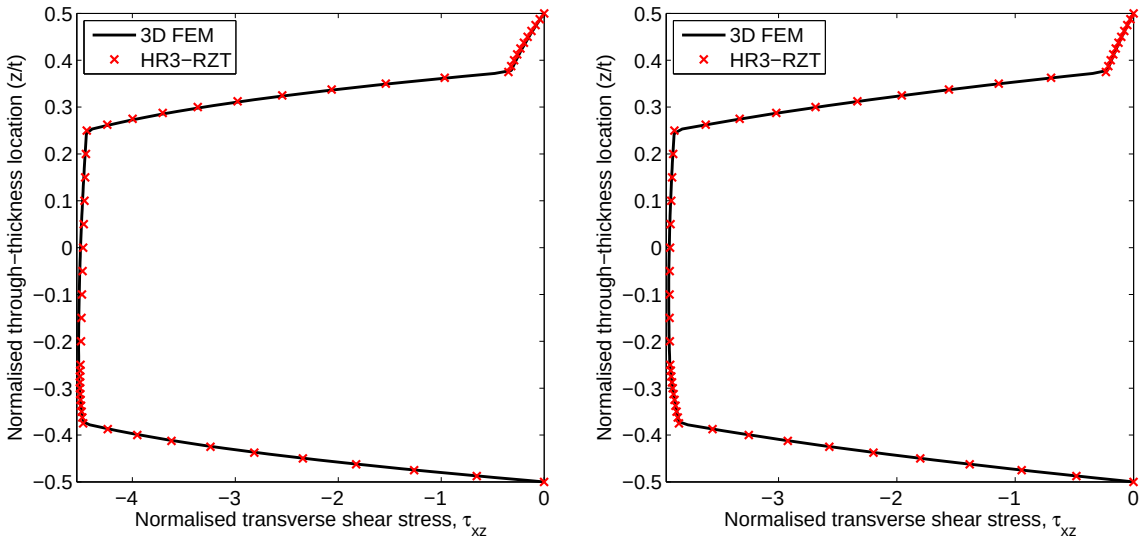

(a) $\bar{\tau}_{xz}$ at 15% **(b)** $\bar{\tau}_{xz}$ at 20%

Figure 5.36: Laminate 2: Through-thickness plot of normalised transverse shear stress $\bar{\tau}_{xz}$ at locations 15% and 20% of the beam span from clamped end x_A.

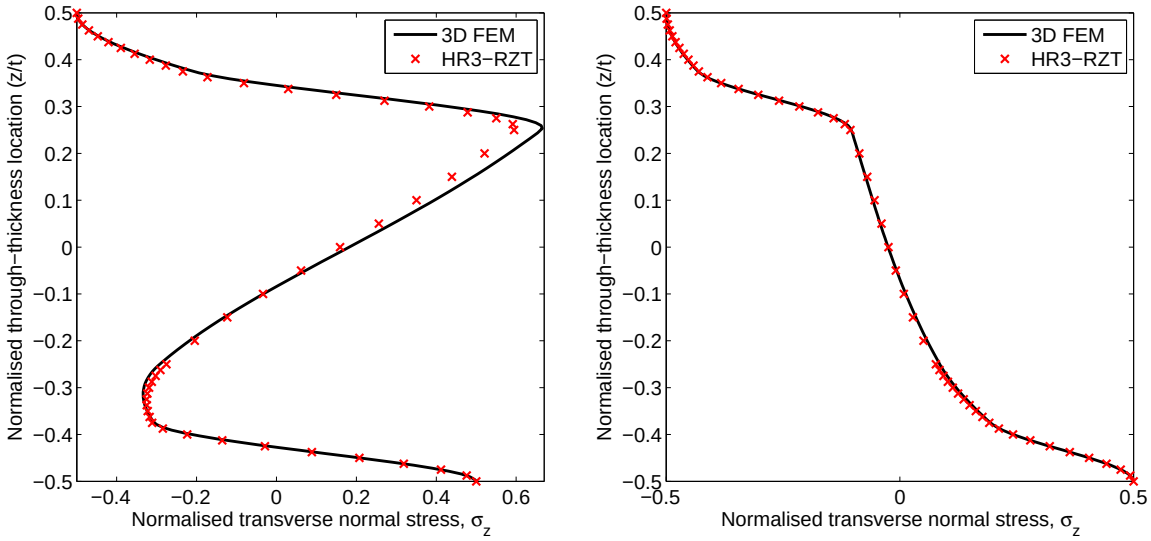

(a) $\bar{\sigma}_z$ at 5% **(b)** $\bar{\sigma}_z$ at 10%

Figure 5.37: Laminate 2: Through-thickness plot of normalised transverse normal stress $\bar{\sigma}_z$ at locations 5% and 10% of the beam span from clamped end x_A.

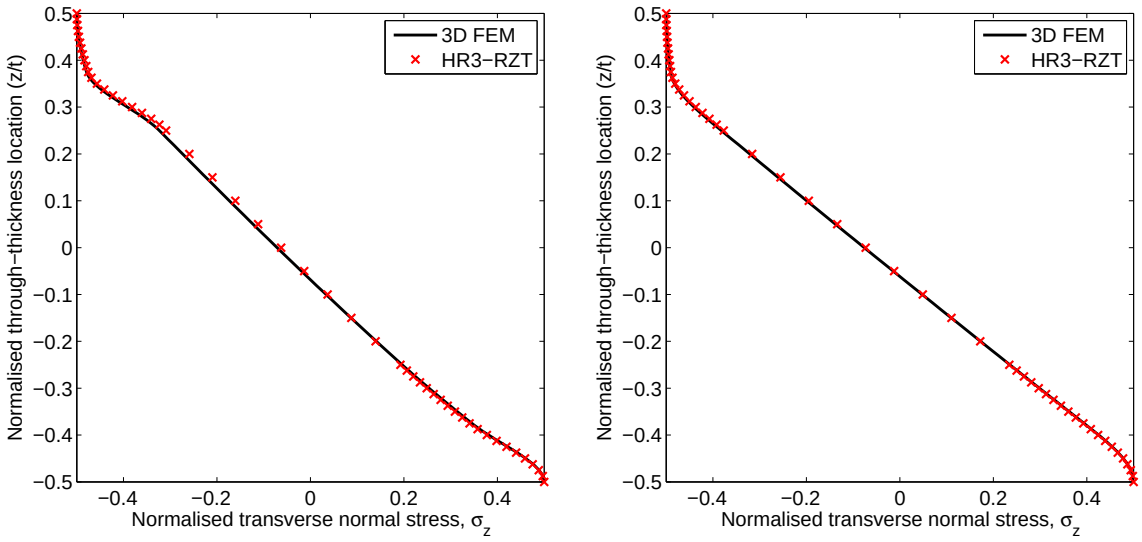

(a) $\bar{\sigma}_z$ at 15% **(b)** $\bar{\sigma}_z$ at 20%

Figure 5.38: Laminate 2: Through-thickness plot of normalised transverse normal stress $\bar{\sigma}_z$ at locations 15% and 20% of the beam span from clamped end x_A.

FEM model is used to verify the results. The beam is modelled in the commercial software package Abaqus using a 3D body 1000 mm long, 100 mm thick and 1 mm wide that is meshed with 96,000 C3D8R brick elements, i.e. 160 elements through the thickness, 600 elements along the length and 1 element across the width. This choice was based on initial convergence studies that ensured that all plotted results converge to within 0.1%. The plane strain condition in the width direction is enforced by using a single element in this direction and by restraining the lateral edges from expanding. A load of $\hat{P}_b = -\hat{P}_t = 50$ kPa is applied as a pressure loading on the top and bottom surfaces. Finally, all nodal degrees of freedom are constrained throughout the thickness of two clamped edges.

The three stress fields σ_x, τ_{xz} and σ_z are normalised using the expressions in Eq (5.5). The through-thickness distributions of these three stress fields are plotted in Figures 5.27-5.38 at the four locations 5%, 10%, 15% and 20% of the beam length from the clamped end x_A of the beam. The nearest position of 5% to the clamped end was chosen to minimise the effect of the boundary singularity on the 3D FEM results. The stress plots of HR3-RZT and 3D FEM are well-correlated in Figures 5.27-5.38, although the correlation is not quite as good as between Pagano's 3D elasticity solution [20] and HR3-RZT in Section 5.2. As Pagano's model is an exact closed-form solution to the 3D elasticity problem, and further refinements in the mesh density did not seem to cause further convergence in the 3D FEM results, it is conjectured that certain inaccuracies appear in the 3D FEM results that lead to this inferior correlation. A more detailed discussion of these arguments is presented in Sections 6.3 and 6.4.

To begin, consider the results for laminate 1. Figures 5.27-5.32 show a clear and definite change in the through-thickness profile of all three stress fields at different locations from the clamped support. The clamped laminate 1 investigated here has the same stacking sequence as the simply supported laminate J studied in Section 5.2. The through-thickness profile of $\bar{\tau}_{xz}$ at the 20% location for laminate 1 (Figure 5.30b) is the same as the $\bar{\tau}_{xz}$ profile at the supports of laminate J (Figure 5.12b). The zero-stress natural boundary condition in the simply supported beam does not induce a boundary layer close to the supports, and therefore the plot for the 20% location in Figure 5.30b represents the converged solution free of boundary layer effects.

Close to the clamped ends, e.g. at the 5% location in Figure 5.29a, the non-zero natural boundary condition induces a boundary layer and this results in a change in shape of the transverse shear stress profile. The maximum $\bar{\tau}_{xz}$ magnitude is redistributed from the midplane towards the surfaces, causing a reversal in the transverse shear stress profile with smaller stress magnitudes towards the midplane. This behaviour was previously observed for sandwich beams, e.g. laminates F and G in Figures 5.8b and 5.9b, and is attributed to the ZZ effect, i.e. in these sandwich beams the extremely soft core is unable to support the transverse shear stress magnitude in the stiff face layers. The [0/90/0/90] stacking sequence of laminate 1 is not affected by the ZZ phenomenon to the same extent as the sandwich beam. However, the plot in Figure 5.29a shows that the clamped support condition exacerbates the ZZ deformations within the laminate towards the boundaries.

The same effect is also evident in the transverse normal stress plots of Figures 5.31-5.32. The transverse normal stress field at the 20% location in Figure 5.32b has the same shape as the midspan transverse normal stress of the simply supported laminate J (Figure 5.20b). How-

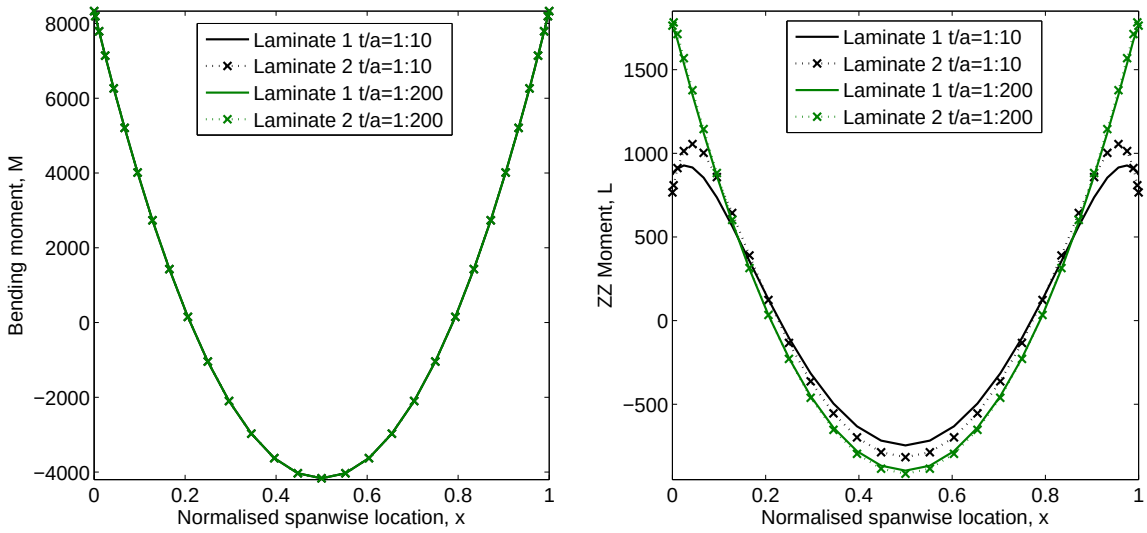

(a) Bending Moment, M **(b)** ZZ Moment, L

Figure 5.39: Bending moment M and ZZ moment L for two different laminates plotted against axial location x for different thickness to length ratios t/a.

ever, closer to the clamped boundary at the 5% location (Figure 5.31a) the through-thickness variation of $\bar{\sigma}_z$ changes considerably due to the increased influence of the ZZ effect.

Finally, the plots of the axial stress fields in Figures 5.27-5.28 show that towards the boundary the third-order "stress-channelling" effects decrease. This manifests itself by a reduction of the cubic z-wise variation of $\bar{\sigma}_x$ between the 20% location in Figure 5.28b and the 5% location in Figure 5.27a. At the 5% location, the additional linear behaviour of the ZZ effect reduces the relative magnitude of the cubic through-thickness variation.

Similarly, the plots for sandwich beam laminate 2 in Figures 5.33-5.38 also show that the through-thickness distributions of the three stress fields change from the 20% to 5% locations. As discussed above, towards the boundaries the increasing effect of ZZ deformations causes transverse shear loads to be redistributed from the beam midplane to the surfaces. In fact, the redistribution of the transverse stresses can be explained intuitively using Cauchy's equilibrium equations. Given that the clamped support causes localised axial stress gradients in σ_x, this rate of change of $\sigma_{x,x}$ must be balanced by a rate of change $\tau_{xz,z}$. Hence, the through-thickness profile of the transverse shear stress is altered by stress gradients of the axial stress. In the same manner, the rate of change in τ_{xz} in the x-direction leads to an increase in the z-wise rate of change of σ_z.

The extent of the boundary layers along the lengths of laminates 1 and 2 are shown graphically in Figure 5.39. The plots show the variation of bending moment M (Figure 5.39a) and ZZ moment L (Figure 5.39b) with span-wise location x along the beams. According to the equilibrium of moments and transverse forces, the bending moments M for laminates 1 and 2 are prescribed fully by the loading and boundary conditions and are independent of stacking sequence. Thus, the bending moments show no observable local variations towards the boundaries. However, the ZZ moments L of the two laminates are not the same due to the different degrees of transverse anisotropy inherent in the stacking sequences. Furthermore, there is an

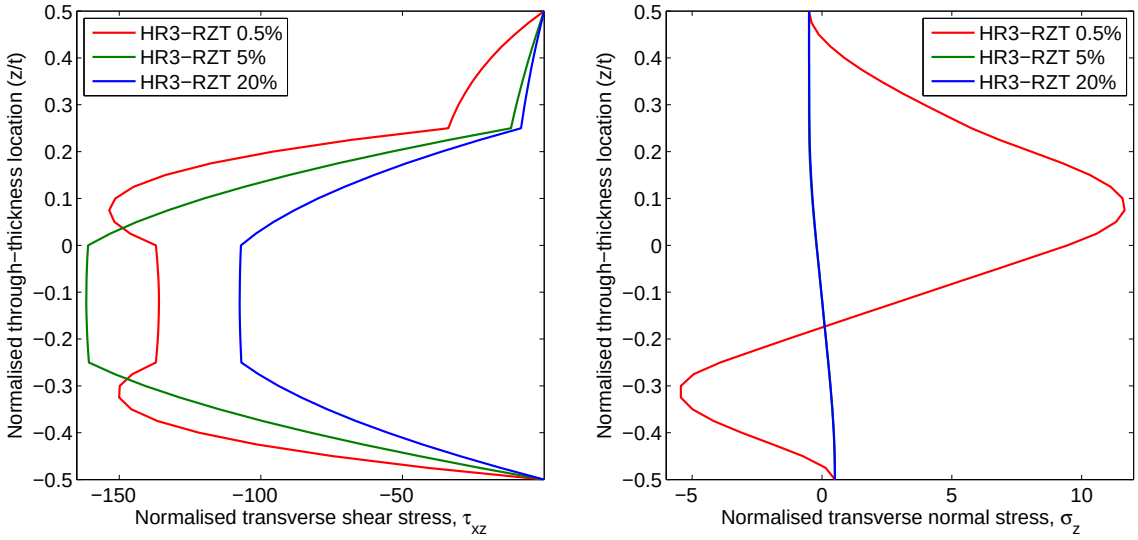

(a) $\bar{\tau}_{xz}$ **(b)** $\bar{\sigma}_z$

Figure 5.40: Laminate 1: Comparison of through-thickness plots of normalised transverse shear stress $\bar{\tau}_{xz}$ and transverse normal stress $\bar{\sigma}_z$ at locations 0.5%, 5% and 20% of the beam span from clamped end x_A with $t/a = 1 : 200$.

observable boundary layer effect as L transitions from the global sinusoidal curve, that also governs the bending moment M, to local high-order behaviour towards the two ends $x = 0$ and $x = 1$.

The boundary layer effect observed here is a higher-order phenomenon that depends on the magnitude of ZZ deformations within the structure. Based on the findings in Section 5.3, this means that the boundary layer effect scales with the thickness to length ratio t/a and with the degree of transverse anisotropy. For example, consider laminates 1 and 2 with reduced thickness to length ratio $t/a = 1 : 200$. The axial plots of the ZZ moment L for these two thinner configurations are shown alongside the plots for the originally thicker configurations ($t/a = 1 : 10$) in Figure 5.39b. The relative magnitudes of the bending moments M and ZZ moments L are not reduced as the thickness to length ratio is decreased from $t/a = 1 : 10$ to $t/a = 1 : 200$. However, in the thinner configuration the boundary layers between $x \in [0, 0.15]$ and $x \in [0.85, 1]$ are no longer present. Thus, reducing the thickness to length ratio has not impacted the magnitude of the ZZ moment but eliminated the boundary layer effects associated with it.

The through-thickness plots of $\bar{\tau}_{xz}$ and $\bar{\sigma}_z$ at locations 0.5%, 5% and 20% for the thinner configurations ($t/a = 1 : 200$) are compared in Figures 5.40-5.41. Compared to the plots for the thicker laminates ($t/a = 1 : 10$), there is no observable boundary layer effect between the shape of the 5% and 20% curves of both $\bar{\tau}_{xz}$ and $\bar{\sigma}_z$. Because the transverse shear force varies with location, the magnitudes of $\bar{\tau}_{xz}$ in Figures 5.40a and 5.41a are different, but the overall through-thickness shape remains the same. However, there is a visible difference between the curves of $\bar{\tau}_{xz}$ and $\bar{\sigma}_z$ at the 0.5% and 5% locations. Thus, compared to the thicker configurations of laminates 1 and 2, the length of the boundary layer from the clamped support has decreased with the thickness to length ratio. This reduction in the boundary layer length is also visible in

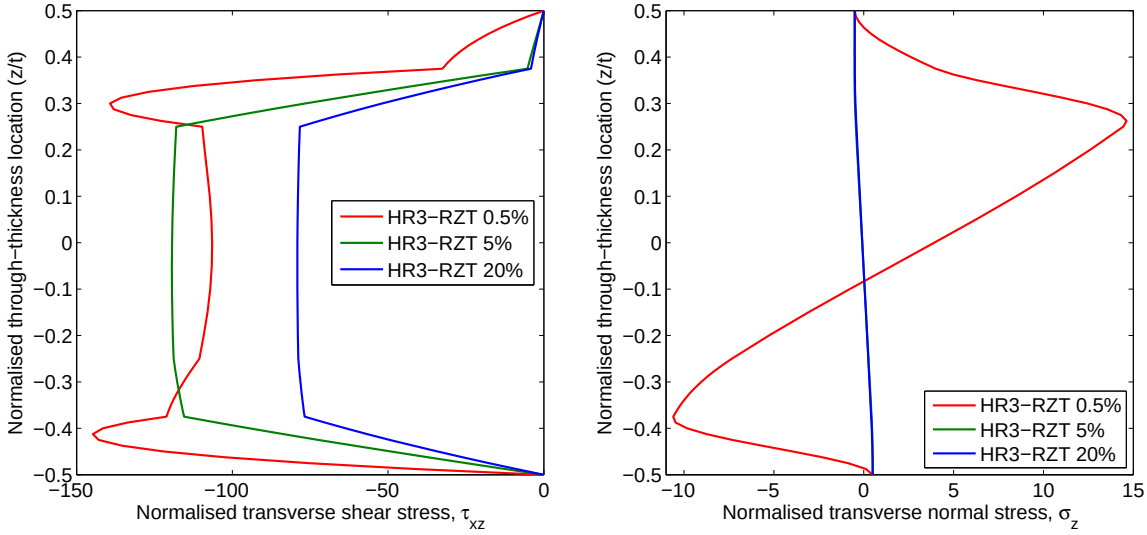

(a) $\bar{\tau}_{xz}$ **(b)** $\bar{\sigma}_z$

Figure 5.41: Laminate 2: Comparison of through-thickness plots of normalised transverse shear stress $\bar{\tau}_{xz}$ and transverse normal stress $\bar{\sigma}_z$ at locations 0.5%, 5% and 20% of the beam span from clamped end x_A with $t/a = 1 : 200$.

the axial variation of the ZZ moment L in Figure 5.39b. When $t/a = 1 : 200$, the local variation of L is constrained to a much smaller interval close to the boundary than when $t/a = 1 : 10$.

Second, consider the effects of maintaining the thickness to length ratio of laminate 1 at $t/a = 1 : 10$ but reducing the transverse anisotropy through the thickness. This is achieved by reducing the ratio G_{13}/G_{23} of material p from 2.5 : 1, as originally defined in Table 5.1, to a lesser ratio of 1.01 : 1, i.e. transverse shear stiffness orthotropy between the 0° and 90° layers is almost removed completely. Figure 5.42 shows that in this case the magnitude of the ZZ moment is much smaller than the higher-order moment O. Furthermore, compared to the case of greater orthotropy ratio in Figure 5.39b, the local boundary layer of ZZ moment L close to the supports is also reduced. Therefore, the boundary layer effect associated with the ZZ moment is not only reduced for a lower thickness to length ratio t/a, but also when the transverse orthotropy ratio is decreased.

However, Figure 5.43 shows that the through-thickness shapes of $\bar{\tau}_{xz}$ and $\bar{\sigma}_z$ do undergo changes in shape at different locations from the clamped boundary, even when the ZZ moment is benign. This second boundary layer effect is related to the higher-order moment O and only becomes visible when ZZ effects are negligible. The axial distribution of the higher-order moment O in Figure 5.42a shows that there is a small boundary layer close to the supports, which manifests itself by $\mathrm{d}O/\mathrm{d}x \approx 0$ at the boundary. This local change in slope modifies the z-wise stress profiles between locations 0.5% and 5% shown in Figure 5.43.

Furthermore, the axial variation of higher-order moment O plotted in Figure 5.42a shows that the local boundary layer in O is eliminated when the thickness to length ratio is reduced to $t/a = 1 : 200$. The through-thickness plots of the transverse stress fields $\bar{\tau}_{xz}$ and $\bar{\sigma}_z$ in Figure 5.44 show that a benign boundary layer effect remains. However, the overall change in shape is considerably reduced and constrained to a much closer region from the boundary, i.e.

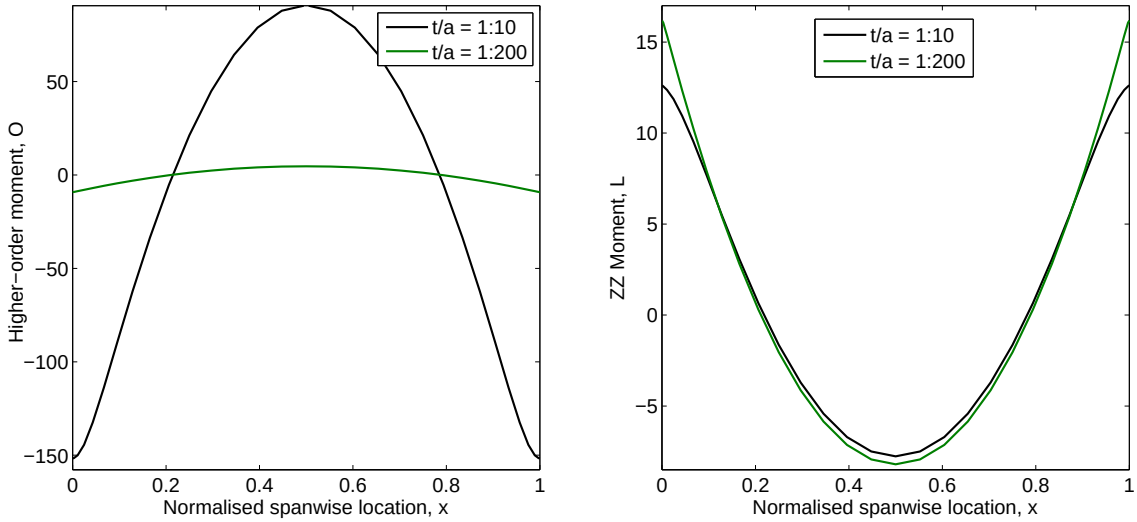

(a) Higher-order moment, O **(b)** ZZ moment, L

Figure 5.42: Axial variation of higher-order moment O and ZZ moment L for laminate 1 with reduced transverse orthotropy ratio $G_{13}/G_{23} = 1.01 : 1$ of material p.

within $x \in [0\%, 2.5\%]$.

In conclusion, boundary layer effects towards clamped boundaries can arise from higher-order global moments or from higher-order ZZ moments. These local effects scale in proportion to the effect of their associated moments on the global behaviour of the structure. When ZZ moments are important, such as for sandwich panels, the associated boundary layer effects dominate, and the metrics introduced in Section 5.3 may be used to assess when this is the case. For laminated structures where the ZZ effects are benign, such as composite laminates with thin plies evenly distributed through the thickness, boundary layer effects associated with higher-order moments play a more important role.

These boundary layer effects lead to changes in the z-wise profiles of the 3D stress fields and the HR formulation is capable of modelling these effects. This capability arises because the stresses are treated as fundamental unknowns and forced to obey Cauchy's equilibrium equations in the variational statement. Second, solving the governing equations in the strong form using DQM means that equilibrium is guaranteed at every point within the solution domain. Modelling boundary layers accurately is important for stress-based failure analyses because stress concentrations arise close to discrete changes in the loading condition, e.g. at boundary conditions, and the stress gradients at these locations are often the critical drivers in failure initiation.

5.5 Conclusions

This chapter analysed multiple straight-fibre composite and sandwich beams using the HR formulation derived in Chapter 4. The accuracy of the model was validated against 3D elasticity and 3D FEM solutions for a wide range of straight-fibre composite and sandwich beams, and the excellent correlation of all three stress fields (σ_x, τ_{xz} and σ_z) with the benchmark solutions

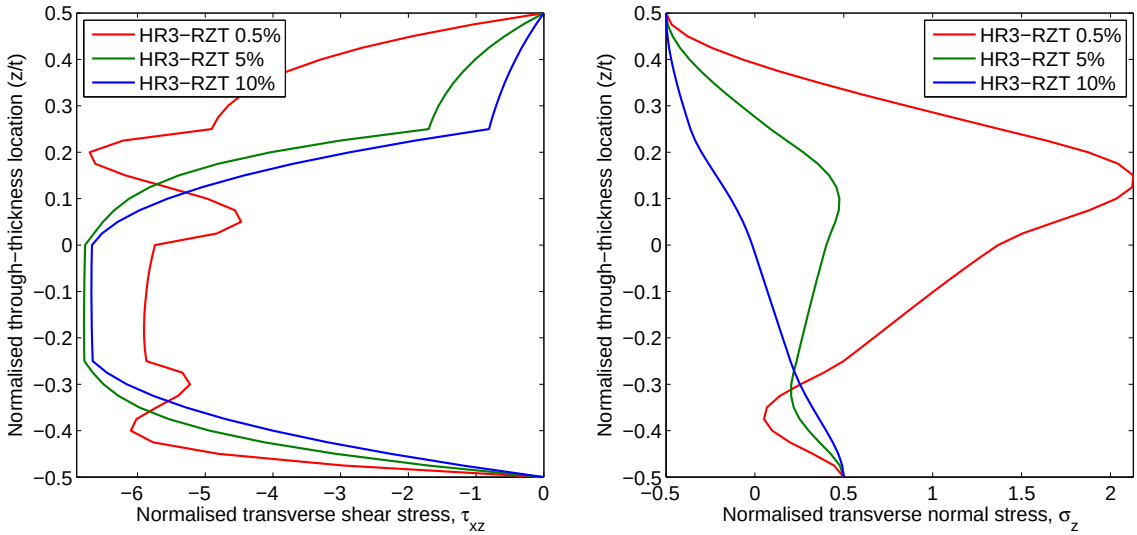

(a) $\bar{\tau}_{xz}$ **(b)** $\bar{\sigma}_z$

Figure 5.43: Laminate 1: Comparison of through-thickness plots of normalised transverse shear stress $\bar{\tau}_{xz}$ and transverse normal stress $\bar{\sigma}_z$ at locations 0.5%, 5% and 10% of the beam span from clamped end x_A with $t/a = 1 : 10$ and reduced transverse orthotropy ratio $G_{13}/G_{23} = 1.01 : 1$ of material p.

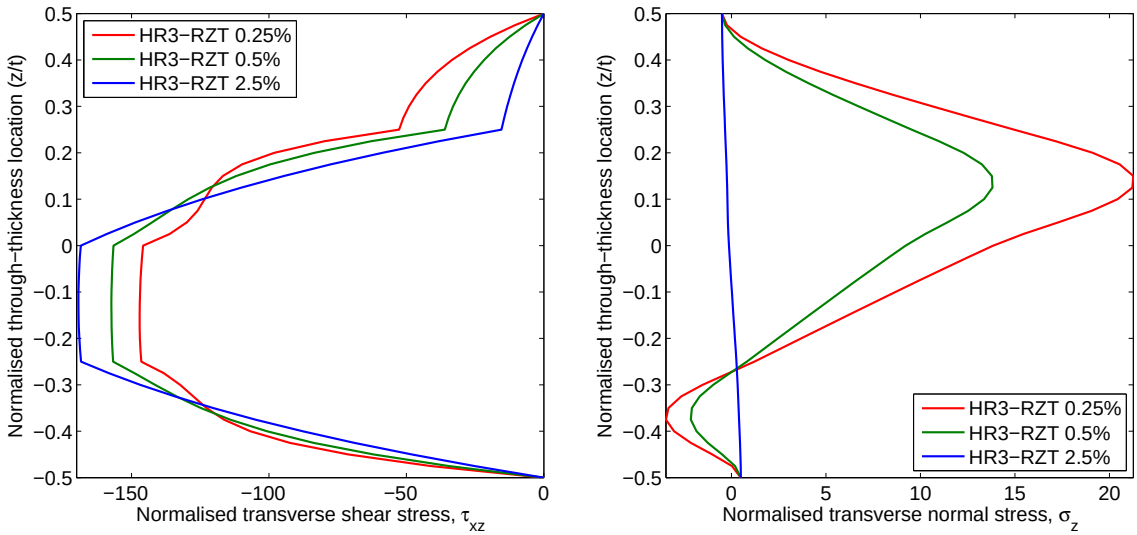

(a) $\bar{\tau}_{xz}$ **(b)** $\bar{\sigma}_z$

Figure 5.44: Laminate 1: Comparison of through-thickness plots of normalised transverse shear stress $\bar{\tau}_{xz}$ and transverse normal stress $\bar{\sigma}_z$ at locations 0.25%, 0.5% and 2.5% of the beam span from clamped end x_A with $t/a = 1 : 200$ and reduced transverse orthotropy ratio $G_{13}/G_{23} = 1.01 : 1$ of material p.

demonstrate the accuracy of the model for commonly used and highly heterogeneous layered structures. The model was also used to analyse axial boundary layer effects towards clamped boundaries and to assess the importance of transverse shearing, transverse normal and zig-zag deformations on the structural behaviour.

The results for the straight-fibre laminates in Section 5.2 showed that a cubic formulation of the HR model coupled with the RZT ZZ function (HR3-RZT) is the best performing model considered herein. The bending deflection and three stress fields (σ_x, τ_{xz} and σ_z) are predicted to an accuracy within 1% of Pagano's solution even for highly heterogeneous laminates with arbitrary thickness ratios, ply material orientations and layer material properties. The results of the HR3-MZZF model showed that this model can predict the three-dimensional stress fields to similar accuracy for some laminates. However, for sandwich beams with very soft cores or laminates with three unique materials, the discrepancies between HR3-MZZF and Pagano's solution are greater than 10% and therefore significantly higher than for HR3-RZT. The performance of the HR formulations was also compared to corresponding theories developed using the RMVT. Whereas the RMVT3-RZT and RMVT3-MZZF give accurate predictions for the bending deflection and axial stress, the model assumptions for transverse shear stress may be highly inaccurate when the number of layers exceeds three. As a result, the RMVT formulations require extra post-processing steps to guarantee accurate transverse stress results. However, compared to the HR formulation, the RMVT formulation reduces the variable count by one. Thus, the overall computational efficiency of the RMVT formulation with respect to the HR model, depends on the effort involved in this extra post-processing step.

The results in Section 5.3 showed that for commonly used non-sandwich beams used in industry, which prohibit thick blocks of 0° and 90° plies, the ZZ effect on the structural behaviour is negligible. In these cases, higher-order effects, such as "stress-channelling", i.e. a cubic variation of the axial stress towards the surfaces of the laminate, are more important. Furthermore, two nondimensional factors were identified that quantify the influence of the ZZ effect on the classical bending deflection and transverse shear behaviour. The results show that including the ZZ effect in the model reduces the effect of transverse shear deformation and generally acts to stiffen the structure in bending.

Section 5.4 demonstrated that the HR3-RZT model is capable of predicting local variations in the stress fields towards clamped edges. These boundary layer effects arise due to local variations in the higher-order stress resultants, i.e. the relative significance of the higher-order effects increases towards the clamped boundaries. For sandwich beams, the boundary layer effects occur due to local variations in the ZZ moment, whereas for commonly used composite laminates, the effects are driven by variations in the higher-order membrane moments. Therefore, the magnitude of the boundary layer effect is a function of both the transverse anisotropy and the thickness to length ratio of the laminate.

Chapter 6

Global and Local Phenomena in Tow-Steered Composite Beam Bending

In the previous Chapter a higher-order ZZ version of the HR model was benchmarked for the bending of highly heterogeneous straight-fibre beams. The validation of the HR model's accuracy is now extended to variable-stiffness laminates. The combination of variable stiffness along the length of the beam and high heterogeneity through the thickness present a challenging test case for a 2D equivalent single-layer model. Based on the good accuracy of the third-order HR formulations HR3-MZZF and HR3-RZT for straight-fibre laminates presented in the previous chapter, these two models are also used here for variable-stiffness beams. A detailed model comparison against 3D FEM solutions, remote from the boundaries, is presented in Section 6.3, and local boundary layer effects are investigated in Section 6.4. Finally, Section 6.6 presents an optimisation study of a variable-stiffness beam with the aim of tailoring the full 3D stress field through the thickness, such that a compromise between maximising bending stiffness and minimising the likelihood of delamination is obtained.

6.1 Load case and model implementation

A multilayered beam with thickness to length ratio $t/a = 1:10$, comprising N_l variable-stiffness composite layers and clamped at both ends $x_A = 0$ and $x_B = a$, is assumed to undergo isothermal, static deformations in plane strain under a uniformly distributed load equally divided between the top and bottom surfaces $\hat{P}_b = -\hat{P}_t = q_0/2$, as shown in Figure 6.1. To the author's knowledge there are no closed-form 3D elasticity solutions for variable-stiffness beams in bending. Therefore, high-fidelity 3D finite element models are used to compare the stress and bending deflection results. A clamped edge load case is chosen herein as this condition is easily modelled in 3D FEM by constraining all through-thickness nodal degrees of freedom at the edges. Furthermore, this load case serves to show that the HR formulation does not lead to static inconsistencies at clamped edges, as was discussed in Chapter 3 for other higher-order theories in the literature.

Variable-stiffness beams with linear fibre angle variations in the spanwise direction of each ply k are defined using the notation by Gürdal and Olmedo [101],

$$\alpha^{(k)}(x) = \frac{2\left(T_1^{(k)} - T_0^{(k)}\right)}{a}\left|x - \frac{a}{2}\right| + T_0^{(k)} \quad \text{written as} \quad \langle T_0^{(k)} | T_1^{(k)} \rangle \tag{6.1}$$

where $\alpha^{(k)}(x)$ is the local fibre angle at coordinate x, and $T_0^{(k)}$ and $T_1^{(k)}$ are the fibre angles at the beam midspan $x = a/2$, and ends $x = 0$ and $x = a$, respectively. Hence, the fibre angle in

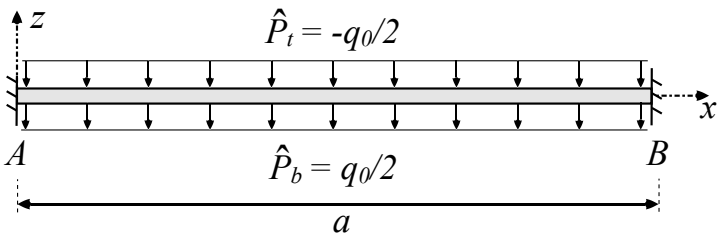

Figure 6.1: A multilayered, variable-stiffness beam clamped at both ends and loaded by a uniformly distributed load. This depicts the load case used to validate the HR formulation for variable-stiffness beams.

Table 6.1: Analysed stacking sequences with $t/a = 1 : 10$ including symmetric and non-symmetric variable stiffness composite laminates and sandwich beams. Subscripts indicate the repetition of a property over the corresponding number of layers.

Laminate	Thickness Ratio	Material	Stacking Sequence
VS A	$[(1/8)_8]$	$[\mathrm{IM7}_8]$	$[\pm\langle 90\|0\rangle/\pm\langle 45\|-45\rangle]_s$
VS B	$[(1/8)_8]$	$[\mathrm{IM7}_8]$	$[\pm[\langle 90\|20\rangle/\langle 45\|-25\rangle]]_s$
VS C	$[(1/3)_3]$	$[\mathrm{IM7}_3]$	$[\langle 0\|90\rangle/\langle 90\|0\rangle/\langle 0\|90\rangle]$
VS D	$[(1/3)_3]$	$[\mathrm{IM7}_3]$	$[\langle 90\|0\rangle/\langle 0\|90\rangle/\langle 90\|0\rangle]$
VS E	$[(1/5)_5]$	$[\mathrm{IM7}_5]$	$[\langle 90\|30\rangle/\langle -70\|50\rangle/\ldots$ $\langle 60\|0\rangle/\langle -25\|35\rangle/\langle 80\|10\rangle]$
VS F	$[(1/4)_4]$	$[\mathrm{IM7}_4]$	$[\langle 0\|70\rangle/\langle 90\|50\rangle/\langle 20\|-40\rangle/\langle 50\|0\rangle]$
VS G	$[(1/8)_2/0.5/(1/8)_2]$	$[\mathrm{p}_2/\mathrm{pvc}/\mathrm{p}_2]$	$[\pm\langle 45\|-45\rangle/0/\mp\langle 45\|-45\rangle]$
VS H	$[(1/12)_4/(1/3)/(1/12)_4]$	$[\mathrm{p}_4/\mathrm{pvc}/\mathrm{p}_4]$	$[\pm[\langle 0\|90\rangle/\langle 90\|0\rangle]/0/\mp[\langle 90\|0\rangle/\langle 0\|90\rangle]]$
VS I	$[(1/8)_2/0.5/(1/8)_2]$	$[\mathrm{p}_2/\mathrm{pvc}/\mathrm{p}_2]$	$[\langle 20\|-60\rangle/\langle -20\|60\rangle/0/0/90]$
VS J	$[(1/12)_4/(1/3)/(1/12)_4]$	$[\mathrm{p}_4/\mathrm{pvc}/\mathrm{p}_4]$	$[\pm\langle 20\|-60\rangle/\pm\langle 45\|-45\rangle/\ldots$ $0/0/90/\pm\langle 35\|-35\rangle]$

each ply takes the value $T_1^{(k)}$ at one end of the beam, is then steered to $T_0^{(k)}$ at the beam centre and returns to $T_1^{(k)}$ at the other end of the beam.

The stacking sequences modelled in this section are shown in Table 6.1. This table includes four symmetrically laminated variable-stiffness composites (VS A - VS D), two non-symmetric variable-stiffness composite laminates (VS E - VS F), two symmetric sandwich beams with variable-stiffness face layers (VS G - VS H), and two non-symmetric sandwich beams with hybrid straight-fibre/variable-stiffness face layers (VS I - VS J).

The stacking sequences include three materials IM7, p and pvc, where IM7 represents IM7 8852, a material commonly used in industry and defined in Table 6.2. Materials p and

Table 6.2: Mechanical properties of IM7 8552.

Material	E_1	E_2	E_3	G_{12}	G_{13}	G_{23}
IM7	163 GPa	12 GPa	12 GPa	5 GPa	4 GPa	3.2 GPa
Material	ν_{12}		ν_{13}		ν_{23}	
IM7	0.3		0.3		0.3	

pvc represent the orthotropic lamina and isotropic closed-cell polyvinyl chloride foam that were previously used in Chapter 5 and are defined in Table 5.1. Material IM7 is exclusively used for the variable-stiffness laminates VS A - VS F, whereas materials p and pvc are used for the sandwich beams VS G - VS J.

For the straight-fibre laminates in Chapter 5, trigonometric assumptions were made for displacement unknowns u_0, w_0 and stress unknowns $\mathcal{F}$ that satisfied boundary conditions Eq. (4.59) exactly and allowed derivations of closed form solutions. In general, such an approach is not possible for variable-stiffness composites because the variable-stiffness distribution across the beam can lead to non-intuitive deformation fields that are not accurately modelled by simple trigonometric functions.

Therefore, the governing field equations (4.58) and associated boundary conditions (4.59) are solved numerically in the strong form at every point within the discretisation domain using the pseudo-spectral DQM. This particular solution technique is chosen as DQM has been shown to be an efficient and robust solution technique for solving both stretching and bending [136], and stability problems [107] of variable-stiffness composites. Following the description of DQM in Section 2.4, the governing differential equations are converted into algebraic ones by replacing the differential operators with weighting matrices that operate on all functional unknowns within the domain. A non-uniform Chebychev-Gauss-Lobatto grid with 31 points is chosen herein based on an initial mesh convergence study.

The third-order ZZ HR model for variable-stiffness beams has two displacement unknowns u_0, w_0 and six stress unknowns $\mathcal{F} = \begin{bmatrix} N & M & O & P & F_{\phi,x} & F_\phi \end{bmatrix}^\top$, where N and O are the classic and second-order membrane stress resultants, respectively, M and P are the classic bending moment and second-order bending moment, respectively, and F_ϕ and $F_{\phi,x}$ are the ZZ moments associated with the ZZ function and axial derivative of the ZZ function, respectively.

For the load case shown in Figure 6.1, the stress resultants do not vanish at the clamped ends $x = 0$ and $x = a$, whereas all displacements vanish, i.e. $\hat{\mathcal{U}}_{bc} = \mathbf{0}$, such that the boundary conditions Eq. (4.59a)

$$\left(\boldsymbol{\eta}^{sbc} + \boldsymbol{\eta}^{nbc}\right)\mathcal{F} + \left(\boldsymbol{\eta}_x^{sbc} + \boldsymbol{\eta}_x^{nbc}\right)\mathcal{F}_{,x} + \boldsymbol{\eta}_{xx}^{nbc}\mathcal{F}_{,xx} + \boldsymbol{\eta}_{xxx}^{nbc}\mathcal{F}_{,xxx} + \hat{T}_b\boldsymbol{\chi}^{sbc} + \hat{T}_{b,x}\boldsymbol{\chi}_x^{nbc} + \hat{T}_{b,xx}\boldsymbol{\chi}_{xx}^{nbc} + \hat{P}_b\boldsymbol{\omega}^{nbc} + \hat{P}_{b,x}\boldsymbol{\omega}_x^{nbc} + \boldsymbol{\Lambda}_{bc_1} = \mathbf{0} \quad (6.2)$$

need to be satisfied. Furthermore, the axial derivatives of the membrane stress resultant $N_{,x}$ vanishes at the clamped ends, whereas the axial derivatives of all other stress resultants are undefined. Therefore, the boundary condition in Eq. (4.59b) is split into two parts,

$$N_{,x} = 0 \quad \text{from} \quad \delta\mathcal{F}_{,x}^\top = 0 \quad (6.3a)$$

$$\begin{bmatrix} \rho_{21}^{nbc} & \rho_{22}^{nbc} & \rho_{23}^{nbc} & \rho_{24}^{nbc} & \rho_{25}^{nbc} & \rho_{26}^{nbc} \\ \rho_{31}^{nbc} & \rho_{32}^{nbc} & \rho_{33}^{nbc} & \rho_{34}^{nbc} & \rho_{35}^{nbc} & \rho_{36}^{nbc} \\ \rho_{41}^{nbc} & \rho_{42}^{nbc} & \rho_{43}^{nbc} & \rho_{44}^{nbc} & \rho_{45}^{nbc} & \rho_{46}^{nbc} \\ \rho_{51}^{nbc} & \rho_{52}^{nbc} & \rho_{53}^{nbc} & \rho_{54}^{nbc} & \rho_{55}^{nbc} & \rho_{56}^{nbc} \\ \rho_{61}^{nbc} & \rho_{62}^{nbc} & \rho_{63}^{nbc} & \rho_{64}^{nbc} & \rho_{65}^{nbc} & \rho_{66}^{nbc} \end{bmatrix} \mathcal{F} + \begin{bmatrix} \rho_{x21}^{nbc} & \rho_{x22}^{nbc} & \rho_{x23}^{nbc} & \rho_{x24}^{nbc} & \rho_{x25}^{nbc} & \rho_{x26}^{nbc} \\ \rho_{x31}^{nbc} & \rho_{x32}^{nbc} & \rho_{x33}^{nbc} & \rho_{x34}^{nbc} & \rho_{x35}^{nbc} & \rho_{x36}^{nbc} \\ \rho_{x41}^{nbc} & \rho_{x42}^{nbc} & \rho_{x43}^{nbc} & \rho_{x44}^{nbc} & \rho_{x45}^{nbc} & \rho_{x46}^{nbc} \\ \rho_{x51}^{nbc} & \rho_{x52}^{nbc} & \rho_{x53}^{nbc} & \rho_{x54}^{nbc} & \rho_{x55}^{nbc} & \rho_{x56}^{nbc} \\ \rho_{x61}^{nbc} & \rho_{x62}^{nbc} & \rho_{x63}^{nbc} & \rho_{x64}^{nbc} & \rho_{x65}^{nbc} & \rho_{x66}^{nbc} \end{bmatrix} \mathcal{F}_{,x} +$$

$$\begin{bmatrix} \rho_{xx21}^{nbc} & \rho_{xx22}^{nbc} & \rho_{xx23}^{nbc} & \rho_{xx24}^{nbc} & \rho_{xx25}^{nbc} & \rho_{xx26}^{nbc} \\ \rho_{xx31}^{nbc} & \rho_{xx32}^{nbc} & \rho_{xx33}^{nbc} & \rho_{xx34}^{nbc} & \rho_{xx35}^{nbc} & \rho_{xx36}^{nbc} \\ \rho_{xx41}^{nbc} & \rho_{xx42}^{nbc} & \rho_{xx43}^{nbc} & \rho_{xx44}^{nbc} & \rho_{xx45}^{nbc} & \rho_{xx46}^{nbc} \\ \rho_{xx51}^{nbc} & \rho_{xx52}^{nbc} & \rho_{xx53}^{nbc} & \rho_{xx54}^{nbc} & \rho_{xx55}^{nbc} & \rho_{xx56}^{nbc} \\ \rho_{xx61}^{nbc} & \rho_{xx62}^{nbc} & \rho_{xx63}^{nbc} & \rho_{xx64}^{nbc} & \rho_{xx65}^{nbc} & \rho_{xx66}^{nbc} \end{bmatrix} \mathcal{F}_{,xx} + \hat{T}_{b,x} \begin{Bmatrix} \gamma_{x2}^{nbc} \\ \gamma_{x3}^{nbc} \\ \gamma_{x4}^{nbc} \\ \gamma_{x5}^{nbc} \\ \gamma_{x6}^{nbc} \end{Bmatrix} + \hat{P}_b \begin{Bmatrix} \mu_2^{nbc} \\ \mu_3^{nbc} \\ \mu_4^{nbc} \\ \mu_5^{nbc} \\ \mu_6^{nbc} \end{Bmatrix} + \begin{Bmatrix} w_0 \\ 0 \\ 0 \\ 0 \\ 0 \end{Bmatrix} = \mathbf{0}. \tag{6.3b}$$

where the first equation associated with membrane stress resultants N is not included in Eq. (6.3b) because it satisfies the condition in Eq. (6.3a). Thus, by writing the governing field equations (4.58), and boundary conditions Eq. (6.2) and (6.3) in DQ matrix form as defined in Eq. (2.36), the functional unknowns at the DQ grid points are found using standard matrix operations. In the present work the numerical solution procedure was implemented in Matlab.

A 3D FEM benchmark model was implemented in the commercial software package Abaqus, which featured a 250 mm long (x-direction), 1000 mm wide (y-direction) and 25 mm thick (z-direction) plate that was meshed using a total of 95,880 linear C3D8R elements with 799 elements in the x-direction, 120 elements in the z-direction, and a single element in the y-direction. Note that the exact dimensions of the 3D FEM model are not important as long as the thickness to length ratio equals 1 : 10. Furthermore, the magnitude of the external pressure q_0 on the top and bottom surfaces is indefinite as the results presented herein are normalised with respect to q_0.

The plane strain condition in the y-direction is enforced by the high width to length aspect ratio, the use of a single element in the y-direction and boundary conditions that prevent the longitudinal sides from expanding laterally. Furthermore, Abaqus' enhanced hour-glassing control was chosen in the element settings to prevent numerical ill-conditioning. For all analysed stacking sequences, mesh convergence studies were carried out to ensure that the number of z-wise elements was sufficient to guarantee interfacial equilibrium conditions. In general, these studies showed that at least 10 elements per ply are required for the transverse shear stress fields of the 3D FEM solution to satisfy interlaminar continuity and equilibrium of surface tractions. Furthermore, the mesh in the x-direction was increased until all stress fields converged to within 0.1%.

Normalised metrics of the bending deflection w_0, axial stress σ_x, transverse shear stress τ_{xz} and transverse normal stress σ_z are used to assess the accuracy of the variable-stiffness HR model. The normalised quantities are defined as follows

$$\bar{w} = \frac{10^6 t^2}{q_0 a^4} \int_{-\frac{t}{2}}^{\frac{t}{2}} u_z \mathrm{d}z, \quad \bar{\sigma}_x = \frac{t^2}{q_0 a^2} \sigma_x, \quad \bar{\tau}_{xz} = \frac{1}{q_0} \tau_{xz}, \quad \bar{\sigma}_z = \frac{1}{q_0} \sigma_z \tag{6.4}$$

and are used for all plots shown throughout this section. The normalised deflections $\bar{w}$ for the HR formulation are constant through the thickness and thus compared against the average through-thickness deflection of the 3D FEM solution.

6.2 Comments on variable-stiffness zig-zag function

At this point, a few comments regarding the choice of the ZZ function for variable-stiffness beams, especially with respect to the numerical implementation in DQM have to be made. When MZZF is chosen, all stiffness terms, shear correction factors and normal correction factors associated with $F_{\phi,x}$ vanish because MZZF is independent of material properties. Thus, MZZF has the advantage of eliminating one degree of freedom from the formulation, albeit at the cost of losing the capability of capturing an extra higher-order structural effect.

On the other hand, the RZT ZZ function depends on the transverse shear moduli of the layers within the laminate as defined in Eq. (4.15). When all layers within a laminate have the same transverse shear modulus, the RZT ZZ function vanishes exactly. A numerical model based on RZT runs into ill-conditioning problems when the RZT ZZ function is zero, because this causes all stiffness terms associated with ZZ moments and their associated governing differential equations to vanish. As a result, the stiffness matrix includes rows of zeros that lead to rank deficiency, i.e. there is no unique solution to the inversion problem. Because MZZF is independent of layer moduli, it does not encounter these numerical issues.

For laminates with variable-stiffness plies, the RZT ZZ function may be finite throughout the majority of the domain but disappear at certain points when the stacking sequence is locally unidirectional, i.e. there is no transverse orthotropy. For sandwich beams, this is generally not an issue as the flexible core always provides a certain degree of transverse orthotropy. Similarly, the axial derivative of the RZT ZZ function $\phi^{(k)}_{,x}$ may be finite in certain regions of the beam but vanish at symmetry points of the axial fibre variation. If the fibre angle variations are defined by Eq. (6.1), then $\phi^{(k)}_{,x} = 0$ at the midspan and this leads to numerical ill-conditioning of the governing differential equation associated with ZZ moment $F_{\phi,x}$.

Furthermore, the stiffness terms in the HR formulation, including all transverse shear and transverse normal correction factors, are derived from the inverse of the laminate stiffness matrix $\boldsymbol{S}$ defined in Eq. (4.22). The inversion of $\boldsymbol{S}^{-1} = \boldsymbol{s}$ can be numerically ill-conditioned if either $\phi^{(k)} \approx 0$ or $\phi^{(k)}_{,x} \approx 0$. For example, consider a $[\langle 0|90\rangle/\text{pvc}/\langle 90|0\rangle]$ sandwich beam with variable-stiffness face layers where all layers have equal thickness and pvc represents the foam core. Figure 6.2a plots the axial variation of $\phi^{(\text{VS1})}_{,x}$ in the top variable-stiffness layer VS1, and the axial variation of $\phi^{(\text{pvc})}_{,x}$ in the pvc core, at the interface between these two layers. As shown in Figure 6.2a, the value of $\phi^{(\text{VS1})}_{,x}$ and $\phi^{(\text{pvc})}_{,x}$ is exactly zero at the midspan and close to zero at the two ends. In fact, this is true for all $\phi^{(k)}_{,x}$ throughout the entire laminate thickness at these axial locations. This means that the stiffness terms in $\boldsymbol{S}_{ll}$ associated with the ZZ moment $F_{\phi,x}$, as calculated from Eq. (4.21), are zero or close to zero at the midspan and the endpoints. Therefore, the laminate stiffness matrix $\boldsymbol{S}$ cannot be inverted accurately at these points because the large difference between terms on the leading diagonal cause a singularity in at least one of the inverted terms.

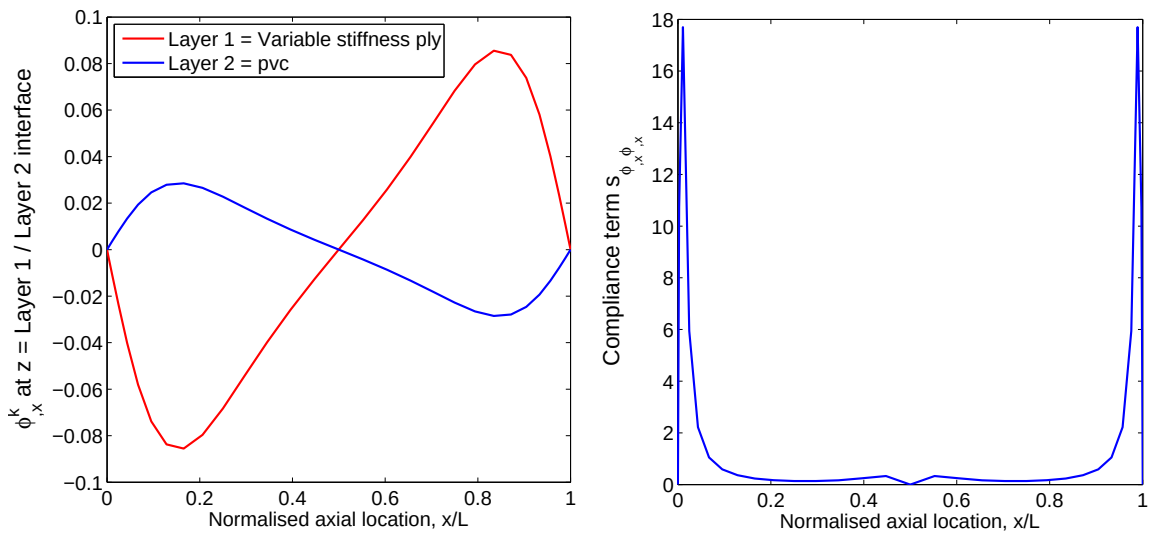

(a) $\phi^{(k)}_{,x}$ at layer 1/layer 2 interface

(b) Compliance term $\boldsymbol{s}_{\phi_{,x}\phi_{,x}}$

Figure 6.2: The presence of $\phi^{(k)}_{,x} = 0$ at certain points along the beam span, as shown in (a), leads to a singularity in the compliance matrix $\boldsymbol{s}$ of a [⟨0|90⟩/pvc/⟨90|0⟩] laminate, as shown in (b).

A near singular matrix can be inverted by using techniques, such as the Moore-Penrose pseudoinverse [170], by breaking the matrix into blocks with terms of similar orders of magnitude, or by damping the leading diagonal using the Levenberg-Marquardt coefficient [171,172]. Whereas these techniques allow computation of an approximate compliance matrix $\boldsymbol{s}$, they nevertheless lead to non-physical results when actually solving the associated equilibrium equations. In fact, the singularity is not eliminated completely by using these techniques but simply reduced in magnitude. For example, consider the axial distribution of the compliance term $\boldsymbol{s}_{\phi_{,x}\phi_{,x}}$ for the [⟨0|90⟩/pvc/⟨0|90⟩] sandwich in Figure 6.2b, where $\boldsymbol{s}_{\phi_{,x}\phi_{,x}}$ is the term on the leading diagonal of $\boldsymbol{s}$ associated with the ZZ moment $F_{\phi_{,x}}$. The plot shows the singularities in the compliance term at the two ends and the midspan of the beam, and this leads to certain knock-on effects. The higher-order shear and transverse normal correction terms are based on axial derivatives of the compliance terms $\boldsymbol{s}$, as shown in Eqs. (A.5) and (A.8), and the high rates of change in the vicinity of the singularities leads to noise in the computations of these derivatives.

One possible remedy to this problem is to eliminate the degree of freedom $F_{\phi_{,x}}$ at the locations where $\phi^{(k)}_{,x} \approx 0$. However, even finite values of $\phi^{(k)}_{,x}$ can lead to local spikes in the axial distribution of $\boldsymbol{s}_{\phi_{,x}\phi_{,x}}$ because the inverse calculation of $\boldsymbol{s} = \boldsymbol{S}^{-1}$ magnifies local differences in $\phi^{(k)}_{,x}$ of just one order of magnitude, which is not unlikely for general variable-stiffness sandwich beams. Second, eliminating degrees of freedom in DQM at certain points within the grid is not viable as the computation of derivatives is based on all functional values within the grid. This is akin to the problem of joining elements with different degrees of freedom in FEM.

On the other hand, this issue does not occur for laminates without a symmetry point in the axial fibre direction. For example, consider a sandwich panel where the two face layers vary linearly from 20° at end x_A to 70° at end x_B, denoted by the laminate notation [⟨20||70⟩/pvc/⟨20||70⟩] herein. The through-thickness plots of the ZZ function $\phi^{(k)}$ and axial

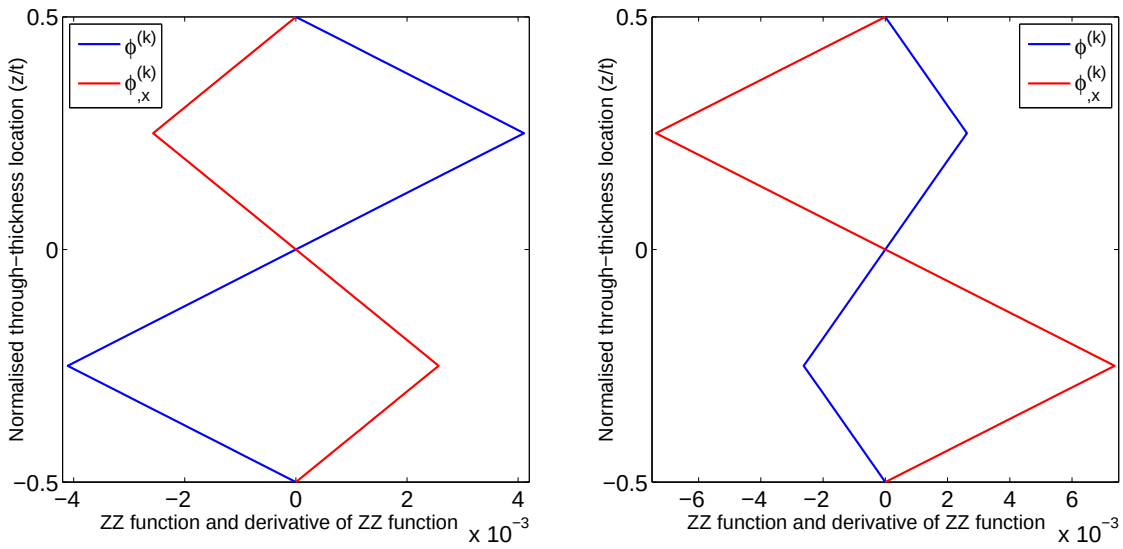

(a) Beam end A **(b)** Beam end B

Figure 6.3: ZZ function $\phi^{(k)}$ and axial derivative of ZZ function $\phi^{(k)}_{,x}$ plotted through the thickness of a $[\langle 20||70\rangle/\text{pvc}/\langle 20||70\rangle]$ laminate at the two ends of the beam.

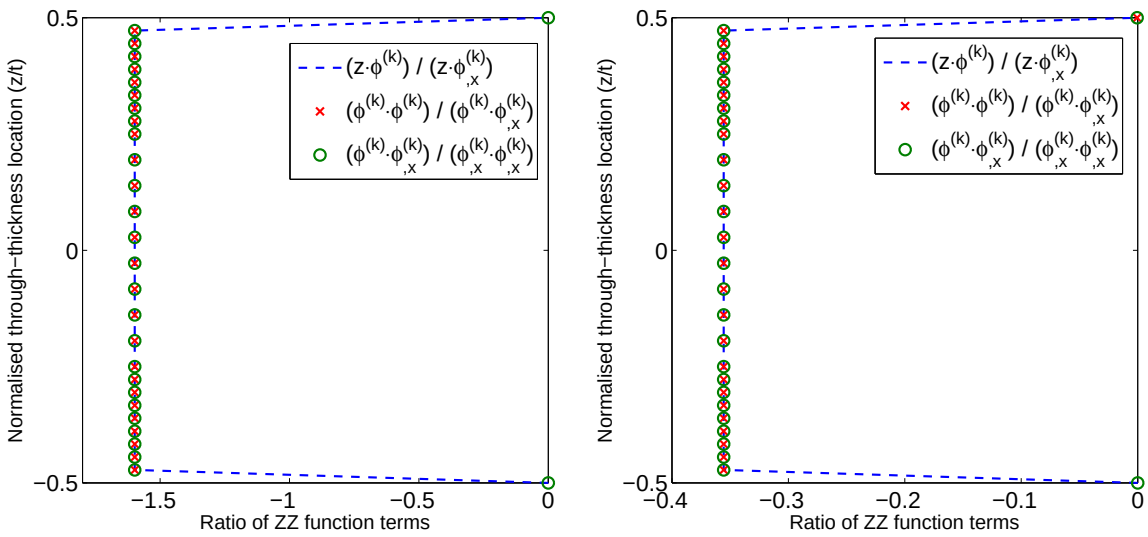

(a) Beam end A **(b)** Beam end B

Figure 6.4: Comparison of various ZZ term products that are used to calculate the stiffness terms in $\boldsymbol{S}$ plotted through the thickness of a $[\langle 20||70\rangle/\text{pvc}/\langle 20||70\rangle]$ laminate at the two ends of the beam.

derivative of the ZZ function $\phi_{,x}^{(k)}$ at the two ends x_A and x_B are shown in Figure 6.3. This plots shows that $\phi^{(k)}$ and $\phi_{,x}^{(k)}$ are unique and of different magnitudes at the two ends. However, permutations of these two functions and the moment arm z are related by a constant of proportionality. For example, the product $z\phi^{(k)}$ defines the coupling stiffness term between the bending moment M and the ZZ moment F_ϕ, whereas ${\phi^{(k)}}^2$ defines the direct bending stiffness of ZZ moment F_ϕ. For a first-order HR ZZ model (HR1-RZT), the stiffness matrices $\boldsymbol{S}_{gl}$ and $\boldsymbol{S}_{ll}$ are calculated from Eq. (4.20) and Eq. (4.21) as follows

$$\boldsymbol{S}_l = \begin{bmatrix} \boldsymbol{S}_{gl} \\ \boldsymbol{S}_{ll} \end{bmatrix} = \begin{bmatrix} \int z\bar{Q}^{(k)}\phi^{(k)}\mathrm{d}z & \int z\bar{Q}^{(k)}\phi_{,x}^{(k)}\mathrm{d}z \\ \int \phi^{(k)}\bar{Q}^{(k)}\phi^{(k)}\mathrm{d}z & \int \phi^{(k)}\bar{Q}^{(k)}\phi_{,x}^{(k)}\mathrm{d}z \\ \int \phi_{,x}^{(k)}\bar{Q}^{(k)}\phi^{(k)}\mathrm{d}z & \int \phi_{,x}^{(k)}\bar{Q}^{(k)}\phi_{,x}^{(k)}\mathrm{d}z \end{bmatrix}. \tag{6.5}$$

Figure 6.4 shows the ratio of the integrands in the first column of matrix $\boldsymbol{S}_l$ in Eq. (6.5) to the integrands in the second column of matrix $\boldsymbol{S}_l$ at the two ends x_A and x_B. In either case, the integral in the z-direction, i.e. the area enclosed by the curves, is the same for all three ratios. Therefore, the two columns in matrix $\boldsymbol{S}_l$ of Eq. (6.5) are not independent and the complete stiffness matrix $\boldsymbol{S}$ is rank deficient, such that the inverse operation $\boldsymbol{s} = \boldsymbol{S}^{-1}$ is not unique. In effect, this suggests that including the ZZ displacement ψ and its derivative $\psi_{,x}$ introduces a redundancy, i.e. the relation between the two variables is known a priori and one of the two variables can be eliminated.

Thus, this section has elucidated certain shortcomings in incorporating the derivative of the ZZ function $\phi_{,x}^{(k)}$ in the HR formulation as it introduces numerical instabilities in calculating the compliance matrix $\boldsymbol{s}$. This is especially a problem for symmetric fibre variations that are typically analysed in the literature. It is worth noting that in a typical finite element implementation $\phi_{,x}^{(k)} = 0$ as the standard element formulations assume constant material properties within elements. It is possible to employ screening algorithms that eliminate rows and columns within the stiffness matrix $\boldsymbol{S}$ that lead to numerical instabilities in the inversion $\boldsymbol{s} = \boldsymbol{S}^{-1}$. Indeed, such approaches are often employed in commercial FEM codes when combining elements with different degrees of freedom, e.g. 2D and 3D elements, but extending these algorithms to the DQM is beyond the scope of the present work.

Based on these considerations, the effect of stress resultant $F_{\phi,x}$ is neglected henceforth. The axial derivative of the ZZ function $\phi_{,x}^{(k)}$ does not vanish completely from the model as the shear correction and normal correction factors are functions of $\boldsymbol{s}_{,x}$ which in turn depends on $\phi_{,x}^{(k)}$. In fact, the accuracy of the 3D stress fields for the HR3-RZT model shown in Figures 6.18-6.25 and discussed in the next section, suggest that stress resultant $F_{\phi,x}$ does not play a significant role in the accuracy of the model for the laminates considered.

6.3 Model validation

To analyse laminates VS A - VS J in Table 6.1, third-order models of the HR formulation using the RZT ZZ function (HR3-RZT) and MZZF (HR3-MZZF) are implemented in Matlab.

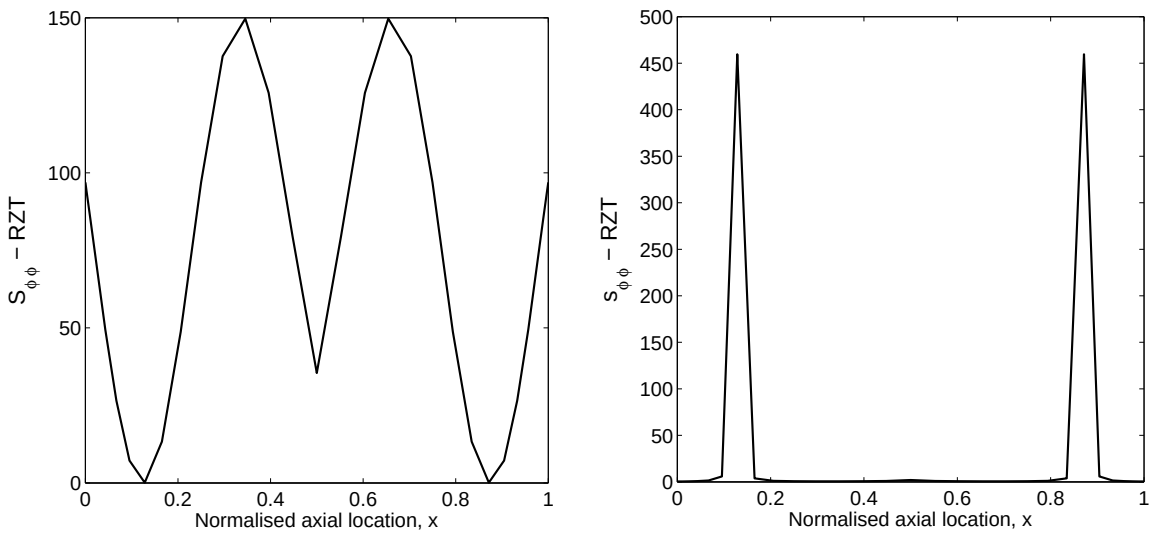

(a) $S_{\phi\phi}$ - RZT **(b)** $s_{\phi\phi}$ - RZT

Figure 6.5: Laminate VS A: Variation of ZZ stiffness term $S_{\phi\phi}$ and ZZ compliance term $s_{\phi\phi}$ of the HR3-RZT model along the length of the beam.

Furthermore, a third-order model without the ZZ term (HR3) is also used herein, in order to qualitatively examine the importance of the ZZ deformations, and assess the magnitude of errors associated with neglecting the ZZ terms.

As discussed in Section 6.2, the RZT ZZ function changes over the length of a variable-stiffness beam as it is based on layerwise transverse shear properties. Therefore, the ZZ effect can be negligible in some regions of the beam and cause numerical ill-conditioning problems during the matrix inversion $\boldsymbol{s} = \boldsymbol{S}^{-1}$. For example, consider the axial variation of the direct ZZ stiffness term $S_{\phi\phi}$ in Figure 6.5a and the corresponding compliance term $s_{\phi\phi}$ in Figure 6.5b. The stiffness term $S_{\phi\phi}$ is close to zero at $x = 0.125$ and $x = 0.875$ and the inversion of matrix $\boldsymbol{S}$ causes two singularities in the variation of $s_{\phi\phi}$ along the beam length. These singularities produce considerable amount of noise in the numerical computations of derivatives $s_{\phi\phi,x}$ and the associated transverse shear and transverse normal correction factors around $x = 0.125$ and $x = 0.875$. Due to these sources of numerical noise, the RZT ZZ function is limited in its application to modelling variable-stiffness laminates using the present HR formulation in the DQM. Hence, the results for HR3-RZT are only used for sandwich beams VS G - VS J but not included for the variable-stiffness composite VS B - VS F.

Figures 6.6a, 6.8a, etc. up to 6.24a show plots of the spanwise bending deflection $\bar{w}$ for the HR and 3D FEM solutions. The in-plane stress field $\bar{\sigma}_x$ and transverse normal stress field $\bar{\sigma}_z$ at the midspan of the beam ($x = a/2$) are plotted in Figures 6.6b, 6.8b, etc. up to 6.24b and Figures 6.7b, 6.9b, etc. up to 6.25b, respectively. The transverse shear stress $\bar{\tau}_{xz}$ at the quarter-span of the beam ($x = a/4$) is plotted in Figures 6.7a, 6.9a, etc. up to 6.25a.

Figures 6.6-6.7 illustrate the numerical instabilities regarding the application of HR3-RZT to variable-stiffness composite laminates mentioned above. The plots show large discrepancies between the HR3-RZT model and the other 3D FEM and HR results. Whereas the HR3 and HR-MZZF model correlate well with 3D FEM, the HR-RZT model shows significant errors for

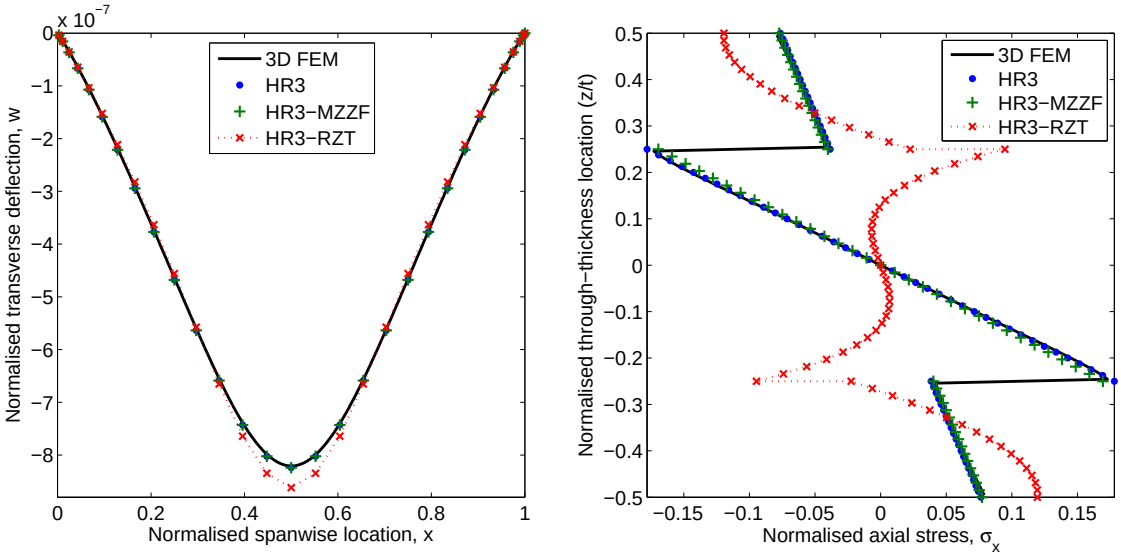

(a) Normalised transverse displacement, $\bar{w}$ **(b)** Normalised axial stress, $\bar{\sigma}_x$

Figure 6.6: Laminate VS A: Normalised bending displacement and through-thickness distribution of the normalised axial stress (at $x = a/2$).

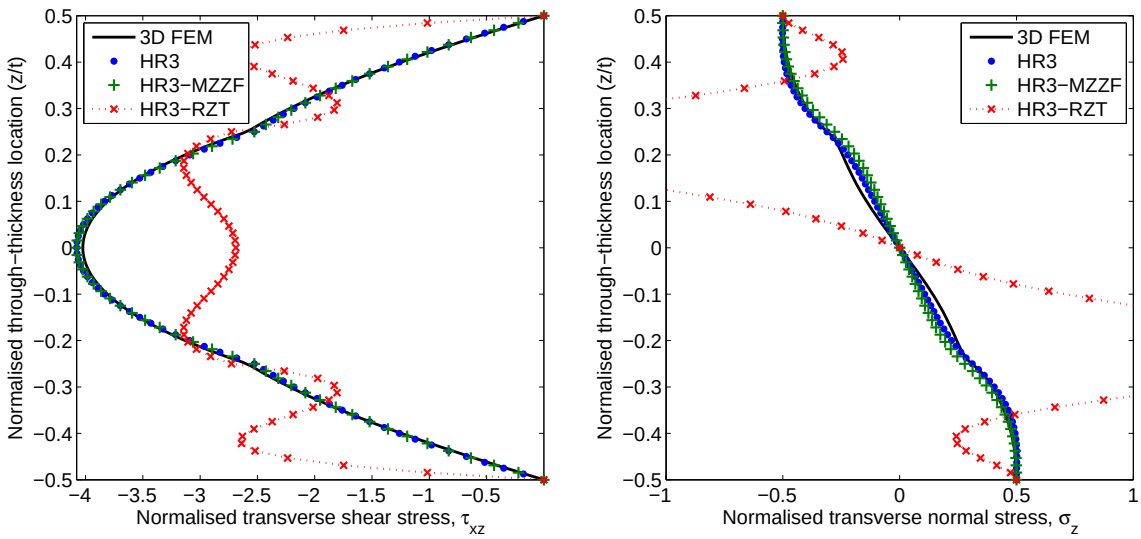

(a) Normalised transverse shear stress, $\bar{\tau}_{xz}$ **(b)** Normalised transverse normal stress stress, $\bar{\sigma}_z$

Figure 6.7: Laminate VS A: Through-thickness distribution of the normalised transverse shear stress (at $x = a/4$) and normalised transverse normal stress (at $x = a/2$).

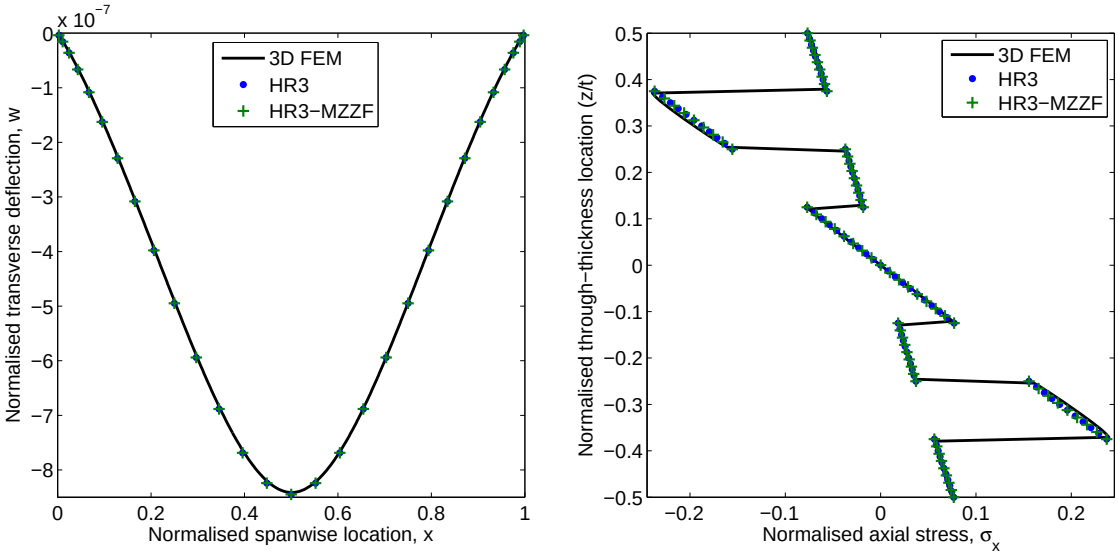

(a) Normalised transverse displacement, $\bar{w}$ **(b)** Normalised axial stress, $\bar{\sigma}_x$

Figure 6.8: Laminate VS B: Normalised bending displacement and through-thickness distribution of the normalised axial stress (at $x = a/2$).

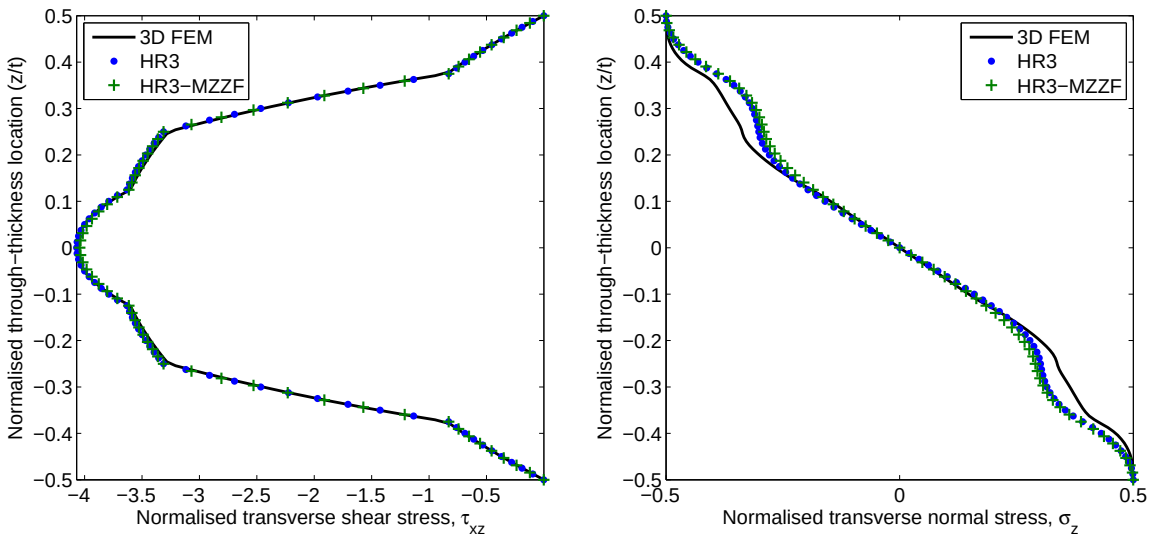

(a) Normalised transverse shear stress, $\bar{\tau}_{xz}$ **(b)** Normalised transverse normal stress stress, $\bar{\sigma}_z$

Figure 6.9: Laminate VS B: Through-thickness distribution of the normalised transverse shear stress (at $x = a/4$) and normalised transverse normal stress (at $x = a/2$).

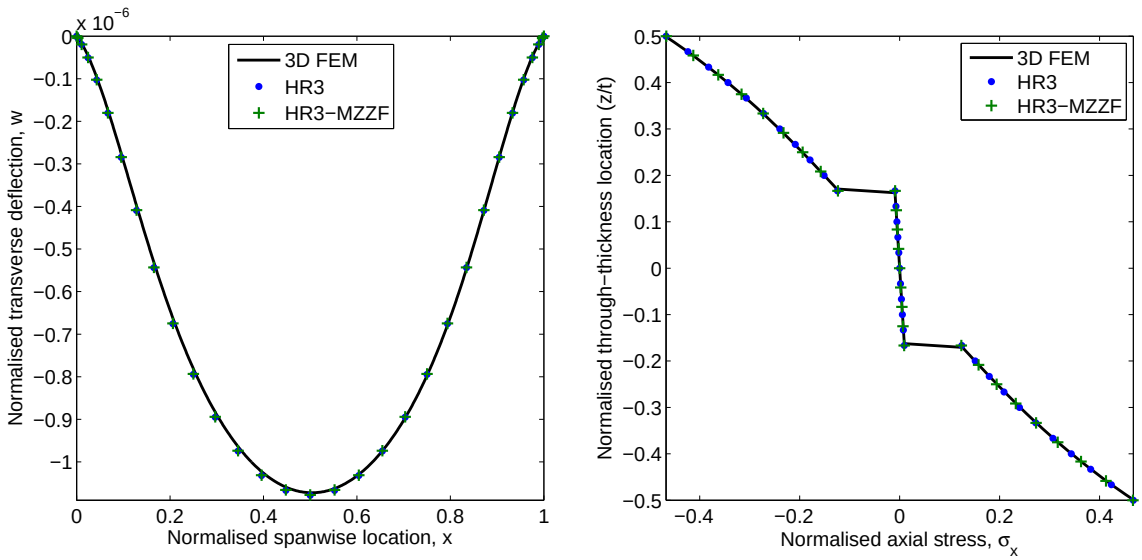

(a) Normalised transverse displacement, $\bar{w}$ **(b)** Normalised axial stress, $\bar{\sigma}_x$

Figure 6.10: Laminate VS C: Normalised bending displacement and through-thickness distribution of the normalised axial stress (at $x = a/2$).

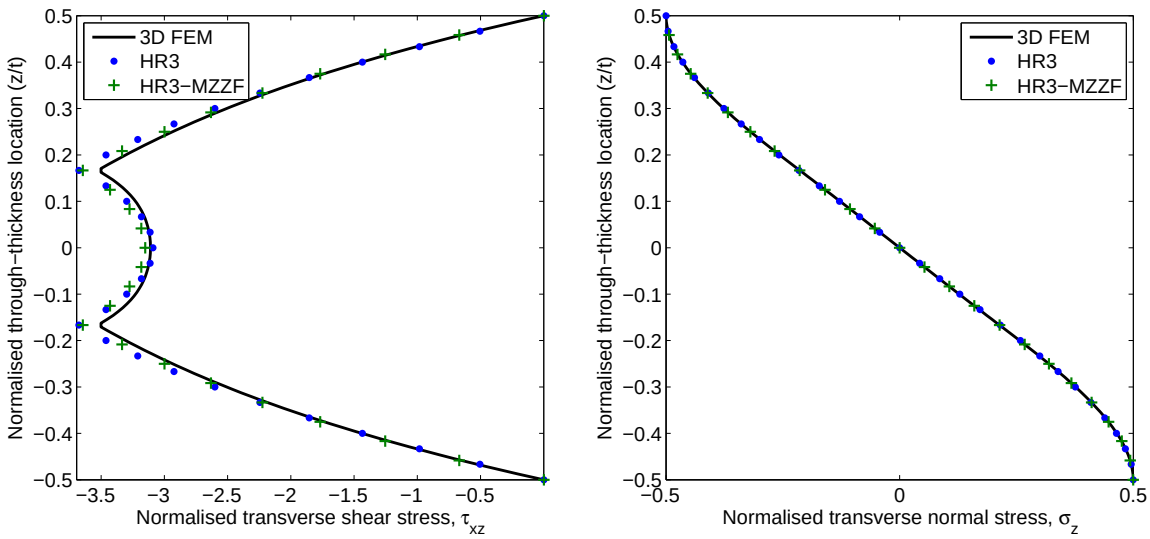

(a) Normalised transverse shear stress, $\bar{\tau}_{xz}$ **(b)** Normalised transverse normal stress stress, $\bar{\sigma}_z$

Figure 6.11: Laminate VS C: Through-thickness distribution of the normalised transverse shear stress (at $x = a/4$) and normalised transverse normal stress (at $x = a/2$).

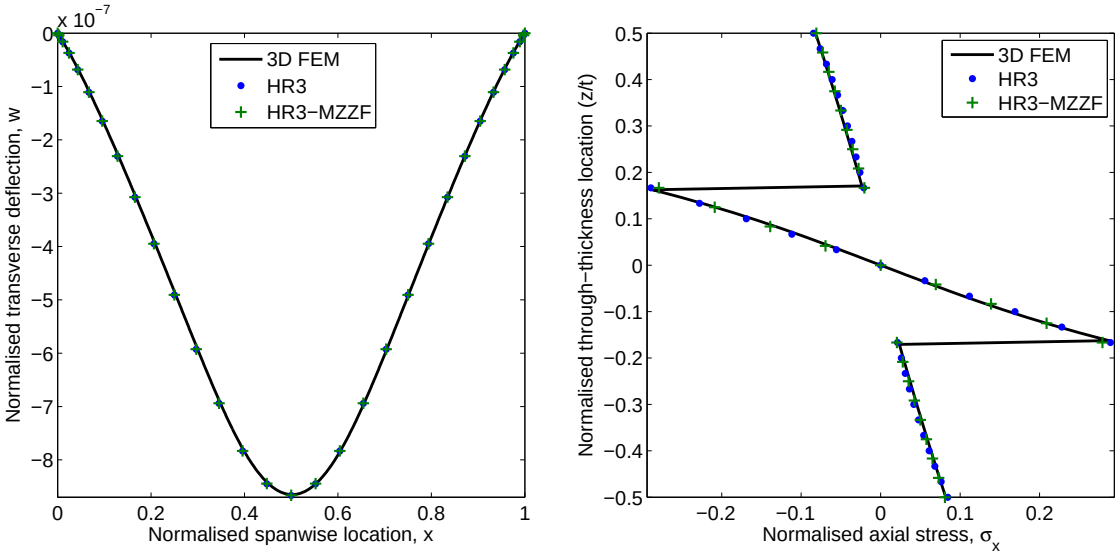

(a) Normalised transverse displacement, $\bar{w}$ **(b)** Normalised axial stress, $\bar{\sigma}_x$

Figure 6.12: Laminate VS D: Normalised bending displacement and through-thickness distribution of the normalised axial stress (at $x = a/2$).

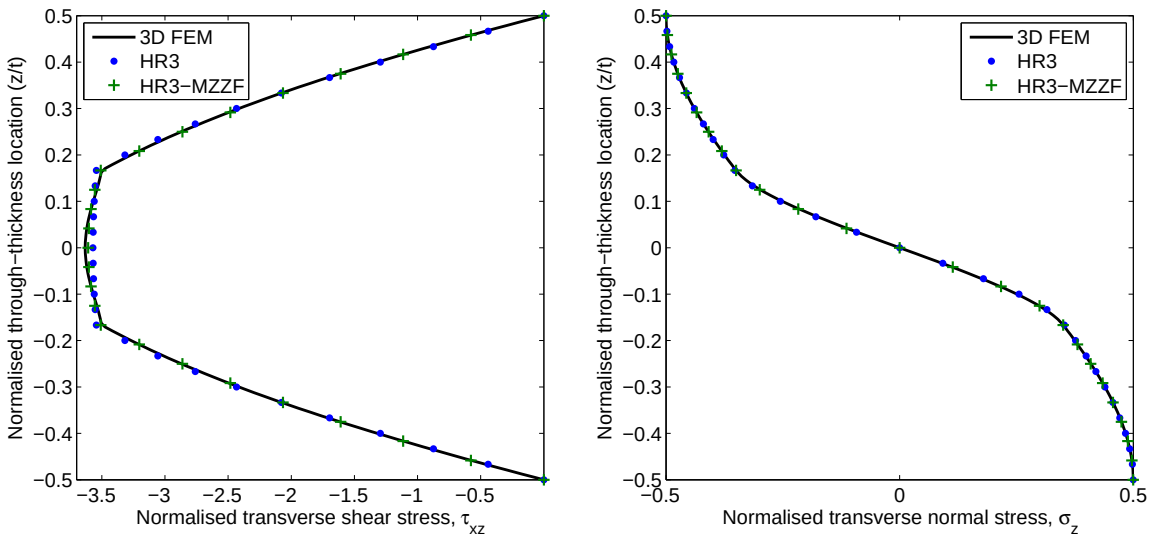

(a) Normalised transverse shear stress, $\bar{\tau}_{xz}$ **(b)** Normalised transverse normal stress stress, $\bar{\sigma}_z$

Figure 6.13: Laminate VS D: Through-thickness distribution of the normalised transverse shear stress (at $x = a/4$) and normalised transverse normal stress (at $x = a/2$).

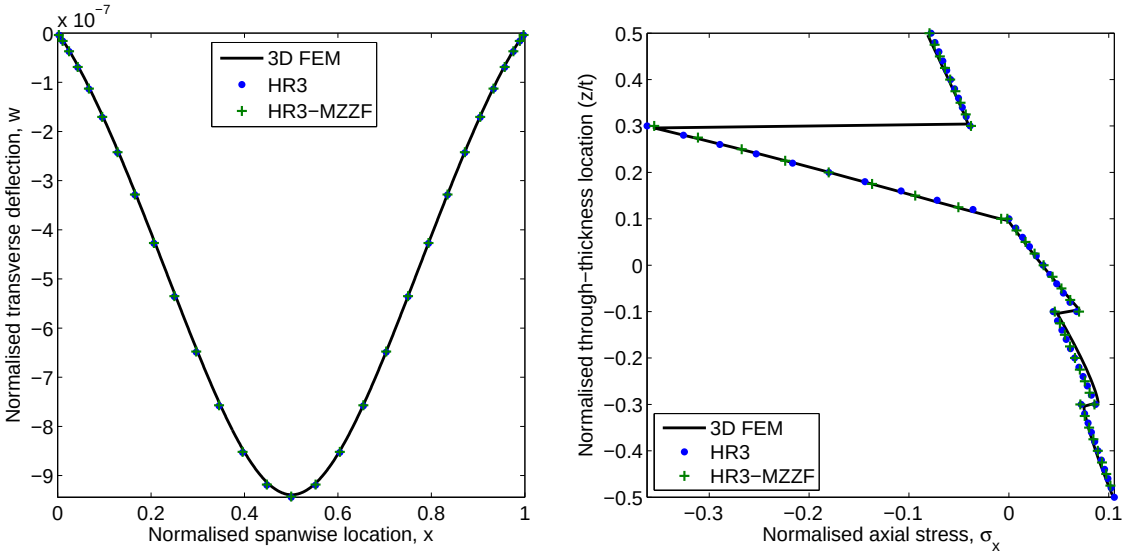

(a) Normalised transverse displacement, $\bar{w}$ **(b)** Normalised axial stress, $\bar{\sigma}_x$

Figure 6.14: Laminate VS E: Normalised bending displacement and through-thickness distribution of the normalised axial stress (at $x = a/2$).

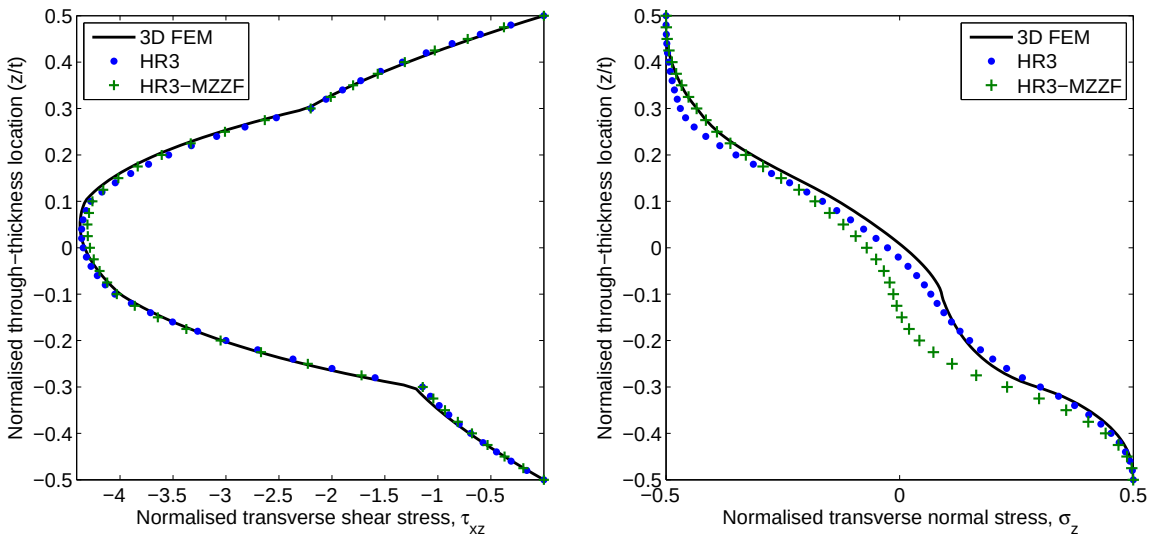

(a) Normalised transverse shear stress, $\bar{\tau}_{xz}$ **(b)** Normalised transverse normal stress stress, $\bar{\sigma}_z$

Figure 6.15: Laminate VS E: Through-thickness distribution of the normalised transverse shear stress (at $x = a/4$) and normalised transverse normal stress (at $x = a/2$).

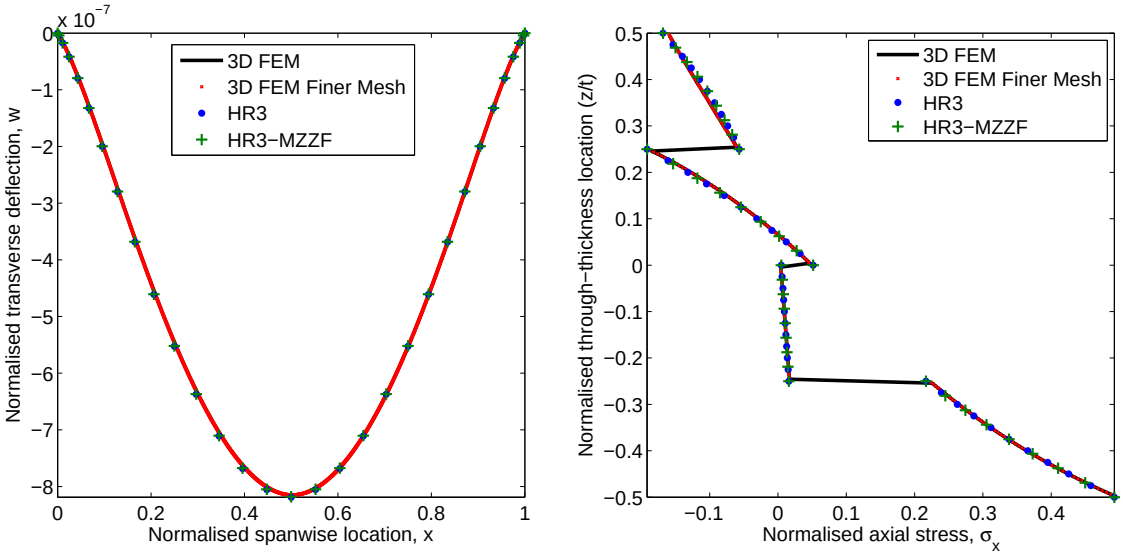

(a) Normalised transverse displacement, $\bar{w}$ **(b)** Normalised axial stress, $\bar{\sigma}_x$

Figure 6.16: Laminate VS F: Normalised bending displacement and through-thickness distribution of the normalised axial stress (at $x = a/2$). The 3D FEM curve is coincident with all other results and hence not visible in the plot.

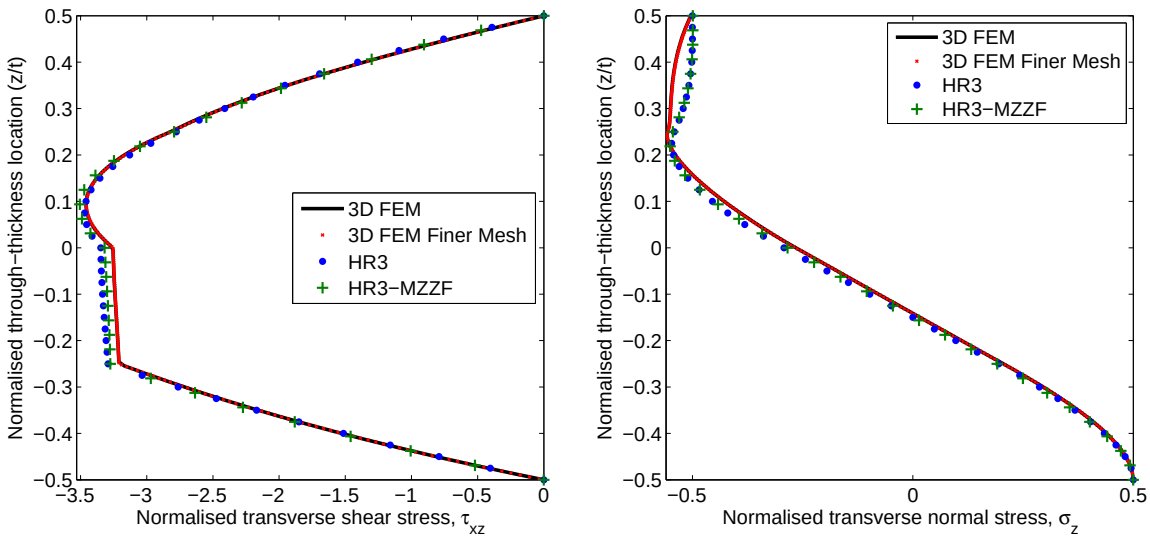

(a) Normalised transverse shear stress, $\bar{\tau}_{xz}$ **(b)** Normalised transverse normal stress stress, $\bar{\sigma}_z$

Figure 6.17: Laminate VS F: Through-thickness distribution of the normalised transverse shear stress (at $x = a/4$) and normalised transverse normal stress (at $x = a/2$).

all displacement and stress fields. For sandwich beams VS G - VS J, this is numerical instability is not an issue as the flexible core always provides a finite degree of transverse orthotropy over the length of the beam. In fact, the results for laminates VS G - VS J in Figures 6.18-6.25 show that the HR3-RZT model provides well-correlated results for the variable-stiffness sandwich beams.

Overall, Figures 6.6-6.25 show good correlation between the 3D FEM results and the HR models. For composite laminates VS A - VS F, the ZZ effects are benign as shown by the close correlation between the HR3 and HR3-MZZF results. This is mainly because the orthotropy ratio of material IM7 8552 of $G_{13}/G_{23} = 1.25$ is relatively close to unity. For some of the variable-stiffness sandwich beams, e.g. laminates VS G and VS H, that are based on materials p and pvc with much higher degrees of transverse orthotropy, the HR3 solution maintains reasonable accuracy compared to the 3D FEM results. However, for the arbitrary sandwich beams laminate VS J, there are significant inaccuracies in the axial stress and transverse shear stress plots (Figures 6.24b and 6.25a). Thus, for general sandwich laminations with variable-stiffness face layers, the ZZ degrees of freedom are required for accurate stress predictions.

The axial stress plots for sandwich beams VS H, VS I and VS J in Figures 6.20b, 6.22b and 6.24b, respectively, show that the RZT ZZ function is more accurate than MZZF at modelling the 3D stress fields in variable-stiffness sandwich beams. The greatest differences are observed for the most challenging test case, the non-symmetric sandwich beam VS J. This corroborates the findings in Section 5.2 that the RZT ZZ function is more suitable for arbitrary laminations as it takes into account the layerwise differences in transverse material properties. Furthermore, ignoring the ZZ moment associated with the axial derivative of the RZT ZZ function ($F_{\phi,x}$) does not seem to adversely affect the accuracy of the HR3-RZT model for the laminates analysed herein. In fact, the 90° variations in fibre angle along the length of the face layers in the sandwich beams represent a degree of stiffness variation that is greater than the manufacturing capability of most tow-steering machines. Therefore, the laminates considered herein are at the extreme case of what is currently manufacturable.

One striking observation between the HR formulation and 3D FEM results is that the axial stress $\bar{\sigma}_x$ is generally well-correlated, whereas discrepancies are observed for the transverse stresses $\bar{\tau}_{xz}$ and $\bar{\sigma}_z$. Overall, the correlation between 3D FEM and the HR model for variable-stiffness beams in this section is inferior to the correlation between Pagano's 3D elasticity solution [20] and the HR model for the straight-fibre beams in Chapter 5. Some discrepancy between Pagano's solution and 3D FEM is expected because the 3D elasticity solution obeys both the 3D kinematic and equilibrium equations explicitly, whereas 3D FEM only approximately guarantees the equilibrium of stresses in a weak sense. Therefore, the 3D FEM solution has weaker functional constraints when minimising the strain energy in the variational statement. Furthermore, in the displacement-based 3D FEM Abaqus model used herein, stresses are derived from displacement variables using kinematic and constitutive equations, whereas in both the HR formulation and Pagano's solution, individual stress assumptions are made. Due to the C^0-continuity of the linear finite elements, the derivation of stresses from derivatives of displacement variables leads to more numerical noise than using the functional assumptions in Pagano's 3D elasticity or the mixed-variational HR approaches.

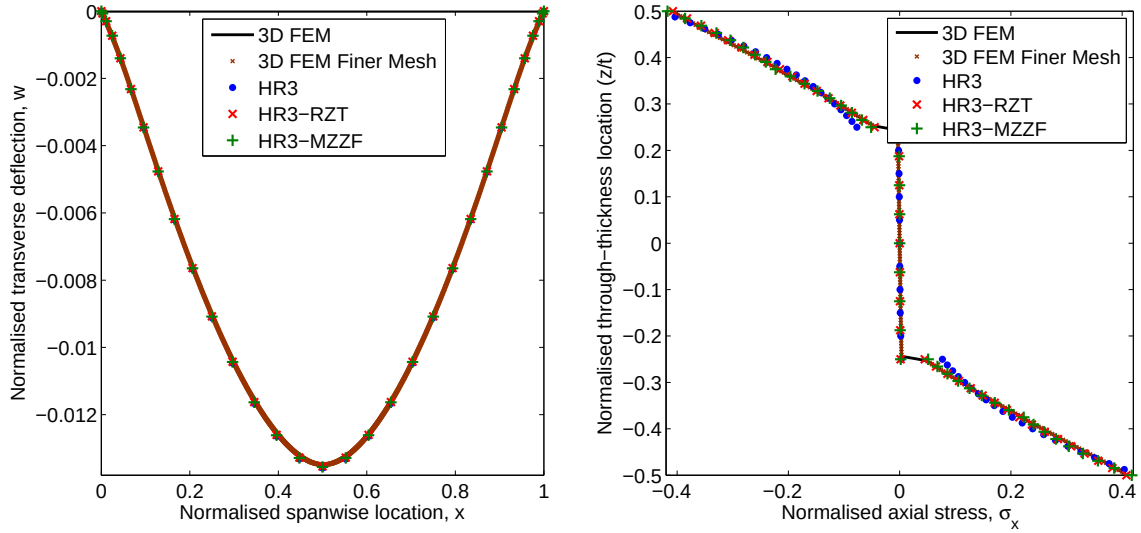

(a) Normalised transverse displacement, $\bar{w}$ **(b)** Normalised axial stress, $\bar{\sigma}_x$

Figure 6.18: Laminate VS G: Normalised bending displacement and through-thickness distribution of the normalised axial stress (at $x = a/2$).

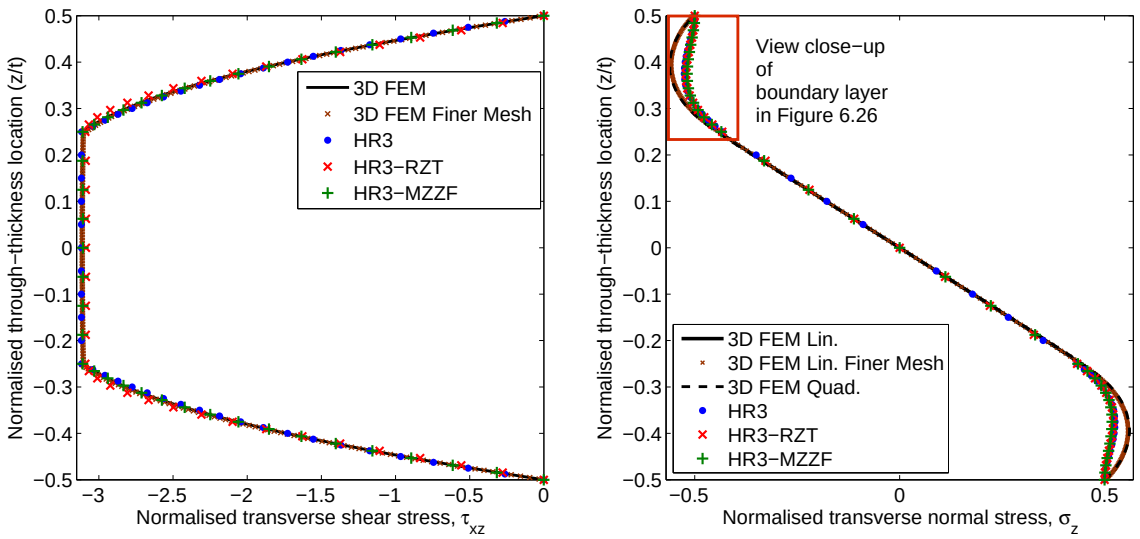

(a) Normalised transverse shear stress, $\bar{\tau}_{xz}$ **(b)** Normalised transverse normal stress stress, $\bar{\sigma}_z$

Figure 6.19: Laminate VS G: Through-thickness distribution of the normalised transverse shear stress (at $x = a/4$) and normalised transverse normal stress (at $x = a/2$).

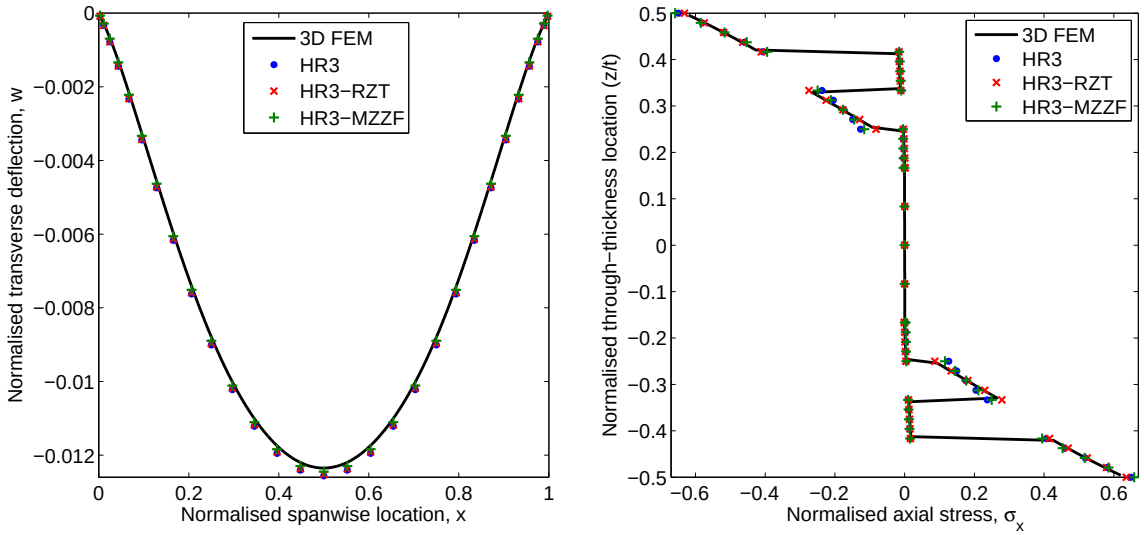

(a) Normalised transverse displacement, $\bar{w}$ **(b)** Normalised axial stress, $\bar{\sigma}_x$

Figure 6.20: Laminate VS H: Normalised bending displacement and through-thickness distribution of the normalised axial stress (at $x = a/2$).

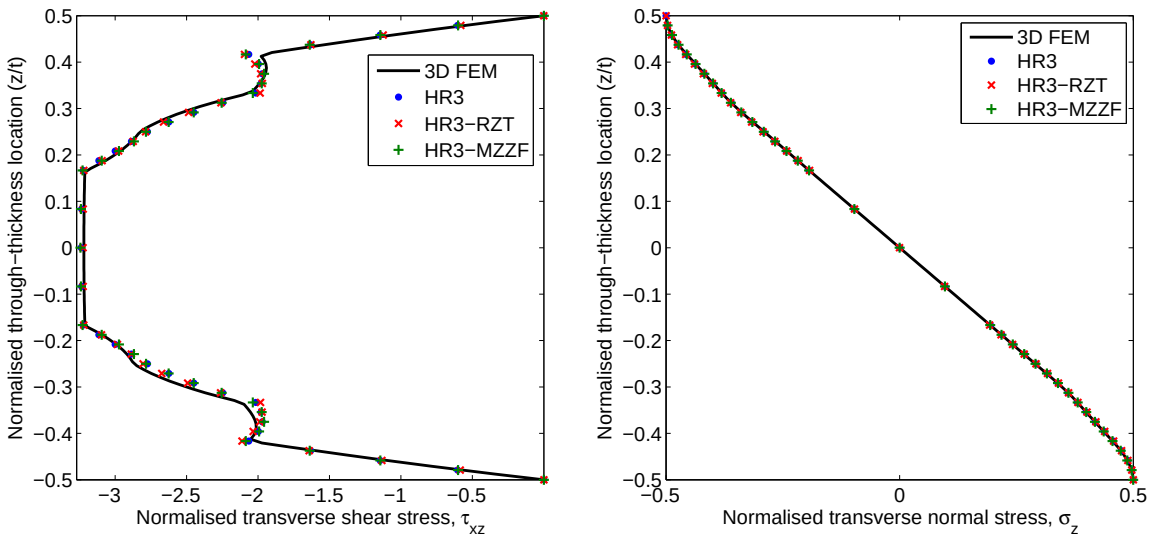

(a) Normalised transverse shear stress, $\bar{\tau}_{xz}$ **(b)** Normalised transverse normal stress stress, $\bar{\sigma}_z$

Figure 6.21: Laminate VS H: Through-thickness distribution of the normalised transverse shear stress (at $x = a/4$) and normalised transverse normal stress (at $x = a/2$).

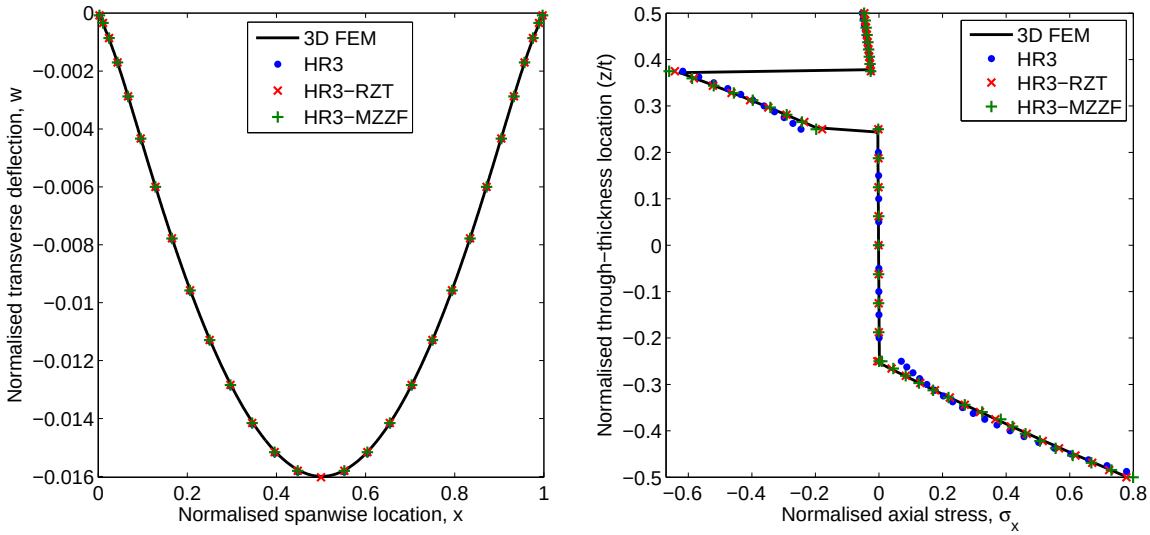

(a) Normalised transverse displacement, $\bar{w}$ **(b)** Normalised axial stress, $\bar{\sigma}_x$

Figure 6.22: Laminate VS I: Normalised bending displacement and through-thickness distribution of the normalised axial stress (at $x = a/2$).

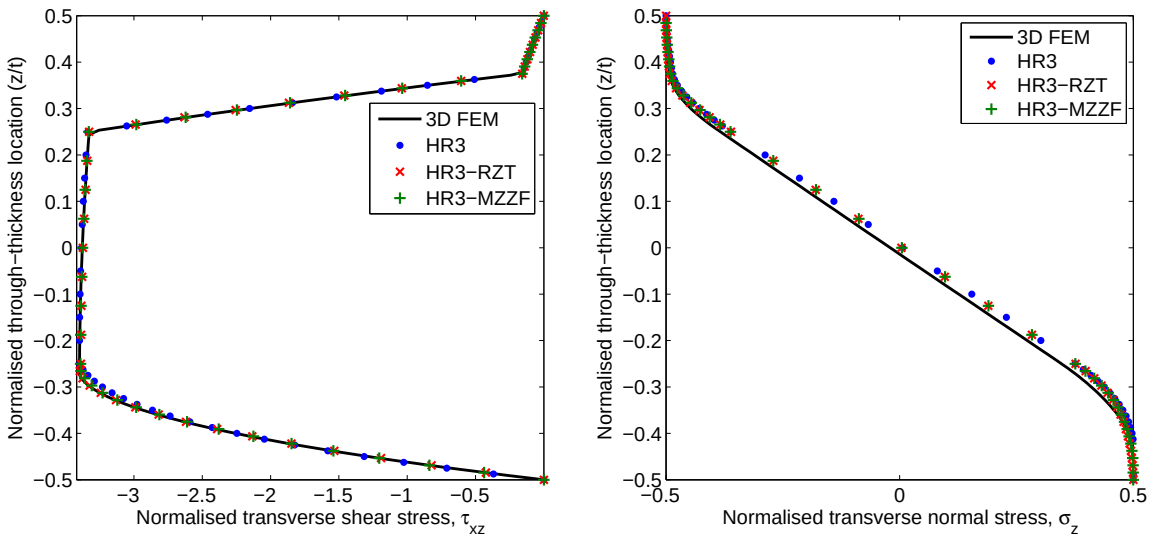

(a) Normalised transverse shear stress, $\bar{\tau}_{xz}$ **(b)** Normalised transverse normal stress stress, $\bar{\sigma}_z$

Figure 6.23: Laminate VS I: Through-thickness distribution of the normalised transverse shear stress (at $x = a/4$) and normalised transverse normal stress (at $x = a/2$).

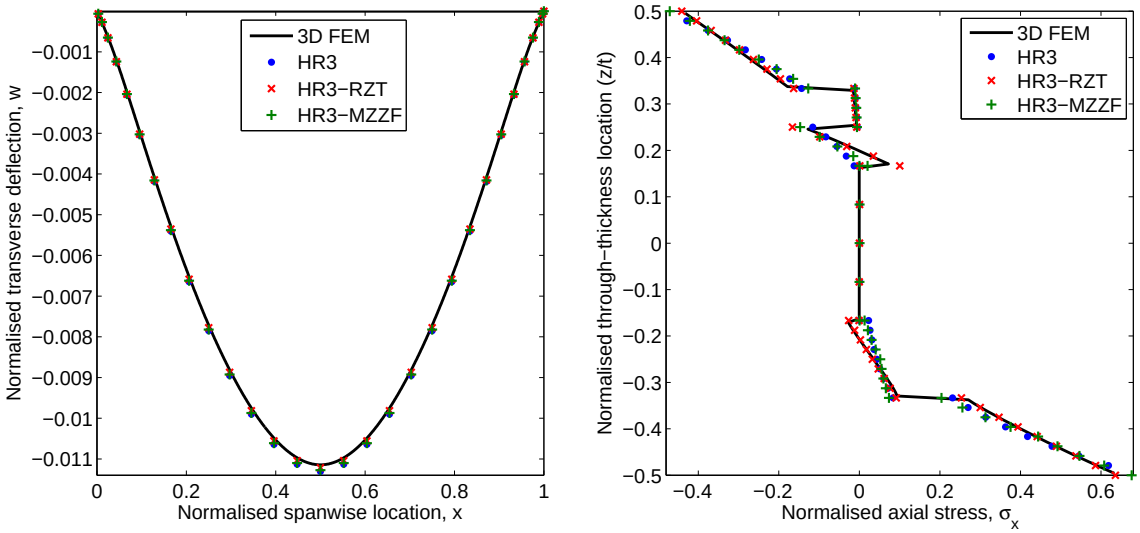

(a) Normalised transverse displacement, $\bar{w}$ **(b)** Normalised axial stress, $\bar{\sigma}_x$

Figure 6.24: Laminate VS J: Normalised bending displacement and through-thickness distribution of the normalised axial stress (at $x = a/2$).

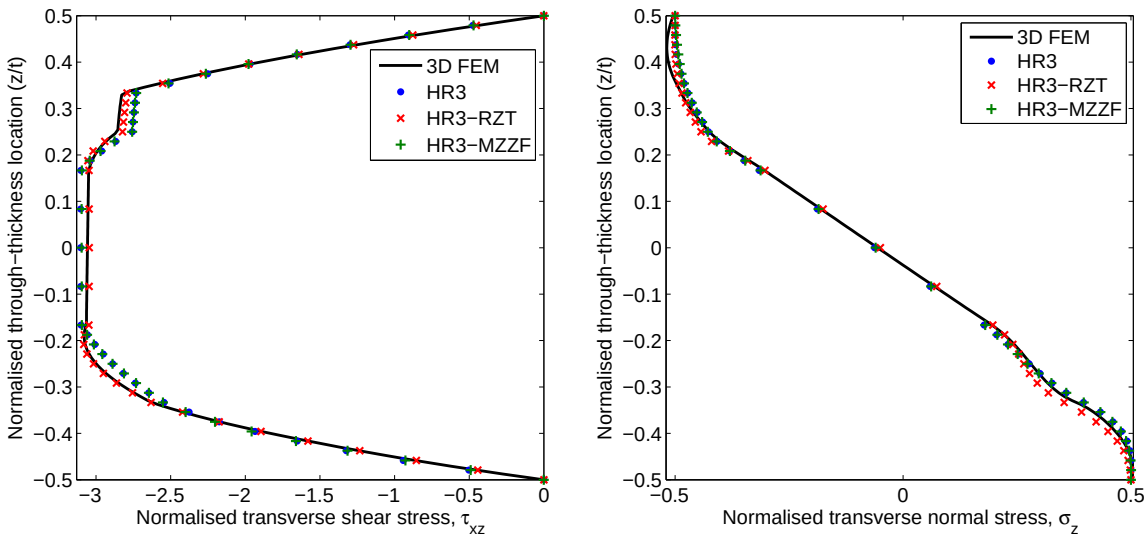

(a) Normalised transverse shear stress, $\bar{\tau}_{xz}$ **(b)** Normalised transverse normal stress stress, $\bar{\sigma}_z$

Figure 6.25: Laminate VS J: Through-thickness distribution of the normalised transverse shear stress (at $x = a/4$) and normalised transverse normal stress (at $x = a/2$).

This example considers a plane strain case of an infinitely wide plate in the lateral y-direction and therefore $\tau_{yz} = 0$. Due to the finite width of a 3D element, this condition is enforced in Abaqus using a single element of high aspect ratio that is constrained from expanding in the y-direction. The 3D FEM results show that $\tau_{yz} = 10^{-2}\tau_{xz}$, and therefore any spurious stress effects due to the finite width of the 3D brick element can be considered negligible.

In fact, the results for laminates VS F, VS G and VS J show that the 3D FEM model does not fully obey the traction equilibrium condition on the top and bottom surfaces. Consider the transverse Cauchy equilibrium equation for a 1D beam in the absence of body forces,

$$\tau_{xz,x} + \sigma_{z,z} = 0. \tag{6.6}$$

In the load case analysed here, the shear tractions applied at the top and bottom surfaces $\hat{T}_b$ and $\hat{T}_t$ are zero, i.e. $\tau_{xz}(z = \pm t/2) = 0$. Due to the uniformity of these shear tractions on the top and bottom surfaces, the axial derivative of the transverse shear stress also vanishes on the top and bottom surfaces, i.e. $\tau_{xz,x}(z = \pm t/2) = 0$. In consideration of Eq. (6.6), this means that $\sigma_{z,z}(z = \pm t/2) = 0$, i.e. the z-wise derivative of the transverse normal stress σ_z is zero on the top and bottom surfaces. The plots of $\bar{\sigma}_z$ in Figures 6.17b, 6.19b and 6.25b show that $\bar{\sigma}_{z,z} \neq 0$ at the surfaces for 3D FEM, whereas the HR model satisfies this boundary condition for all cases.

The displacement-based, weak formulation of the structural problem in the 3D FEM Abaqus model, combined with the piecewise-continuous assumption of the displacement variables, are possible explanations for this shortcoming. The displacement-based formulation inherently entails that the equilibrium of stresses and natural stress-based boundary conditions are satisfied approximately in the variational statement. Second, the weak formulation of the 3D FEM model means that the underlying equilibrium equations and natural boundary conditions are solved in an average sense across the mesh domain. The FEM solutions rely on increases in mesh density to enforce the equilibrium of stresses asymptotically.

In fact, the interfacial continuity conditions are satisfied for all 3D FEM plots of τ_{xz} and σ_z shown in this section. On the other hand, the boundary layers towards the surfaces are not modelled accurately for some 3D FEM solutions, even when the mesh density is doubled to 240 through-thickness elements and 1499 lengthwise elements (359,760 elements in total). This solution is shown by the "3D FEM Lin. Finer Mesh" curve in Figure 6.19b and in the close-up Figure 6.26 of the boundary layer of laminate VS G. Furthermore, this solution is also shown as "3D FEM Finer Mesh" in all other plots of Figures 6.16-6.19. The close-up plot of the boundary layer in Figure 6.26 also shows the results for $\bar{\sigma}_z$ using the original courser mesh of 95,880 elements but based on quadratic C3D20R elements ("3D FEM Quad." in Figure 6.26). The difference compared to the 3D FEM solution using linear C3D8R elements is negligible, and these quadratic results do not capture the surface boundary layer either. Based on these observations, it seems that seemingly converged 3D FEM values of $\bar{\sigma}_z$ from Abaqus using very fine meshes of more than 20 elements per ply, are not guaranteed to satisfy local equilibrium conditions towards the top and bottom surfaces.

Note that in 3D FEM, stresses are calculated at interior Gauss collocation points, such that the stresses on the surfaces $z = \pm t/2$ are never calculated explicitly. The through-thickness

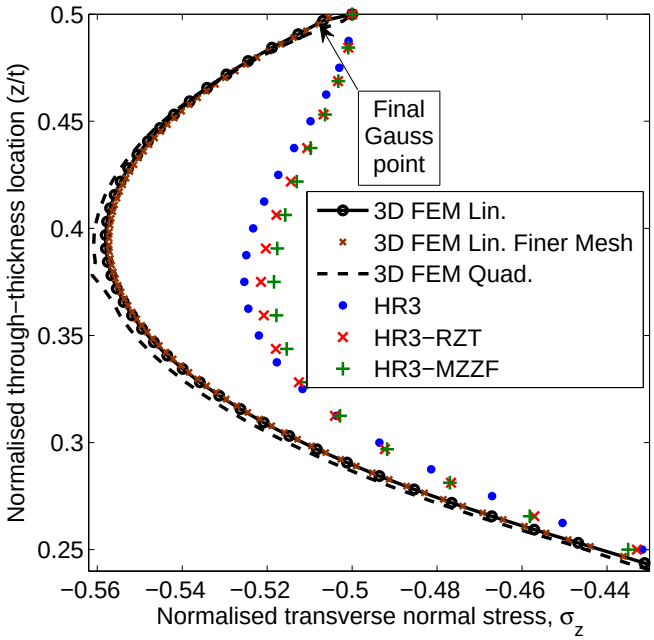

Figure 6.26: Surface boundary layer in the transverse normal stress $\bar{\sigma}_z$ for laminate VS G. 3D FEM does not capture the local boundary condition $\sigma_{z,z} = 0$ at the top surface.

mesh density used for all 3D FEM models, places the outermost Gauss points within 0.3% of the laminate thickness from the outer surfaces. The close-up view of the top surface boundary layer for laminate VS G in Figure 6.26, shows that the 3D FEM mesh density is sufficiently fine to capture the local variations of the boundary layer predicted by the HR models. However, the 3D FEM model clearly does not capture these local variations in σ_z resulting in differences of up to 6.7%. The significance of these findings for local failure predictions based on 3D FEM models in Abaqus, e.g. for impact studies, should be a topic for future investigation.

As discussed in Section 5.4, the HR formulation accurately models boundary layers due to the enforcement of Cauchy's equilibrium equations in the variational statement, and this characteristic contributes to the accurate representation of the z-wise boundary layers observed here. Furthermore, the HR implementation used herein solves the governing equations in the strong form, such that all natural stress boundary conditions are enforced explicitly and do not depend on the choice of mesh density. Based on these observations, it seems that an inherent degree of error is present in the 3D FEM solution that accounts for some of the discrepancies with respect to the HR formulation. This hypothesis is examined quantitatively in the following section.

6.4 Comments on 3D equilibrium conditions and strain energy

The accuracy in satisfying the axial and transverse Cauchy equilibrium equations of laminates VS A - VS J for the load case introduced in Section 6.1, is assessed using the two residuals $\bar{R}_x$

and $\bar{R}_z$ defined by

$$\bar{R}_x = \frac{1}{q_0} \int_{-t/2}^{t/2} (\sigma_{x,x} + \tau_{xz,z}) \, \mathrm{d}z \tag{6.7}$$

$$\bar{R}_z = \frac{1}{q_0} \int_{-t/2}^{t/2} (\tau_{xz,x} + \sigma_{z,z}) \, \mathrm{d}z \tag{6.8}$$

which capture the sum of the equilibrium residuals throughout the thickness of the beam, normalised by the applied loading magnitude q_0. Thus, these metrics do not assess the local equilibrium of stresses at every z-wise location through the beam but rather give an overall measure of accuracy for every axial domain point.

Second, the transverse equilibrium equation at the top surface of the beam $z = t/2$ is tested explicitly using the normalised residual $\bar{R}_z^t$ defined by

$$\bar{R}_z^t = \frac{1}{q_0} \left(\tau_{xz,x} + \sigma_{z,z} \right) \Big|_{z=\frac{t}{2}} . \tag{6.9}$$

This latter metric gives a more detailed measurement of how accurately the models capture the z-wise boundary layers towards the outside surfaces. The smaller the magnitude of the three residuals $\bar{R}_x$, $\bar{R}_z$ and $\bar{R}_z^t$ the more accurately the results satisfy Cauchy's equilibrium equations.

For the HR model, the derivatives of the stresses and the associated residuals are calculated directly using DQ weighting matrices in the implemented Matlab code. In the case of 3D FEM, the stress fields are exported from Abaqus using a Python script and then imported into Matlab in order to calculate the derivatives using Matlab's internal `gradient` function. This function uses central differences for interior data points and single-sided differences for boundary points, giving second-order accuracy for the former and first-order accuracy for the latter points. Thus, the local truncation error is proportional to the step size but the error magnitude is kept small due to the fine x-wise mesh of 799 elements, which results in a step size of order 0.1% of the beam length. However, it must be pointed out that the computations of axial x-wise derivatives of the HR and 3D FEM models are different, and therefore the respective results are subjected to different degrees of numerical error.

Table 6.3 summarises the maximum and minimum magnitudes of the three residuals along the length of the beam. Individually, the maximum and minimum values indicate the greatest and least errors in satisfying Cauchy's equilibrium equations along the beam. Furthermore, when taken in combination, these two values also provide information about the range of error inherent in the model.

For composite laminates VS A - VS F, the minimum values of $\bar{R}_x$, $\bar{R}_z$ and $\bar{R}_z^t$, for both 3D FEM and the HR solution, are close to zero and of similar orders of magnitude. For sandwich beams VS G - VS J, the minimum residual of the HR model is up to eight orders of magnitude less than for the 3D FEM model. However, given the small overall magnitude of the residuals, these differences are negligible.

However, when the maximum magnitude of the three metrics is taken into account, the HR model is shown to be more accurate than the 3D FEM model. For every laminate, the maximum magnitude of residuals $\bar{R}_x$, $\bar{R}_z$ and $\bar{R}_z^t$ is smaller for the HR model than for 3D FEM.

Table 6.3: Maximum and minimum values of the normalised residuals of Cauchy's x- and z-direction equilibrium equations ($\bar{R}_x$ and $\bar{R}_z$, respectively), and the normalised residual of Cauchy's z-direction equilibrium equation at the top surface ($\bar{R}_z^t$).

Lam.	Model	$\min\left\lvert\bar{R}_x\right\rvert$	$\max\left\lvert\bar{R}_x\right\rvert$	$\min\left\lvert\bar{R}_z\right\rvert$	$\max\left\lvert\bar{R}_z\right\rvert$	$\min\left\lvert\bar{R}_z^t\right\rvert$	$\max\left\lvert\bar{R}_z^t\right\rvert$
VS A	3D FEM	0	7.8×10^{-6}	3.9×10^{-6}	4.1	1.1×10^{-3}	6.9×10^{3}
	HR3-MZZF	4.4×10^{-13}	2.4×10^{-9}	6.7×10^{-7}	6.7×10^{-5}	2.8×10^{-3}	2.7
VS B	3D FEM	0	1.4×10^{-5}	1.7×10^{-5}	4.4	1.7×10^{-3}	7.3×10^{3}
	HR3-MZZF	2.97×10^{-13}	5.8×10^{-10}	1.6×10^{-7}	6.6×10^{-5}	8.2×10^{-3}	1.1
VS C	3D FEM	0	1.1×10^{-5}	1.3×10^{-6}	1.6×10^{1}	2.9×10^{-3}	2.3×10^{4}
	HR3-MZZF	2.9×10^{-11}	2.7×10^{-8}	3.2×10^{-7}	7.2×10^{-4}	3.7×10^{-3}	2.1×10^{1}
VS D	3D FEM	0	8.3×10^{-6}	8.7×10^{-5}	4.2	1.3×10^{-2}	7.0×10^{3}
	HR3-MZZF	1.5×10^{-11}	1.2×10^{-7}	6.1×10^{-6}	1.2×10^{-4}	1.6×10^{-1}	9.3
VS E	3D FEM	1.7×10^{-5}	8.9×10^{-1}	1.3×10^{-5}	4.8	8.1×10^{-3}	7.2×10^{3}
	HR3-MZZF	3.7×10^{-9}	2.0×10^{-5}	1.0×10^{-7}	1.4×10^{-4}	2.6×10^{-3}	4.6
VS F	3D FEM	3.9×10^{-5}	1.8	3.3×10^{-4}	8.8	5.0×10^{-3}	7.6×10^{3}
	HR3-MZZF	7.9×10^{-9}	4.0×10^{-4}	1.5×10^{-6}	5.5×10^{-5}	8.1×10^{-3}	4.7
VS G	3D FEM	1.0×10^{-4}	1.6×10^{1}	2.9×10^{-3}	7.4	4.7×10^{-2}	1.5×10^{4}
	HR3-RZT	3.0×10^{-12}	9.9×10^{-9}	5.2×10^{-8}	5.9×10^{-5}	4.2×10^{-2}	7.7
VS H	3D FEM	7.0×10^{-4}	8.4	9.6×10^{-3}	8.9	1.2×10^{-3}	1.1×10^{4}
	HR3-RZT	2.5×10^{-12}	7.4×10^{-9}	4.6×10^{-8}	6.5×10^{-6}	6.2×10^{-3}	5.3
VS I	3D FEM	2.7×10^{-3}	1.3×10^{1}	5.1×10^{-3}	1.3×10^{1}	2.8×10^{-1}	1.9×10^{4}
	HR3-RZT	1.2×10^{-12}	5.7×10^{-4}	3.6×10^{-7}	7.3×10^{-5}	4.6×10^{-2}	7.8
VS J	3D FEM	2.5×10^{-4}	1.5×10^{1}	1.4×10^{-2}	7.3	4.4×10^{-1}	1.3×10^{4}
	HR3-RZT	1.7×10^{-12}	1.5×10^{-5}	5.2×10^{-8}	6.7×10^{-6}	5.8×10^{-2}	2.3

For laminate VS G, the residual $\max|\bar{R}_x|$ of HR3-RZT is ten orders of magnitude less than for the 3D FEM model. In general, the magnitudes of residuals $\bar{R}_x$ and $\bar{R}_z$ are least for the symmetric composite and sandwich beams, and increase in magnitude for the non-symmetric laminations VS E, VS F, VS I and VS J. Furthermore, the minimum and maximum values also show that the range of the residuals is generally less for the HR model than for 3D FEM. Hence, the variation of the residuals along the length of the beam is less for the present HR model.

In absolute terms, the maximum magnitude of the residual for the HR model is of order 10^1, whereas for 3D FEM, it is of order 10^4. Given that the residuals are normalised with respect to q_0, the maximum error in the 3D FEM solution is considerable when compared to the applied loading magnitude. In particular, the magnitude of the residuals $\bar{R}_x$ and $\bar{R}_z$ of the HR model is never greater than 10^{-4} along the length of the beams. This is not surprising as the integral expressions of the equilibrium equations that are used to calculate residuals $\bar{R}_x$ and $\bar{R}_z$ in Eqs. (6.7)-(6.8) are enforced explicitly in the HR functional via Lagrange multipliers. In 3D FEM, the equilibrium equations are not applied as constraints in the variational statement, and this leads to larger magnitudes of the residuals $\bar{R}_x$ and $\bar{R}_z$.

In the previous Section 6.3, it was shown qualitatively that the 3D FEM model violates the transverse equilibrium equation $\tau_{xz,x} + \sigma_{z,z} = 0$ at the top and bottom surfaces of laminates VS F, VS G and VS J. The residual $\bar{R}_z^t$ represents the quantitative measurement of how accurately this equilibrium condition is satisfied by the HR and 3D FEM models. The magnitudes $\max|\bar{R}_z^t|$ in Table 6.3 suggest that the maximum residual of the HR model is at least three orders of magnitude smaller than the 3D FEM residual.

However, consider the axial plots of residual $\bar{R}_z^t$ for laminates VS G and VS J in Figures 6.27a and 6.28a. These plots show that residual $\bar{R}_z^t$ for the 3D FEM model, increases considerably towards the ends of the beam due to the singularity of the boundary condition at these locations. Remote from the ends the magnitude of $\bar{R}_z^t$ converges to that of the HR model. Therefore, Figures 6.27a and 6.28a suggest that the large differences in $\max|\bar{R}_z^t|$ between 3D FEM and the HR model are constrained to local regions towards the boundaries. At the same time, the axial plots of the ratio between $\bar{R}_z^t$ of the HR model and the 3D FEM model for the same laminates in Figures 6.27b and 6.28b, show that the HR residual $\bar{R}_z^t$ is always at least one order of magnitude smaller than the 3D FEM residual. Finally, both Figures 6.27b and 6.28b show that residuals $\bar{R}_x$ and $\bar{R}_z$ of the HR model are negligible compared to the 3D FEM model along the entire beam length.

In summary, these quantitative findings show that the HR model leads to stress results that obey Cauchy's 3D equilibrium equations more accurately than 3D FEM. In effect, this explains the qualitative observations in Section 6.3 regarding the errors in the 3D FEM model of accurately predicting the boundary condition $\bar{\sigma}_{z,z} = 0$ at the surfaces. Based on these qualitative and quantitative findings, it is concluded that the present higher-order HR formulation provides more accurate stress results compared to the 3D FEM model for the laminates and load case considered here.

Combined with the residual in Cauchy's equilibrium equations, the total strain energy can be used to assess the accuracy of the two models. Any structure under external loading, and constrained by certain boundary conditions, deforms in such a manner as to minimise the total

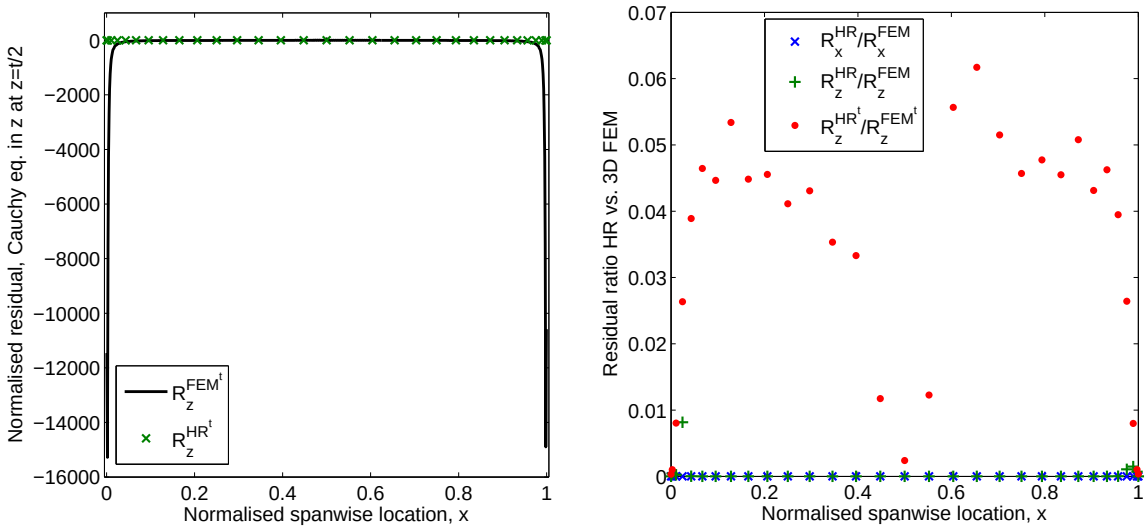

(a) Normalised residual, $\bar{R}_z^t$ **(b)** Normalised residual ratios, $\bar{R}^{HR}/\bar{R}^{FEM}$

Figure 6.27: Laminate VS G: Spanwise distribution of the normalised residual of Cauchy's z-direction equilibrium equation at the top surface in (a), and spanwise distributions of the residual ratios of Cauchy's x- and z-direction equilibrium equations in (b), as calculated from the HR and 3D FEM models.

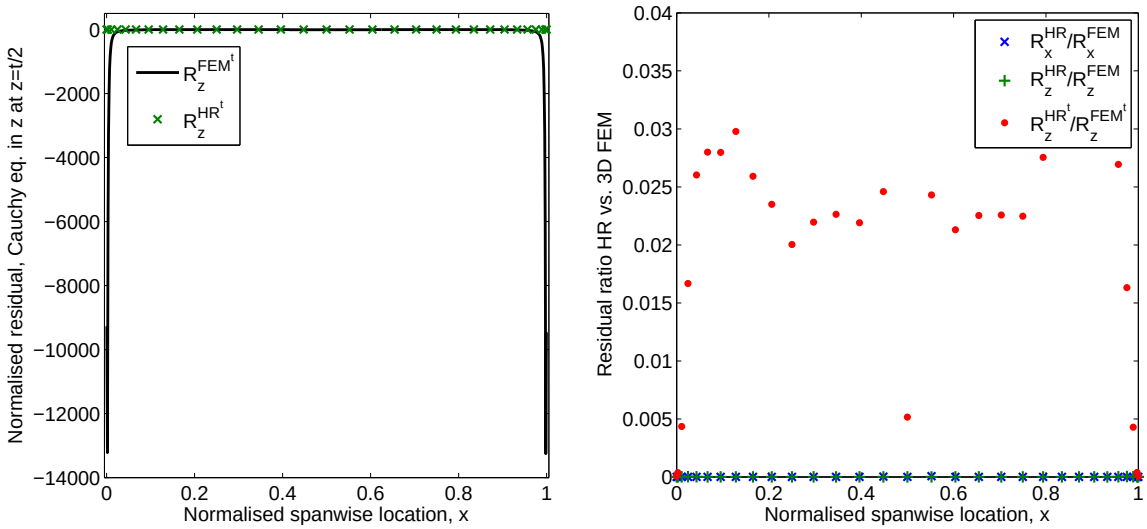

(a) Normalised residual, $\bar{R}_z^t$ **(b)** Normalised residual ratios, $\bar{R}^{HR}/\bar{R}^{FEM}$

Figure 6.28: Laminate VS J: Spanwise distribution of the normalised residual of Cauchy's z-direction equilibrium equation at the top surface in (a), and spanwise distributions of the residual ratios of Cauchy's x- and z-direction equilibrium equations in (b), as calculated from the HR and 3D FEM models.

Table 6.4: Total strain energy U in the model of the structure, and percentage contributions of axial deformation (U_{σ_x}/U), transverse shear deformation ($U_{\tau_{xz}}/U$) and transverse normal deformation (U_{σ_z}/U).

Lam.	Model	U_{σ_x}/U (%)	$U_{\tau_{xz}}/U$ (%)	U_{σ_z}/U (%)	U (J/m)
VS A	HR3-MZZF	45.3	54.3	0.37	0.142
	3D FEM	44.6	55.1	0.37	0.142
VS B	HR3-MZZF	46.3	53.4	0.35	0.148
	3D FEM	45.5	54.1	0.33	0.147
VS C	HR3-MZZF	58.5	41.1	0.40	0.215
	3D FEM	57.4	42.2	0.44	0.214
VS D	HR3-MZZF	45.1	54.5	0.39	0.149
	3D FEM	44.2	55.4	0.39	0.147
VS E	HR3-MZZF	50.7	48.9	0.37	0.162
	3D FEM	50.0	49.6	0.37	0.161
VS F	HR3-MZZF	46.6	53.1	0.34	0.156
	3D FEM	45.5	54.1	0.34	0.155
VS G	HR3-RZT	27.7	72.0	0.27	2573
	3D FEM	26.4	73.4	0.19	2572
VS H	HR3-RZT	28.0	71.9	0.18	2478
	3D FEM	28.3	71.6	0.18	2433
VS I	HR3-RZT	27.0	72.6	0.40	3174
	3D FEM	26.1	73.6	0.24	3142
VS J	HR3-RZT	29.8	69.9	0.35	2180
	3D FEM	28.8	71.0	0.18	2168

strain energy U. Thus, if the HR model more accurately obeys Cauchy's equilibrium equations, and at the same time corresponds to a lower strain energy configuration than 3D FEM, then its solution must necessarily be a more accurate representation of the 3D stress field within the structure.

Table 6.4 compares the total strain energy per unit width U of the HR and 3D FEM models for all variables stiffness laminates VS A-VS J, and also shows the respective percentage energy contributions of the axial stress U_{σ_x}, transverse shear stress $U_{\tau_{xz}}$ and transverse normal stress U_{σ_z} potentials. These quantities are calculated as follows:

$$U = \int_0^a \int_{-t/2}^{t/2} \left[\frac{\sigma_x^{(k)^2}}{2\bar{Q}^{(k)}} + \frac{\tau_{xz}^{(k)^2}}{2G_{xz}^{(k)}} + \frac{\sigma_z^{(k)}}{2} \left(R_{33}^{(k)} \sigma_z^{(k)} + R_{13}^{(k)} \sigma_x^{(k)} \right) \right] \mathrm{d}z\mathrm{d}x = U_{\sigma_x} + U_{\tau_{xz}} + U_{\sigma_z} \quad (6.10)$$

where σ_x, τ_{xz} and σ_z are derived from Eqs. (4.23), (4.40) and (4.41) for the HR model, respectively, and are extracted from Abaqus using a Python script for the 3D FEM model.

Table 6.4 shows that the percentage contributions of three stress fields for the HR and 3D FEM models, are correlated to within 1.5% for all laminates considered. For composite laminates VS A-VS F, the strain energy within the beam is almost equally shared between the axial stress and the transverse shear stress. For the sandwich beams VS G-VS J, the effect of

transverse shear deformations is increased due to the relatively high shear flexibility of the core, and contributes to more than 70% of the strain energy within the structure. Furthermore, for all laminates analysed, the energy contribution of the transverse normal stress field is less than 0.5% and negligible compared to the axial and transverse shear stress fields.

Finally, for all laminates, the internal strain energy of the 3D FEM model is less than the strain energy of the HR model. For most laminates, the difference between the two models is less than 1% but for the laminate VS H the strain energy of the HR model is 1.8% greater than for 3D FEM. Thus, in general, we cannot conclude that the HR model leads to a lower strain energy solution than 3D FEM, and therefore does not correspond to a lower energy state. However, it is well-known that the displacement-based weak-form FEM overestimates the stiffness matrix and results in the lowest possible strain energy solution [11]. Based on the previous observation that the HR formulation predicts higher internal strain energy states than the 3D FEM model; more accurately obeys Cauchy's 3D equilibrium equations; and correlates to within 1% of Pagano's 3D elasticity solution [20], provides compelling evidence that the HR formulation, combined with the strong form DQM, more accurately predicts the 3D stress fields for the laminates considered here. This is especially noteworthy as the computational effort in the HR3-RZT formulation is reduced by *four* orders of magnitude compared to 3D FEM; 217 degrees of freedom (5 moments and 2 Lagrange multipliers at 31 grid points) in HR3-RZT compared to 1.16×10^6 degrees of freedom (6 unknowns for 95,880 elements, i.e. 193,600 nodes) in 3D FEM.

6.5 Localised stress gradients driven by tow steering

This section investigates non-classical transverse shear stress profiles that for straight-fibre laminates have previously only been observed at clamped boundaries [173, 174]. The results in this section show that stiffness variations along a beam can induce the same boundary layer effects but remote from any singularities or boundary conditions. It is shown that tow-steering can lead to non-intuitive stress gradients that may adversely affect the damage tolerance of these laminates.

To study the effect in straight-fibre laminates, consider a square [0/90/0] laminate with in-plane dimensions $a = b$ and characteristic length to thickness ratio of $a/t = 10$, clamped along all four edges and loaded by a uniform pressure on the top surface. The bending behaviour of this laminate is readily investigated using the HR plate model derived in Chapter 7. The example of a plate is used here as the four clamped conditions induce a particular boundary layer with non-intuitive transverse shear stresses in the four corners of the straight-fibre laminate, and this particular behaviour is not possible for 1D beams.

Figure 6.29 shows the through-thickness plots of the transverse shear stresses at a distance of $(x, y) = (0.066a, 0.066b)$ from one of the corners of the plate. The stress distributions of the HR3-RZT and 3D FEM model are closely matched at this location. Conversely, Figure 6.30 shows the through-thickness plots of the transverse shear stresses at a corner of the plate, i.e. at $(x, y) = (0, 0)$. It is apparent that the transverse shear plots in the corner are considerably different from the plots slightly away from the corner. The 3D FEM solution is not plotted for

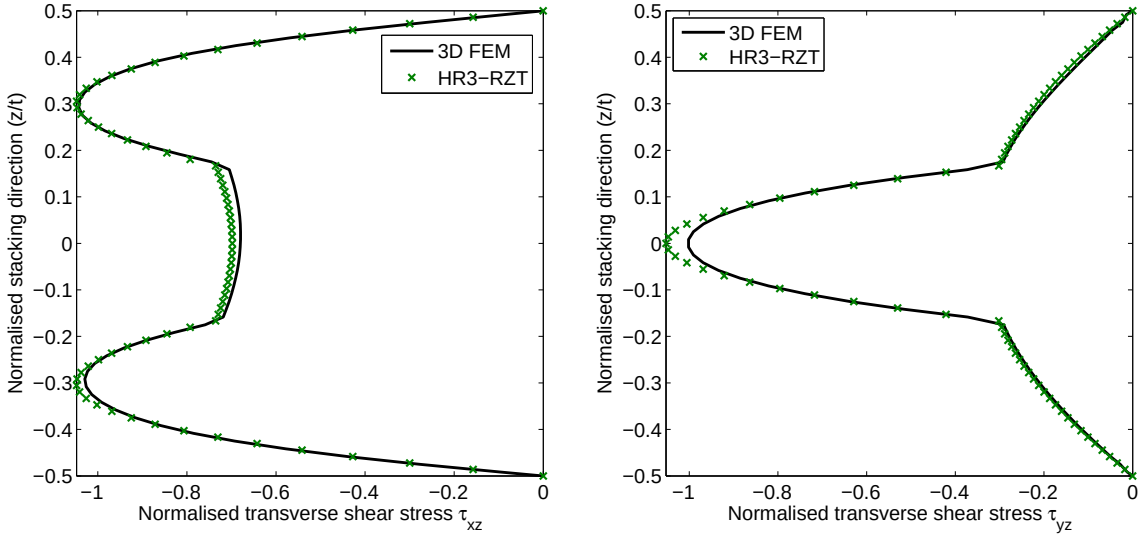

(a) τ_{xz} **(b)** τ_{yz}

Figure 6.29: Through-thickness distribution of the normalised transverse shear stresses τ_{xz} and τ_{yz} at location $(0.066a, 0.066b, z)$.

the corner location in Figure 6.30 because the clamped edges create a singularity that prevents convergence of the stresses to meaningful values.

Slightly away from the corner in Figure 6.29, we observe the classical result of single sign, piecewise parabolic transverse shear stresses, i.e. the applied pressure loading on the top surface is causing the cross-section to shear in one direction only. However, at the corner in Figure 6.30, the HR3-RZT solution shows that both transverse shear stresses change sign through the thickness, i.e. some parts of the cross-section are shearing in one direction, whereas other parts are shearing in the opposite direction. This non-intuitive stress distribution arises from the strong dual boundary condition of two coincident clamped edges at the corner point. Small movements away from the corner, as shown in Figure 6.29, completely eliminate this phenomenon suggesting that this is a boundary layer effect for straight-fibre laminates.

Similar plots are shown in the works by Vel and Batra [173] and Shah and Batra [174] but these authors did not point out or study the peculiarity of these stress fields in further detail. As is shown below, the same effects can be replicated in variable-stiffness beams at locations considerably removed from any boundaries. Thus, boundary layers that occur in the vicinity of strong 2D boundary conditions for straight-fibre laminates can be induced in 1D structures by varying the material properties alone.

For example, consider a multilayered beam with characteristic length to thickness ratio $a/t = 20$, comprised of N_l variable-stiffness composite layers and clamped at both ends $x_A = 0$ and $x_B = a = 250$ mm, and subjected to a uniformly distributed load equally divided between the top and bottom surfaces $\hat{P}_b = -\hat{P}_t = 50$ kPa.

Table 6.5 summarises two balanced and symmetric, variable-stiffness layups VS X and VS Y that are analysed using the HR3 model. The two laminates feature eight tow-steered plies of equal thickness manufactured using the IM7 8552 carbon-fibre reinforced plastic previously defined in Table 6.2. Laminate VS X features fibre variations of 90° within each layer, whereas

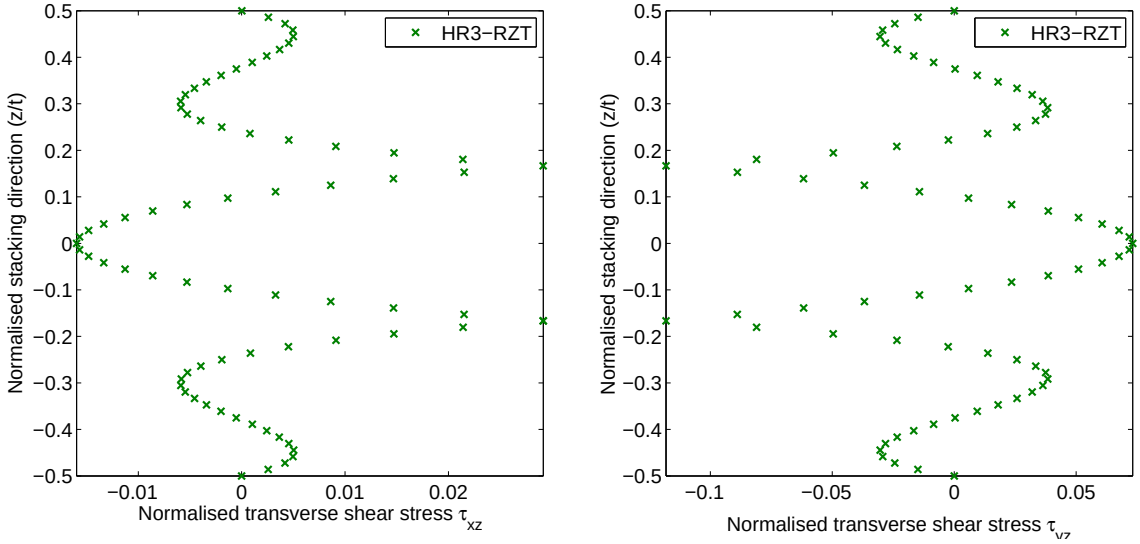

(a) τ_{xz} **(b)** τ_{yz}

Figure 6.30: Through-thickness distribution of the normalised transverse shear stresses τ_{xz} and τ_{yz} at location $(0, 0, z)$. Note the change of sign of the transverse shear stresses through the thickness.

Table 6.5: Stacking sequences and material properties of two tow-steered laminates used to investigate localised stress fields due to in-plane stiffness variations.

Laminate	**Layup**	t_{ply} (mm)
VS X	$[\langle 90\|0\rangle/\langle -90\|0\rangle/\langle 45\| -45\rangle/\langle -45\|45\rangle]_s$	1.5625
VS Y	$[\langle 90\|20\rangle/\langle 45\| -25\rangle/\langle -90\| -20\rangle/\langle -45\|25\rangle]_s$	1.5625

the fibre variations for laminate VS Y are slightly more benign at 70° for each layer.

A 3D FEM model in Abaqus is implemented that features a 250 mm long (x-direction), 1000 mm wide (y-direction) and 12.5 mm thick (z-direction) plate that is meshed using a total of 95,880 C3D8R elements with 799 elements in the x-direction, 120 elements in the z-direction, i.e. 15 elements per ply, and a single element in the y-direction. The plane strain condition in the y-direction is enforced by the high width-to-length aspect ratio, the use of a single element in the y-direction and boundary conditions that prevent the shorter sides from expanding laterally.

Figure 6.31 plots the through-thickness profile of the normalised (see Eq. (6.4)) transverse shear stress $\bar{\tau}_{xz}$ for laminates VS X and VS Y at the quarterspan ($x = a/4$) of the beam. The plots show that the 3D FEM solution from Abaqus and the HR3 results are well correlated throughout the entire thickness.

Most importantly, both plots show that the transverse shear stress is both negative and positive throughout the thickness. For both laminate VS X and VS Y, the external surface layers shear in one direction, whereas the internal layers shear in the opposite direction. Hence, this behaviour is similar to results at the clamped corner point of a straight-fibre laminate shown in Figure 6.30. In this case, the two coincident clamped edges induced strong localised boundary layers in the transverse shear stress profiles. Remote from such singularities, the transverse shear stress profiles in isotropic and straight-fibre composite beams and plates is either positive or

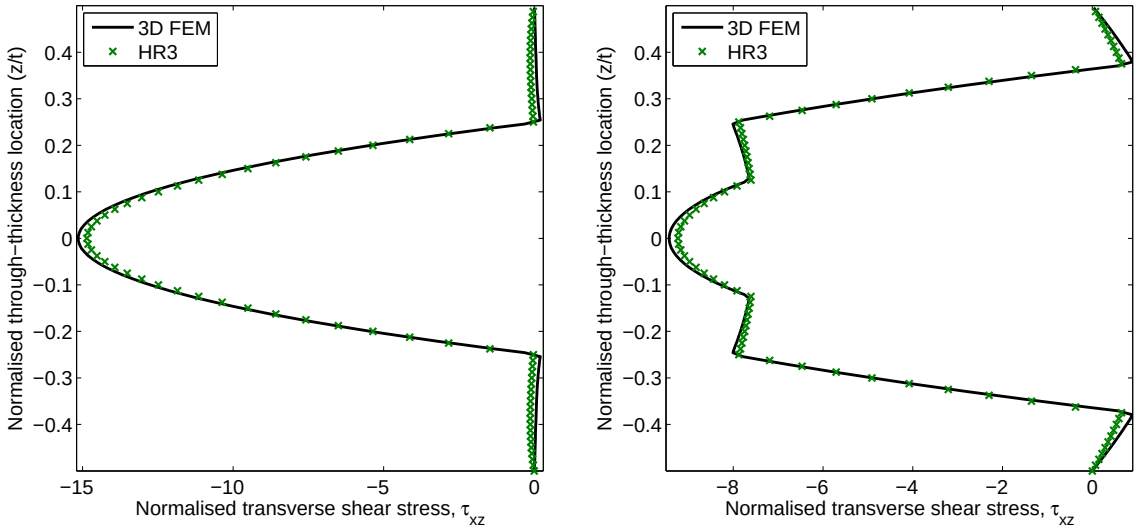

(a) Laminate VS X **(b)** Laminate VS Y

Figure 6.31: Through-thickness distribution of the normalised transverse shear stress (at $x = a/4$). Note the change of sign of the transverse shear stress through the thickness.

negative throughout the entire thickness. However, for the two tow-steered beams VS X and VS Y, the transverse shearing reversal occurs at the quarterspan, i.e. significantly removed from any localised boundary condition.

The physical reason of why this is possible in tow-steered beams is readily explained by investigating the transverse shear stress equation of the HR model in the absence of surface shear tractions, reproduced from Chapter 4 below,

$$\tau_{xz}^{(k)} = \frac{\mathrm{d}}{\mathrm{d}x}\left[\left\{-\bar{Q}^{(k)}\boldsymbol{g}^{(k)} + \boldsymbol{\alpha}^{(k)}\right\}\boldsymbol{s}\mathcal{F}\right]. \tag{6.11}$$

In Eq. (6.11), the only quantities that can influence the layerwise sign of the transverse shear stress are the ply stiffness $\bar{Q}^{(k)}$ and integration constant $\boldsymbol{\alpha}^{(k)}$, where the latter is a function of the ply stiffness terms $\bar{Q}^{(k)}$ itself. All other terms $\boldsymbol{s}$ and $\mathcal{F}$ are equivalent single-layer quantities that are the same for all plies. For any material that satisfies the second law of thermodynamics, the definition $\bar{Q}^{(k)} > 0$ holds and as the value of $\bar{Q}^{(k)}$ for each layer is fixed along the entire length of a straight-fibre beam, the sign of the transverse shear stress is completely defined by the stress resultants $\mathcal{F}$ along the beam length. However, for tow-steered laminates, the derivative $\dfrac{\mathrm{d}\bar{Q}^{(k)}}{\mathrm{d}x} \neq 0$ and can be positive for some layers and negative for others. Hence, the sign of the transverse shear stress can change sign based on the local rate of change of the material stiffness $\bar{Q}^{(k)}$.

The practicality of these non-intuitive transverse shear stress profiles is yet to be determined. Perhaps, these localised stress fields can be used for actuation purposes in morphing structures or for sensing of interlaminar damage sites. On the contrary, these transverse shear stress profiles of opposite sign could be detrimental for the damage tolerance of tow-steered laminates. The transverse shear force, i.e. the through-thickness integral of the transverse shear stress, is fully defined by the external loading and boundary conditions, and hence is independent of the

stacking sequence or material properties of the laminate. As a result, locally positive transverse shear stresses must result in increased negative transverse shear stresses at other locations throughout the cross-section and vice versa if the overall transverse shear force is to remain constant.

As debonding of layers in laminated composites is driven by the magnitude of transverse shear stresses, these locally accentuated levels of transverse shear stress could lead to premature delamination initiation. Current studies on the buckling and postbuckling optimisation of tow-steered laminates in the literature rarely account for transverse shear stresses. If the non-intuitive through-thickness stresses outlined in this section are detrimental to the damage tolerance of tow-steered laminates, and these effects occur remote from boundaries and singularities, which are traditionally seen as the areas of localised stress concentration, then current design guidelines need to be reviewed to take account of these effects. Thus, further work into the potential uses and effects of this particular non-classical effect are pertinent topics for future research.

6.6 Full-field stress tailoring for delamination prevention

The aim of the following study is to use the variable fibre angle technology to tailor the through-thickness stress distributions of the transverse shear and normal stresses. The motivation behind this goal is to reach a compromise between maintaining high overall bending stiffness and reducing local interfacial stress concentrations.

An often cited metric for predicting the onset of delamination in layered composites is the quadratic failure criterion of Camanho et al. [175]

$$f = \left(\frac{\langle \sigma_{zz} \rangle}{\check{N}}\right)^2 + \left(\frac{\tau_{xz}}{\check{S}}\right)^2 + \left(\frac{\tau_{yz}}{\check{T}}\right)^2 \tag{6.12}$$

where $\check{N}$ is the interlaminar tensile strength, and $\check{S}$ and $\check{T}$ are the interlaminar shear strengths. Delamination initiation is assumed to occur when $f \geq 1$. Macaulay brackets $\langle\rangle$[1] are used because compressive transverse normal stresses do not contribute to the initiation of delaminations. In the beam problem considered here, $\tau_{yz} = 0$, such that delamination initiation is driven by σ_{zz} and τ_{xz} at the interface between two plies with different material properties. In the HR formulation, the interfacial shear and normal stresses are calculated using Eqs. (4.40) and (4.41).

Consider the problem of a simply supported, four layer cross-ply beam in bending, loaded by a uniform pressure on the top surface. Depending on the arrangement of the four layers, the transverse shear stress profile changes considerably. Figure 6.32 compares the transverse shear stress profile at the support $x = 0$ through the thickness of a $[0/90]_s$ and a $[90/0]_s$ laminate. For both laminates, the maximum shear stress occurs at the midplane and the transverse shear stress vanishes at both surfaces due to the absence of external shear tractions. Classical beam theory states that the transverse shear force, i.e. the integral of the transverse shear stress through the thickness, is independent of the layup and only depends on the loading condition. Based on these two insights, it is apparent that to distribute stresses most evenly, the shear stress

[1] $\langle x \rangle = 0$ for $x \leq 0$ and $\langle x \rangle = x$ for $x > 0$

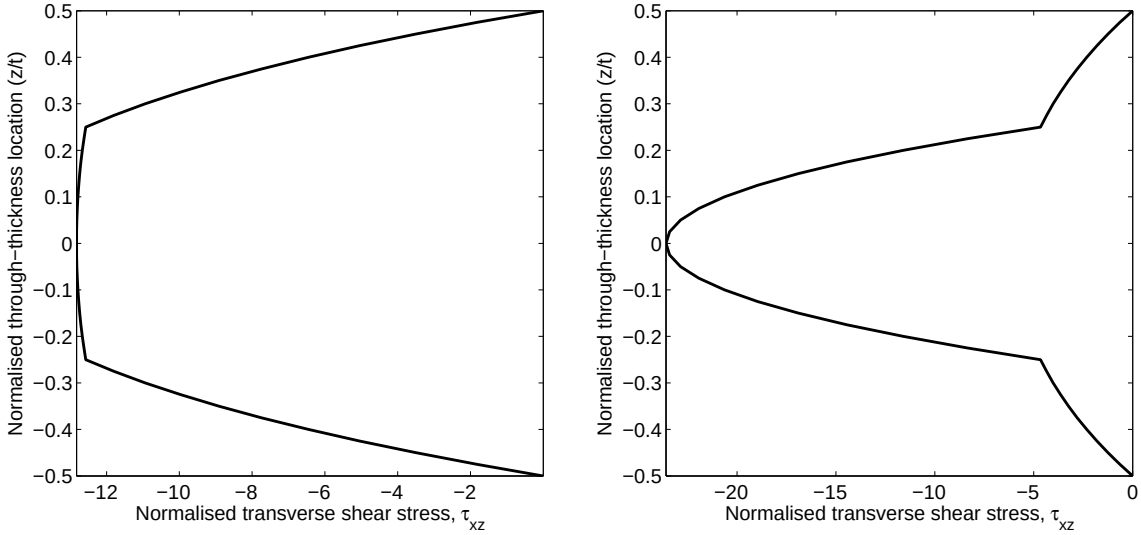

(a) [0/90/90/0] **(b)** [90/0/0/90]

Figure 6.32: Through-thickness distribution of normalised transverse shear stress $\bar{\tau}_{xz}$ at $x = 0$ for two cross-ply laminates. Profiles calculated using Pagano's 3D elasticity solution [20].

should increase as rapidly as possible away from the outer surfaces and then remain constant for the rest of the cross-section (see Figure 6.32a). In the ideal case the entire cross-section is sheared by the same amount, thereby spreading load equally and minimising the shear stress amplitude. Alternatively, if delaminations are to be tolerated, and their location constrained to the midplane where sublaminate buckling in compression is least likely, a transverse shear stress profile as shown in Figure 6.32b is preferable.

Due to the greater axial and transverse shear rigidity of the 0° layers, the former scenario can be realised by placing the stiffer 0° on the outside and using the less stiff 90° layers as a core. In the opposite case, the transverse shear stress remains close to zero in the outer 90° layers causing a local stress concentration in the central 0° layers with an overall greater shear stress magnitude.

Even for such a simple scenario the two cases present a non-trivial trade-off. The $[0/90]_s$ laminate maximises bending stiffness and reduces the maximum shear stress magnitude throughout the thickness by placing the stiffer 0° towards the surfaces. Conversely, the $[90/0]_s$ laminate significantly reduces the shear stress at the interface between the 0° and 90° layers, which is a critical factor in delamination initiation. Thus, a compromise needs to be reached between minimising bending deflection and reducing the chance of intraply transverse cracking.

This trade-off ultimately depends on the structural requirements and material strengths being considered, and is not only restricted to this illustrative case of a cross-ply laminate. To an extent, a similar phenomenon occurs for a quasi-isotropic laminate, whereby a $[\pm 45/90/0]_s$ stacking sequence is comparable to the $[90/0]_s$ laminate, whereas a $[0/\pm 45/90]$ stacking sequence is the analogue to the $[0/90]_s$ laminate.

An optimisation study was conducted to ascertain if beams manufactured using variable-stiffness composite plies could:

1. Reduce the likelihood of delaminations compared to an optimised straight-fibre, quasi-isotropic beam, i.e. reduce the maximum value of the initiation criterion f in Eq. (6.12) at the interfaces of layers with different material properties.

2. Find a compromise between maximising overall bending rigidity and minimising the likelihood of delaminations.

For both opimisation studies above, a 250 mm long and 16 mm thick beam with either simply supported (SS) or clamped (CC) boundary conditions was analysed, i.e. a total of four optimisation studies 1-CC, 1-SS, 2-SS and 2-CC. In all cases, the beam is loaded by a uniform distributed load of unit magnitude on the top surface only. The material properties are those of IM7-8552 defined in Table 6.2, and the interlaminar strengths are $\check{N} = 99$ MPa and $\check{S} = 113$ MPa. Initially, a 16-ply quasi-isotropic, balanced and symmetric baseline design comprised of straight-fibre $\pm 45°, 0°$ and $90°$ plies is sought for each of the four optimisation cases. For example, in a $[45, -45, 0, 90, 0, 90, -45, 45]_s$ stacking sequence, each fibre angle represents a stack of four 0.25mm plies within which delaminations cannot occur. Thus, the goal is to rearrange the ply blocks such as to minimise the appropriate fitness function.

For the variable-stiffness designs, the laminate is constrained to the balanced and symmetric form $[\pm\langle T_0^{(1)}|T_1^{(1)}\rangle, \cdots, \pm\langle T_0^{(8)}|T_1^{(8)}\rangle]_s$. There are 32 blocks of variable-stiffness layers each comprised of two 0.25 mm IM7-8552 plies, such that each $\pm$ pair of variable-stiffness plies is equivalent to a stack of four straight-fibre plies in the quasi-isotropic baseline designs.

Initial numerical studies showed that for the type of composite laminate investigated, ZZ deformations have negligible effects on the global structural behaviour and local boundary layers towards the clamped edges. The benign orthotropy ratio $G_{13}/G_{23} = 1.25$ of IM7-8552, and the large number of unique plies through the thickness, limit the effect of ZZ deformations. Thus, the implemented optimisation problem is based on the HR3 model formulation, i.e. a third-order expansion without a ZZ term.

For the variable-stiffness laminates, the two optimisation problems are formulated as follows:

$$\begin{aligned}
&1) \quad \text{Minimise:} \quad \max\{f(\boldsymbol{v})\} \\
&2) \quad \text{Minimise:} \quad \max\{f(\boldsymbol{v})\} \cdot \max\{w_0(\boldsymbol{v})\} \\
&\quad\;\; \text{Variables:} \quad \boldsymbol{v}: \quad \begin{bmatrix} T_0^{(1)} & \dots & T_0^{(8)} & T_1^{(1)} & \dots & T_1^{(8)} \end{bmatrix} \\
&\text{Subject to:} \quad 0° \leq T_s^{(k)} \leq 90° \quad (s = 0, 1 \text{ and } k = 1 \dots 8)
\end{aligned} \tag{6.13}$$

where w_0 is the bending deflection and f the delamination initiation factor defined in Eq. (6.12). The delamination initiation factor f is calculated at the top and bottom of each ply, i.e. at the layer interfaces, and at all DQM grid points X_i throughout the grid.

Note that the second optimisation study is a multi-objective optimisation, and therefore a Pareto front of optimised designs exist for different combinations of $f(\boldsymbol{v})$ and $w_0(\boldsymbol{v})$. Thus, designs with varying degrees of importance assigned to the two objectives f and w_0 can be found. As the focus of this work is on the underlying higher-order model, a more straightforward option was chosen here. Hence, an optimised solution that gives equal weight to both objectives, displacement and fracture, is sought here, which represent a simple compromise between the

Table 6.6: Optimised straight-fibre and variable stiffness laminates with associated value of the fitness function. The percentage change indicates the reduction in fitness function magnitude of the variable stiffness designs compared to the straight-fibre designs.

Optimisation	Layup	Fit. Function	Change
1 - SS	$[0_2/45/-45/90_2/-45/45]_s$	7.10×10^{-3}	-
	$[0_2/\pm\langle 90\|71\rangle/\pm\langle 90\|84\rangle/90_4/\pm\langle 81\|89\rangle/\pm\langle 0\|83\rangle/\pm\langle 0\|77\rangle]_s$	6.20×10^{-3}	-12.6%
1 - CC	$[0/45/90/-45/90/45/-45/0]_s$	5.91×10^{-3}	-
	$[\pm\langle 70\|10\rangle/\pm\langle 2\|73\rangle/\pm\langle 10\|74\rangle/\pm\langle 34\|66\rangle/\pm\langle 82\|85\rangle/\pm\langle 41\|48\rangle/\pm\langle 4\|65\rangle/\pm\langle 0\|17\rangle]_s$	5.47×10^{-3}	-7.4%
2 - SS	$[0_2/45/-45/45/90/90/-45]_s$	1.05×10^{-5}	-
	$[0_4/\pm\langle 0\|62\rangle/\pm\langle 0\|72\rangle/\pm\langle 0\|76\rangle_3/\pm\langle 0\|71\rangle]_s$	7.82×10^{-6}	-25.3%
2 - CC	$[0/-45/0/90/45/-45/90/45]_s$	2.93×10^{-6}	-
	$[0_2/\pm\langle 0\|3\rangle/\pm\langle 0\|35\rangle/\pm\langle 0\|26\rangle/\pm\langle 0\|9\rangle/\pm\langle 0\|3\rangle/0_4]_s$	2.26×10^{-6}	-22.8%

two objectives.

The optimisation problem is solved using a genetic algorithm (GA) in the commercial software package Matlab. The crossover probability is chosen to be 0.8 and the children of future generations are created using a weighted average of the parents. The mutation function is a Matlab adaptive-feasible algorithm that creates random changes in the population individuals with the direction and step length adaptive to the prior successful or unsuccessful generation. Due to the large number of design variables and the non-convexity of the optimisation problem, the convergence of the GA is relatively slow and a global minimum is not guaranteed. To improve the convergence rate, a hybrid optimisation scheme is implemented, whereby the GA is used to find the region near an optimum point after only a small number of generations, typically less than 20, and a pattern-search algorithm is then used for a faster and more efficient local search. To prevent entrapment in local minima, a variety of random and specific initial seed populations are tested, with the range of individuals in the initial population set to include the whole design space $T_s^{(k)} \in [0°, 90°]$, and the population size set to 15-20 times the number of design variables.

Table 6.6 summarises the optimised straight-fibre and variable-stiffness laminates found using the GA for the four optimisation studies. In all cases, the variable-stiffness design improves upon the optimal straight-fibre design.

The structural mechanism behind the improvements is readily explained by example of case 2-SS. Classical beam theory states that the maximum transverse shear force must occur at the supports for a simply supported beam loaded by a uniformly distributed load. Ideally, the stiffness of the beam can be reduced over the supports as the transverse deflection is constrained at these points. To reduce the likelihood of delaminations in this area, the magnitude of the maximum transverse shear stress is minimised using the mechanism previously described in Figure 6.32a, i.e. stiffer layers towards the surfaces with a softer core. In the optimal design for case 2-SS, the local layup above the supports is $[0_4/\pm 62/\pm 72/\pm 76_3/\pm 71]_s$ which agrees

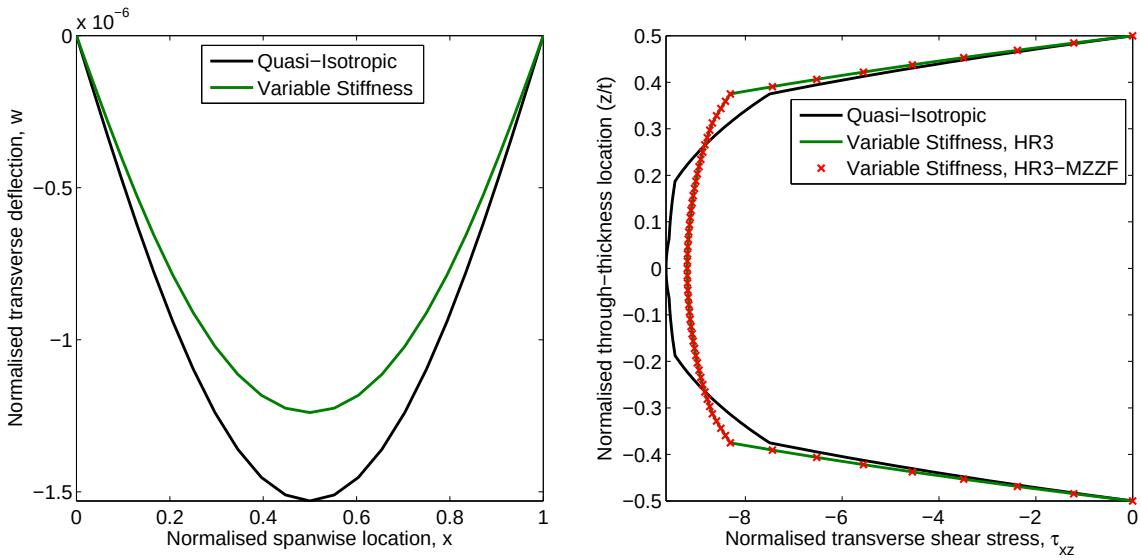

(a) Bending deflection $\bar{w}_0$

(b) Transverse shear stress $\bar{\tau}_{xz}$ at $x = 0$

Figure 6.33: Case 2 - SS: Comparison of normalised bending deflection $\bar{w}$ and through-thickness profile of transverse shear stress $\bar{\tau}_{xz}$ at the support $x = 0$ for quasi-isotropic and variable-stiffness optimal designs.

with the above qualitative explanation. Furthermore, the layup at the centre of the beam, i.e. the point of maximum bending deflection, is $[0_{32}]$ which gives the maximum possible bending stiffness.

Compared to the quasi-isotropic design, variable-stiffness laminates therefore have the capability of increasing the bending stiffness towards unsupported areas, and optimising the layup for distributing transverse stresses at supported locations where stress concentrations are more likely. Overall, this results in decreased bending deflection, a reduction in the peak transverse shear stress and more distributed transverse loading, as shown in Figure 6.33. This figure also shows that the variable-stiffness design reduces the peak bending displacement more than the peak transverse shear stress. This explains why the fitness function in Table 6.6 is improved more for case 2 (bending and delamination) than for case 1 (delamination only).

A similar explanation is applicable for the clamped optimisation case 2-CC. The optimised design for case 2-CC in Table 6.6 shows that the fibre orientation at the midspan of the beam is $[0_{32}]$ to minimise the bending deflection, and varies linearly to $[0_2/\pm 3/\pm 35/\pm 26/\pm 9/\pm 3/0_4]_s$ over the supports. Compared to the optimised design for case 2-SS, the magnitude of stiffness variation across the beam is reduced, such that the bending stiffness is relatively high along the whole beam. Indeed, Figure 6.34 shows that the improvements in the fitness function with respect to the straight-fibre design are mostly due to reductions in the bending deformation w_0 than reductions in the peak transverse shear stress over the supports.

However, Figure 6.34b does show that the transverse shear stress is more evenly distributed throughout the cross-section for the variable-stiffness laminate than the straight-fibre laminate. The plot shows that the clamped edge introduces a non-intuitive transverse shear stress profile at the supports. The pronounced through-thickness variation makes it harder to evenly spread the load throughout the cross-section. This mechanism also explains why the improvements

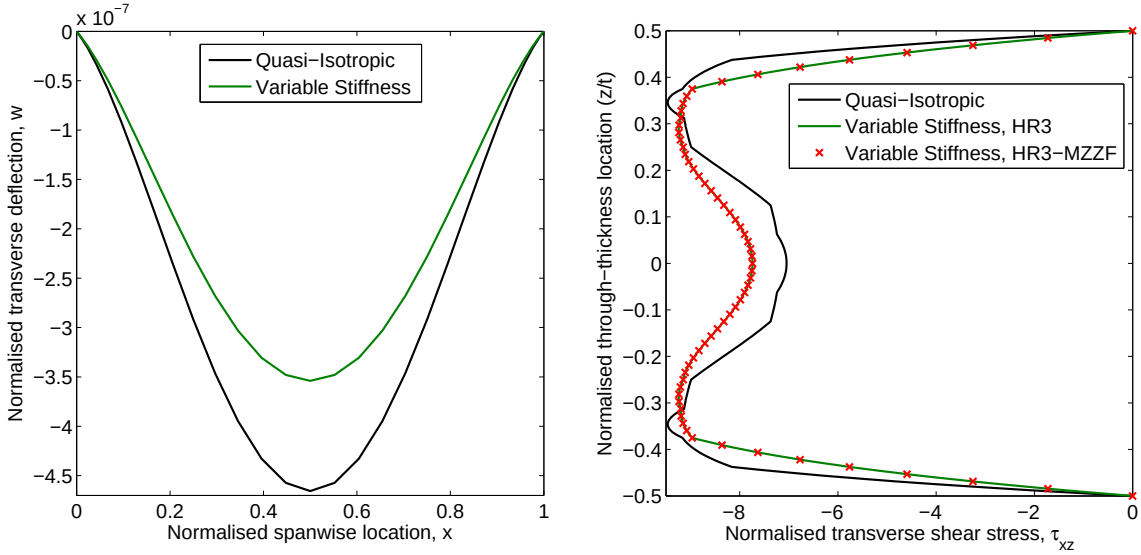

(a) Bending deflection $\bar{w}_0$

(b) Transverse shear stress $\bar{\tau}_{xz}$ at $x = 0$

Figure 6.34: Case 2 - CC: Comparison of normalised bending deflection $\bar{w}$ and through-thickness profile of transverse shear stress $\bar{\tau}_{xz}$ at the support $x = 0$ for quasi-isotropic and variable-stiffness optimal designs.

in the fitness function for case 1-SS are better than for case 1-CC in Table 6.34, i.e. for the cases where only the delamination failure criterion f is minimised. Namely, the higher-order variation of transverse shear stress at the clamped supports makes it harder to redistribute the transverse shear stress for delamination prevention purposes.

Finally, the transverse shear stress plots in Figures 6.33b and 6.34b show the model results for both HR3 and HR3-MZZF, i.e. with and without inclusion of a ZZ function, respectively. These plots show no difference between the two models, such that ZZ effects can safely be ignored. These results support the initial assumption of basing this optimisation study on the HR3 model.

6.7 Conclusions

This chapter extended the benchmarking exercise of a third-order zig-zag implementation of the HR model derived in Chapter 4 to variable-stiffness beams. The accuracy of the model was validated against 3D FEM solutions and the good correlation of all three stress fields (σ_x, τ_{xz} and σ_z) with the benchmark solutions demonstrate the accuracy of the model for layered structures with material properties that may vary continuously in-plane and discretely through the thickness. The HR model was also used to analyse transverse boundary layers towards external surfaces that are not captured rigorously by 3D FEM, and to find a compromise between increased bending stiffness and reduced chance of delaminations by full-field stress tailoring.

The results for the variable-stiffness laminates in this chapter, revealed numerical instabilities in the implementation of the HR-RZT formulation within the DQM. The dependence of the RZT ZZ function on transverse shear rigidities means that the ZZ effect, as predicted by RZT,

can be finite in some areas of the beam and vanish in others. Local areas with negligible ZZ effect lead to numerical instabilities in the model due to vanishing degrees of freedom or due to local singularities in the axial variation of laminate compliance terms. As DQM computes derivatives based on all functional values within the domain, local singularities cause significant noise in the numerical calculation of derivatives, and in turn, in the transverse shear and normal correction factors that underpin the model. These effects are not observed for MZZF as this ZZ function does not vary with axial location for variable-stiffness laminates, and thus the HR3-MZZF model performs robustly for all laminates considered.

Despite these numerical instabilities in the HR3-RZT model for certain laminates, the results in Section 6.3 demonstrate that the HR3, HR3-MZZF, HR3-RZT and 3D FEM results are well-correlated for the comprehensive range of variable-stiffness composite and sandwich beams modelled herein. These laminates represent a challenging test case for any ESLT as local material properties change both in the axial and transverse directions, and layer properties can vary by orders of magnitude. In fact, Section 6.4 revealed that the HR models more accurately predict transverse boundary layers towards external surfaces, i.e. Cauchy's 3D equilibrium equations are obeyed more closely on a local layer and global laminate level, than in the 3D FEM implementation in Abaqus. Section 6.5 then showed that non-intuitive localised stress fields in straight-fibre laminates that are induced towards clamped supports can occur in tow-steered laminates remote from any boundaries or singularities.

Finally, the HR model was used to develop the new concept of tailoring the full 3D stress field throughout composite laminates. Transverse cracking between layers is a problematic failure criterion for commonly used structures as this form of damage is often invisibly hidden within the laminate but can significantly reduce the load-carrying capacity. As initiation of delaminations is driven by interlaminar transverse shear and transverse normal stresses [175], and as these stress fields are accurately predicted in the HR formulation, the present model was used as the basis for a computationally efficient optimisation study that minimises transverse stress concentrations at layer interfaces while maintaining high bending rigidity. The results in Section 6.6 show that variable-stiffness laminates can lead to a better compromise for these objectives than quasi-isotropic straight-fibre laminates by facilitating smooth layup transitions between the central portion of the beam, where high bending stiffness is required, and portions of the beam subject to local stress concentrations.

Chapter 7

Hellinger-Reissner Model for Heterogeneous Laminated Plates

This chapter extends the higher-order model for laminated 1D beams presented in Chapter 4 to 2D flat plates. The classical equivalent single-layer membrane and bending equilibrium equations are enforced within the PMCE via Lagrange multipliers, resulting in a contracted HR functional that is used to derive a set of governing equations[1] from higher-order displacement and stress fields that inherently guarantee interlaminar and surface traction equilibrium. Even though local layerwise properties are taken into account via a ZZ function, all variables of the model are independent of the number of layers. The governing equations are derived in a generalised framework, such that the order of the model is readily increased when implemented in a computer code. By increasing the order of the model and including or disregarding the local ZZ fidelity, the model is easily tailored to plate-like structures ranging from thin engineering laminates to highly heterogeneous thick laminates comprised of straight-fibre or tow-steered reinforced plastics, foam, honeycomb and other compliant layers.

7.1 Higher-order zig-zag in-plane stress fields

Consider a multilayered plate of uniform thickness t comprised of N_l perfectly bonded laminae with individual thicknesses $t^{(k)}$ as represented in Figure 7.1. The initial configuration of the plate is referenced in orthogonal Cartesian coordinates (x, y, z) with x and y defining the two in-plane dimensions and $z \in [-t/2, t/2]$ defining the thickness coordinate. In the following, this multilayered structure is condensed onto an equivalent single layer Ω coincident with the (x, y)-plane by integrating the structural properties and 3D governing equations in the direction of the smallest dimension z. The plate is bounded by two boundary surfaces S_1 and S_2 on which the displacement and traction boundary conditions are specified, respectively, and where the complete bounding surface $S = S_1 \cup S_2$, hence S includes the top and bottom surfaces, and the circumferential boundary surface. The intersection of the bounding surface S and the reference surface Ω describes the perimeter curve Γ of the reference surface. This perimeter is split into two disjoint curves C_1 and C_2 on which displacement and stress resultant boundary conditions are prescribed, respectively. The plate is assumed to undergo static isothermal deformations under a specific set of externally applied shear and normal tractions $\left(\hat{T}_{bx}, \hat{T}_{by}, \hat{P}_b\right)$ and $\left(\hat{T}_{tx}, \hat{T}_{ty}, \hat{P}_t\right)$ on the bottom and top surfaces of the 3D body, respectively. Note that henceforth a superposed "hat" $\hat{}$ refers to a prescribed quantity, and the list $a = (a_1, a_2, a_3, \dots)$ refers to a column vector.

The in-plane displacement fields $u_x(x, y, z)$ and $u_y(x, y, z)$ are expanded as generalised expansions of z in terms of global displacement variables $u_{i_n}(x, y)$ and local layerwise ZZ variables

[1] Governing field equations and boundary conditions.

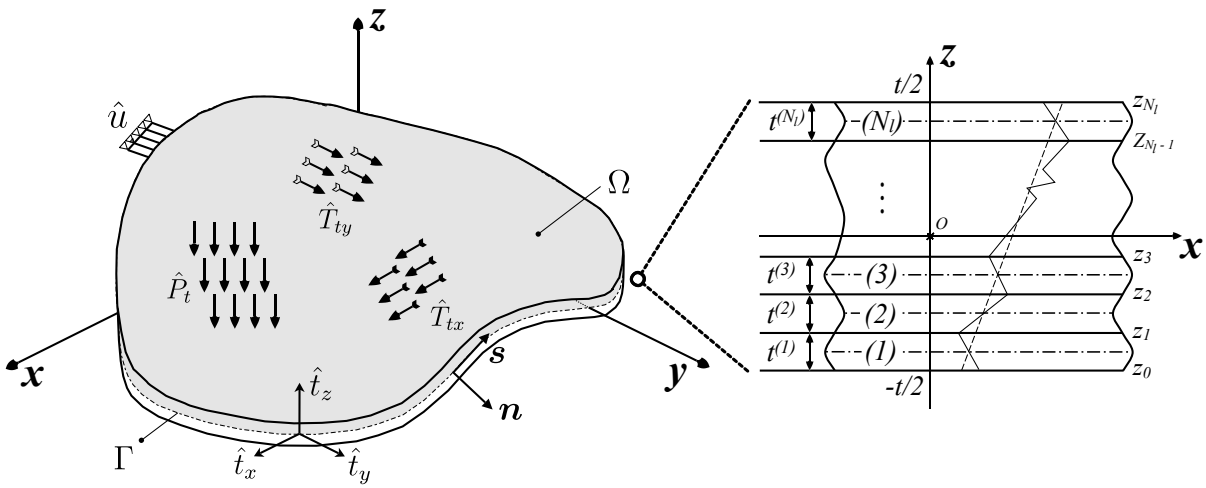

Figure 7.1: A 3D multilayered plate condensed onto an equivalent single layer. The assumed through-thickness displacement field accounts for layerwise ZZ discontinuities which are disregarded in classical theories.

$u_i^{\phi}(x,y)$ for $i = x, y$ and $n = 0, 1, \ldots, N_{o_i}$, where N_{o_i} is the highest-order expansion term in the ith direction. As most practical engineering laminates maintain a high degree of transverse normal rigidity, the present formulation ignores the occurrence of thickness stretch. Hence, $u_z(x,y)$ is independent of z. Therefore, only Kirchhoff's hypotheses regarding plane sections remaining plane and normals remaining perpendicular to the midplane are relaxed. Nevertheless, thickness stretch could readily be incorporated within the present formulation by assuming a higher-order global/local expansion for u_z.

The displacement at any point (x, y, z) within the plate domain is assumed to be

$$u_x^{(k)}(x,y,z) = u_{x_0}(x,y) + zu_{x_1}(x,y) + z^2u_{x_2}(x,y) + z^3u_{x_3}(x,y) + \cdots + \phi_x^{(k)}(x,y,z)u_x^{\phi}(x,y) \tag{7.1a}$$

$$u_y^{(k)}(x,y,z) = u_{y_0}(x,y) + zu_{y_1}(x,y) + z^2u_{y_2}(x,y) + z^3u_{y_3}(x,y) + \cdots + \phi_y^{(k)}(x,y,z)u_y^{\phi}(x,y) \tag{7.1b}$$

$$u_z(x,y) = w_0 \tag{7.1c}$$

where u_{i_0} are the reference surface in-plane displacements, u_{i_1} are the rotations of the plate cross-section, $u_{i_2}, u_{i_3}, \ldots$ are higher-order stretching and rotation terms, u_i^{ϕ} are the ZZ rotations and $\phi_i^{(k)}$ are the pertinent ZZ functions where superscript (k) refers to ply k.

Most ZZ functions in the literature can be written in the linear form

$$\phi_i^{(k)}(x,y,z) = m_i^{(k)}(x,y) \cdot z + c_i^{(k)}(x,y) \quad \text{for} \quad i = x, y \tag{7.2}$$

where $m_i^{(k)}$ and $c_i^{(k)}$ take different layerwise values depending on the particular choice of the ZZ function. Also note that for advanced composites with curvilinear fibre paths, the RZT ZZ function is dependent on both in-plane (x, y)- and through-thickness z-coordinates, whereas MZZF is independent of (x, y). The RZT ZZ function $\phi_{RZT}^{(k)}$ in two dimensions, introduced by

Tessler et al. [78], previously discussed for 1D beam models in Chapter 4, is defined by

$$\left.\begin{aligned}
\phi^{(1)}_{i_{RZT}}(x,y,z) &= \left(z+\frac{t}{2}\right)\left(\frac{G_i}{G^{(1)}_{iz}}-1\right) \\
\phi^{(k)}_{i_{RZT}}(x,y,z) &= \left(z+\frac{t}{2}\right)\left(\frac{G_i}{G^{(k)}_{iz}}-1\right)+\sum_{j=2}^{k} t^{(j-1)}\left(\frac{G_i}{G^{(j-1)}_{iz}}-\frac{G_i}{G^{(k)}_{iz}}\right)
\end{aligned}\right\} \text{ for } i=x,y \tag{7.3}$$

$$\text{and } G_i(x,y) = \left[\frac{1}{t}\sum_{k=1}^{N_l}\frac{t^{(k)}}{G^{(k)}_{iz}(x,y)}\right]^{-1}.$$

For variable-stiffness composites, the RZT ZZ function is not only a layerwise quantity but also varies with the in-plane coordinates (x,y) as the transverse shear moduli $G^{(k)}_{iz}(x,y)$ can change from point to point over surface Ω.

MZZF is invariant of transverse material properties and therefore only varies with location (x,y) when the thickness of the plate changes. In the case of a constant thickness plate, MZZF is purely a layerwise function given by

$$\phi^{(k)}_{i_{MZZF}}(z) = (-1)^k\frac{2}{t^{(k)}}\left(z-z^{(k)}_m\right) \quad \text{for} \quad i=x,y \tag{7.4}$$

where $z^{(k)}_m$ is the midplane coordinate of layer k. Note that for a constant thickness plate $\phi^{(k)}_{x_{MZZF}} = \phi^{(k)}_{y_{MZZF}}$.

To facilitate the concise derivation of the governing equations, the displacement field Eq. (7.1) is written in condensed matrix form as follows:

$$\mathcal{U}^{(k)}_{xy} = \begin{Bmatrix} u^{(k)}_x \\ u^{(k)}_y \end{Bmatrix} = \begin{bmatrix} \boldsymbol{I}_2 & \boldsymbol{Z}_2 & \boldsymbol{Z}^2_2 & \dots \end{bmatrix} \begin{Bmatrix} \mathcal{U}^g_0 \\ \mathcal{U}^g_1 \\ \mathcal{U}^g_2 \\ \vdots \end{Bmatrix} + \begin{bmatrix} \phi^{(k)}_x & 0 \\ 0 & \phi^{(k)}_y \end{bmatrix} \begin{Bmatrix} u^{\phi}_x \\ u^{\phi}_y \end{Bmatrix} \tag{7.5}$$

where the matrices and vectors in Eq. (7.5) are given by

$$\boldsymbol{I}_2 = \begin{bmatrix} 1 & 0 \\ 0 & 1 \end{bmatrix},\ \boldsymbol{Z}_2 = \begin{bmatrix} z & 0 \\ 0 & z \end{bmatrix},\ \boldsymbol{Z}^2_2 = \begin{bmatrix} z^2 & 0 \\ 0 & z^2 \end{bmatrix},\ \dots \tag{7.6}$$

$$\mathcal{U}^g_0 = \begin{bmatrix} u_{x_0} & u_{y_0} \end{bmatrix}^\top,\ \mathcal{U}^g_1 = \begin{bmatrix} u_{x_1} & u_{y_1} \end{bmatrix}^\top,\ \mathcal{U}^g_2 = \begin{bmatrix} u_{x_2} & u_{y_2} \end{bmatrix}^\top,\ \dots \tag{7.7}$$

with superscript g henceforth defined to refer to global quantities and $\top$ denoting the matrix transpose. By defining

$$\boldsymbol{f}^g_u = \begin{bmatrix} \boldsymbol{I}_2 & \boldsymbol{Z}_2 & \boldsymbol{Z}^2_2 & \dots \end{bmatrix} \quad \text{and} \quad \boldsymbol{f}^l_u = \begin{bmatrix} \phi^{(k)}_x & 0 \\ 0 & \phi^{(k)}_y \end{bmatrix}, \tag{7.8}$$

$$\mathcal{U}^g = \begin{bmatrix} \mathcal{U}^g_0 & \mathcal{U}^g_1 & \mathcal{U}^g_2 & \dots \end{bmatrix}^\top \quad \text{and} \quad \mathcal{U}^l = \begin{bmatrix} u^{\phi}_x & u^{\phi}_y \end{bmatrix}^\top \tag{7.9}$$

where superscript l is henceforth defined to refer to local ZZ quantities, Eq. (7.5) now reads

$$\mathcal{U}_{xy}^{(k)} = \boldsymbol{f}_u^g \mathcal{U}^g + \boldsymbol{f}_u^l \mathcal{U}^l = \begin{bmatrix} \boldsymbol{f}_u^g & \boldsymbol{f}_u^l \end{bmatrix} \begin{Bmatrix} \mathcal{U}^g \\ \mathcal{U}^l \end{Bmatrix} = \boldsymbol{f}_u^{(k)} \mathcal{U} \tag{7.10}$$

The in-plane strains ϵ in Voigt-Kelvin vector notation are now derived from the kinematic relations,

$$\epsilon = \begin{Bmatrix} \epsilon_x \\ \epsilon_y \\ \epsilon_{xy} \end{Bmatrix} = \begin{Bmatrix} \dfrac{\partial u_x}{\partial x} \\ \dfrac{\partial u_y}{\partial y} \\ \dfrac{\partial u_x}{\partial y} + \dfrac{\partial u_y}{\partial x} \end{Bmatrix} = \begin{bmatrix} \dfrac{\partial}{\partial x} & 0 \\ 0 & \dfrac{\partial}{\partial y} \\ \dfrac{\partial}{\partial y} & \dfrac{\partial}{\partial x} \end{bmatrix} \begin{Bmatrix} u_x \\ u_y \end{Bmatrix} = \boldsymbol{D}\mathcal{U}_{xy} \tag{7.11}$$

where a new differential operator matrix $\boldsymbol{D}$ has been defined. Substituting the expression for $\mathcal{U}_{xy}$ from Eq. (7.10) into the kinematic relations Eq. (7.11) gives

$$\epsilon^{(k)} = \begin{bmatrix} \boldsymbol{I}_3 & \boldsymbol{Z}_3 & \boldsymbol{Z}_3^2 & \dots \end{bmatrix} \begin{bmatrix} \boldsymbol{D} & 0 & 0 & \dots \\ 0 & \boldsymbol{D} & 0 & \dots \\ 0 & 0 & \boldsymbol{D} & \dots \\ \vdots & \vdots & \vdots & \ddots \end{bmatrix} \begin{Bmatrix} \mathcal{U}_0^g \\ \mathcal{U}_1^g \\ \mathcal{U}_2^g \\ \vdots \end{Bmatrix} +$$

$$\begin{bmatrix} \phi_x^{(k)} & 0 & 0 & 0 \\ 0 & \phi_y^{(k)} & 0 & 0 \\ 0 & 0 & \phi_x^{(k)} & \phi_y^{(k)} \end{bmatrix} \begin{bmatrix} \dfrac{\partial}{\partial x} & 0 \\ 0 & \dfrac{\partial}{\partial y} \\ \dfrac{\partial}{\partial y} & 0 \\ 0 & \dfrac{\partial}{\partial x} \end{bmatrix} \begin{Bmatrix} u_x^\phi \\ u_y^\phi \end{Bmatrix} + \left(\begin{bmatrix} \dfrac{\partial}{\partial x} & 0 \\ 0 & \dfrac{\partial}{\partial y} \\ \dfrac{\partial}{\partial y} & \dfrac{\partial}{\partial x} \end{bmatrix} \begin{bmatrix} \phi_x^{(k)} & 0 \\ 0 & \phi_y^{(k)} \end{bmatrix} \right) \begin{Bmatrix} u_x^\phi \\ u_y^\phi \end{Bmatrix} \tag{7.12}$$

where $\boldsymbol{I}_3$, $\boldsymbol{Z}_3$, $\boldsymbol{Z}_3^2$ etc. are 3x3 versions of the 2x2 matrices defined in Eq. (7.6), and the differential operator matrix in the third term of Eq. (7.12) is only applied on the ZZ function matrix within the parentheses. Note that this particular term in parentheses vanishes when MZZF is used. By defining

$$\boldsymbol{f}_\epsilon^g = \begin{bmatrix} \boldsymbol{I}_3 & \boldsymbol{Z}_3 & \boldsymbol{Z}_3^2 & \dots \end{bmatrix} \quad \text{and} \quad \boldsymbol{f}_\epsilon^l = \begin{bmatrix} \phi_x^{(k)} & 0 & 0 & 0 \\ 0 & \phi_y^{(k)} & 0 & 0 \\ 0 & 0 & \phi_x^{(k)} & \phi_y^{(k)} \end{bmatrix}, \tag{7.13}$$

$$\boldsymbol{D}^g = \begin{bmatrix} \boldsymbol{D} & 0 & 0 & \dots \\ 0 & \boldsymbol{D} & 0 & \dots \\ 0 & 0 & \boldsymbol{D} & \dots \\ \vdots & \vdots & \vdots & \ddots \end{bmatrix} \quad \text{and} \quad \boldsymbol{D}^l = \begin{bmatrix} \dfrac{\partial}{\partial x} & 0 \\ 0 & \dfrac{\partial}{\partial y} \\ \dfrac{\partial}{\partial y} & 0 \\ 0 & \dfrac{\partial}{\partial x} \end{bmatrix} \tag{7.14}$$

Eq. (7.12) is simplified to

$$\epsilon^{(k)} = \boldsymbol{f}_\epsilon^g \left(\boldsymbol{D}^g \mathcal{U}^g \right) + \boldsymbol{f}_\epsilon^l \left(\boldsymbol{D}^l \mathcal{U}^l \right) + \left(\boldsymbol{D} \boldsymbol{f}_u^l \right) \mathcal{U}^l. \tag{7.15}$$

Finally, by defining the global and local strain fields ϵ^g and ϵ^l, respectively,

$$\epsilon^g = \boldsymbol{D}^g \mathcal{U}^g \quad \text{and} \quad \epsilon^l = \boldsymbol{D}^l \mathcal{U}^l \tag{7.16}$$

the strain can simply be expressed as

$$\epsilon^{(k)} = \begin{bmatrix} \boldsymbol{f}_\epsilon^g & \boldsymbol{f}_\epsilon^l & \boldsymbol{D}\boldsymbol{f}_u^l \end{bmatrix} \begin{Bmatrix} \epsilon^g \\ \epsilon^l \\ \mathcal{U}^l \end{Bmatrix} = \boldsymbol{f}_\epsilon^{(k)} \mathcal{E}. \tag{7.17}$$

As a result, the in-plane strains are now defined as a product of a through-thickness function $\boldsymbol{f}_\epsilon^{(k)}$ and unknown field variables $\mathcal{E}$. Note that when MZZF is used $\boldsymbol{D}\boldsymbol{f}_u^l = \boldsymbol{0}$ and therefore the variables $\mathcal{U}^l$ in $\mathcal{E}$ are eliminated.

The in-plane stresses σ written in Voigt-Kelvin vector notation are now calculated from the strains using the reduced stiffness matrix $\bar{\boldsymbol{Q}}$ for plane stress in z. Hence,

$$\sigma^{(k)} = \begin{Bmatrix} \sigma_x \\ \sigma_y \\ \sigma_{xy} \end{Bmatrix}^{(k)} = \begin{bmatrix} \bar{Q}_{11} & \bar{Q}_{12} & \bar{Q}_{16} \\ \bar{Q}_{12} & \bar{Q}_{22} & \bar{Q}_{26} \\ \bar{Q}_{16} & \bar{Q}_{26} & \bar{Q}_{66} \end{bmatrix}^{(k)} \begin{Bmatrix} \epsilon_x \\ \epsilon_y \\ \epsilon_{xy} \end{Bmatrix}^{(k)} = \bar{\boldsymbol{Q}}^{(k)} \epsilon^{(k)} = \bar{\boldsymbol{Q}}^{(k)} \boldsymbol{f}_\epsilon^{(k)} \mathcal{E}. \tag{7.18}$$

The stress resultants $\mathcal{F}$ are defined as the through-thickness integrals of the in-plane stresses $\sigma^{(k)}$ multiplied by the assumed strain field function $\boldsymbol{f}_\epsilon^{(k)}$. As the in-plane stress dyad $\boldsymbol{\sigma} = \sigma_{ij},\ i,j = x,y$ has been written as a vector in Voigt-Kelvin notation, i.e. $\sigma^{(k)} = (\sigma_x, \sigma_y, \sigma_{xy})$, $\mathcal{F}$ is a collection of stress resultants written in Voigt-Kelvin notation as well. Thus,

$$\mathcal{F} = \int_{-t/2}^{t/2} \boldsymbol{f}_\epsilon^{(k)^\top} \sigma^{(k)} \mathrm{d}z = \int_{-t/2}^{t/2} \boldsymbol{f}_\epsilon^{(k)^\top} \bar{\boldsymbol{Q}}^{(k)} \boldsymbol{f}_\epsilon^{(k)} \mathrm{d}z \cdot \mathcal{E} = \boldsymbol{S} \cdot \mathcal{E} \tag{7.19}$$

where the first six terms of the column vector $\mathcal{F} = (N_x, N_y, N_{xy}, M_x, M_y, M_{xy}, \dots)$ are the classical membrane forces and bending moments $\mathcal{N} = (N_x, N_y, N_{xy})$ and $\mathcal{M} = (M_x, M_y, M_{xy})$, and the following terms in $\mathcal{F}$ are higher-order moments.

In general, the orders of expansion in the x- and y-directions are chosen to be the same, such that $N_{o_x} = N_{o_y} = N_o$. In this case, the length $\mathcal{O}$ of the stress resultant vector $\mathcal{F}$ is given by:

- Global expansion up to z^{N_o}, no ZZ variables: $\mathcal{O} = 3\,(N_o + 1)$
- Global expansion up to z^{N_o}, MZZF: $\mathcal{O} = 3\,(N_o + 1) + 3$
- Global expansion up to z^{N_o}, RZT: $\mathcal{O} = 3\,(N_o + 1) + 6$. Note, $\mathcal{O} = 3\,(N_o + 1) + 4$ for straight-fibre laminates.

Thus, a model based on RZT can lead up to three more variables in $\mathcal{F}$ than a model based on MZZF. In the general case of RZT $\phi_x^{(k)} \neq \phi_y^{(k)}$, and therefore the ZZ twisting moments

$$M_{xy}^\phi = \int_{-t/2}^{t/2} \phi_x^{(k)} \sigma_{xy}^{(k)} \mathrm{d}z \quad \neq \quad M_{yx}^\phi = \int_{-t/2}^{t/2} \phi_y^{(k)} \sigma_{xy}^{(k)} \mathrm{d}z, \tag{7.20}$$

whereas for MZZF $M^{\phi}_{xy} = M^{\phi}_{yx}$. Second, in the general case of varying material properties over the planform, e.g. for tow-steered laminates, the RZT coefficient matrix $\boldsymbol{D}\boldsymbol{f}^{l}_{u} \neq \boldsymbol{0}$, which leads to two extra moments associated with the derivatives of the ZZ function. Hence,

$$M^{\partial\phi}_{x} = \int_{-t/2}^{t/2} \left(\frac{\partial \phi^{(k)}_{x}}{\partial x}\sigma_x + \frac{\partial \phi^{(k)}_{x}}{\partial y}\sigma_{xy} \right) \mathrm{d}z \quad \text{and} \quad M^{\partial\phi}_{y} = \int_{-t/2}^{t/2} \left(\frac{\partial \phi^{(k)}_{y}}{\partial y}\sigma_y + \frac{\partial \phi^{(k)}_{y}}{\partial x}\sigma_{xy} \right) \mathrm{d}z \tag{7.21}$$

and therefore, combined with the fact that $M^{\phi}_{xy} \neq M^{\phi}_{yx}$, RZT defines three more stress resultants than MZZF.

Finally, matrix $\boldsymbol{S}$ in Eq. (7.19) is the higher-order ABD stiffness matrix of dimensions $\mathcal{O} \times \mathcal{O}$ defined by

$$\boldsymbol{S} = \int_{-t/2}^{t/2} \boldsymbol{f}^{(k)\top}_{\epsilon} \bar{\boldsymbol{Q}}^{(k)} \boldsymbol{f}^{(k)}_{\epsilon} \mathrm{d}z \tag{7.22}$$

which can be inverted to express the unknown strain field $\mathcal{E}$ in Eq. (7.19) in terms of the stress resultants $\mathcal{F}$. Hence,

$$\mathcal{E} = \boldsymbol{S}^{-1}\mathcal{F} = \boldsymbol{s}\mathcal{F} \quad \text{where} \quad \boldsymbol{s} = \boldsymbol{S}^{-1}. \tag{7.23}$$

Thus, we have derived a general expression for the layerwise in-plane stresses $\sigma^{(k)}$ given by

$$\sigma^{(k)} = \bar{\boldsymbol{Q}}^{(k)} \boldsymbol{f}^{(k)}_{\epsilon} \boldsymbol{s}\mathcal{F} \tag{7.24}$$

in terms of layerwise constitutive matrices $\bar{\boldsymbol{Q}}^{(k)}$, the higher-order compliance matrix $\boldsymbol{s}$, through-thickness shape functions $\boldsymbol{f}^{(k)}_{\epsilon}$ and the stress resultants $\mathcal{F}$, where the latter are the only functional unknowns. Note, the advantage of expressing the in-plane stresses in terms of stress resultants rather than displacements, is that the stresses are now functions of the unknown variables themselves rather than their derivatives, and this helps to reduce the order of the derived differential equations. In general, lower-order differential equations can be solved with less numerical discretisation error.

7.2 Derivation of transverse shear stress fields

An expression for the transverse shear stresses is found by integrating the axial stresses of Eq. (7.24) in Cauchy's in-plane equilibrium equations in the absence of body forces,

$$\left.\begin{aligned} \frac{\partial \sigma^{(k)}_{xz}}{\partial z} &= -\frac{\partial \sigma^{(k)}_{x}}{\partial x} - \frac{\partial \sigma^{(k)}_{xy}}{\partial y} \\ \frac{\partial \sigma^{(k)}_{yz}}{\partial z} &= -\frac{\partial \sigma^{(k)}_{xy}}{\partial x} - \frac{\partial \sigma^{(k)}_{y}}{\partial y} \end{aligned}\right\} \Rightarrow \frac{\partial \tau^{(k)}}{\partial z} = \frac{\partial}{\partial z}\begin{Bmatrix} \sigma_{xz} \\ \sigma_{yz} \end{Bmatrix}^{(k)} = -\begin{bmatrix} \frac{\partial}{\partial x} & 0 & \frac{\partial}{\partial y} \\ 0 & \frac{\partial}{\partial y} & \frac{\partial}{\partial x} \end{bmatrix} \begin{Bmatrix} \sigma_x \\ \sigma_y \\ \sigma_{xy} \end{Bmatrix}^{(k)}$$

$$\frac{\partial \tau^{(k)}}{\partial z} = -\boldsymbol{D}^{\top}\sigma^{(k)} = -\boldsymbol{D}^{\top}\left[\bar{\boldsymbol{Q}}^{(k)} \boldsymbol{f}^{(k)}_{\epsilon} \boldsymbol{s}\mathcal{F}\right]. \tag{7.25}$$

Note, the differential operator matrix $\boldsymbol{D}^{\top}$ is applied to all terms within the square brackets as both the material dependent quantities $\bar{\boldsymbol{Q}}^{(k)}$, $\boldsymbol{f}^{(k)}_{\epsilon}$ and $\boldsymbol{s}$, as well as the stress resultants $\mathcal{F}$ can vary over the domain Ω of a plate with curvilinear fibres. The only term in Eq. (7.25) that is a function of z is $\boldsymbol{f}^{(k)}_{\epsilon}$ and therefore only this term is integrated to derive the transverse shear

stresses. Hence,

$$\tau^{(k)} = -\boldsymbol{D}^\top \left[\bar{\boldsymbol{Q}}^{(k)} \left(\int \boldsymbol{f}_\epsilon^{(k)}(z)\mathrm{d}z\right) \boldsymbol{s}\mathcal{F}\right] = -\boldsymbol{D}^\top \left[\bar{\boldsymbol{Q}}^{(k)} \boldsymbol{g}^{(k)}(z)\boldsymbol{s}\mathcal{F}\right] + \boldsymbol{a}^{(k)} \tag{7.26}$$

where $\boldsymbol{g}^{(k)}(z)$ captures the variation of $\tau^{(k)}$ through the thickness of each ply k and is derived by simple integration of the local and global polynomial shape functions.

The N_l layerwise constants $\boldsymbol{a}^{(k)}$ are found by enforcing the $N_l - 1$ interfacial continuity conditions $\tau^{(k)}(z_{k-1}) = \tau^{(k-1)}(z_{k-1})$ for $k = 2, \ldots, N_l$, and one of the prescribed surface tractions, i.e. either the bottom surface $\tau^{(1)}(z_0) = \hat{T}_b = \begin{bmatrix}\hat{T}_{bx} & \hat{T}_{by}\end{bmatrix}^\top$ or the top surface $\tau^{(N_l)}(z_{N_l}) = \hat{T}_t = \begin{bmatrix}\hat{T}_{tx} & \hat{T}_{ty}\end{bmatrix}^\top$ tractions. Here, we choose to enforce the bottom surface tractions, such that the layerwise constants are found to be

$$\boldsymbol{a}^{(k)} = \sum_{i=1}^{k} \boldsymbol{D}^\top \left[\left\{\bar{\boldsymbol{Q}}^{(i)}\boldsymbol{g}^{(i)}(z_{i-1}) - \bar{\boldsymbol{Q}}^{(i-1)}\boldsymbol{g}^{(i-1)}(z_{i-1})\right\} \boldsymbol{s}\mathcal{F}\right] + \hat{T}_b = \boldsymbol{D}^\top \left[\boldsymbol{\alpha}^{(k)}\boldsymbol{s}\mathcal{F}\right] + \hat{T}_b \tag{7.27}$$

where by definition $\bar{\boldsymbol{Q}}^0 = \boldsymbol{0}$ and the variable

$$\boldsymbol{\alpha}^{(k)} = \sum_{i=1}^{k} \left\{\bar{\boldsymbol{Q}}^{(i)}\boldsymbol{g}^{(i)}(z_{i-1}) - \bar{\boldsymbol{Q}}^{(i-1)}\boldsymbol{g}^{(i-1)}(z_{i-1})\right\} \tag{7.28}$$

has been introduced. Additional physical insight into the layerwise integration constants $\boldsymbol{\alpha}^{(k)}$ can be gleaned when considering that the higher-order ABD matrix defined in Eq. (7.22) is equal to the through-thickness integral of layerwise constitutive matrices $\bar{\boldsymbol{Q}}^{(k)}$ multiplied by shape functions $\boldsymbol{f}_\epsilon^{(k)}$. As $\boldsymbol{g}^{(k)}$ is equal to the indefinite integral of $\boldsymbol{f}_\epsilon^{(k)}$, the $\boldsymbol{\alpha}^{(k)}$ terms can be interpreted as the partial higher-order ABD matrices up to the kth layer.

The final expression for $\tau^{(k)}$ is established by substituting the layerwise integration constants of Eq. (7.27) back into Eq. (7.26). Thus,

$$\tau^{(k)} = \boldsymbol{D}^\top \left[\left(-\bar{\boldsymbol{Q}}^{(k)}\boldsymbol{g}^{(k)}(z) + \boldsymbol{\alpha}^{(k)}\right) \boldsymbol{s}\mathcal{F}\right] + \hat{T}_b. \tag{7.29}$$

In the derivation of Eq. (7.27), the surface traction on the top surface is not enforced explicitly. As the proof below shows, this condition is automatically satisfied if equilibrium of the axial stress field Eq. (7.24) and transverse shear stress Eq. (7.29) is enforced. As we are dealing with an equivalent single layer, Cauchy's two in-plane equilibrium equations in the absence of body forces are integrated in the thickness z-direction to give

$$\int_{-t/2}^{t/2} \left(\boldsymbol{D}^\top \sigma^{(k)} + \frac{\partial \tau^{(k)}}{\partial z}\right) \mathrm{d}z = \boldsymbol{D}^\top \mathcal{N} + \tau^{(N_l)}(z_{N_l}) - \tau^{(1)}(z_0) = \boldsymbol{0} \tag{7.30}$$

where the column vector $\mathcal{N} = (N_x, N_y, N_{xy})$ represents the membrane stress resultants. An expression for $\boldsymbol{D}^\top \mathcal{N}$ is easily derived by applying the differential operator matrix $\boldsymbol{D}^\top$ to the

expression for $\sigma^{(k)}$ in Eq. (7.24) and then integrating in the z-direction. Hence,

$$\boldsymbol{D}^\top \mathcal{N} = \int_{-t/2}^{t/2} \boldsymbol{D}^\top \sigma^{(k)} \mathrm{d}z = \sum_{k=1}^{N_l} \boldsymbol{D}^\top \left[\left\{ \bar{\boldsymbol{Q}}^{(k)} \boldsymbol{g}^{(k)}(z_k) - \bar{\boldsymbol{Q}}^{(k)} \boldsymbol{g}^{(k)}(z_{k-1}) \right\} \boldsymbol{s}\mathcal{F} \right]. \tag{7.31}$$

Now, the only undefined quantity in Eq. (7.30) is $\tau^{(N_l)}(z_{N_l})$ and an expression for this is sought using the expression for $\tau^{(k)}$ in Eq. (7.29),

$$\begin{aligned} \tau^{(N_l)}(z_{N_l}) &= \boldsymbol{D}^\top \left[\left\{ -\bar{\boldsymbol{Q}}^{(N_l)} \boldsymbol{g}^{(N_l)}(z_{N_l}) + \boldsymbol{\alpha}^{(N_l)} \right\} \boldsymbol{s}\mathcal{F} \right] + \hat{T}_b \\ &= -\sum_{k=1}^{N_l} \boldsymbol{D}^\top \left[\left\{ \bar{\boldsymbol{Q}}^{(k)} \boldsymbol{g}^{(k)}(z_k) - \bar{\boldsymbol{Q}}^{(k)} \boldsymbol{g}^{(k)}(z_{k-1}) \right\} \boldsymbol{s}\mathcal{F} \right] + \hat{T}_b. \end{aligned}$$

Substituting Eq. (7.31) into the above expression we have

$$\tau^{(N_l)}(z_{N_l}) = -\boldsymbol{D}^\top \mathcal{N} + \hat{T}_b \tag{7.32}$$

and substituting Eq. (7.32) back into Cauchy's equilibrium Eq. (7.30) gives

$$\boldsymbol{D}^\top \mathcal{N} + \left(-\boldsymbol{D}^\top \mathcal{N} + \hat{T}_b \right) - \tau^{(1)}(z_0) = \boldsymbol{0}. \tag{7.33}$$

Hence, as $\tau^{(1)}(z_0) = \hat{T}_b$ the expression in Eq. (7.33) is satisfied. This is the first important characteristic of the higher-order model presented herein; as long as Cauchy's in-plane equilibrium equations Eq. (7.30) are satisfied when deriving the governing equations from a variational statement, equilibrium of the interfacial and surface shear tractions is automatically guaranteed *a priori* using the stress assumptions in Eqs. (7.24) and (7.29).

Finally, the layerwise coefficients in the expression for $\tau^{(k)}$ in Eq. (7.29), namely $-\bar{\boldsymbol{Q}}^{(k)} \boldsymbol{g}^{(k)} + \boldsymbol{\alpha}^{(k)}$ are conveniently combined into a single layerwise vector $\boldsymbol{c}^{(k)}(z)$, such that

$$\tau^{(k)} = \boldsymbol{D}^\top \left[\boldsymbol{c}^{(k)} \boldsymbol{s}\mathcal{F} \right] + \hat{T}_b. \tag{7.34}$$

To shed some further insight into the above equation of the transverse shear stresses, the term $\boldsymbol{R}^{(k)} = \boldsymbol{c}^{(k)} \boldsymbol{s}$ is defined and the differential product rule is applied to expand the term

$$\begin{aligned} \boldsymbol{D}^\top \left(\boldsymbol{c}^{(k)} \boldsymbol{s}\mathcal{F} \right) = \boldsymbol{D}^\top \left(\boldsymbol{R}^{(k)} \mathcal{F} \right) &= \left(\boldsymbol{D}^\top \boldsymbol{R}^{(k)} \right) \mathcal{F} + \boldsymbol{I}_x \boldsymbol{R}^{(k)} \frac{\partial \mathcal{F}}{\partial x} + \boldsymbol{I}_y \boldsymbol{R}^{(k)} \frac{\partial \mathcal{F}}{\partial y} \\ &= \left(\boldsymbol{D}^\top \boldsymbol{R}^{(k)} \right) \mathcal{F} + \boldsymbol{R}_x^{(k)} \frac{\partial \mathcal{F}}{\partial x} + \boldsymbol{R}_y^{(k)} \frac{\partial \mathcal{F}}{\partial y} \end{aligned} \tag{7.35}$$

where the parentheses in the first term indicate that the differential operator matrix $\boldsymbol{D}^\top$ is only applied to matrix $\boldsymbol{R}^{(k)}$, and the matrices

$$\boldsymbol{I}_x = \begin{bmatrix} 1 & 0 & 0 \\ 0 & 0 & 1 \end{bmatrix} \text{ and } \boldsymbol{I}_y = \begin{bmatrix} 0 & 0 & 1 \\ 0 & 1 & 0 \end{bmatrix} \tag{7.36}$$

have been introduced to allow the partial derivatives $\partial/\partial x$ and $\partial/\partial y$ to be applied directly to $\mathcal{F}$ with coefficients of $\boldsymbol{R}_x^{(k)} = \boldsymbol{I}_x \boldsymbol{R}^{(k)}$ and $\boldsymbol{R}_y^{(k)} = \boldsymbol{I}_y \boldsymbol{R}^{(k)}$. By substituting Eq. (7.35) into

Eq. (7.34), an alternative definition of $\tau^{(k)}$ in terms of the layerwise constitutive matrices $\boldsymbol{R}^{(k)}$, $\boldsymbol{R}_x^{(k)}$ and $\boldsymbol{R}_y^{(k)}$ is derived,

$$\tau^{(k)} = \left(\boldsymbol{D}^\top \boldsymbol{R}^{(k)}\right)\mathcal{F} + \boldsymbol{R}_x^{(k)}\frac{\partial \mathcal{F}}{\partial x} + \boldsymbol{R}_y^{(k)}\frac{\partial \mathcal{F}}{\partial y} + \hat{T}_b. \tag{7.37}$$

The significance of Eq. (7.37) is two-fold. First, separating the derivatives of $\mathcal{F}$ allows for straightforward manipulations of the integration by parts step involved in the calculus of variations. Second, the first term $\boldsymbol{D}^\top \boldsymbol{R}^{(k)}$ in Eq. (7.37) is only non-zero for variable-stiffness laminates as it includes derivatives of material properties $\boldsymbol{R}^{(k)}$. Thus, Eq. (7.37) decomposes the contributions of the transverse shear stresses into variable-stiffness and constant-stiffness components.

7.3 Derivation of transverse normal stress field

An expression for the transverse normal stress is derived in a similar fashion by integrating Cauchy's transverse equilibrium equation in the absence of body forces. Thus,

$$\frac{\partial \sigma_z^{(k)}}{\partial z} = -\begin{bmatrix}\frac{\partial}{\partial x} & \frac{\partial}{\partial y}\end{bmatrix}\begin{Bmatrix}\sigma_{xz}^{(k)}\\ \sigma_{yz}^{(k)}\end{Bmatrix} = -\nabla^\top \tau^{(k)}$$

where $\nabla = \left(\frac{\partial}{\partial x}, \frac{\partial}{\partial y}\right)$ is the del operator used to calculate the divergence of $\tau^{(k)}$. By integrating in the z-direction,

$$\begin{aligned}\sigma_z^{(k)} &= \nabla^\top \boldsymbol{D}^\top \left[\int \left(\bar{\boldsymbol{Q}}^{(k)}\boldsymbol{g}^{(k)}(z) - \boldsymbol{\alpha}^{(k)}\right)\mathrm{d}z\boldsymbol{s}\mathcal{F}\right] - \nabla^\top \hat{T}_b z\\ &= \nabla^\top \boldsymbol{D}^\top \left[\left\{\bar{\boldsymbol{Q}}^{(k)}\boldsymbol{h}^{(k)}(z) - \boldsymbol{\alpha}^{(k)}z\right\}\boldsymbol{s}\mathcal{F}\right] - \nabla^\top \hat{T}_b z + \boldsymbol{b}^{(k)}\end{aligned} \tag{7.38}$$

where $\boldsymbol{h}^{(k)}(z)$ captures the variation of $\sigma_z^{(k)}$ through the thickness of each ply k and is readily derived by integrating the assumed polynomial shape functions.

The N_l layerwise constants $\boldsymbol{b}^{(k)}$ are found by enforcing the $N_l - 1$ continuity conditions $\sigma_z^{(k)}(z_{k-1}) = \sigma_z^{(k-1)}(z_{k-1})$ for $k = 2, \ldots, N_l$, and one of the prescribed surface tractions, i.e. either the bottom surface $\sigma_z^{(1)}(z_0) = \hat{P}_b$ or the top surface $\sigma_z^{(N_l)}(z_{N_l}) = \hat{P}_t$ traction. Here, we choose to enforce the bottom traction condition, such that the integration constants are

$$\begin{aligned}\boldsymbol{b}^{(k)} &= \nabla^\top \boldsymbol{D}^\top \sum_{i=1}^{k}\left[\left\{\bar{\boldsymbol{Q}}^{(i-1)}\boldsymbol{h}^{(i-1)}(z_{i-1}) - \bar{\boldsymbol{Q}}^{(i)}\boldsymbol{h}^{(i)}(z_{i-1}) + \left(\boldsymbol{\alpha}^{(i)} - \boldsymbol{\alpha}^{(i-1)}\right)z_{i-1}\right\}\boldsymbol{s}\mathcal{F}\right] +\\ &\quad \nabla^\top \hat{T}_b z_0 + \hat{P}_b\\ &= \nabla^\top \boldsymbol{D}^\top \left[\boldsymbol{\beta}^{(k)}\boldsymbol{s}\mathcal{F}\right] + \nabla^\top \hat{T}_b z_0 + \hat{P}_b\end{aligned} \tag{7.39}$$

where by definition $\bar{\boldsymbol{Q}}^0 = \boldsymbol{\alpha}^0 = \boldsymbol{0}$ and the variable $\boldsymbol{\beta}^{(k)}$ has been introduced where

$$\boldsymbol{\beta}^{(k)} = \sum_{i=1}^{k}\left\{\bar{\boldsymbol{Q}}^{(i-1)}\boldsymbol{h}^{(i-1)}(z_{i-1}) - \bar{\boldsymbol{Q}}^{(i)}\boldsymbol{h}^{(i)}(z_{i-1}) + \left(\boldsymbol{\alpha}^{(i)} - \boldsymbol{\alpha}^{(i-1)}\right)z_{i-1}\right\}. \tag{7.40}$$

The final expression for $\sigma_z^{(k)}$ is established by substituting the layerwise integration constants of Eq. (7.39) back into Eq. (7.38). Thus,

$$\sigma_z^{(k)} = \nabla^\top \boldsymbol{D}^\top \left[\left\{ \bar{\boldsymbol{Q}}^{(k)} \boldsymbol{h}^{(k)}(z) - \boldsymbol{\alpha}^{(k)} z + \boldsymbol{\beta}^{(k)} \right\} \boldsymbol{s}\mathcal{F} \right] - \nabla^\top \hat{T}_b \left(z - z_0 \right) + \hat{P}_b. \tag{7.41}$$

In the derivation of the layerwise integration constants of Eq. (7.39), the surface traction $\hat{P}_t$ on the top surface is not enforced explicitly. As the proof below shows, this condition is automatically satisfied if equilibrium of the transverse shear stress field Eq. (7.29) and transverse normal stress Eq. (7.41) is enforced. As we are dealing with an equivalent single layer, Cauchy's transverse equilibrium equation is integrated through the thickness to give

$$\int_{-t/2}^{t/2} \left(\nabla^\top \tau^{(k)} + \frac{\partial \sigma_z^{(k)}}{\partial z} \right) \mathrm{d}z = \nabla^\top \mathcal{Q} + \sigma_z^{(N_l)}(z_{N_l}) - \sigma_z^{(1)}(z_0) = 0 \tag{7.42}$$

where $\mathcal{Q} = (Q_{xz}, Q_{yz})$ are the transverse shear forces. An expression for $\nabla^\top \mathcal{Q}$ is derived by taking the divergence of $\tau^{(k)}$ in Eq. (7.29) and integrating in the z-direction. Thus,

$$\begin{aligned} \nabla^\top \mathcal{Q} &= \int_{-t/2}^{t/2} \nabla^\top \tau^{(k)} \mathrm{d}z \\ &= \nabla^\top \boldsymbol{D}^\top \sum_{k=1}^{N_l} \left[\left\{ \bar{\boldsymbol{Q}}^{(k)} \left(\boldsymbol{h}^{(k)}(z_{k-1}) - \boldsymbol{h}^{(k)}(z_k) \right) + \boldsymbol{\alpha}^{(k)} t^{(k)} \right\} \boldsymbol{s}\mathcal{F} \right] + \nabla^\top \hat{T}_b \sum_{k=1}^{N_l} t^{(k)} \end{aligned} \tag{7.43}$$

where $t^{(k)}$ is the thickness of the kth layer. Now, an expression for $\sigma_z^{(N_l)}(z_{N_l})$ is found by substituting $z = z_{N_l}$ into the expression for $\sigma_z^{(k)}$ of Eq. (7.41),

$$\begin{aligned} \sigma_z^{(N_l)}(z_{N_l}) &= \nabla^\top \boldsymbol{D}^\top \left[\left\{ \bar{\boldsymbol{Q}}^{(N_l)} \boldsymbol{h}^{(N_l)}(z_{N_l}) - \boldsymbol{\alpha}^{(N_l)} z_{N_l} + \boldsymbol{\beta}^{(N_l)} \right\} \boldsymbol{s}\mathcal{F} \right] - \nabla^\top \hat{T}_b \left(z_{N_l} - z_0 \right) + \hat{P}_b \\ &= \nabla^\top \boldsymbol{D}^\top \sum_{k=1}^{N_l} \left[\left\{ \bar{\boldsymbol{Q}}^{(k)} \left(\boldsymbol{h}^{(k)}(z_k) - \boldsymbol{h}^{(k)}(z_{k-1}) \right) - \boldsymbol{\alpha}^{(k)} t^{(k)} \right\} \boldsymbol{s}\mathcal{F} \right] - \nabla^\top \hat{T}_b \sum_{k=1}^{N_l} t^{(k)} + \hat{P}_b. \end{aligned}$$

By consideration of Eq. (7.43), the above expression is transformed into

$$\sigma_z^{(N_l)}(z_{N_l}) = -\nabla^\top \mathcal{Q} + \hat{P}_b \tag{7.44}$$

such that by substituting Eq. (7.44) back into Cauchy's single-layer equilibrium Eq. (7.42),

$$\nabla^\top \mathcal{Q} + \left(-\nabla^\top \mathcal{Q} + \hat{P}_b \right) - \sigma_z^{(1)}(z_0) = 0. \tag{7.45}$$

Hence, as $\sigma_z^{(1)}(z_0) = \hat{P}_b$ the expression in Eq. (7.45) is satisfied. This is the second significant characteristic of the present higher-order model; as long as Eq. (7.42) is satisfied when deriving the governing field equations and boundary conditions from a variational statement, equilibrium of the interfacial and surface normal tractions is automatically enforced *a priori* using the stress assumptions in Eqs. (7.24), (7.29) and (7.41).

Finally, the layerwise coefficients in the expression for $\sigma_z^{(k)}$ in Eq. (7.41) are conveniently

combined into a single layerwise vector, such that

$$\sigma_z^{(k)} = \nabla^\top \boldsymbol{D}^\top \left[\boldsymbol{d}^{(k)} \boldsymbol{s} \mathcal{F}\right] - \nabla^\top \hat{T}_b \left(z - z_0\right) + \hat{P}_b. \tag{7.46}$$

7.4 Governing equations from the Hellinger-Reissner mixed-variational statement

The HR mixed-variational statement for a 3D continuum was introduced in Eq. (2.19) of Chapter 2. In the HR principle, the PMCE functional is enhanced by enforcing Cauchy's equilibrium equations and natural boundary conditions using displacement Lagrange multipliers. Hence,

$$\Pi_{HR}(\boldsymbol{u}, \boldsymbol{\sigma}) = \int_V U_0^*(\sigma_{ij}) \mathrm{d}V - \int_{S_1} \hat{u}_i t_i \mathrm{d}S + \int_V u_i \left(\sigma_{ij,j} + f_i\right) \mathrm{d}V - \int_{S_2} u_i \left(t_i - \hat{t}_i\right) \mathrm{d}S \tag{7.47}$$

where $U_0^*(\sigma_{ij})$ is the complementary energy density written in terms of the Cauchy stress tensor σ_{ij}, and the displacements u_i are the Lagrange multipliers that enforce Cauchy's equilibrium equations $\sigma_{ij,j} + f_i$ in a variational sense throughout the volume of the continuum and the traction boundary conditions $t_i - \hat{t}_i$ on the boundary surface S_2. The tractions $t_i = \sigma_{ij} n_j = (\sigma_{nx}, \sigma_{ny}, \sigma_{nz})$ are the tractions in the (x, y, z) directions acting on the boundary surface with outward normal $\boldsymbol{n} = (n_x, n_y, n_z)$.

In the present work, the model assumption of the in-plane displacements is given by Eq. (7.10), i.e. $(u_x, u_y) = \boldsymbol{f}_u^{(k)} \mathcal{U}$, whereas the transverse displacement $u_z = w_0$ is constant throughout the thickness. Thus, the term associated with Cauchy's equilibrium equations in the HR functional in the absence of body forces is written as

$$\Pi_{\mathcal{L}} = \int_V u_i \sigma_{ij,j} \mathrm{d}V = \int_V \left[\mathcal{U}^\top \boldsymbol{f}_u^{(k)^\top} \left(\boldsymbol{D}^\top \sigma^{(k)} + \frac{\partial \tau^{(k)}}{\partial z}\right) + w_0 \left(\nabla^\top \tau^{(k)} + \frac{\partial \sigma_z^{(k)}}{\partial z}\right)\right] \mathrm{d}V \tag{7.48}$$

where all quantities are defined as in the previous two sections. Taking the first variation of this functional with respect to the displacement variables, i.e. $\delta\mathcal{U}$ and δw_0, results in the higher-order equilibrium equations of the theory. For example, by integrating the first term in Eq. (7.48) by parts in the z-direction and taking the first variation with respect to the displacement variables we have

$$\begin{aligned}
\delta\Pi_{\mathcal{L}_1} &= \iiint_{-t/2}^{t/2} \delta\mathcal{U}^\top \left(\boldsymbol{f}_u^{(k)^\top} \boldsymbol{D}^\top \sigma^{(k)} - \frac{\partial \boldsymbol{f}_u^{(k)^\top}}{\partial z} \tau^{(k)}\right) \mathrm{d}z\mathrm{d}y\mathrm{d}x + \iint \delta\mathcal{U}^\top \boldsymbol{f}_u^{(k)^\top} \tau^{(k)} \Big|_{-t/2}^{t/2} \mathrm{d}y\mathrm{d}x \\
&= \iint \delta\mathcal{U}^\top \left[\boldsymbol{D}^F \mathcal{F}^* - \mathcal{T} + \boldsymbol{f}_u^{(N_l)^\top}(z_{N_l}) \hat{T}_t - \boldsymbol{f}_u^{(1)^\top}(z_0) \hat{T}_b\right] \mathrm{d}y\mathrm{d}x
\end{aligned} \tag{7.49}$$

where we have made use of Eq. (7.19) that the stress resultants $\mathcal{F}$ are the z-direction integrals of the in-plane stresses $\sigma^{(k)}$ multiplied by through-thickness shape functions. The vector of stress resultants $\mathcal{F}^*$ used in Eq. (7.49) is the same as $\mathcal{F}$ defined in Eq. (7.19) but does not contain the stress resultants associated with the derivatives of the ZZ function $\phi_{,i}^{(k)}$, i.e. $M_x^{\partial\phi}$ and $M_y^{\partial\phi}$, as these do not feature in $\boldsymbol{f}_u^{(k)}$. Furthermore, $\boldsymbol{D}^F = \boldsymbol{I}_{N_o} \otimes \boldsymbol{D}^\top$ with $\otimes$ denoting the Kronecker

matrix product[2] and $\boldsymbol{I}_{N_o}$ the $(N_o+2)\times(N_o+2)$ identity matrix. Thus,

$$\boldsymbol{D}^F\mathcal{F}^* = \int_{-t/2}^{t/2} \boldsymbol{f}_u^{(k)^\top} \boldsymbol{D}^\top \sigma^{(k)} \mathrm{d}z. \tag{7.50}$$

Finally, a vector of transverse shear stress resultants, i.e. a vector of higher-order transverse shear forces
$\mathcal{T} = (0, 0, Q_x, Q_y, \ldots, Q_x^\phi, Q_y^\phi)$ that balances the gradients of the stress resultants $\mathcal{F}^*$ in the higher-order equilibrium equations, has been defined as follows:

$$\mathcal{T} = \int_{-t/2}^{t/2} \frac{\partial \boldsymbol{f}_u^{(k)^\top}}{\partial z} \tau^{(k)} \mathrm{d}z. \tag{7.51}$$

When the first variation is set to zero, the term in square brackets of Eq. (7.49) represents the collection of equilibrium equations of the equivalent single-layer written in matrix form. These are the same higher-order equilibrium equations that are derived from the assumed displacement field if the PVD is applied. For clarity, the equilibrium equations and associated Lagrange multipliers for a theory with $N_o = 1$ and ZZ functionality are

$$\begin{aligned}
\delta u_{x_0} &: N_{x,x} + N_{xy,y} + \hat{T}_{tx} - \hat{T}_{bx} = 0 \\
\delta u_{y_0} &: N_{xy,x} + N_{y,y} + \hat{T}_{ty} - \hat{T}_{by} = 0 \\
\delta u_{x_1} &: M_{x,x} + M_{xy,y} - Q_x + z_{N_l}\hat{T}_{tx} - z_0\hat{T}_{bx} = 0 \\
\delta u_{y_1} &: M_{xy,x} + M_{y,y} - Q_y + z_{N_l}\hat{T}_{ty} - z_0\hat{T}_{by} = 0 \\
\delta u_x^\phi &: M_{x,x}^\phi + M_{xy,y}^\phi - Q_x^\phi + \phi_x^{(N_l)}(z_{N_l})\hat{T}_{tx} - \phi_x^{(1)}(z_0)\hat{T}_{bx} = 0 \\
\delta u_y^\phi &: M_{xy,x}^\phi + M_{y,y}^\phi - Q_y^\phi + \phi_y^{(N_l)}(z_{N_l})\hat{T}_{ty} - \phi_y^{(1)}(z_0)\hat{T}_{by} = 0
\end{aligned} \tag{7.52}$$

where the comma notation is used to denote differentiation, (N_x, N_y, N_{xy}), (M_x, M_y, M_{xy}) and (Q_x, Q_y) are the classical membrane forces, bending moments and transverse shear forces respectively, whereas $(M_x^\phi, M_y^\phi, M_{xy}^\phi)$ and $(Q_x^\phi, Q_y^\phi,)$ are the ZZ bending moments and ZZ transverse shear forces, respectively.

For a general assumption of displacements $\boldsymbol{u}$ and stresses $\boldsymbol{\sigma}$, the entire set of higher-order equilibrium equations in the square brackets of Eq. (7.49) needs to be satisfied. However, in the present work, the in-plane stresses and transverse shear stresses are inherently equilibrated due to the *a priori* integration step in Cauchy's equilibrium equations. As shown in the following, this means that the equilibrium equations of Eq. (7.49) are, in fact, automatically satisfied and do not need to be enforced in the variational statement.

Returning to the definition of the transverse shear stress resultants and integrating by parts,

$$\mathcal{T} = \int_{-t/2}^{t/2} \frac{\partial \boldsymbol{f}_u^{(k)^\top}}{\partial z} \tau^{(k)} \mathrm{d}z = \boldsymbol{f}_u^{(k)^\top} \tau^{(k)} \Big|_{-t/2}^{t/2} - \int_{-t/2}^{t/2} \boldsymbol{f}_u^{(k)^\top} \frac{\partial \tau^{(k)}}{\partial z} \mathrm{d}z. \tag{7.53}$$

[2]If $\boldsymbol{A}$ is an $m\times n$ matrix and $\boldsymbol{B}$ is a $q\times r$ matrix, then the Kronecker matrix product $\boldsymbol{A}\otimes\boldsymbol{B}$ is the $mq\times nr$ block matrix $\boldsymbol{A}\otimes\boldsymbol{B} = \begin{bmatrix} A_{11}\boldsymbol{B} & \ldots & A_{1n}\boldsymbol{B} \\ \vdots & \ddots & \vdots \\ A_{m1}\boldsymbol{B} & \ldots & A_{mn}\boldsymbol{B} \end{bmatrix}$.

As the model assumption for the transverse shear stresses is derived exactly from Cauchy's equilibrium equations in Eq. (7.25), we can replace $\tau_{,z}^{(k)}$ with $-\boldsymbol{D}^\top \sigma^{(k)}$. Hence,

$$\mathcal{T} = \boldsymbol{f}_u^{(N_l)^\top}(z_{N_l})\hat{T}_t - \boldsymbol{f}_u^{(1)^\top}(z_0)\hat{T}_b + \int_{-t/2}^{t/2} \boldsymbol{f}_u^{(k)^\top} \boldsymbol{D}^\top \sigma^{(k)} \mathrm{d}z \tag{7.54}$$

and by using the expression in Eq. (7.50)

$$\mathcal{T} = \boldsymbol{f}_u^{(N_l)^\top}(z_{N_l})\hat{T}_t - \boldsymbol{f}_u^{(1)^\top}(z_0)\hat{T}_b + \boldsymbol{D}^F \mathcal{F}^*. \tag{7.55}$$

Thus, in consideration of Eq. (7.55), all higher-order equilibrium equations in the square brackets of Eq. (7.49) vanish identically when using the present equilibrated assumptions for in-plane stresses $\sigma^{(k)}$ Eq. (7.24) and transverse shear stresses $\tau^{(k)}$ Eq. (7.29), and therefore need not be enforced in the HR principle via Lagrange multipliers.

However, as discussed in Sections 7.2 and 7.3, equilibrium of the membrane forces $\mathcal{N} = (N_x, N_y, N_{xy})$ with the applied surface shear tractions, and equilibrium of the transverse shear forces $\mathcal{Q} = (Q_x, Q_y)$ with the applied surface normal tractions needs to be enforced to guarantee that the tractions on the top surface are recovered accurately. Therefore, a new set of governing equations for linear plate stretching and bending is derived by means of a modified HR principle with only the membrane equilibrium Eq. (7.30) and bending equilibrium Eq. (7.42) enforced via Lagrange multipliers $\boldsymbol{u} = (u_{x_0}, u_{y_0}, w_0)$. Thus,

$$\begin{aligned}\Pi(\boldsymbol{u}, \mathcal{F}) = \int_V U_0^*(\mathcal{F})\mathrm{d}V - \int_{S_1} \hat{u}_i t_i \mathrm{d}S + \iint \begin{bmatrix} u_{x_0} & u_{y_0} \end{bmatrix} \left(\boldsymbol{D}^\top \mathcal{N} + \hat{T}_t - \hat{T}_b\right) \mathrm{d}y\mathrm{d}x + \\ \iint w_0 \left(\nabla^\top \mathcal{Q} + \hat{P}_t - \hat{P}_b\right) \mathrm{d}y\mathrm{d}x - \int_{S_2} u_i \left(t_i - \hat{t}_i\right) \mathrm{d}S, \quad i, j = x, y, z.\end{aligned} \tag{7.56}$$

As observed by other authors, such as Batra et al. [58, 59], enforcing the equilibrium equations in the variational statement is a powerful technique for predicting accurate 3D stress fields in multilayered structures in a variationally consistent manner. However, the present HR functional results in a structural model with fewer degree of freedom than the generalised model of Batra et al. as the in-plane and transverse shear stresses are based on the same degrees of freedom. A possible disadvantage of this approach is that the reduction of variables leads to a loss in fidelity or general applicability of the model. However, this is offset by a considerable reduction in computational cost due to fewer equilibrium equations and variables. As the numerical results in the following Chapter 8 document, the reduced number of degrees of freedom in the present HR formulation is not detrimental to the accuracy of the model, even for highly heterogeneous straight-fibre or tow-steered composite laminates and sandwich beams. Therefore, the model strikes a favourable balance between modelling accuracy and computational effort.

For a linear elastic body with a predefined constitutive relation, the complementary energy density is written in terms of σ_{ij} and the compliance tensor S_{ijkl}. Hence,

$$U_0^*(\sigma_{ij}) = \frac{1}{2} S_{ijkl}\sigma_{ij}\sigma_{kl}. \tag{7.57}$$

In Chapters 5 and 6 it was found that the transverse normal stress is at least one order of magnitude smaller than the in-plane and transverse shear stresses for practical engineering laminates under classical load cases. Thus, the effect of transverse normal stresses is henceforth assumed to be small. Therefore, the contribution of σ_z in the complementary energy density Eq. (7.57) is ignored, such that for a structure comprised of monoclinic laminae we can write

$$U_0^*(\mathcal{F}) = \frac{1}{2}\sigma^{(k)\top}\bar{\boldsymbol{Q}}^{(k)^{-1}}\sigma^{(k)} + \frac{1}{2}\tau^{(k)\top}\boldsymbol{G}^{(k)^{-1}}\tau^{(k)} \tag{7.58}$$

where the in-plane stresses and transverse shear stresses are defined in Eqs. (7.24) and (7.34), respectively, $\bar{\boldsymbol{Q}}$ is the transformed reduced stiffness matrix for plane stress in z as defined in Eq. (7.18), and the transverse shear constitutive matrix is given by

$$\boldsymbol{G}^{(k)} = \begin{bmatrix} C_{55} & C_{54} \\ C_{45} & C_{44} \end{bmatrix}^{(k)} \tag{7.59}$$

where $C_{55} = G_{xz}$, $C_{44} = G_{yz}$, and $C_{54} = C_{45}$ are the coupling terms between the two orthogonal transverse shear deformations. For orthotropic 0° and 90° lamina $C_{54} = C_{45} = 0$, whereas for general angle-ply laminae $C_{54} = C_{45} \neq 0$. As indicated by Eq. (7.58), once the substitutions for $\sigma^{(k)}$ and $\tau^{(k)}$ have been made from Eqs. (7.24) and (7.34), respectively, the complementary energy density is a function of the stress resultants $\mathcal{F}$ only. Note that even though the transverse normal stress $\sigma_z^{(k)}$ is ignored in the complementary energy density Eq. (7.58), the transverse normal stress is readily calculated from the model assumption Eq. (7.46) once the stress resultant field $\mathcal{F}$ is computed.

For equilibrium of the system, the first variation of the functional Π in Eq. (7.56) must vanish. Thus, substituting Eq. (7.58) back into the functional in absence of the body forces f_i, the first variation of the modified HR functional reads

$$\begin{aligned}\delta\Pi(\boldsymbol{u},\mathcal{F}) = \delta\Bigg[&\int_V \left\{\frac{1}{2}\sigma^{(k)\top}\bar{\boldsymbol{Q}}^{(k)^{-1}}\sigma^{(k)} + \frac{1}{2}\tau^{(k)\top}\boldsymbol{G}^{(k)^{-1}}\tau^{(k)}\right\}\mathrm{d}V + \\ &\iint \left\{\begin{bmatrix} u_{x_0} & u_{y_0}\end{bmatrix}\left(\boldsymbol{D}^\top\mathcal{N} + \hat{T}_t - \hat{T}_b\right) + w_0\left(\nabla^\top\mathcal{Q} + \hat{P}_t - \hat{P}_b\right)\right\}\mathrm{d}y\mathrm{d}x - \\ &\int_{S_1}\left(\hat{u}_x t_x + \hat{u}_y t_y + \hat{u}_z t_z\right)\mathrm{d}S - \int_{S_2}\left\{u_x\left(t_x - \hat{t}_x\right) + u_y\left(t_y - \hat{t}_y\right) + u_z\left(t_z - \hat{t}_z\right)\right\}\mathrm{d}S\Bigg] = 0.\end{aligned} \tag{7.60}$$

The new set of governing equations is derived by substituting the stress fields for $\sigma^{(k)}$ and $\tau^{(k)}$ from Eqs. (7.24) and (7.34) into Eq. (7.60) and expanding the first variation. The corresponding Euler-Lagrange field equations in terms of the functional unknowns $\boldsymbol{u}$ and $\mathcal{F}$ are

$$\delta\begin{bmatrix} u_{x_0} & u_{y_0}\end{bmatrix} : \boldsymbol{D}^\top\mathcal{N} + \hat{T}_t - \hat{T}_b = \boldsymbol{0} \tag{7.61a}$$

$$\delta w_0 : \nabla^\top\boldsymbol{D}^\top\mathcal{M} + \nabla^\top\left(z_{N_l}\hat{T}_t - z_0\hat{T}_b\right) + \hat{P}_t - \hat{P}_b = 0 \tag{7.61b}$$

$$\begin{aligned}\delta\mathcal{F}^\top :\ &(\boldsymbol{s}+\boldsymbol{\eta})\,\mathcal{F} + \boldsymbol{\eta}_x\frac{\partial\mathcal{F}}{\partial x} + \boldsymbol{\eta}_y\frac{\partial\mathcal{F}}{\partial y} + \boldsymbol{\eta}_{xx}\frac{\partial^2\mathcal{F}}{\partial x^2} + \boldsymbol{\eta}_{xy}\frac{\partial^2\mathcal{F}}{\partial x\partial y} + \boldsymbol{\eta}_{yy}\frac{\partial^2\mathcal{F}}{\partial y^2} + \\ &\boldsymbol{\chi}\hat{T}_b + \boldsymbol{\chi}_x\frac{\partial\hat{T}_b}{\partial x} + \boldsymbol{\chi}_y\frac{\partial\hat{T}_b}{\partial y} + \mathcal{L}_{eq} = \boldsymbol{0}\end{aligned} \tag{7.61c}$$

where $\mathcal{N}$ and $\mathcal{M}$ are the classical membrane stress resultants and bending moments, respectively, and are subsets of the full stress resultant vector $\mathcal{F}$. The pertinent essential and natural boundary conditions are given by

$$\left.\begin{aligned} &\delta\mathcal{F}_{bc}^{\top} : \boldsymbol{\eta}^{bc}\mathcal{F} + \boldsymbol{\eta}_x^{bc}\frac{\partial\mathcal{F}}{\partial x} + \boldsymbol{\eta}_y^{bc}\frac{\partial\mathcal{F}}{\partial y} + \boldsymbol{\chi}^{bc}\hat{T}_b + \mathcal{L}_{bc} = \hat{\mathcal{U}}_{bc} \\ &\delta Q_{nz} : w_0 = \hat{w}_0 \end{aligned}\right\} \quad \text{on} \quad C_1 \tag{7.62a}$$

$$\delta\mathcal{U}_{bc}^{\top} : \ \mathcal{F}_{bc}^{*} = \hat{\mathcal{F}}_{bc}^{*} \quad \text{and} \quad \delta w_0 : \ Q_{nz} = \hat{Q}_{nz} \quad \text{on} \quad C_2 \tag{7.62b}$$

where $\mathcal{F}_{bc} = (N_n, N_{ns}, M_n, M_{ns}, \dots)$ is the column vector of stress resultants transformed to the local normal-tangential coordinate system (n, s, z) of the boundary curve Γ, Q_{nz} is the transverse shear force acting normal to the boundary surface, and $\hat{\mathcal{U}}_{bc} = \left(\hat{u}_{n_0}, \hat{u}_{s_0}, \hat{u}_{n_1}, \hat{u}_{s_1}, \dots, \hat{u}_n^{\phi}, \hat{u}_s^{\phi}, 0, 0\right)$ is a column vector of prescribed displacement variables on the boundary. Similarly, $\mathcal{F}_{bc}^{*}$ is the stress resultant vector previously defined in Eq. (7.50), which is the same as $\mathcal{F}$ without the stress resultants associated with $\phi_{,i}^{(k)}$, i.e. $M_x^{\partial\phi}$ and $M_y^{\partial\phi}$, and transformed to the local normal-tangential coordinate system (n, s, z) of the boundary curve.

The governing field equations related to $\delta\begin{bmatrix} u_{x_0} & u_{y_0} \end{bmatrix}$ and $\delta\mathcal{F}^{\top}$ are written in vector form with each row defining a separate equation. The equations related to $\delta\boldsymbol{u}$ are the classical in-plane membrane and bending equilibrium equations. These equilibrium equations are supplemented by "enhanced" constitutive equations from $\delta\mathcal{F}^{\top}$ in Eqs. (7.61c). In these equations, the well-known constitutive equations of CLA written in inverted form, i.e.

$$\begin{Bmatrix} \epsilon_0 \\ \kappa \end{Bmatrix} = \begin{bmatrix} \boldsymbol{A} & \boldsymbol{B} \\ \boldsymbol{B} & \boldsymbol{D} \end{bmatrix}^{-1} \begin{Bmatrix} \mathcal{N} \\ \mathcal{M} \end{Bmatrix} = \boldsymbol{s}\mathcal{F}, \tag{7.63}$$

are enhanced with differential terms of the stress resultants $\mathcal{F}$, where $\mathcal{F}$ may also include higher-order moments beyond $\mathcal{N}$ and $\mathcal{M}$. Thus, all $\mathcal{O} \times \mathcal{O}$ matrices $\boldsymbol{\eta}$ in Eqs. (7.61c) are collections of transverse shear correction factors that when multiplied by their corresponding higher-order moment terms $\dfrac{\partial^n\mathcal{F}}{\partial x_i^n}$ correct the product of the direct $\mathcal{O} \times \mathcal{O}$ compliance matrix $\boldsymbol{s}$ and moments $\mathcal{F}$. Similarly, the $\mathcal{O} \times 2$ matrices $\boldsymbol{\chi}$ are correction factors related to the applied surface shear tractions. In general, the addition of the superscript bc to any matrix denotes correction factors that are applicable to the boundary curve Γ and therefore include the outward normal vector $\boldsymbol{n} = (n_x, n_y)$.

Finally, $\mathcal{L}_{eq}$ is a $\mathcal{O}\times 1$ column vector that only includes derivatives of the Lagrange multipliers $\boldsymbol{u} = (u_{x_0}, u_{y_0}, w_0)$ and captures the reference surface stretching strains ϵ_0 and curvatures κ,

$$\mathcal{L}_{eq} = \begin{bmatrix} -\dfrac{\partial u_{x0}}{\partial x} & -\dfrac{\partial u_{y0}}{\partial y} & -\dfrac{\partial u_{x0}}{\partial y} - \dfrac{\partial u_{y0}}{\partial x} & \dfrac{\partial^2 w_0}{\partial x^2} & \dfrac{\partial^2 w_0}{\partial y^2} & 2\dfrac{\partial^2 w_0}{\partial x \partial y} & 0 & \dots \end{bmatrix}^{\top}. \tag{7.64}$$

Similarly, $\mathcal{L}_{bc}$ is a $\mathcal{O} \times 1$ column vector that includes the transformed Lagrange multipliers $u_{n_0} = n_x u_{x_0} + n_y u_{y_0}$, $u_{s_0} = -n_y u_{x_0} + n_x u_{y_0}$ and rotations $\dfrac{\partial w_0}{\partial n}$ and $\dfrac{\partial w_0}{\partial s}$ of the boundary perimeter Γ,

$$\mathcal{L}_{bc} = \begin{bmatrix} u_{n_0} & u_{s_0} & -\dfrac{\partial w_0}{\partial n} & -\dfrac{\partial w_0}{\partial s} & 0 & \dots \end{bmatrix}^{\top}. \tag{7.65}$$

Thus, the physical significance of the displacement boundary conditions in Eq. (7.62a) is that Kirchhoff rotations normal and tangential to the boundary curve $\frac{\partial w_0}{\partial n}$ and $\frac{\partial w_0}{\partial s}$, respectively, are modified by transverse shear rotations. Therefore, the static inconsistency that occurs for Reddy-type models discussed in Chapter 3 does not arise here because the slope of the middle surface of the plate can change at the boundary.

The full derivation of the governing equations, including details of all transverse shear correction coefficients, are given in Appendix B. The governing field equations Eq. (7.61) and boundary conditions Eq. (7.62) above are valid for any multilayered laminate comprised of linear elastic anisotropic laminae. Therefore, the HR model derived herein is applicable to straight-fibre and tow-steered composites as well as isotropic single-layer plates or multilayered ceramic structures, such as laminated glass. For plates with material properties invariant of the planar (x, y) directions, the governing equations simplify considerably as any terms involving planar derivatives vanish. Thus, for straight-fibre laminates and isotropic plates $\boldsymbol{\eta} = \boldsymbol{\eta}_x = \boldsymbol{\eta}_y = \boldsymbol{\chi} = \boldsymbol{\eta}^{bc} = \mathbf{0}$.

7.5 Conclusions

In this chapter, the higher-order HR formulation for laminated one-dimensional beams presented in Chapter 4 was extended to two-dimensional plates. Higher-order fidelity is introduced into the model by writing the in-plane stress field as a Taylor series expansion of global and local higher-order stress resultants.

The derivation of the HR model in Section 7.4 is based on the notion that accurate transverse shear and transverse normal stress fields can be derived by integrating the in-plane stresses of displacement-based, higher-order theories in Cauchy's equilibrium equations. Based on the assumption of a generalised in-plane displacement field, a higher-order in-plane stress field in terms of stress resultant variables was defined in Section 7.1 and used to derive equilibrated transverse stresses in Sections 7.2 and 7.3. As shown in Sections 7.2 and 7.3, transverse stress fields that satisfy the surface and interfacial equilibrium conditions are mathematically guaranteed in the present model if the classical membrane and bending equilibrium equations are enforced in a variational statement. Furthermore, as the transverse shear stresses are derived by integrating the in-plane stresses in Cauchy's equilibrium equations, the higher-order equilibrium equations need not be enforced. Thus, a contracted Hellinger-Reissner-type functional is used to derive a new set of governing field equations and boundary conditions. In this contracted HR functional, the number of variables in the model is greatly reduced; for an expansion of the in-plane variables up to the order of z^{N_o} the reduction in the number of variables is $2N_o$.

Due to the higher-order fidelity, the model can be applied to laminates comprised of layers with structural properties that vary by orders of magnitude and also to advanced composites with curvilinear fibre paths. Thus, the model is applicable for modelling the bending and stretching of plates with heterogeneity in all three dimensions.

In the present approach the accuracy of the transverse stresses is dependent on the order of the assumed in-plane stress field expansion because, for computational efficiency, the transverse stress fields are based on the same variables as the in-plane stress fields. In the derivation presented herein, the effect of the transverse normal stress was neglected. Based on the findings

in Chapters 5 and 6 this is believed to be a valid assumption for practical engineering laminates under classical loading conditions. Nevertheless, the author would like to suggest two possible ways of incorporating the effects of transverse normal deformation if these effects are deemed to be significant. The first is to use the generalised approach presented by Batra and co-workers [58, 59] of assuming separate Taylor or Legendre series expansions for the six stress and three displacement fields. The drawback of this approach is that the number of variables is significantly increased. To maintain the computational efficiency of shared variables presented herein, only the normal displacement field for u_z in Eq. (7.1) can be expanded as a Taylor series. In this case, the vector of stress resultants $\mathcal{F}$ will include extra higher-order moments that capture the stretching in the normal direction and its Poisson effect on the in-plane stresses. Once the expression for the in-plane stresses incorporating the effects of transverse normal deformation has been established, the rest of the model derivation follows the outline presented in this chapter.

Chapter 8

Three-Dimensional Stress Fields in Straight-Fibre and Tow-Steered Plates

The previous chapter introduced a mixed displacement/stress-based, higher-order ZZ theory derived from the HR mixed-variational statement. The displacement and stress fields were expanded in a Taylor series of the through-thickness coordinate z, such that the governing equations were derived in generalised notation that allows the order of the model to be specified *a priori* without having to re-derive the equations. Thus, the model is suited for modelling highly heterogeneous laminated plates comprised of straight-fibre and variable-stiffness plies, honeycomb and foam cores, or other material combinations where material properties vary by orders of magnitude.

In this chapter the derived HR formulation is compared against 3D elasticity and 3D FEM results for a number of straight-fibre and variable-stiffness laminates, as well as sandwich plates. Overall, four different implementations of the HR formulation are considered. The first is a third-order model that does not account for ZZ effects denoted by HR3. The displacement and stress field expansions are truncated after the z^3 term, such that there are twelve global stress resultants in $\mathcal{F}$. A third-order global expansion field is important for capturing "stress-channelling" effects that arise in highly-orthotropic laminates. Second, the third-order model is enhanced via a ZZ degree of freedom using either MZZF, denoted by HR3-MZZF, or the RZT ZZ function. In the latter case, a distinction is made between the classic implementation of the RZT ZZ function, denoted by HR3-RZT, and Gherlone's adaptation [54] that accounts for the presence of Externally Weak Layers (EWLs) discussed in Section 4.1.1, and denoted by HR3-RZTmx, where mx stands for "modified external". For RZTmx the RZT ZZ function is calculated from modified values of the transverse shear moduli $G_{xz}^{(k)}$ and $G_{yz}^{(k)}$ of layer k:

$$\begin{aligned} &\bullet \text{ If } G_{iz}^{(1)} < G_{iz}^{(2)}, \text{ then } G_{iz}^{(1)} = G_{iz}^{(2)} \quad \text{for} \quad i = x, y. \\ &\bullet \text{ If } G_{iz}^{(N_l)} < G_{iz}^{(N_l-1)}, \text{ then } G_{iz}^{(N_l)} = G_{iz}^{(N_l-1)} \quad \text{for} \quad i = x, y. \end{aligned} \tag{8.1}$$

where N_l is the total number of layers. The rule does not apply if the condition reduces the laminate to have the same transverse shear moduli for all layers, as would be the case for [0/90], [90/0] and [90/0/90] laminates. The ZZ functionality adds three additional ZZ bending moments in the case of MZZF and four in the case of RZT (see itemised list on page 161), such that the number of unknowns in $\mathcal{F}$ is increased to fifteen and sixteen, respectively. For straight-fibre laminates, the ZZ moments associated with $\phi_{,i}^{(k)}$ vanish as the ZZ function does not vary over the planform of the plate.

The presentation of the results is split into two sections. Section 8.1 shows the benchmarking results for straight-fibre laminates, whereas Section 8.2 treats tow-steered laminates. In

Section 8.1.1, orthotropic laminates are compared with Pagano's 3D elasticity solution [69] of an orthotropic plate simply supported along all four edges and loaded by a sinusoidal pressure loading on the top surface. This 3D elasticity solution is not applicable to anisotropic laminates with extension/shear coupling, bend/twist coupling or load cases involving shear tractions applied to the top and bottom surfaces as the transverse displacement is restricted to a double sine wave. Therefore, high-fidelity 3D FEM solutions from Abaqus are used to compare more general laminations and load cases in Section 8.1.2. This second test case considers general anisotropic laminates that are fully clamped along all four edges and loaded by a constant pressure loading and shear traction on the top surface. Similar 3D FEM solutions are used in Section 8.2.1 to test the accuracy of the model for tow-steered laminates. A large number of different stacking sequences and characteristic in-plane length to width ratios are considered to validate the general applicability of the HR model. Finally, the relative effects of transverse shear deformation on tow-steered laminates, as compared to a quasi-isotropic straight-fibre laminate, is presented in Section 8.2.2.

8.1 3D stress fields in straight-fibre laminates and sandwich plates

Consider a square plate of unit in-plane dimensions $a = b = 1$ m and total thickness $t < a, b$. The plate is comprised of N_l orthotropic, straight-fibre laminae of layer thickness $t^{(k)}$, material stiffness tensor $\boldsymbol{C}^{(k)}$ and fibre orientation $\alpha^{(k)}$. The individual layers can be arranged in any general fashion but are assumed to be perfectly bonded, such that displacement and traction continuity at the interfaces is guaranteed. The plate is subjected to certain displacement or traction boundary conditions along its four straight-edge surfaces, e.g. simply supported or rigidly built-in, and is loaded via certain external tractions on the top and bottom surfaces. In reaction to the applied loading and constraining boundary conditions, the plate is assumed to deform isothermally into a new static equilibrium state.

8.1.1 Benchmarking of 3D stresses in orthotropic laminates

8.1.1.1 Model implementation

As a first test, consider the multilayered plate loaded by a sinusoidally distributed pressure load on the top surface and simply supported along all four edges shown in Figure 8.1. In the HR formulation, the 3D continuum is compressed onto an equivalent single layer Ω coincident with the midplane of the plate as depicted by the grey surface. All externally applied tractions are zero except for the sinusoidal pressure on the top surface $\hat{P}_t = p_0 \sin(\pi x/a) \sin(\pi y/b)$.

Following Pagano [69], an exact 3D elasticity solution exists for this problem with arbitrary number of orthotropic or isotropic layers, and this is readily implemented in software packages, such as Matlab. Thus, Pagano's solution serves as the benchmark for the orthotropic composite laminates and sandwich plates considered in this section.

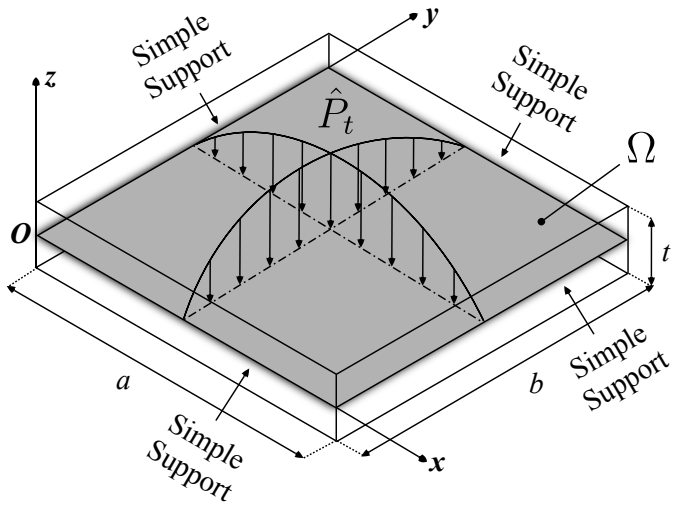

Figure 8.1: A composite plate loaded by a sinusoidally distributed pressure load on the top surface and simply supported along all four edges. In the HR formulation, the 3D continuum is compressed onto an equivalent single layer Ω coincident with the midplane of the plate.

For straight-fibre laminates the HR governing field equations (7.61) are given by

$$\boldsymbol{s}\mathcal{F} + \boldsymbol{\eta}_{xx}\mathcal{F}_{,xx} + \boldsymbol{\eta}_{yy}\mathcal{F}_{,yy} + \boldsymbol{\eta}_{xy}\mathcal{F}_{,xy} + \mathcal{L}_{eq} = \mathbf{0} \tag{8.2a}$$

$$N_{x,x} + N_{xy,y} = 0 \tag{8.2b}$$

$$N_{xy,x} + N_{y,y} = 0 \tag{8.2c}$$

$$M_{x,xx} + 2M_{xy,xy} + M_{y,yy} + \hat{P}_t = 0 \tag{8.2d}$$

where the comma notation is used to denote differentiation, and N_x, N_y, N_{xy} and M_x, M_y, M_{xy} are the classical membrane forces and bending moments, respectively, and are the first six entries in the stress resultant array $\mathcal{F}$.

The simply supported boundary conditions, i.e. each edge can rotate and move normal to its boundary curve but not tangential to it, are expressed mathematically as

$$\text{at} \quad x = 0, a: \qquad \sigma_x = u_{y_0} = w_0 = 0 \tag{8.3a}$$

$$\text{at} \quad y = 0, b: \qquad \sigma_y = u_{x_0} = w_0 = 0. \tag{8.3b}$$

Variable assumptions that satisfy the conditions in Eq. (8.3) and that are sufficiently general to solve the boundary value problem depicted in Figure 8.1, are given by

$$u_{x_0} = U\cos\left(\frac{\pi x}{a}\right)\sin\left(\frac{\pi y}{b}\right), \quad u_{y_0} = V\sin\left(\frac{\pi x}{a}\right)\cos\left(\frac{\pi y}{b}\right), \quad w_0 = W\sin\left(\frac{\pi x}{a}\right)\sin\left(\frac{\pi y}{b}\right) \tag{8.4a}$$

$$\mathcal{F}_x = F_{x_0}\sin\left(\frac{\pi x}{a}\right)\sin\left(\frac{\pi y}{b}\right), \quad \mathcal{F}_y = F_{y_0}\sin\left(\frac{\pi x}{a}\right)\sin\left(\frac{\pi y}{b}\right), \quad \mathcal{F}_{xy} = F_{xy_0}\cos\left(\frac{\pi x}{a}\right)\cos\left(\frac{\pi y}{b}\right) \tag{8.4b}$$

where $\mathcal{F}_x = (N_x, M_x, \ldots, M_x^{\phi})$ are the x-wise axial stress resultants, $\mathcal{F}_y = (N_y, M_y, \ldots, M_y^{\phi})$

are the y-wise lateral stress resultants, and $\mathcal{F}_{xy} = (N_{xy}, M_{xy}, \dots, \boldsymbol{M}^{\phi}_{xy})$ are the in-plane shear stress resultants. Note that $\boldsymbol{M}^{\phi}_{xy}$ does not exist for HR3, $\boldsymbol{M}^{\phi}_{xy} = (M^{\phi}_{xy}, M^{\phi}_{yx})$ for HR3-RZT and $\boldsymbol{M}^{\phi}_{xy} = M^{\phi}_{xy}$ for HR3-MZZF (see itemised list on page 161).

Substituting Eq. (8.4) into the governing differential equations (8.2) results in a set of N_{eq} algebraic equations in N_{eq} variables $(F_{x_0}, F_{y_0}, F_{xy_0}, U, V, W)$, where $N_{eq} = 15$ for HR3, $N_{eq} = 18$ for HR3-MZZF and $N_{eq} = 19$ for HR3-RZT. Note that for orthotropic laminates considered in this problem, the extension/shear coupling stiffness terms $\bar{Q}_{16} = \bar{Q}_{26} = 0$. As a result, all extension/shear and bend/twist coupling terms s_{ij} in the direct compliance matrix $\boldsymbol{s}$ must vanish, i.e. $s_{13} = s_{16} = \cdots = s_{23} = s_{26} = \cdots = s_{31} = s_{32} = s_{34} = s_{35} = \cdots = 0$ because all components in $\boldsymbol{s}$ are linearly dependent on $\bar{\boldsymbol{Q}}$. For the direct shear correction matrix $\boldsymbol{\eta}_{xx}$, the terms associated with $\bar{Q}_{16}$ and $\bar{Q}_{26}$ also vanish, i.e. $\eta_{xx_{13}} = \eta_{xx_{16}} = \cdots = \eta_{xx_{23}} = \eta_{xx_{26}} = \cdots = \eta_{xx_{31}} = \eta_{xx_{32}} = \eta_{xx_{34}} = \eta_{xx_{35}} = \cdots = 0$, and similarly for the direct stiffness matrix $\boldsymbol{\eta}_{yy}$. On the contrary, for the in-plane coupling shear correction matrix $\boldsymbol{\eta}_{xy}$, these aforementioned vanishing terms are the only non-zero values, such that $\eta_{xy_{11}} = \eta_{xy_{12}} = \eta_{xy_{14}} = \eta_{xy_{15}} = \cdots = \eta_{xy_{21}} = \eta_{xy_{22}} = \eta_{xy_{24}} = \eta_{xy_{25}} = \cdots = \eta_{xy_{33}} = \eta_{xy_{36}} = \cdots = 0$.

According to the definition of $\boldsymbol{\eta}_{xx}$ and $\boldsymbol{\eta}_{yy}$ in Eqs. (B.27d) and (B.27e), these two direct shear correction matrixes are functions of the products $\boldsymbol{R}^{(k)^\top}_x \cdot \boldsymbol{R}^{(k)}_x$ and $\boldsymbol{R}^{(k)^\top}_y \cdot \boldsymbol{R}^{(k)}_y$, respectively, and by extension of Eq. (7.35) functions of $\left(\boldsymbol{I}_x \bar{\boldsymbol{Q}}^{(k)}\right)^\top \cdot \left(\boldsymbol{I}_x \bar{\boldsymbol{Q}}^{(k)}\right)$ and $\left(\boldsymbol{I}_y \bar{\boldsymbol{Q}}^{(k)}\right)^\top \cdot \left(\boldsymbol{I}_y \bar{\boldsymbol{Q}}^{(k)}\right)$, respectively. The in-plane coupling shear correction matrix $\boldsymbol{\eta}_{xy}$ in Eq. (B.27f), however, is a function of mixed terms $\boldsymbol{R}^{(k)^\top}_x \cdot \boldsymbol{R}^{(k)}_y + \boldsymbol{R}^{(k)^\top}_y \cdot \boldsymbol{R}^{(k)}_x$, and therefore depends on $\left(\boldsymbol{I}_x \bar{\boldsymbol{Q}}^{(k)}\right)^\top \cdot \left(\boldsymbol{I}_y \bar{\boldsymbol{Q}}^{(k)}\right) + \left(\boldsymbol{I}_y \bar{\boldsymbol{Q}}^{(k)}\right)^\top \cdot \left(\boldsymbol{I}_x \bar{\boldsymbol{Q}}^{(k)}\right)$. By computing these matrix products involving $\boldsymbol{I}_x, \boldsymbol{I}_y$ and $\bar{\boldsymbol{Q}}^{(k)}$ with $\bar{Q}_{16} = \bar{Q}_{26} = 0$, the set of vanishing shear correction factors above is readily verified.

Thus, in consideration of these vanishing compliance and shear correction terms, and the fact that $a = b = 1$ m, the set of algebraic governing field equations reads

$$\boldsymbol{K}_f F_0 + \boldsymbol{K}_u U_0 = \boldsymbol{0} \tag{8.5a}$$

$$N_{x_0} - N_{xy_0} = 0 \tag{8.5b}$$

$$N_{y_0} - N_{xy_0} = 0 \tag{8.5c}$$

$$\pi^2 \left(M_{x_0} + M_{y_0} - 2M_{xy_0}\right) = p_0 \tag{8.5d}$$

where $F_0 = (N_{x_0}, N_{y_0}, N_{xy_0}, M_{x_0}, M_{y_0}, M_{xy_0}, \dots)$ and $U_0 = (U, V, W)$. The stiffness matrices $\boldsymbol{K}_f$ and $\boldsymbol{K}_u$ multiplying the unknowns F_0 and U_0 are given by,

$$\boldsymbol{K}_f : \begin{array}{ll} K_{f_{ii}} = s_{ii} - \pi^2 \left(\eta_{xx_{ii}} + \eta_{yy_{ii}}\right), & K_{f_{ij}} = \pi^2 \eta_{xy_{ij}} \\ K_{f_{ji}} = \pi^2 \eta_{xy_{ji}}, & K_{f_{jj}} = s_{jj} - \pi^2 \left(\eta_{xx_{jj}} + \eta_{yy_{jj}}\right) \end{array} \quad \text{and} \quad \boldsymbol{K}_u = \begin{bmatrix} \pi & 0 & 0 \\ 0 & \pi & 0 \\ -\pi & -\pi & 0 \\ 0 & 0 & -\pi^2 \\ 0 & 0 & -\pi^2 \\ 0 & 0 & 2\pi^2 \\ 0 & 0 & 0 \\ \vdots & \vdots & \vdots \end{bmatrix}$$

where subscripts ij denote components of the associated matrices with indices i and j defined by

$$
\begin{aligned}
i &= (1,2,4,5,\ldots,10,11), \quad j = (3,6,\ldots,12) \quad \text{for HR3} \\
i &= (1,2,4,5,\ldots,13,14), \quad j = (3,6,\ldots,15) \quad \text{for HR3-MZZF} \\
i &= (1,2,4,5,\ldots,13,14), \quad j = (3,6,\ldots,15,16) \quad \text{for HR3-RZT.}
\end{aligned}
$$

Thus, Eqs. (8.5) represent a system of N_{eq} simultaneous algebraic equations that are readily solved for the N_{eq} unknowns (F_0, U_0) by standard matrix inversion. In the present work, computations of all stiffness terms and shear correction factors, and the matrix inversion operations were carried out in Matlab.

8.1.1.2 Model validation

To test the general applicability of the HR models a variety of different symmetric and non-symmetric composite laminates and sandwich plates are tested. Table 8.1 shows the two different materials used throughout the analysis. The first material c is representative of a high-performance carbon-fibre reinforced plastic with high orthotropy of in-plane modulus to transverse shear modulus. The second material h is a transversely isotropic honeycomb core and features significantly lower transverse shear stiffness than material c to exacerbate the ZZ effect. The stacking sequences of different laminates including layer orientations, layer thicknesses and layer material codes are summarised in Table 8.2.

Table 8.1: Mechanical properties of materials c and h.

Material	E_1	E_2	E_3	G_{12}	G_{13}	G_{23}
c	172.5 GPa	6.9 GPa	6.9 GPa	3.45 GPa	3.45 GPa	1.38 GPa
h	276 MPa	276 MPa	3.45 GPa	110.4 MPa	414 MPa	414 MPa
Material	ν_{12}		ν_{13}		ν_{23}	
c	0.25		0.25		0.25	
h	0.25		0.02		0.02	

Table 8.2: Analysed orthotropic stacking sequences. Subscripts indicate the repetition of a property over the corresponding number of layers. Layer thicknesses stated as ratios of total laminate thickness.

Laminate	**Thickness Ratio**	**Material**	**Stacking Sequence**
A	[0.3/0.7]	[c_2]	[0/90]
B	[$(1/3)_3$]	[c_3]	[0/90/0]
C	[0.25_4]	[c_4]	[0/90/0/90]
D	[0.2_5]	[c_5]	[0/90/0/90/0]
E	[$(1/20)_2/0.8/(1/20)_2$]	[c_2/h/c_2]	[0/90/0/90/0]
F	[$0.1_2/0.2_3/0.1_2$]	[c_2/h/0.01h/h/c_2]	[90/0_5/90]
G	[0.1/0.3/0.35/0.25]	[c_2/h/c]	[0/90/0/90]
H	[$0.1_2/0.3/0.4/0.05_2$]	[c_2/0.01h/h/c_2]	[90/0_3/90/0]

Laminates A-D are composite laminates, whereas laminates E-H are sandwich plates. Laminates F and H feature two different kinds of sandwich cores, the full constitutive core h and the degraded core 0.01h, for which all material moduli of material h are degraded by a factor of 100. As a variety of thin and thick laminates with characteristic length to thickness ratios ranging from $a/t = 100$ to $a/t = 5$ are investigated in this section, the layer thicknesses are quoted as ratios of the total laminate thickness. Overall, the laminates in Table 8.2 were chosen to represent a set of highly heterogeneous laminates that test the full capability of the HR models and reveal shortcomings that require further refinement.

Henceforth, all deflection and stress results are presented in normalised form. The chosen metrics for assessing the accuracy of the HR models are the maximum transverse bending deflection w_0 and the full 3D stress field, i.e. axial stress σ_x, lateral stress σ_y, in-plane shear stress σ_{xy}, transverse shear stresses τ_{xz} and τ_{yz}, and transverse normal stress σ_z. The normalised quantities are defined as follows:

$$\begin{aligned}
\bar{w}_0 &= \frac{E_2^{(c)} t^2}{p_0 a^2 b^2} \int_{-\frac{t}{2}}^{\frac{t}{2}} u_z \left(\frac{a}{2}, \frac{b}{2}, z\right) \mathrm{d}z \\
\bar{\sigma}_x(z) &= \frac{t^2}{p_0 a^2} \cdot \sigma_x \left(\frac{a}{2}, \frac{b}{2}, z\right), \quad \bar{\sigma}_y(z) = \frac{t^2}{p_0 b^2} \cdot \sigma_y \left(\frac{a}{2}, \frac{b}{2}, z\right), \quad \bar{\sigma}_{xy}(z) = \frac{t^2}{p_0 ab} \cdot \sigma_{xy} \left(\frac{a}{4}, \frac{b}{4}, z\right) \\
\bar{\sigma}_{xz}(z) &= \frac{1}{p_0} \cdot \sigma_{xz} \left(0, \frac{b}{2}, z\right), \quad \bar{\sigma}_{yz}(z) = \frac{1}{p_0} \cdot \sigma_{yz} \left(\frac{a}{2}, 0, z\right), \quad \bar{\sigma}_z(z) = \frac{1}{p_0} \cdot \sigma_z \left(\frac{a}{2}, \frac{b}{2}, z\right)
\end{aligned} \tag{8.6}$$

and are calculated at the indicated locations (x, y, z) throughout the 3D plate. Note that the bending deflection is normalised using the matrix-dominated modulus $E_2^{(c)}$ of material c. Furthermore, the normalised bending deflection $\bar{w}_0$ for the HR models is constant through the thickness of each laminate and is thus compared against Pagano's [69] normalised average through-thickness deflection. As $\bar{w}_0$ is calculated at the in-plane centroid of the plate, this metric corresponds to the maximum bending deflection. Similarly, the normal stress metrics $\bar{\sigma}_x$, $\bar{\sigma}_y$ and $\bar{\sigma}_z$ are also computed at the in-plane centroid of the plate. The two transverse shear stress metrics $\bar{\sigma}_{xz}$ and $\bar{\sigma}_{yz}$ are calculated at the midspan locations of the supported edges, whereas the in-plane shear stress is taken at the quarterspan of both in-plane x- and y-dimensions.

The relative percentage errors in the normalised metrics of Eq. (8.6) for the four HR models HR3, HR3-RZT, HR3-RZTmx and HR3-MZZF with respect to Pagano's 3D elasticity solution [69] are shown Tables 8.3-8.10. The results for Pagano's solution are given to four significant figures, whereas the percentage errors are cited to two decimal places. These tables allow the accuracy of the four HR models to be compared for a number of different stacking sequences and characteristic length to thickness ratios ranging from thin laminates with $a/t = 100$ to thick laminates with $a/t = 5$.

As indicated by the table headings, the results in Tables 8.3-8.10 compare the absolute maximum through-thickness values of the stress metrics $\bar{\sigma}_x$, $\bar{\sigma}_y$, $\bar{\sigma}_{xy}$, $\bar{\sigma}_{xz}$ and $\bar{\sigma}_{yz}$, where the notation $\vee |m|$ is used to indicate the absolute maximum value of metric m. For the transverse normal stress metric $\bar{\sigma}_z$, the value at the interface $z = z_{N_l - 1}$ between layer N_l and $N_l - 1$, i.e. at the first layer interface from the top of the laminate, is used. Laminates A and B are two- and three-layer laminates, respectively, and therefore the RZT modification rule for EWLs given in

Table 8.3: Orthotropic laminate A: Percentage error in normalised bending deflection and 3D stresses for various HR models and a/t ratios with respect to Pagano's solution [69].

a/t	Model	$\lvert\bar{w}_0\rvert$	$\vee\lvert\bar{\sigma}_x\rvert$	$\vee\lvert\bar{\sigma}_y\rvert$	$\vee\lvert\bar{\sigma}_{xy}\rvert$	$\vee\lvert\bar{\sigma}_{xz}\rvert$	$\vee\lvert\bar{\sigma}_{yz}\rvert$	$\bar{\sigma}_z(z_{N_l-1})$
100	**Pagano**	**0.01065**	**0.7159**	**0.7159**	**0.02625**	**33.56**	**33.56**	**-0.5000**
	HR3 (%)	0.01	-0.01	-0.01	0.00	-0.01	0.00	0.00
	HR3-RZT	0.01	0.00	-0.02	0.02	0.00	-0.02	0.01
	HR3-MZZF	0.01	-0.01	-0.01	0.00	-0.01	0.00	0.00
50	**Pagano**	**0.01070**	**0.7164**	**0.7163**	**0.02627**	**16.78**	**16.77**	**-0.5000**
	HR3 (%)	0.02	-0.05	-0.04	-0.01	0.00	0.02	0.00
	HR3-RZT	-0.02	-0.03	-0.05	0.02	-0.01	0.00	0.01
	HR3-MZZF	0.02	-0.05	-0.04	-0.01	0.00	0.02	0.00
20	**Pagano**	**0.01104**	**0.7196**	**0.7193**	**0.02641**	**6.698**	**6.690**	**-0.5000**
	HR3 (%)	0.13	-0.28	-0.24	-0.05	0.06	0.18	0.01
	HR3-RZT	0.13	-0.28	-0.24	-0.05	0.06	0.18	0.01
	HR3-MZZF	0.13	-0.28	-0.24	-0.05	0.06	0.18	0.01
10	**Pagano**	**0.01226**	**0.7304**	**0.7309**	**0.02688**	**3.326**	**3.316**	**-0.4996**
	HR3 (%)	0.47	-1.02	-1.08	-0.17	0.33	0.64	0.08
	HR3-RZT	0.47	-1.02	-1.08	-0.17	0.34	0.64	0.08
	HR3-MZZF	0.47	-1.02	-1.08	-0.17	0.34	0.64	0.08
5	**Pagano**	**0.01711**	**0.7671**	**0.7894**	**0.02853**	**1.610**	**1.621**	**-0.4954**
	HR3 (%)	1.33	-2.97	-5.71	-0.33	2.09	1.40	0.93
	HR3-RZT	1.33	-2.99	-5.73	-0.33	2.12	1.43	0.93
	HR3-MZZF	1.33	-2.99	-5.73	-0.33	2.12	1.43	0.93

Eq. (8.1) need not be applied. As a result, the models HR3-RZT and HR3-RZTmx are the same and are combined under a single heading HR3-RZT in Tables 8.3 and 8.4.

The results in Tables 8.3-8.6 show that the error in the HR3 model without ZZ functionality is around 1% for the non-sandwich laminates A-D with a/t ratios up to 20. For composite laminate A, the errors of the HR3 and the HR models with ZZ functionality are essentially the same, indicating that the ZZ effect for this [0/90] laminate is negligible. For the other three composite laminates B-D, the HR3 model loses accuracy compared to the ZZ HR models when $a/t \leq 10$. For laminate B, the error in $\bar{\sigma}_x$ is as great as 4.25% for $a/t = 10$ and then increases to 8.05% for $a/t = 5$. However, as plies are blocked together into relatively thick groups in laminates B-D, part of the error in HR3 is due to the ZZ effect that arises from the difference in transverse shear moduli of the 0° and 90° layers. In practical engineering laminates, where plies are regularly dispersed to prevent transverse matrix cracking, the accuracy of the HR3 model is expected to be similar to laminate A. Thus, for general engineering laminates, the HR3 model can safely be considered to be applicable for composite, non-sandwich plates up to a/t ratios of around 10. The increasing discrepancy for $a/t = 5$ is due to the increasing effects of normal through-thickness deformation as previously observed for 1D beams in Figure 5.23 of Chapter 5. Thus, under these circumstances the HR formulation needs to be modified to account for thickness stretch.

For sandwich plates E-H the accuracy of the HR3 model is inferior to the HR models with ZZ functionality. Without the ZZ degree of freedom, the HR3 model cannot account for the fact that layerwise differences in transverse shear moduli lead to changes in the z-wise slopes of the

Table 8.4: Orthotropic laminate B: Percentage error in normalised bending deflection and 3D stresses for various HR models and a/t ratios with respect to Pagano's solution [69].

a/t	Model	$\lvert\bar{w}_0\rvert$	$\vee\lvert\bar{\sigma}_x\rvert$	$\vee\lvert\bar{\sigma}_y\rvert$	$\vee\lvert\bar{\sigma}_{xy}\rvert$	$\vee\lvert\bar{\sigma}_{xz}\rvert$	$\vee\lvert\bar{\sigma}_{yz}\rvert$	$\bar{\sigma}_z(z_{N_l-1})$
100	**Pagano**	**0.004347**	**0.5393**	**0.1808**	**0.01068**	**39.47**	**8.282**	**-0.7407**
	HR3 (%)	0.01	0.05	-0.02	0.03	0.01	-0.01	0.00
	HR3-RZT	0.01	0.00	-0.02	-0.01	0.00	-0.01	0.00
	HR3-MZZF	0.01	0.00	-0.02	0.00	0.00	-0.01	0.00
50	**Pagano**	**0.004451**	**0.5410**	**0.1846**	**0.01082**	**19.67**	**4.212**	**-0.7406**
	HR3 (%)	0.03	0.22	-0.07	0.13	0.03	-0.03	0.01
	HR3-RZT	0.02	0.01	-0.07	0.01	0.01	-0.04	0.00
	HR3-MZZF	0.03	0.01	-0.07	0.01	0.01	-0.04	0.00
20	**Pagano**	**0.005162**	**0.5525**	**0.2101**	**0.01170**	**7.692**	**1.875**	**-0.7398**
	HR3 (%)	0.15	1.28	-0.39	0.76	0.17	-0.16	0.04
	HR3-RZT	0.14	0.09	-0.27	0.40	0.04	-0.19	0.00
	HR3-MZZF	0.14	0.07	-0.38	0.04	0.04	-0.19	0.01
10	**Pagano**	**0.007524**	**0.5906**	**0.2882**	**0.01449**	**3.573**	**1.228**	**-0.7371**
	HR3 (%)	0.50	4.25	-1.17	2.37	0.64	-0.29	0.17
	HR3-RZT	0.33	0.02	-1.09	0.91	0.11	-0.30	0.06
	HR3-MZZF	0.42	0.08	-1.17	0.19	0.15	-0.44	0.05
5	**Pagano**	**0.01528**	**0.7180**	**0.4784**	**0.02185**	**1.471**	**0.9557**	**-0.7264**
	HR3 (%)	1.28	8.05	-2.97	5.56	-0.35	0.25	0.76
	HR3-RZT	0.97	-2.18	-3.03	1.07	0.41	-0.15	0.45
	HR3-MZZF	0.97	-2.20	-3.05	1.03	0.39	-0.15	0.44

Table 8.5: Orthotropic laminate C: Percentage error in normalised bending deflection and 3D stresses for various HR models and a/t ratios with respect to Pagano's solution [69].

a/t	Model	$\lvert\bar{w}_0\rvert$	$\vee\lvert\bar{\sigma}_x\rvert$	$\vee\lvert\bar{\sigma}_y\rvert$	$\vee\lvert\bar{\sigma}_{xy}\rvert$	$\vee\lvert\bar{\sigma}_{xz}\rvert$	$\vee\lvert\bar{\sigma}_{yz}\rvert$	$\bar{\sigma}_z(z_{N_l-1})$
50	**Pagano**	**0.005169**	**0.4887**	**0.4886**	**0.01259**	**14.02**	**14.02**	**-0.8599**
	HR3 (%)	0.03	-0.01	0.01	0.08	0.03	0.04	0.00
	HR3-RZT	0.05	0.07	0.00	0.51	-0.05	-0.05	-0.04
	HR3-RZTmx	0.03	-0.03	-0.01	0.02	0.00	0.00	0.00
	HR3-MZZF	0.03	0.03	0.04	0.08	0.00	0.00	0.00
20	**Pagano**	**0.005713**	**0.4982**	**0.4979**	**0.01305**	**5.567**	**5.567**	**-0.8590**
	HR3 (%)	0.16	-0.03	0.03	0.50	0.21	0.21	0.00
	HR3-RZT	0.15	0.19	0.25	0.50	0.02	0.02	0.00
	HR3-RZTmx	0.15	-0.15	-0.09	0.12	0.01	0.01	0.00
	HR3-MZZF	0.15	0.18	0.25	0.50	0.02	0.02	0.00
10	**Pagano**	**0.007617**	**0.5306**	**0.5309**	**0.01460**	**2.715**	**2.720**	**-0.8557**
	HR3 (%)	0.57	-0.02	-0.07	1.80	0.90	0.72	0.01
	HR3-RZT	0.44	0.75	0.67	1.93	0.15	-0.02	0.04
	HR3-RZTmx	0.44	-0.48	-0.53	0.46	0.13	-0.04	0.02
	HR3-MZZF	0.44	0.74	0.69	1.75	0.15	-0.02	0.03
5	**Pagano**	**0.01475**	**0.6384**	**0.6560**	**0.01985**	**1.245**	**1.264**	**-0.8430**
	HR3 (%)	1.73	0.77	-1.94	5.02	3.16	1.55	0.21
	HR3-RZT	0.87	2.64	-0.28	4.98	0.81	-0.72	0.31
	HR3-RZTmx	0.86	-0.95	-3.61	1.54	1.03	-0.54	0.25
	HR3-MZZF	0.86	2.56	-0.20	4.73	0.83	-0.74	0.31

Table 8.6: Orthotropic laminate D: Percentage error in normalised bending deflection and 3D stresses for various HR models and a/t ratios with respect to Pagano's solution [69].

a/t	Model	$\lvert\bar{w}_0\rvert$	$\vee\lvert\bar{\sigma}_x\rvert$	$\vee\lvert\bar{\sigma}_y\rvert$	$\vee\lvert\bar{\sigma}_{xy}\rvert$	$\vee\lvert\bar{\sigma}_{xz}\rvert$	$\vee\lvert\bar{\sigma}_{yz}\rvert$	$\bar{\sigma}_z(z_{N_l-1})$
	Pagano	**0.004418**	**0.5390**	**0.3271**	**0.01073**	**15.51**	**8.385**	**-0.8961**
	HR3 (%)	0.03	-0.05	-0.13	0.00	-0.07	0.01	0.00
50	HR3-RZT	0.03	-0.01	0.01	0.03	0.00	-0.01	0.00
	HR3-RZTmx	0.03	-0.01	-0.04	0.01	0.00	-0.01	0.00
	HR3-MZZF	0.03	-0.01	0.01	0.03	0.00	-0.01	0.00
	Pagano	**0.004964**	**0.5410**	**0.3463**	**0.01118**	**6.119**	**3.481**	**-0.8966**
	HR3 (%)	0.15	-0.31	-0.78	0.02	-0.44	0.09	0.00
20	HR3-RZT	0.14	-0.08	0.09	0.18	0.02	-0.06	0.00
	HR3-RZTmx	0.14	-0.08	-0.23	0.05	0.02	-0.07	0.00
	HR3-MZZF	0.14	-0.08	0.09	0.18	0.02	-0.06	0.00
	Pagano	**0.006861**	**0.5538**	**0.4007**	**0.01267**	**2.948**	**1.895**	**-0.8972**
	HR3 (%)	0.53	-1.17	-2.74	0.37	-1.74	0.48	0.03
10	HR3-RZT	0.41	-0.33	0.46	0.80	0.05	-0.15	0.01
	HR3-RZTmx	0.41	-0.35	-0.73	0.30	0.05	-0.17	0.01
	HR3-MZZF	0.41	-0.33	0.46	0.80	0.05	-0.15	0.01
	Pagano	**0.01397**	**0.6422**	**0.5286**	**0.01756**	**1.375**	**1.039**	**-0.8928**
	HR3 (%)	1.56	-5.40	-7.80	2.35	-6.63	2.35	0.20
5	HR3-RZT	0.75	-2.98	2.18	2.85	0.08	-0.08	0.18
	HR3-RZTmx	0.76	-3.03	-1.57	1.28	0.07	-0.15	0.18
	HR3-MZZF	0.76	-2.97	2.20	2.85	0.09	-0.07	0.18

Table 8.7: Orthotropic laminate E: Percentage error in normalised bending deflection and 3D stresses for various HR models and a/t ratios with respect to Pagano's solution [69].

a/t	Model	$\lvert\bar{w}_0\rvert$	$\vee\lvert\bar{\sigma}_x\rvert$	$\vee\lvert\bar{\sigma}_y\rvert$	$\vee\lvert\bar{\sigma}_{xy}\rvert$	$\vee\lvert\bar{\sigma}_{xz}\rvert$	$\vee\lvert\bar{\sigma}_{yz}\rvert$	$\bar{\sigma}_z(z_{N_l-1})$
	Pagano	**0.009121**	**1.099**	**0.9896**	**0.02175**	**9.249**	**8.437**	**-0.9852**
	HR3 (%)	0.01	-0.02	-0.03	-0.06	0.00	0.00	0.00
50	HR3-RZT	0.01	-0.01	0.00	0.00	0.00	0.00	0.00
	HR3-RZTmx	0.01	-0.01	0.00	0.00	0.00	0.00	0.00
	HR3-MZZF	0.01	0.00	0.00	-0.04	0.00	0.00	0.00
	Pagano	**0.01090**	**1.108**	**1.001**	**0.02217**	**3.693**	**3.380**	**-0.9852**
	HR3 (%)	0.06	-0.11	-0.16	-0.37	-0.01	-0.02	0.00
20	HR3-RZT	0.06	-0.04	0.02	-0.02	0.00	-0.01	0.00
	HR3-RZTmx	0.06	-0.04	-0.02	-0.02	0.00	-0.01	0.00
	HR3-MZZF	0.06	0.00	-0.01	-0.24	-0.01	-0.02	0.00
	Pagano	**0.01725**	**1.145**	**1.039**	**0.02367**	**1.839**	**1.694**	**-0.9850**
	HR3 (%)	0.14	-0.42	-0.58	-1.36	-0.06	-0.08	0.00
10	HR3-RZT	0.14	-0.16	0.10	-0.04	-0.01	-0.03	0.00
	HR3-RZTmx	0.14	-0.16	-0.06	-0.04	-0.01	-0.02	0.00
	HR3-MZZF	0.14	0.01	0.00	-0.87	-0.05	-0.07	0.00
	Pagano	**0.04251**	**1.296**	**1.174**	**0.02949**	**0.9118**	**0.8460**	**-0.9839**
	HR3 (%)	0.22	-1.28	-1.79	-4.06	-0.17	-0.19	0.01
5	HR3-RZT	0.18	-0.40	0.60	0.18	-0.09	-0.08	0.00
	HR3-RZTmx	0.18	-0.37	0.02	0.17	-0.09	-0.07	0.00
	HR3-MZZF	0.21	0.21	0.23	-2.46	-0.18	-0.21	0.01

Table 8.8: Orthotropic laminate F: Percentage error in normalised bending deflection and 3D stresses for various HR models and a/t ratios with respect to Pagano's solution [69].

a/t	Model	$\lvert\bar{w}_0\rvert$	$\vee\lvert\bar{\sigma}_x\rvert$	$\vee\lvert\bar{\sigma}_y\rvert$	$\vee\lvert\bar{\sigma}_{xy}\rvert$	$\vee\lvert\bar{\sigma}_{xz}\rvert$	$\vee\lvert\bar{\sigma}_{yz}\rvert$	$\bar{\sigma}_z(z_{N_l-1})$
	Pagano	**0.01579**	**0.6563**	**0.8200**	**0.01847**	**8.519**	**10.67**	**-0.9607**
	HR3 (%)	0.14	-1.43	3.60	8.25	-0.05	-0.08	-0.04
50	HR3-RZT	0.01	0.02	-0.01	0.00	0.00	0.00	0.00
	HR3-RZTmx	0.01	0.00	-0.01	0.00	0.00	0.00	0.00
	HR3-MZZF	0.10	1.82	2.90	4.71	-0.12	-0.14	-0.01
	Pagano	**0.06419**	**1.181**	**1.433**	**0.04163**	**3.587**	**4.339**	**-0.9446**
	HR3 (%)	1.09	-4.04	12.34	21.66	-6.10	-1.36	-0.24
20	HR3-RZT	0.01	0.04	-0.07	-0.03	-0.07	0.01	0.00
	HR3-RZTmx	0.01	-0.03	-0.07	-0.03	-0.07	0.01	0.00
	HR3-MZZF	0.77	6.12	9.84	12.40	-1.87	-0.60	-0.07
	Pagano	**0.1843**	**2.489**	**2.951**	**0.09918**	**3.028**	**3.255**	**-0.9048**
	HR3 (%)	3.57	-4.40	20.03	29.92	-8.42	4.33	-0.92
10	HR3-RZT	0.01	-0.32	-0.58	-0.51	-0.51	-0.26	0.05
	HR3-RZTmx	0.01	-0.43	-0.58	-0.51	-0.53	-0.26	0.04
	HR3-MZZF	2.53	9.89	15.61	17.11	0.04	-0.17	-0.30
	Pagano	**0.3758**	**4.886**	**5.481**	**0.1948**	**2.648**	**2.706**	**-0.8383**
	HR3 (%)	7.70	-9.37	22.40	32.18	-8.51	7.50	-2.02
5	HR3-RZT	0.11	-4.59	-4.39	-4.15	-3.86	-3.46	0.74
	HR3-RZTmx	0.11	-4.59	-4.38	-4.13	-3.89	-3.46	0.74
	HR3-MZZF	5.43	4.76	16.19	17.19	-0.18	0.34	-0.44

Table 8.9: Orthotropic laminate G: Percentage error in normalised bending deflection and 3D stresses for various HR models and a/t ratios with respect to Pagano's solution [69].

a/t	Model	$\lvert\bar{w}_0\rvert$	$\vee\lvert\bar{\sigma}_x\rvert$	$\vee\lvert\bar{\sigma}_y\rvert$	$\vee\lvert\bar{\sigma}_{xy}\rvert$	$\vee\lvert\bar{\sigma}_{xz}\rvert$	$\vee\lvert\bar{\sigma}_{yz}\rvert$	$\bar{\sigma}_z(z_{N_l-1})$
	Pagano	**0.006048**	**0.2451**	**0.6576**	**0.01883**	**3.268**	**19.69**	**-0.8002**
	HR3 (%)	0.03	0.07	0.46	0.08	-0.15	0.08	0.01
50	HR3-RZT	0.03	-0.07	0.03	0.04	-0.08	0.01	0.00
	HR3-RZTmx	0.03	-0.06	0.01	0.04	-0.08	0.01	0.00
	HR3-MZZF	0.03	-0.04	0.19	0.16	-0.10	0.02	0.00
	Pagano	**0.008037**	**0.3159**	**0.6757**	**0.02216**	**1.605**	**7.357**	**-0.7997**
	HR3 (%)	0.24	0.54	2.64	0.50	-0.62	0.47	0.08
20	HR3-RZT	0.15	-0.30	0.16	0.21	-0.38	0.09	-0.01
	HR3-RZTmx	0.15	-0.30	0.04	0.21	-0.39	0.09	-0.01
	HR3-MZZF	0.16	-0.16	1.06	0.84	-0.40	0.14	0.01
	Pagano	**0.01384**	**0.4927**	**0.7746**	**0.03001**	**1.154**	**3.193**	**-0.7970**
	HR3 (%)	1.02	2.31	10.82	1.82	-0.87	-2.97	0.26
10	HR3-RZT	0.44	-0.68	0.91	0.72	-0.80	0.20	-0.02
	HR3-RZTmx	0.44	-0.67	0.17	0.72	-0.81	0.26	-0.03
	HR3-MZZF	0.52	-0.12	6.97	2.46	-0.64	-0.77	0.02
	Pagano	**0.02969**	**0.8067**	**1.081**	**0.04158**	**0.8103**	**1.649**	**-0.7829**
	HR3 (%)	2.74	7.49	21.13	5.28	-0.08	-6.96	0.81
5	HR3-RZT	0.95	-1.03	1.64	1.96	-0.95	1.54	0.10
	HR3-RZTmx	0.95	-1.02	0.32	1.95	-0.96	1.56	0.10
	HR3-MZZF	1.23	0.79	12.57	6.08	-0.20	0.35	0.22

Table 8.10: Orthotropic laminate H: Percentage error in normalised bending deflection and 3D stresses for various HR models and a/t ratios with respect to Pagano's solution [69].

a/t	Model	$\lvert\bar{w}_0\rvert$	$\vee\lvert\bar{\sigma}_x\rvert$	$\vee\lvert\bar{\sigma}_y\rvert$	$\vee\lvert\bar{\sigma}_{xy}\rvert$	$\vee\lvert\bar{\sigma}_{xz}\rvert$	$\vee\lvert\bar{\sigma}_{yz}\rvert$	$\bar{\sigma}_z(z_{N_l-1})$
	Pagano	**0.02123**	**1.153**	**1.190**	**0.02576**	**9.003**	**9.478**	**-0.9849**
	HR3 (%)	0.25	6.07	3.64	16.16	-0.50	-0.41	-0.05
50	HR3-RZT	0.00	0.01	0.02	0.00	0.00	0.00	0.00
	HR3-RZTmx	0.00	0.00	0.01	0.01	0.00	0.00	0.00
	HR3-MZZF	0.23	7.24	0.69	21.83	-0.52	-0.37	-0.06
	Pagano	**0.08638**	**1.599**	**1.643**	**0.05179**	**4.072**	**4.285**	**-0.9817**
	HR3 (%)	2.02	25.88	11.18	28.06	-8.98	-2.42	-0.27
20	HR3-RZT	0.00	0.01	0.04	0.05	0.03	0.01	0.00
	HR3-RZTmx	0.00	-0.02	0.03	0.06	0.01	0.01	0.00
	HR3-MZZF	1.79	30.62	9.49	44.21	-5.93	-3.73	-0.34
	Pagano	**0.2483**	**3.169**	**3.668**	**0.1281**	**3.723**	**3.792**	**-0.9738**
	HR3 (%)	6.71	29.18	20.13	26.56	-10.86	3.32	-0.91
10	HR3-RZT	-0.06	0.51	0.43	0.45	0.46	0.42	0.01
	HR3-RZTmx	-0.06	0.42	0.42	0.48	0.42	0.42	0.01
	HR3-MZZF	5.90	36.23	17.20	46.60	-5.84	-1.31	-1.14
	Pagano	**0.5129**	**6.188**	**6.565**	**0.2376**	**3.131**	**3.148**	**-0.9600**
	HR3 (%)	13.38	24.97	35.38	38.74	-1.89	16.38	-2.07
5	HR3-RZT	-1.12	4.19	4.38	4.37	4.42	4.46	0.18
	HR3-RZTmx	-1.12	4.15	4.37	4.52	4.37	4.47	0.18
	HR3-MZZF	11.50	31.84	30.70	61.03	3.37	9.34	-2.52

displacement and stress fields at layer interfaces, as described in Section 4.1.1. The pronounced transverse orthotropy between the composite layers c and the honeycomb layers h increases the ZZ effect in the sandwich plates E-H compared to composite laminates A-D. The errors in the HR3 model are especially pronounced for laminates F and H which feature both the honeycomb core h and the degraded core 0.01h. For these two laminates, the errors in the in-plane shear stress metric $\bar{\sigma}_{xy}$ is around 10% for the relatively thin a/t ratio of 50. For thicker laminates with $a/t = 10$, this error increases to over 25%. However, for sandwich plates E and G, which are only comprised of core h, the HR3 model maintains reasonable accuracy even for relatively thick laminates of $a/t = 10$.

The HR3-RZT and HR3-RZTmx models are the most accurate of the HR formulations investigated herein, with a maximum error of 1.93% (Laminate C) for a/t ratios up to 10. When the thickness of the plate is further increased to $a/t = 5$, the HR-RZT models are accurate to within 6% (Laminate A). As previously noted, the increasing inaccuracy for $a/t = 5$ arises because the effects of through-thickness normal deformation can no longer be ignored. However, given the highly orthotropic material properties and "cube"-like nature of a plate with $a/t = 5$, errors to within a few percent of a 3D elasticity solution are acceptable given the reduced computational effort of the HR model compared to the alternative of full 3D FEM analyses. Interestingly, for sandwich plates E and G both the HR3-RZT and HR3-RZTmx models are accurate to within 2% for the thick configurations with $a/t = 5$. One possible explanation for this behaviour is that the low transverse shear rigidity of the sandwich core

(414 MPa) with respect to the transverse normal modulus (3.45 GPa) makes it energetically favourable for the plate to deform via transverse shearing and ZZ mechanisms rather than by transverse normal deformation, thereby reducing the relative influence of inaccuracies associated with neglecting thickness stretch.

Based on these findings, the difference in accuracy between the HR3-RZT and HR3-RZTmx models is benign. Gherlone [54] modified the definition of the RZT ZZ function based on observations of the in-plane displacement fields but the present results suggest that the effect of EWLs is less pronounced for stress fields. Stresses are based on the derivatives of displacements, such that differences in the displacements of the HR3-RZT and HR3-RZTmx models do not necessarily mean the displacement gradients are different. However, given that accurate internal displacement fields are needed in many nonlinear failure analyses, such as cohesive zone models, Gherlone's [54] modified version of the RZT ZZ function is recommended for most accurate results.

The other third-order ZZ model based on MZZF, HR3-MZZF, shows similar accuracy to the HR models based on the RZT ZZ function for composite laminates A-D and sandwich plates E and G. For composite laminates A-D, all seven metrics are accurate to within 2% for a/t ratios up to 10. When the thickness of the plate is further increased to $a/t = 5$, the HR3-MZZF model also suffers from a loss in accuracy to around 6% due to the thickness stretch effect. The first discrepancy between the accuracy of the RZT- and MZZF-based HR models can be observed for sandwich plates E and G. Although the HR3-MZZF model considerably improves on the HR3 model, the maximum error in $\bar{\sigma}_{xy}$ for laminate E at $a/t = 10$ is around 1% and increases to 2.5% for $a/t = 5$, whereas the error for the RZT HR models is close to zero in both cases. Furthermore, for sandwich plate G the error in $\bar{\sigma}_y$ is close to 7% when $a/t = 10$, whereas the HR3-RZTmx model remains within 2% even for the thicker configuration of $a/t = 5$.

For sandwich plates F and H, which are comprised of two different core materials h and 0.01h, the errors in HR3-MZZF are more pronounced and are in fact comparable to the accuracy of the HR3 model without ZZ functionality. For laminate F, the error in $\bar{\sigma}_{xy}$ is around 5% for the relatively thin configuration of $a/t = 50$ and increases to 17% for the moderately thick configuration at $a/t = 10$. For laminate H, the errors are exacerbated with a 22% discrepancy in $\bar{\sigma}_{xy}$ for $a/t = 50$ which increases to 47% when $a/t = 10$. In comparison, the error in the RZT-based HR models is less than 1% for both sandwich plates F and H up to $t/a = 10$.

These observations corroborate the findings in Section 5.2 that MZZF loses accuracy for laminates comprised of three different constitutive materials. This is because MZZF does not formally account for differences in the transverse shear moduli that underlie the mechanics of the ZZ effect. It is perhaps appropriate to point out the caveat in the original paper by Toledano and Murakami [168] that the "inclusion of the zig-zag shaped C^0 function was motivated by the displacement micro-structure of *periodic* laminated composites" and that "for general laminate configurations, this periodicity is destroyed", such that the "theory should be expected to break down in these particular cases". However, the author would like to emphasise that, in general, MZZF provides accurate solutions for most commonly used laminates when employed in a third-order HR theory. For sandwich plates with very flexible cores or laminates with pronounced heterogeneity, the constitutive independence of MZZF can lead to large errors. Thus, the RZT

ZZ function should be used for the most general straight-fibre laminations.

To qualitatively compare the accuracy of the four HR models, the through-thickness variations of all six stress metrics are plotted in Figures 8.2-8.9 for the characteristic length to thickness ratio $a/t = 10$. The in-plane (x, y) locations of each z-wise plot are provided in the stress metric definitions of Eq. (8.6) and are additionally indicated in the figure captions. The observations previously made about the data in Tables 8.3-8.10 are corroborated in these figures, namely:

1. The HR3-RZT and HR3-RZTmx through-thickness plots of the 3D stress fields are closely matched to Pagano's 3D elasticity solution for any type of stacking sequence investigated herein. Most importantly, the transverse stress profiles are captured accurately from the *a priori* model assumptions, precluding the need for stress recovery steps.

2. The difference in the 3D stress fields between HR3-RZT and HR3-RZTmx models is benign.

3. The HR3 model generally only provides accurate 3D stress fields to within nominal errors for composite laminates with $a/t \geq 10$. In the case of sandwich plates or laminates that feature materials with transverse shear properties that vary by orders of magnitude, a ZZ term is generally recommended. However for practical engineering laminates most commonly used in industry, the HR3 model provides the best trade-off between accuracy and computational effort.

4. A third-order model with a ZZ term based on MZZF is accurate for most composite laminates and stiff sandwich cores. In the case of more flexible or degraded sandwich cores, laminates with two different types of cores or laminates with more than two unique constitutive materials, the HR3-MZZF model leads to large errors.

5. For characteristic length to thickness ratios $a/t \leq 5$, thickness stretch should be incorporated for generally accurate 3D stress fields. Thus, the assumed displacement field for u_z in Eq. (7.1) needs to be modified to account for a higher-order variation through the thickness.

Note that the discrepancies between the two HR models HR3 and HR3-MZZF, and Pagano's 3D elasticity solution are most evident for sandwich laminates F and H comprised of two different sandwich cores (see Figures 8.7 and Figures 8.9, respectively).

An interesting phenomenon is observed in the transverse shear stress profiles of laminates F and H in Figures 8.7e and 8.7f, and Figures 8.9e and 8.9f, respectively. In these plots, a reversal of the transverse shear stresses in the stiffer face layers is observed. This behaviour only occurs for extreme cases of transverse orthotropy, i.e. when the transverse shear rigidity of an inner layer is insufficient to support the peak transverse shear stress of the adjacent outer layer. In essence, it is a load redistribution effect that arises because the transverse shear force must remain constant for a unique loading configuration, i.e. the transverse shear stress through-thickness distribution may change with layup, but the through-thickness integral of this transverse shear stress is independent of layup.

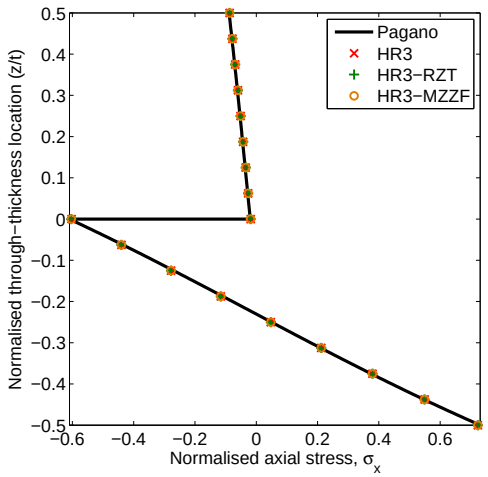

(a) Normalised axial stress, $\bar{\sigma}_x(a/2, b/2, z)$

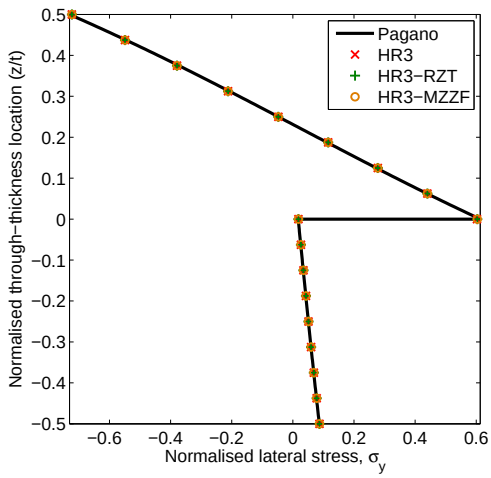

(b) Normalised lateral stress, $\bar{\sigma}_y(a/2, b/2, z)$

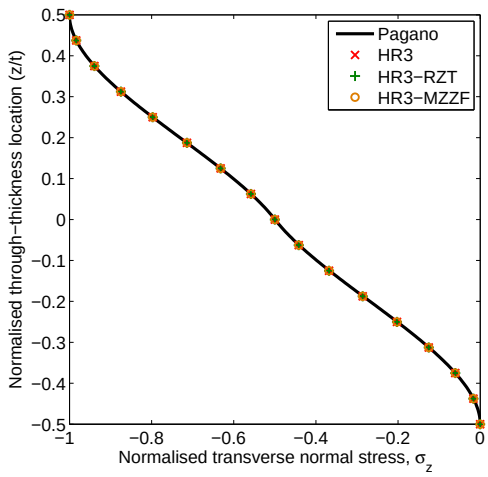

(c) Normalised transverse normal stress, $\bar{\sigma}_z(a/2, b/2, z)$

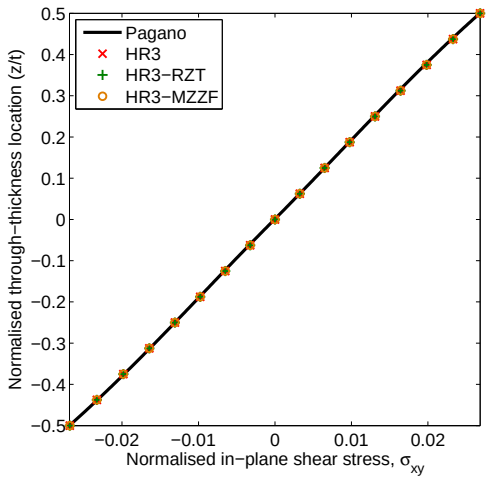

(d) Normalised in-plane shear stress, $\bar{\sigma}_{xy}(a/4, b/4, z)$

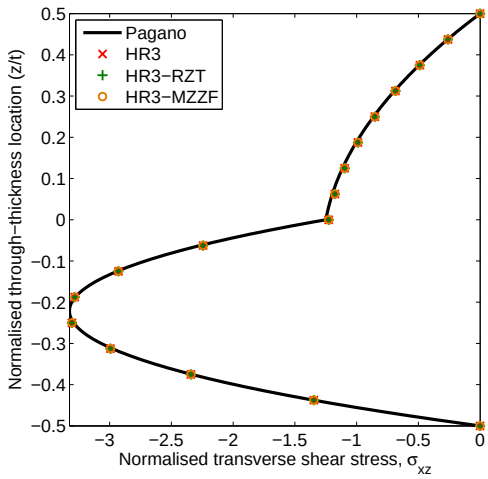

(e) Normalised transverse shear stress, $\bar{\sigma}_{xz}(0, b/2, z)$

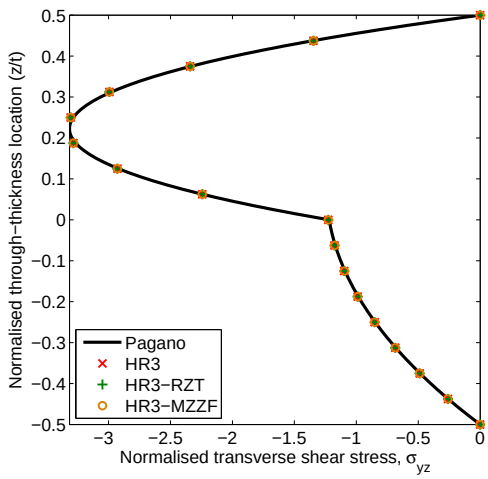

(f) Normalised transverse shear stress, $\bar{\sigma}_{yz}(a/2, 0, z)$

Figure 8.2: Laminate A: Through-thickness distribution of the 3D stress field at different planar locations for $a/t = 10$. The figures compare different implementations of the HR model with Pagano's elasticity solution.

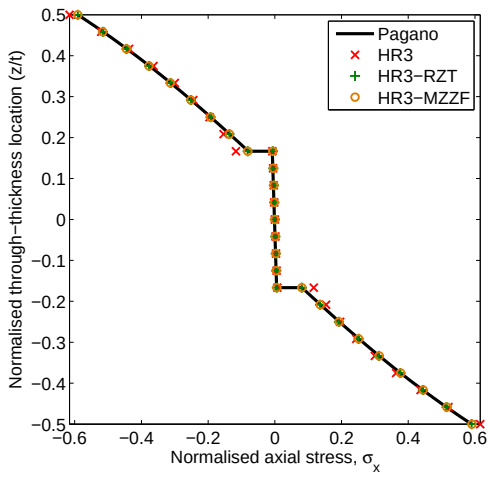

(a) Normalised axial stress, $\bar{\sigma}_x(a/2, b/2, z)$

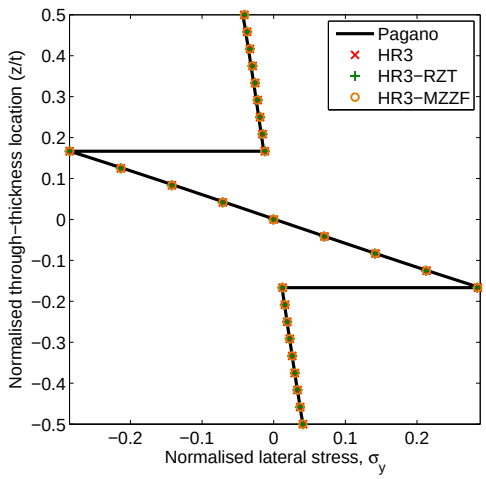

(b) Normalised lateral stress, $\bar{\sigma}_y(a/2, b/2, z)$

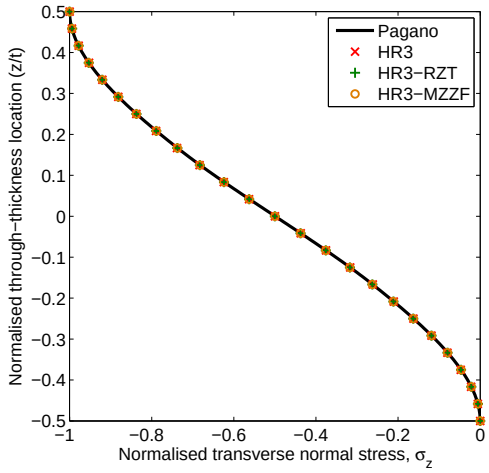

(c) Normalised transverse normal stress, $\bar{\sigma}_z(a/2, b/2, z)$

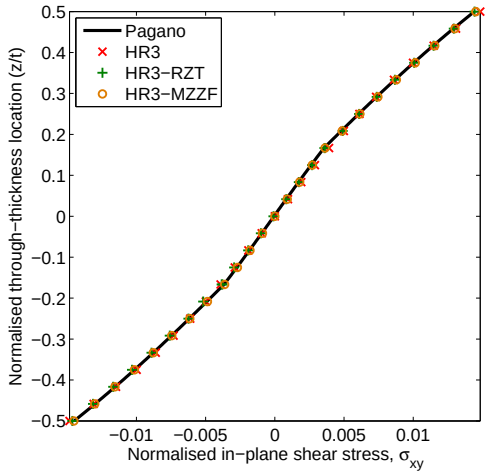

(d) Normalised in-plane shear stress, $\bar{\sigma}_{xy}(a/4, b/4, z)$

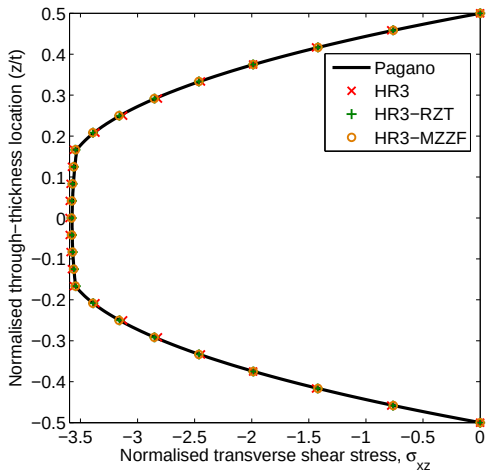

(e) Normalised transverse shear stress, $\bar{\sigma}_{xz}(0, b/2, z)$

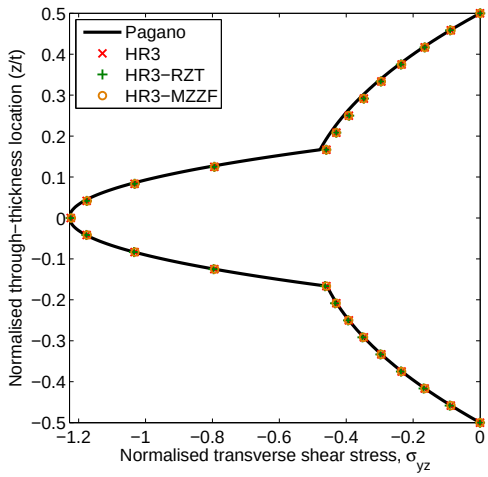

(f) Normalised transverse shear stress, $\bar{\sigma}_{yz}(a/2, 0, z)$

Figure 8.3: Laminate B: Through-thickness distribution of the 3D stress field at different planar locations for $a/t = 10$. The figures compare different implementations of the HR model with Pagano's elasticity solution.

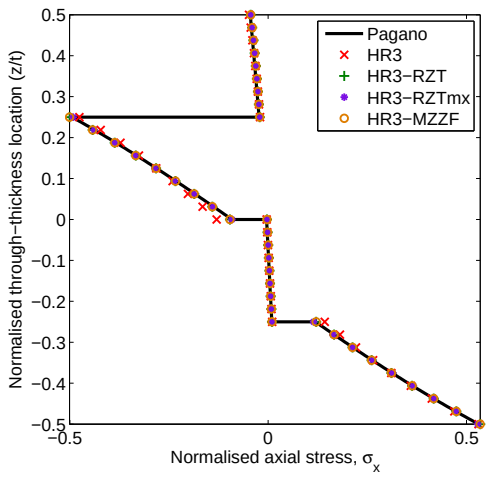

(a) Normalised axial stress, $\bar{\sigma}_x(a/2, b/2, z)$

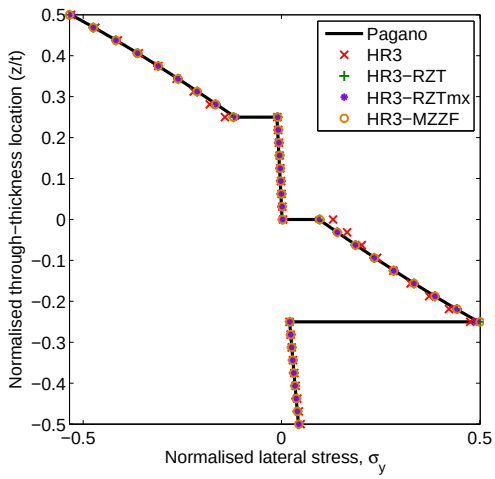

(b) Normalised lateral stress, $\bar{\sigma}_y(a/2, b/2, z)$

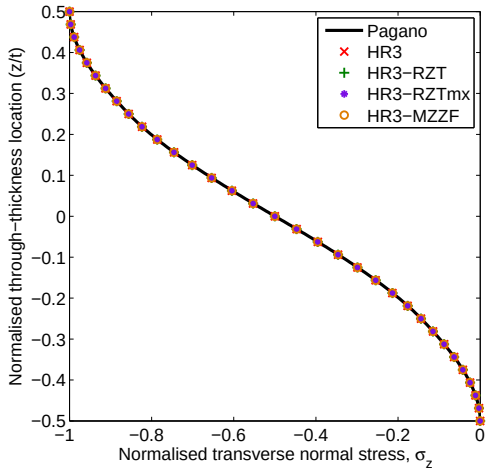

(c) Normalised transverse normal stress, $\bar{\sigma}_z(a/2, b/2, z)$

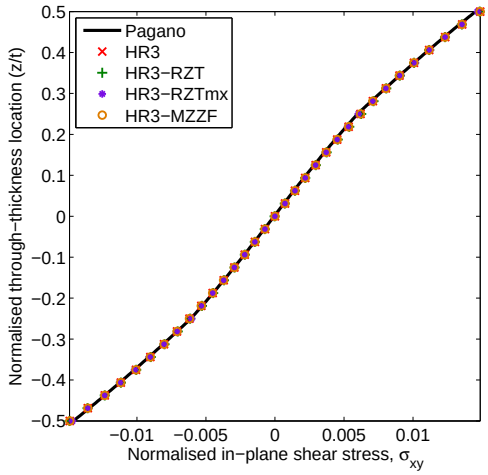

(d) Normalised in-plane shear stress, $\bar{\sigma}_{xy}(a/4, b/4, z)$

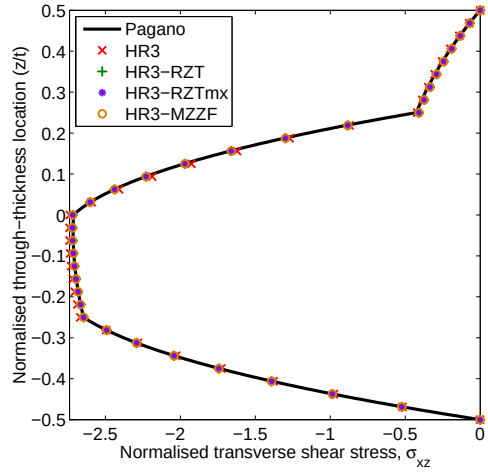

(e) Normalised transverse shear stress, $\bar{\sigma}_{xz}(0, b/2, z)$

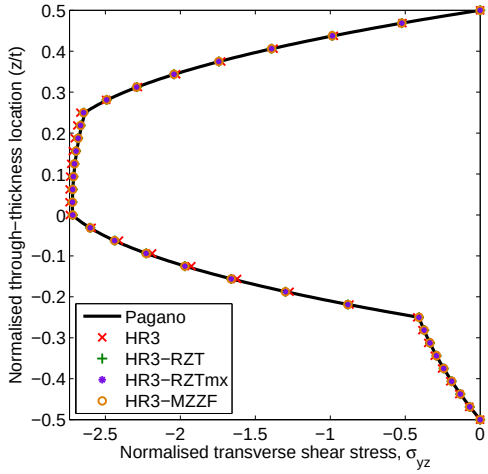

(f) Normalised transverse shear stress, $\bar{\sigma}_{yz}(a/2, 0, z)$

Figure 8.4: Laminate C: Through-thickness distribution of the 3D stress field at different planar locations for $a/t = 10$. The figures compare different implementations of the HR model with Pagano's elasticity solution.

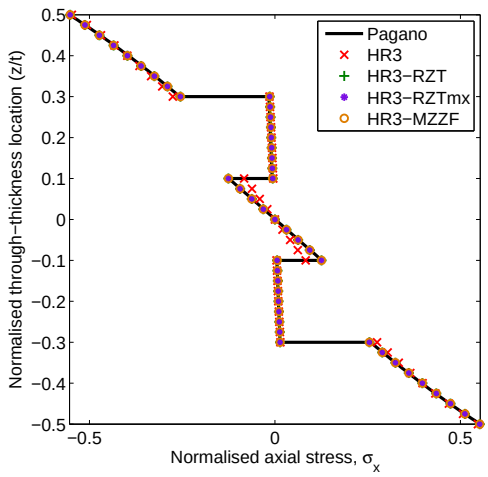

(a) Normalised axial stress, $\bar{\sigma}_x(a/2, b/2, z)$

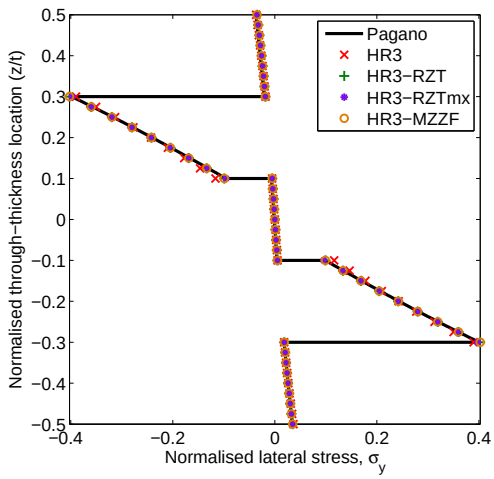

(b) Normalised lateral stress, $\bar{\sigma}_y(a/2, b/2, z)$

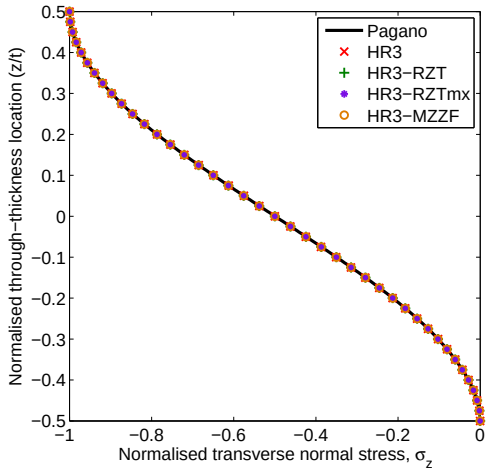

(c) Normalised transverse normal stress, $\bar{\sigma}_z(a/2, b/2, z)$

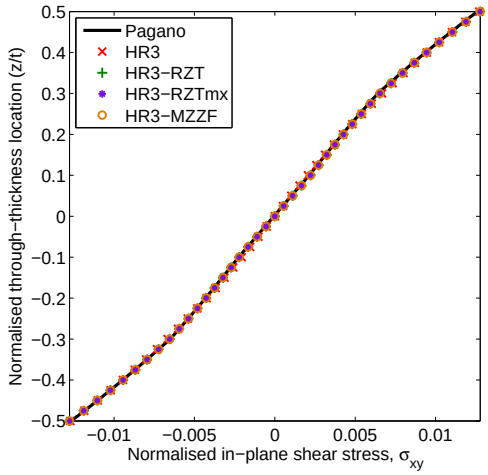

(d) Normalised in-plane shear stress, $\bar{\sigma}_{xy}(a/4, b/4, z)$

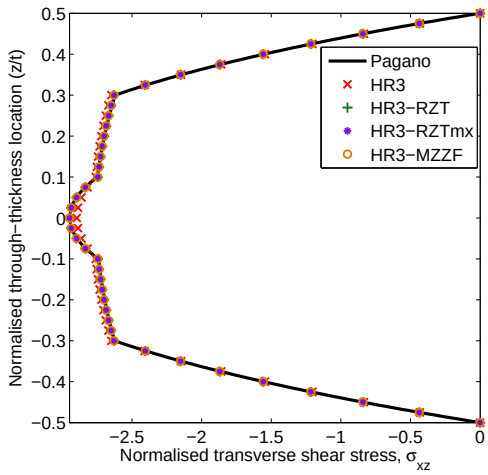

(e) Normalised transverse shear stress, $\bar{\sigma}_{xz}(0, b/2, z)$

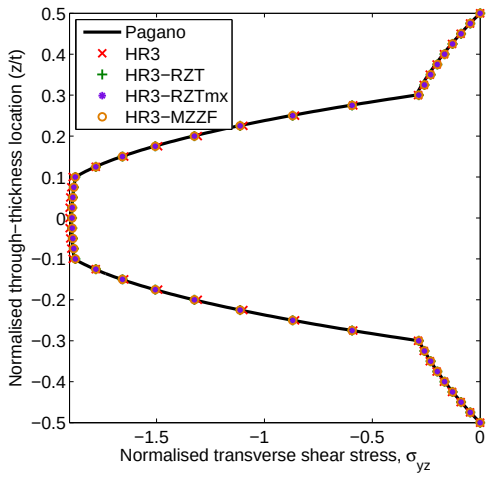

(f) Normalised transverse shear stress, $\bar{\sigma}_{yz}(a/2, 0, z)$

Figure 8.5: Laminate D: Through-thickness distribution of the 3D stress field at different planar locations for $a/t = 10$. The figures compare different implementations of the HR model with Pagano's elasticity solution.

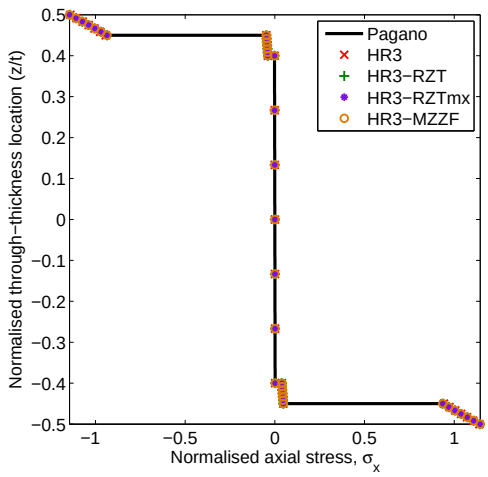

(a) Normalised axial stress, $\bar{\sigma}_x(a/2, b/2, z)$

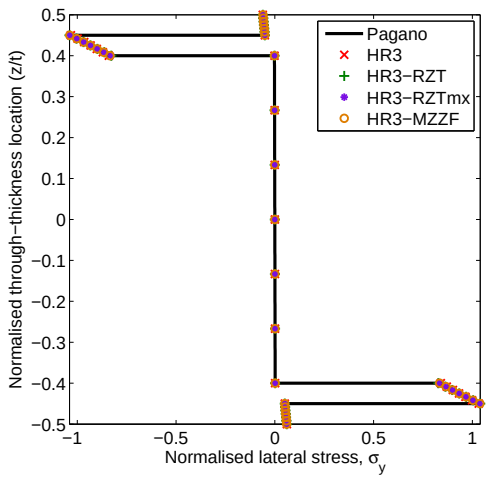

(b) Normalised lateral stress, $\bar{\sigma}_y(a/2, b/2, z)$

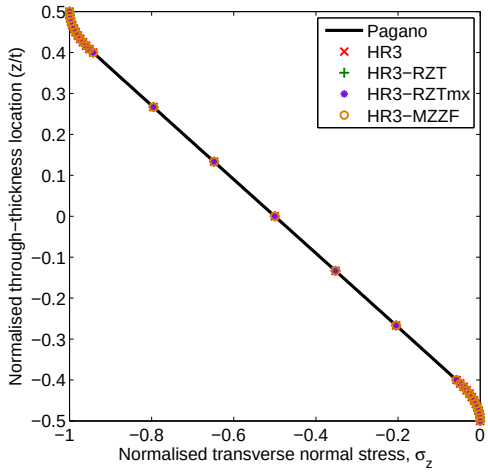

(c) Normalised transverse normal stress, $\bar{\sigma}_z(a/2, b/2, z)$

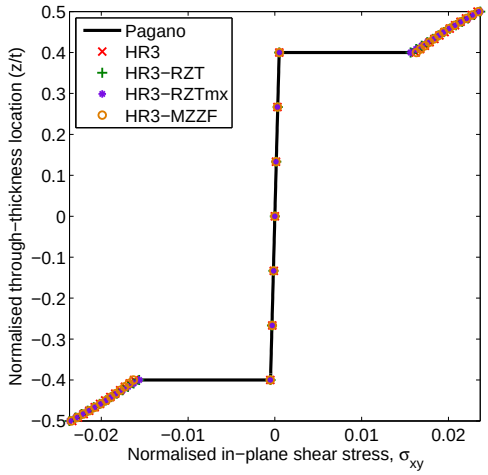

(d) Normalised in-plane shear stress, $\bar{\sigma}_{xy}(a/4, b/4, z)$

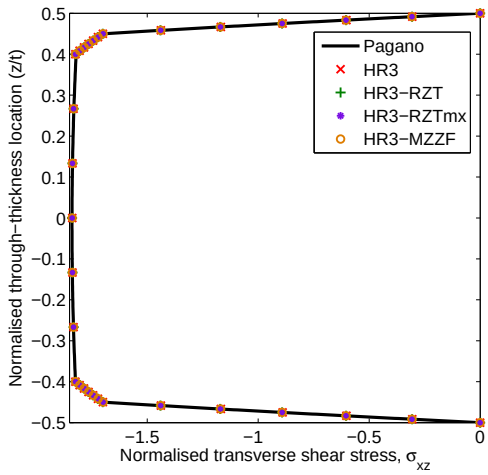

(e) Normalised transverse shear stress, $\bar{\sigma}_{xz}(0, b/2, z)$

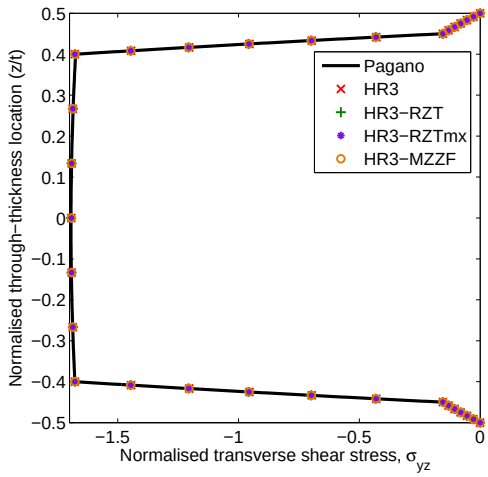

(f) Normalised transverse shear stress, $\bar{\sigma}_{yz}(a/2, 0, z)$

Figure 8.6: Laminate E: Through-thickness distribution of the 3D stress field at different planar locations for $a/t = 10$. The figures compare different implementations of the HR model with Pagano's elasticity solution.

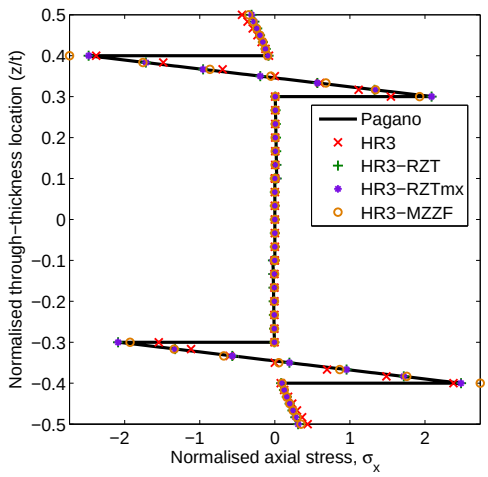

(a) Normalised axial stress, $\bar{\sigma}_x(a/2, b/2, z)$

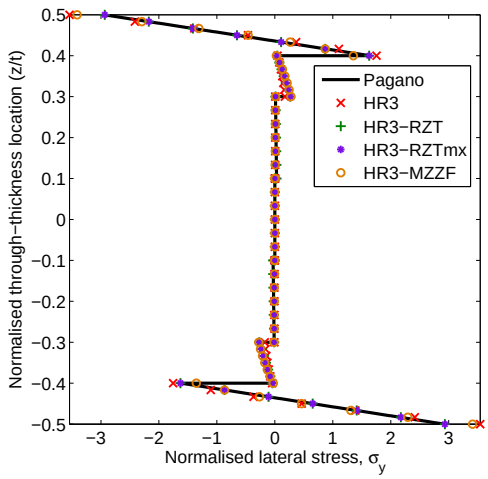

(b) Normalised lateral stress, $\bar{\sigma}_y(a/2, b/2, z)$

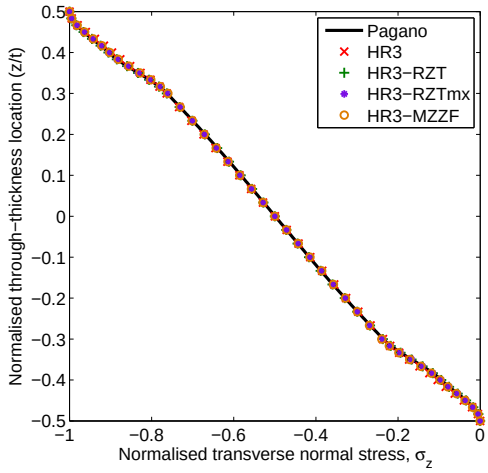

(c) Normalised transverse normal stress, $\bar{\sigma}_z(a/2, b/2, z)$

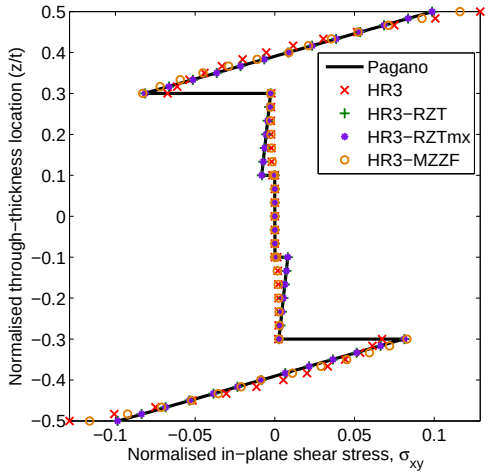

(d) Normalised in-plane shear stress, $\bar{\sigma}_{xy}(a/4, b/4, z)$

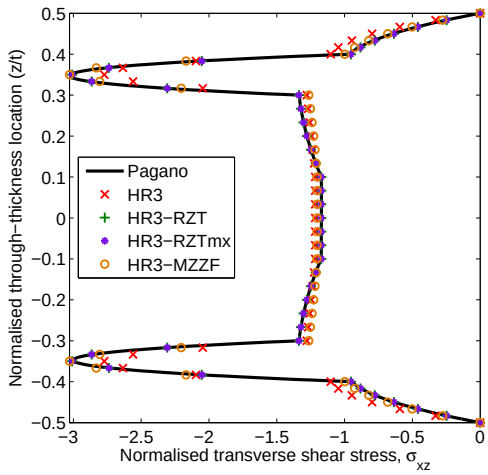

(e) Normalised transverse shear stress, $\bar{\sigma}_{xz}(0, b/2, z)$

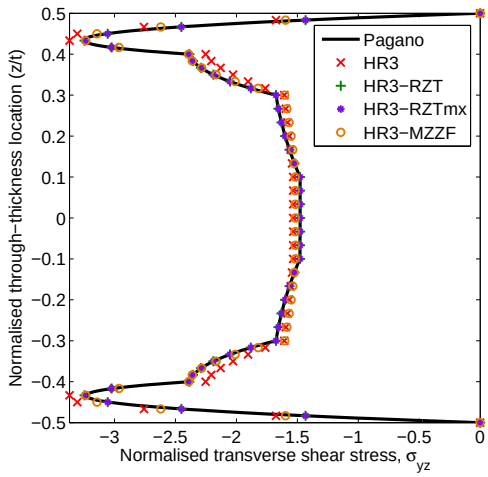

(f) Normalised transverse shear stress, $\bar{\sigma}_{yz}(a/2, 0, z)$

Figure 8.7: Laminate F: Through-thickness distribution of the 3D stress field at different planar locations for $a/t = 10$. The figures compare different implementations of the HR model with Pagano's elasticity solution.

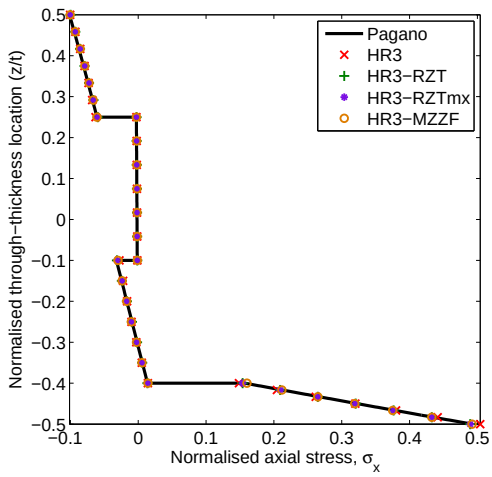

(a) Normalised axial stress, $\bar{\sigma}_x(a/2, b/2, z)$

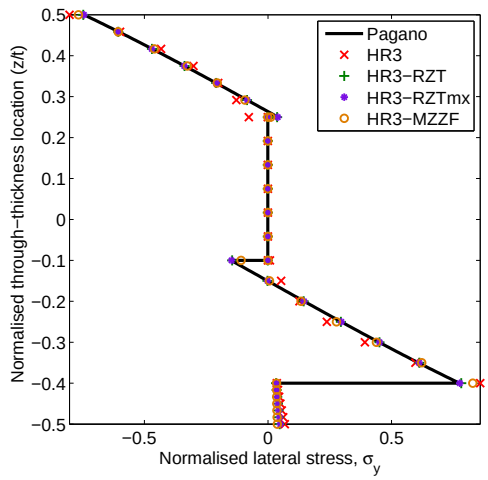

(b) Normalised lateral stress, $\bar{\sigma}_y(a/2, b/2, z)$

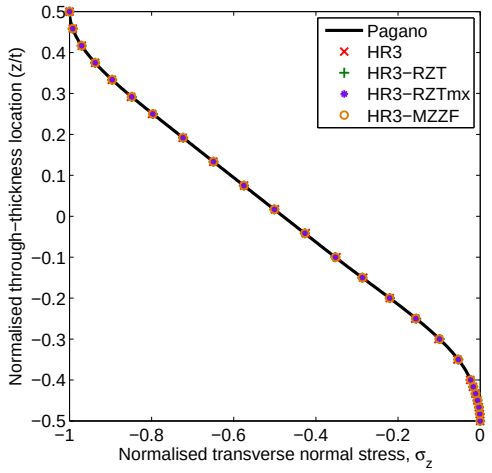

(c) Normalised transverse normal stress, $\bar{\sigma}_z(a/2, b/2, z)$

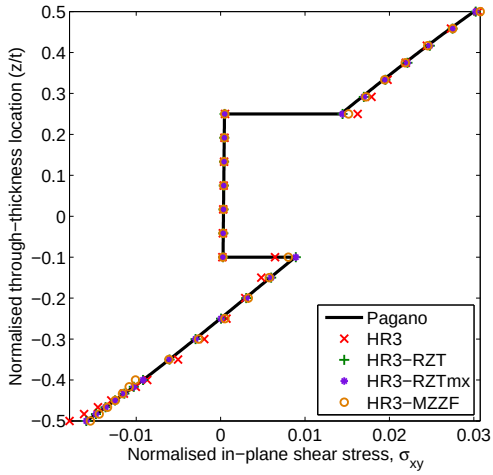

(d) Normalised in-plane shear stress, $\bar{\sigma}_{xy}(a/4, b/4, z)$

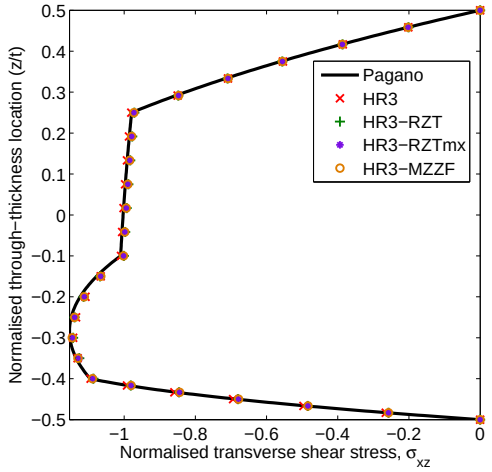

(e) Normalised transverse shear stress, $\bar{\sigma}_{xz}(0, b/2, z)$

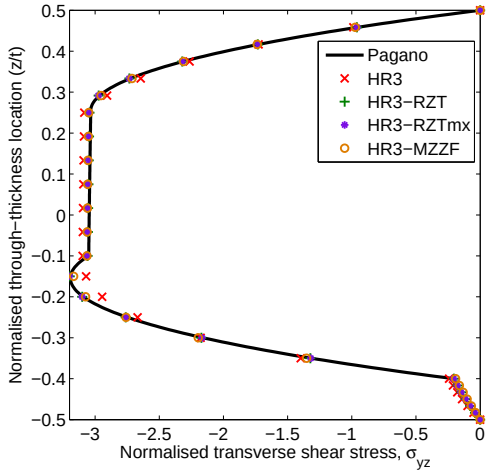

(f) Normalised transverse shear stress, $\bar{\sigma}_{yz}(a/2, 0, z)$

Figure 8.8: Laminate G: Through-thickness distribution of the 3D stress field at different planar locations for $a/t = 10$. The figures compare different implementations of the HR model with Pagano's elasticity solution.

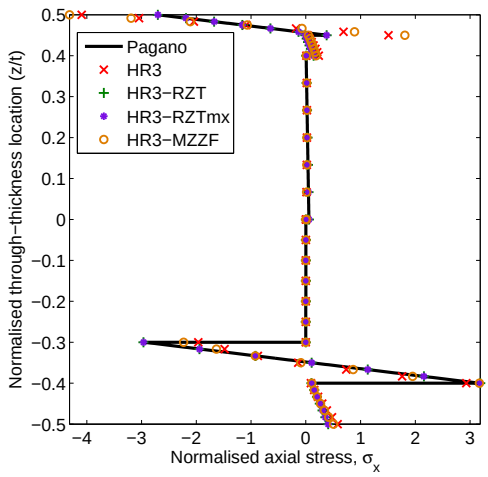

(a) Normalised axial stress, $\bar{\sigma}_x(a/2, b/2, z)$

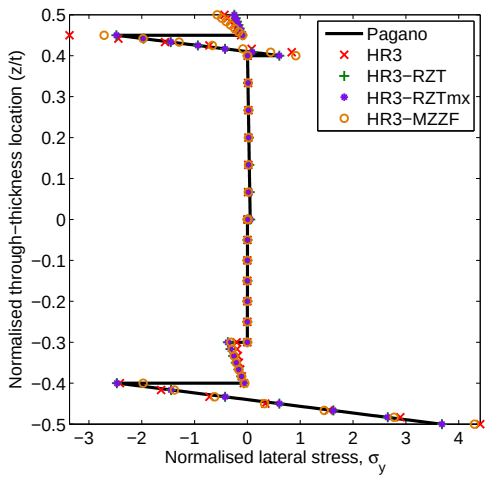

(b) Normalised lateral stress, $\bar{\sigma}_y(a/2, b/2, z)$

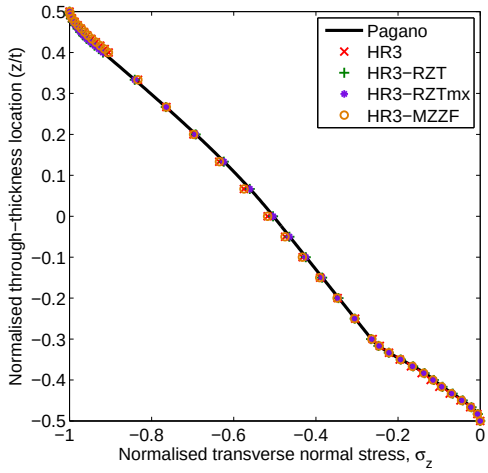

(c) Normalised transverse normal stress, $\bar{\sigma}_z(a/2, b/2, z)$

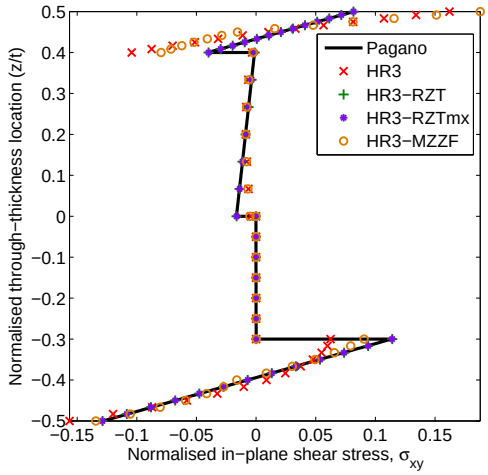

(d) Normalised in-plane shear stress, $\bar{\sigma}_{xy}(a/4, b/4, z)$

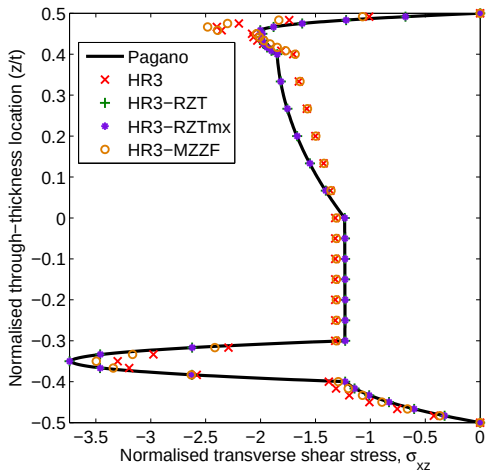

(e) Normalised transverse shear stress, $\bar{\sigma}_{xz}(0, b/2, z)$

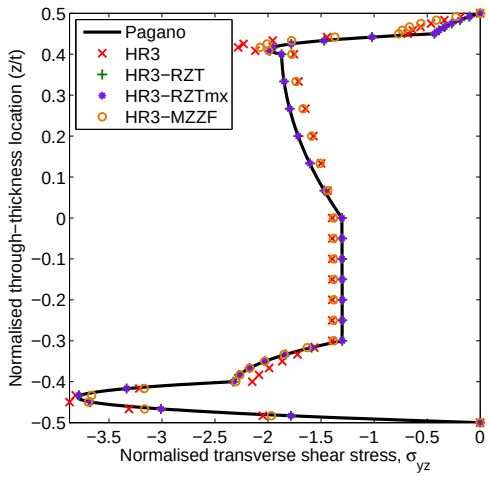

(f) Normalised transverse shear stress, $\bar{\sigma}_{yz}(a/2, 0, z)$

Figure 8.9: Laminate H: Through-thickness distribution of the 3D stress field at different planar locations for $a/t = 10$. The figures compare different implementations of the HR model with Pagano's elasticity solution.

As the transverse shear stresses and in-plane stresses must equilibrate in Cauchy's equilibrium equations, we can also observe that the corresponding plots of $\bar{\sigma}_x$, $\bar{\sigma}_y$ and $\bar{\sigma}_{xy}$ for sandwich plates F and H change sign in some layers remote from the neutral axis. As a result, some of the layers are both in tension and compression even when they are situated far away from the neutral axis. This is especially evident for the symmetric sandwich plate F in Figures 8.7a and 8.7b where the neutral axis is located on the midplane, i.e. the geometric centroid, but the second layers from the top and bottom of the laminate are both in tension and compression. Fundamentally this means that a cross-section of the plate no longer has one unique neutral axis. The extreme case of transverse orthotropy occurs when the stiffer outer layers are bending independently with fully reversed in-plane stress profiles within one layer, i.e. equal amounts of tension and compression. Such a scenario occurs if the properties of the sandwich core are negligible, such that they have "air-like" properties that cannot support any shear loading.

In conclusion, the results for the orthotropic plates presented in this section corroborate the findings for orthotropic beams in Section 5.2. The third-order RZT-based model is the most accurate of the formulations investigated herein for predicting bending deflections and 3D stress fields from *a priori* model assumptions. This is because the RZT ZZ function is derived from actual transverse shear material properties. The HR3-MZZF model provides similar accuracy for composite laminates and sandwich plates with benign transverse anisotropy between the core and face layers. For more pronounced anisotropy, the constitutive independence of MZZF can lead to large errors, such that the HR3-RZTmx model is deemed to provide the most accurate 3D stress predictions for arbitrary straight-fibre laminations.

8.1.2 Benchmarking of 3D stresses in anisotropic laminates

8.1.2.1 Model implementation

As a second test, consider the multilayered square plate ($a = b = 1$ m) shown in Figure 8.10, loaded on the top surface by a uniformly distributed pressure load $\hat{P}_t = p_0$ and a uniform shear traction in the x-direction $\hat{T}_{tx} = t_0$. The plate is rigidly built-in along all four edges, such that the three translations and three rotations are constrained through the entire cross-section. In the HR model, the 3D continuum is compressed onto an equivalent single layer Ω coincident with the midplane of the plate, depicted by the grey surface. This loading configuration represents a more challenging test case than the orthotropic plate subjected to sinusoidal pressure loading in the previous section as both the layer fibre orientations and the loading condition are more general.

For the anisotropic laminates investigated herein, the third-order model HR3, and third-order ZZ models HR3-RZT, HR3-RZTmx and HR3-MZZF are again implemented. As general anisotropic laminates with off-axis plies exhibit extension/shear and bend/twist coupling, it is more challenging to ascertain an analytical solution for the bending behaviour than for the orthotropic laminates in Section 8.1.1.1. For general anisotropic laminates, $\bar{Q}_{16} \neq 0$ and $\bar{Q}_{26} \neq 0$, such that the simple double sine series solution previously implemented no longer exactly satisfies the governing differential equations.

The general governing equations are therefore solved using the DQM introduced in Chapter 2. The DQM is a versatile numerical discretisation technique that can be used to develop

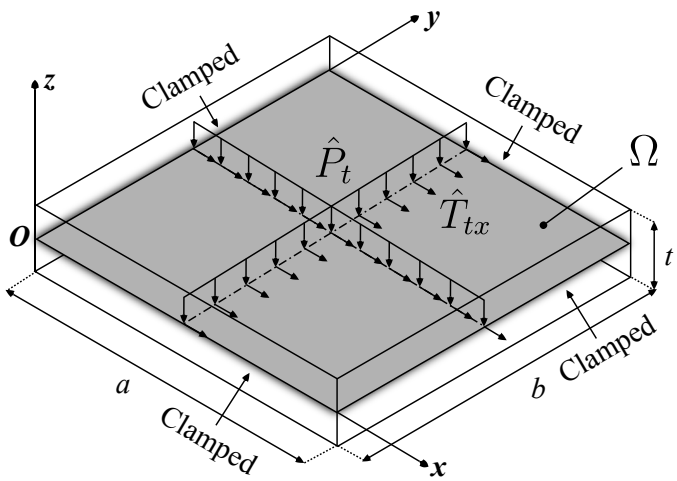

Figure 8.10: A composite plate loaded on the top surface by a uniformly distributed pressure load and a uniform shear traction. All four edges are clamped. In the HR model, the 3D continuum is compressed onto an equivalent single layer Ω coincident with the midplane of the plate.

strong-form finite elements [150]. Using this technique, the relatively simple geometry of a square, flat plate investigated here can be extended to the analysis of more complex geometries.

Following the description of DQM in Section 2.4, the governing differential equations are converted into algebraic ones by replacing the differential operators in the governing field equations (7.61) and boundary conditions (7.62) with DQ weighting matrices that operate on all functional unknowns within the domain. Thus, each differential operator is converted into a linear weighted sum of the functional unknowns at predetermined grid points. In this work, the non-uniform Chebychev-Gauss-Lobatto grid is used to discretise the planar domain of the continuum $x \in [0, 1]$ and $y \in [0, 1]$ into a computational domain with N_p grid points in either direction. In the Chebychev-Gauss-Lobatto grid, the location of the grid points X_i in direction X is given by

$$X_i = \frac{1}{2}\left(1 - \cos\frac{(i-1)\,\pi}{N_p - 1}\right) \quad \text{for} \quad i = 1, 2, \ldots, N_p. \tag{8.7}$$

An important characteristic of the Chebychev-Gauss-Lobatto grid is that it results in the minimum discretisation error, and by biasing the grid points towards the boundaries, avoids Runge's phenomenon[1] associated with a uniform grid [149]. Based on an initial mesh convergence study, a disretisation grid with 19 points in both the x- and y- directions was chosen (see Figure 8.11). The chosen mesh size of 361 grid points provides a good trade-off between computational time and accuracy of the results.

As shown in Eq. (2.35), the governing field equations (7.61) are discretised only for the internal grid points, whereas the boundary conditions (7.62) are only applied on the boundary points. Both sets of equations are written in terms of two unknown vectors: a vector of internal

[1]Runge's phenomenon is a problem of oscillation between discretisation points which occurs when high-order interpolation polynomials are used in a grid of uniformly spaced points. Thus, increasing the interpolation order of the polynomial on a uniform grid spacing does not necessarily lead to better numerical solutions. The Chebychev-Gauss-Lobatto grid, on the other hand, guarantees that the maximum error reduces with increasing polynomial order.

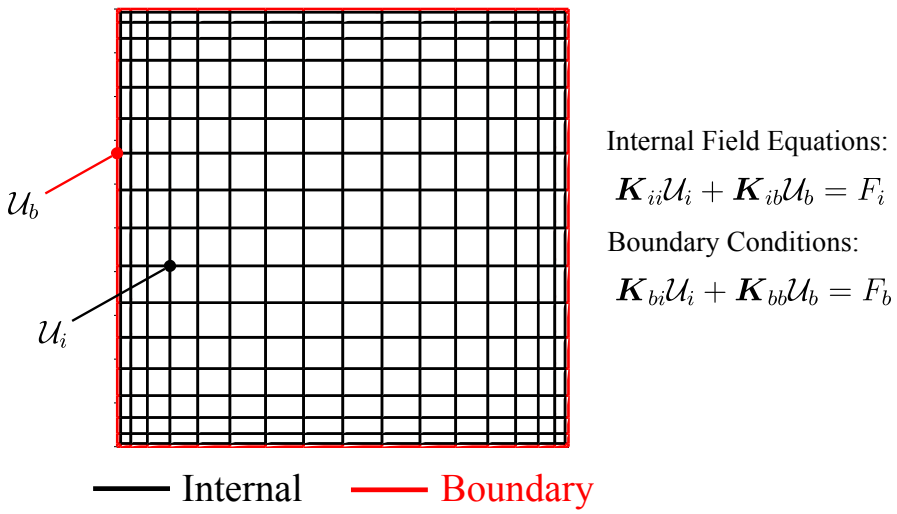

Figure 8.11: A non-uniform Chebychev-Gauss-Lobatto grid broken into a set of internal grid points and a grid of boundary points. The governing field equations are only applied at the internal points and the boundary conditions only at the boundary points. Thus, the problem is substructured into four unique matrices and solved for the field and boundary unknowns $\mathcal{U}_i$ and $\mathcal{U}_b$, respectively.

field unknowns $\mathcal{U}_i$ and a vector of boundary unknowns $\mathcal{U}_b$. This step of splitting the problem into internal and boundary points, as well as into field and boundary equations, is depicted in Figure 8.11. In this manner, the complete set of governing equations is substructured into four unique matrices that allow the boundary unknowns to be eliminated,

$$\mathcal{U}_i = \left[\boldsymbol{K_{ii}} - \boldsymbol{K_{ib}}\boldsymbol{K_{bb}}^{-1}\boldsymbol{K_{bi}}\right]^{-1} \cdot \left(F_i - \boldsymbol{K_{ib}}\boldsymbol{K_{bb}}^{-1} \cdot F_b\right) \tag{8.8a}$$

$$\mathcal{U}_b = \boldsymbol{K_{bb}}^{-1} \cdot \left(F_b - \boldsymbol{K_{bi}} \cdot \mathcal{U}_i\right) \tag{8.8b}$$

where i refers to the internal field and b to the boundary. Thus, the final matrix inversion problem in Eq. (8.8a) includes both the discretised field and boundary equations in one matrix, which is solved for the vector of internal field unknowns $\mathcal{U}_i$. The unknowns on the boundary $\mathcal{U}_b$ are subsequently post-processed using the internal field variables in Eq. (8.8b).

It is important to point out that the stiffness matrices in Eq. (8.8) are densely populated, such that certain pre-conditioning steps are recommended to reduce the condition number[2] of the associated matrices and to improve the accuracy of the matrix inversion. For variable-stiffness laminates, the material properties change across the discretisation grid, such that the magnitudes of the terms along the rows of the stiffness matrices may vary significantly. Moreover, in the governing field equations and boundary conditions Eqs. (7.61)-(7.62), the unknown stress resultants $\mathcal{F}$ and their in-plane derivatives are multiplied by compliance terms $\boldsymbol{s}$ and shear correction factors $\boldsymbol{\eta}$. These material property-dependent terms can be orders of

[2]In linear algebra, the condition number of a matrix is a metric to gauge how sensitive the solution to a system of linear equations is to errors in the inputs. Thus, the condition number indicates the expected accuracy of matrix inversion and of the solution. In general, the condition number κ of a matrix $\boldsymbol{A}$ is given by the product of two norms $\kappa(\boldsymbol{A}) = \|\boldsymbol{A}^{-1}\| \cdot \|\boldsymbol{A}\|$, such that by definition $\kappa(\boldsymbol{A}) \geq 1$ with values near unity indicating a well-conditioned matrix [176, p. 321].

magnitude smaller than the DQM weighting coefficients which appear in the strain vectors $\mathcal{L}_{eq}$ and $\mathcal{L}_{bc}$ (see Eqs. (7.64) and (7.65), respectively). Thus, elements along the rows of the stiffness matrices, where each row corresponds to a unique equilibrium equation at a discretisation grid point, can vary by orders of magnitude and lead to a large condition number. The use of the compliance matrix $\boldsymbol{s}$ is an inherent numerical drawback of the chosen theoretical framework in terms of solving the problem numerically using the DQM. This drawback can be partially remedied by normalising each row K_r of the stiffness matrix, i.e. each equilibrium equation, using the root-mean-square of the corresponding row,

$$K_r^n = \frac{K_r}{\sqrt{\sum_c K_{rc}^2}} \tag{8.9}$$

where K_{rc} are the c components of row K_r, and K_r^n is a normalised row.

Finally, the stiffness matrices in Eq. (8.8) are generally non-symmetric and can have zeros on the leading diagonal. This occurs because the in-plane and bending equilibrium equations Eqs. (7.61a) and (7.61b), as well as the enhanced constitutive equations Eqs. (7.61c), are discretised into the same matrix due to the mixed displacement- and stress-based nature of the HR model. To overcome the issue of zeros on the leading diagonal, the idea of damping, as proposed in the works of Levenberg [171] and Marquardt [172], is used by replacing the zeros with small terms of magnitude 10^{-10}. Even though this method considerably reduces the condition number of the stiffness matrix, the author is aware that damping the diagonal in this manner perturbs the underlying numerical problem and more elegant solutions may be possible. One possible solution is to discretise the plate into multiple DQM elements using the method proposed by Tornabene et al. [150]. Such an approach is equivalent to a strong-form FEM and considerably reduces the bandwidth of the matrices to improve the conditioning of the stiffness matrix.

As Pagano's 3D elasticity solution [69] is only valid for simply supported orthotropic plates, a 3D FEM model is used to benchmark the HR model results for anisotropic laminates. The plate is modelled in the commercial software package Abaqus using a 3D body that is 1 m long, 50 mm thick and 1 m wide. This plate, with characteristic length to thickness aspect ratio of $a/t = 20$, is meshed with 784,080 linear C3D8R reduced integration brick elements with enhanced hourglassing control, i.e. 80 elements through the thickness and 99 elements in both in-plane dimensions. This choice was based on initial convergence criteria and on the constraint of keeping the runtime at less than 12 hrs. In Section 8.1.2.2 laminates with up to eight unique layers are analysed, such that each laminate features a minimum of ten elements per layer. A pressure loading of $\hat{P}_t = -100$ kPa and a shear traction of $\hat{T}_{tx} = -50$ kPa are applied on the top surface. Finally, all six degrees of freedom (three translations and three rotations) are constrained at the four clamped edges throughout the entire plate cross-section. With 810,000 nodes and six degrees of freedom per node (4.86 million variables) the run-time on the local desktop PC equipped with an Intel i7-2600S processor with 2.80 GHz and 8 GB of RAM is about 12 hrs, whereas the HR3 (15 variables) and HR3-RZT (19 variables) codes in Matlab have a run-times of around 120 sec and 180 sec, respectively, at the chosen mesh size of 361 grid points (5,415 and 6,859 variables, respectively). Thus, the HR model in Matlab reduces the number of degrees of freedom by three orders of magnitude compared to the 3D FEM model in Abaqus.

However, it must be noted that the runtime in Abaqus is highly dependent on the available RAM and not the CPU speed. Therefore, the Abaqus model can be sped-up considerably if the available RAM is increased.

8.1.2.2 Model validation

To test the general applicability of the HR formulation a variety of different symmetric and non-symmetric composite laminates and sandwich plates are tested. The two materials used throughout the analysis are as defined in Table 8.1 of Section 8.1.1.2. The stacking sequences of different laminates including layer orientations, layer thickness and layer material codes are summarised in Table 8.11. All laminates have a total thickness of 50 mm, i.e. $a/t = 20$.

Laminates I and J are general composite laminates with orthotropic and off-axis plies with respect to the (x, y) coordinate system. Laminate I is a balanced, non-symmetric laminate that exhibits in-plane/out-of-plane coupling and bend/twist coupling. Laminate J is an unbalanced, symmetric laminate which exhibits both extension/shear and bend/twist coupling. Laminates K and L extend the two coupling mechanisms mentioned above to a soft-core sandwich plate that accentuates the ZZ effect. Thus, these two latter test cases represent non-classical laminates with arbitrary fibre orientations and material heterogeneity, which intend to test the full capability of the different HR models. Finally, laminate M is a quasi-isotropic composite laminate, which is the most commonly used layup in industry.

Henceforth, all deflection and stress results are presented in normalised form. The same definitions of the normalised metrics as previously defined in Eq. (8.6) are used but due to the change in load case the factor p_0 in the denominators of the metrics is replaced by the norm $\sqrt{p_0^2 + t_0^2}$. Furthermore, the transverse shear stresses σ_{xz} and σ_{yz} are no longer computed at the edges of the plate, as this represents a singularity in the 3D FEM model, but at the quarterspan. Hence, the new definition of the stress metrics is given by

$$\begin{aligned}
\bar{w}_0 &= \frac{E_2^{(c)} t^2}{a^2 b^2 \sqrt{p_0^2 + t_0^2}} \int_{-\frac{t}{2}}^{\frac{t}{2}} u_z \left(\frac{a}{2}, \frac{b}{2}, z\right) \mathrm{d}z \\
\bar{\sigma}_x(z) &= \frac{t^2}{a^2 \sqrt{p_0^2 + t_0^2}} \cdot \sigma_x \left(\frac{a}{2}, \frac{b}{2}, z\right), \quad \bar{\sigma}_y(z) = \frac{t^2}{b^2 \sqrt{p_0^2 + t_0^2}} \cdot \sigma_y \left(\frac{a}{2}, \frac{b}{2}, z\right) \\
\bar{\sigma}_z(z) &= \frac{1}{\sqrt{p_0^2 + t_0^2}} \cdot \sigma_z \left(\frac{a}{2}, \frac{b}{2}, z\right), \quad \bar{\sigma}_{xy}(z) = \frac{t^2}{ab \sqrt{p_0^2 + t_0^2}} \cdot \sigma_{xy} \left(\frac{a}{4}, \frac{b}{4}, z\right) \\
\bar{\sigma}_{xz}(z) &= \frac{1}{\sqrt{p_0^2 + t_0^2}} \cdot \sigma_{xz} \left(\frac{a}{4}, \frac{b}{2}, z\right), \quad \bar{\sigma}_{yz}(z) = \frac{1}{\sqrt{p_0^2 + t_0^2}} \cdot \sigma_{yz} \left(\frac{a}{2}, \frac{b}{4}, z\right).
\end{aligned} \tag{8.10}$$

The normalised deflection $\bar{w}_0$ for the HR models is compared against the normalised average through-thickness deflection of the 3D model.

The accuracy of the different HR models in predicting the bending deflection of laminates I-M, with characteristic length to thickness ratio $a/t = 20$, under the load case defined in Figure 8.10 is presented in Table 8.12. The table summarises the percentage error in the maximum normalised bending deflection $|\bar{w}_0|$ to six decimal places with respect to the 3D FEM result. The results show that the models with and without ZZ functionality predict the bending deflection to within 1% of the 3D FEM solution, with the exception of a 2.59% error in the

Table 8.11: Analysed anisotropic stacking sequences. Subscripts indicate the repetition of a property over the corresponding number of layers. Layer thicknesses stated as ratios of total laminate thickness.

Laminate	Thickness Ratio	Material	Stacking Sequence
I	$[0.25_4]$	$[c_4]$	$[45/-45/0/90]$
J	$[0.2_5]$	$[c_5]$	$[60/30/75/30/60]$
K	$[0.125_2/0.5/0.125_2]$	$[c_2/h/c_2]$	$[45/-45/0/0/90]$
L	$[(1/12)_3/0.5/(1/12)_3]$	$[c_3/h/c_3]$	$[15/75/45/0/45/75/15]$
M	$[0.125_8]$	$[c_8]$	$[45/-45/90/0]_s$

Table 8.12: Anisotropic laminates I-M with $a/t = 20$: Percentage error in normalised bending deflection $|\bar{w}_0|$ to six decimal places for different HR models with respect to a 3D FEM solution.

	Lam. I	Lam. J	Lam. K	Lam. L	Lam. M
3D FEM	**0.002525**	**0.002613**	**0.004148**	**0.004282**	**0.002260**
HR3 (%)	0.18	0.23	0.04	0.20	0.10
HR3-RZT	0.06	2.59	-0.05	-0.38	-0.46
HR3-RZTmx	0.19	0.80	-0.09	-0.21	-0.46
HR3-MZZF	0.13	0.06	-0.08	0.15	0.10

HR3-RZT model for laminate J.

There are two possible explanations for the larger discrepancy of the HR3-RZT result for laminate J. A possible first source of error is the numerical conditioning of the problem. However, as shown in Table 8.13, the condition number κ of the DQM stiffness matrix $\boldsymbol{K}$ is of equal magnitude as $\kappa(\boldsymbol{K})$ of HR3-RZTmx, and in fact slightly less than the condition number for HR3. In all cases the condition number is relatively high and as discussed in Section 8.1.2.1 future work should focus on strategies to reduce $\kappa(\boldsymbol{K})$. One possible solution is to reduce the bandwidth of the matrices, either by using localised DQ methods or by implementing the strong-form DQ finite element method developed by Tornabene and co-workers [150]. An alternative would be to transform the governing differential equations Eqs. (7.61) into the weak form by using the generalised Galerkin method. One drawback of this latter approach is that derivatives are not computed as accurately in C^0 continuous finite elements as they are with DQ weighting matrices. For the HR formulation presented herein, this would lead to a reduction in computational accuracy of the transverse stresses as these are derived from the in-plane derivatives of the stress resultants $\mathcal{F}$.

A second source of error in the HR3-RZT model is that it does not account for EWLs. As the error in the HR3 model for laminate J is small (0.23%) and the presence of EWLs only

Table 8.13: Laminate J: Condition number κ of the DQM stiffness matrix $\boldsymbol{K}$ that is inverted to solved the structural problem.

	HR3	HR3-RZT	HR3-RZTmx	HR3-MZZF
$\kappa(\boldsymbol{K})$	1.929×10^{16}	1.367×10^{16}	1.326×10^{16}	1.391×10^{16}

influences the definition of the ZZ function, which is not included in HR3, it is possible that failing to account for EWLs artificially alters the stiffness of the structure. This explanation is likely as the HR3-RZTmx model, which does account for EWLs, reduces the error by a factor of three. Furthermore, the through-thickness plots of the two transverse shear stress metrics $\bar{\sigma}_{xz}$ and $\bar{\sigma}_{yz}$ in Figure 8.13 show that the HR3-RZT solution does not exactly correlate with the 3D FEM solution, whereas the other three HR models are almost coincident with the benchmark. As the ZZ effect, and by extension the influence of EWLs, arises from differences in the transverse shear moduli, the results suggest that the discrepancy in the HR3-RZT model is due to a failure to account for EWLs. Thus, the modified RZT ZZ function implemented in HR3-RZTmx is recommended for most accurate results.

To compare the accuracy of the HR 3D stress fields, the through-thickness variations of all six stress metrics are plotted in Figures 8.12-8.16 for the characteristic length to thickness ratio $a/t = 20$. The in-plane (x, y) locations of each z-wise plot are given in the stress metric definitions of Eq. (8.10) and are also indicated in the figure captions.

For all laminates investigated herein, the HR3, HR3-RZTmx and HR3-MZZF model results follow the 3D FEM solutions closely throughout the entire thickness. The HR3-RZT model also correlates well with the 3D FEM solution for most laminates with the exception of the transverse shear stresses for laminate J (Figure 8.13). As previously discussed, this inaccuracy arises because the HR3-RZT model does not account for EWLs in the definition of the RZT ZZ function, and is therefore less robust than the modified HR3-RZTmx model. Most importantly, the through-thickness variations of all six stress fields closely follow the 3D FEM solution for the quasi-isotropic laminate M (Figure 8.16), which is the most commonly used engineering stacking sequence.

The through-thickness plots support the findings of Table 8.12 that both the HR3 model without ZZ functionality and the HR3 ZZ models accurately predict the structural behaviour of the anisotropic laminates. As shown in Figure 8.12, Figure 8.13 and Figure 8.16 the HR3 model remains accurate for all three anisotropic composite laminate I, J and M. In general, most composite laminae have $G_{13} < G_{23}$, such that the maximum and minimum values of transverse shear stiffness occur for 0° and 90° plies, respectively. Thus, the HR3 model is expected to be more accurate for general anisotropic than for orthotropic 0/90 laminates as the layerwise differences in transverse shear moduli is reduced. However, for sandwich laminate L the HR3 model is less accurate than the HR3-RZTmx model, with the discrepancies especially pronounced for the in-plane shear stress plot in Figure 8.15d.

As for the orthotropic laminates investigated in Section 8.1.1.2, the HR3-RZTmx model most consistently correlates with the 3D benchmark solution for the full range of anisotropic laminates investigated. The only marked discrepancy between the 3D FEM solution and the HR3-RZTmx model, and in fact all other HR models, is the in-plane shear stress $\bar{\sigma}_{xy}$ for laminate J shown in Figure 8.13d. To ascertain which of these stress fields, the 3D FEM or the HR solutions, is the most accurate result, the residuals in Cauchy's x- and y-direction equilibrium equations are calculated. Only these two equilibrium equations explicitly contain the in-plane shear stress σ_{xy}. Furthermore, as the 3D FEM and HR solutions of the two in-plane stresses σ_x and σ_y, and the two transverse shear stresses σ_{xz} and σ_{yz} are well correlated, the model that satisfies Cauchy's

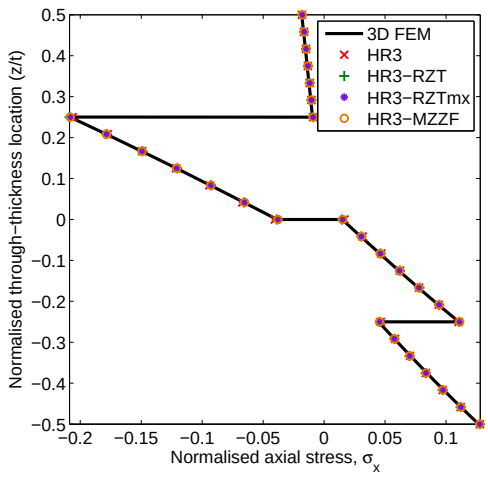

(a) Normalised axial stress, $\bar{\sigma}_x(a/2, b/2, z)$

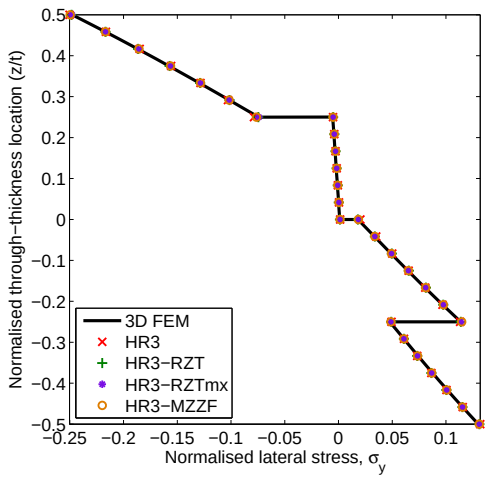

(b) Normalised lateral stress, $\bar{\sigma}_y(a/2, b/2, z)$

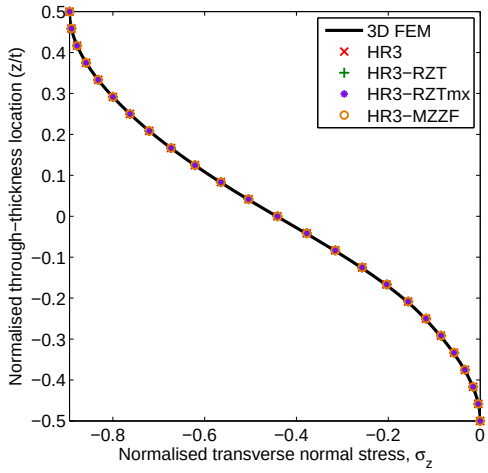

(c) Normalised transverse normal stress, $\bar{\sigma}_z(a/2, b/2, z)$

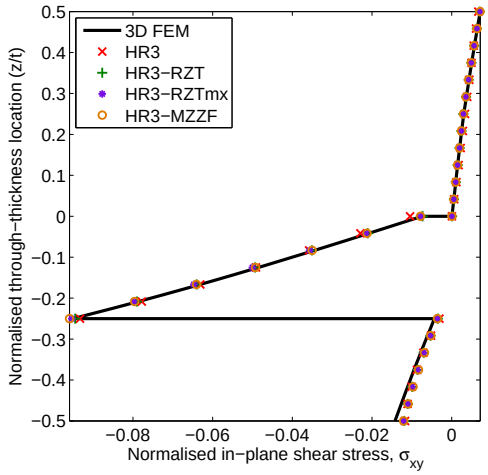

(d) Normalised in-plane shear stress, $\bar{\sigma}_{xy}(a/4, b/4, z)$

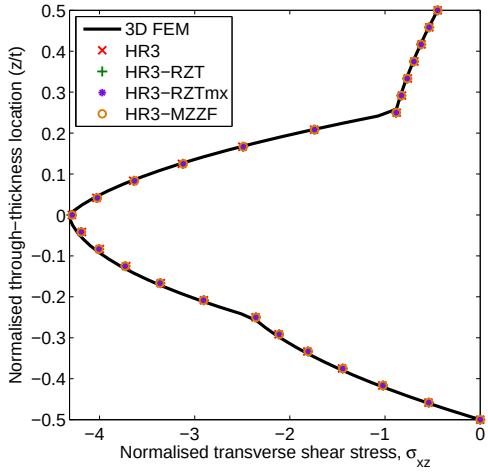

(e) Normalised transverse shear stress, $\bar{\sigma}_{xz}(a/4, b/2, z)$

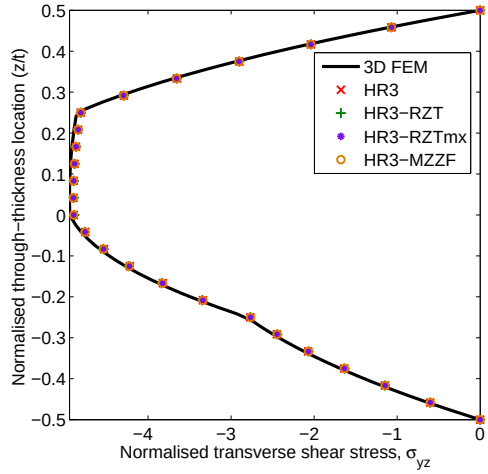

(f) Normalised transverse shear stress, $\bar{\sigma}_{yz}(a/2, b/4, z)$

Figure 8.12: Laminate I: Through-thickness distribution of the 3D stress field at different planar locations for $a/t = 20$. The figures compare different implementations of the HR model with a 3D FEM model.

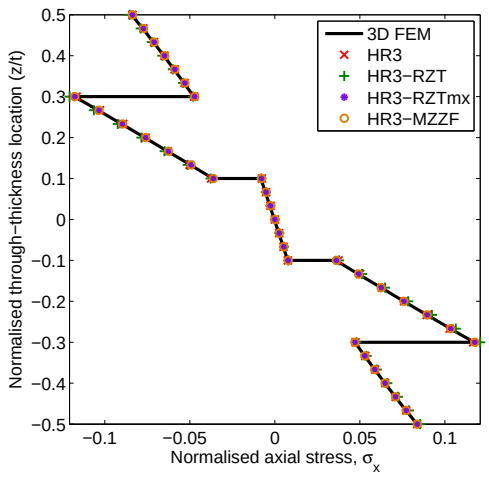

(a) Normalised axial stress, $\bar{\sigma}_x(a/2, b/2, z)$

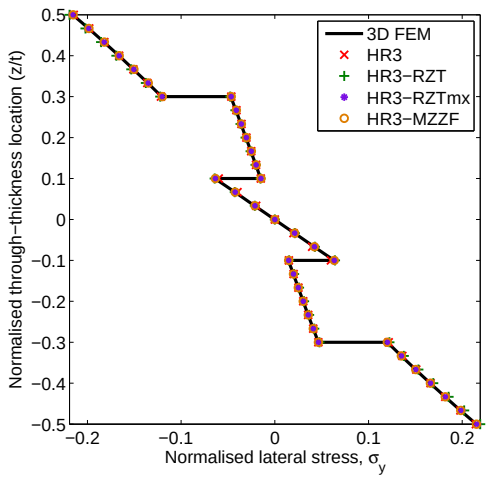

(b) Normalised lateral stress, $\bar{\sigma}_y(a/2, b/2, z)$

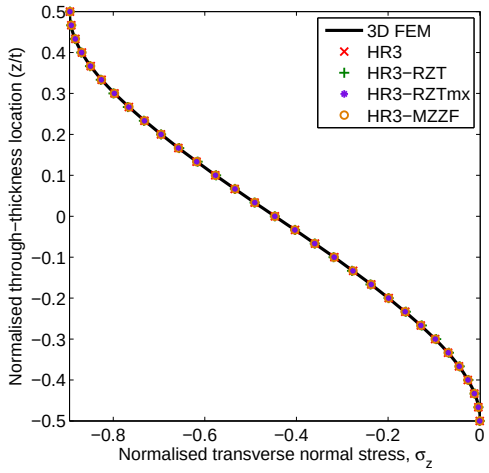

(c) Normalised transverse normal stress, $\bar{\sigma}_z(a/2, b/2, z)$

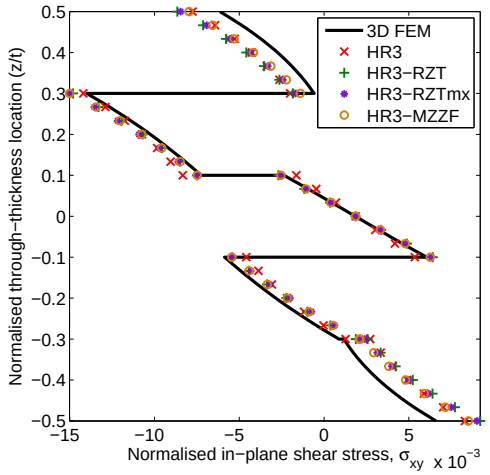

(d) Normalised in-plane shear stress, $\bar{\sigma}_{xy}(a/4, b/4, z)$

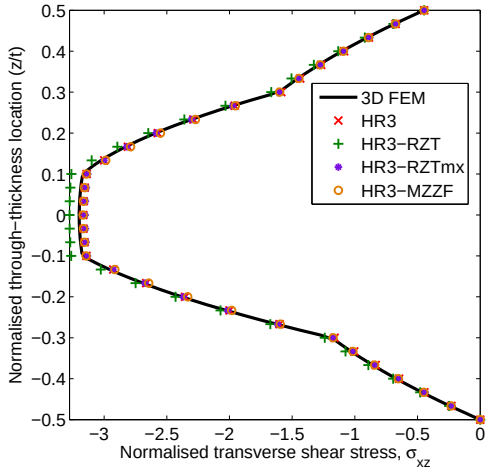

(e) Normalised transverse shear stress, $\bar{\sigma}_{xz}(a/4, b/2, z)$

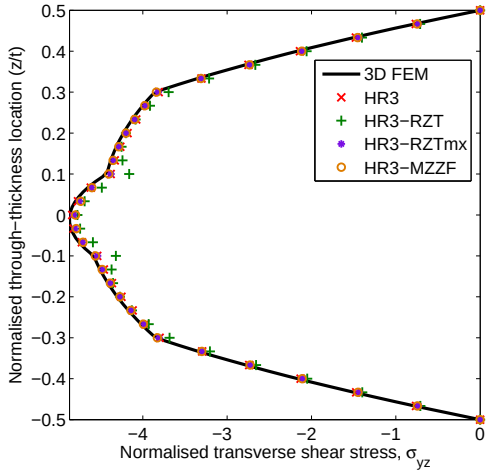

(f) Normalised transverse shear stress, $\bar{\sigma}_{yz}(a/2, b/4, z)$

Figure 8.13: Laminate J: Through-thickness distribution of the 3D stress field at different planar locations for $a/t = 20$. The figures compare different implementations of the HR model with a 3D FEM model.

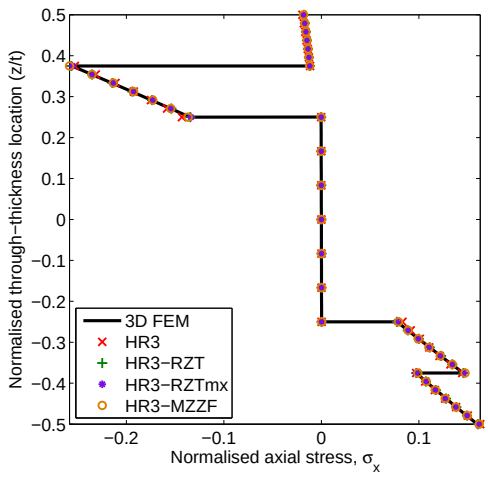

(a) Normalised axial stress, $\bar{\sigma}_x(a/2, b/2, z)$

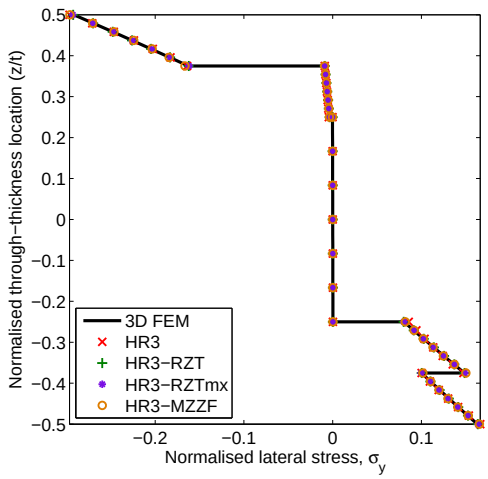

(b) Normalised lateral stress, $\bar{\sigma}_y(a/2, b/2, z)$

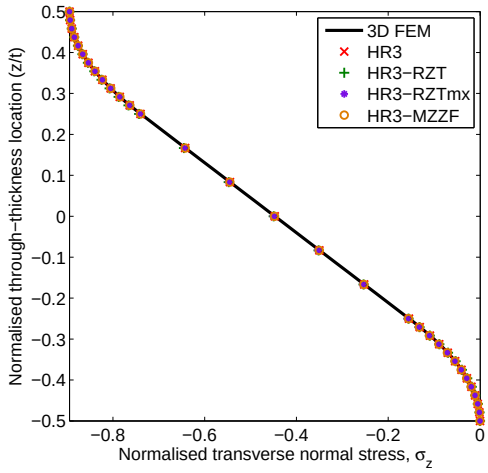

(c) Normalised transverse normal stress, $\bar{\sigma}_z(a/2, b/2, z)$

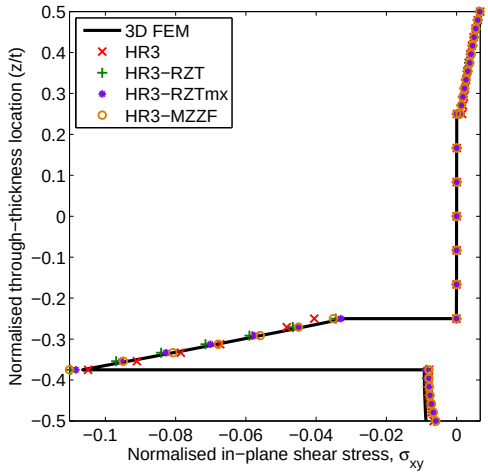

(d) Normalised in-plane shear stress, $\bar{\sigma}_{xy}(a/4, b/4, z)$

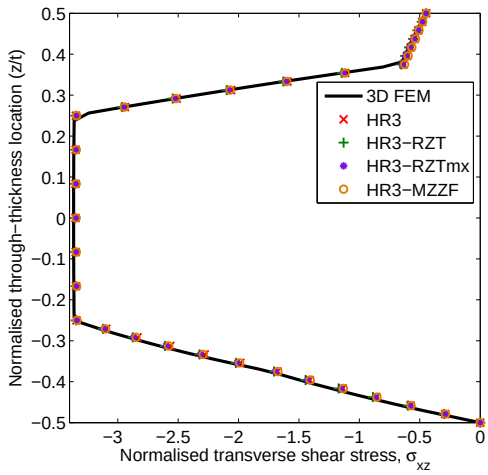

(e) Normalised transverse shear stress, $\bar{\sigma}_{xz}(a/4, b/2, z)$

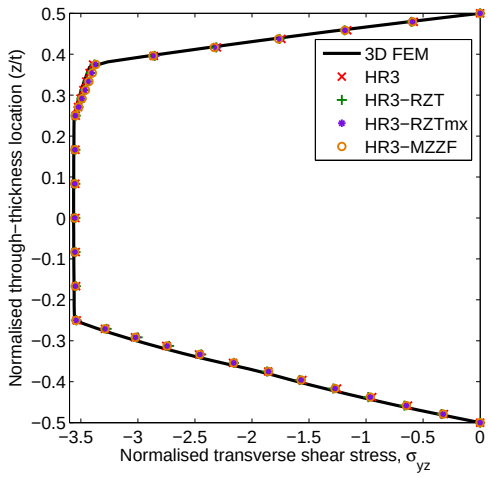

(f) Normalised transverse shear stress, $\bar{\sigma}_{yz}(a/2, b/4, z)$

Figure 8.14: Laminate K: Through-thickness distribution of the 3D stress field at different planar locations for $a/t = 20$. The figures compare different implementations of the HR model with a 3D FEM model.

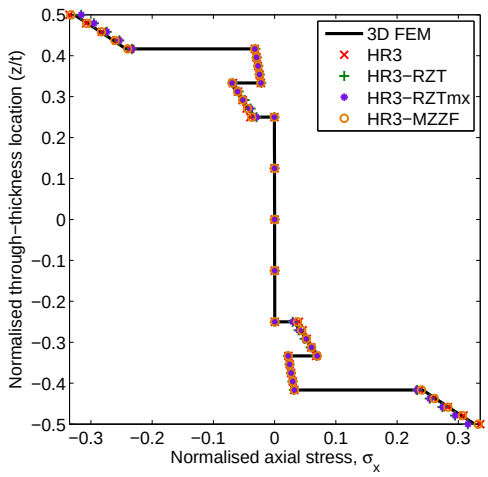

(a) Normalised axial stress, $\bar{\sigma}_x(a/2, b/2, z)$

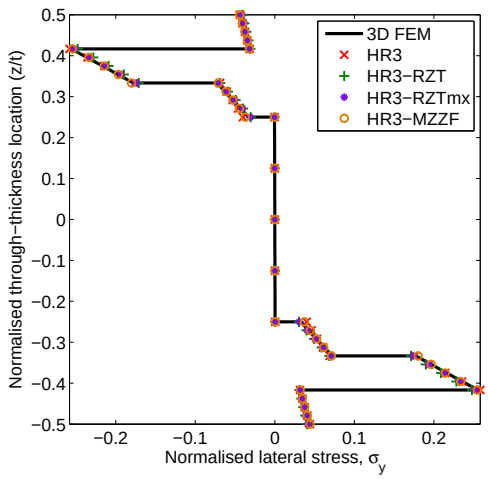

(b) Normalised lateral stress, $\bar{\sigma}_y(a/2, b/2, z)$

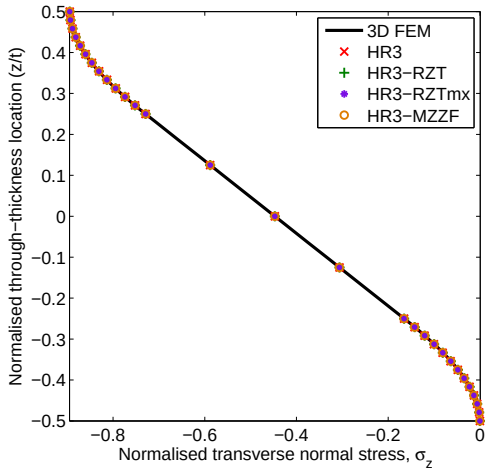

(c) Normalised transverse normal stress, $\bar{\sigma}_z(a/2, b/2, z)$

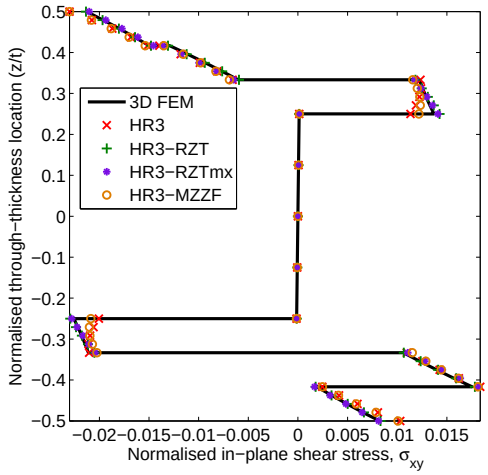

(d) Normalised in-plane shear stress, $\bar{\sigma}_{xy}(a/4, b/4, z)$

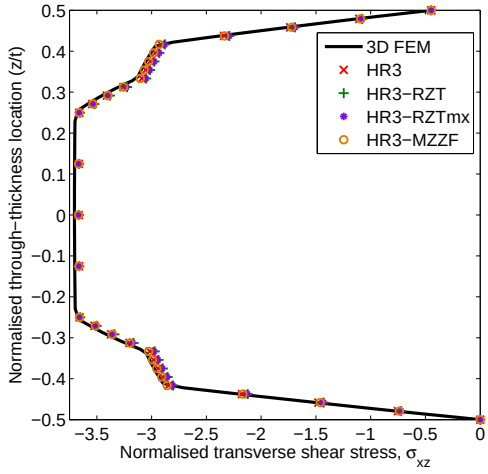

(e) Normalised transverse shear stress, $\bar{\sigma}_{xz}(a/4, b/2, z)$

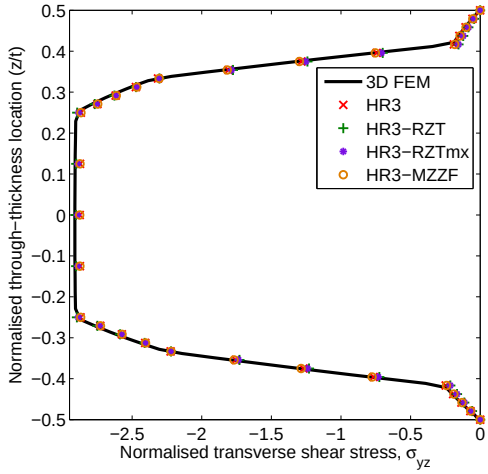

(f) Normalised transverse shear stress, $\bar{\sigma}_{yz}(a/2, b/4, z)$

Figure 8.15: Laminate L: Through-thickness distribution of the 3D stress field at different planar locations for $a/t = 20$. The figures compare different implementations of the HR model with a 3D FEM model.

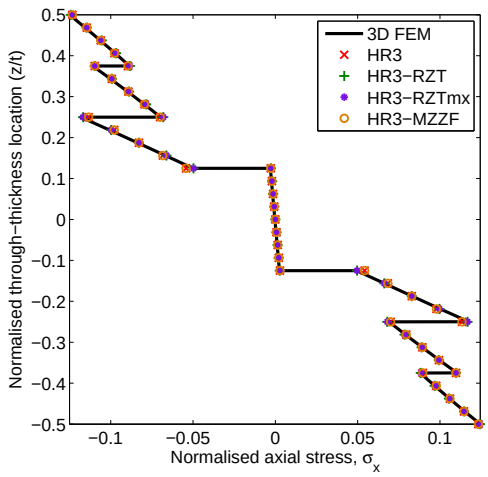

(a) Normalised axial stress, $\bar{\sigma}_x(a/2, b/2, z)$

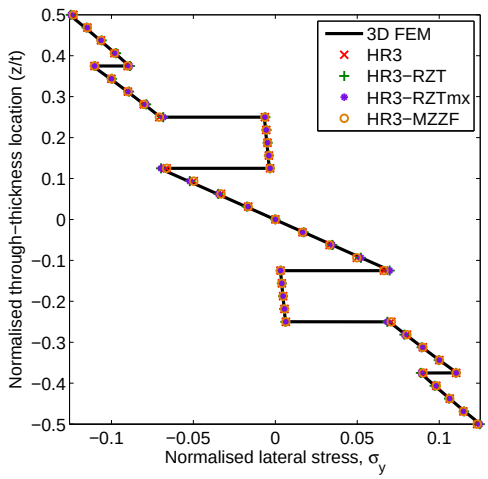

(b) Normalised lateral stress, $\bar{\sigma}_y(a/2, b/2, z)$

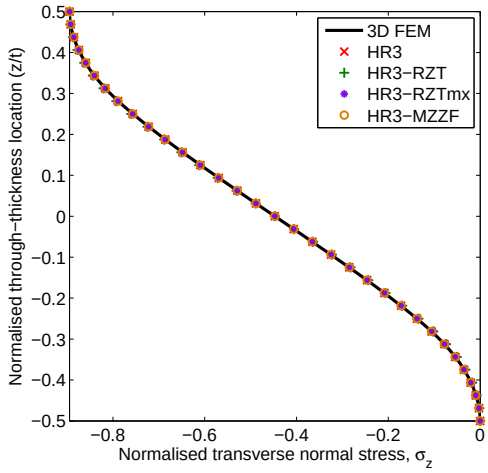

(c) Normalised transverse normal stress, $\bar{\sigma}_z(a/2, b/2, z)$

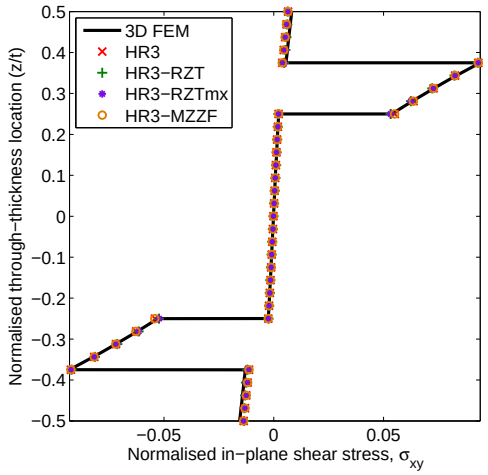

(d) Normalised in-plane shear stress, $\bar{\sigma}_{xy}(a/4, b/4, z)$

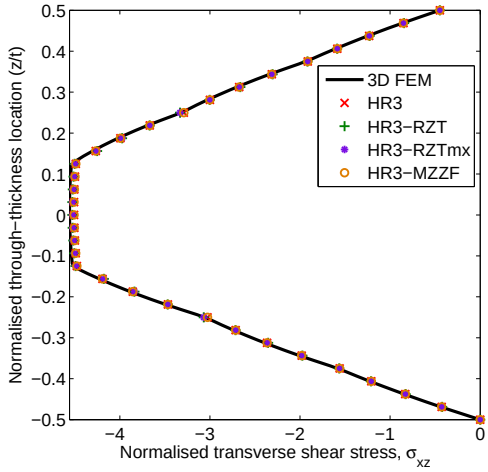

(e) Normalised transverse shear stress, $\bar{\sigma}_{xz}(a/4, b/2, z)$

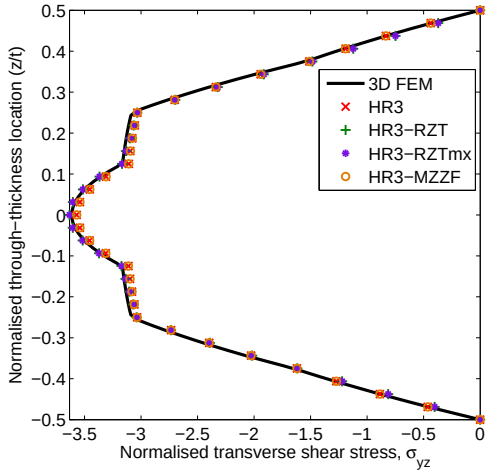

(f) Normalised transverse shear stress, $\bar{\sigma}_{yz}(a/2, b/4, z)$

Figure 8.16: Laminate M: Through-thickness distribution of the 3D stress field at different planar locations for $a/t = 20$. The figures compare different implementations of the HR model with a 3D FEM model.

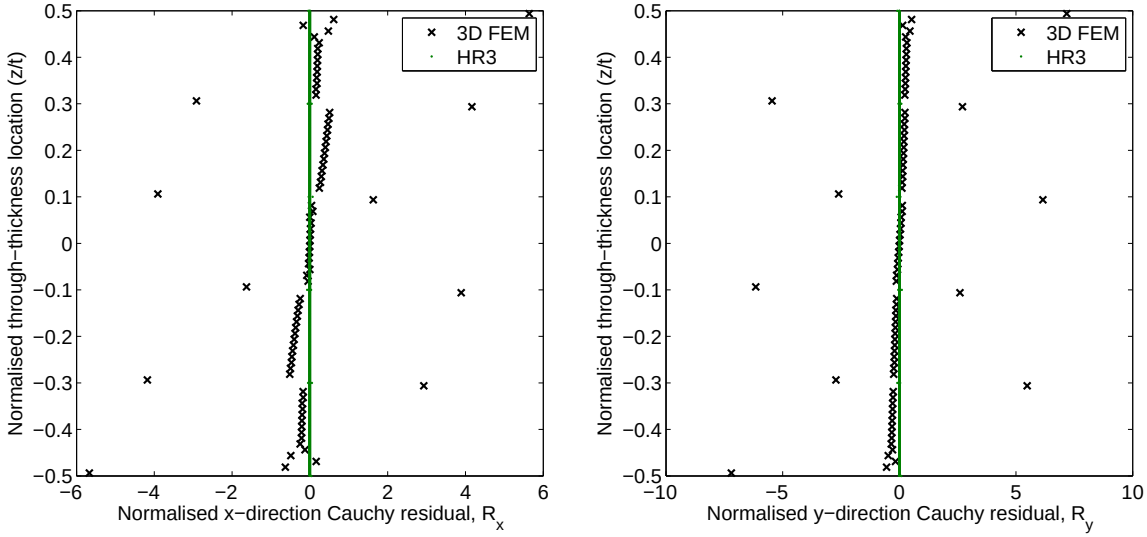

(a) Normalised x-direction Cauchy residual, $\bar{R}_x$ **(b)** Normalised y-direction Cauchy residual, $\bar{R}_y$

Figure 8.17: Laminate J: Normalised x-direction and y-direction Cauchy residuals $\bar{R}_x$ and $\bar{R}_y$, respectively, for 3D FEM and HR models at $(a/4, b/4, z)$ with $a/t = 20$.

equilibrium equations with the least residual is deemed to be the most accurate. Hence, the two normalised residuals

$$\bar{R}_x\left(\frac{a}{4}, \frac{b}{4}, z\right) = \frac{1}{\sqrt{p_0^2 + t_0^2}}\left[\frac{\partial\sigma_x\left(\frac{a}{4}, \frac{b}{4}, z\right)}{\partial x} + \frac{\partial\sigma_{xy}\left(\frac{a}{4}, \frac{b}{4}, z\right)}{\partial y} + \frac{\partial\sigma_{xz}\left(\frac{a}{4}, \frac{a}{b}, z\right)}{\partial z}\right] \tag{8.11a}$$

$$\bar{R}_y\left(\frac{a}{4}, \frac{b}{4}, z\right) = \frac{1}{\sqrt{p_0^2 + t_0^2}}\left[\frac{\partial\sigma_{xy}\left(\frac{a}{4}, \frac{b}{4}, z\right)}{\partial x} + \frac{\partial\sigma_y\left(\frac{a}{4}, \frac{b}{4}, z\right)}{\partial y} + \frac{\partial\sigma_{yz}\left(\frac{a}{4}, \frac{b}{4}, z\right)}{\partial z}\right] \tag{8.11b}$$

are used to compare the accuracy of the in-plane shear stress field σ_{xy} of laminate J at $\left(\frac{a}{4}, \frac{b}{4}, z\right)$. The 3D FEM stress results are extracted from Abaqus using a Python script and then post-processed in Matlab using the internal `gradient` function to calculate the derivatives in Eq. (8.11).

Figure 8.17 compares the normalised residuals $\bar{R}_x$ and $\bar{R}_y$ of 3D FEM and the HR3 model through the thickness of laminate J at $\left(\frac{a}{4}, \frac{b}{4}, z\right)$. The plots show that the residuals for the HR3 model are always less than the residual for the 3D FEM model. Figure 8.18 shows that the residuals $\bar{R}_x$ and $\bar{R}_y$ for all four HR models are close to zero throughout the whole laminate thickness. For the 3D FEM and HR models, the maximum residuals always occur at the ply interfaces due to the relatively higher numerical error associated with calculating derivatives at interval ends. The maximum error in the HR models at the ply interfaces is of order 10^{-1}, whereas the maximum 3D FEM residual is almost two orders of magnitude greater, i.e. of the order of the applied loading norm $\sqrt{p_0^2 + t_0^2}$. In fact, remote from the layer interfaces the HR model residuals are of order 10^{-6} and therefore negligibly small compared to the loading norm.

Thus, similar to the comments made in Section 6.4, even the detailed 3D FEM meshes considered here, with more than ten elements per layer and multiple hours of runtime on a high-performance computer, do not guarantee that Cauchy's equilibrium equations are satisfied

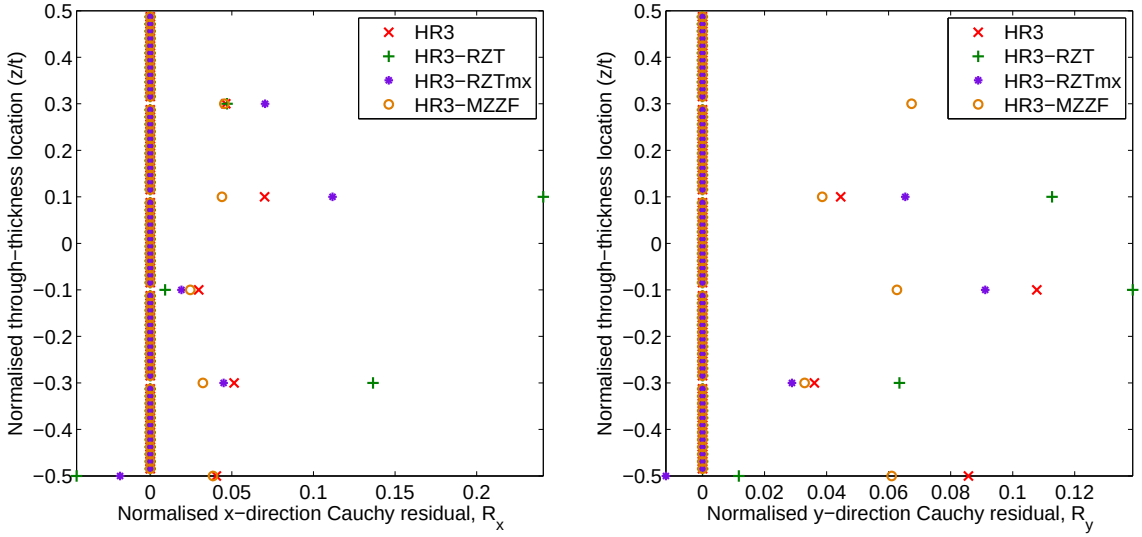

(a) Normalised x-direction Cauchy residual, $\bar{R}_x$ **(b)** Normalised y-direction Cauchy residual, $\bar{R}_y$

Figure 8.18: Laminate J: Normalised x-direction and y-direction Cauchy residuals $\bar{R}_x$ and $\bar{R}_y$, respectively, for all HR models at $(a/4, b/4, z)$ with $a/t = 20$.

with negligible error. The results in Figure 8.18 suggest that the HR formulation 3D stress fields equilibrate more accurately in Cauchy's equations than the 3D FEM stresses. At the same time the HR models reduce the number of variables by three orders of magnitude, thereby cutting the computational runtime from multiple hours to 1-2 minutes.

8.2 3D stress fields in tow-steered laminates

In this section the laminates considered are generalised further by allowing the fibre paths to vary continuously across the planform of the plate, i.e. with (x, y) location. Thus, these laminates exhibit what is henceforth called *full 3D heterogeneity* as the material properties can vary in both planar dimensions and through the thickness of the plate. These variable-stiffness plates are manufactured by steering fibre tows in curvilinear paths using advanced automated manufacturing methods, such as Advanced Fibre Placement (AFP) or Continuous Tow Shearing (CTS). The aim of this section is to benchmark the 3D stress fields in these tow-steered plates using the HR formulation and 3D FEM solutions, and to compare the relative effects of transverse shear deformation of tow-steered plates and an equivalent quasi-isotropic straight-fibre laminate.

8.2.1 Benchmarking of 3D stresses in tow-steered laminates

Consider a square plate of unit in-plane dimensions $a = b = 1$ m and $t = 0.1$ m thickness $(a/t = 10)$ as depicted graphically in Figure 8.19. The plate is comprised of N_l orthotropic, tow-steered laminae of arbitrary thickness $t^{(k)}$ with the fibre orientation $\alpha^{(k)}(x, y)$ varying smoothly over the planform of the plate. Due to the variable-stiffness design of the curvilinear tow paths, the material stiffness tensor $\boldsymbol{C}^{(k)}(x, y)$ is a function of the in-plane location. As a result, the

complete laminated plate has varying stiffness properties in all three Cartesian coordinates.

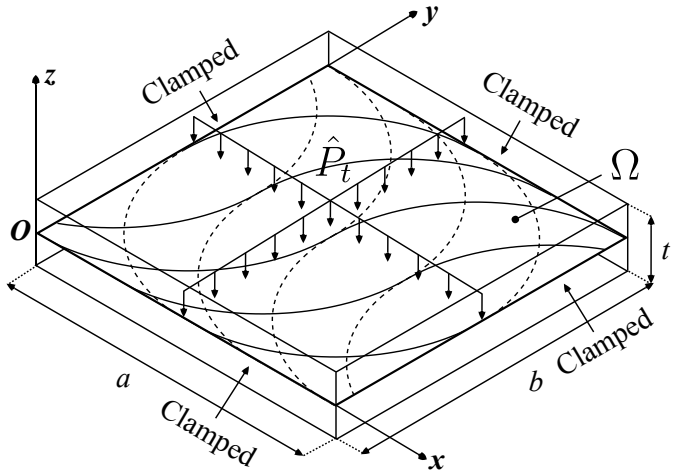

Figure 8.19: A composite plate with tow-steered fibre paths, loaded on the top surface by a uniformly distributed pressure load. All four edges are clamped. In the HR model, the 3D continuum is compressed onto an equivalent single layer Ω coincident with the midplane of the plate. For reference, the curvilinear fibre paths have been superimposed onto this equivalent single layer.

The individual tow-steered layers can be arranged in any general fashion but are assumed to be perfectly bonded, such that displacement and traction continuity at the interfaces is guaranteed. The plate is rigidly built-in along all four edges and is loaded via a uniformly distributed pressure $\hat{P}_t = p_0$ on the top surface. In reaction to the applied loading and constraining boundary conditions, the plate is assumed to deform isothermally into a new static equilibrium state.

In this work only linear fibre variations in one direction, i.e. prismatic variations, are considered. Such tow-steered fibre paths are conveniently defined using the notation of Gürdal and Olmedo [101],

$$\alpha(x, y) = \Phi\langle T_0|T_1\rangle \tag{8.12}$$

where Φ denotes the rotation of the fibre path with respect to the global x-axis, and angles T_0 and T_1 are the fibre directions at the ply centre and at a characteristic length d from the centre, respectively, with respect to the global rotation Φ. Thus, angle Φ also represents the direction of fibre variation. To cover the whole planform of the plate the fibre trajectories are shifted perpendicular to Φ.

Manufacturing techniques that steer fibres by in-plane bending, such as AFP, inevitably cause gaps and overlaps when the reference path is shifted perpendicular to Φ. The CTS technique, which steers fibre tows by in-plane shearing, allows the fibres to be tessellated without any gaps or overlaps but induces an asymmetric variable thickness profile. Throughout this analysis the presence of tow gaps, tow overlaps and thickness variations is neglected as the main aim of the current work is to demonstrate the capability of modelling accurate 3D stresses for an idealised flat plate with variable stiffness. However, the HR models are readily extended to account for discrete or continuous thickness variations by locally changing the limits of

through-thickness integration and by taking account of the ensuing curvature of the neutral axis [124].

The third-order model HR3 and third-order ZZ model HR3-MZZF are used to model the tow-steered plates. The governing differential field equations (7.61) and boundary conditions (7.62) are converted into algebraic equations using the DQM approach outlined in Section 8.1.2.1. Thus, a system of algebraic equations in the form of Eqs. (8.8) is derived that is solved via standard matrix inversion, taking into account the normalisation of the equilibrium equations via Eq. (8.9).

As discussed in Section 6.3 regarding the analysis of variable-stiffness beams, the RZT ZZ function leads to certain numerical conditioning problems for variable-stiffness laminates when the governing equations are solved using the DQM. The RZT ZZ function varies over the planform of a variable-stiffness plate as it is based on actual transverse shear material properties. For a general fibre variation, the orthotropy in transverse shear moduli that drives the ZZ effect can be finite in some areas of the plate but vanish locally if the layup is unidirectional or close to unidirectional at a specific point. Under these circumstances the RZT ZZ function vanishes and leads to numerical ill-conditioning in the matrix inversion $\boldsymbol{s} = \boldsymbol{S}^{-1}$ (See Figure 6.5). For finite element techniques that define constant fibre angles per element, this singularity in the RZT ZZ function may not be a problem as the ZZ degree of freedom may be neglected locally for the affected element. In the pseudo-spectral DQM implemented herein, this approach is not possible as the fibre variations and all functional degrees of freedom vary smoothly across the single DQM element used to discretise the plate.

Furthermore, it was found here that for variable-stiffness plates, the in-plane derivatives of the RZT ZZ function can vary significantly over the planform and thus lead to local singularities that ill-condition the DQ stiffness matrix. When using MZZF, this is not an issue as this ZZ function is invariant with location (x, y). Hence, due to the numerical ill-conditioning issues faced with the RZT ZZ function, the HR3-RZT and HR3-RZTmx models were not used for the variable-stiffness panels analysed in this section.

The ill-conditioning problem due to the in-plane derivatives of the RZT ZZ function may partially be remedied by using a local DQM approach, where only a small number of grid points rather than the full domain is used to compute derivatives. Alternatively, the strong-form FEM by Tornabene et al. [150] may provide a similar solutions. Further investigating the numerical stability of the HR3-RZT model within a DQM framework should be the focus of future work.

Similar to Section 8.1.2.1, a 3D FEM model is used to benchmark the HR model results for the tow-steered laminates. After the plate geometry is meshed, a Python script is used to assign the pertinent material orientations to the elements depending on the exact location of the element centroid in 3D Cartesian space. To achieve converged results, the in-plane mesh density has to be increased to 149 elements in both in-plane directions to guarantee sufficiently smooth fibre variations from the discrete element angles in the x- and y-directions. Combined with 80 elements through the thickness, the 3D body is thus meshed with 1,776,080 linear C3D8R reduced integration brick elements with enhanced hourglassing control. A pressure loading of $\hat{P}_t = -100$ kPa is applied on the top surface and all six degrees of freedom (three translations and three rotations) are constrained at the four clamped edges for all nodes throughout the

Table 8.14: Analysed tow-steered stacking sequences. Subscripts indicate the repetition of a property over the corresponding number of layers. Layer thicknesses stated as ratios of total laminate thickness.

Laminate	Thickness Ratio	Material	Stacking Sequence
VAT A	$[0.25_4]$	$[\mathrm{IM7}_4]$	$[0 \pm \langle 0\|90\rangle]_s$
VAT B	$[0.25_4]$	$[\mathrm{IM7}_4]$	$[90 \pm \langle 0\|90\rangle]_s$
VAT C	$[0.125_8]$	$[\mathrm{IM7}_8]$	$[0 \pm \langle 0\|45\rangle/0 \pm \langle 90\|45\rangle]_s$
VAT D	$[0.125_8]$	$[\mathrm{IM7}_8]$	$[90 \pm \langle 0\|70\rangle/90 \pm \langle 90\|20\rangle]_s$
VAT E	$[0.125_8]$	$[\mathrm{IM7}_8]$	$[90 \pm \langle 0\|45\rangle/0 \pm \langle 45\|0\rangle]_s$
VAT F	$[0.125_2/0.5/0.125_2]$	$[\mathrm{IM7}_2/\mathrm{h}/\mathrm{IM7}_2]$	$[0 \pm \langle 90\|0\rangle/0/0 \mp \langle 90\|0\rangle]$
VAT G	$[0.0625_4/0.5/0.0625_2]$	$[\mathrm{IM7}_4/\mathrm{h}/\mathrm{IM7}_4]$	$[90 \pm \langle 0\|70\rangle/90 \pm \langle 45\| - 20\rangle/0/$ $90 \mp \langle 45\| - 20\rangle/90 \mp \langle 0\|70\rangle]$

Table 8.15: Tow-steered laminates VAT A-G with $a/t = 10$: Percentage error in normalised bending deflection $|\bar{w}_0|$ to six decimal places for different HR models with respect to a 3D FEM solution.

	VAT A	**VAT B**	**VAT C**	**VAT D**	**VAT E**	**VAT F**	**VAT G**
3D FEM	**.004690**	**.003279**	**.003857**	**.003265**	**.003427**	**.010392**	**.010388**
HR3 (%)	0.58	0.24	0.15	0.22	0.18	3.72	1.94
HR3-MZZF	0.58	0.24	0.15	0.22	0.18	-0.25	1.48

entire plate cross-section.

The laminates investigated here are restricted to symmetrically laminated variable-stiffness composites and sandwich plates and are tabulated in Table 8.14. These laminates are comprised of the commonly used industrial material system IM7 8552 with $E_1 = 163$ GPa, $E_2 = E_3 = 12$ GPa, $G_{12} = 5$ GPa, $G_{13} = 4$ GPa, $G_{23} = 3.2$ GPa, $\upsilon_{12} = \upsilon_{13} = \upsilon_{23} = 0.3$, and the sandwich core h previously defined in Table 8.1. Laminates A-D are tow-steered composite laminates, whereas laminates E-F are sandwich plates with tow-steered face sheets. The laminates have layers with fibre variations that vary explicitly in the x-direction (laminates A, C and F), y-direction (laminates B, D and G) or both directions (laminate E).

All deflection and stress results are presented as normalised metrics. The same definitions and spatial locations of the normalised metrics as previously defined in Eq. (8.10) is used. Due to the change in load case, the factor $t_0 = 0$ in the denominators of the metrics. The accuracy of the different HR models in predicting the bending deflection of laminates VAT A-VAT G, with characteristic length to thickness ratio $a/t = 10$ under the load case defined in Figure 8.19, is presented in Table 8.15. The table summarises the percentage error in the maximum normalised bending deflection $|\bar{w}_0|$ to six decimal places with respect to the 3D FEM result. The results show that the models with and without ZZ functionality predict the bending deflection to within 1% of the 3D FEM solution for the variable-stiffness composites laminates VAT A-VAT E. For the variable-stiffness sandwich plates VAT F and VAT G, the maximum error in the HR3 model (3.72%) is greater than for the HR3-MZZF model. As was previously shown for orthotropic and anisotropic straight-fibre laminates in Sections 8.1.1.2 and 8.1.2.2, the inclusion of ZZ functionality is important for accurate modelling of sandwich panels.

Next, consider the through-thickness variations of all six stress metrics for laminates VAT A-VAT G as plotted in Figures 8.20-8.26 for the characteristic length to thickness ratio $a/t = 10$. The in-plane (x, y) locations of each z-wise plot are given in the stress metric definitions of Eq. (8.10) and are also indicated in the figure captions. For the variable-stiffness composite laminates VAT A-VAT E, both the HR3 and HR3-MZZF model results closely correlate the 3D FEM solutions throughout the entire thickness.

For laminates VAT A and VAT B, small discrepancies are visible in the in-plane $\bar{\sigma}_y$ stress plot (Figures 8.20b and 8.21b) towards the top surface of the laminates. The 3D FEM solution has a 6.2% higher magnitude of compressive stress on the top surface than tensile stress on the bottom surface. This result suggests that the applied transverse pressure loading on the top surface is locally affecting the in-plane stress field via Poisson's coupling. Therefore, the effect of transverse normal deformation on $\bar{\sigma}_y$ is more pronounced for these two laminates (all other laminates do not show this behaviour) and a higher-order expansion of the through-thickness displacement u_z in Eq. (7.1) is warranted. The discrepancy between the maximum compressive stress $\bar{\sigma}_y$ of 3D FEM and the HR models is around 5% for both VAT A-VAT B, and may therefore not be worth the extra computational effort in an industrial setting given the practical uncertainties around material properties and fibre angles.

The plots for laminates VAT F and VAT G in Figures 8.25-8.26 confirm the inferior accuracy of the HR3 model in modelling sandwich panels previously observed for the deflection results in Table 8.15. For laminate VAT F, both the in-plane stress plots for $\bar{\sigma}_x$ (Figure 8.25a), $\bar{\sigma}_y$ (Figure 8.25b) and $\bar{\sigma}_{xy}$ (Figure 8.25d), as well as the transverse shear plots for $\bar{\sigma}_{xz}$ (Figure 8.25e) and $\bar{\sigma}_{yz}$ (Figure 8.25f) show inaccuracies of 5-16% in the HR3 results compared to 3D FEM. The HR3-MZZF model follows the 3D FEM results more closely, with a maximum through-thickness error ranging from 1.5% for σ_{xz} to 8% for σ_{xy}.

As previously observed in Section 8.1.2.2, the in-plane shear stresses $\bar{\sigma}_{xy}$ are generally the worst-matching plots for the laminates investigated. For example, consider the in-plane shear stress distribution for VAT D in Figure 8.23d. The HR and 3D FEM results are closely matched for four plies but show some differences for the central two layers and the two surface layers. The other stress fields that equilibrate the in-plane shear stress in Cauchy's x-direction equilibrium equations, σ_x and σ_{xz}, and Cauchy's y-direction equilibrium equations, σ_y and σ_{yz}, are closely correlated. Thus, as introduced in Section 8.1.2.2, the extent to which the 3D FEM and HR stress fields satisfy Cauchy's x- and y-direction equilibrium equations is ascertained using a metric capturing the general accuracy of the stress fields. Hence, the two normalised residuals in Eq. (8.11) are used to compare the accuracy of the in-plane shear stress field σ_{xy} of laminate D at $\left(\frac{a}{4}, \frac{b}{4}, z\right)$.

Figure 8.27 compares the normalised residuals $\bar{R}_x$ and $\bar{R}_y$ of 3D FEM and the HR3 model through the thickness of laminate D at $\left(\frac{a}{4}, \frac{b}{4}, z\right)$. The residuals for the HR3 model are always less than the residual in the 3D FEM model. Furthermore, Figure 8.28 shows that the residuals $\bar{R}_x$ and $\bar{R}_y$ for both HR models are close to zero throughout the whole laminate thickness. The maximum residual in the HR models at the ply interfaces is of order 10^{-2} and reduces to 10^{-6} away from the interfaces. The maximum 3D FEM residual at the ply interfaces is of the order

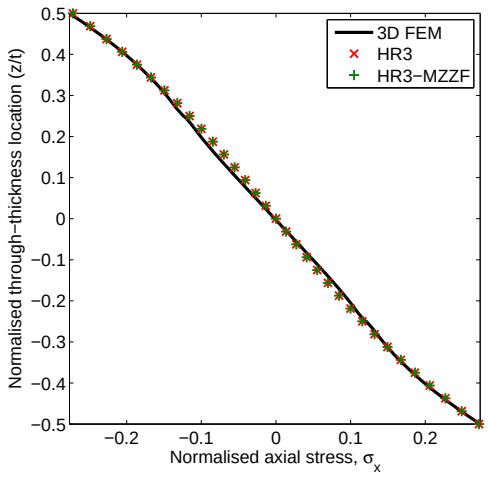

(a) Normalised axial stress, $\bar{\sigma}_x(a/2, b/2, z)$

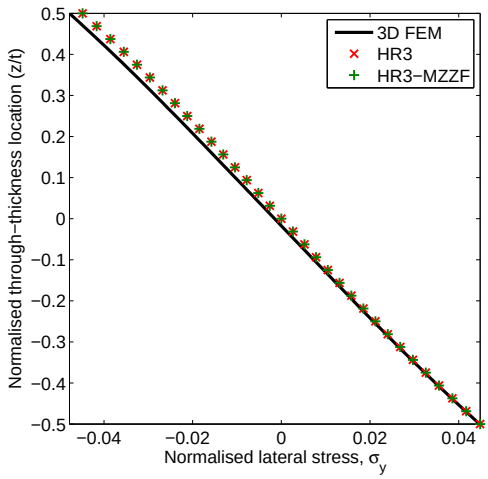

(b) Normalised lateral stress, $\bar{\sigma}_y(a/2, b/2, z)$

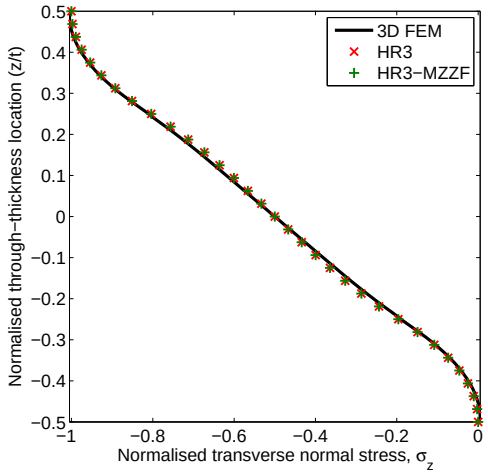

(c) Normalised transverse normal stress, $\bar{\sigma}_z(a/2, b/2, z)$

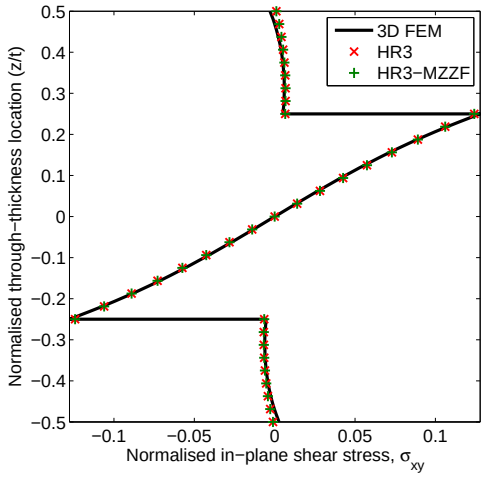

(d) Normalised in-plane shear stress, $\bar{\sigma}_{xy}(a/4, b/4, z)$

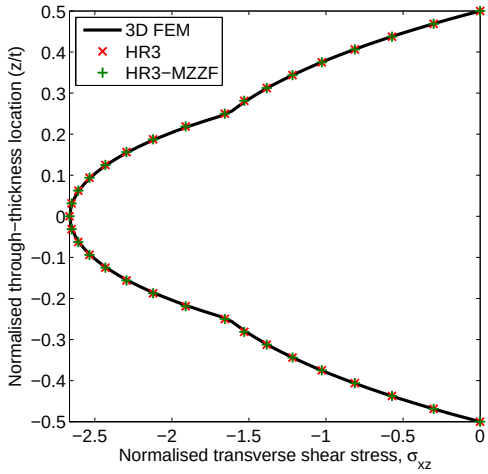

(e) Normalised transverse shear stress, $\bar{\sigma}_{xz}(a/4, b/2, z)$

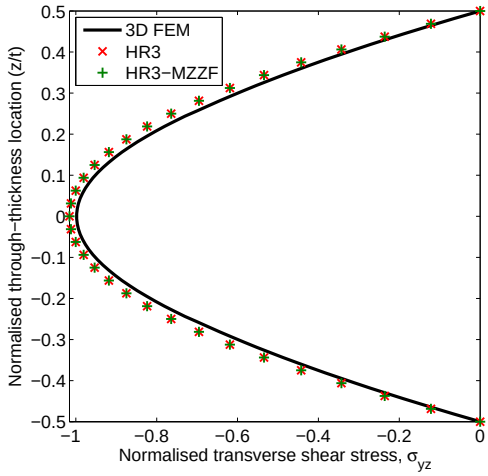

(f) Normalised transverse shear stress, $\bar{\sigma}_{yz}(a/2, b/4, z)$

Figure 8.20: Laminate VAT A: Through-thickness distribution of the 3D stress field at different planar locations for $a/t = 10$. The figures compare different implementations of the HR model with a 3D FEM model.

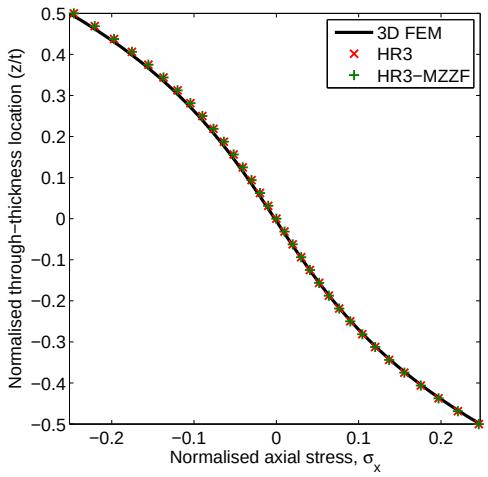

(a) Normalised axial stress, $\bar{\sigma}_x(a/2, b/2, z)$

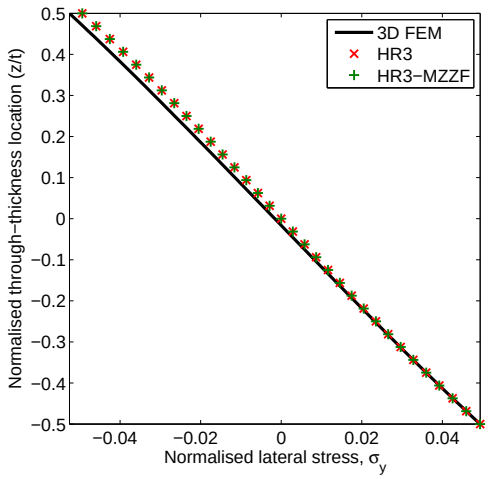

(b) Normalised lateral stress, $\bar{\sigma}_y(a/2, b/2, z)$

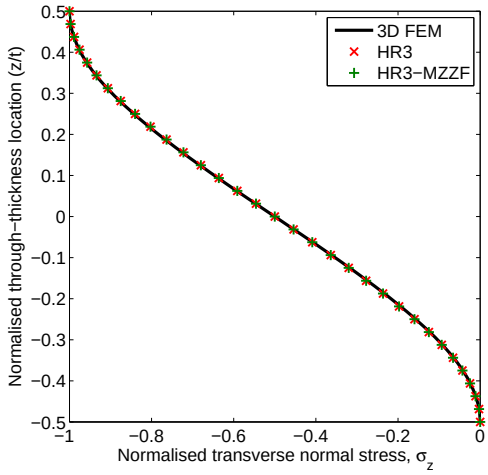

(c) Normalised transverse normal stress, $\bar{\sigma}_z(a/2, b/2, z)$

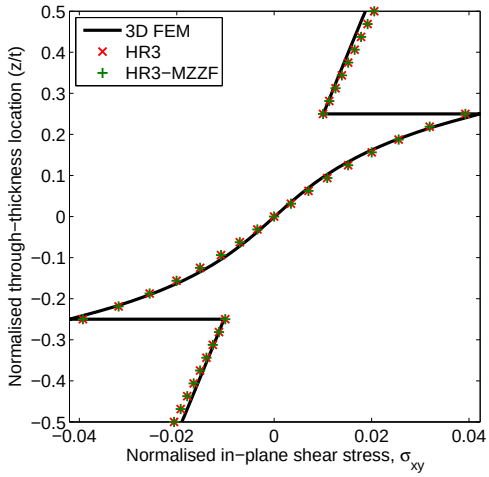

(d) Normalised in-plane shear stress, $\bar{\sigma}_{xy}(a/4, b/4, z)$

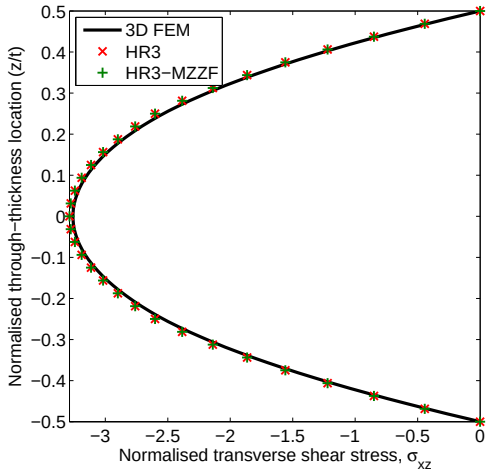

(e) Normalised transverse shear stress, $\bar{\sigma}_{xz}(a/4, b/2, z)$

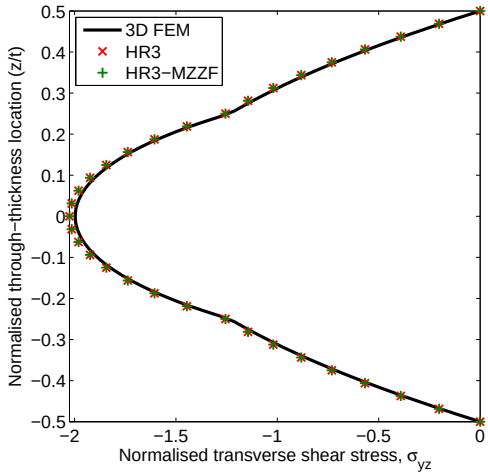

(f) Normalised transverse shear stress, $\bar{\sigma}_{yz}(a/2, b/4, z)$

Figure 8.21: Laminate VAT B: Through-thickness distribution of the 3D stress field at different planar locations for $a/t = 10$. The figures compare different implementations of the HR model with a 3D FEM model.

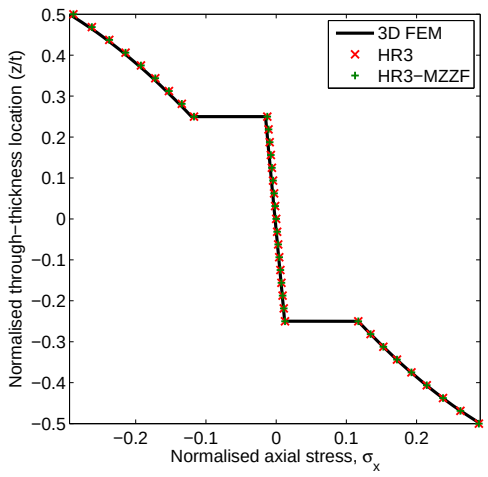

(a) Normalised axial stress, $\bar{\sigma}_x(a/2, b/2, z)$

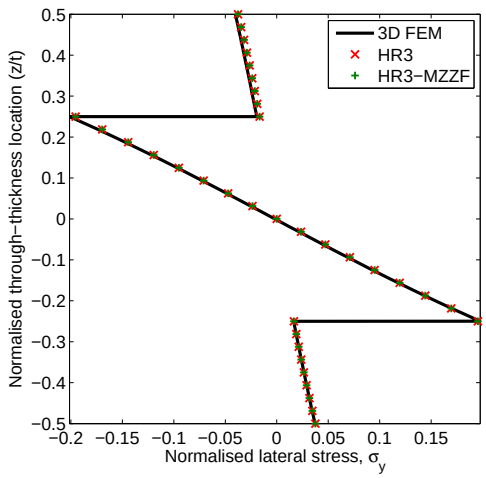

(b) Normalised lateral stress, $\bar{\sigma}_y(a/2, b/2, z)$

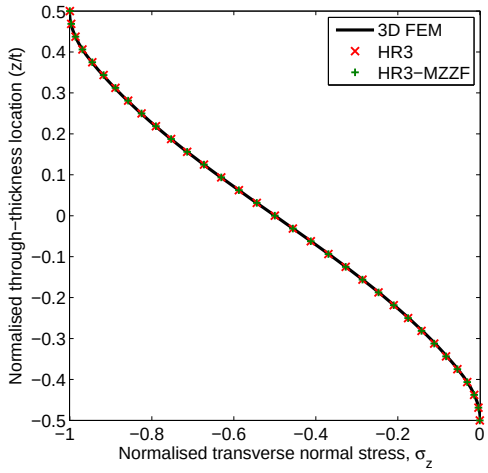

(c) Normalised transverse normal stress, $\bar{\sigma}_z(a/2, b/2, z)$

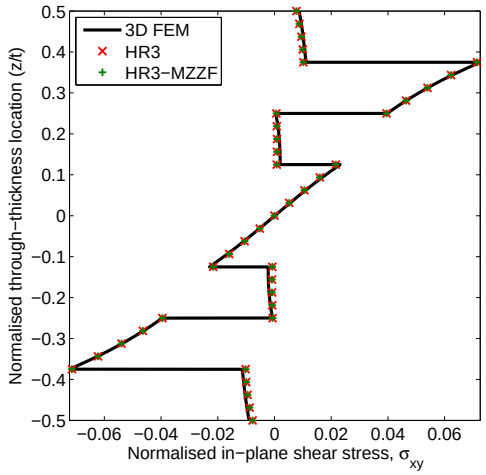

(d) Normalised in-plane shear stress, $\bar{\sigma}_{xy}(a/4, b/4, z)$

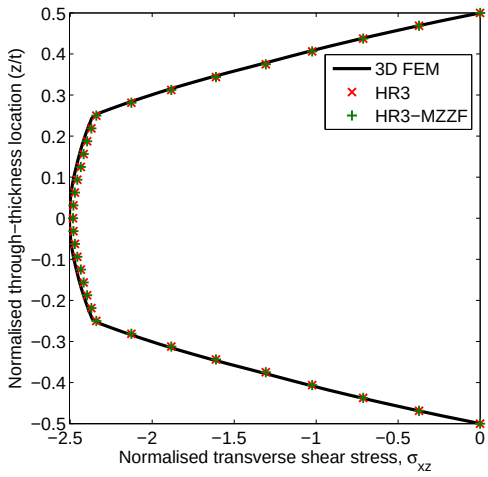

(e) Normalised transverse shear stress, $\bar{\sigma}_{xz}(a/4, b/2, z)$

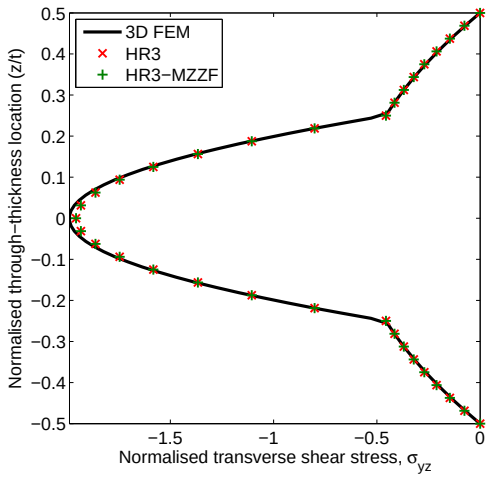

(f) Normalised transverse shear stress, $\bar{\sigma}_{yz}(a/2, b/4, z)$

Figure 8.22: Laminate VAT C: Through-thickness distribution of the 3D stress field at different planar locations for $a/t = 10$. The figures compare different implementations of the HR model with a 3D FEM model.

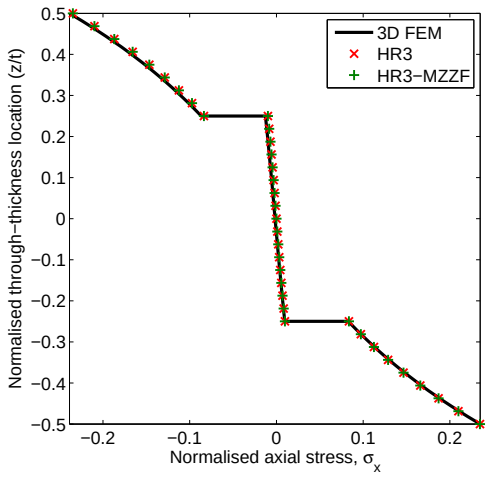

(a) Normalised axial stress, $\bar{\sigma}_x(a/2, b/2, z)$

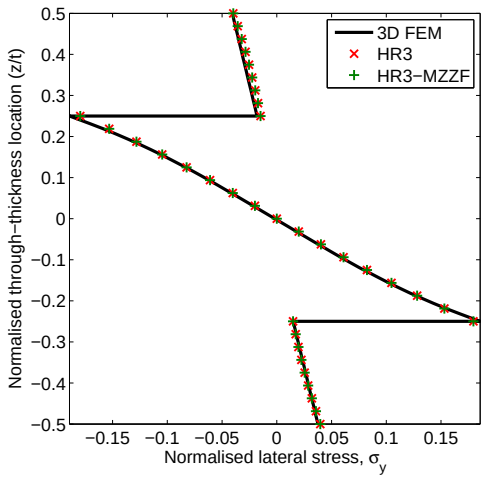

(b) Normalised lateral stress, $\bar{\sigma}_y(a/2, b/2, z)$

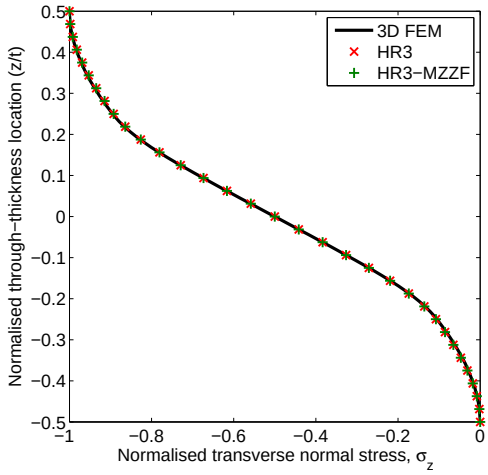

(c) Normalised transverse normal stress, $\bar{\sigma}_z(a/2, b/2, z)$

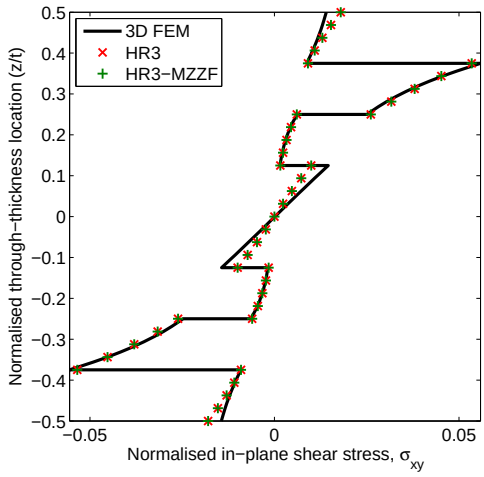

(d) Normalised in-plane shear stress, $\bar{\sigma}_{xy}(a/4, b/4, z)$

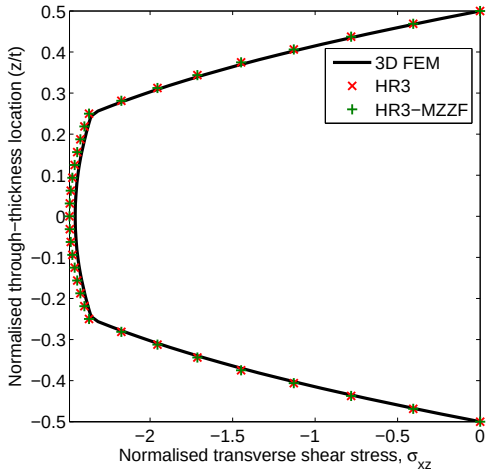

(e) Normalised transverse shear stress, $\bar{\sigma}_{xz}(a/4, b/2, z)$

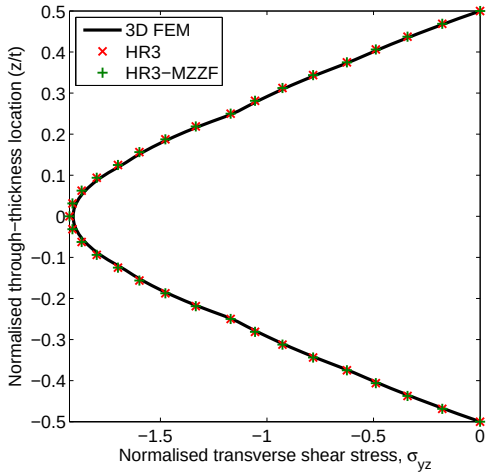

(f) Normalised transverse shear stress, $\bar{\sigma}_{yz}(a/2, b/4, z)$

Figure 8.23: Laminate VAT D: Through-thickness distribution of the 3D stress field at different planar locations for $a/t = 10$. The figures compare different implementations of the HR model with a 3D FEM model.

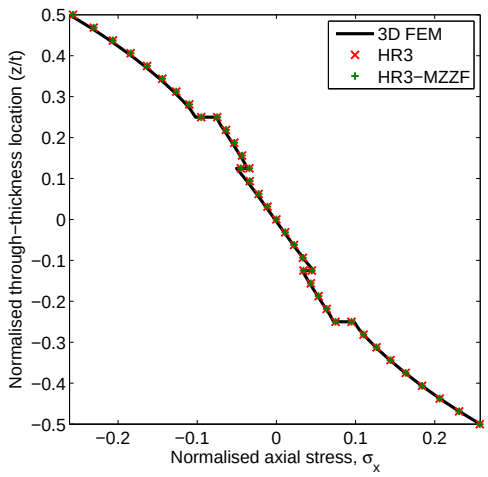

(a) Normalised axial stress, $\bar{\sigma}_x(a/2, b/2, z)$

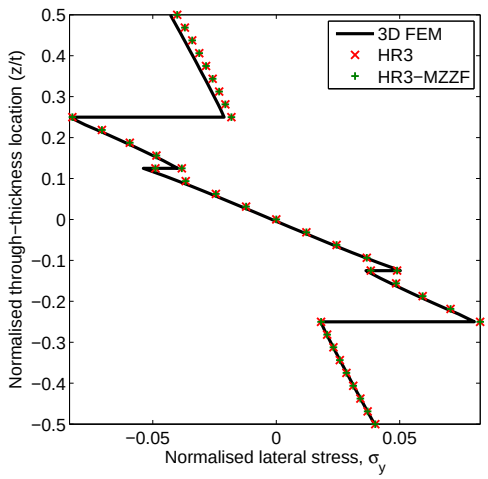

(b) Normalised lateral stress, $\bar{\sigma}_y(a/2, b/2, z)$

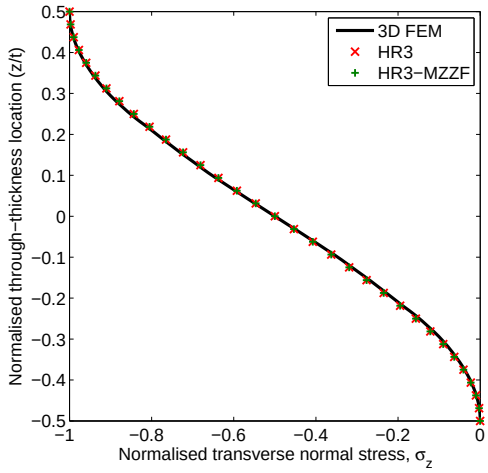

(c) Normalised transverse normal stress, $\bar{\sigma}_z(a/2, b/2, z)$

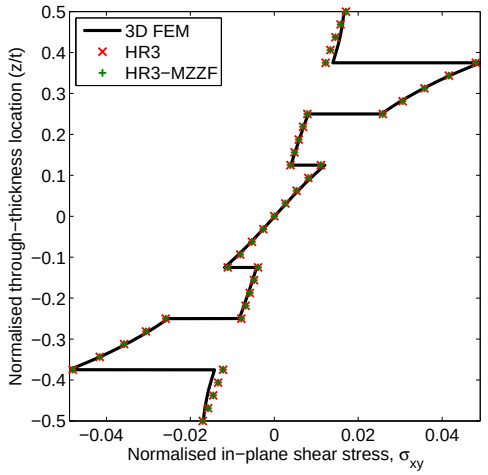

(d) Normalised in-plane shear stress, $\bar{\sigma}_{xy}(a/4, b/4, z)$

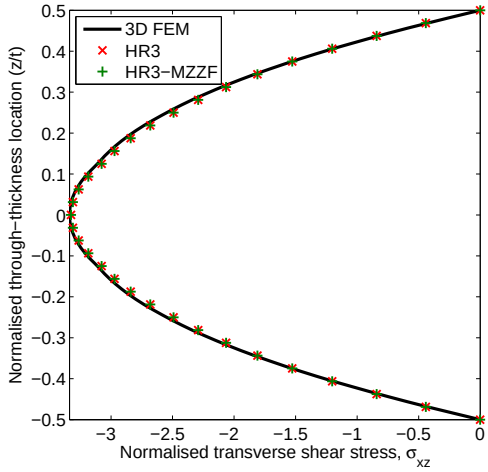

(e) Normalised transverse shear stress, $\bar{\sigma}_{xz}(a/4, b/2, z)$

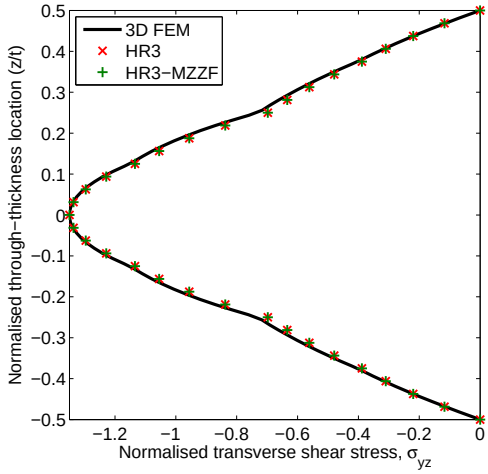

(f) Normalised transverse shear stress, $\bar{\sigma}_{yz}(a/2, b/4, z)$

Figure 8.24: Laminate VAT E: Through-thickness distribution of the 3D stress field at different planar locations for $a/t = 10$. The figures compare different implementations of the HR model with a 3D FEM model.

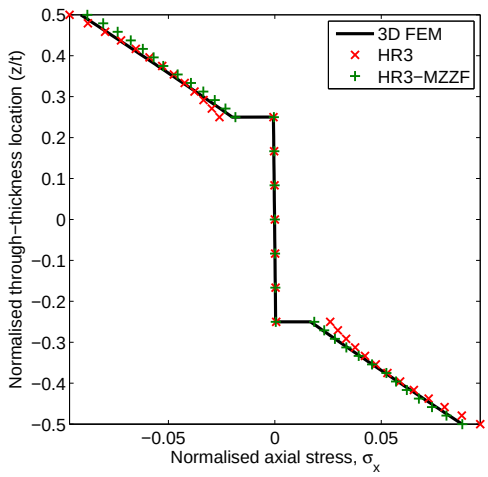

(a) Normalised axial stress, $\bar{\sigma}_x(a/2, b/2, z)$

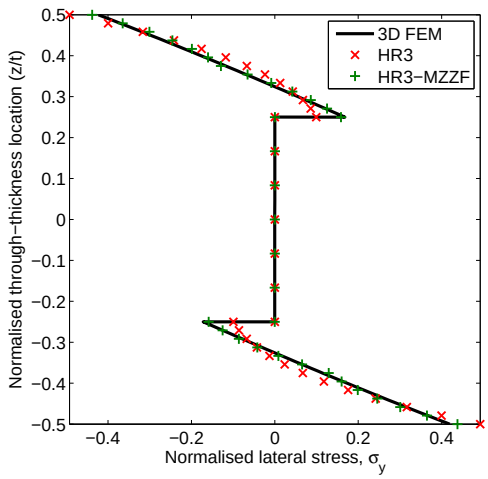

(b) Normalised lateral stress, $\bar{\sigma}_y(a/2, b/2, z)$

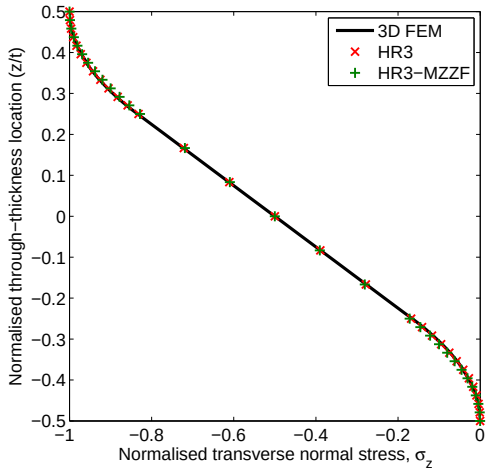

(c) Normalised transverse normal stress, $\bar{\sigma}_z(a/2, b/2, z)$

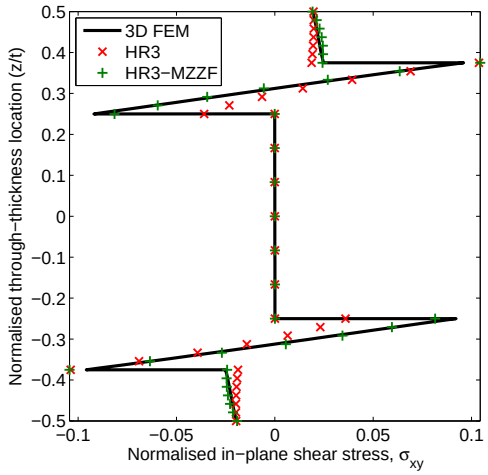

(d) Normalised in-plane shear stress, $\bar{\sigma}_{xy}(a/4, b/4, z)$

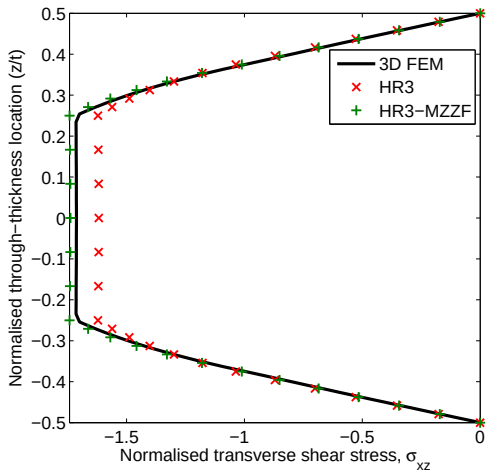

(e) Normalised transverse shear stress, $\bar{\sigma}_{xz}(a/4, b/2, z)$

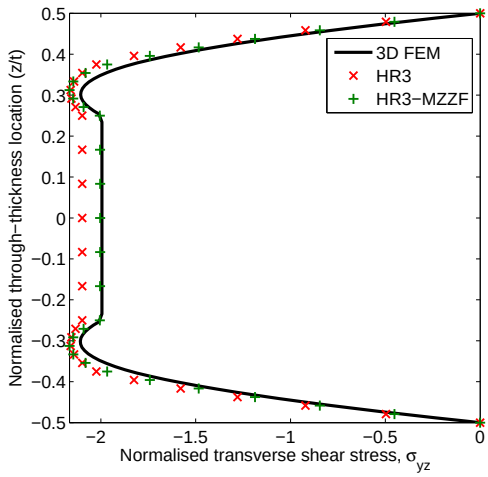

(f) Normalised transverse shear stress, $\bar{\sigma}_{yz}(a/2, b/4, z)$

Figure 8.25: Laminate VAT F: Through-thickness distribution of the 3D stress field at different planar locations for $a/t = 10$. The figures compare different implementations of the HR model with a 3D FEM model.

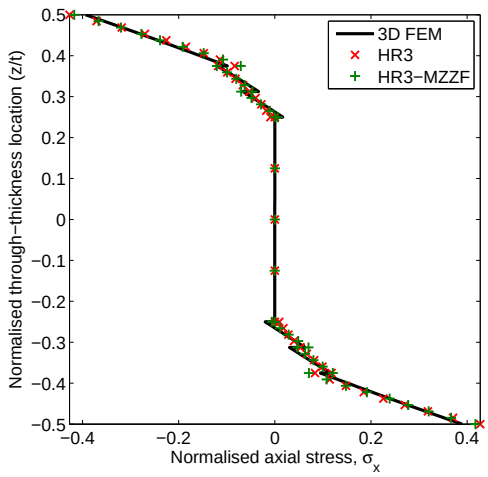

(a) Normalised axial stress, $\bar{\sigma}_x(a/2, b/2, z)$

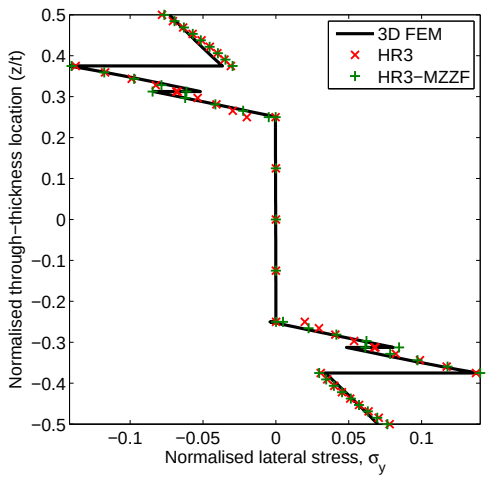

(b) Normalised lateral stress, $\bar{\sigma}_y(a/2, b/2, z)$

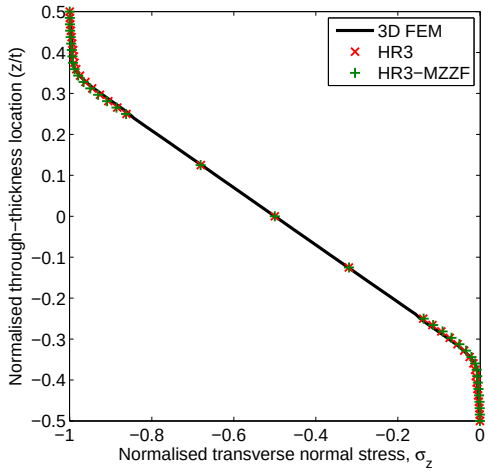

(c) Normalised transverse normal stress, $\bar{\sigma}_z(a/2, b/2, z)$

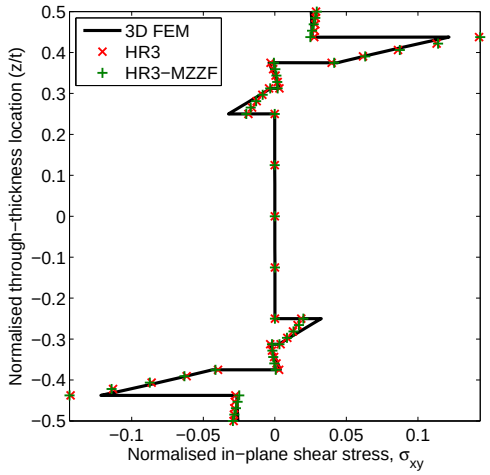

(d) Normalised in-plane shear stress, $\bar{\sigma}_{xy}(a/4, b/4, z)$

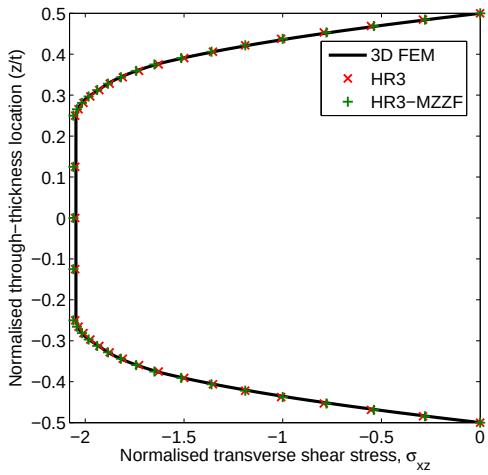

(e) Normalised transverse shear stress, $\bar{\sigma}_{xz}(a/4, b/2, z)$

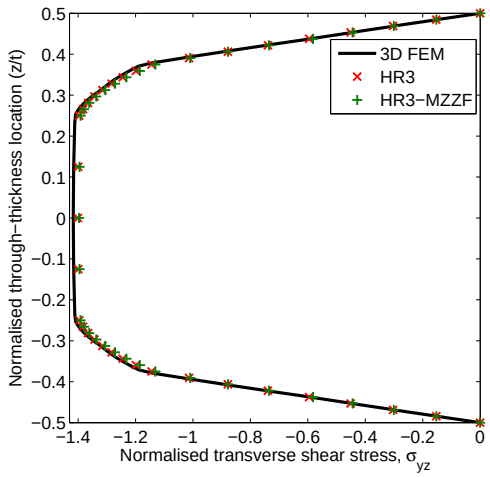

(f) Normalised transverse shear stress, $\bar{\sigma}_{yz}(a/2, b/4, z)$

Figure 8.26: Laminate VAT G: Through-thickness distribution of the 3D stress field at different planar locations for $a/t = 10$. The figures compare different implementations of the HR model with a 3D FEM model.

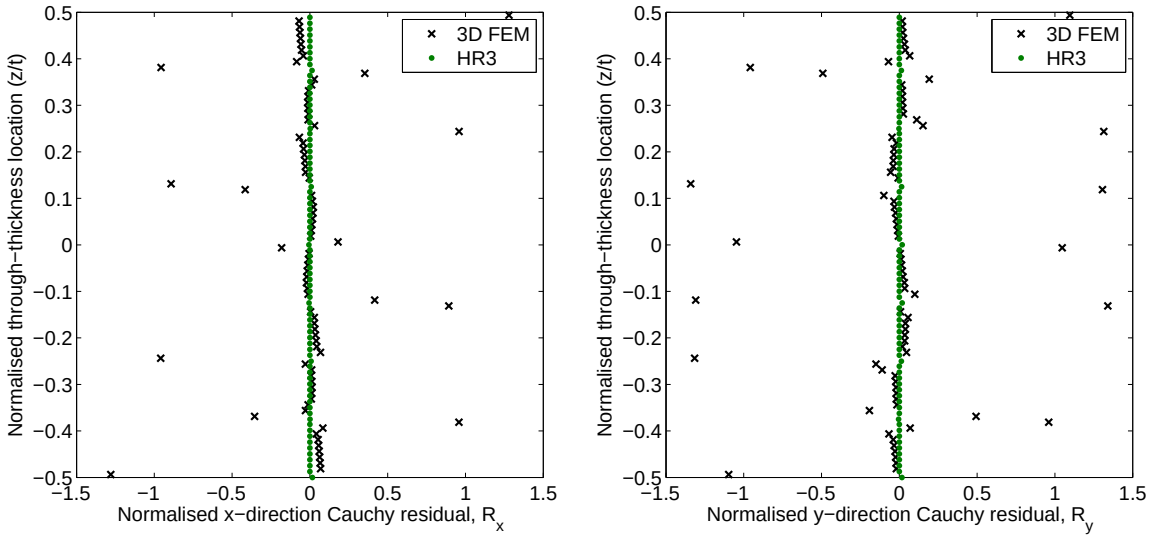

(a) Normalised x-direction Cauchy residual, $\bar{R}_x$ **(b)** Normalised y-direction Cauchy residual, $\bar{R}_y$

Figure 8.27: Laminate VAT D: Normalised x-direction and y-direction Cauchy residuals $\bar{R}_x$ and $\bar{R}_y$, respectively, for 3D FEM and HR models at $(a/4, b/4, z)$ for $a/t = 10$.

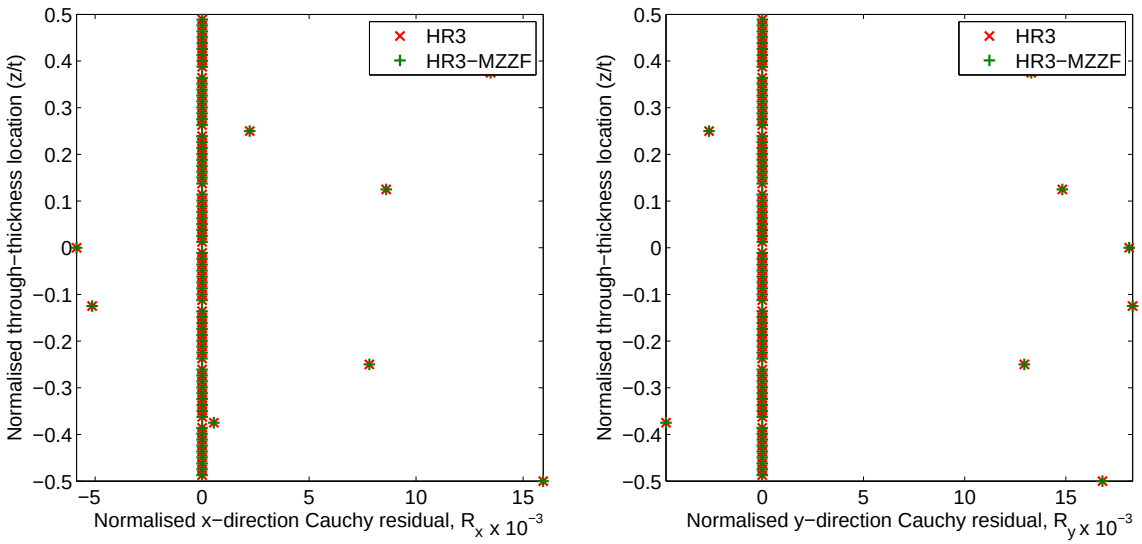

(a) Normalised x-direction Cauchy residual, $\bar{R}_x$ **(b)** Normalised y-direction Cauchy residual, $\bar{R}_y$

Figure 8.28: Laminate VAT D: Normalised x-direction and y-direction Cauchy residuals $\bar{R}_x$ and $\bar{R}_y$, respectively, for all HR models at $(a/4, b/4, z)$ for $a/t = 10$.

of the applied loading norm p_0, and even at layer midplane level the residual can be of order 10^{-2}, and is four orders of magnitude greater than the HR models.

As a result, we observe that very detailed 3D FEM meshes with more than ten elements per layer and multiple hours of runtime, do not guarantee that Cauchy's equilibrium equations are satisfied with negligible error. The HR formulation presented herein predicts 3D stress fields that equilibrate more accurately than 3D FEM. At the same time, the HR models reduce the number of variables by four orders of magnitude when analysing variable-stiffness laminates, which leads to a reduction in run-time from 10 hours in Abaqus on a high-performance computer with 128 GB of RAM to 1-2 minutes on a standard desktop PC running interpreted Matlab.

This combination of accuracy and computational expense makes the HR formulation an attractive basis for industrial design tools. Two important reasons for the performance of the HR models is their mixed displacement- and stress-based nature, which inherently satisfies the equilibrium of stresses in a variational sense, compared to the displacement-based 3D FEM model in Abaqus, which only guarantees the compatibility of displacements and strains. Second, the strong-form DQM solution technique used herein allows more accurate computation of derivatives and enforces both essential and natural boundary conditions explicitly.

8.2.2 Effect of transverse shear deformation on tow-steered plates

Finally, the relative effects of transverse shear deformation on tow-steered composite plates are investigated for a range of characteristic length to thickness ratios $a/t \in [100, 10]$, i.e. from relatively thin to moderately thick plates. A variety of different tow-steered laminates are tested including panels with fibre variations in the x- and y-directions only, as well as panels with fibre variations in both directions. The loading configuration in Figure 8.19 is maintained with a uniform pressure loading of magnitude $\hat{P}_t = p_0$ applied to the top surface but the boundary conditions are changed from clamped to simply supported. Thus, the midplane of the boundary cross-section is assumed to be supported on a knife edge, such that translation and rotation of the edges normal to the boundary is not constrained, whereas translation and rotation tangential to the boundary is constrained.

To eliminate the influence of the ZZ effect, transverse shear anisotropy is removed by assuming material properties with equal transverse shear moduli. As a result, $G_{13} = G_{23}$ and any layer of arbitrary fibre orientation has the same transverse shear rigidity with no discontinuity in transverse shear strains at layer interfaces. The material properties $E_1 = 150$ GPa, $E_2 = E_3 = 10$ GPa, $G_{12} = 5$ GPa, $G_{13} = G_{12} = 4$ GPa, $\upsilon_{12} = \upsilon_{13} = \upsilon_{23} = 0.3$ are assumed herein and are representative of a typical carbon-fibre reinforced plastic.

As the influence of the ZZ effect is eliminated using these material properties, the HR3 model is used throughout this section. The relative effect of transverse shear deformation is gauged by comparing the bending deflection of this higher-order HR3 model to the results of a CLA model which neglects the effects of transverse shear deformation. The bending deflection is expressed in terms of the normalised parameter

$$\bar{w}_0 = \frac{E_1 t^3}{0.15 p_0 a^2 b^2} w_0 \left(\frac{a}{2}, \frac{b}{2}, z \right). \tag{8.13}$$

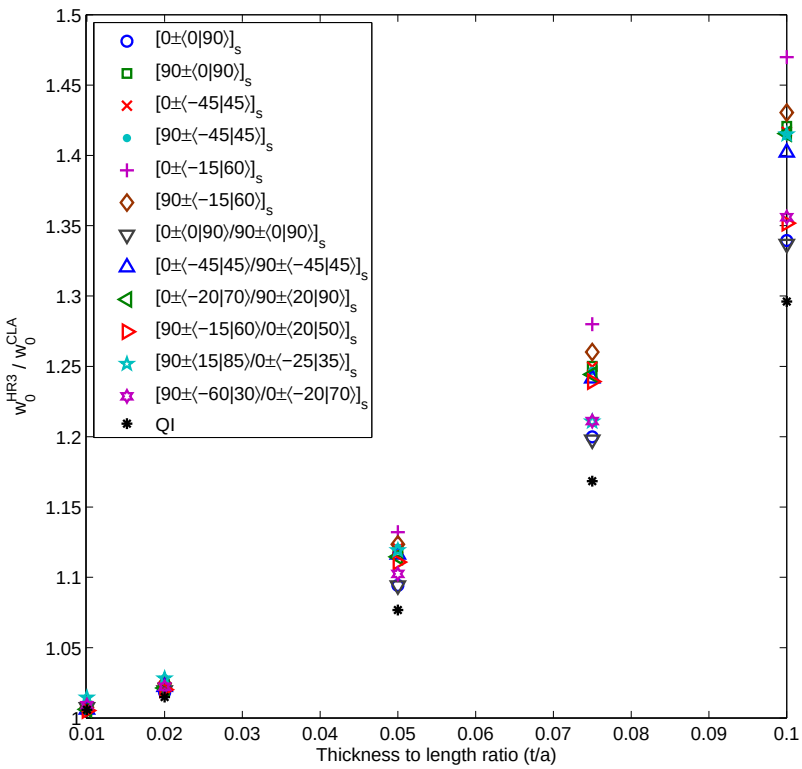

Figure 8.29: Ratio of normalised HR3 and CLA bending deflections for 12 different tow-steered laminates at various thickness to characteristic length ratio t/a. The curves indicate the increasing effect of transverse shear deformation on the global behaviour with increasing t/a. The deflections ratios of the tow-steered laminates are compared against a homogeneous, specially orthotropic, symmetric and quasi-isotropic laminate denoted by QI.

For the CLA mode, this metric is invariant with the characteristic length to thickness ratio a/t. Thus, the ratio between the normalised HR3 deflection and the normalised CLA deflection $\bar{w}_0^{HR3}/\bar{w}_0^{CLA}$ gives an indication of the influence of transverse shear deformation for different values of a/t. For $a/t \to \infty$, the ratio $\bar{w}_0^{HR3}/\bar{w}_0^{CLA} \to 1$.

The results of $\bar{w}_0^{HR3}/\bar{w}_0^{CLA}$ for a large set of tow-steered laminates at different values of thickness to characteristic length ratio within the range $t/a \in [.01, .1]$ are shown in Figure 8.29. The bending deflection ratios follow a general parabolic trend with t/a, which confirms the well-known relationship between the influence of transverse shear deformation and thickness of a plate. Thus, increasing the thickness of the plate causes a parabolically increasing effect of transverse shear deformation on the global behaviour of the plate.

Figure 8.29 also compares the tow-steered bending deflection ratios against that of a corresponding homogeneous, specially orthotropic, symmetric and quasi-isotropic laminate denoted by QI. Weaver [177] has shown that the minimum number of unidirectional layers required to produce a homogeneous, specially orthotropic, symmetric and quasi-isotropic layup using only the standard $0°$, $90°$, $-45°$ and $45°$ layers is 48. A layup is defined to be homogeneous if the

condition

$$\frac{D_{ij}}{A_{ij}} = \frac{t^2}{12}, \quad j \neq 6$$

is satisfied where A_{ij} and D_{ij} are the classical membrane and bending rigidity matrices, respectively. Thus, a homogeneous laminate obeys the classic ratio of membrane and bending stiffness for isotropic plates. One possible layup that satisfies these requirements is a

$$[0/-45/90/45/0/-45/45/90/-45/90/45/45/90/0/0/90/45/-45/45/-45/0/0/90/-45]_s\,.$$

stacking sequence, and this layup is henceforth be referred to as QI.

As the tow-steered laminates considered here feature a continuous range of fibre angles across the plate of up to 90°, they can be considered to be akin to a quasi-isotropic laminate. Thus, the comparison against the QI laminate gives a measure of the effect of transverse shear deformation on the two-steered panels compared to a realistic laminate of the same material invariants. An interesting finding of Figure 8.29 is that all tow-steered panels investigated here are affected more by transverse shear deformation than the QI laminate.

The effect of transverse shear deformation on the tow-steered laminates is most evident for the maximum thickness of $t/a = 0.1$. Interestingly, the tow-steered laminates tend to agglomerate into two groups with the $[0 \pm \langle -15|60\rangle]$ laminate being an exception to this rule. In fact, this laminate is affected most by transverse shear deformation for $t/a = 0.1$. However, from pure visual investigation it is difficult to ascertain whether certain trends exist that correlate the magnitude of transverse shear effects and tow-steering. This is not surprising given the complexity of the structural behaviour due to the variable-stiffness nature of the laminates. Thus, an interesting topic of future work would be to ascertain and quantify the relationship between the effects of transverse shear deformation and variable-stiffness designs. Due to the complexity of the problem, finding a closed-form solution for this relationship in terms of structural parameters may prove difficult. In this reagrd, statistical regression techniques could be a promising first approach.

8.3 Conclusions

In this chapter, a comprehensive set of straight-fibre and variable-stiffness composite and sandwich beams was analysed under different bending load cases, boundary conditions and thickness to characteristic length ratios using the 2D ESLT derived from the HR principle in Chapter 7. The tested laminates include a variety of symmetric and non-symmetric, balanced and unbalanced, multimaterial sandwich plates as well as laminates with *3D heterogeneity*, i.e. laminates with material properties that vary in all three dimensions.

The orthotropic straight-fibre laminates were validated against 3D elasticity solutions, whereas the anisotropic straight-fibre and variable-stiffness laminates were compared against 3D FEM results. Overall, the through-thickness stress fields of the HR model show excellent correlation with the 3D elasticity and 3D FEM results for characteristic length to thickness ratios of 10 : 1. In some applications, e.g. wind turbine blade roots, where the characteristic length to thickness ratio exceeds this value, transverse normal deformation needs to be accounted for. The accuracy

of the HR model combined with the three-order-of-magnitude reduction in runtime compared to high-fidelity 3D FEM models, are attractive qualities for industrial design tools.

The results in Section 8.1.1.2 show that the HR3-RZTmx model, i.e. using the RZT ZZ function accounting for EWLs, correlates most accurately with Pagano's 3D elasticity solution for orthotropic straight-fibre laminates. Thus, Gherlone's adaptation [54] of the RZT ZZ function is recommended to obtain the most accurate stress results. The HR model using MZZF (HR3-MZZF) is also accurate for simple sandwich laminates comprised of stiff face layers and a soft core. When two different cores or three unique material properties are used within a laminate, MZZF results in large errors. This discrepancy occurs because MZZF is based on an arbitrary ad hoc assumption of the ZZ slope changes between layers, and not on actual material properties like the RZT ZZ function. For non-sandwich laminates, the HR3 model without ZZ functionality gives similar accuracy to the HR3-RZTmx and HR3-MZZF models, and as a result of the reduced computational expense, is the preferred option for typical non-sandwich composite laminates used in engineering applications.

The anisotropic laminates in Section 8.1.2.2 are influenced less by the ZZ effect as the layerwise differences in transverse shear moduli is reduced for combinations of off-axis layers compared to orthotropic 0/90 laminates. Furthermore, the results for anisotropic, straight-fibre laminates confirm that the HR3-RZTmx model predicts the 3D stress fields most accurately for general multimaterial laminations, where layer material properties may vary by orders of magnitude. However, for the variable-stiffness plates studied in Section 8.2.1, the RZT ZZ function leads to ill-conditioning of the numerical DQM stiffness matrix due to local singularities in the in-plane derivatives of the RZT ZZ function. Thus, within the present global DQM framework, the HR3-RZTmx is not suited for robust analysis of variable-stiffness laminates. To remedy this, a local DQM approach, where only small number of grid points rather than the full domain is used to compute derivatives, should be tested. Alternatively, a strong-form or weak-form FEM that assigns constant fibre-angles to each element within the discretisation mesh would also remove the numerical ill-conditioning.

The results presented in Sections 8.1.2.2 and 8.2.1 corroborate earlier findings, that the HR 3D stress fields satisfy Cauchy's 3D equilibrium equations more accurately, and at a fraction of the computational cost, than high-fidelity 3D FEM models in Abaqus. This point highlights an important advantage of the HR variational statement: it is computationally more efficient to enforce the equilibrium of stresses explicitly in a variational sense than relying on the assumption that finer discretisation meshes in displacement-based theories converge to a negligible residual. The largest errors between the present HR plate model and the 3D FEM results for both straight-fibre and tow-steered composites, occur for the in-plane shear stress σ_{xy}. To date, the author has not been able to elucidate the origin of this bias towards the in-plane shear stress accuracy, and this issue is to be investigated further in future work.

Finally, the results in Section 8.2.2 suggest that tow-steered panels are affected more by transverse shear effects than a quasi-isotropic, homogeneous plate of the same material invariants. Due to the complexity of the governing equations, it is difficult to ascertain closed-form relations between the transverse shearing effects and tow-steering. An interesting topic of future work would be to implement statistical regression techniques to quantify this relationship.

Chapter 9

Conclusions and Future Work

The *Carbon Fibre Industry Worldwide 2011-2020* [178] research report published in 2011 forecasts an optimistic outlook for the worldwide demand for carbon-fibre reinforced plastics within the next decade. By 2020, the two biggest industrial applications, namely the automotive and wind energy sectors, are projected to increase their demand for carbon fibre fivefold - from just over 10 ktonnes in 2011 to over 50 ktonnes in 2020. Over the same period, the use of carbon fibre composites in the aerospace sector is forecast to double. The two major drivers behind these trends are an increasing focus on efficient lightweight structural design and the falling costs of carbon fibre raw materials as increasing demand allows for better economies of scale [4].

Falling costs will not only increase utilisation of reinforced plastics in traditional industries but also open the door for novel applications. In fact, the additive layer-by-layer manufacturing process of multilayered composites is ideally suited for rapid prototyping in niche applications and is starting to interface with research on 3D printing [179]. With this diversification to new applications, laminated composites are likely to be used in a host of new service environments. Furthermore, different applications benefit from different laminate configurations in terms of layer material properties, stacking sequences and geometric configurations.

As introduced in Chapter 1, laminated composites feature a number of non-classical effects which do not occur at all, or are not as pronounced in isotropic metallic or ceramic structures. Examples of these include:

- Transverse shearing of the cross-section, which leads to reductions in the bending rigidity and also induces higher-order distortions of the cross-section that concentrate stresses at the surfaces of laminates. For fibre-reinforced plastics, the ratio of longitudinal to shear modulus is approximately one order of magnitude greater than for isotropic materials ($E_{iso}/G_{iso} = 2.6,\ E_{11}/G_{13} \approx 28$). Second, as the orthotropy ratios $\lambda_i = E_{ii}/G_{i3}(t/L_i)^2$ for $i = 1, 2$ increase, stresses are increasingly channelled towards the surface.

- Transverse normal deformation, which compresses or extends the laminate in the stacking direction, and is particularly important for soft core sandwiches and pronounced asymmetric loading between the top and bottom surfaces. For isotropic materials $E_{xx} = E_{zz}$, whereas for composites $E_{11}/E_{33} \approx 15$, and hence thickness stretching is significantly increased for the same surface pressure loading.

- The zig-zag effect, which is a particular multilayered phenomenon that results in non-intuitive internal load redistributions towards layers with greater transverse shear and transverse normal rigidity. For purely isotropic beams and plates, this phenomenon does not exist, and this greatly reduces the complexity of the structural analysis.

- Localised boundary layers towards singularities, which exacerbate all three of the previously mentioned effects and lead to stress gradients that are drivers of failure initiation. In multilayered fibre-reinforced composites, higher-order moments that drive these boundary layers are more pronounced when compared to isotropic materials due to the presence of ZZ discontinuities and greater orthotropy ratios.

Hence, the reliable design of present and future multilayered structures requires accurate tools for stress predictions that account for these non-classical effects.

9.1 Review of the research objectives

The objective of this dissertation is to develop a computationally efficient structural model that accounts for the wide range of non-classical effects present in beam- and plate-like structures comprised of multiple layers of fibre-reinforced plastic, foam, honeycomb, or other high-performance materials. Particular focus is placed on finding a favourable combination of an accurate mathematical framework and an efficient numerical solver in order to make the developed model attractive for industrial design purposes. In this respect, a guiding principle of the present work is to provide insight into the origins and drivers of non-classical effects in multilayered structures, hence, to elucidate the underlying physics of the studied phenomena in order to aid the intuition of structural engineers in mitigating some of the unique structural effects that are characteristic of multilayered plates and beams.

A particular novelty of the work is that non-classical effects in both straight-fibre and tow-steered laminates are investigated. Hence, the research aims to develop a robust modelling framework for multilayered beams and plates with so-called *3D heterogeneity*, i.e. the material properties change discretely through the thickness due to the layered construction of the laminates, and also vary continuously in-plane as a result of curvilinear fibre paths. Whereas a number of works in the literature deal with global structural phenomena of tow-steered composites laminates, such as vibration and buckling, relatively little work has been conducted on localised higher-order effects in these laminates.

9.2 Research contributions

Overall, the work presented herein can be summarised by four overarching themes:

1. An in-depth literature review on 2D ESLTs for composite laminates, including an investigation of some of the shortcomings of popular displacement-based theories.

2. The mathematical derivation of a computationally efficient 2D modelling framework for straight-fibre and tow-steered multilayered beams and plates using the HR mixed-variational statement, and implemented within a meshless pseudo-spectral numerical solution scheme.

3. The application of the model to a wide range of laminated *3D heterogeneous* beams and plates under a variety of loading conditions. The results suggest that the model predicts 3D stress fields and local stress gradients towards boundaries to within a few percent of 3D elasticity and 3D finite element solutions.

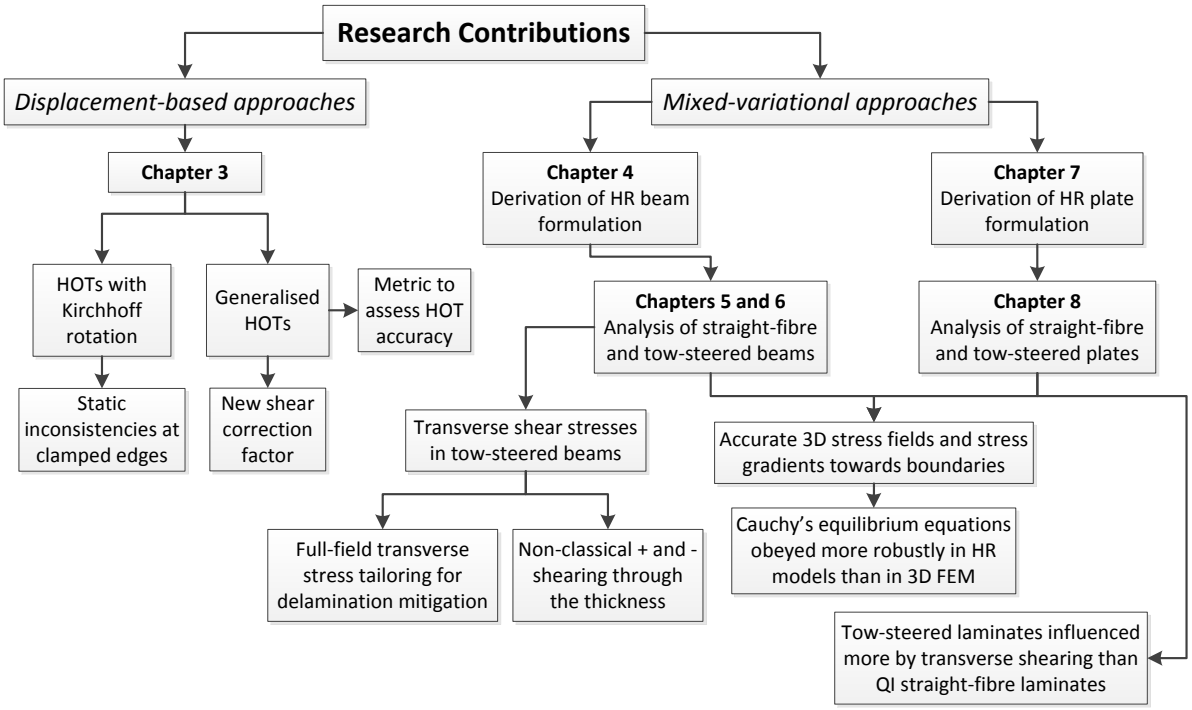

Figure 9.1: A hierarchy of the most significant research contributions presented in this dissertation. In the author's opinion the HR formulation presented herein is well-suited for accurate and computationally efficient stress analysis in industrial applications.

4. Using the derived model to study non-classical behaviour arising from in-plane and transverse anisotropy in layered structures in order to provide physical insight into the governing factors that drive higher-order effects, and to highlight some of the differences between straight-fibre and tow-steered laminates.

The most significant findings of the present work, as summarised by the four themes above, are addressed in more detail below. To accompany this, a flowchart of the major contributions of each chapter is presented in Figure 9.1.

Displacement-based theories

Chapter 3 elucidated static inconsistencies in axiomatic displacement-based HOTs that include the Kirchhoff rotations $\partial w_0/\partial x$ and $\partial w_0/\partial y$ in the assumptions of the in-plane displacement fields u_x and u_y, respectively. Originally, these terms arose in the third-order theories of Ambartsumyan [35] and Reddy [34] as a means of enforcing the transverse shear strains to vanish at the top and bottom surfaces. Throughout the decades since, their work has inspired many theories that use the linear displacement field of CLA as a basis, enhanced by a through-thickness shear strain shape function that vanishes on the surfaces (see Eq. (2.24) and Table 2.1). However, the presence of the Kirchhoff rotations in the displacement field of an HOT overconstrains the model and leads to underpredictions of bending displacements for clamped boundary conditions. Specifically, the Kirchhoff rotations induce essential boundary conditions $\delta\partial w_0/\partial x_i = 0$ in the PVD derivation of the governing equations, which need to be enforced at clamped edges

to mathematically constrain the boundary value problem. At clamped boundaries, the normal rotation $\partial w_0/\partial n$ is therefore forced to vanish, even though this condition is physically incorrect as the plate can rotate at the clamped edge due to the presence of transverse shearing. Furthermore, in these theories the transverse shear force derived from the constitutive equations is zero at clamped edges, which contradicts the shear force and bending moment equilibrium condition of classical beam theory.

It was shown that removing this artificial constraint, and writing the displacement field as a generalised power series of the through-thickness coordinate z, does not cause any of these static inconsistencies at clamped edges. In fact, if the order of the theory, i.e. the order of expansion of the displacement fields, is sufficient to capture all pertinent higher-order effects then the transverse shear stresses automatically vanish at the top and bottom surfaces. It was found that the residual at the top and bottom surfaces could thus be used as a metric to gauge the accuracy of the HOT.

The degree of higher-order shearing effects in bending can be captured using the nondimensional parameters $\lambda_x = \dfrac{E_{xx}}{G_{xz}}\left(\dfrac{t}{L_x}\right)^2$ and $\lambda_y = \dfrac{E_{yy}}{G_{yz}}\left(\dfrac{t}{L_y}\right)^2$. This parameter λ can be used to derive shear correction factors for FSDT that correct the transverse bending deflection results to be consistent with a particular HOT. Hence, these transverse shear correction factors are tailored to the actual geometry and material properties of the structure, and provide more accurate bending deflection results than the classic value of 5/6, which is the value of an infinitesimally thin beam or plate.

Derivation of Hellinger-Reissner model

As previously demonstrated by other authors [58, 59], the HR principle is a powerful mixed-variational statement for deriving 2D ESLTs due to its ability to predict accurate 3D stress fields and localised stress gradients towards boundaries. This characteristic stems from the fact that Cauchy's equilibrium equations are enforced explicitly in the variational statement. In purely displacement-based theories derived from the PVD, the constitutive and kinematic relations are satisfied *a priori* and the equilibrium of stresses is only enforced approximately. In other popular mixed-variational statements for multilayered structures, such as RMVT, the equilibrium of stresses is not enforced explicitly either. Hence, accurate transverse stress fields need to be post-processed from the in-plane stresses of these theories. Recent work by Tessler [82] suggests that the RMVT can be used to derive a theory that predicts accurate transverse shear stresses from the underlying model assumptions if the transverse shear stress assumptions inherently equilibrate with the in-plane stresses.

This same insight was used herein to derive a computationally efficient 2D ESLT for the bending and stretching of flat beams and plates from the HR principle. The derivations of the HR beam model in Chapter 4 and the HR plate model in Chapter 7 are based on the notion that accurate transverse shear and normal stress fields can be derived by integrating the in-plane stresses of a generalised, displacement-based HOT in Cauchy's equilibrium equations. These inherently equilibrated stress fields are thus written in terms of the same set of functional unknowns that are chosen to be the set of higher-order stress resultants. The use of stress

resultants is preferred over the use of displacement variables as this reduces the order of the ensuing governing differential equations.

Using inherently equilibrated 3D stress assumptions in the HR variational statement has a number of advantages. First, as a result of using the same set of functional unknowns for all stress fields, the number of unknown variables in the theory is reduced compared to generalised theories [58, 59]. Second, the higher-order 2D equivalent single-layer equilibrium equations, which arise from the variation of the Lagrange multipliers enforcing Cauchy's equilibrium equations in the HR principle, are inherently satisfied and do not need to be solved. Finally, the equilibrium of interfacial and surface tractions is mathematically guaranteed as long as the classical membrane and bending equilibrium equations of CLA are enforced in the variational statement. Hence, these three factors result in a *contracted* HR-type functional with considerably fewer unknowns than the full generalised functional, namely the reference plane translations (u_0, v_0, w_0) and a set of higher-order membrane forces and bending moments $\mathcal{F}$. Most importantly, the static inconsistencies noted above do not occur at clamped edges.

Higher-order fidelity was introduced in the formulation by a Taylor series expansion of the in-plane displacement and stress fields including the effect of ZZ moments. In fact, the governing equations were derived in a generalised framework, such that the order of the model can be readily increased when implemented in a computer code. By increasing the order of the model, and including or disregarding the local ZZ fidelity, the model is easily tailored to a variety of different engineering laminates. In Chapter 4, the fundamental mechanics of the ZZ effect in multilayered structures was shown to arise from differences in transverse shear strains at layer interfaces that, by means of the kinematic relations, lead to discrete changes in the slope of the in-plane displacement fields. The dual requirement of transverse shear stress and displacement continuity at layer interfaces led to the notion of modelling the transverse shear mechanics of a multilayered structure using a "springs-in-series" system. This approach resulted in the RZT ZZ function proposed by Tessler et al. [77] and is based on the ratio of layerwise transverse shear moduli to the equivalent transverse rigidity of the entire laminate. Throughout this work, this constitutive ZZ approach was compared to a constitutively independent ZZ function, namely MZZF, which is extensively used in the literature and only accounts for differences in layer thicknesses.

Modelling of laminated *3D heterogeneous* beams and plates

The application of the present HR formulation to the bending of flat beams and plates was presented in Chapters 5, 6 and 8. Particular focus was placed on modelling a large set of different stacking sequences and material systems to test the full capability of the model and highlight shortcomings that require further refinement. Furthermore, a number of different modelling orders were tested to assess the respective influence of different higher-order effects.

The results presented herein suggest that the HR model predicts 3D stress fields and local stress gradients towards boundaries to within nominal errors compared to 3D elasticity and 3D FEM solutions for laminates with thickness to length ratios down to 5 : 1. Of particular significance is that the derived HR formulation robustly captures 3D stress fields in multilayered beams and plates with *3D heterogeneity* at a fraction of the computational cost of 3D FEM

models. For thicker laminates, transverse normal deformation may be significant, such that the transverse displacement field needs to account for the occurrence of thickness stretch. However, it should be noted that most engineering laminates used in industry do not exceed characteristic length to thickness ratios of 5 : 1.

Indeed, the results show that a third-order HR model enhanced by the RZT ZZ function can robustly model straight-fibre composites and sandwich panels with layer properties that vary by multiple orders of magnitude. Previously, the consensus in the literature was that accurate 3D stress fields for such laminates can only be predicted using LWTs. As a 2D ESLT, the HR model is not capable of enforcing unique boundary conditions for different layers. However, these loading conditions are rare in practical engineering structures as the interface between different components typically involves the entire cross-section. Hence, the present work questions the necessity of using LWTs for practical engineering structures, and suggests that future work should re-examine when these approaches are worth their computational effort.

Another important finding of the present work is that the HR models more accurately obey Cauchy's 3D equilibrium equations, and at significantly reduced computational cost, than high-fidelity 3D FEM solutions from Abaqus. This means that local boundary layers towards surfaces, interfacial traction conditions and local stress fields are modelled more robustly using the HR formulation. This highlights an important advantage of the HR variational statement: it is computationally more efficient to enforce the equilibrium of stresses explicitly in a variational sense than to rely on the assumption that finer discretisation meshes in displacement-based theories will converge to negligible residuals.

Overall, the results suggest that a third-order HR model is sufficient to account for most higher-order effects that occur in practical engineering laminates used in industry. For these laminates, ZZ effects are benign as thick blocks of unidirectional plies are typically forbidden in engineering laminates to prevent issues with interlaminar cracking, and sandwich panels typically use thin face sheets and core materials with sufficient transverse shear rigidity that collectively minimise the ZZ effect. At the same time, the third-order HR model does account for higher-order transverse shearing effects, such as "stress-channelling", which occur for laminates with pronounced in-plane to transverse shear modulus orthotropy, as for example, common carbon fibre-reinforced composites.

However, the present work also shows that ZZ effects are accentuated towards clamped boundaries, such that ZZ functionality is required to capture the localised stress gradients that occur here. These boundary layer effects arise due to local variations in the higher-order stress resultants, i.e. the relative significance of the higher-order effects increases towards the clamped boundaries. In some niche sandwich applications where layerwise material properties can vary by orders of magnitude, as is the case for laminated glass and solar panels, the ZZ effect cannot be neglected. Furthermore, recent work by the present author shows that a ZZ variable can be used to model delaminations in laminates via a cohesive law [180]. The basic premise behind this approach is that the debonding process is akin to modelling a thin interfacial resin layer with heavily degraded material properties, i.e. giving rise to a ZZ deformation field. Hence, the ability to incorporate ZZ fidelity robustly in the HR formulation is a useful capability for accurate stress predictions.

In this respect, the current work has shown that the HR model based on the modified RZT ZZ function [54], which accounts for the presence of EWLs, most robustly captures ZZ effects in highly heterogeneous multilayered beams and plates. An HR model based on MZZF can predict the three-dimensional stress fields to similar accuracy for simple sandwich laminates comprised of stiff face layers and a soft core. For sandwich beams with very soft cores, or laminates with more than two unique materials, the errors of a MZZF-based HR model can be an order of magnitude greater than for RZT-based HR models. The reason for this is that the RZT ZZ function incorporates differences in layerwise transverse shear moduli, i.e. accounts for the underlying physics of the ZZ effect, whereas MZZF only incorporates differences in layer thicknesses.

However, the results for variable-stiffness beams and plates in Chapters 6 and 8, respectively, revealed numerical instabilities in the implementation of the HR-RZT formulation within the DQM due to local singularities in the in-plane derivatives of the RZT ZZ function. The dependence of the RZT ZZ function on transverse shear rigidities means that the ZZ effect can be finite in some areas of the numerical domain and vanish in others. Discretisation points with negligible ZZ effect lead to local singularities in the in-plane variations of the laminate compliance terms, and these cause significant noise in the numerical calculation of derivatives and, in turn, in the transverse shear and normal correction factors that underpin the HR model. The MZZF-based HR model performs more robustly under these circumstances as this ZZ function does not vary with in-plane location for variable-stiffness laminates.

Finally, the analysis of variable-stiffness laminates revealed some interesting non-classical phenomena that do not occur for straight-fibre laminates. First, Section 6.5 showed that non-intuitive stress fields induced towards the corners of straight-fibre laminates clamped along all four edges, can occur in tow-steered laminates remote from any boundaries or singularities. These localised stress fields are noteworthy as some parts of the cross-section are sheared in one direction and other parts are sheared in the opposite direction. Thus, local boundary layers in straight-fibre laminates that occur in the vicinity of strong 2D boundary conditions, can be induced in 1D structures purely by varying the material properties. Second, the results in Section 8.2.2 suggest that tow-steered panels are affected more by transverse shearing effects than a quasi-isotropic, homogeneous plate of the same material properties. Finally, the HR model was used to develop a new concept of tailoring the full 3D stress field throughout composite laminates. The results in Section 6.6 show that variable-stiffness laminates can lead to a better compromise between maximising bending stiffness and minimising the likelihood of delaminations. This is achieved by facilitating smooth layup transitions between the central unsupported portion of the structure, where high bending stiffness is required, and portions of the structure subject to local stress concentrations.

9.3 Future work

Throughout the preceding chapters, certain shortcomings of the present HR formulation have been highlighted. Suggestions for future work and improvement of the developed model are therefore summarised below.

The results in Chapter 5 and 8 showed that the effect of transverse normal deformation on composite laminates and sandwich beams under classical loading conditions is important for characteristic thickness to length ratios of about 5 : 1. To include these effects, the transverse displacement assumption for u_z in Eq. (4.9) for beams and Eq. (7.1) for plates, should be expanded in a power series of the through-thickness displacement z. In this manner, the thickness of the laminate is allowed to stretch and contract, such that pronounced asymmetric loads, e.g. blast loads, laminates with one transversely flexible and one transversely rigid layer, and very thick laminates can be modelled robustly. If ZZ effects due to layerwise differences in transverse normal moduli are to be included, an additional ZZ term can also be added to this displacement field. The derivation of the HR model based on the ensuing stress resultants and equilibrated in-plane stresses, which now account for the Poisson's effect from transverse normal deformations, then follows in the same manner as outlined herein.

In this work, the HR formulation was derived for flat beams and plates. A valuable contribution to the literature, and indeed for industrial stress analysis tools, would be an extension of the formulation to polar and/or curvilinear coordinates. This model could be applied to predict the transverse stresses in curved laminates, such as in corners of box- and C-spars on aircraft wings, or the curved blade-flange connection region in T-stringers. In singly or doubly curved laminates, high interlaminar stresses, i.e. transverse shear and transverse normal stresses, occur when the laminate is subjected to an opening bending moment that acts to flatten the structure. As a result, delamination is a common failure mode for curved laminates. Although simple analytical formulae for calculating these interlaminar stresses exist [181], recent industrial research suggests that the application of these models is limited due to the underlying geometric, material and boundary condition assumptions [182]. Even though these interlaminar stresses can be analysed using 3D FEM models, their computational cost is high, and alternative methods are needed. The development of a 1D HR model for arches and a 2D HR model for shells would therefore be a valuable contribution to this field.

In general, an important next step is to generalise the application of the HR formulation to a broader category of geometries. Two possible ways to achieve this are the development of weak-form finite elements from the HR functional, or the extension of the present single-element DQM to the finite-element DQM presented by Tornabene and coworkers [150]. The advantage of this latter strong-form FEM is that both the essential and natural boundary conditions are enforced, and interelement continuity of both displacements and stresses is guaranteed. In classic weak-form displacement-based finite elements, the displacement fields are generally chosen to be C^0-continuous, and therefore very fine meshes are required to predict accurate stress fields from the first derivatives of the displacements. Furthermore, the present work has shown that the strong-form DQM is advantageous in that the governing equations are solved at each discretisation point, rather than in an average sense over the whole domain, and this leads to accurate predictions of localised boundary layers towards supports and laminate surfaces. Hence, a strong-form FEM implementation would extend the applicability of the HR formulation to more general geometries while maintaining the benefits of computing pointwise accurate stress fields.

One interesting application of the HR model in a strong-form FEM framework would be the

analysis of stress concentrations around cutouts. It is well known that cutouts lead to localised stress concentrations around holes but also to the so-called "free-edge effect" in laminated composites. In the latter, the mismatch of elastic material properties between two adjacent layers at a free edge induces concentrated transverse shear and transverse normal stresses at the interfaces of dissimilar layers. The driver of these transverse interlaminar effects are decaying in-plane stresses towards the free edge, which are balanced with transverse shear and transverse normal stress gradients. As Cauchy equilibrium of the 3D stress fields is enforced in the HR formulation, a strong-form finite element model is likely to capture these effects robustly. Such a model could then be used in an optimisation study, and build on the work of previous authors [99, 100], to alleviate the interlaminar stresses around the hole using tow steering.

A strong-form FEM code could also be used to investigate some of the numerical instabilities of the present single-element DQ solution scheme. This single-element approach leads to densely populated stiffness matrices as the derivative at a point within the discretisation domain is based on all functional values within the domain. Second, the mixed-variational approach in terms of displacement and stress resultant variables means that significant off-diagonal terms arise in the stiffness matrices. Furthermore, the transverse shear correction factors of the HR formulation are orders of magnitude smaller than the DQ differential weighting matrices. This means that the enhanced constitutive equations for beams in Eq. (4.58c) and for plates in Eq. (7.61c), which feature derivatives of unknown variables and shear correction factors multiplying derivatives of unknown variables, have terms of significantly different orders of magnitude when discretised using the DQM. The advantage of a FEM approach is that the bandwidth of the stiffness matrix reduces with increasing number of elements as functional derivatives are only based on the functional values in each element, rather than the entire domain. Hence, non-zero values within the stiffness matrix are constrained close to the leading diagonal producing a sparser matrix that is inverted with less numerical error.

Finally, an interesting topic of future study are the non-intuitive transverse shear stress profiles that occur in tow-steered laminates introduced in Section 6.5. A pertinent question worth answering is in what manner the opposite transverse shear strains in different layers can be manipulated via stiffness variations. Are these effects only possible for laminates with a certain number of layers? And could an optimisation study shed light on the extents to which these effects can be maximised? Moreover, further research into the possible implications of these effects are required. Current design studies on the buckling and postbuckling optimisation of tow-steered laminates rarely account for transverse shear stresses as these effects are deemed to be negligible for thin-walled structures. However, if non-intuitive through-thickness stresses, such as these transverse shear stress reversals, are detrimental to the damage tolerance of tow-steered laminates, and these effects occur remote from boundaries and singularities, then changes in the design guidelines are needed to account for these effects. In this case, higher-order modelling of non-classical effects is required throughout the entire structure, not just in areas with local boundary features, such that computationally efficient 2D modelling techniques, as presented in this work, will become critical for safe design.

Overall, the HR model derived herein has been shown to be a robust modelling framework for straight-fibre and tow-steered beams and plates, and is well-suited for accurate and compu-

tationally efficient stress analysis. In the author's opinion, an extension of the model using finite element techniques would present a compelling analysis tool for many industrial applications and for future research projects on optimised lightweight structures.

Appendices

Appendix A

This appendix supplements Chapter 4. Detailed derivations of the HR beam governing equations, and the definitions of pertinent transverse shear and transverse normal correction factors are shown herein.

The contracted HR functional in Eq. (4.55) is split into separate components representing the potential of axial stress Π_{σ_x}, transverse shear stress $\Pi_{\tau_{xz}}$, transverse normal Π_{σ_z} stress, the potential of boundary tractions Π_Γ and the potential of the Lagrange multiplier constraints $\Pi_\mathcal{L}$. Substituting the pertinent expressions for stresses and strains into the functional of Eq. (4.55) yields,

$$\delta\Pi = \delta\left(\Pi_{\sigma_x} + \Pi_{\tau_{xz}} + \Pi_{\sigma_z} + \Pi_\mathcal{L} + \Pi_\Gamma\right) = 0$$

$$\Pi_{\sigma_x} = \frac{1}{2}\int_V \sigma_x^\top \epsilon_x \mathrm{d}V = \frac{1}{2}\int_V \mathcal{F}^\top \boldsymbol{s}^\top \boldsymbol{f}_\epsilon^{(k)\top} \bar{Q}^{(k)} \boldsymbol{f}_\epsilon^{(k)} \boldsymbol{s}\mathcal{F}\mathrm{d}V \tag{A.1a}$$

$$\Pi_{\tau_{xz}} = \frac{1}{2}\int_V \tau_{xz}^\top \gamma_{xz}\mathrm{d}V = \frac{1}{2}\int_V \left[\frac{\mathrm{d}}{\mathrm{d}x}\left\{\boldsymbol{c}^{(k)}\boldsymbol{s}\mathcal{F}\right\} + \hat{T}_b\right]^\top \frac{1}{G_{xz}^{(k)}}\left[\frac{\mathrm{d}}{\mathrm{d}x}\left\{\boldsymbol{c}^{(k)}\boldsymbol{s}\mathcal{F}\right\} + \hat{T}_b\right]\mathrm{d}V \tag{A.1b}$$

$$\begin{aligned}\Pi_{\sigma_z} = \frac{1}{2}\int_V \sigma_z^\top \epsilon_z \mathrm{d}V = \frac{1}{2}\int_V &\left[\frac{\mathrm{d}^2}{\mathrm{d}x^2}\left\{\boldsymbol{e}^{(k)}\boldsymbol{s}\mathcal{F}\right\} - \hat{T}_{b,x}\left(z - z_0\right) + \hat{P}_b\right]^\top \cdot \\ &\left[R_{13}^{(k)}\bar{Q}^{(k)}\boldsymbol{f}_\epsilon^{(k)}\boldsymbol{s}\mathcal{F} + R_{33}^{(k)}\left\{\frac{\mathrm{d}^2}{\mathrm{d}x^2}\left(\boldsymbol{e}^{(k)}\boldsymbol{s}\mathcal{F}\right) - \hat{T}_{b,x}\left(z - z_0\right) + \hat{P}_b\right\}\right]\mathrm{d}V\end{aligned} \tag{A.1c}$$

$$\Pi_\mathcal{L} = \int u_0\left(N_{,x} + \hat{T}_t - \hat{T}_b\right)\mathrm{d}x + \int w_0\left(M_{,xx} + z_{N_l}\hat{T}_{t,x} - z_0\hat{T}_{b,x} + \hat{P}_t - \hat{P}_b\right)\mathrm{d}x \tag{A.1d}$$

$$\begin{aligned}\Pi_\Gamma &= -\int_{S_1}\left(\sigma_x\hat{u}_x^{(k)} + \tau_{xz}\hat{w}_0\right)\mathrm{d}S - \int_{S_2}\left\{u_x^{(k)}\left(\sigma_x - \hat{\sigma}_x\right) + w_0\left(\tau_{xz} - \hat{\tau}_{xz}\right)\right\}\mathrm{d}S \\ &= -\int\left[\sigma_x\boldsymbol{f}_u^{(k)}\hat{\mathcal{U}} + \tau_{xz}\hat{w}_0\right]\Big|_{C_1}\mathrm{d}z - \int\left\{\boldsymbol{f}_u^{(k)}\mathcal{U}\left(\sigma_x - \hat{\sigma}_x\right) + w_0\left(\tau_{xz} - \hat{\tau}_{xz}\right)\right\}\Big|_{C_2}\mathrm{d}z.\end{aligned} \tag{A.1e}$$

Performing the variations on the functionals in Eqs. (A.1a)-(A.1e) following the rules of the calculus of variations results in the following expressions. For the potential of axial stress we have,

$$\begin{aligned}\delta\Pi_{\sigma_x} &= \delta\left\{\frac{1}{2}\int\mathcal{F}^\top\boldsymbol{s}^\top\left(\int\boldsymbol{f}_\epsilon^{(k)\top}\bar{Q}^{(k)}\boldsymbol{f}_\epsilon^{(k)}\mathrm{d}z\right)\boldsymbol{s}\mathcal{F}\mathrm{d}x\right\} \\ &= \delta\left\{\frac{1}{2}\int\mathcal{F}^\top\boldsymbol{s}^\top\boldsymbol{S}\boldsymbol{s}\mathcal{F}\mathrm{d}x\right\} = \delta\left\{\frac{1}{2}\int\mathcal{F}^\top\boldsymbol{s}^\top\mathcal{F}\mathrm{d}x\right\} = \int\mathcal{F}^\top\boldsymbol{s}^\top\delta\mathcal{F}\mathrm{d}x.\end{aligned} \tag{A.2}$$

For the potential of transverse shear stress,

$$\begin{aligned}
\delta\Pi_{\tau_{xz}} &= \delta\left\{\frac{1}{2}\int_V\left[\frac{\mathrm{d}}{\mathrm{d}x}\left(\boldsymbol{c}^{(k)}\boldsymbol{s}\mathcal{F}\right)^\top\frac{1}{G_{xz}^{(k)}}\frac{\mathrm{d}}{\mathrm{d}x}\left(\boldsymbol{c}^{(k)}\boldsymbol{s}\mathcal{F}\right)+2\frac{\hat{T}_b}{G_{xz}^{(k)}}\frac{\mathrm{d}}{\mathrm{d}x}\left(\boldsymbol{c}^{(k)}\boldsymbol{s}\mathcal{F}\right)+\frac{\hat{T}_b^2}{G_{xz}^{(k)}}\right]\mathrm{d}V\right\}\\
&= \int_V\left[\mathcal{F}^\top\left\{\left(\boldsymbol{c}^{(k)}\boldsymbol{s}\right)_{,x}^\top\frac{1}{G_{xz}^{(k)}}\left(\boldsymbol{c}^{(k)}\boldsymbol{s}\right)_{,x}\right\}+\mathcal{F}_{,x}^\top\left\{\boldsymbol{s}^\top\boldsymbol{c}^{(k)\top}\frac{1}{G_{xz}^{(k)}}\left(\boldsymbol{c}^{(k)}\boldsymbol{s}\right)_{,x}\right\}+\right.\\
&\quad\left.\hat{T}_b\left\{\frac{1}{G_{xz}^{(k)}}\left(\boldsymbol{c}^{(k)}\boldsymbol{s}\right)_{,x}\right\}\right]\delta\mathcal{F}\mathrm{d}V+\int_V\left[\mathcal{F}^\top\left\{\left(\boldsymbol{c}^{(k)}\boldsymbol{s}\right)_{,x}^\top\frac{1}{G_{xz}^{(k)}}\boldsymbol{c}^{(k)}\boldsymbol{s}\right\}+\right.\\
&\quad\left.\mathcal{F}_{,x}^\top\left\{\boldsymbol{s}^\top\boldsymbol{c}^{(k)\top}\frac{1}{G_{xz}^{(k)}}\boldsymbol{c}^{(k)}\boldsymbol{s}\right\}+\hat{T}_b\left\{\frac{1}{G_{xz}^{(k)}}\boldsymbol{c}^{(k)}\boldsymbol{s}\right\}\right]\delta\mathcal{F}_{,x}\mathrm{d}V.
\end{aligned}\tag{A.3}$$

Performing integration by parts on Eq. (A.3), and defining pertinent shear correction matrices by integrating in the z-direction results in,

$$\begin{aligned}
\delta\Pi_{\tau_{xz}} &= \left[\mathcal{F}^\top\boldsymbol{\eta}^{sbc^\top}+\mathcal{F}_{,x}^\top\boldsymbol{\eta}_x^{sbc^\top}+\hat{T}_b\boldsymbol{\chi}^{sbc^\top}\right]\Big|_{C_1}\delta\mathcal{F}+\\
&\quad\int\left[\mathcal{F}^\top\boldsymbol{\eta}^{s^\top}+\mathcal{F}_{,x}^\top\boldsymbol{\eta}_x^{s^\top}+\mathcal{F}_{,xx}^\top\boldsymbol{\eta}_{xx}^{s^\top}+\hat{T}_b\boldsymbol{\chi}^{s^\top}+\hat{T}_{b,x}\boldsymbol{\chi}_x^{s^\top}\right]\delta\mathcal{F}\mathrm{d}x
\end{aligned}\tag{A.4}$$

where all $\boldsymbol{\eta}_\alpha^s$ are $\mathcal{O}$x$\mathcal{O}$ matrices of shear coefficients that automatically include pertinent shear correction factors. Matrices $\boldsymbol{\chi}_\alpha^s$ are $\mathcal{O}$x1 column vectors of correction factors that enforce transverse shearing effects of the surface shear tractions. In each case the additional superscript *bc* refers to coefficients used in the boundary conditions. The size of these matrices depends on the chosen order of the model. For example a first-order shear theory has $\mathcal{O}=2$ with in-plane stress resultant N and bending stress resultant M, i.e. $\mathcal{F}=\begin{bmatrix}N & M\end{bmatrix}^\top$, whereas a third-order zigzag theory has $\mathcal{O}=6$ with in-plane stress resultants N,O, bending stress resultants M,P and zig-zag resultant $F_{\phi,x},F_\phi$, i.e. $\mathcal{F}=\begin{bmatrix}N & M & O & P & F_{\phi,x} & F_\phi\end{bmatrix}^\top$. The transposes of the different shear coefficient matrices $\boldsymbol{\eta}_\alpha^{s^\top}$ and $\boldsymbol{\chi}_\alpha^{s^\top}$ are defined as follows

$$\boldsymbol{\eta}^{s^\top}=\int_{-t/2}^{t/2}\left[-\left(\boldsymbol{c}^{(k)}\boldsymbol{s}\right)_{,xx}^\top\frac{1}{G_{xz}^{(k)}}\boldsymbol{c}^{(k)}\boldsymbol{s}-\left(\boldsymbol{c}^{(k)}\boldsymbol{s}\right)_{,x}^\top\left(\frac{1}{G_{xz}^{(k)}}\right)_{,x}\boldsymbol{c}^{(k)}\boldsymbol{s}\right]\mathrm{d}z\tag{A.5a}$$

$$\boldsymbol{\eta}_x^{s^\top}=\int_{-t/2}^{t/2}\left[-\boldsymbol{s}^\top\boldsymbol{c}^{(k)\top}\left(\frac{1}{G_{xz}^{(k)}}\right)_{,x}\boldsymbol{c}^{(k)}\boldsymbol{s}-2\left(\boldsymbol{c}^{(k)}\boldsymbol{s}\right)_{,x}^\top\frac{1}{G_{xz}^{(k)}}\boldsymbol{c}^{(k)}\boldsymbol{s}\right]\mathrm{d}z\tag{A.5b}$$

$$\boldsymbol{\eta}_{xx}^{s^\top}=\int_{-t/2}^{t/2}\left[-\boldsymbol{s}^\top\boldsymbol{c}^{(k)\top}\frac{1}{G_{xz}^{(k)}}\boldsymbol{c}^{(k)}\boldsymbol{s}\right]\mathrm{d}z=-\boldsymbol{\eta}_x^{sbc^\top}\tag{A.5c}$$

$$\boldsymbol{\chi}^{s^\top}=\int_{-t/2}^{t/2}\left[-\left(\frac{1}{G_{xz}^{(k)}}\right)_{,x}\boldsymbol{c}^{(k)}\boldsymbol{s}\right]\mathrm{d}z\tag{A.5d}$$

$$\boldsymbol{\chi}_x^{s^\top}=\int_{-t/2}^{t/2}\left[-\frac{1}{G_{xz}^{(k)}}\boldsymbol{c}^{(k)}\boldsymbol{s}\right]\mathrm{d}z=-\boldsymbol{\chi}^{sbc^\top}\tag{A.5e}$$

$$\boldsymbol{\eta}^{sbc^\top}=\int_{-t/2}^{t/2}\left[\left(\boldsymbol{c}^{(k)}\boldsymbol{s}\right)_{,x}^\top\frac{1}{G_{xz}^{(k)}}\boldsymbol{c}^{(k)}\boldsymbol{s}\right]\mathrm{d}z.\tag{A.5f}$$

For the potential of transverse normal stress we expand the parentheses in Eq. (A.1c) and take the first variation to get

$$\begin{aligned}\delta\Pi_{\sigma_z} = \int \Big[& \mathcal{F}^\top \left(\boldsymbol{e}^{(k)}\boldsymbol{s}\right)^\top_{,xx} R^{(k)}_{13}\bar{Q}^{(k)}\boldsymbol{f}^{(k)}_\epsilon \boldsymbol{s} + \mathcal{F}^\top_{,x}\left(\boldsymbol{e}^{(k)}\boldsymbol{s}\right)^\top_{,x} R^{(k)}_{13}\bar{Q}^{(k)}\boldsymbol{f}^{(k)}_\epsilon\boldsymbol{s} + \\ & \frac{1}{2}\mathcal{F}^\top_{,xx}\left(\boldsymbol{e}^{(k)}\boldsymbol{s}\right)^\top R^{(k)}_{13}\bar{Q}^{(k)}\boldsymbol{f}^{(k)}_\epsilon\boldsymbol{s} - \hat{T}_{b,x}\left(z-z_0\right)R^{(k)}_{33}\left(\boldsymbol{e}^{(k)}\boldsymbol{s}\right)_{,xx} + \hat{P}_b R^{(k)}_{33}\left(\boldsymbol{e}^{(k)}\boldsymbol{s}\right)_{,xx} - \\ & \frac{1}{2}\hat{T}_{b,x}\left(z-z_0\right)R^{(k)}_{13}\bar{Q}^{(k)}\boldsymbol{f}^{(k)}_\epsilon\boldsymbol{s} + \frac{1}{2}\hat{P}_b R^{(k)}_{13}\bar{Q}^{(k)}\boldsymbol{f}^{(k)}_\epsilon\boldsymbol{s} + \Big\{\left(\boldsymbol{e}^{(k)}\boldsymbol{s}\right)_{,xx}\mathcal{F} + 2\left(\boldsymbol{e}^{(k)}\boldsymbol{s}\right)_{,x}\mathcal{F}_{,x} + \\ & \left(\boldsymbol{e}^{(k)}\boldsymbol{s}\right)\mathcal{F}_{,xx}\Big\}^\top R^{(k)}_{33}\left(\boldsymbol{e}^{(k)}\boldsymbol{s}\right)_{,xx}\Big]\,\delta\mathcal{F}\mathrm{d}V + \int\Big[\mathcal{F}^\top\boldsymbol{s}^\top\boldsymbol{f}^{(k)^\top}_\epsilon\bar{Q}^{(k)}R^{(k)}_{13}\left(\boldsymbol{e}^{(k)}\boldsymbol{s}\right)_{,x} - \\ & 2\hat{T}_{b,x}\left(z-z_0\right)R^{(k)}_{33}\left(\boldsymbol{e}^{(k)}\boldsymbol{s}\right)_{,x} + 2\hat{P}_b R^{(k)}_{33}\left(\boldsymbol{e}^{(k)}\boldsymbol{s}\right)_{,x} + 2\Big\{\left(\boldsymbol{e}^{(k)}\boldsymbol{s}\right)_{,xx}\mathcal{F} + \\ & 2\left(\boldsymbol{e}^{(k)}\boldsymbol{s}\right)_{,x}\mathcal{F}_{,x} + \left(\boldsymbol{e}^{(k)}\boldsymbol{s}\right)\mathcal{F}_{,xx}\Big\}^\top R^{(k)}_{33}\left(\boldsymbol{e}^{(k)}\boldsymbol{s}\right)_{,x}\Big]\,\delta\mathcal{F}_{,x}\mathrm{d}V + \\ & \int\Big[\frac{1}{2}\mathcal{F}^\top\boldsymbol{s}^\top\boldsymbol{f}^{(k)^\top}_\epsilon\bar{Q}^{(k)}R^{(k)}_{13}\left(\boldsymbol{e}^{(k)}\boldsymbol{s}\right) - \hat{T}_{b,x}\left(z-z_0\right)R^{(k)}_{33}\left(\boldsymbol{e}^{(k)}\boldsymbol{s}\right) + \hat{P}_b R^{(k)}_{33}\left(\boldsymbol{e}^{(k)}\boldsymbol{s}\right) + \\ & \Big\{\left(\boldsymbol{e}^{(k)}\boldsymbol{s}\right)_{,xx}\mathcal{F} + 2\left(\boldsymbol{e}^{(k)}\boldsymbol{s}\right)_{,x}\mathcal{F}_{,x} + \left(\boldsymbol{e}^{(k)}\boldsymbol{s}\right)\mathcal{F}_{,xx}\Big\}^\top R^{(k)}_{33}\left(\boldsymbol{e}^{(k)}\boldsymbol{s}\right)\Big]\,\delta\mathcal{F}_{,xx}\mathrm{d}V. \end{aligned} \tag{A.6}$$

Next, the first and second derivatives are removed from the first variation of $\delta\mathcal{F}$ in Eq. (A.6) by using integration by parts, and pertinent transverse normal correction matrices are defined by integrating in the z-direction to give,

$$\begin{aligned}\delta\Pi_{\sigma_z} = & \Big[\mathcal{F}^\top\boldsymbol{\eta}^{nbc^\top} + \mathcal{F}^\top_{,x}\boldsymbol{\eta}^{nbc^\top}_x + \mathcal{F}^\top_{,xx}\boldsymbol{\eta}^{nbc^\top}_{xx} + \mathcal{F}^\top_{,xxx}\boldsymbol{\eta}^{nbc^\top}_{xxx} + \hat{T}_{b,x}\boldsymbol{\chi}^{nbc^\top}_x + \hat{T}_{b,xx}\boldsymbol{\chi}^{nbc^\top}_{xx} + \\ & \hat{P}_b\boldsymbol{\omega}^{nbc^\top} + \hat{P}_{b,x}\boldsymbol{\omega}^{nbc^\top}_x\Big]\Big|_{C_1}\delta\mathcal{F} + \Big[\mathcal{F}^\top\boldsymbol{\rho}^{nbc^\top} + \mathcal{F}^\top_{,x}\boldsymbol{\rho}^{nbc^\top}_x + \mathcal{F}^\top_{,xx}\boldsymbol{\rho}^{nbc^\top}_{xx} + \hat{T}_{b,x}\boldsymbol{\gamma}^{nbc^\top}_x + \\ & \hat{P}_b\boldsymbol{\mu}^{nbc^\top}\Big]\Big|_{C_1}\delta\mathcal{F}_{,x} + \int\Big[\mathcal{F}^\top\boldsymbol{\eta}^{n^\top} + \mathcal{F}^\top_{,x}\boldsymbol{\eta}^{n^\top}_x + \mathcal{F}^\top_{,xx}\boldsymbol{\eta}^{n^\top}_{xx} + \mathcal{F}^\top_{,xxx}\boldsymbol{\eta}^{n^\top}_{xxx} + \mathcal{F}^\top_{,xxxx}\boldsymbol{\eta}^{n^\top}_{xxxx} + \\ & \hat{T}_{b,x}\boldsymbol{\chi}^{n^\top}_x + \hat{T}_{b,xx}\boldsymbol{\chi}^{n^\top}_{xx} + \hat{T}_{b,xxx}\boldsymbol{\chi}^{n^\top}_{xxx} + \hat{P}_b\boldsymbol{\omega}^{n^\top} + \hat{P}_{b,x}\boldsymbol{\omega}^{n^\top}_x + \hat{P}_{b,xx}\boldsymbol{\omega}^{n^\top}_{xx}\Big]\,\delta\mathcal{F}\mathrm{d}x \end{aligned} \tag{A.7}$$

where all $\boldsymbol{\eta}^n_\alpha$ are $\mathcal{O}$x$\mathcal{O}$ matrices of transverse normal coefficients that include pertinent correction factors. matrices $\boldsymbol{\chi}^n_\alpha$ and $\boldsymbol{\omega}^n_\alpha$ are $\mathcal{O}$x1 column vectors of correction factors that enforce transverse normal effects of the surface shear and normal tractions, respectively. Correction matrices $\boldsymbol{\rho}^{nbc}_\alpha$, $\boldsymbol{\gamma}^{nbc}_x$ and $\boldsymbol{\mu}^{nbc}$ only appear in the boundary condition associated with $\delta\mathcal{F}_{,x}$. The full set of correction matrices in Eq. (A.7) is defined as follows,

$$\begin{aligned}\boldsymbol{\eta}^{n^\top} = \int_{-t/2}^{t/2}\Big[& \left(\boldsymbol{e}^{(k)}\boldsymbol{s}\right)^\top_{,xx} R^{(k)}_{13}\bar{Q}^{(k)}\boldsymbol{f}^{(k)}_\epsilon\boldsymbol{s} - \frac{1}{2}\boldsymbol{s}^T\boldsymbol{f}^{(k)^\top}_\epsilon R^{(k)}_{13}\bar{Q}^{(k)}\left(\boldsymbol{e}^{(k)}\boldsymbol{s}\right)_{,xx} + \\ & \frac{1}{2}\left(\boldsymbol{f}^{(k)}_\epsilon\boldsymbol{s}\right)^\top_{,xx} R^{(k)}_{13}\bar{Q}^{(k)}\boldsymbol{e}^{(k)}\boldsymbol{s} + \frac{1}{2}\boldsymbol{s}^\top\boldsymbol{f}^{(k)^\top}_\epsilon\left(R^{(k)}_{13}\bar{Q}^{(k)}\right)_{,xx}\boldsymbol{e}^{(k)}\boldsymbol{s} + \\ & \left(\boldsymbol{f}^{(k)}_\epsilon\boldsymbol{s}\right)^\top_{,x}\left(R^{(k)}_{13}\bar{Q}^{(k)}\right)_{,x}\boldsymbol{e}^{(k)}\boldsymbol{s} + \left(\boldsymbol{e}^{(k)}\boldsymbol{s}\right)^\top_{,xxxx} R^{(k)}_{33}\boldsymbol{e}^{(k)}\boldsymbol{s} + \left(\boldsymbol{e}^{(k)}\boldsymbol{s}\right)^\top_{,xx} R^{(k)}_{33,xx}\boldsymbol{e}^{(k)}\boldsymbol{s} + \\ & 2\left(\boldsymbol{e}^{(k)}\boldsymbol{s}\right)^\top_{,xxx} R^{(k)}_{33,x}\boldsymbol{e}^{(k)}\boldsymbol{s}\Big]\,\mathrm{d}z \end{aligned} \tag{A.8a}$$

$$\boldsymbol{\eta}_x^{n^\top} = \int_{-t/2}^{t/2} \Big[\left(\boldsymbol{e}^{(k)}\boldsymbol{s}\right)_{,x}^\top R_{13}^{(k)} \bar{Q}^{(k)} \boldsymbol{f}_\epsilon^{(k)} \boldsymbol{s} + \left(\boldsymbol{f}_\epsilon^{(k)}\boldsymbol{s}\right)_{,x}^\top R_{13}^{(k)} \bar{Q}^{(k)} \boldsymbol{e}^{(k)} \boldsymbol{s} + \boldsymbol{s}^\top \boldsymbol{f}_\epsilon^{(k)^\top} \left(R_{13}^{(k)} \bar{Q}^{(k)}\right)_{,x} \boldsymbol{e}^{(k)} \boldsymbol{s} + 4 \left(\boldsymbol{e}^{(k)}\boldsymbol{s}\right)_{,xxx}^\top R_{33}^{(k)} \boldsymbol{e}^{(k)} \boldsymbol{s} + 2 \left(\boldsymbol{e}^{(k)}\boldsymbol{s}\right)_{,x}^\top R_{33,xx}^{(k)} \boldsymbol{e}^{(k)} \boldsymbol{s} + 6 \left(\boldsymbol{e}^{(k)}\boldsymbol{s}\right)_{,xx}^\top R_{33,x}^{(k)} \boldsymbol{e}^{(k)} \boldsymbol{s} \Big] \mathrm{d}z \quad \text{(A.8b)}$$

$$\boldsymbol{\eta}_{xx}^{n^\top} = \int_{-t/2}^{t/2} \Big[\frac{1}{2} \boldsymbol{s}^\top \boldsymbol{e}^{(k)^\top} R_{13}^{(k)} \bar{Q}^{(k)} \boldsymbol{f}_\epsilon^{(k)} \boldsymbol{s} + \frac{1}{2} \boldsymbol{s}^\top \boldsymbol{f}_\epsilon^{(k)^\top} R_{13}^{(k)} \bar{Q}^{(k)} \boldsymbol{e}^{(k)} \boldsymbol{s} + 6 \left(\boldsymbol{e}^{(k)}\boldsymbol{s}\right)_{,xx}^\top R_{33}^{(k)} \boldsymbol{e}^{(k)} \boldsymbol{s} + 6 \left(\boldsymbol{e}^{(k)}\boldsymbol{s}\right)_{,x}^\top R_{33,x}^{(k)} \boldsymbol{e}^{(k)} \boldsymbol{s} + \boldsymbol{s}^\top \boldsymbol{e}^{(k)^\top} R_{33,xx}^{(k)} \boldsymbol{e}^{(k)} \boldsymbol{s} \Big] \mathrm{d}z \quad \text{(A.8c)}$$

$$\boldsymbol{\eta}_{xxx}^{n^\top} = \int_{-t/2}^{t/2} \Big[4 \left(\boldsymbol{e}^{(k)}\boldsymbol{s}\right)_{,x}^\top R_{33}^{(k)} \boldsymbol{e}^{(k)} \boldsymbol{s} + 2 \boldsymbol{s}^\top \boldsymbol{e}^{(k)^\top} R_{33,x}^{(k)} \boldsymbol{e}^{(k)} \boldsymbol{s} \Big] \mathrm{d}z \quad \text{(A.8d)}$$

$$\boldsymbol{\eta}_{xxxx}^{n^\top} = \int_{-t/2}^{t/2} \Big[\boldsymbol{s}^\top \boldsymbol{e}^{(k)^\top} R_{33}^{(k)} \boldsymbol{e}^{(k)} \boldsymbol{s} \Big] \mathrm{d}z = -\boldsymbol{\eta}_{xxx}^{nbc^\top} = \boldsymbol{\rho}_{xx}^{nbc^\top} \quad \text{(A.8e)}$$

$$\boldsymbol{\chi}_x^{n^\top} = \int_{-t/2}^{t/2} (z - z_0) \Big[-\frac{1}{2} R_{13}^{(k)} \bar{Q}^{(k)} \boldsymbol{f}_\epsilon^{(k)} \boldsymbol{s} - R_{33,xx}^{(k)} \boldsymbol{e}^{(k)} \boldsymbol{s} \Big] \mathrm{d}z \quad \text{(A.8f)}$$

$$\boldsymbol{\chi}_{xx}^{n^\top} = \int_{-t/2}^{t/2} (z - z_0) \Big[-2 R_{33,x}^{(k)} \boldsymbol{e}^{(k)} \boldsymbol{s} \Big] \mathrm{d}z \quad \text{(A.8g)}$$

$$\boldsymbol{\chi}_{xxx}^{n^\top} = \int_{-t/2}^{t/2} (z - z_0) \Big[-R_{33}^{(k)} \boldsymbol{e}^{(k)} \boldsymbol{s} \Big] \mathrm{d}z = -\boldsymbol{\chi}_{xx}^{nbc^\top} = \boldsymbol{\gamma}_x^{nbc^\top} \quad \text{(A.8h)}$$

$$\boldsymbol{\omega}^{n^\top} = \int_{-t/2}^{t/2} \Big[\frac{1}{2} R_{13}^{(k)} \bar{Q}^{(k)} \boldsymbol{f}_\epsilon^{(k)} \boldsymbol{s} + R_{33,xx}^{(k)} \boldsymbol{e}^{(k)} \boldsymbol{s} \Big] \mathrm{d}z \quad \text{(A.8i)}$$

$$\boldsymbol{\omega}_x^{n^\top} = \int_{-t/2}^{t/2} \Big[2 R_{33,x}^{(k)} \boldsymbol{e}^{(k)} \boldsymbol{s} \Big] \mathrm{d}z, \quad \boldsymbol{\omega}_{xx}^{n^\top} = \int_{-t/2}^{t/2} \Big[R_{33}^{(k)} \boldsymbol{e}^{(k)} \boldsymbol{s} \Big] \mathrm{d}z = -\boldsymbol{\omega}_x^{nbc^\top} = \boldsymbol{\mu}^{nbc^\top} \quad \text{(A.8j)}$$

$$\boldsymbol{\eta}^{nbc^\top} = \int_{-t/2}^{t/2} \Big[\frac{1}{2} \boldsymbol{s}^\top \boldsymbol{f}_\epsilon^{(k)^\top} R_{13}^{(k)} \bar{Q}^{(k)} \left(\boldsymbol{e}^{(k)}\boldsymbol{s}\right)_{,x} - \frac{1}{2} \left(\boldsymbol{s}^\top \boldsymbol{f}_\epsilon^{(k)^\top} R_{13}^{(k)} \bar{Q}^{(k)}\right)_{,x} \boldsymbol{e}^{(k)} \boldsymbol{s} + \left(\boldsymbol{e}^{(k)}\boldsymbol{s}\right)_{,xx}^\top R_{33}^{(k)} \left(\boldsymbol{e}^{(k)}\boldsymbol{s}\right)_{,x} - \left\{ \left(\boldsymbol{e}^{(k)}\boldsymbol{s}\right)_{,xx}^\top R_{33}^{(k)} \right\}_{,x} \boldsymbol{e}^{(k)} \boldsymbol{s} \Big] \mathrm{d}z \quad \text{(A.8k)}$$

$$\boldsymbol{\eta}_x^{nbc^\top} = \int_{-t/2}^{t/2} \Big[-\frac{1}{2} \boldsymbol{s}^\top \boldsymbol{f}_\epsilon^{(k)^\top} R_{13}^{(k)} \bar{Q}^{(k)} \boldsymbol{e}^{(k)} \boldsymbol{s} + 2 \left(\boldsymbol{e}^{(k)}\boldsymbol{s}\right)_{,x}^\top R_{33}^{(k)} \left(\boldsymbol{e}^{(k)}\boldsymbol{s}\right)_{,x} - 3 \left(\boldsymbol{e}^{(k)}\boldsymbol{s}\right)_{,xx}^\top R_{33}^{(k)} \boldsymbol{e}^{(k)} \boldsymbol{s} - 2 \left(\boldsymbol{e}^{(k)}\boldsymbol{s}\right)_{,x}^\top R_{33,x}^{(k)} \boldsymbol{e}^{(k)} \boldsymbol{s} \Big] \mathrm{d}z \quad \text{(A.8l)}$$

$$\boldsymbol{\eta}_{xx}^{nbc^\top} = \int_{-t/2}^{t/2} \Big[\boldsymbol{s}^\top \boldsymbol{e}^{(k)^\top} R_{33}^{(k)} \left(\boldsymbol{e}^{(k)}\boldsymbol{s}\right)_{,x} - 3 \left(\boldsymbol{e}^{(k)}\boldsymbol{s}\right)_{,x}^\top R_{33}^{(k)} \boldsymbol{e}^{(k)} \boldsymbol{s} - \boldsymbol{s}^\top \boldsymbol{e}^{(k)^\top} R_{33,x}^{(k)} \boldsymbol{e}^{(k)} \boldsymbol{s} \Big] \mathrm{d}z \quad \text{(A.8m)}$$

$$\boldsymbol{\chi}_x^{nbc^\top} = \int_{-t/2}^{t/2} (z - z_0) \Big[-R_{33}^{(k)} \left(\boldsymbol{e}^{(k)}\boldsymbol{s}\right)_{,x} + R_{33,x}^{(k)} \boldsymbol{e}^{(k)} \boldsymbol{s} \Big] \mathrm{d}z \quad \text{(A.8n)}$$

$$\boldsymbol{\omega}^{nbc^\top} = \int_{-t/2}^{t/2} \Big[R_{33}^{(k)} \left(\boldsymbol{e}^{(k)}\boldsymbol{s}\right)_{,x} - R_{33,x}^{(k)} \boldsymbol{e}^{(k)} \boldsymbol{s} \Big] \mathrm{d}z \quad \text{(A.8o)}$$

$$\boldsymbol{\rho}^{nbc^\top} = \int_{-t/2}^{t/2} \Big[\frac{1}{2} \boldsymbol{s}^\top \boldsymbol{f}_\epsilon^{(k)^\top} R_{13}^{(k)} \bar{Q}^{(k)} \boldsymbol{e}^{(k)} \boldsymbol{s} + \left(\boldsymbol{e}^{(k)}\boldsymbol{s}\right)_{,xx}^\top R_{33}^{(k)} \boldsymbol{e}^{(k)} \boldsymbol{s} \Big] \mathrm{d}z \quad \text{(A.8p)}$$

$$\boldsymbol{\rho}_x^{nbc^\top} = \int_{-t/2}^{t/2} \Big[2 \left(\boldsymbol{e}^{(k)}\boldsymbol{s}\right)_{,x}^\top R_{33}^{(k)} \boldsymbol{e}^{(k)} \boldsymbol{s} \Big] \mathrm{d}z. \quad \text{(A.8q)}$$

The potential of the Lagrange multipliers is given by,

$$\delta\Pi_{\mathcal{L}} = \int \left(N_{,x} + \hat{T}_t - \hat{T}_b\right)\delta u_0 \mathrm{d}x - \int u_{0,x}\delta N \mathrm{d}x + u_0 \delta N|_{C_1} + \\ \int \left(M_{,xx} + z_{N_l}\hat{T}_{t,x} - z_0\hat{T}_{b,x} + \hat{P}_t - \hat{P}_b\right)\delta w_0 \mathrm{d}x + \int w_{0,xx}\delta M \mathrm{d}x + w_0 \delta M_{,x}|_{C_1} - w_{0,x}\delta M|_{C_1} \tag{A.9}$$

Finally, the potential of the work done by the applied loads on the boundary is,

$$\delta\Pi_{\Gamma} = -\left\{\begin{bmatrix}\delta\mathcal{F}^{g^\top} & \delta F_{\phi,x} & \delta F_\phi\end{bmatrix}\begin{pmatrix}\hat{\mathcal{U}}^g \\ 0 \\ \hat{\psi}\end{pmatrix} + \delta Q \hat{w}_0\right\}\Bigg|_{C_1} \\ - \left\{\begin{bmatrix}\delta\mathcal{U}^g & \delta\psi\end{bmatrix}\begin{pmatrix}\mathcal{F}^g - \hat{\mathcal{F}}^g \\ F_\phi - \hat{F}_\phi\end{pmatrix} + \delta w_0\left(Q - \hat{Q}\right)\right\}\Bigg|_{C_2}$$

$$\begin{aligned}\delta\Pi_{\Gamma} &= -\left\{\delta\mathcal{F}^\top\hat{\mathcal{U}}_{bc} + \delta M_{,x}\hat{w}_0\right\}\Big|_{C_1} - \left\{\delta\mathcal{U}^\top\left(\mathcal{F}^* - \hat{\mathcal{F}}^*\right) + \delta w_0\left(Q - \hat{Q}\right)\right\}\Big|_{C_2} \\ &= -\left\{\delta\mathcal{F}^\top\hat{\mathcal{U}}_{bc} + \delta\mathcal{F}_{,x}^\top\hat{\mathcal{W}}\right\}\Big|_{C_1} - \left\{\delta\mathcal{U}^\top\left(\mathcal{F}^* - \hat{\mathcal{F}}^*\right) + \delta w_0\left(Q - \hat{Q}\right)\right\}\Big|_{C_2}.\end{aligned} \tag{A.10}$$

The integral expressions in equations (A.2), (A.4), (A.7), (A.9) and (A.10) combine to form the governing field equations (4.58), whereas the terms evaluated on C_1 and C_2 combine to form the governing boundary equations (4.59). These equations feature three column vectors $\mathbf{\Lambda}_{eq}, \mathbf{\Lambda}_{bc1}, \mathbf{\Lambda}_{bc2}$ that include the Lagrange multipliers u_0, w_0 and their derivatives. These are given by,

$$\mathbf{\Lambda}_{eq} = \begin{pmatrix}-u_{0,x} \\ w_{0,xx} \\ 0 \\ \vdots\end{pmatrix}, \ \mathbf{\Lambda}_{bc1} = \begin{pmatrix}u_0 \\ -w_{0,x} \\ 0 \\ \vdots\end{pmatrix}, \ \mathbf{\Lambda}_{bc2} = \begin{pmatrix}0 \\ w_0 \\ 0 \\ \vdots\end{pmatrix}. \tag{A.11}$$

The boundary displacement $\hat{w}_0$ in Eq. (A.10) is contained in the vector $\hat{\mathcal{W}} = \begin{bmatrix}0 & \hat{w}_0 & 0 & \ldots\end{bmatrix}^\top$.

Appendix B

This appendix supplements Chapter 7. Detailed derivations of the HR plate governing equations and the definitions of pertinent transverse shear correction factors are shown herein.

The HR functional in Eq. (7.60) is split into separate components representing the potential of in-plane stresses Π_σ, transverse shear stresses Π_τ, the potential of the work done on the boundary Π_Γ and the potential of the Lagrange multipliers $\Pi_\mathcal{L}$. Substituting the pertinent expressions for in-plane and transverse shear stresses Eq. (7.24) and Eq. (7.34), respectively, into the functional of Eq. (7.60) yields

$$\delta\Pi(\boldsymbol{u},\mathcal{F}) = \delta\left\{\Pi_\sigma(\mathcal{F}) + \Pi_\tau(\mathcal{F}) + \Pi_\mathcal{L}(\boldsymbol{u},\mathcal{F}) + \Pi_\Gamma(\boldsymbol{u},\mathcal{F})\right\} = 0 \tag{B.12}$$

where

$$\Pi_\sigma = \frac{1}{2}\int_V \sigma^{(k)\top}\bar{\boldsymbol{Q}}^{(k)^{-1}}\sigma^{(k)}\mathrm{d}V = \frac{1}{2}\int_V \left(\bar{\boldsymbol{Q}}^{(k)}\boldsymbol{f}_\epsilon^{(k)}\boldsymbol{s}\mathcal{F}\right)^\top \bar{\boldsymbol{Q}}^{(k)^{-1}}\left(\bar{\boldsymbol{Q}}^{(k)}\boldsymbol{f}_\epsilon^{(k)}\boldsymbol{s}\mathcal{F}\right)\mathrm{d}V \tag{B.13a}$$

$$\Pi_\tau = \frac{1}{2}\int_V \tau^{(k)\top}\boldsymbol{G}^{(k)^{-1}}\tau^{(k)}\mathrm{d}V = \frac{1}{2}\int_V \left\{\boldsymbol{D}^\top\left(\boldsymbol{c}^{(k)}\boldsymbol{s}\mathcal{F}\right) + \hat{T}_b\right\}^\top \boldsymbol{G}^{(k)^{-1}}\left\{\boldsymbol{D}^\top\left(\boldsymbol{c}^{(k)}\boldsymbol{s}\mathcal{F}\right) + \hat{T}_b\right\}\mathrm{d}V \tag{B.13b}$$

$$\Pi_\mathcal{L} = \iint \left\{\begin{bmatrix} u_{x_0} & u_{y_0}\end{bmatrix}\left(\boldsymbol{D}^\top\mathcal{N} + \hat{T}_t - \hat{T}_b\right) + w_0\left(\nabla^\top\mathcal{Q} + \hat{P}_t - \hat{P}_b\right)\right\}\mathrm{d}y\mathrm{d}x \tag{B.13c}$$

$$\Pi_\Gamma = -\int_{S_1}\left(\hat{u}_x t_x + \hat{u}_y t_y + \hat{u}_z t_z\right)\mathrm{d}S - \int_{S_2}\left\{u_x\left(t_x - \hat{t}_x\right) + u_y\left(t_y - \hat{t}_y\right) + u_z\left(t_z - \hat{t}_z\right)\right\}\mathrm{d}S. \tag{B.13d}$$

Performing the variations on the functionals in Eqs. (B.13a)-(B.13d) following the rules of the calculus of variations results in the following expressions. For the potential of in-plane stresses,

$$\begin{aligned}\delta\Pi_\sigma &= \delta\left\{\frac{1}{2}\iint \mathcal{F}^\top\boldsymbol{s}^\top\left(\int \boldsymbol{f}_\epsilon^{(k)\top}\bar{\boldsymbol{Q}}^{(k)}\boldsymbol{f}_\epsilon^{(k)}\mathrm{d}z\right)\boldsymbol{s}\mathcal{F}\mathrm{d}y\mathrm{d}x\right\}\\ &= \delta\left\{\frac{1}{2}\iint \mathcal{F}^\top\boldsymbol{s}^\top\boldsymbol{S}\boldsymbol{s}\mathcal{F}\mathrm{d}y\mathrm{d}x\right\} = \delta\left\{\frac{1}{2}\iint \mathcal{F}^\top\boldsymbol{s}^\top\mathcal{F}\mathrm{d}y\mathrm{d}x\right\} = \iint \mathcal{F}^\top\boldsymbol{s}^\top\delta\mathcal{F}\mathrm{d}y\mathrm{d}x.\end{aligned} \tag{B.14}$$

For the potential of transverse shear stresses with $\boldsymbol{q}^{(k)} = \boldsymbol{G}^{(k)^{-1}}$

$$\begin{aligned}\Pi_\tau &= \frac{1}{2}\int_V \left\{\boldsymbol{D}^\top\left(\boldsymbol{c}^{(k)}\boldsymbol{s}\mathcal{F}\right) + \hat{T}_b\right\}^\top \boldsymbol{q}^{(k)}\left\{\boldsymbol{D}^\top\left(\boldsymbol{c}^{(k)}\boldsymbol{s}\mathcal{F}\right) + \hat{T}_b\right\}\mathrm{d}V\\ \delta\Pi_\tau &= \int_V \left\{\boldsymbol{D}^\top\left(\boldsymbol{c}^{(k)}\boldsymbol{s}\mathcal{F}\right) + \hat{T}_b\right\}^\top \boldsymbol{q}^{(k)}\left\{\boldsymbol{D}^\top\left(\boldsymbol{c}^{(k)}\boldsymbol{s}\delta\mathcal{F}\right)\right\}\mathrm{d}V.\end{aligned} \tag{B.15}$$

By using the alternative definition of $\tau^{(k)}$ in terms of the layerwise constitutive matrices $\boldsymbol{R}^{(k)}$, $\boldsymbol{R}_x^{(k)}$ and $\boldsymbol{R}_y^{(k)}$ of Eq. (7.37), i.e.

$$\tau^{(k)} = \left(\boldsymbol{D}^\top\boldsymbol{R}^{(k)}\right)\mathcal{F} + \boldsymbol{R}_x^{(k)}\frac{\partial\mathcal{F}}{\partial x} + \boldsymbol{R}_y^{(k)}\frac{\partial\mathcal{F}}{\partial y} + \hat{T}_b, \tag{B.16}$$

the variation of the transverse shear functional in Eq. (B.15) now reads

$$\delta\Pi_\tau = \int_V \left[\tau^{(k)\top} \boldsymbol{q}^{(k)} \left\{ \left(\boldsymbol{D}^\top \boldsymbol{R}^{(k)} \right) \delta\mathcal{F} + \boldsymbol{R}_x^{(k)} \delta \frac{\partial \mathcal{F}}{\partial x} + \boldsymbol{R}_y^{(k)} \delta \frac{\partial \mathcal{F}}{\partial y} \right\} \right] \mathrm{d}V. \tag{B.17}$$

Expanding Eq. (B.17) and collecting common terms of $\delta\mathcal{F}$ results in

$$\delta\Pi_\tau = \int_V \left[\tau^{(k)\top} \boldsymbol{q}^{(k)} \left(\boldsymbol{D}^\top \boldsymbol{R}^{(k)} \right) \delta\mathcal{F} + \tau^{(k)\top} \boldsymbol{q}^{(k)} \boldsymbol{R}_x^{(k)} \delta \frac{\partial \mathcal{F}}{\partial x} + \tau^{(k)\top} \boldsymbol{q}^{(k)} \boldsymbol{R}_y^{(k)} \delta \frac{\partial \mathcal{F}}{\partial y} \right] \mathrm{d}V. \tag{B.18}$$

Next, by performing integration by parts on the terms $\delta \dfrac{\partial \mathcal{F}}{\partial x}$ and $\delta \dfrac{\partial \mathcal{F}}{\partial y}$ in Eq. (B.18),

$$\begin{aligned} \delta\Pi_\tau = & \int_V \left[\tau^{(k)\top} \boldsymbol{q}^{(k)} \left(\boldsymbol{D}^\top \boldsymbol{R}^{(k)} \right) - \frac{\partial}{\partial x} \left\{ \tau^{(k)\top} \boldsymbol{q}^{(k)} \boldsymbol{R}_x^{(k)} \right\} - \frac{\partial}{\partial y} \left\{ \tau^{(k)\top} \boldsymbol{q}^{(k)} \boldsymbol{R}_y^{(k)} \right\} \right] \delta\mathcal{F} \mathrm{d}V \\ & + \int_{S_1} \left[n_x \left\{ \tau^{(k)\top} \boldsymbol{q}^{(k)} \boldsymbol{R}_x^{(k)} \right\} + n_y \left\{ \tau^{(k)\top} \boldsymbol{q}^{(k)} \boldsymbol{R}_y^{(k)} \right\} \right] \delta\mathcal{F} \mathrm{d}S \end{aligned} \tag{B.19}$$

where n_x and n_y are the (x, y) components of the normal vector $\boldsymbol{n}$ to the boundary surface S. Thus, Eq. (B.19) shows that the variation of the transverse shear stresses is a function of the transverse shear stresses themselves multiplied by the layerwise constitutive matrices $\boldsymbol{R}^{(k)}$, $\boldsymbol{R}_x^{(k)}$ and $\boldsymbol{R}_y^{(k)}$ and their in-plane derivatives.

The boundary integral in Eq. (B.19) is simplified further by combining the normal vector components n_x and n_y into a single matrix term, such that the constitutive $\boldsymbol{R}_x^{(k)}$ and $\boldsymbol{R}_y^{(k)}$ matrices can be combined back into $\boldsymbol{R}^{(k)}$. Hence,

$$\int_{S_1} \left[\tau^{(k)\top} \boldsymbol{q}^{(k)} \left\{ n_x \boldsymbol{R}_x^{(k)} + n_y \boldsymbol{R}_y^{(k)} \right\} \right] \delta\mathcal{F} \mathrm{d}S = \int_{S_1} \left[\tau^{(k)\top} \boldsymbol{q}^{(k)} \boldsymbol{n}_D \boldsymbol{R}^{(k)} \right] \delta\mathcal{F} \mathrm{d}S \tag{B.20}$$

where

$$\boldsymbol{n}_D = n_x \boldsymbol{I}_x + n_y \boldsymbol{I}_y = \begin{bmatrix} n_x & 0 & n_y \\ 0 & n_y & n_x \end{bmatrix}. \tag{B.21}$$

In the boundary integral of Eq. (B.20) the virtual stress resultants in the column vector $\delta\mathcal{F}$ are defined in a global (x, y) reference system. For example, the first six terms of $\mathcal{F}$ are the classical membrane forces $\mathcal{N} = (N_x, N_y, N_{xy})$ and bending moments $\mathcal{M} = (M_x, M_y, M_{xy})$. In order to transform the stress resultants in $\mathcal{F}$ from the global coordinate system (x, y, z) to the local normal-tangential coordinate system (n, s, z) of the boundary surface, the transformation matrix $\boldsymbol{T}$ is applied,

$$\begin{Bmatrix} F_x \\ F_y \\ F_{xy} \end{Bmatrix} = \boldsymbol{T} \begin{Bmatrix} F_n \\ F_s \\ F_{ns} \end{Bmatrix} \quad \text{where} \quad \boldsymbol{T} = \begin{bmatrix} n_x^2 & n_y^2 & -2n_x n_y \\ n_y^2 & n_x^2 & 2n_x n_y \\ n_x n_y & -n_x n_y & n_x^2 - n_y^2 \end{bmatrix}. \tag{B.22}$$

After converting all stress resultants to the local normal-tangential coordinate system (n, s, z), the orthogonality condition of n and s is used to conclude that the stress resultants F_s can do no work normal to the boundary surface. Thus, the second column of $\boldsymbol{T}$ can be disregarded in

the stress resultant transformation of δF, such that

$$\boldsymbol{T}_n = \begin{bmatrix} n_x^2 & -2n_x n_y \\ n_y^2 & 2n_x n_y \\ n_x n_y & n_x^2 - n_y^2 \end{bmatrix}. \tag{B.23}$$

The complete column vector of all stress resultants $\mathcal{F} = (N_x, N_y, N_{xy}, M_x, M_y, M_{xy}, \dots)$ is transformed into the boundary stress resultant $\mathcal{F}_{bc} = (N_n, N_{ns}, M_n, M_{ns}, \dots)$ as follows

$$\mathcal{F} = \boldsymbol{T}_{bc}\mathcal{F}_{bc} \quad \text{where} \quad \boldsymbol{T}_{bc} = \boldsymbol{I}_{\mathcal{O}} \otimes \boldsymbol{T}_n \tag{B.24}$$

where $\otimes$ is the Kronecker matrix product[1] and $\boldsymbol{I}_{\mathcal{O}}$ is the $\mathcal{O}\times\mathcal{O}$ identity matrix. Thus, Eq. (B.19) is rewritten to accommodate the new boundary integral,

$$\begin{aligned}\delta\Pi_\tau = &\int_V \left[\tau^{(k)\top}\boldsymbol{q}^{(k)}\left(\boldsymbol{D}^\top\boldsymbol{R}^{(k)}\right) - \frac{\partial}{\partial x}\left\{\tau^{(k)\top}\boldsymbol{q}^{(k)}\boldsymbol{R}_x^{(k)}\right\} - \frac{\partial}{\partial y}\left\{\tau^{(k)\top}\boldsymbol{q}^{(k)}\boldsymbol{R}_y^{(k)}\right\}\right]\delta\mathcal{F}\mathrm{d}V + \\ &\int_{S_1}\left[\tau^{(k)\top}\boldsymbol{q}^{(k)}\boldsymbol{n}_D\boldsymbol{R}^{(k)}\boldsymbol{T}_{bc}\right]\delta\mathcal{F}_{bc}\mathrm{d}S.\end{aligned} \tag{B.25}$$

Finally, all that is left is to expand the derivatives in Eq. (B.25) using the differential product rule and integrate in the z-direction to collapse the terms onto an equivalent single layer. Thus, by defining pertinent shear correction matrices in the final z-wise integration step, we arrive at

$$\begin{aligned}\delta\Pi_\tau = \iint &\left[\boldsymbol{\eta}\mathcal{F} + \boldsymbol{\eta}_x\frac{\partial\mathcal{F}}{\partial x} + \boldsymbol{\eta}_y\frac{\partial\mathcal{F}}{\partial y} + \boldsymbol{\eta}_{xx}\frac{\partial^2\mathcal{F}}{\partial x^2} + \boldsymbol{\eta}_{xy}\frac{\partial^2\mathcal{F}}{\partial x\partial y} + \boldsymbol{\eta}_{yy}\frac{\partial^2\mathcal{F}}{\partial^2 y} + \boldsymbol{\chi}\hat{T}_b + \boldsymbol{\chi}_x\frac{\partial\hat{T}_b}{\partial x}\right. \\ &\left.+\boldsymbol{\chi}_y\frac{\partial\hat{T}_b}{\partial y}\right]^\top\delta\mathcal{F}\mathrm{d}y\mathrm{d}x + \int_{C_1}\left[\boldsymbol{\eta}^{bc}\mathcal{F} + \boldsymbol{\eta}_x^{bc}\frac{\partial\mathcal{F}}{\partial x} + \boldsymbol{\eta}_y^{bc}\frac{\partial\mathcal{F}}{\partial y} + \boldsymbol{\chi}^{bc}\hat{T}_b\right]^\top\delta\mathcal{F}_{bc}\mathrm{d}s\end{aligned} \tag{B.26}$$

where all $\boldsymbol{\eta}_\alpha$ are $\mathcal{O}\times\mathcal{O}$ matrices of shear coefficients that automatically include pertinent shear correction factors. The $\mathcal{O}\times 2$ matrices $\boldsymbol{\chi}_\alpha$ are correction factors that enforce transverse shearing effects of the surface shear tractions. In each case the additional superscript bc refers to coefficients used in the boundary conditions. The size of these matrices depends on the chosen order of the model $\mathcal{O}$. For example, a first-order shear theory has $\mathcal{O} = 6$ with membrane forces $\mathcal{N}$ and bending moments $\mathcal{M}$, i.e. $\mathcal{F} = (N_x, N_y, N_{xy}, M_x, M_y, M_{xy})$.

The transposes of the shear correction matrices $\boldsymbol{\eta}_\alpha^\top$ and $\boldsymbol{\chi}_\alpha^\top$ in the double integral are

$$\begin{aligned}\boldsymbol{\eta}^\top = \sum_{k=1}^{N_l}\int_{z_{k-1}}^{z_k}&\left[\left(\boldsymbol{D}^\top\boldsymbol{R}^{(k)}\right)^\top\left\{\boldsymbol{q}^{(k)}\left(\boldsymbol{D}^\top\boldsymbol{R}^{(k)}\right) - \frac{\partial}{\partial x}\left(\boldsymbol{q}^{(k)}\boldsymbol{R}_x^{(k)}\right) - \frac{\partial}{\partial y}\left(\boldsymbol{q}^{(k)}\boldsymbol{R}_y^{(k)}\right)\right\}\right. \\ &\left.-\frac{\partial}{\partial x}\left(\boldsymbol{D}^\top\boldsymbol{R}^{(k)}\right)^\top\boldsymbol{q}^{(k)}\boldsymbol{R}_x^{(k)} - \frac{\partial}{\partial y}\left(\boldsymbol{D}^\top\boldsymbol{R}^{(k)}\right)^\top\boldsymbol{q}^{(k)}\boldsymbol{R}_y^{(k)}\right]\mathrm{d}z\end{aligned} \tag{B.27a}$$

$$\boldsymbol{\eta}_x^\top = \sum_{k=1}^{N_l}\int_{z_{k-1}}^{z_k}\left[\boldsymbol{R}_x^{(k)\top}\left\{\boldsymbol{q}^{(k)}\left(\boldsymbol{D}^\top\boldsymbol{R}^{(k)}\right) - \frac{\partial}{\partial x}\left(\boldsymbol{q}^{(k)}\boldsymbol{R}_x^{(k)}\right) - \frac{\partial}{\partial y}\left(\boldsymbol{q}^{(k)}\boldsymbol{R}_y^{(k)}\right)\right\}\right.$$

[1] Defined on page 168.

$$- \left(\boldsymbol{D}^\top \boldsymbol{R}^{(k)}\right)^\top \boldsymbol{q}^{(k)} \boldsymbol{R}_x^{(k)} - \frac{\partial \boldsymbol{R}_x^{(k)^\top}}{\partial x} \boldsymbol{q}^{(k)} \boldsymbol{R}_x^{(k)} - \frac{\partial \boldsymbol{R}_x^{(k)^\top}}{\partial y} \boldsymbol{q}^{(k)} \boldsymbol{R}_y^{(k)} \Bigg] \mathrm{d}z \quad \text{(B.27b)}$$

$$\boldsymbol{\eta}_y^\top = \sum_{k=1}^{N_l} \int_{z_{k-1}}^{z_k} \Bigg[\boldsymbol{R}_y^{(k)^\top} \left\{ \boldsymbol{q}^{(k)} \left(\boldsymbol{D}^\top \boldsymbol{R}^{(k)}\right) - \frac{\partial}{\partial x}\left(\boldsymbol{q}^{(k)} \boldsymbol{R}_x^{(k)}\right) - \frac{\partial}{\partial y}\left(\boldsymbol{q}^{(k)} \boldsymbol{R}_y^{(k)}\right) \right\}$$
$$- \left(\boldsymbol{D}^\top \boldsymbol{R}^{(k)}\right)^\top \boldsymbol{q}^{(k)} \boldsymbol{R}_y^{(k)} - \frac{\partial \boldsymbol{R}_y^{(k)^\top}}{\partial x} \boldsymbol{q}^{(k)} \boldsymbol{R}_x^{(k)} - \frac{\partial \boldsymbol{R}_y^{(k)^\top}}{\partial y} \boldsymbol{q}^{(k)} \boldsymbol{R}_y^{(k)} \Bigg] \mathrm{d}z \quad \text{(B.27c)}$$

$$\boldsymbol{\eta}_{xx}^\top = -\sum_{k=1}^{N_l} \int_{z_{k-1}}^{z_k} \boldsymbol{R}_x^{(k)^\top} \boldsymbol{q}^{(k)} \boldsymbol{R}_x^{(k)} \mathrm{d}z \quad \text{(B.27d)}$$

$$\boldsymbol{\eta}_{yy}^\top = -\sum_{k=1}^{N_l} \int_{z_{k-1}}^{z_k} \boldsymbol{R}_y^{(k)^\top} \boldsymbol{q}^{(k)} \boldsymbol{R}_y^{(k)} \mathrm{d}z \quad \text{(B.27e)}$$

$$\boldsymbol{\eta}_{xy}^\top = -\sum_{k=1}^{N_l} \int_{z_{k-1}}^{z_k} \left[\boldsymbol{R}_x^{(k)^\top} \boldsymbol{q}^{(k)} \boldsymbol{R}_y^{(k)} + \boldsymbol{R}_y^{(k)^\top} \boldsymbol{q}^{(k)} \boldsymbol{R}_x^{(k)} \right] \mathrm{d}z \quad \text{(B.27f)}$$

$$\boldsymbol{\chi}^\top = \sum_{k=1}^{N_l} \int_{z_{k-1}}^{z_k} \left[\boldsymbol{q}^{(k)} \left(\boldsymbol{D}^\top \boldsymbol{R}^{(k)}\right) - \frac{\partial}{\partial x}\left(\boldsymbol{q}^{(k)} \boldsymbol{R}_x^{(k)}\right) - \frac{\partial}{\partial y}\left(\boldsymbol{q}^{(k)} \boldsymbol{R}_y^{(k)}\right) \right] \mathrm{d}z \quad \text{(B.27g)}$$

$$\boldsymbol{\chi}_x^\top = -\sum_{k=1}^{N_l} \int_{z_{k-1}}^{z_k} \boldsymbol{q}^{(k)} \boldsymbol{R}_x^{(k)} \mathrm{d}z \quad \text{(B.27h)}$$

$$\boldsymbol{\chi}_y^\top = -\sum_{k=1}^{N_l} \int_{z_{k-1}}^{z_k} \boldsymbol{q}^{(k)} \boldsymbol{R}_y^{(k)} \mathrm{d}z \quad \text{(B.27i)}$$

and in the boundary integral $\boldsymbol{\eta}_\alpha^{bc^\top}$ and $\boldsymbol{\chi}^{bc^\top}$ are given by

$$\boldsymbol{\eta}^{bc^\top} = \sum_{k=1}^{N_l} \int_{z_{k-1}}^{z_k} \left(\boldsymbol{D}^\top \boldsymbol{R}^{(k)}\right)^\top \boldsymbol{q}^{(k)} \boldsymbol{n}_D \boldsymbol{R}^{(k)} \boldsymbol{T}_{bc} \mathrm{d}z \quad \text{(B.28a)}$$

$$\boldsymbol{\eta}_x^{bc^\top} = \sum_{k=1}^{N_l} \int_{z_{k-1}}^{z_k} \boldsymbol{R}_x^{(k)^\top} \boldsymbol{q}^{(k)} \boldsymbol{n}_D \boldsymbol{R}^{(k)} \boldsymbol{T}_{bc} \mathrm{d}z \quad \text{(B.28b)}$$

$$\boldsymbol{\eta}_y^{bc^\top} = \sum_{k=1}^{N_l} \int_{z_{k-1}}^{z_k} \boldsymbol{R}_y^{(k)^\top} \boldsymbol{q}^{(k)} \boldsymbol{n}_D \boldsymbol{R}^{(k)} \boldsymbol{T}_{bc} \mathrm{d}z \quad \text{(B.28c)}$$

$$\boldsymbol{\chi}^{bc^\top} = \sum_{k=1}^{N_l} \int_{z_{k-1}}^{z_k} \boldsymbol{q}^{(k)} \boldsymbol{n}_D \boldsymbol{R}^{(k)} \boldsymbol{T}_{bc} \mathrm{d}z. \quad \text{(B.28d)}$$

The expressions in Eq. (B.27) and (B.28) above are valid for any multilayered plate comprised of linear elastic anisotropic laminae. Thus, the expressions are applicable to straight-fibre and tow-steered composites, as well as for isotropic single-layer plates or multilayered ceramic structures, such as laminated glass. For plates with material properties invariant of the planar (x, y) directions, the expressions in Eq. (B.27) and (B.28) simplify considerably as any terms involving $\boldsymbol{D}^\top, \partial/\partial x, \partial/\partial y$ vanish. Thus, for straight-fibre laminates $\boldsymbol{\eta}^\top = \boldsymbol{\eta}_x^\top = \boldsymbol{\eta}_y^\top = \boldsymbol{\chi}^\top = \boldsymbol{\eta}^{bc^\top} = \boldsymbol{0}$.

The potential of the Lagrange multipliers Eq. (B.13c) is given by

$$\Pi_{\mathcal{L}} = \iint \left\{ \begin{bmatrix} u_{x_0} & u_{y_0} \end{bmatrix} \left(\boldsymbol{D}^\top \mathcal{N} + \hat{T}_t - \hat{T}_b \right) + w_0 \left(\nabla^\top \mathcal{Q} + \hat{P}_t - \hat{P}_b \right) \right\} \mathrm{d}y\mathrm{d}x. \tag{B.29}$$

An expression for the transverse shear stress resultants $\mathcal{Q} = (Q_{xz}, Q_{yz})$ in terms of bending moments $\mathcal{M}$ is found by using the bending moment equilibrium from Cauchy's in-plane equilibrium equations. Hence,

$$\int_{-t/2}^{t/2} z \left(\boldsymbol{D}^\top \sigma^{(k)} + \frac{\partial \tau^{(k)}}{\partial z} \right) \mathrm{d}z = \boldsymbol{D}^\top \mathcal{M} + \int_{-t/2}^{t/2} z \frac{\partial \tau^{(k)}}{\partial z} \mathrm{d}z = \boldsymbol{0}$$

and through integration by parts,

$$\begin{aligned} \boldsymbol{D}^\top \mathcal{M} + \left[z\tau^{(k)} \right]_{z_0}^{z_{N_l}} - \int_{-t/2}^{t/2} \tau^{(k)} \mathrm{d}z &= \boldsymbol{D}^\top \mathcal{M} + \left[z_{N_l} \tau^{(N_l)}(z_{N_l}) - z_0 \tau^{(1)}(z_0) \right] - \mathcal{Q} = \boldsymbol{0} \\ \therefore \mathcal{Q} &= \boldsymbol{D}^\top \mathcal{M} + \left(z_{N_l} \hat{T}_t - z_0 \hat{T}_b \right). \end{aligned} \tag{B.30}$$

Note, that Eq. (B.30) is the expression seen in the third and fourth equations of Eq. (7.52). Substituting the expression for $\mathcal{Q}$ from Eq. (B.30) into Eq. (B.29) results in

$$\begin{aligned} \Pi_{\mathcal{L}} = \iint \begin{bmatrix} u_{x_0} & u_{y_0} \end{bmatrix} \left(\boldsymbol{D}^\top \mathcal{N} + \hat{T}_t - \hat{T}_b \right) \mathrm{d}y\mathrm{d}x + \\ \iint w_0 \left(\nabla^\top \boldsymbol{D}^\top \mathcal{M} + \nabla^\top \left(z_{N_l} \hat{T}_t - z_0 \hat{T}_b \right) + \hat{P}_t - \hat{P}_b \right) \mathrm{d}y\mathrm{d}x. \end{aligned} \tag{B.31}$$

Now, taking the first variation of Eq. (B.31),

$$\begin{aligned} \delta\Pi_{\mathcal{L}} = \iint \left\{ \begin{bmatrix} \delta u_{x_0} & \delta u_{y_0} \end{bmatrix} \left(\boldsymbol{D}^\top \mathcal{N} + \hat{T}_t - \hat{T}_b \right) + \begin{bmatrix} u_{x_0} & u_{y_0} \end{bmatrix} \left(\boldsymbol{D}^\top \delta\mathcal{N} \right) \right\} \mathrm{d}y\mathrm{d}x + \\ \iint \left\{ \delta w_0 \left(\nabla^\top \boldsymbol{D}^\top \mathcal{M} + \nabla^\top \left(z_{N_l} \hat{T}_t - z_0 \hat{T}_b \right) + \hat{P}_t - \hat{P}_b \right) + w_0 \left(\nabla^\top \boldsymbol{D}^\top \delta\mathcal{M} \right) \right\} \mathrm{d}y\mathrm{d}x \end{aligned} \tag{B.32}$$

and then integrating the expressions involving derivatives of $\delta\mathcal{N}$ and $\delta\mathcal{M}$ by parts we have

$$\begin{aligned} \delta\Pi_{\mathcal{L}} = \iint \left\{ \begin{bmatrix} \delta u_{x_0} & \delta u_{y_0} \end{bmatrix} \left(\boldsymbol{D}^\top \mathcal{N} + \hat{T}_t - \hat{T}_b \right) - \left(\boldsymbol{D} \begin{Bmatrix} u_{x_0} \\ u_{y_0} \end{Bmatrix} \right)^\top \delta\mathcal{N} \right\} \mathrm{d}y\mathrm{d}x + \\ \iint \left\{ \delta w_0 \left(\nabla^\top \boldsymbol{D}^\top \mathcal{M} + \nabla^\top \left(z_{N_l} \hat{T}_t - z_0 \hat{T}_b \right) + \hat{P}_t - \hat{P}_b \right) + \left(\nabla^\top \boldsymbol{D}^\top w_0 \right) \delta\mathcal{M} \right\} \mathrm{d}y\mathrm{d}x + \\ \int_{C_1} \begin{bmatrix} u_{n_0} & u_{s_0} \end{bmatrix} \delta\mathcal{N}_{bc} \mathrm{d}s - \int_{C_1} \left(\nabla_{ns} w_0 \right)^\top \delta\mathcal{M}_{bc} \mathrm{d}s + \int_{C_1} w_0 \delta Q_{nz} \mathrm{d}s \end{aligned} \tag{B.33}$$

where $\nabla_{ns} = \left(\frac{\partial}{\partial n}, \frac{\partial}{\partial s} \right)$, $\mathcal{N}_{bc} = (N_n, N_{ns})$, $\mathcal{M}_{bc} = (M_n, M_{ns})$, Q_{nz} is the transverse shear force acting on the normal boundary surface, and two new variables $u_{n_0} = n_x u_{x_0} + n_y u_{y_0}$ and $u_{s_0} = -n_y u_{x_0} + n_x u_{y_0}$ have been introduced to capture the displacement Lagrange multipliers

on the boundary. In general, this transformation follows the rule

$$\begin{Bmatrix} \hat{e}_x \\ \hat{e}_y \end{Bmatrix} = \begin{bmatrix} n_x & -n_y \\ n_y & n_x \end{bmatrix} \begin{Bmatrix} \hat{e}_n \\ \hat{e}_s \end{Bmatrix} \tag{B.34}$$

where $\hat{\boldsymbol{e}}$ is a unit vector.

Finally, the first variation of the work done on the boundary surface S of Eq. (B.13d) has to be evaluated. Thus,

$$\delta\Pi_\Gamma = -\int_{S_1} (\hat{u}_x \delta t_x + \hat{u}_y \delta t_y + \hat{u}_z \delta t_z)\, \mathrm{d}S - \int_{S_2} \left\{ \delta u_x \left(t_x - \hat{t}_x\right) + \delta u_y \left(t_y - \hat{t}_y\right) + \delta u_z \left(t_z - \hat{t}_z\right) \right\} \mathrm{d}S. \tag{B.35}$$

When the displacements are transformed from $(\hat{u}_x, \hat{u}_y, \hat{u}_z)$ to $(\hat{u}_n, \hat{u}_s, \hat{u}_z)$ and tractions transfomed from $(t_x, t_y, t_z) = (\sigma_{nx}, \sigma_{ny}, \sigma_{nz})$ to $(t_n, t_s, t_z) = (\sigma_{nn}, \sigma_{ns}, \sigma_{nz})$ using Eq. (B.34), the first variation of the work done on the boundary surface Eq. (B.35) reads

$$\delta\Pi_\Gamma = -\int_{S_1} (\hat{u}_n \delta t_n + \hat{u}_s \delta t_s + \hat{u}_z \delta t_z)\, \mathrm{d}S - \int_{S_2} \left\{ \delta u_n \left(t_n - \hat{t}_n\right) + \delta u_s \left(t_s - \hat{t}_s\right) + \delta u_z \left(t_z - \hat{t}_z\right) \right\} \mathrm{d}S. \tag{B.36}$$

Following the generalised displacement field for u_x and u_y of Eq. (7.1), the normal-tangential displacements u_n and u_s are expanded as follows:

$$u_n^{(k)}(n,s,z) = u_{n_0}(n,s) + z u_{n_1}(n,s) + z^2 u_{n_2}(n,s) + \cdots + \phi_n^{(k)}(n,s,z) u_n^\phi(n,s) \tag{B.37a}$$

$$u_s^{(k)}(n,s,z) = u_{s_0}(n,s) + z u_{s_1}(n,s) + z^2 u_{s_2}(n,s) + \cdots + \phi_s^{(k)}(n,s,z) u_s^\phi(n,s) \tag{B.37b}$$

$$u_z(n,s) = w_0. \tag{B.37c}$$

Writing Eq. (B.37) in a more concise matrix notation we have

$$\mathcal{U}_{ns}^{(k)} = \begin{Bmatrix} u_n^{(k)} \\ u_s^{(k)} \end{Bmatrix} = \begin{bmatrix} \boldsymbol{I}_2 & \boldsymbol{Z}_2 & \boldsymbol{Z}_2^2 & \dots \end{bmatrix} \begin{Bmatrix} \mathcal{U}_{0bc}^g \\ \mathcal{U}_{1bc}^g \\ \mathcal{U}_{2bc}^g \\ \vdots \end{Bmatrix} + \begin{bmatrix} \phi_n^{(k)} & 0 \\ 0 & \phi_s^{(k)} \end{bmatrix} \begin{Bmatrix} u_n^\phi \\ u_s^\phi \end{Bmatrix} \tag{B.38}$$

where $\boldsymbol{I}_2, \boldsymbol{Z}_2, \boldsymbol{Z}_2^2, \dots$ are as previously defined in Eq. (7.6) and

$$\mathcal{U}_{0bc}^g = \begin{bmatrix} u_{n_0} & u_{s_0} \end{bmatrix}^\top,\ \mathcal{U}_{1bc}^g = \begin{bmatrix} u_{n_1} & u_{s_1} \end{bmatrix}^\top,\ \mathcal{U}_{2bc}^g = \begin{bmatrix} u_{n_2} & u_{s_2} \end{bmatrix}^\top,\ \dots \tag{B.39}$$

By defining,

$$\boldsymbol{f}_{ubc}^l = \begin{bmatrix} \phi_n^{(k)} & 0 \\ 0 & \phi_s^{(k)} \end{bmatrix},\ \mathcal{U}_{bc}^g = \begin{bmatrix} \mathcal{U}_{0bc}^g & \mathcal{U}_{1bc}^g & \mathcal{U}_{2bc}^g & \dots \end{bmatrix}^\top,\ \mathcal{U}_{bc}^l = \begin{bmatrix} u_n^\phi & u_s^\phi \end{bmatrix}^\top \tag{B.40}$$

Eq. (B.38) now reads

$$\mathcal{U}_{ns}^{(k)} = \boldsymbol{f}_u^g \mathcal{U}_{bc}^g + \boldsymbol{f}_{ubc}^l \mathcal{U}_{bc}^l = \begin{bmatrix} \boldsymbol{f}_u^g & \boldsymbol{f}_{ubc}^l \end{bmatrix} \begin{Bmatrix} \mathcal{U}_{bc}^g \\ \mathcal{U}_{bc}^l \end{Bmatrix} = \boldsymbol{f}_{ubc}^{(k)} \mathcal{U}_{bc}. \tag{B.41}$$

Substituting Eq. (B.41) into the variation of the work done on the boundary Eq. (B.36) gives

$$\delta\Pi_\Gamma = -\int_{S_1}\left(\begin{bmatrix}\hat{u}_n & \hat{u}_s\end{bmatrix}\begin{Bmatrix}\delta t_n\\ \delta t_s\end{Bmatrix} + \hat{u}_z\delta t_z\right)\mathrm{d}S - \int_{S_2}\left(\begin{bmatrix}\delta u_n & \delta u_s\end{bmatrix}\begin{Bmatrix}t_n-\hat{t}_n\\ t_s-\hat{t}_s\end{Bmatrix} + \delta u_z\left(t_z-\hat{t}_z\right)\right)\mathrm{d}S$$

$$\delta\Pi_\Gamma = -\int_{S_1}\left(\hat{\mathcal{U}}_{bc}^\top \boldsymbol{f}_{ubc}^{(k)\top}\begin{Bmatrix}\delta\sigma_{nn}\\ \delta\sigma_{ns}\end{Bmatrix} + \hat{w}_0\delta\sigma_{nz}\right)\mathrm{d}S - \int_{S_2}\left(\delta\mathcal{U}_{bc}^\top \boldsymbol{f}_{ubc}^{(k)\top}\begin{Bmatrix}\sigma_{nn}-\hat{\sigma}_{nn}\\ \sigma_{ns}-\hat{\sigma}_{ns}\end{Bmatrix} + \delta w_0\left(\sigma_{nz}-\hat{\sigma}_{nz}\right)\right)\mathrm{d}S \quad \text{(B.42)}$$

and finally, by integrating in the z-direction

$$\delta\Pi_\Gamma = -\int_{C_1}\left(\hat{\mathcal{U}}_{bc}^\top\delta\mathcal{F}_{bc}^* + \hat{w}_0\delta Q_{nz}\right)\mathrm{d}s - \int_{C_2}\left[\delta\mathcal{U}_{bc}^\top\left(\mathcal{F}_{bc}^* - \hat{\mathcal{F}}_{bc}^*\right) + \delta w_0\left(Q_{nz}-\hat{Q}_{nz}\right)\right]\mathrm{d}s \quad \text{(B.43)}$$

where C_1 and C_2 are the boundary curves corresponding to the intersections of the reference surface Ω with the boundary surfaces S_1 and S_2, respectively, and Q_{nz} is the transverse shear force normal to the boundary. Furthermore, $\mathcal{F}_{bc}^*$ is the stress resultant vector without the stress resultants associated with $\phi_{,i}^{(k)}$, i.e. $M_x^{\partial\phi}$ and $M_y^{\partial\phi}$, transformed to the local normal-tangential coordinate system (n, s, z) of the boundary curve. Thus, when combining the coefficient of $\delta\mathcal{F}_{bc}^*$, i.e. $\hat{\mathcal{U}}_{bc}^\top$, with the boundary coefficients of $\delta\mathcal{F}_{bc}$ in equation Eq. (B.26), two extra zeros need to be added to the end of vector $\hat{\mathcal{U}}_{bc}^\top$.

The double integral expressions in equations (B.14), (B.26), (B.33) and (B.43) combine to form the governing field equations (7.61), whereas the line integrals combine to form the governing boundary conditions (7.62). These equations feature two column vectors $\mathcal{L}_{eq}$ and $\mathcal{L}_{bc}$ that include the Lagrange multipliers (u_{x_0}, u_{y_0}, w_0) and (u_{n_0}, u_{s_0}, w_0), respectively, and their derivatives. These column vectors are derived from the Lagrange multiplier terms in Eq. (B.33), and are given by

$$\begin{aligned}\mathcal{L}_{eq} &= \left[-\left(\boldsymbol{D}\begin{Bmatrix}u_{x_0}\\ u_{y_0}\end{Bmatrix}\right)^\top \quad \nabla^\top\boldsymbol{D}^\top w_0 \quad 0 \quad \ldots\right]^\top \\ &= \left[-\frac{\partial u_{x_0}}{\partial x} \quad -\frac{\partial u_{y_0}}{\partial y} \quad -\frac{\partial u_{x_0}}{\partial y} - \frac{\partial u_{y_0}}{\partial x} \quad \frac{\partial^2 w_0}{\partial x^2} \quad \frac{\partial^2 w_0}{\partial y^2} \quad 2\frac{\partial^2 w_0}{\partial x\partial y} \quad 0 \quad \ldots\right]^\top \end{aligned} \quad \text{(B.44)}$$

$$\begin{aligned}\mathcal{L}_{bc} &= \left[u_{n_0} \quad u_{s_0} \quad -\left(\nabla_{ns}w_0\right)^\top \quad 0 \quad \ldots\right]^\top \\ &= \left[u_{n_0} \quad u_{s_0} \quad -\frac{\partial w_0}{\partial n} \quad -\frac{\partial w_0}{\partial s} \quad 0 \quad \ldots\right]^\top .\end{aligned} \quad \text{(B.45)}$$

References

[1] M. Darecki, C. Edelstenne, T. Enders, E. Fernandez, P. Hartman, J-P. Herteman, M. Kerkloh, I. King, P. Ky, M. Mathieu, G. Orsi, G. Schotman, C. Smith, and J-D. Woerner. Flightpath 2050 - Europe's vision for aviation. Research report, The High Level Group on Aviation Research - European Commission of the European Union, 2011.

[2] The Boeing Company. 787 Design Highlights - Advanced Composites Use. `http://www.boeing.com/commercial/787/#/design-highlights/visionary-design/composites/advanced-composite-use/`. Accessed: 22-09-2015.

[3] S. Azau and C. Rose. Design limits and solutions for very large wind turbines - A 20 MW turbine is feasible. Research report, The European Wind Energy Association, March 2011.

[4] Lucintel. Opportunities for composites in European automotive market 2013-2018. Research report, Lucintel - Global Management Consulting & Market Research Firm, 2013.

[5] P. Brondstedt, H. Lilholt, and A. Lystrup. Composite materials for wind power turbine blades. *Annual Review of Materials Research*, 35:505–538, 2005.

[6] L. Holloway. A review of the present and future utilisation of FRP composites in the civil infrastructure with reference to their important in-service properties. *Construction and Building Materials*, 24:2419–2445, 2010.

[7] D. Griffin and T. Ashwill. Alternative composite materials for megawatt-scale wind turbine blades: Design considerations and recommended testing. *Journal of Solar Energy Engineering*, 125:515–521, 2003.

[8] JN. Reddy. *Energy and Variational Methods in Applied Mechanics.* John Wiley & Sons, 1st edition, 1984.

[9] K. Washizu. *Variational Methods in Elasticity and Plasticity.* Pergamon Press Ltd., London, UK, 1st edition, 1968.

[10] E. Reissner. On a variational theorem in elasticity. *Journal of Mathematical Physics*, 29:90–95, 1950.

[11] BF. Vebeuke. *Stress Analysis*, chapter Displacement and equilibrium models in the finite element method. Holister GS (eds). Wiley, 1965.

[12] E. Carrera. Theories and finite elements for multilayered, anisotropic, composite plates and shells. *Archives of Computational Methods in Engineering*, 9(2):87–140, 2002.

[13] PC. Ciarlet, L. Trabucho, and JM. Viano. *Asymptotic Methods for Elastic Structures.* Walter de Gruyter & Co., 1995.

[14] W. Yu, VV. Volovoi, DH. Hodges, and X. Hong. Validation of the variational asymptotic beam sectional analysis (VABS). *AIAA Journal*, 40(10):2105–2113, 2002.

[15] G. Kirchhoff. Uber das Gleichgewicht und die Bewegung einer elastischen Scheibe. *Journal fur reine und angewandte Mathematik*, 40:51–88, 1850.

[16] AEH. Love. *The Mathematical Theory of Elasticity.* Cambridge University Press, London, 1934.

[17] RM. Jones. *Mechanics of Composite Materials.* Taylor & Francis Ltd., London, UK, 2nd edition, 1998.

[18] GC. Everstine and AC. Pipkin. Stress channelling in transversely isotropic elastic composites. *Zeitung fuer angewandte Mathematik und Physik*, 22:825–834, 1971.

[19] PM. Weaver. *Mechanical Behaviour of a Novel Three-Dimensional Composite.* PhD thesis, University of Newcastle upon Tyne, 1992.

[20] NJ. Pagano. Exact solutions for composite laminates in cylindrical bending. *Journal of Composite Materials*, 3(3):398–411, 1969.

[21] E. Carrera. Developments, ideas and evaluations based upon Reissner's mixed variational theorem in the modeling of multilayered plates and shells. *Applied Mechanics Reviews*, 54(4):301–329, 2001.

[22] L. Demasi. Partially zig-zag advanced higher order shear deformation theories based on the generalized unified formulation. *Composite Structures*, 94(2):363–375, 2012.

[23] E. Carrera. Theories and finite elements for multilayered plates and shells: A unified compact formulation with numerical assessment and benchmarking. *Archives of Computational Methods in Engineering*, 10(3):5216–5296, 2003.

[24] L. Demasi. ∞^3 hierarchy plate theories for thick and thin composite plates: The generalized unified formulation. *Composite Structures*, 84:256–270, 2008.

[25] S. Timoshenko. *Theory of Elasticity.* McGraw-Hill Book Company, Inc., New York, 1934.

[26] RD. Mindlin. Influence of rotary inertia and shear on flexural motion of isotropic elastic plates. *Journal of Applied Mechanics*, 18:31–38, 1951.

[27] PC. Yang, CH. Norris, and Y. Stavsky. Elastic wave propagation in heterogeneous plates. *International Journal of Solids and Structures*, 2:665–684, 1966.

[28] JM. Whitney and NJ. Pagano. Shear deformation in heterogeneous anisotropic plates. *Journal of Applied Mechanics*, 37:1031–1036, 1970.

[29] J. Prescott. Elastic waves and vibrations in thin rods. *Philosophical Magazine*, 33:703–754, 1942.

[30] G. Cowper. The shear coefficient in Timoshenko's beam theory. *Journal of Applied Mechanics*, 33(5):335–340, 1966.

[31] G. Kennedy, J. Hansen, and J. Martins. A Timoshenko beam theory with pressure corrections for layered orthotropic beams. *International Journal of Solids and Structures*, 48(16–17):2373–2382, 2011.

[32] BF. Vlasov. On the equations of bending of plates. *Dokla. Ak. Nauk. Azerbeijanskoi-SSR*, 3:955–979, 1957.

[33] M. Levinson. A new rectangular beam theory. *Journal of Sound and Vibration*, 74(1):81–87, 1981.

[34] JN. Reddy. A refined nonlinear theory of plates with transverse shear deformation. *International Journal of Solids and Structures*, 20(9):881–896, 1983.

[35] SA. Ambartsumyan. On a general theory of anisotropic shells. *Prikl. Mat. Mekh.*, 22:226–237, 1958.

[36] JN. Reddy. A refined shear deformation theory for the analysis of laminated plates. Contractor Report 3955, National Aeronautics and Space Administration, 1986.

[37] M. Touratier. An efficient standard plate theory. *International Journal of Engineering Science*, 29:901–916, 1991.

[38] KP. Soldatos. A transverse shear deformation theory for homogeneous monoclinic plates. *Acta Mechanica*, 94:195–220, 1992.

[39] M. Karama, KS. Afaq, and S. Mistou. Mechanical behaviour of laminated composite beam by the new multi-layered laminated composite structures model with transverse shear stress continuity. *International Journal of Solids and Structures*, 40:1525–1546, 2003.

[40] E. Reissner. On transverse bending of plates, including the effect of transverse shear deformation. *International Journal of Solids and Structures*, 11:569–573, 1975.

[41] M. Levy. Memoire sur la theorie des plaques elastique planes. *Journal de Mathmatiques Pures et Appliquées*, 30:219–306, 1877.

[42] M. Stein. Nonlinear theory for plates and shells including the effect of transverse shearing. *AIAA Journal*, 24:1537–1544, 1986.

[43] M. Karama, B. Abou Harb, S. Mistou, and S. Caperaa. Bending, buckling and free vibration of laminated composite with a transverse shear stress continuity model. *Composites Part B: Engineering*, 29B:223–234, 1998.

[44] AJM. Ferreira, CMC. Roque, and RMN. Jorge. Analysis of composite plates by trigonometric shear deformation theory and multiquadrics. *Computers & Structures*, 83:2225–2237, 2005.

[45] AMA. Neves, AJM. Ferreira, E. Carrera, M. Cinefra, CMC. Roque, and RMN. Jorge. Free vibration analysis of functionally graded shells by a higher-order shear deformation theory and radial basis functions collocation, accounting for through-the-thickness deformations. *European Journal of Mechanics - A/Solids*, 37:24–34, 2013.

[46] JL. Mantari, AS. Oktem, and C. Guedes Soares. Static and dynamic analysis of laminated composite and sandwich plates and shells by using a new higher-order shear deformation theory. *Composite Structures*, 94:37–49, 2011.

[47] RP. Shimpi. Refined plate theory and its variants. *AIAA Journal*, 40(1):137–146, 2002.

[48] WT. Koiter. A consistent first approximation in the general theory of thin elastic shells. In *Proceedings of the First Symposium on the Theory of Thin Elastic Shells*, pages 12–23, Amsterdam, Netherlands, 1960.

[49] FB. Hildebrand, E. Reissner, and GB. Thomas. Notes on the foundations of the theory of small displacements of orthotropic shells. Technical Note 1833, National Advisory Committee for Aeronautics, 1938.

[50] KH. Lo, RM. Christensen, and EM. Wu. A high-order theory of plate deformation - Part 2: Laminated plates. *Journal of Applied Mechanics*, 44(4):669–676, 1977.

[51] A. Tessler. An improved theory of {1,2}-order for thick composite laminates. *International Journal of Solids and Structures*, 30(7):981–1000, 1993.

[52] G. Cook and A. Tessler. A {3,2}-order bending theory for laminated composite and sandwich beams. *Composites Part B: Engineering*, 29B:565–576, 1998.

[53] A. Barut, E. Madenci, J. Heinrich, and A. Tessler. Analysis of thick sandwich construction by a {3,2}-order theory. *International Journal of Solids and Structures*, 38(34):6063–6067, 2001.

[54] M. Gherlone. On the use of zigzag functions in equivalent single layer theories for laminated composite and sandwich beams: A comparative study and some observations on external weak layers. *Journal of Applied Mechanics*, 80:1–19, 2013.

[55] JM. Whitney. Stress analysis of thick laminated composite and sandwich plates. *Journal of Composite Materials*, 6(4):426–440, 1972.

[56] E. Reissner. On the theory of bending of elastic plates. *Journal of Mathematics and Physics*, 23:184–191, 1944.

[57] E. Reissner. The effect of transverse shear deformation on the bending of elastic plates. *Journal of Applied Mechanics*, 12(30):A69–A77, 1945.

[58] RC. Batra and S. Vidoli. Higher-order piezoelectric plate theory derived from a three-dimensional variational principle. *AIAA Journal*, 40(1):91–104, 2002.

[59] RC. Batra, S. Vidoli, and F. Vestroni. Plane wave solutions and modal analysis in higher order shear and normal deformable plate theories. *Journal of Sound and Vibration*, 257(1):63–88, 2002.

[60] E. Cosentino and PM. Weaver. An enhanced single-layer variational formulation for the effect of transverse shear on laminated orthotropic plates. *European Journal of Mechanics A/Solids*, 29:567–590, 2010.

[61] E. Reissner. On a certain mixed variational theorem and a proposed application. *International Journal for Numerical Methods in Engineering*, 20(7):1366–1368, 1984.

[62] F. Auricchio and E. Sacco. Refined first-order shear deformation theory models for composite laminates. *Journal of Applied Mechanics*, 70(3):381–390, 2003.

[63] E. Carrera. Historical review of zig-zag theories for multilayered plates and shells. *Applied Mechanics Reviews*, 56(3):287–308, 2003.

[64] SG. Lekhnitskii. Strength calculation of composite beams. *Vestn. Inzh. Tekh.*, 9, 1935.

[65] JG. Ren. A new theory of laminated plates. *Composites Science and Technology*, 26:225–239, 1986.

[66] JG. Ren. Bending theory of laminated plates. *Composites Science and Technology*, 27:225–248, 1986.

[67] SA. Ambartsumyan. *Theory of anisotropic plates: strength, stability, vibration.* Technomic Publishing Company, 1970.

[68] JM. Whitney. The effect of transverse shear deformation on the bending of laminated plates. *Journal of Composite Materials*, 3:534–547, 1969.

[69] NJ. Pagano. Exact solutions for rectangular bidirectional composites and sandwich plates. *Journal of Composite Materials*, 4(20):20–34, 1970.

[70] NJ. Pagano. Influence of shear coupling in cylindrical bending of anisotropic laminates. *Journal of Composite Materials*, 4(3):330–343, 1970.

[71] AO. Rasskazov. Theory of multilayer orthotropic shallow shells. *Prikl. Mekh.*, 12:50–76, 1976.

[72] BK. Rath and YC. Das. Vibration of layered shells. *J. Sound Vibration*, 28:737–757, 1973.

[73] M. Di Sciuva. A refinement of the transverse shear deformation theory for multilayered orthotropic plates. *L'aerotecnica missile e spazio*, 62:84–92, 1984.

[74] M. Di Sciuva. Development of an anisotropic, multilayered, shear-deformable rectangular plate element. *Composite Structures*, 21(4):789–796, 1985.

[75] RC. Averill. Static and dynamic response of moderately thick laminated beams with damage. *Composites Engineering*, 4(4):381–395, 1994.

[76] RC. Averill and YC. Yip. Development of simple, robust finite elements based on refined theories for thick laminated beams. *Composite Structures*, 59(3):3529–546, 1996.

[77] A. Tessler, M. Di Sciuva, and M. Gherlone. Refinement of Timoshenko beam theory for composite and sandwich beams using zigzag kinematics. Technical Publication 215086, National Aeronautics and Space Administration, 2007.

[78] A. Tessler, M. Di Sciuva, and M. Gherlone. Refined zigzag theory for laminated composite and sandwich plates. Technical Publication 215561, National Aeronautics and Space Administration, 2009.

[79] A. Tessler, M. Di Sciuva, and M. Gherlone. Refined zigzag theory for homogeneous, laminated composite, and sandwich plates: A homogeneous limit methodology for zigzag function selection. Technical Publication 216214, National Aeronautics and Space Administration, 2010.

[80] A. Tessler, M. Di Sciuva, and M. Gherlone. A consistent refinement of first-order shear deformation theory for laminated composite and sandwich plates using improved zigzag kinematics. *Journal of Mechanics of Materials and Structures*, 5(2):341–367, 2010.

[81] A. Barut, E. Madenci, and A. Tessler. A refined zigzag theory for laminated composite and sandwich plates incorporating thickness stretch deformation. In *Proceedings of the 53rd AIAA/ASME/ASCE/AHS/ASC Structures, Structural Dynamics, and Materials Conference*, Honolulu, Hawaii, USA, 2012.

[82] A. Tessler. Refined zigzag theory for homogeneous, laminated composite, and sandwich beams derived from Reissner's mixed variational principle. *Meccanica*, Advances In The Mechanics Of Composite And Sandwich Structures:1–26, 2015.

[83] L. Iurlaro, M. Gherlone, M. Di Sciuva, and A. Tessler. Refined zigzag theory for laminated composite and sandwich plates derived from Reissner's mixed-variational theorem. *Composite Structures*, 133:809–817, 2015.

[84] M. Di Sciuva, M. Gherlone, L. Iurlaro, and A. Tessler. A class of higher-order C0 composite and sandwich beam elements based on the refined zigzag theory. *Composite Structures*, 132:784–803, 2015.

[85] L. Iurlaro, M. Gherlone, and M. Di Sciuva. The (3,2)-mixed Refined zigzag theory for generally laminated beams: Theoretical development and C0 finite element formulation. *International Journal of Solids and Structures*, 73-74:1–19, 2015.

[86] H. Murakami. Laminated composite plate theory with improved in-plane responses. *Journal of Applied Mechanics*, 53:661–666, 1986.

[87] A. Toledano and H. Murakami. A high-order laminated plate theory with improved in-plane responses. *International Journal of Solids and Structures*, 23(1):111–131, 1986.

[88] S. Brischetto, E. Carrera, and L. Demasi. Free vibration of sandwich plates and shells by using zig-zag function. *Shock and Vibration*, 16:495–503, 2009.

[89] S. Brischetto, E. Carrera, and L. Demasi. Improved bending analysis of sandwich plates using zig-zag functions. *Composite Structures*, 89:408–415, 2009.

[90] E. Carrera, M. Filippi, and E. Zappino. Free vibration analysis of laminated beam by polynomial, trigonometric, exponential and zig-zag theories. *Journal of Composite Materials*, 0(0):1–18, 2013.

[91] E. Carrera, M. Filippi, and E. Zappino. Laminated beam analysis by polynomial, trigonometric, exponential and zig-zag theories. *European Journal of Mechanics A/Solids*, 41:58–69, 2013.

[92] E. Carrera. On the use of the Murakami's zig-zag function in the modeling of layered plates and shells. *Computers & Structures*, 82(7–8):541–554, 2004.

[93] TO. Williams. A generalized, multilength scale framework for thermo-diffusional-mechanically coupled, nonlinear, laminated plate theories with delaminations. *International Journal of Solids and Structures*, 42(5–6):1465–1490, 2005.

[94] TO. Williams. Efficiency and accuracy considerations in a unified plate theory with delamination. *Composite Structures*, 52:27–40, 2001.

[95] TO. Williams. A new theoretical framework for the formulation of general, nonlinear, multiscale plate theories. *International Journal of Solids and Structures*, 45(9):2534–2560, 2008.

[96] E. Carrera and G. Giunta. Refined beam theories based on Carrera's unified formulation. *International Journal of Applied Mechanics*, 2(1):117–143, 2010.

[97] E. Carrera and M. Petrolo. Refined one-dimensional formulations for laminated structure analysis. *AIAA Journal*, 50(1):176–189, 2012.

[98] AAG. Cooper. *Trajectorial fiber reinforcement of composite structures.* PhD thesis, Department of Mechanical and Aerospace Engineering, Washington University, 1972.

[99] MW. Hyer and HH. Lee. The use of curvilinear fiber format to improve buckling resistance of composite plates with central circular holes. *Composite Structures*, 18:239–261, 1991.

[100] MW. Hyer and RF. Charette. The use of curvilinear fiber format in composite structure design. *AIAA Journal*, 29(6):1011–1015, 1991.

[101] Z. Gurdal and R. Olmedo. In-plane response of laminates with spatially varying fiber orientations: Variable stiffness concept. *AIAA Journal*, 31(4):751–758, 1993.

[102] Z. Gurdal, BF. Tatting, and CK. Wu. Variable stiffness composite panels: Effects of stiffness variation on the in-plane and buckling response. *Composites Part A: Applied Science and Manufacturing*, 39:911–922, 2008.

[103] S. Setoodeh, MM. Abdalla, ST. Ijsselmuiden, and Z. Gurdal. Design of variable stiffness composite panels for maximum buckling load. *Composite Structures*, 87:109–117, 2008.

[104] PM. Weaver, KD. Potter, K. Hazra, MAR. Saverymuthapulle, and MT. Hawthorne. Buckling of variable angle tow plates: From concept to experiment. In *Proceedings of the 50th AIAA/ASME/ASCE/AHS/ASC Structures, Structural Dynamics, and Materials Conference*, Palm Springs, California, USA, 2009.

[105] CS. Lopes, Z. Gurdal, and PP. Camanho. Tailoring for strength of composite steered-fibre panels with cutouts. *Composites Part A: Applied Science and Manufacturing*, 41:1760–1767, 2010.

[106] Z. Wu, PM. Weaver, G. Raju, and BC. Kim. Buckling analysis and optimisation of variable angle tow composite plates. *Thin-Walled Structures*, 60:163–172, 2012.

[107] G. Raju, Z. Wu, BC. Kim, and PM. Weaver. Prebuckling and buckling analysis of variable angle tow plates with general boundary conditions. *Composite Structures*, 94(9):2961–2970, 2012.

[108] W. Liu and R. Butler. Buckling optimization of variable-angle-tow panels using the infinite-strip method. *AIAA Journal*, 51:1442–1449, 2013.

[109] G. Raju, Z. Wu, and PM. Weaver. Buckling and postbuckling of variable angle tow composite plates under in-plane shear loading. *International Journal of Solids and Structures*, 58:270–287, 2015.

[110] WM. van den Brink, WJ. Vankan, and R. Maas. Buckling optimized variable stiffness laminates for a composite fuselage window section. In *Proceedings of the 28th International Congress of the Aeronautical Sciences*, Brisbane, Australia, 2012.

[111] A. Alhajahmad, MM. Abdalla, and Z. Gurdal. Optimal design of tow-placed fuselage panels for maximum strength with buckling considerations. *Journal of Aircraft*, 47(3):775–782, 2010.

[112] BH. Coburn, Z. Wu, and PM. Weaver. Buckling analysis of stiffened variable angle tow panels. *Composite Structures*, 111:259–270, 2014.

[113] BH. Coburn, Z. Wu, and PM. Weaver. Buckling analysis and optimization of blade stiffened variable stiffness panels. In *Proceedings of the 56th AIAA/ASME/ASCE/AHS/ASC Structures, Structural Dynamics and Materials Conference*, number 1438, Kissimmee, Florida, USA, 2015.

[114] Z. Wu, G. Raju, and PM. Weaver. Postbuckling analysis of variable angle tow composite plates. *International Journal of Solids and Structures*, 50:1770–1780, 2013.

[115] Z. Wu, PM. Weaver, and G. Raju. Postbuckling optimisation of variable angle tow composite plates. *Composite Structures*, 103:34–42, 2013.

[116] JP. Peterson, P. Seide, and VI. Weingarten. Buckling of thin-walled circular cylinders. Technical Report NASA-SP-8007, NASA, 1968.

[117] SC. White and PM. Weaver. Towards imperfection insensitive buckling response of shell structures shells with plate-like post-buckled responses. In *Proceedings of the 4th Aircraft Structural Design Conference of the Royal Aeronautical Society*, Belfast, UK, 2014.

[118] SC. White and PM. Weaver. Bend-free shells under uniform pressure with variable-angle tow derived anisotropy. *Composite Structures*, 94(11):3207–3214, 2012.

[119] BC. Kim, K. Potter, and PM. Weaver. Continuous tow shearing for manufacturing variable angle tow composites. *Composites Part A: Applied Science and Manufacturing*, 43(8):1347–1356, 2012.

[120] AW. Blom. *Structural performance of fiberplaced variable-stiffness composite conical and cylindrical shells*. PhD thesis, University of Delft, 2010.

[121] A. Beakou, M. Cano, J-B. Le Cam, and V. Verney. Modelling slit tape buckling during automated prepreg manufacturing: A local approach. *Composite Structures*, 93:2628–2635, 2011.

[122] K. Fayazbakhsh, M. Arian Nik, D. Pasini, and L. Lessard. Defect layer method to capture effect of gaps and overlaps in variable stiffness laminates made by Automated Fiber Placement. *Composite Structures*, 97:245–251, 2013.

[123] BC. Kim, PM. Weaver, and K. Potter. Manufacturing characteristics of the continuous tow shearing method for manufacturing of variable angle tow composites. *Composites Part A: Applied Science and Manufacturing*, 61(8):141–151, 2014.

[124] RMJ. Groh and PM. Weaver. Buckling analysis of variable angle tow, variable thickness panels with transverse shear effects. *Composite Structures*, 107:482–493, 2014.

[125] RMJ. Groh and PM. Weaver. Mass optimization of variable angle tow, variable thickness panels with static failure and buckling constraints. In *Proceedings of the 56th AIAA/ASME/ASCE/AHS/ASC Structures, Structural Dynamics and Materials Conference*, Kissimmee, Florida, USA, 2015.

[126] ST. Ijsselmuiden, MM. Abdalla, and Z. Gurdal. Optimization of variable-stiffness panels for maximum buckling load using lamination parameters. *Journal of Aircraft*, 48(1):134–143, 2010.

[127] JMJF. van Campen, C. Kassapoglou, and Z. Gurdal. Generating realistic laminate fiber angle distributions for optimal variable stiffness laminates. *Composites Part B: Engineering*, 43:354–360, 2012.

[128] M. Arian Nik, K. Fayazbakhsh, D. Pasini, and L. Lessard. Surrogate-based multi-objective optimization of a composite laminate with curvilinear fibres. *Composite Structures*, 94:2306–2313, 2012.

[129] M. Arian Nik, K. Fayazbakhsh, D. Pasini, and L. Lessard. Optimization of variable stiffness composites with embedded defects induced by Automated Fiber Placement. *Composite Structures*, 107:160–166, 2014.

[130] G. Raju, S. White, and Z. Wu. Optimal postbuckling design of variable angle tow composites using lamination parameters. In *Proceedings of the 56th AIAA/ASME/ASCE/AHS/ASC Structures, Structural Dynamics and Materials Conference*, Kissimmee, Florida, USA, 2015.

[131] Z. Wu, G. Raju, and PM. Weaver. Framework for the buckling optimization of variable-angle tow composite plates. *AIAA Journal*, Article in Advance:1–17, 2015.

[132] H. Akhavan and P. Ribeiro. Natural modes of vibration of variable stiffness composite laminates with curvilinear fibers. *Composite Structures*, 93:3040–3047, 2011.

[133] H. Akhavan, P. Ribeiro, and MFSF. Moura. Large deflection and stresses in variable stiffness composite laminate with curvilinear fibres. *International Journal of Mechanical Sciences*, 73:14–26, 2013.

[134] H. Akhavan and P. Ribeiro. Non-linear vibrations of variable stiffness composite laminated plates. *Composite Structures*, 94:2424–2432, 2012.

[135] AH. Akbarzadeh, M. Arian Nik, and D. Pasini. The role of shear deformation in laminated plates with curvilinear fiber paths and embedded defects. *Composite Structures*, 118:217–227, 2014.

[136] RMJ. Groh, PM. Weaver, SC. White, G. Raju, and Z. Wu. A 2D equivalent single-layer formulation for the effect of transverse shear on laminated plates with curvilinear fibres. *Composite Structures*, 100:464–478, 2013.

[137] S. Yazdani and P. Ribeiro. A layerwise p-version finite element formulation for free vibration analysis of thick composite laminates with curvilinear fibres. *Composite Structures*, 120:531–542, 2015.

[138] S. Yazdani, P. Ribeiro, and JD. Rodrigues. A p-version layerwise model for large deflection of composite plates with curvilinear fibres. *Composite Structures*, 108:181–190, 2014.

[139] F. Tornabene, N. Fantuzzi, M. Bacciocchi, and E. Viola. Higher-order theories for the free vibrations of doubly-curved laminated panels with curvilinear reinforcing fibers by means of a local version of the GDQ method. *Composites Part B: Engineering*, 81:196–230, 2015.

[140] G. Raju, Z. Wu, and PM. Weaver. Postbuckling analysis of variable angle tow plates using differential quadrature method. *Composite Structures*, 106:74–84, 2013.

[141] SC. White, G. Raju, and PM. Weaver. Initial post-buckling of variable-stiffness curved panels. *Journal of the Mechanics and Physics of Solids*, 71:132–155, 2014.

[142] E. Viola, F. Tornabene, and N. Fantuzzi. General higher-order shear deformation theories for the free vibration analysis of completely doubly-curved laminated shells and panels. *Composite Structures*, 95:639–666, 2013.

[143] F. Tornabene, E. Viola, and N. Fantuzzi. General higher-order equivalent single layer theory for free vibrations of doubly-curved laminated composite shells and panels. *Composite Structures*, 104:94–117, 2013.

[144] E. Viola, F. Tornabene, and N. Fantuzzi. Static analysis of completely doubly-curved laminated shells and panels using general higher-order shear deformation theories. *Composite Structures*, 101:59–93, 2013.

[145] R. Bellman, G. Kashef, and J. Casti. Differential quadrature: A technique for the rapid solution of nonlinear partial differential equations. *Journal of Computational Physics*, 10:40–52, 1972.

[146] C. Shu and BE. Richards. High resolution of natural convection in a square cavity by generalized differential quadrature. In *Proceedings of the 3rd International Conference on Advances in Numerical Methods in Engineering, Theory and Applications*, pages 978–985, Swansea, UK, 1990.

[147] C. Shu and BE. Richards. Application of generalized differential quadrature to solve two-dimensional incompressible Navier-Stokes equations. *International Journal for Numerical Methods in Fluids*, 15:791–798, 1992.

[148] JR. Quan and CT. Chang. New insights in solving distributed system equations by the quadrature method – I. Analysis. *Computers & Chemical Engineering*, 13(7):779–788, 1989.

[149] C. Shu. *Differential Quadrature and its Application in Engineering*. Springer Verlag, 1st edition, 2000.

[150] F. Tornabene, N. Fantuzzi, F. Ubertini, and E. Viola. Strong formulation finite element method based on differential quadrature: A survey. *Applied Mechanics Reviews*, 67:1–55, 2015.

[151] F. Tornabene, N. Fantuzzi, E. Viola, and RC. Batra. Stress and strain recovery for functionally graded free-form and doubly-curved sandwich shells using higher-order equivalent single layer theory. *Composite Structures*, 119:67–89, 2015.

[152] A. Tessler and HR. Riggs. Accurate interlaminar stress recovery from Finite Element Analysis. Technical Memorandum 109149, NASA, 1994.

[153] CW. Bert, SK. Jang, and AG. Striz. Two new approximate methods for analyzing free vibration of structural components. *AIAA Journal*, 26:612–620, 1988.

[154] X. Wang and CW. Bert. A new approach in applying differential quadrature to static and free vibrational analyses of beams and plates. *Journal of Sound and Vibration*, 162(3):566–572, 1993.

[155] M. Malik and CW. Bert. Implementing multiple boundary conditions in the DQ solution of higher-order PDE's: Application to free vibration of plates. *International Journal for Numerical Methods in Engineering*, 39(7):1237–1258, 1996.

[156] C. Shu and H. Du. Implementation of clamped and simply supported boundary conditions in the GDQ free vibration analysis of beams and plates. *International Journal of Solids and Structures*, 34(7):819–835, 1997.

[157] H. Du, MK. Lim, and NR. Lin. Application of generalized differential quadrature method to structural problems. *International Journal for Numerical Methods in Engineering*, 37:1881–1896, 1994.

[158] H. Du, MK. Lim, and NR. Lin. Application of generalized differential quadrature to vibration analysis. *Journal of Sound and Vibration*, 181:279–293, 1995.

[159] C. Shu and H. Du. A generalized approach for implementing general boundary conditions in the GDQ free vibration analysis of plates. *International Journal of Solids and Structures*, 34(7):837–846, 1997.

[160] JN. Reddy. *Mechanics of Laminated Composite Plates and Shells.* CRC Press LLC, Boca Raton, Florida, USA, 2nd edition edition, 2004.

[161] AA. Khdeir, JN. Reddy, and L. Librescu. Analytical solution of a refined shear deformation theory for rectangular composite plates. *International Journal of Solids and Structures*, 23(10):1447–1463, 1986.

[162] F. Yeli and L. Fangyong. An analytical solution of rectangular laminated plates by higher-order theory. *Applied Mathematics and Mechanics*, 19(8):793–806, 1998.

[163] AS. Oktem and RA. Chaudhuri. Fourier solution to a thick cross-ply Levy-type clamped problem. *Composite Structures*, 79:481–492, 2007.

[164] M. Bodaghi and AR. Saidi. Levy-type solution for buckling analysis of thick functionally graded rectangular plates based on the higher-order shear deformation plate theory. *Applied Mathematical Modelling*, 34(11):3659–3673, 1986.

[165] HT. That and SE. Kim. Analytical solution of a two variable refined plate theory for bending analysis of orthotropic Levy-type plates. *International Journal of Mechanical Sciences*, 54:269–276, 2012.

[166] MZ. Hu, H. Kolsky, and AC. Pipkin. Bending theory for fiber-reinforced beams. *Journal of Composite Materials*, 19:235–249, 1985.

[167] RMJ. Groh and PM. Weaver. On displacement-based and mixed-variational equivalent single layer theories for modelling highly heterogeneous laminated beams. *International Journal of Solids and Structures*, 59:147–170, 2015.

[168] A. Toledano and H. Murakami. A composite plate theory for arbitrary laminate configurations. *Journal of Applied Mechanics*, 54(1):181–189, 1987.

[169] E. Carrera. A priori vs. a posteriori evaluation of transverse stresses in multilayered orthotropic plates. *Composite Structures*, 48(4):245–260, 2000.

[170] R. Penrose. A generalised inverse for matrices. In *Proceedings of Cambridge Philosophical Society*, volume 51, pages 406–413, 1955.

[171] K. Levenberg. A method for the solution of certain non-linear problems in least squares. *Quarterly of Applied Mathematics*, 2:164–168, 1944.

[172] D. Marquardt. An algorithm for least-squares estimation of nonlinear parameters. *SIAM Journal on Applied Mathematics*, 11(2):431–441, 1963.

[173] SS. Vel and RC. Batra. Analytical solution for rectangular thick laminated plates subjected to arbitrary boundary conditions. *AIAA Journal*, 37(11):1464–1473, 1999.

[174] PH. Shah and RC. Batra. Through-the-thickness stress distributions near edges of composite laminates using stress recovery scheme and third order shear and normal deformable theory. *Composite Structures*, 131:397–413, 2015.

[175] PP. Camanho, CG. Dávila, and MF. de Moura. Numerical simulation of mixed-mode progressive delamination in composite materials. *Journal of Composite Materials*, 37(16):1415–1435, 2003.

[176] E. Cheney and D. Kincaid. *Numerical Mathematics and Computing*. Cengage Learning, 6th edition, 2007.

[177] PM. Weaver, J. Driesen, and P. Roberts. The effect of flexural/twist anisotropy on compression buckling of quasi-isotropic laminated cylindrical shells. *Composite Structures*, 55:195–204, 2002.

[178] A. Roberts. The carbon fibre industry worldwide 2011-2020: An evaluation of current markets and future supply and demand. Research report ID: 2519726, Materials Technology Publications, 2011.

[179] S. Black. 3D printing continuous carbon fiber composites? `http://www.compositesworld.com/articles/3d-printing-continuous-carbon-fiber-composites`, January 2014. Accessed: 03-10-2015.

[180] RMJ. Groh, PM. Weaver, and A. Tessler. Application of the Refined Zigzag Theory to the modeling of delaminations in laminated composites. Technical Memorandum NASA/TM-2015-218808, NASA, 2015.

[181] KT. Kedward, RS. Wilson, and SK. McLean. Flexure of simply curved composite shapes. *Composites Part A: Applied Science and Manufacturing*, 20(6):527–536, 1989.

[182] J. Most, D. Stegmair, and D. Petry. Error estimation between simple, closed-form analytical formulae and full-scale FEM for interlaminar stress prediction in curved laminates. *Composite Structures*, 131:72–81, 2015.